NASA SR-54

Scientific Findings from EXPLORER VI

NATIONAL AERONAUTICS AND SPACE ADMINISTRATION

NASA SP-54

Scientific findings from

EXPLORER VI

Scientific and Technical Information Division 1965
NATIONAL AERONAUTICS AND SPACE ADMINISTRATION
Washington, D.C.

FOR SALE BY THE SUPERINTENDENT OF DOCUMENTS, U.S. GOVERNMENT PRINTING OFFICE
WASHINGTON, D.C., 20402 - PRICE $2.25

PREFACE

Explorer VI was the first successful scientific satellite launched by the National Aeronautics and Space Administration after its creation. This volume is the first of a projected series of the collected scientific results of the NASA Space Science Program. It assembles the significant scientific publications from Explorer VI, and succeeding volumes will assemble the papers from later spacecraft.

HOMER E. NEWELL,
Associate Administrator for
Space Science and Applications.

Page intentionally left blank

Foreword

On August 7, 1959, NASA launched its first successful scientific satellite, Explorer VI. Explorer VI carried experiments to investigate the trapped radiations, micrometeoroids, magnetic fields, very low frequency electromagnetic transmission, and cloud cover.

During the years since the launch of Explorer VI, experimenters have analyzed their data and have published the results. These results have been discussed and reviewed by other scientists and incorporated in our knowledge and understanding of space science. The data taken with Explorer VI provided new insights into space phenomena and in turn raised new questions which its successors—Explorers XII, XIV, and XV—are helping to answer.

The purpose of this document is to bring together the significant scientific papers resulting from Explorer VI so that historians can place the contributions of Explorer VI to the National Space Science Program in their proper historical context.

Considerable national resources and much effort by both scientists and engineers were required for the success of Explorer VI. It is impossible to acknowledge the contributions of all the people who helped to make Explorer VI a success. However, it is appropriate to list some people of NASA, the Air Force, and Space Technology Laboratories, Inc., who made major contributions, without which Explorer VI would not have been possible. Their names and affiliations at the time of their contributions to Explorer VI are listed below:

John C. Lindsey—NASA, Project Manager
Charles P. Sonett—STL, Project Scientist
Paul F. Glasser—STL
George J. Gleghorn—STL
George E. Mueller—STL
Adolph K. Thiel —STL
Maj. Donald Latham—USAF
Maj. John Richards—USAF
Harry J. Goett—NASA
Morton J. Stoller—NASA
John W. Townsend—NASA

JOHN E. NAUGLE,
Director of Physics and Astronomy Programs, Office of Space Science and Applications.

Page intentionally left blank

Contents

PAGE

PART III: ENERGETIC PARTICLES IN MAGNETIC FIELDS

Section 1. Ion Chamber and Geiger Counter Experiments Designed by the University of Minnesota

Section 2. Cosmic and Trapped Radiation Studies Designed by the University of Chicago

Introduction

BY H. E. STAUSS

Physics and Astronomy Programs
Office of Space Science and Applications

The National Aeronautics and Space Administration began life officially in October 1958; Explorer VI, launched August 7, 1959, was its first artificial Earth satellite to return useful data.

In the five years that have elapsed since then the experimenters have analyzed their data and published their results. This compilation contains the scientific papers that have been prepared on the basis of data acquired from Explorer VI. It omits the technological developments that were associated with the spacecraft, as these will be presented in a separate volume. The papers included here are chiefly those published in the open professional literature. Duplication between papers presented to different groups of readers has been avoided if possible by assigning priorities to papers containing similar material in the following order: professional magazines, reports to COSPAR, and NASA Technical Notes—contractors' reports have not been used. Papers of experimenters have not been edited and are presented as published, and any omission has been inadvertent. Papers by persons who did not have experiments on the spacecraft have been included where they seemed important; this was true in the area of orbital calculations or celestial mechanics.

Explorer VI, also called the paddlewheel satellite, was designed to provide a coordinated, comprehensive group of measurements of scientific interest over as large a region of the magnetosphere as was possible with the capability of the rocket boosters available at the time. This goal was attained by placing the spacecraft in a highly elliptical orbit with an apogee of 42,500 km. Simultaneous studies were made of the trapped radiation in the Van Allen region, galactic cosmic rays, geomagnetism, radio propagation in the upper atmosphere, and the flux of micrometeorites or cosmic dust. Secondary to these investigations was the testing of a scanning device used for photographing the Earth's cloud cover; this was the forerunner of the TV cameras carried in later satellites.

Explorer VI was launched into an orbit with an initial apogee of almost 42,500 km (26,300 miles) and a perigee of 250 km (156 miles). Its period of revolution in this orbit was approximately 12.5 hours, and the inclination of the orbit to the Earth's equatorial plane was 46.9°. The satellite was spin-oriented at the rate of 2.7 rps. Although a lifetime of 1 year had been hoped for, the satellite transmitted useful data only for a period of between 1 and 2 months of service, varying for different experiments. All transmission ceased on October 6, 1959.

The satellite was spheroidal, or nearly spherical, with a flattened bottom as seen in figure 1. Its height was 66 cm (26 in.) along the spin axis, its equatorial diameter was 73 cm (29 in.) in the plane of circular symmetry, and its weight was 64.5 kg (142 lb). Four solar-cell paddles were mounted near the equator to recharge the storage batteries in orbit. In flight, the plane of the solar-cell paddles formed angles of 30° to the equator of the spacecraft. Each panel was 46 cm×46 cm

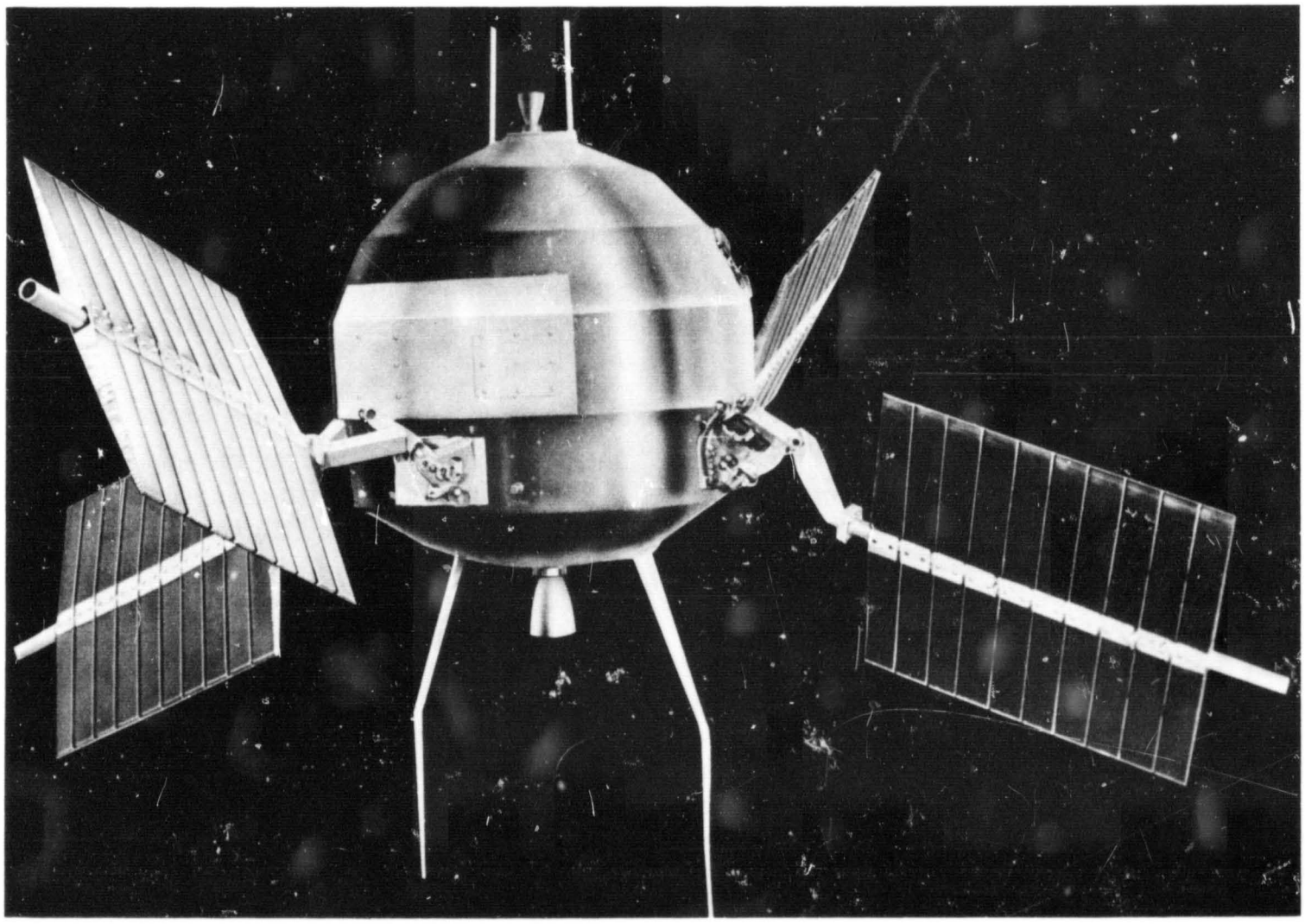

FIGURE 1.—*Explorer VI spacecraft.*

and contained 2,000 solar cells. It had been calculated that 25 percent of the cells would be in the sunlight at all times; however, at launch one paddle failed to deploy correctly, and the power available on the spacecraft was reduced. The outer shell of the spacecraft was made of 0.012-in.-thick aluminum sheet and carried no load. The inside of the shell had been anodized black and the outside painted with a black, hard, epoxy-base paint. White patches of paint and of aluminum foil coated with titanium oxide provided passive temperature control. The arrangement of equipment within Explorer VI is shown in figure 2.

Explorer VI contained the first of the telemetry systems known as Telebit, which operated in a digital transmission mode. Transmission was at 378 Mcps. Telemetry signals were transmitted on FM subcarriers by three transmitters: two 80-mW VHF transmitters broadcasting at 108.06 and 108.09 Mcps and carrying analog data, and one 5-W UHF transmitter broadcasting at 378 Mcps. A payload receiver permitted reception of earth-transmitted commands.

Primarily three ground stations were used for communicating with the satellite: in England at the University of Manchester, in Hawaii, and in Singapore. Telemetered digital data were received at these stations and at Cape Kennedy as well. The digital telemetry system served chiefly to evaluate the satellite's usefulness in transmitting information over long distances. From launch to October 2, 1959, telemetered data were transmitted by the satellite upon command from the primary ground tracking stations. Difficulties in ground reception were often occasioned by extremely deep fading in signal strength. In particular, the signal was often weak at the apogee, at which times reliance

was placed upon the 250-ft radio telescope of the University of Manchester in England, which was made available by Professor A. C. B. Lovell. When interconnected coherently (108 Mcps and 378 Mcps), the transmitters formed a transponder capable of providing velocity and range information as an aid in tracking.

An important event during the flight of Explorer VI was a solar flare that occurred on August 14, 1959, beginning at 0040Z, and which could be observed both visually and photographically. Its occurrence permitted correlations of the data obtained by the radiation and magnetometer experiments with solar activity.

An unexpected consequence of the Explorer VI launch was the confirmation of the prediction of Y. Kozai of the Smithsonian Astrophysical Observatory that lunar perturbations of a satellite orbit of a highly eccentric form,

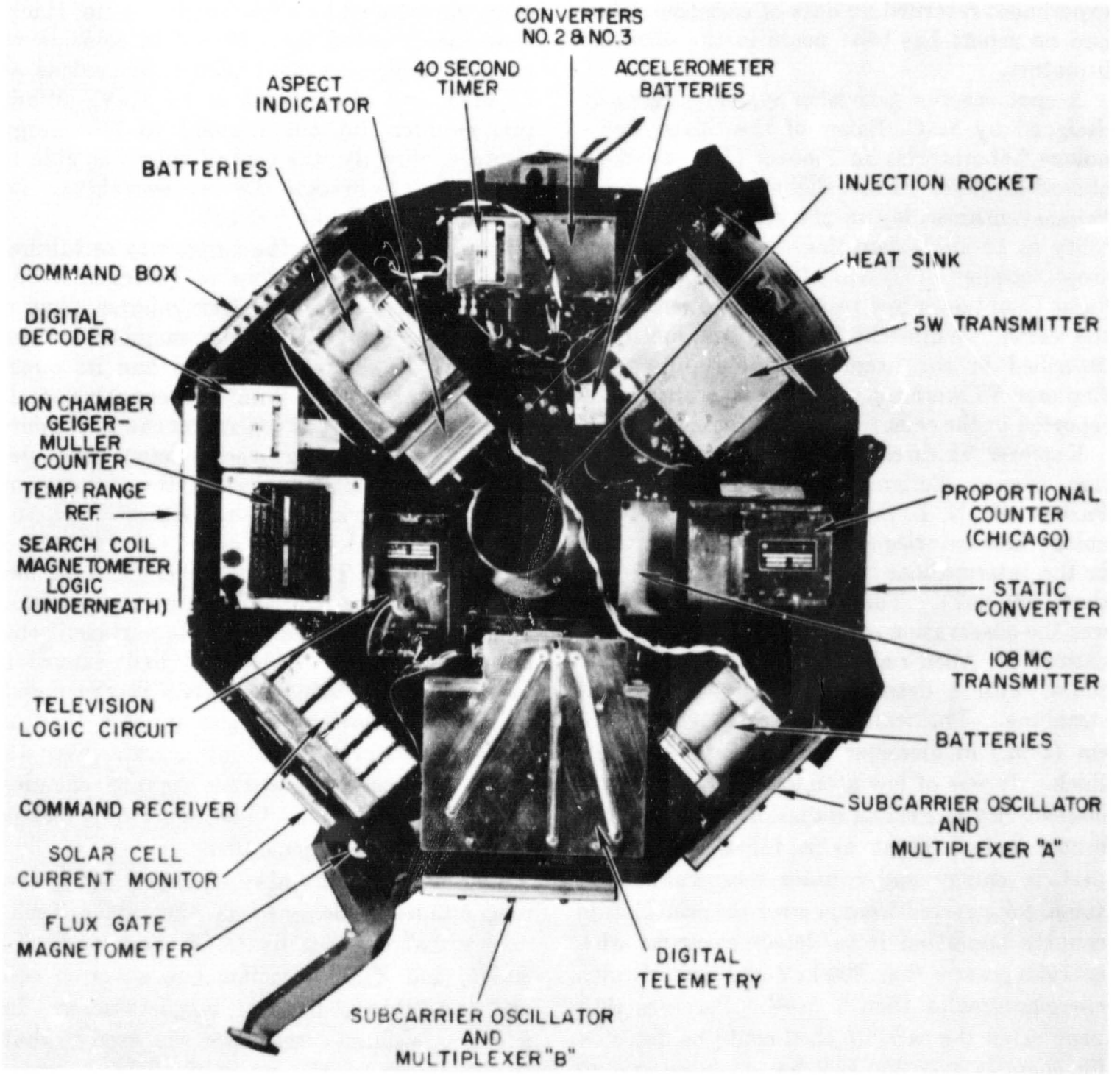

FIGURE 2.—*Top view of payload of Explorer VI.*

such as that of Explorer VI, would result in a depression of the perigee and consequent shortening of the lifetime below that calculated from air drag for the unperturbed orbit.

A micrometeorite experiment was flown to obtain statistics on the momentum flux and the variations of flux of micrometeorites. Planned by M. Dubin, W. M. Alexander, and H. A. Cohen of NASA and the Air Force Geophysics Research Division, it employed piezoelectric crystal microphones as sensing elements. Although pulses were detected, the experiment returned no data of scientific value, and no report has been made in the scientific literature.

A spot scanner television system, originally designed by S. C. Baker of the Space Technology Laboratories for Pioneer II, was carried aboard Explorer VI in a slightly modified form. Primary interest lay in the study of its feasibility as an angle-detecting device for spectroscopic studies in space. It was used in this flight to obtain a low resolution photograph of the earth. While the device itself has been described in the literature, the results from Explorer VI were not of sufficient value to be reported in the scientific literature.

Explorer VI carried a small plastic scintillation counter designed by A. Rosen, T. A. Farley, and N. L. Sanders of the Space Technology Laboratories to be sensitive to electrons in the intermediate range of energies (greater than 200 keV). The purpose of the counter was the observation of electrons throughout the entire Van Allen region, both inner and outer zones, with a detector insensitive to bremsstrahlung. The scintillator was a cylinder 2.5 cm (1 in.) in diameter and 0.6 cm (0.25 in.) thick. It was of low atomic number to insure insensitivity to gamma radiation, and was calibrated before flight as a function of both particle energy and counter temperature. A small, foil-covered window over the scintillation counter permitted it to detect electrons with energies greater than 200 keV and protons with energies greater than 2 MeV. Particles that penetrated the satellite shell could be detected for energies over 500 keV for electrons and 10 MeV for protons.

The spacecraft carried a proportional counter telescope for investigating variations in the galactic cosmic radiation and for studying the trapped radiation in the Van Allen region. It was designed by a University of Chicago group led by Professor J. A. Simpson to respond to electrons of energies greater than 500 keV and to protons of energies greater than 70 MeV. The telescope consisted of seven semiproportional counter tubes arranged in a closely packed, hexagonal array of six tubes surrounding the seventh central tube, with the entire array surrounded by a lead shield 5 g/cm^2 thick. Low energy cutoff for a three-fold coincidence gave unambiguous identification of protons at 75 MeV and of electrons at 13 MeV. While this counter did not respond to low-energy electrons directly, the central tube was able to detect them through the bremsstrahlung for energies greater than 500 keV.

A unit designed at the University of Minnesota under the leadership of Professor J. R. Winckler contained a geiger counter (Anton 302) and a Neher ionization chamber for the study of the trapped radiation and its mean specific ionization; the unit was sensitive to all radiation types. The ionization chamber operated on the pulsing electrometer principle. The geiger counter measured the number of impinging particles, while the ionization chamber measured the number of ion pairs produced per unit time. The two together gave the ion pairs per unit path produced by each particle, and thus gave the energy of the particle if the mass was known. This unit had extensive previous use in balloon flights. It responded to electrons having energies greater than 2 MeV and to protons having energies over 16 MeV. Low-energy electrons having energies greater than 30 keV could be detected by means of the X-rays they generated.

Explorer VI was also equipped with two magnetometers designed at the Space Technology Laboratories by C. P. Sonett, D. L. Judge, and P. J. Coleman, one a search coil and the other a fluxgate magnetometer. In addition, a phase comparator was used so that the direction of the magnetic field in space could be determined. The search coil was a

solenoid of 30,000 turns wound on an iron-nickel core attached to the shell of the spin-stabilized payload. The spin of the vehicle generated a sinusoidal voltage proportional to the component of the magnetic field, B, perpendicular to the spin axis of the vehicle. Steady fields and slow variations in the field could be measured. Automatic gain control was incorporated in the amplifier to reduce instrument sensitivity with increasing field. The fluxgate magnetometer failed some minutes subsequent to launch and returned no data.

A magnetic field aspect indicator, or phase comparator, reported the direction of the magnetic field in the plane normal to the spin direction by giving the angle between the measured vector of the magnetic field and the projection of the sun's direction in this plane. It measured the phase angle by measuring the time delay between two pulses, one from a photodiode sun scanner, and the other representing the zero voltage crossing of the sinusoidal signal from the search coil.

The component of the ambient magnetic field parallel to the spin axis of the spacecraft was to have been measured with the fluxgate magnetometer. The combined measurements of the two magnetometers and the phase comparator would have given the direction and the magnitude of the ambient magnetic field in space.

A VLF electromagnetic wave propagation experiment was designed at Stanford University under Professor R. A. Helliwell. It consisted of a VLF (15.5 kc) receiver keyed to transmissions from the U.S. Navy Station NSS at Annapolis. The experiment was designed for studying VLF transmission through the lower ionosphere from the ground station to the satellite during launch. Transmission was investigated during a period beginning before liftoff and continuing until the rocket was over the horizon. A bandwidth of 100 cps gave a time resolution of approximately 10 msec for measurements of group delay. Antenna impedance and receiver gain were calibrated automatically. Telemetered information was compared with the outputs of 15.5-kcps receivers located at the STL tracking stations. Observations of the whistler mode were also made from a Stanford University ground station near the NSS magnetic conjugate point.

An experiment, using Doppler-Faraday radio propagation measurements, to measure the electron density in the vicinity of the satellite was designed by C. D. Graves of the Space Technology Laboratories. In this experiment two coherent signals, one from the 108-Mcps analog UHF transmitter and one from the digital transmitter at 378 Mcps, were used to measure the Doppler difference frequency. Supplementary measurements of the rate of change of the Faraday polarization rotation were made on the signal at 108 kcps. Limited, but useful, data were obtained.

The accomplishments of Explorer VI were important in space research in several ways. They sharpened the focus of scientific knowledge of the terrestrial magnetosphere by providing simultaneous measurements of energetic particles, the magnetic field, and the electron density in the upper atmosphere. They also provided information on the boundary of the Earth's magnetic field and confirmed interrelationships between solar activity such as flares and phenomena in the terrestrial exosphere. Above all, the accomplishments of Explorer VI provided a sound stepping stone to subsequent space experimentation. Some of the more specific results are as listed.

(1) The orbital characteristics of Explorer VI confirmed an earlier theory that the Sun and Moon have important perturbing influences on an orbit of high eccentricity.

(2) The eccentric character of the orbit of Explorer VI stimulated further investigations of methods of calculating orbits of near-Earth artificial satellites.

(3) The electron density in the vicinity of the spacecraft itself was determined by means of combined measurements of Doppler frequency and of Faraday polarization rotation. The actual results were unexpectedly higher than what had been anticipated from the whistler propagation studies. The difficulties encountered in the experiment, inherent in this type of propagation measurement, led the experimenter to conclude that a more direct method of density measurement is desirable.

(4) An experiment was conducted relative to the generation of whistlers, using VHF transmission from a ground station to the spacecraft during the launch period. Sufficient data were obtained to permit development of a theory relative to the generation of the whistler mode.

(5) The particle intensity detected in the outer zone of trapped radiation showed a decrease following the sudden commencement of a geomagnetic storm followed by a slower recovery; however, apparently the number of energetic protons increased simultaneously.

(6) A differential energy spectrum for trapped protons of energy above 30 MeV in the inner radiation belt was developed on the basis of an assumed power law and was found to be $E^{-1.65}$ at about $-28°$ geomagnetic latitude.

(7) Visual observations of aurorae were made simultaneously with radiation measurements on the same lines of force.

(8) Explorer VI data on the radiation in the outer radiation zone were found not to be in complete agreement with earlier measurements.

(9) The spectrum of trapped particles along a line of force was found not to change greatly along the line.

(10) Evidence was obtained suggestive of coupling between the solar plasma and the outer radiation zone.

(11) Measurements of electron flux along a magnetic line of force in the outer radiation belt led to the conclusion that other processes besides electron injection by neutron decay are necessary to explain the observed flux distribution.

(12) Gross fluctuations in radiation intensity were observed at the edge of the outer zone of trapped radiation during a magnetic storm.

(13) Magnetic field measurements showed fair accord with calculations based on a terrestrial magnetic dipole to the altitude of 5 Earth radii. From 5 to 8 Earth radii, deviations between the two were observed. Calculations were made of the extraterrestrial current system that would be necessary to explain the deviations. Comparison of results from Explorer VI and Explorer X indicated that the deviations could also result from a tail in the terrestrial magnetic field.

Page intentionally left blank

PART I: ASTRONOMY AND CELESTIAL MECHANICS

765-698 O-65—2

Anticipated Orbital Perturbations of Satellite 1959 Delta Two[1]

BY YOSHIHIDE KOZAI[2] AND CHARLES A. WHITNEY[3]

Astrophysical Observatory
Smithsonian Institution

1. INTRODUCTION

As announced by the Smithsonian Astrophysical Observatory in a press release dated August 21, 1959 (see Appendix), the orbit of Satellite 1959 Delta Two, the "Paddle-Wheel," is significantly affected by lunar and solar perturbations. Thus, Satellite 1959 Delta Two is unique among satellites launched to date and we believe it worth while to publish the present analysis to provide a basis for anticipating its orbital behavior.

Starting from the orbital elements provided by the National Aeronautics and Space Administration for September 3, 1959, we have carried out numerical integration to predict the future behavior of this satellite. These integrations, based on variation of parameters, are preliminary in nature. Techniques for a more precise analysis of the orbit are in preparation.

The equations employed are outlined in Section 2. The technique of integration was a simple one taking the semi-major axis as independent variable.

2. THE PERTURBATION EQUATIONS

Solar and Lunar Perturbations.—Variations of the orbital eccentricity due to the moon and the sun are expressed by the equation (Kozai, 1959),

$$\frac{de}{dt}=-\frac{\sqrt{1-e^2}}{na^2e}\frac{\partial R}{\partial \omega}, \tag{1}$$

where the principal terms of R are:

$$\begin{aligned} R = \frac{15}{8}\, e^2a^2 \Big[& n_\odot^2 \cos^4\frac{i}{2}\cos^4\frac{\epsilon}{2}\cos 2(\lambda_\odot-\omega) \\ & + \frac{1}{2}\,(n_\mathbb{C}^2 m_\mathbb{C} + n_\odot^2)\sin^2 i\left(1-\frac{3}{2}\sin^2\epsilon\right)\cos 2\omega \\ & + \frac{1}{2}\, n_\mathbb{C}^2 m_\mathbb{C}\Big\{\sin^2\epsilon\cos^4\frac{i}{2}\cos 2(\omega+\Omega-\Omega_\mathbb{C}) \\ & - \sin i\cos^2\frac{i}{2}\sin 2\epsilon\cos(2\omega+\Omega-\Omega_\mathbb{C})\Big\} \\ & + \frac{1}{2}\, n_\odot^2\Big\{\sin^2\epsilon\cos^4\frac{i}{2}\cos 2(\omega+\Omega) \\ & - \sin i\cos^2\frac{i}{2}\sin 2\epsilon\cos(2\omega+\Omega)\Big\} + n_\odot^2\sin i \\ & \cos^2\frac{i}{2}\sin\epsilon\cos^2\frac{\epsilon}{2}\cos(2\lambda_\odot-2\omega-\Omega)\Big]. \end{aligned} \tag{2}$$

Here, $n_\odot$ is the mean motion of the sun; $n_\mathbb{C}$, that of the moon; ϵ, the obliquity; $\lambda_\odot$, the mean longitude of the sun; $m_\odot$, the mass of the moon (the unit is the mass of the earth); and $\Omega_\mathbb{C}$, the longitude of the ascending node of the moon with respect to the earth's equator. On the right side of equation (2), i, Ω and ω may be considered not to be affected by the moon and the sun.

[1] Published in Special Report No. 30, November 12, 1959. Reprinted by permission.

[2] Astronomer, Satellite Tracking Program. Now at Tokyo Astronomical Observatory.

[3] Physicist, Division of Solar Radiation Studies, Smithsonian Astrophysical Observatory, and Research Associate, Harvard College Observatory.

As the semi-major axis does not change rapidly due to the moon and the sun, the variation of the perigee distance, q, is

$$\frac{dq}{dt} = -a\frac{de}{dt}. \tag{3}$$

Oblateness Perturbations.—The rates of change of the argument of perigee and the right ascension of the ascending node were computed from the usual first-order equations,

$$\frac{d\omega}{dN} = \frac{J}{p^2}(2\text{–}2.5\sin^2 i),$$

$$\frac{d\Omega}{dN} = -\frac{J}{p^2}\cos i, \tag{4}$$

where N is the revolution number and $p = a(1 - e^2)$. The value $J = .0016230$ was employed as well as the equation,

$$P = .0586745a^{3/2} \tag{5}$$

relating the orbital period in days to the semi-major axis in units of 6378.388 km.

Atmospheric-Drag Perturbations.—The effects of atmospheric drag on the orbital energy and the perigee height were introduced in the following manner.

The effect on perigee height was computed from the approximation,

$$\frac{dq}{dQ} = \frac{H}{ae}, \tag{6}$$

where H is the atmospheric scale height. This relation can be transformed to the equation,

$$\frac{dq}{da} = \frac{2}{Kae+1} \tag{7}$$

where $K = H^{-1}$.

This approximation is valid for orbits of high eccentricity, but clearly is very poor for low eccentricities. We do not feel that the present calculations would be significantly affected by a more precise computation of dq/da.

The drag effect on orbital period was evaluated with a formula derived to be valid for a wide range of eccentricities.

The loss of energy due to drag may be written as

$$du = \frac{C_D}{2}A\rho w^2 ds, \tag{8}$$

where C_D is the drag coefficient, A is the satellite's effective cross-sectional area, ρ is the atmospheric density, w is the orbital velocity, and ds is the differential of distance along the orbit.

For the orbital velocity we substituted the value at perigee,

$$w^2 = k^2\frac{1+e}{a(1-e)}.$$

For ds we used the equations,

$$\frac{ds}{dv} = r\left(1+\left(\frac{1}{r}\frac{dr}{dv}\right)^2\right)^{1/2},$$

$$\frac{dr}{dv} = r\frac{\sin v}{1+e\cos v}. \tag{9}$$

On the assumption that v, the true anomaly, is much less than one radian in the region of significant drag, we derived the equation,

$$ds = a(1-e)\left(1+\frac{e}{1+e}v^2\right)dv. \tag{10}$$

We further assumed that the atmospheric density above perigee can be represented by an exponential function of height, writing $\rho(v) = \rho(q)\exp(-K(q)(r(v)-q))$.

We then found that

$$du = \frac{C_D}{2}A\rho(q)k^2(1+e)\left(1+\frac{e}{1+e}v^2\right)\exp\left(\frac{-Kqe}{2(1+e)}v^2\right)dv. \tag{11}$$

Integrating over true anomaly and employing the relation

$$da = \frac{a^2}{mk^2}du,$$

where m is the satellite mass, leads to the following expression for Δa, the change of semimajor axis per revolution,

$$\Delta a = \sqrt{\frac{\pi}{2}}C_D\frac{A}{m}\rho(q)\frac{(1+e)^{3/2}}{\sqrt{Kqe}}a^2\left(1+\frac{1}{Kq}\right). \tag{12}$$

We note that the integration around an orbit is performed with an exponential atmosphere. However, because of the wide range of perigee height produced by the lunar and solar perturbations it was not sufficiently accurate to

assume that the entire atmosphere was isothermal.

We employed the following formulae for $\rho(q)$ and $K(q)$:

$$\rho(q) = 7.94 \times 10^{-11} \exp(-161.55(q-1) + 2.3029 \exp(-138.46(q-1) + 2.8)),$$
$$K(q) = 161.55 + 318.86 \exp(-138.46(q-1) + 2.8), \quad (13)$$

where ρ is in gm/cm^3, q is in units of 6378.388 km, and K is in km^{-1}.

Table 1 lists the values of $\log_{10}\rho$ derived from this model and from the Smithsonian Astrophysical Observatory Interim Model Atmosphere No. 4.

TABLE 1.—*Atmospheric Densities*

Height (Km)	$\log_{10}\rho$ (gm/cm^3)	
	Approximation	Model 4
150	−11.12	−11.08
180	−11.75	−11.77
210	−12.24	−12.29
240	−12.65	−12.73
270	−13.02	−13.09

3. NUMERICAL RESULTS

The perturbed orbit has been calculated from the following initial orbit:

Epoch 1959 September 3.150 GMT

$a = 4.3446$
$e = .7604$
$i = 47.10$
$\omega = 41.66$
$\Omega = 55.62$

The results are summarized in figures 1, 2, and 3. The arrows indicate the date of launching. In these figures the integrations for two values of A/m are shown, in order to indicate the sensitivity of the orbit to variations of atmospheric density and effective area of the satellite.

The semi-annual variation of perigee distance is produced by the solar perturbation and does not drastically affect the satellite lifetime. The lunar perturbation produces the rapid drop of perigee around 600 days after September 3, 1959 and ends the life of the satellite.

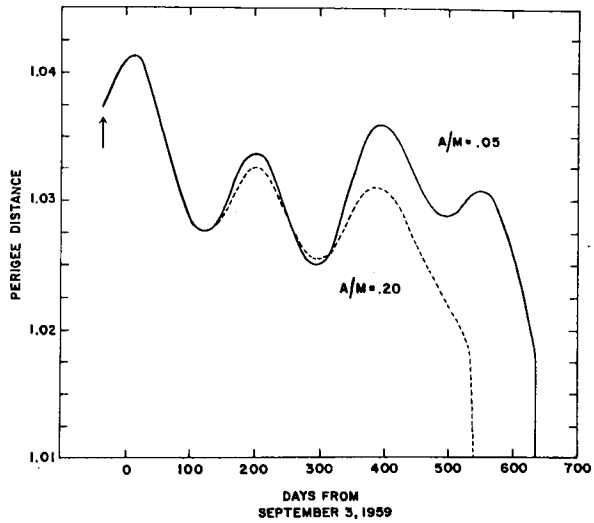

FIGURE 1.—*Expected perigee distance of 1959 Delta Two measured in units of Earth radii.*

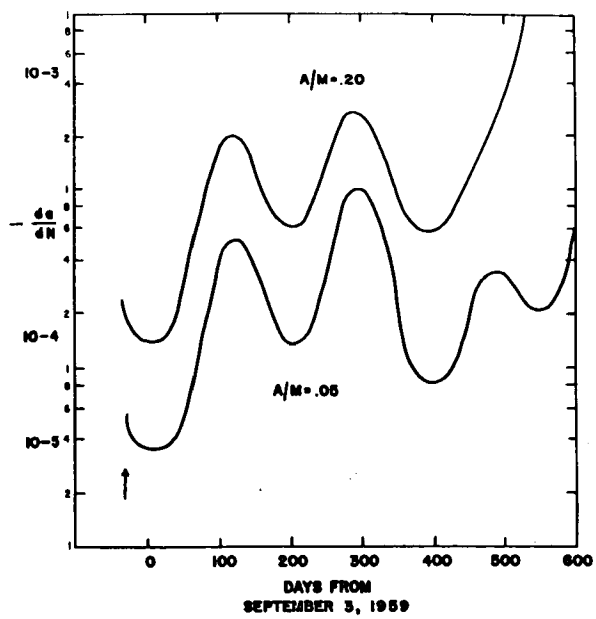

FIGURE 2.—*Expected acceleration of satellite 1959 Delta Two given in terms of the decrease of semi-major axis (in Earth radii) per revolution.*

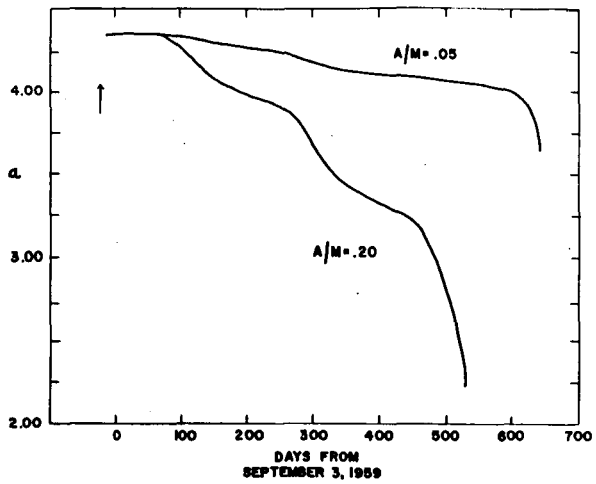

FIGURE 3.—*Expected semi-major axis of 1959 Delta Two measured in Earth radii.*

The two "acceleration" curves of da/dN, plotted logarithmetically, are essentially mirror images of the perigee height.

Dr. Don Lautman has derived an acceleration of

$$\frac{da}{dN} = -1.5 \times 10^{-4} \text{ earth radii}$$

from observations of this satellite during the first month of flight, and this value falls between the plotted curves.

REFERENCE

KOZAI, Y. On the effects of the sun and the moon upon the motion of a close earth satellite. *Special Rep. No. 22*, Smithsonian Astrophys. Obs., p. 7. 1959.

APPENDIX—REDUCTION OF "PADDLE-WHEEL" SATELLITE'S LIFETIME

Dr. Yoshihide Kozai, Astronomer of the Smithsonian Astrophysical Observatory, has predicted that the lifetime of the recently launched "paddle-wheel" satellite, Explorer VI, will be greatly reduced by perturbations of the moon's orbit. Perturbations are irregularities in the motion or orbit of a heavenly body caused by some force other than that which determines its usual path.

The "paddle-wheel" satellite's apogee of 25,000 miles is the greatest distance from the earth ever reached by any artificial satellite. Based on his prior investigation of the relation between satellite orbital irregularities and lunar perturbations, Dr. Kozai has determined that Explorer VI will be affected by the moon's gravitational field. This, in turn, will affect the perigee, drawing it down into the earth's atmosphere, leading to a significant increase in the air-drag effect.

Because of the severity of the moon's effect, the apogee of Explorer VI will be little affected by the atmospheric density at high altitudes responsible for bringing down other artificial satellites. Hence, the "paddle-wheel" will be the first satellite to have its lifetime appreciably disturbed by the moon.

The sun's attraction adds a small contribution to the shortening of this object's lifetime.

Dr. Charles A. Whitney, Physicist in charge, Research and Analysis, Smithsonian Astrophysical Observatory, has performed a detailed numerical integration of Dr. Kozai's perturbation equations in combination with equations describing the effects of air-drag.

These calculations, performed with a high-speed electronic computer, show that although the lifetime of the satellite would be more than two decades in the absence of the moon, the lunar perturbations reduce the expected lifetime to about two years.

The Orbit of Explorer VI—A Test of the Dynamic Model Atmospheres[1]

BY KENNETH MOE[2]

Space Technology Laboratories, Inc.

A new orbit has been computed for the "Paddlewheel Satellite", Explorer VI (1959 δ–1), using all available tracking observations. This orbit covers the period of time from injection into orbit on 7 August 1959 to final transmitter failure on 6 October 1959, the period during which scientific data were received from the satellite. The orbit was constructed by a new method in which only the initial elements are obtained by conventional least-squares fitting. At subsequent times, all the conservative forces acting on the satellite are assumed to be known, and the drag force is solved for by minimizing the residuals of each day's observations. The derived atmospheric densities are compared with the ARDC 1959 Model Atmosphere and with the dynamic models devised by Paetzold, Jacchia, and Priester. None of the early dynamic model atmospheres agree well with the derived densities; however, Paetzold's 1962 Model usually does agree within the standard deviation of the derived densities.

The purpose of this paper is to describe briefly a new method for determining the definitive orbit of a satellite which is significantly affected by drag, and to use the Explorer VI (1959 δ–1) orbit, obtained by this method, to test several of the proposed dynamic model atmospheres.

THE METHOD OF ORBIT FITTING

The orbits of artificial satellites are usually determined in the following way: The observations are separated into groups, each group covering an interval of N revolutions. Then a least-square fitting procedure is used to derive the six orbital elements and the rate of change of period for each group of observations. The rate of change of period (or drag) is assumed constant in each interval. Thus the orbit is a succession of independent segments each of which is N revolutions long.

The new method (1)‡ of orbit determination utilizes the conventional least-square fitting technique to derive only the initial elements. The elements at subsequent times are obtained by allowing the gravitational and drag forces to perturb the initial elements. The gravitational forces are assumed known, while the drag force is determined as a byproduct of the orbital fitting, which is carried out by minimizing the residuals of each day's observations. The essential feature of this method of computing orbits is that it assumes that all forces acting on the satellite except the air drag are known, and it solves for the air drag. Thus it allows the true anomaly to be up-dated (by varying the drag) without rejecting the old information on those elements which are less

[1] Published in the Proceedings of the American Rocket Society 17th Annual Meeting and Space Flight Symposium, Los Angeles, California, November 1964. Reprinted by permission.

[2] Consultant, Systems Analysis Department.

‡Numbers in parentheses indicate References at end of paper.

affected by drag. This advantage can be employed either to construct good orbits when the available tracking data are poorly distributed, or to refine the orbital elements by smoothing over longer time intervals without having the residuals become excessively large. This method of fitting is also of assistance in the rejection of erroneous observations in the following way: If an observation does not fit, the air density can be varied by an amount which is considered reasonable on the basis of past experience, such as is contained in References 2, 3, and 4. If a reasonable adjustment does not cause the observation to fit in with the other observations, it is rejected. Conventional differential orbital improvement programs merely reject observations on the basis of the residuals, using a fixed atmospheric density within the fitting interval.

The present method is useful for constructing satellite orbits when drag fluctuations are the main source of uncertainty in the orbit; hence it is especially good in cases where the perigee is low. The method should not be used when searching for harmonics of the earth's gravitational field, because the method of projecting the elements forward in time necessarily implies that all the conservative forces acting on the satellite are included in the calculation.

THE ORBIT OF EXPLORER VI

The "Paddlewheel Satellite," Explorer VI (1959 δ-1), had an orbit of large eccentricity (e=0.76), and an initial perigee height of 138 nautical miles. During the period from August 7, 1959 to October 6, 1959, this satellite transmitted valuable scientific measurements, which could not be interpreted satisfactorily unless an accurate orbit were available. Unfortunately, the tracking data were not well distributed statistically. For this reason, and because the satellite's perigee was low enough that drag variations could significantly affect the orbit, the new method of orbit fitting was chosen for the determination of the definitive orbit.

The definitive orbit of Explorer VI is given in Reference 1. In this paper, we present only the results related to the satellite orbital accelerations, because of their special interest in studies of the density of the upper atmosphere. The orbital accelerations of Explorer VI did not directly yield the atmospheric density at a particular altitude because the orbit was so eccentric that solar and lunar forces perturbed the height of perigee (6, 7, 8). The height of perigee as a function of time is shown in figure 1a and the rates of change of perigee height caused by solar and lunar perturbations are plotted in figure 1b. (The height is measured from a standard ellipsoid.) If one wants to determine the variations in atmospheric density at a fixed height, one must remove the effects of solar and lunar perturbations from the derived accelerations. This was done, and the resulting adjusted orbital accelerations, giving the variations in atmospheric density at a fixed height of 145 nautical miles, are shown in figure 2a. After 9 September the derived accelerations have been indicated by a dashed line because the relative paucity of data caused the derived accelerations to be more uncertain than during the previous part of the orbit. The satellite was spin-stabilized, so its effective area was unaffected by tumbling. Figures 2b and 2c show two of the quantities which are correlated with variations in atmospheric density: The decimeter solar flux, and the geomagnetic planetary amplitude, A_p. These two correlations are utilized in the dynamic model atmospheres.

TEST OF THE DYNAMIC MODEL ATMOSPHERES

Figure 3 shows the density variations which would have been expected on the basis of several theoretical models of atmospheric density (2, 3, 5) available in 1961, which utilize the known correlations with decimeter solar flux, the local solar time at perigee, and, in the case of Paetzold's atmosphere (5), A_p and the time of year. An exact comparison between the derived accelerations and the theoretical models is difficult to make because they do not all use the same scale heights nor do they employ the same method of computing density from the observed rates of change of period.

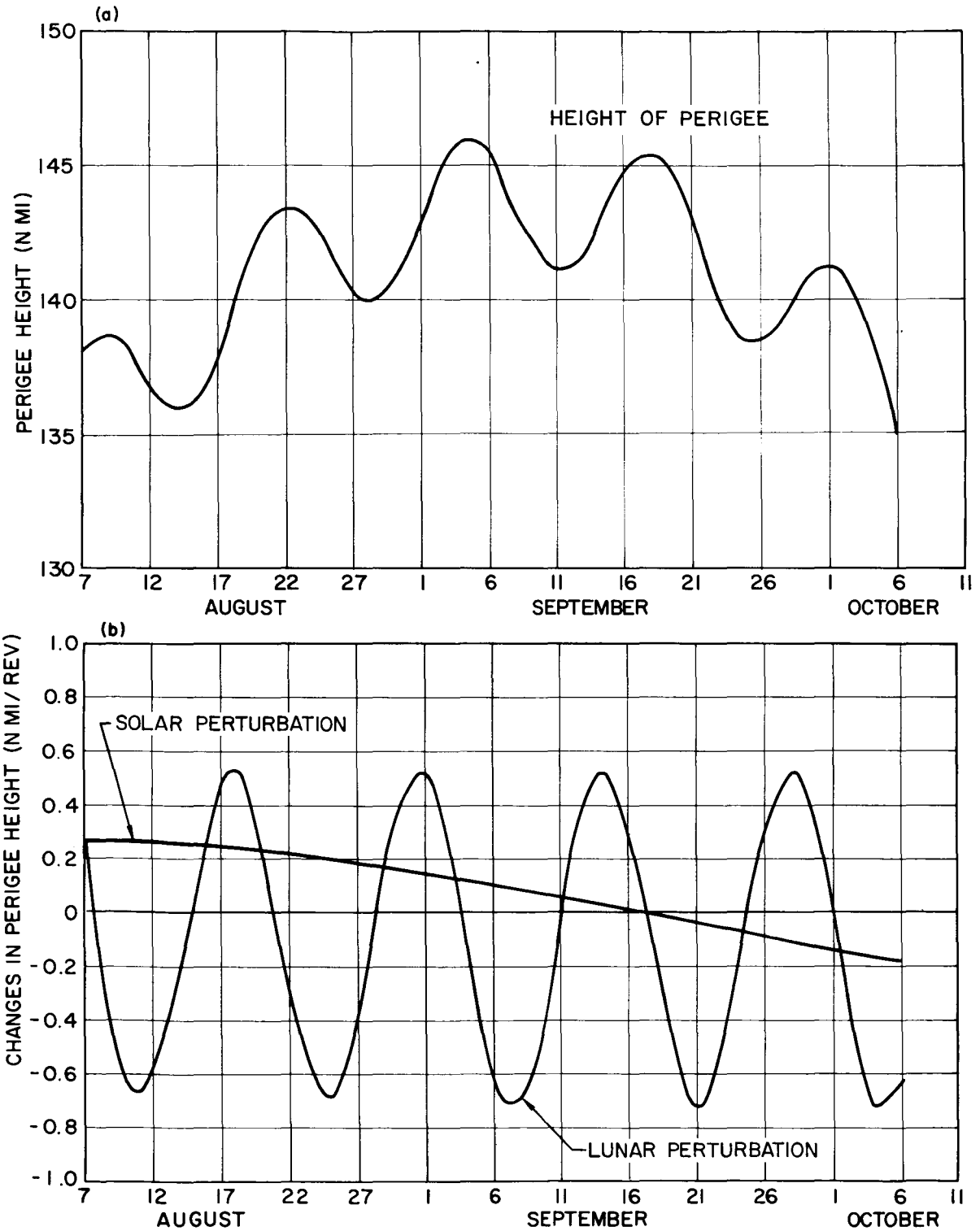

FIGURE 1.—*The height of perigee.*

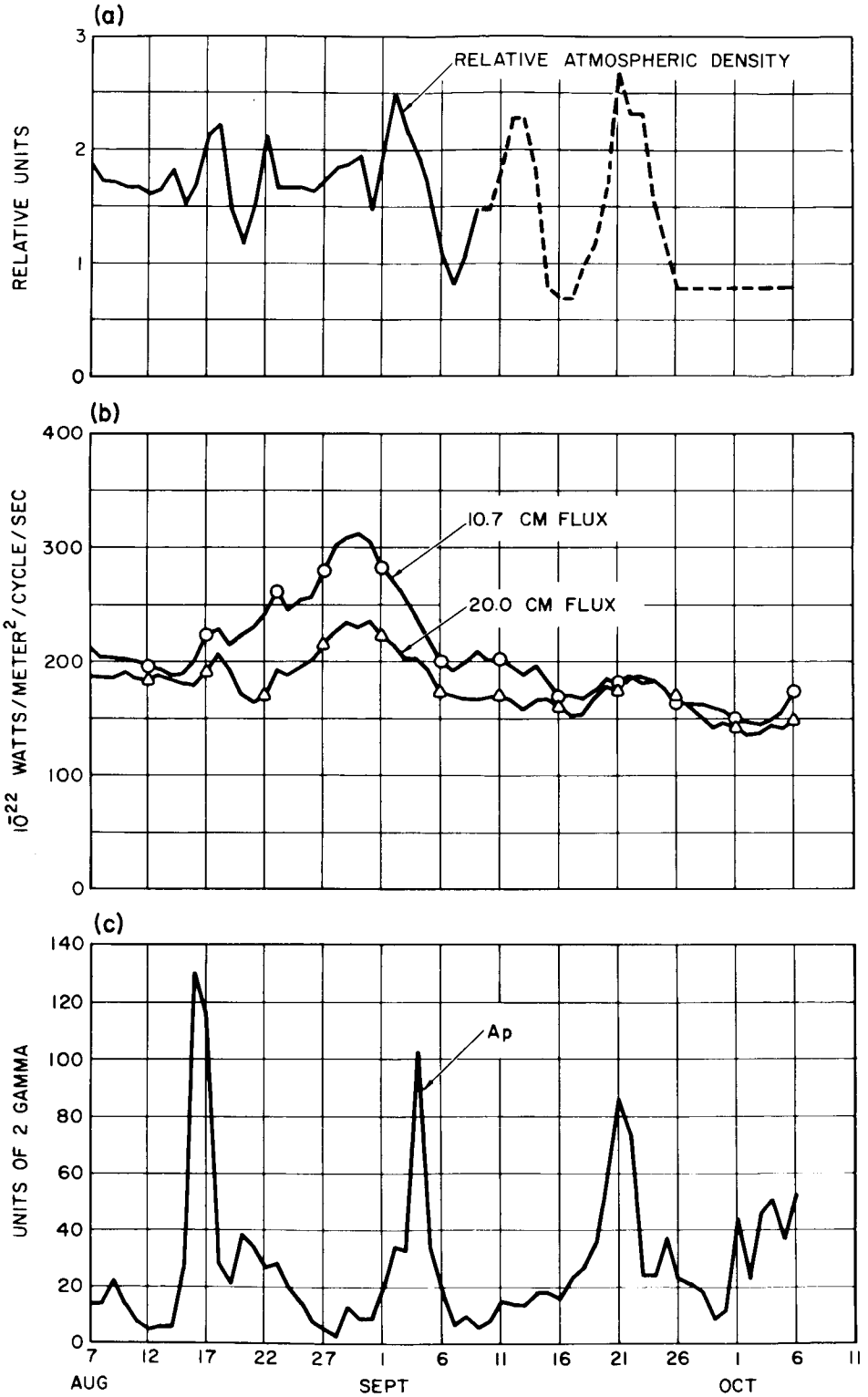

FIGURE 2.—*The relative atmospheric density and related solar and geophysical data.*

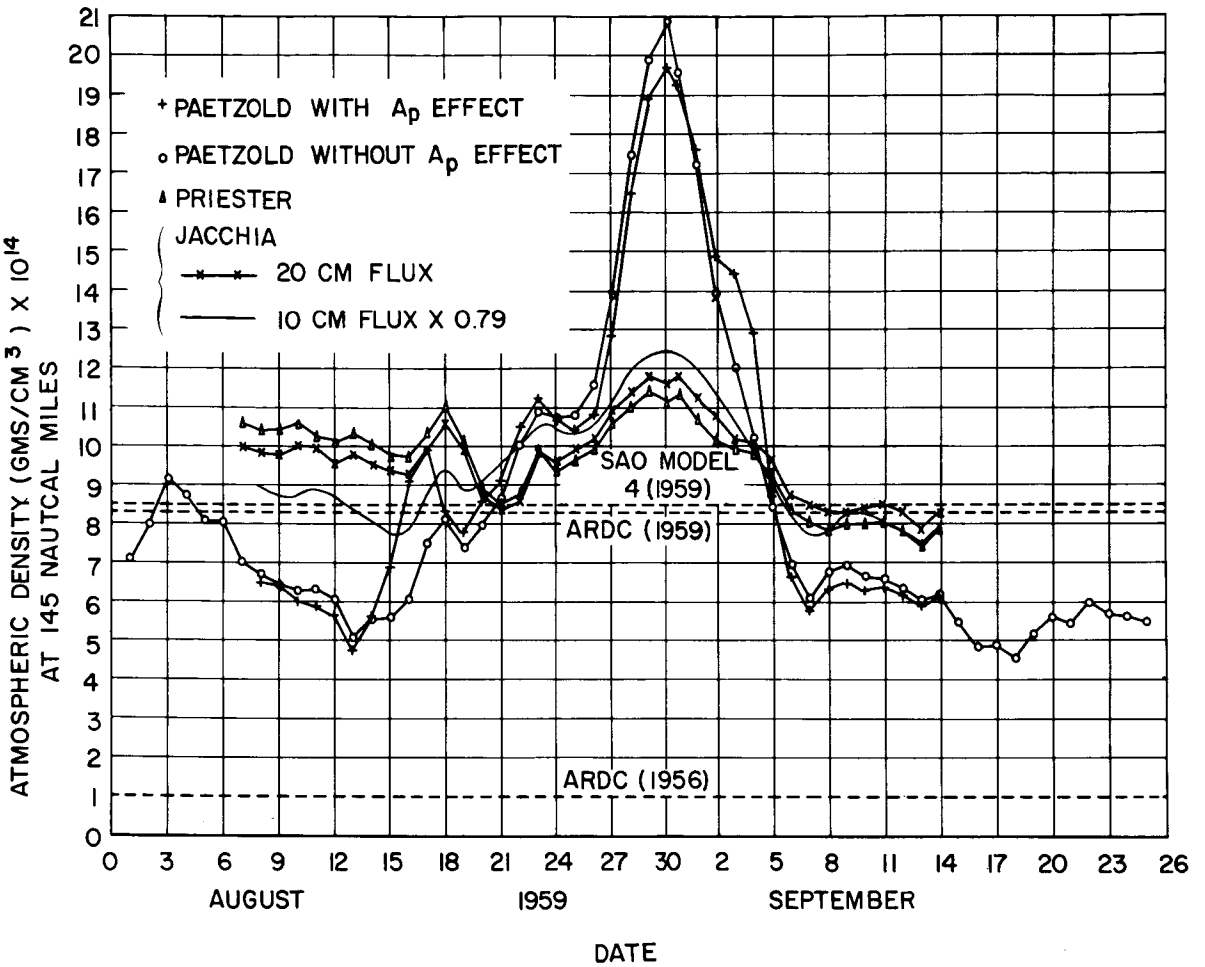

FIGURE 3.—*Atmospheric density models.*

One obvious conclusion that can be drawn from an examination of figures 2 and 3 is that Paetzold's 1961 model has a larger range of variation than either of the other models or the accelerations derived from Explorer VI. Another conclusion that can be drawn by comparing the derived orbital accelerations with the theoretical atmospheres is that the correlation with A_p which Paetzold used improved the agreement, especially around 17 August. The use of two sets of decimeter flux data with Jacchia's atmosphere in figure 3 reveals a limitation on the possible accuracy of model atmospheres which utilize the correlation with decimeter flux. The fact that the ratio of the 10 and 20 centimeter flux varies by 10 to 20 percent over periods of weeks and months was first observed by Allen (9) and has more recently been pointed out in connection with satellite accelerations by Nicolet (10).

Knowledge has advanced so rapidly that the model atmospheres which were available in 1961 are already obsolescent. In 1962, Paetzold has published a revised model (11), of the variations in atmospheric density. The atmospheric density at a fixed height of 145 nautical miles near the perigee point of Explorer VI is graphed in figure 4, according to Paetzold's 1962 model, the ARDC 1959 model, and as derived from the satellite accelerations by making the same assumptions about the scale height, diurnal bulge, and drag coefficient (C_D=1.813) as Paetzold made, because the purpose was to

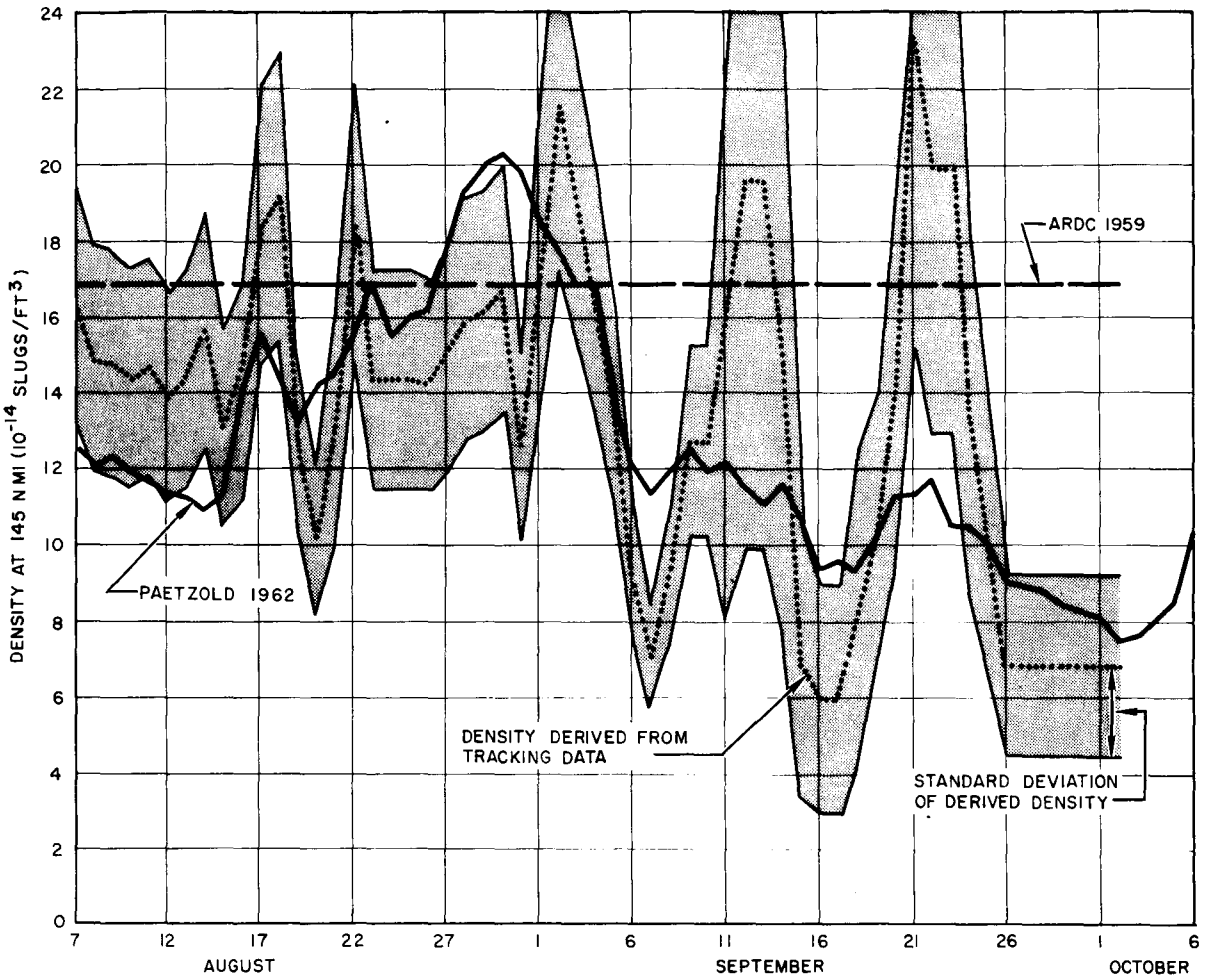

FIGURE 4.—*Comparison of the derived densities with Paetzold's 1962 model.*

determine how closely Paetzold's model would give the observed rates of change of period. Exact numerical integration was used for calculating the rate of change of period, rather than Paetzold's Equation (1), which is not a good approximation for orbits of large eccentricity. The density was calculated for the ARDC Atmosphere by assuming the nominal weight to area ratio ($W/A=14$ lbs/ft^2) and nominal drag coefficient ($C_D=2$) for the satellite. The ARDC 1959 Atmosphere represents average conditions in the twilight zone near the peak of the sunspot cycle. In figure 4, the standard deviation of the derived density is indicated by the gray band. Paetzold's atmospheric densities usually lie within the band, so Paetzold's 1962 model is a valid representation of the upper atmosphere, insofar as this study is capable of testing it.

ACKNOWLEDGMENTS

This work was supported by the Goddard Space Flight Center of the National Aeronautics and Space Administration under Contract No. NAS 5–1246. The author is indebted to the directors of the many satellite tracking agencies for supplying him with observations, and especially to Dr. J. W. Siry of the Goddard Space Flight Center who made many valuable comments as well. This study could not have been made without the interest and encouragement of Professor J. A. Simpson.

REFERENCES

1. Final Report on EXPLORER VI Definitive Orbit, 8650–6001–RU–000, Space Technology Laboratories, 25 June 1962.
2. W. Priester and H. A. Martin, Mitteilung der Universitäts—Sternwarte Bonn, No. 29, 1960.
3. L. G. Jacchia, Smithsonian Astrophysical Observatory, Special Report No. 39, March 1960.
4. L. G. Jacchia and J. W. Slowey, Smithsonian Astrophysical Observatory, Special Report No. 84, February 1962.
5. H. K. Paetzold and H. Zschörner, in COSPAR International Reference Atmosphere, 1961, North-Holland Publishing Co., Amsterdam, 1961.
6. Y. Kozai and C. A. Whitney, Smithsonian Astrophysical Observatory, Special Report No. 30, November 1959.
7. M. Moe, ARS Journal, *30*, 485 (1960).
8. P. Musen in SPACE RESEARCH, Ed. H. Kallman—Bijl, North-Holland Publishing Co., Amsterdam, 1960, p. 440.
9. C. W. Allen, Monthly Notices of the Royal Astronomical Society, *117*, 174 (1957).
10. M. Nicolet, Planetary and Space Science, *5*, 1 (1961).
11. H. K. Paetzold, Model for the Variability of the Terrestrial Atmosphere Above 150 km after Satellite Acceleration, University of Cologne, 1962.

Solar-Lunar Perturbations of the Orbit of an Earth Satellite [1]

BY MILDRED M. MOE [2]
Space Technology Laboratories, Inc.

The gravitational fields of the sun and moon can produce significant pertubations of the orbit of a highly eccentric Earth satellite. The importance of their effect on the lifetime of 1959 delta (Explorer VI) has been pointed out by Kozai (1),[3] who has made a study (2) of solar-lunar perturbations of Earth satellites. The purpose of this note is to treat these perturbations by a different method, based on some simplifying assumptions. It is assumed that the angular velocity of the disturbing body (sun or moon) is small enough compared to the angular velocity of the satellite that we may consider the disturbing body fixed during one revolution of the satellite. This simplification makes possible the integration of the instantaneous rate of change of the orbital elements over one revolution of the satellite to obtain the change in orbital elements per revolution. The magnitude of the error made by holding the disturbing body fixed is estimated. This leads to an evaluation of the effect of the motion of the disturbing body on the semimajor axis (hence energy) of the satellite orbit. The importance of the solar-lunar perturbations of orbits with high eccentricity is illustrated by computing the perturbations of the perigee distance of 1959 delta.

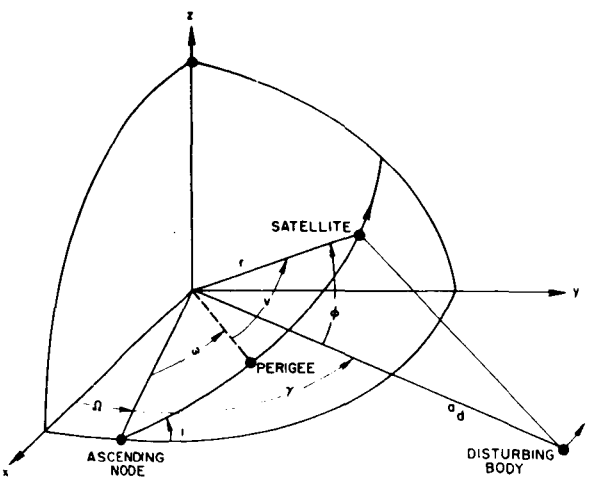

FIGURE 1.—*Satellite orbit*

PERTURBATIONS OF THE ORBITAL ELEMENTS

The analysis of the perturbations is simplified if we choose a geocentric coordinate system having its z axis along the orbital angular momentum vector of the disturbing body. The orbit of the satellite is described by the instantaneous osculating ellipse (3) which has a semimajor axis a, an eccentricity e, an inclination i (with respect to the orbital plane of the disturbing body), an argument of perigee ω, and a longitude of the ascending node Ω (see fig. 1). If there were no perturbing forces, these orbital elements would remain constant (assuming that our coordinate system is fixed in inertial space), and the orbit would be a Kepler orbit (4). If there is a perturbing acceleration having a radial component R, a transverse component S (measured in the plane of the instantaneous osculating ellipse and taken positive when making an angle less than

[1] Published in the May 1960 issue of *American Rocket Society Journal*. Reprinted by permission.
[2] Member of the Technical Staff.
[3] Numbers in parentheses indicate References at end of paper.

90 deg with the velocity vector), and a normal component W (normal to the plane of the instantaneous osculating ellipse and taken positive when making an angle less than 90 deg with the z axis), the orbital elements change at the rates (5).

$$\frac{da}{dt} = \frac{2e \sin v}{n\sqrt{1-e^2}} R + \frac{2a\sqrt{1-e^2}}{nr} S$$

$$\frac{de}{dt} = \frac{\sqrt{1-e^2} \sin v}{na} R + \frac{\sqrt{1-e^2}}{na^2 e}\left[\frac{a^2(1-e^2)}{r} - r\right] S$$

$$\frac{di}{dt} = \frac{r \cos(\omega+v)}{na^2\sqrt{1-e^2}} W$$

$$\frac{d\Omega}{dt} = \frac{r \sin(\omega+v)}{na^2\sqrt{1-e^2} \sin i} W$$

$$\frac{d\omega}{dt} = -\cos i \frac{d\Omega}{dt} - \frac{\sqrt{1-e^2}}{nae} \times \left[R \cos v - \left(\frac{2+e \cos v}{1+e \cos v}\right) S \sin v\right] \quad (1)$$

where

n = satellite's mean angular motion
r = radial distance of the satellite from Earth center
v = true anomaly (the angular distance of the satellite from perigee)

The rate of change of perigee distance q can be found from its relationship to a and e

$$q = a(1 - e).$$

The components R, S and W are given by Moulton (6). If r is always small compared to the distance a_d of the disturbing body from Earth's center, these components may be expanded in powers of r/a_d. Keeping only the first-order term, one obtains

$$R = K_d r(1 + 3 \cos 2\phi)$$

$$S = -6K_d r[\cos\gamma \sin(\omega + v) - \sin\gamma \cos(\omega + v) \cos i] \cos\phi$$

$$W = -6K_d r \cos\phi \sin i \sin\gamma$$

where

$K_d = GM_d/2a_d^3$
G = universal gravitational constant
M_d = the mass of the disturbing body
ϕ = angle between r and a_d
γ = angle from the line of nodes to a_d

We make an additional simplification by taking a_d constant.

Letting ϵ stand for any orbital element and $\Delta\epsilon$ for the change in that element after one revolution of the satellite (from perigee to perigee), we have

$$\Delta\epsilon = \int_{t-0}^{t-2\pi/n} \frac{d\epsilon}{dt} dt = \int_{v-0}^{2\pi} \frac{d\epsilon}{dt}\frac{dt}{dv} dv \quad (2)$$

where t is time measured from perigee passage of the satellite. Since $\Delta\epsilon$ is supposed to be small compared to ϵ, it is permissible to approximate all variables in the expressions (1) for $d\epsilon/dt$ by the values they would have in the unperturbed orbit, and to approximate dt/dv by its relationship to the conservation of angular momentum h

$$\frac{dt}{dv} = \frac{r^2}{h}$$

where $h = na^2\sqrt{1 - e^2}$ is assumed constant. Since the angular velocity of the satellite is usually large compared to the angular velocity of the disturbing body, we may assume that γ is constant during the time the satellite takes to complete one revolution. Then integrals of the type (2) can be evaluated easily. The results are

$$\Delta a = 0 \quad (3)$$

$$\Delta q = \frac{15K_d a\pi e\sqrt{1 - e^2}}{n^2} \times \{\sin 2\gamma \cos 2\omega \cos i - [\cos^2\gamma - \sin^2\gamma \cos^2 i] \sin 2\omega\} \quad (4)$$

$$\Delta e = -(1/a)\Delta q \quad (5)$$

$$\Delta i = \frac{-6K_d\pi \sin i \sin\gamma}{n^2\sqrt{1 - e^2}} \times \left\{\frac{5}{2} e^2 \sin 2\omega \sin\gamma \cos i + [1 - e^2(1 - 5\cos^2\omega)] \cos\gamma\right\} \quad (6)$$

$$\Delta\Omega = \frac{-6K_d\pi \sin\gamma}{n^2\sqrt{1-e^2}} \times \left\{\frac{5}{2} e^2 \sin 2\omega \cos\gamma + [1 + 4e^2 - 5e^2\cos^2\omega]\cos i \sin\gamma\right\} \quad (7)$$

$$\Delta\omega = -\Delta\Omega \cos i - \frac{6K_d\pi\sqrt{1-e^2}}{n^2} \left[1 - 3\sin^2\gamma\cos^2 i - \frac{5}{2}\sin 2\gamma \sin 2\omega \cos i + (1 - 5\cos^2\omega)(\cos^2\gamma - \sin^2\gamma\cos^2 i)\right]. \quad (8)$$

If, now, we let γ take values from zero to 2π, we see how the orbital elements change as a function of the time of month or year.

ERROR DUE TO NEGLECTING THE MOTION OF THE DISTURBING BODY

To estimate the error we have made by taking γ constant, let us consider the special case of co-planar motion of the satellite and the disturbing body ($i = 0$) and set $\omega = 0$. Then Equation (4) for the change in perigee per revolution becomes simply

$$\Delta q_0 = [(15K_d a\pi e\sqrt{1-e^2})/n^2] \sin 2\gamma_0 \quad (9)$$

where we have used the subscript zero to indicate that the disturbing body is held fixed. Now let us evaluate Δq when the disturbing body is moving, by taking $\gamma = \gamma_0 + n_d t$ where n_d is the angular velocity of the disturbing body. Equation (2) for Δq will contain integrals of the form

$$I = \int_0^{2\pi} f(\cos v, \sin v, \cos 2\gamma, \sin 2\gamma)\, dv \quad (10)$$

where f stands for some function. We replace $\cos 2\gamma$ and $\sin 2\gamma$ by their Taylor expansions

$$\cos 2\gamma = \cos 2\gamma_0 - 2n_d t \sin 2\gamma_0 + \ldots$$
$$\sin 2\gamma = \sin 2\gamma_0 + 2n_d t \cos 2\gamma_0 + \ldots$$

and retain only the first two terms. Our integral now contains both v and t as variables of integration. These may be related to the eccentric anomaly E via the relations

$$t = (E - e\sin E)/n$$
$$\sin v = (\sqrt{1-e^2}\sin E)/(1 - e\cos E)$$
$$\cos v = (\cos E - e)/(1 - e\cos E).$$

Equation (10) now takes the form

$$I = \int_0^{2\pi} F(\gamma_0, E, \sin E, \cos E)\, dE \quad (11)$$

where F stands for the new function. This type of integral can be readily evaluated, and yields for Δq

$$\Delta q = \frac{15K_d a\pi e\sqrt{1-e^2}}{n^2} \sin 2\gamma_0 \times \left\{1 + \frac{n_d}{n}\left[2\pi \cot 2\gamma_0 + \frac{(1-e)(4 + 45e + 58e^2 + 17e^3)}{15e(1+e)\sqrt{1-e^2}}\right]\right\} \quad (12)$$

which shows that the additional term, contributed by the motion of the disturbing body, is of the order n_d/n which is usually less than 0.03.

It is also of interest to find how much the semimajor axis is perturbed, and this can be found only by considering the motion of the disturbing body. We return to the three-dimensional problem ($i \neq 0$) and find, by a procedure similar to that used to obtain Equation (12), that

$$\Delta a = (4K_d a\pi n_d/n^3)\{(4 - 6e - 5e^2)[\sin 2\omega \cos 2\gamma_0 \cos i - (1 + \cos^2 i)\sin 2\gamma_0 \cos^2\omega] + [2(1-e^2) + (2 - 6e - 3e^2)\cos^2 i]\sin 2\gamma_0\}$$

EXAMPLE

To illustrate the size of the perturbations, let us compute their effect on the perigee distance of 1959 delta (Explorer VI). Considering first the lunar perturbation and assuming that the orbital elements do not change significantly over the first few weeks of the satellite's life, we may average Equation (4) over one lunar month to obtain for the average value of Δq.

$$\overline{\Delta q_m} = \frac{-15K_m a\pi e\sqrt{1-e^2}}{2n^2} \sin 2\omega_m \sin^2 i_m \quad (13)$$

where the subscript m indicates that the disturbing body is the moon. For 1959 delta the initial values of the orbital elements were ap-

proximately $a = 15{,}000$ nautical miles, $e = 0.76$, $i_m = 41.5$ deg and $\omega_m = 10.4$ deg. With these values, we obtain $\bar{\Delta}q_m = -0.06$ nautical mile per revolution. Remembering that the satellite made about two revolutions a day, we see that the moon's perturbation can lead to a nonnegligible lowering of perigee.

The sun's influence, on the other hand, tends to raise perigee at first. Relative to the sun's plane (or ecliptic), the argument of perigee started at 2.7 deg, the orbital inclination was 40.3 deg, and γ_s was about 48 deg. The initial change in perigee, determined from Equation (4), is therefore $\Delta q_s = 0.26$ nautical mile per revolution. At the end of one month $\Delta q_s = 0.14$ nautical mile per revolution. Eventually the sun moves to such an angular position that Δq_s becomes negative. Then the combined solar-lunar forces produce an important lowering of perigee with the consequent reduction of lifetime. To obtain accurate results, one must evaluate Equation (4) for each revolution, taking into account the changing values of i_s, i_m, ω_s, ω_m, etc., dependent on all perturbations including those caused by Earth's oblateness and atmosphere.

ACKNOWLEDGMENTS

The writer is indebted to Dr. Leon Blitzer for helpful discussions and suggestions for evaluating integrals and to Silvia Marcus for valuable conversations on astronomical language.

REFERENCES

1. Kozai, Y., private communication.
2. Kozai, Y., "On the Effects of the Sun and Moon Upon the Motion of a Close Earth Satellite," Smithsonian Institution Astrophysical Observatory, Research in Space Science, Special Rep. no. 22.
3. Moulton, F. R., "An Introduction to Celestial Mechanics." Macmillan Co., N.Y., 1956, second ed., p. 322.
4. *Ibid.*, pp. 82–83.
5. *Ibid.*, pp. 404–405.
6. *Ibid.*, p. 340.

(Received November 11, 1957.)

Development of the Lunar and Solar Perturbations in the Motion of an Artificial Satellite[1]

BY P. MUSEN, A. BAILIE AND E. UPTON

NASA Goddard Space Flight Center

Problems relating to the influence of lunar and solar perturbations on the motion of artificial satellites are analyzed by an extension of Cayley's development of the perturbative function in the lunar theory. In addition, the results are modified for incorporation into the Hansen-type theory used by the NASA Space Computing Center. The theory is applied to the orbits of the Vanguard I and Explorer VI satellites, and the results of detailed computations for these satellites are given together with a physical description of the perturbations in terms of resonance effects.

INTRODUCTION

This paper is concerned primarily with problems related to the influence of lunar and solar perturbations on the motion of artificial satellites. The importance of these problems is indicated by Kozai's discovery that the perigee height and lifetime of a satellite may be strongly affected by these perturbations.

The basis for the computations is provided by an analytical development of the disturbing function, which is an extension of Cayley's development of the solar perturbative function in the lunar theory. The relations between perigee-height variations and launch conditions have been investigated by using a modification of this development. Values of perturbations in the perigee height for the satellites Vanguard I (1958 β_2) and Explorer VI (1959 δ) were computed from the resultant trigonometric series. A program was developed for computing lunar and solar perturbations with the aid of the IBM 704. This program permits the inclusion of any value of the eccentricity and of the inclination, and gives the variation of the perigee height in the form of a trigonometric series with numerical coefficients. Also, the perturbations in Hansen's coordinates have been computed; this program can be included in the existing Vanguard scheme for general oblateness perturbations. The formulas used in these computations can be applied to the development of a Hansen-type numerical theory for an artificial satellite.

[1] Originally presented at the First International Space Symposium, sponsored by the Committee on Space Research (COSPAR), Nice, France, January 1960. Reprinted by permission.

DEVELOPMENT OF THE DISTURBING FUNCTION

The importance of determining the lunar and solar perturbations in the motion of an artificial satellite was indicated by Kozai's discovery that certain long-period terms in the development of the disturbing function cause large perturbations in the elements and that, in this way, the orbital lifetime of the satellite can be considerably affected (Reference 1). In the present treatment, the analytical development of the two main terms of the disturbing function are expressed

$$\frac{m'r^2}{r'^3}\left(\frac{3}{2}S^2-\frac{1}{2}\right)+\frac{m'r^3}{r'^4}\left(\frac{5}{2}S^3-\frac{3}{2}S\right),$$

where

$$S = \cos(\mathbf{r}, \mathbf{r}').$$

In this expression $(\mathbf{r}, \mathbf{r}')$ is the angle between the position vectors of the satellite and of the perturbing body, either the sun or the moon, with respect to the earth. The main term is the second Legendre polynomial in the harmonic expansion of the disturbing function. The third Legendre polynomial is known as the parallactic term.

The analytical development is important because it permits investigation of the perturbations for an entire group of satellites having similar elements and, in particular, is useful in investigating problems connected with the effects of resonance, i.e., stability problems.

The problem of developing the disturbing effects caused by the sun and the moon is related to the lunar problem but with the difference that the orbital inclinations of both the disturbed and the disturbing body to the basic reference plane can be large in the case considered here. The arrangement given for the development of the disturbing function, based on Cayley's work (Reference 2), permits the inclusion of any power of the eccentricity and is valid for all inclinations (Reference 3).

For the time being, only long-period terms are evaluated, and the terms depending on the mean anomaly of the satellite are excluded. The resultant "abbreviated version" is given on pages 43 through 48. This last development was used to investigate the influence of the combined effect of drag and lunar and solar perturbations on the orbital lifetime of the satellite and in further investigations of the orbits of satellites in the NASA space research program. Future satellite orbits undoubtedly will have elements such that the terms depending on the mean anomaly of the satellite and the higher powers of the eccentricity can be expected to become more important, especially regarding the possible development of resonances associated with the commensurability of satellite and lunar periods.

The perturbations may also be developed by a purely numerical method based on the use of fast computing machines. In this method the values of the orbit elements a, e, i, a', e', i' are substituted into the coefficients. The numerical method is convenient in developing the perturbations according to Hansen's theory and in investigating the variation of the perigee distance. A program for the development in terms of the eccentric anomaly and a program for the development in terms of the mean anomaly have been prepared. Both programs can help to supply information concerning the optimum condition for launching in connection with the solar and lunar perturbations.

Direct numerical integration of the equations of motion with the solar and lunar perturbations, by means of a computer program, has confirmed the results of the analytical treatment and the Fourier series development.

COMPUTATION OF SATELLITE PERTURBATIONS

The following notations are used:

a = semimajor axis of satellite orbit
e = eccentricity
i = angle of inclination to equatorial plane
ω = argument of perigee
Ω = right ascension of ascending node
g = mean anomaly
$\mathbf{r}$ = position vector
x, y, z = rectangular coordinates
r = radius
f = true anomaly
$\gamma = \sin \frac{i}{2}$.

The corresponding elements of the disturbing body are designated by primes: a', e', etc. The equatorial plane is taken as the basic reference plane, and the precession and nutation of the earth's axis are neglected. The disturbing function has the form

$$\Omega = m' \left(\frac{1}{|r - r'|} - \frac{\mathbf{r}' \cdot \mathbf{r}}{r'^3} \right), \tag{1}$$

or

$$\Omega = \frac{m' r^2}{r'^3} P_2(S) + \frac{m' r^3}{r'^4} P_3(S) + \ldots . \tag{2}$$

In the latter expression

$$S = \cos(\mathbf{r},\mathbf{r}') = (1-\gamma^2)(1-\gamma'^2)\cos(f+\omega+\theta-f'-\omega') + \gamma^2(1-\gamma'^2)\cos(f+\omega-\theta+f'+\omega') + \gamma'^2(1-\gamma^2)\cos(f+\omega+\theta+f'+\omega') + \gamma^2\gamma'^2\cos(f+\omega-\theta-f'-\omega') + 2\gamma\gamma'\sqrt{1-\gamma^2}\sqrt{1-\gamma'^2}\cos(f+\omega-f'-\omega') - 2\gamma\gamma'\sqrt{1-\gamma^2}\sqrt{1-\gamma'^2}\cos(f+\omega+f'+\omega'), \quad (3)$$

where

$$\theta = \Omega - \Omega',$$

and P_2, P_3, . . . are Legendre polynomials. Only the first two terms of Equation 2 are considered:

$$a\Omega = \frac{m'a^3}{a'^3}\left(\frac{r}{a}\right)^2\left(\frac{a'}{r'}\right)^3\left(\frac{3}{2}S^2-\frac{1}{2}\right) + \frac{m'a^4}{a'^4}\left(\frac{r}{a}\right)^3\left(\frac{a'}{r'}\right)^4\left(\frac{5}{2}S^3-\frac{3}{2}S\right). \quad (4)$$

If $i' \neq 0$, then it is convenient to represent Equation 4 in the form of Radau (Reference 4):

$$a\Omega = \frac{m'a^3}{a'^3}\left(\frac{r}{a}\right)^2\left(\frac{a'}{r'}\right)^3\left(\frac{1}{4}\frac{r^2-3z^2}{r^2}\frac{r'^2-3z'^2}{r'^2} + \frac{3}{4}\frac{x^2-y^2}{r^2}\frac{x'^2-y'^2}{r'^2} + 3\frac{xyx'y'}{r^2r'^2} + 3\frac{xzx'z'}{r^2r'^2} + 3\frac{yzy'z'}{r^2r'^2}\right) + \frac{m'a^4}{a'^4}\left(\frac{r}{a}\right)^3\left(\frac{a'}{r'}\right)^4\left(\frac{3}{8}\frac{r^2x-5xz^2}{r^3}\frac{r'^2x'-5x'z'^2}{r'^3} + \frac{3}{8}\frac{r^2y-5yz^2}{r^3}\frac{r'^2y'-5y'z'^2}{r'^3} + \frac{1}{4}\frac{3r^2z-5z^3}{r^3}\frac{3r'^2z'-5z'^3}{r'^3} + \frac{5}{8}\frac{x^3-3xy^2}{r^3}\frac{x'^3-3x'y'^2}{r'^3} + \frac{5}{8}\frac{3x^2y-y^3}{r^3}\frac{3x'^2y'-y'^3}{r'^3} + \frac{15}{4}\frac{x^2z-y^2z}{r^3}\frac{x'^2z'-y'^2z}{r'^3} + 15\frac{xyz}{r^3}\frac{x'y'z'}{r'^3}\right); \quad (5)$$

and to substitute

$$\frac{x}{r} = (1-\gamma^2)\cos(f+\omega+\theta) + \gamma^2\cos(f+\omega-\theta),$$

$$\frac{y}{r} = (1-\gamma^2)\sin(f+\omega+\theta) - \gamma^2\sin(f+\omega-\theta),$$

$$\frac{z}{r} = 2\gamma\sqrt{1-\gamma^2}\sin(f+\omega),$$

$$\frac{x'}{r'} = \cos(f'+\omega),$$

$$\frac{y'}{r'} = (1-2\gamma'^2)\sin(f'+\omega'),$$

$$\frac{z'}{r'} = 2\gamma'\sqrt{1-\gamma'^2}\sin(f'+\omega').$$

Substitution of these expressions into Equation 5 results in the following development for Ω in terms of the true anomalies:

$$a\Omega = \frac{m'a^3}{a'^3}\left(\frac{r}{a}\right)^2\left(\frac{a'}{r'}\right)^3 \times (\text{sum of terms of Types I–V}) + \frac{m'a^4}{a'^4}\left(\frac{r}{a}\right)^3\left(\frac{a'}{r'}\right)^4 \times (\text{sum of terms of Types VI–XIII}): \quad (6)$$

Type I

$$+\frac{1}{4}(1-6\gamma^2+6\gamma^4)(1-6\gamma'^2+6\gamma'^4) + 3(\gamma^2-\gamma^4)(\gamma'^2-\gamma'^4)\cos 2\theta + 3(\gamma-2\gamma^3)(\gamma'-2\gamma'^3)\sqrt{1-\gamma^2}\sqrt{1-\gamma'^2}\cos\theta;$$

Type II

$$+\frac{9}{2}(\gamma^2-\gamma^4)(\gamma'^2-\gamma'^4)\cos(2f+2\omega-2f'-2\omega') + \frac{3}{4}(1-\gamma^2)^2(1-\gamma'^2)^2\cos(2f+2\omega-2f'-2\omega'+2\theta) + \frac{3}{4}\gamma^4\gamma'^4\cos(2f+2\omega-2f'-2\omega'-2\theta) + 3(\gamma-\gamma^3)(\gamma'-\gamma'^3)\sqrt{1-\gamma^2}\sqrt{1-\gamma'^2}\cos(2f+2\omega-2f'-2\omega'+\theta) + 3\gamma^3\gamma'^3\sqrt{1-\gamma^2}\sqrt{1-\gamma'^2}\cos(2f+2\omega-2f'-2\omega'-\theta);$$

Type III

$$+\frac{3}{2}(\gamma^2-\gamma^4)(1-6\gamma'^2+6\gamma'^4)\cos(2f+2\omega) + \frac{3}{2}(1-\gamma^2)^2(\gamma'^2-\gamma'^4)\cos(2f+2\omega+2\theta)$$

$$+\frac{3}{2}\gamma^4(\gamma'^2-\gamma'^4)\cos(2f+2\omega-2\theta)$$

$$-3(\gamma-\gamma^3)(\gamma'-2\gamma'^3)\sqrt{1-\gamma^2}\sqrt{1-\gamma'^2}\cos(2f+2\omega+\theta)$$

$$+3\gamma^3(\gamma'-2\gamma'^3)\sqrt{1-\gamma^2}\sqrt{1-\gamma'^2}\cos(2f+2\omega-\theta);$$

Type IV

$$+\frac{3}{2}(\gamma'^2-\gamma'^4)(1-6\gamma^2+6\gamma^4)\cos(2f'+2\omega')$$

$$+\frac{3}{2}(\gamma^2-\gamma^4)(1-\gamma'^2)^2\cos(2f'+2\omega'-2\theta)$$

$$+\frac{3}{2}(\gamma^2-\gamma^4)\gamma'^4\cos(2f'+2\omega'+2\theta)$$

$$+3(\gamma-2\gamma^3)\gamma'^3\sqrt{1-\gamma^2}\sqrt{1-\gamma'^2}\cos(2f'+2\omega'+\theta)$$

$$-3(\gamma-2\gamma^3)(\gamma'-\gamma'^3)\sqrt{1-\gamma^2}\sqrt{1-\gamma'^2}\cos(2f'+2\omega'-\theta);$$

Type V

$$+\frac{9}{2}(\gamma^2-\gamma^4)(\gamma'^2-\gamma'^4)\cos(2f+2\omega+2f'+2\omega')$$

$$+\frac{3}{4}(1-\gamma^2)^2\gamma'^4\cos(2f+2\omega+2f'+2\omega'+2\theta)$$

$$+\frac{3}{4}\gamma^4(1-\gamma'^2)^2\cos(2f+2\omega+2f'+2\omega'-2\theta)$$

$$-3(\gamma-\gamma^3)\gamma'^3\sqrt{1-\gamma^2}\sqrt{1-\gamma'^2}\cos(2f+2\omega+2f'+2\omega'+\theta)$$

$$-3\gamma^3(\gamma'-\gamma'^3)\sqrt{1-\gamma^2}\sqrt{1-\gamma'^2}\cos(2f+2\omega+2f'+2\omega'-\theta);$$

Type VI

$$-\frac{9}{2}(\gamma-5\gamma^3+5\gamma^5)(\gamma'-5\gamma'^3+5\gamma'^5)\sqrt{1-\gamma^2}\sqrt{1-\gamma'^2}\cos(f+\omega+f'+\omega')$$

$$+\frac{3}{8}(1-\gamma^2)(1-10\gamma^2+15\gamma^4)(6\gamma'^2-20\gamma'^4+15\gamma'^6)\cos(f+\omega+f'+\omega'+\theta)$$

$$+\frac{3}{8}(6\gamma^2-20\gamma^4+15\gamma^6)(1-\gamma'^2)(1-10\gamma'^2+15\gamma'^4)\cos(f+\omega+f'+\omega'-\theta)$$

$$+\frac{15}{4}(\gamma-4\gamma^3+3\gamma^5)(2\gamma'^2-3\gamma'^5)\sqrt{1-\gamma^2}\sqrt{1-\gamma'^2}\cos(f+\omega+f'+\omega'+2\theta)$$

$$+\frac{15}{4}(2\gamma^3-3\gamma^5)(\gamma'-4\gamma'^3+3\gamma'^5)\sqrt{1-\gamma^2}\sqrt{1-\gamma'^2}\cos(f+\omega+f'+\omega'-2\theta)$$

$$+\frac{45}{8}(\gamma^2-2\gamma^4+\gamma^6)(\gamma'^4-\gamma'^6)\cos(f+\omega+f'+\omega'+3\theta)$$

$$+\frac{45}{8}(\gamma^4-\gamma^6)(\gamma'^2-2\gamma'^4+\gamma'^6)\cos(f+\omega+f'+\omega'-3\theta);$$

Type VII

$$+\frac{9}{2}(\gamma-5\gamma^3+5\gamma^5)(\gamma'-5\gamma'^3+5\gamma'^5)\sqrt{1-\gamma^2}\sqrt{1-\gamma'^2}\cos(f+\omega-f'-\omega')$$

$$+\frac{3}{8}(1-\gamma^2)(1-10\gamma^2+15\gamma^4)(1-\gamma'^2)(1-10\gamma'^2+15\gamma'^4)\cos(f+\omega-f'-\omega'+\theta)$$

$$+\frac{3}{8}(6\gamma^2-20\gamma^4+15\gamma^6)(6\gamma'^2-20\gamma'^4+15\gamma'^6)\cos(f+\omega-f'-\omega'-\theta)$$

$$+\frac{15}{4}(\gamma-4\gamma^3+3\gamma^5)(\gamma'-4\gamma'^3+3\gamma'^5)\sqrt{1-\gamma^2}\sqrt{1-\gamma'^2}\cos(f+\omega-f'-\omega'+2\theta)$$

$$+\frac{15}{4}(2\gamma^3-3\gamma^5)(2\gamma'^3-3\gamma'^5)\sqrt{1-\gamma^2}\sqrt{1-\gamma'^2}\cos(f+\omega-f'-\omega'-2\theta)$$

$$+\frac{45}{8}(\gamma^2-2\gamma^4+\gamma^6)(\gamma'^2-2\gamma'^4+\gamma'^6)\cos(f+\omega-f'-\omega'+3\theta)$$

$$+\frac{45}{8}(\gamma^4-\gamma^6)(\gamma'^4-\gamma'^6)\cos(f+\omega-f'-\omega'-3\theta);$$

Type VIII

$$-\frac{15}{2}(\gamma-5\gamma^3+5\gamma^5)(\gamma'^3-\gamma'^5)\sqrt{1-\gamma^2}\sqrt{1-\gamma'^2}\cos(f+\omega+3f'+3\omega')$$

$$+\frac{15}{8}(1-\gamma^2)(1-10\gamma^2+15\gamma^4)(\gamma'^4-\gamma'^6)\cos(f+\omega+3f'+3\omega'+\theta)$$

$$+\frac{15}{8}(6\gamma^2-20\gamma^4+15\gamma^6)(\gamma'-\gamma'^3)^2\cos(f+\omega+3f'+3\omega'-\theta)$$

$$+\frac{15}{4}(\gamma-4\gamma^3+3\gamma^5)\gamma'^5\sqrt{1-\gamma^2}\sqrt{1-\gamma'^2}\cos(f+\omega+3f'+3\omega'+2\theta)$$

$$-\frac{15}{4}(2\gamma^3-3\gamma^5)\gamma'(1-\gamma'^2)^2\sqrt{1-\gamma^2}\sqrt{1-\gamma'^2}\cos(f+\omega+3f'+3\omega'-2\theta)$$

$$+\frac{15}{8}(\gamma-\gamma^3)^2\gamma'^6\cos(f+\omega+3f'+3\omega'+3\theta)$$

$$+\frac{15}{8}(\gamma^4-\gamma^6)(1-\gamma'^2)^3\cos(f+\omega+3f'+3\omega'-3\theta);$$

Type IX

$$+\frac{15}{2}(\gamma-5\gamma^3+5\gamma^5)(\gamma'^3-\gamma'^5)\sqrt{1-\gamma^2}\sqrt{1-\gamma'^2}\cos(f+\omega-3f'-3\omega')$$

$$+\frac{15}{8}(1-\gamma^2)(1-10\gamma^2+15\gamma^4)(\gamma'-\gamma'^3)^2\cos(f+\omega-3f'-3\omega'+\theta)$$

$$+\frac{15}{8}(6\gamma^2-20\gamma^4+15\gamma^6)(\gamma'^4-\gamma'^6)\cos(f+\omega-3f'-3\omega'-\theta)$$

$$-\frac{15}{4}(\gamma-4\gamma^3+3\gamma^5)(\gamma'-2\gamma'^3+\gamma'^5)\sqrt{1-\gamma^2}\sqrt{1-\gamma'^2}\cos(f+\omega-3f'-3\omega'+2\theta)$$

$$+\frac{15}{4}(2\gamma^3-3\gamma^5)\gamma'^5\sqrt{1-\gamma^2}\sqrt{1-\gamma'^2}\cos(f+\omega-3f'-3\omega'-2\theta)$$

$$+\frac{15}{8}\gamma^2(1-\gamma^2)^2(1-\gamma'^2)^3\cos(f+\omega-3f'-3\omega'+3\theta)$$

$$+\frac{15}{8}(\gamma^4-\gamma^6)\gamma'^6\cos(f+\omega-3f'-3\omega'-3\theta);$$

Type X

$$-\frac{15}{2}(\gamma^3-\gamma^5)(\gamma'-5\gamma'^3+5\gamma'^5)\sqrt{1-\gamma^2}\sqrt{1-\gamma'^2}\cos(3f+3\omega+f'+\omega')$$

$$+\frac{15}{8}(\gamma-\gamma^3)^2(6\gamma'^2-20\gamma'^4+15\gamma'^6)\cos(3f+3\omega+f'+\omega'+\theta)$$

$$+\frac{15}{8}(\gamma^4-\gamma^6)(1-\gamma'^2)(1-10\gamma'^2+15\gamma'^4)\cos(3f+3\omega+f'+\omega'-\theta)$$

$$-\frac{15}{4}(\gamma-2\gamma^3+\gamma^5)(2\gamma'^3-3\gamma'^5)\sqrt{1-\gamma^2}\sqrt{1-\gamma'^2}\cos(3f+3\omega+f'+\omega'+2\theta)$$

$$+\frac{15}{4}\gamma^5(\gamma'-4\gamma'^3+3\gamma'^5)\sqrt{1-\gamma^2}\sqrt{1-\gamma'^2}\cos(3f+3\omega+f'+\omega'-2\theta)$$

$$+\frac{15}{8}(1-\gamma^2)^3(\gamma'^4-\gamma'^6)\cos(3f+3\omega+f'+\omega'+3\theta)$$

$$+\frac{15}{8}\gamma^6(\gamma'-\gamma'^3)^2\cos(3f+3\omega+f'+\omega'-3\theta);$$

Type XI

$$+\frac{15}{2}(\gamma^3-\gamma^5)(\gamma'-5\gamma'^3+5\gamma'^5)\sqrt{1-\gamma^2}\sqrt{1-\gamma'^2}\cos(3f+3\omega-f'-\omega')$$

$$+\frac{15}{8}(\gamma-\gamma^3)^2(1-\gamma'^2)(1-10\gamma'^2+15\gamma'^4)\cos(3f+3\omega-f'-\omega'+\theta)$$

$$+\frac{15}{8}(\gamma^4-\gamma^6)(6\gamma'^2-20\gamma'^4+15\gamma'^6)\cos(3f+3\omega-f'-\omega'-\theta)$$

$$-\frac{15}{4}(\gamma-2\gamma^3+\gamma^5)(\gamma'-4\gamma'^3+3\gamma'^5)\sqrt{1-\gamma^2}\sqrt{1-\gamma'^2}\cos(3f+3\omega-f'-\omega'+2\theta)$$

$$+\frac{15}{4}\gamma^5(2\gamma'^3-3\gamma'^5)\sqrt{1-\gamma^2}\sqrt{1-\gamma'^2}\cos(3f+3\omega-f'-\omega'-2\theta)$$

$$+\frac{15}{8}(1-\gamma^2)^3(\gamma'-\gamma'^3)^2\cos(3f+3\omega-f'-\omega'+3\theta)$$

$$+\frac{15}{8}\gamma^6(\gamma'^4-\gamma'^6)\cos(3f+3\omega-f'-\omega'-3\theta);$$

Type XII

$$-\frac{25}{2}(\gamma^3-\gamma^5)(\gamma'^3-\gamma'^5)\sqrt{1-\gamma^2}\sqrt{1-\gamma'^2}\cos(3f+3\omega+3f'+3\omega')$$

$$+\frac{75}{8}(\gamma-\gamma^3)^2(\gamma'^4-\gamma'^6)\cos(3f+3\omega+3f'+3\omega'+\theta)$$

$$+\frac{75}{8}(\gamma^4-\gamma^6)(\gamma'-\gamma'^3)^2\cos(3f+3\omega+3f'+3\omega'-\theta)$$

$$-\frac{15}{4}(\gamma-2\gamma^3+\gamma^5)\gamma'^5\sqrt{1-\gamma^2}\sqrt{1-\gamma'^2}\cos(3f+3\omega+3f'+3\omega'+2\theta)$$

$$-\frac{15}{4}\gamma^5(\gamma'-2\gamma'^3+\gamma'^5)\sqrt{1-\gamma^2}\sqrt{1-\gamma'^2}\cos(3f+3\omega+3f'+3\omega'-2\theta)$$

$$+\frac{5}{8}(1-\gamma^2)^3\gamma'^6\cos(3f+3\omega+3f'+3\omega'+3\theta)$$

$$+\frac{5}{8}\gamma^6(1-\gamma'^2)^3\cos(3f+3\omega+3f'+3\omega'-3\theta);$$

Type XIII

$$+\frac{25}{2}(\gamma^3-\gamma^5)(\gamma'^3-\gamma'^5)\sqrt{1-\gamma^2}\sqrt{1-\gamma'^2}\cos(3f+3\omega-3f'-3\omega')$$

$$+\frac{75}{8}(\gamma^2-2\gamma^4+\gamma^6)(\gamma'^2-2\gamma'^4+\gamma'^6)\cos(3f+3\omega-3f'-3\omega'+\theta)$$

$$+\frac{75}{8}(\gamma^4-\gamma^6)(\gamma'^4-\gamma'^6)\cos(3f+3\omega-3f'-3\omega'-\theta)$$

$$+\frac{15}{4}(\gamma-2\gamma^3+\gamma^5)(\gamma'-2\gamma^3+\gamma'^5)\sqrt{1-\gamma^2}\sqrt{1-\gamma'^2}\cos(3f+3\omega-3f'-3\omega'+2\theta)$$

$$+\frac{15}{4}\gamma^5\gamma'^5\sqrt{1-\gamma^2}\sqrt{1-\gamma'^2}\cos(3f+3\omega-3f'-3\omega'-2\theta)$$

$$+\frac{5}{8}(1-\gamma^2)^3(1-\gamma'^2)^3\cos(3f+3\omega-3f'-3\omega'+3\theta)$$

$$+\frac{5}{8}\gamma^6\gamma'^6\cos(3f+3\omega-3f'-3\omega'-3\theta).$$

Then, by using Cayley's notations, we obtain

$$\left(\frac{r}{a}\right)^{p} \cos(qf + \alpha) = \sum_{-\infty}^{+\infty} [\cos + \sin]^{i}_{p,q} \cos(ig + \alpha),$$

$$\left(\frac{r'}{a'}\right)^{p'} \cos(q'f' + \alpha') = \sum_{-\infty}^{+\infty} [\cos + \sin]^{i'}_{p',q'} \cos(i'g' + \alpha').$$

Evidently

$$\left(\frac{r}{a}\right)^{p}\left(\frac{r'}{a'}\right)^{p'} \cos(qf + q'f' + \alpha) = \sum_{-\infty}^{+\infty}\sum_{-\infty}^{+\infty} [\cos + \sin]^{i}_{p,q} [\cos + \sin]^{i'}_{p',q'} \cos(ig + i'g' + \alpha). \quad (7)$$

The coefficients $[\cos + \sin]^{i}_{p,q}$ and $[\cos + \sin]^{i'}_{p',q'}$ are functions of the eccentricities and can be taken, in a general case, from Cayley's tables (Reference 5).

For the development of

$$\left(\frac{r}{a}\right)^{p}\left(\frac{r'}{a'}\right)^{p'} \cos(qf + q'f' + \alpha),$$

Equation 7 leads to the following computational scheme (Reference 2):

$[\cos + \sin]^{-1}_{p',q'}$	$-g'$
$[\cos + \sin]^{0}_{p',q'}$	$0.g'$
$[\cos + \sin]^{+1}_{p',q'}$	$+g'$

$[\cos + \sin]^{-1}_{p,q}$	$-g+\alpha$
$[\cos + \sin]^{0}_{p,q}$	$0.g+\alpha$
$[\cos + \sin]^{+1}_{p,q}$	$+g+\alpha$

Each coefficient in the upper part is multiplied by each coefficient in the lower part, while the corresponding arguments are added together.

A comparison of Cayley's development with Equation 6 shows that the same types of terms appear in both cases:

(I) $\left(\frac{r}{a}\right)^{2}\left(\frac{a'}{r'}\right)^{3}\cos\alpha,$

(II) $\left(\frac{r}{a}\right)^{2}\left(\frac{a'}{r'}\right)^{3}\cos(2f - 2f' + \alpha),$

(III) $\left(\frac{r}{a}\right)^{2}\left(\frac{a'}{r'}\right)^{3}\cos(2f + \alpha),$

(IV) $\left(\frac{r}{a}\right)^{2}\left(\frac{a'}{r'}\right)^{3}\cos(2f' + \alpha),$

(V) $\left(\frac{r}{a}\right)^{2}\left(\frac{a'}{r'}\right)^{3}\cos(2f + 2f' + \alpha),$

(VI) $\left(\frac{r}{a}\right)^{3}\left(\frac{a'}{r'}\right)^{4}\cos(f + f' + \alpha),$

(VII) $\left(\frac{r}{a}\right)^{3}\left(\frac{a'}{r'}\right)^{4}\cos(f - f' + \alpha),$

(VIII) $\left(\frac{r}{a}\right)^{3}\left(\frac{a'}{r'}\right)^{4}\cos(f + 3f' + \alpha),$

(IX) $\left(\frac{r}{a}\right)^{3}\left(\frac{a'}{r'}\right)^{4}\cos(f - 3f' + \alpha),$

(X) $\left(\frac{r}{a}\right)^{3}\left(\frac{a'}{r'}\right)^{4}\cos(3f + f' + \alpha),$

(XI) $\left(\frac{r}{a}\right)^{3}\left(\frac{a'}{r'}\right)^{4}\cos(3f - f' + \alpha),$

(XII) $\left(\frac{r}{a}\right)^3\left(\frac{a'}{r'}\right)^4\cos(3f + 3f' + \alpha)$,

(XIII) $\left(\frac{r}{a}\right)^3\left(\frac{a'}{r'}\right)^4\cos(3f - 3f' + \alpha)$,

and the same arrangement of

$$[\cos + \sin]^{i}_{p,q}, \qquad [\cos + \sin]^{i'}_{p',q'}$$

can be used. *The arrangement for the development of* aΩ *in terms of the mean anomalies, given in pages 30 through 42, has the following forms:*

On the top, the factors depending on γ *and* γ' *are given. Each factor is a product of a polynomial in* γ *and a polynomial in* γ'. *These factors are analogous to the polynomials of Tisserand from the planetary theories. On the right are the angles that correspond to the* γ, γ' *factors and that must be added to the arguments. Each coefficient above must be multiplied by each coefficient below, and the arguments are added. The common factors,* $m'a^3/a'^3$ *for Types I–V and* $m'a^4/a'^4$ *for Types VI–XIII, are omitted.*

As an example, from the arrangement for Type $a\Omega_1$ (below) we take, to order e^2 and e'^2,

$$3(\gamma - 2\gamma^3)(\gamma' - 2\gamma'^3)\sqrt{1-\gamma^2}\sqrt{1-\gamma'^2}\,\frac{m'a^3}{a'^3}\,\frac{9}{4}\,e'^2\left(-\frac{1}{4}\,e^2\right)\cos(+2g + 2g' + \theta).$$

There is no necessity to perform the actual multiplication; it can be done separately in each case.

Type $a\Omega_1$

Factors	*cos terms*
$+\frac{1}{4}(1 - 6\gamma^2 + 6\gamma^4)(1 - 6\gamma'^2 + 6\gamma'^4)$	$2\tau = 0$
$+ 3(\gamma^2 - \gamma^4)(\gamma'^2 - \gamma'^4)$	$2\tau = 2\theta$
$+ 3(\gamma - 2\gamma^3)(\gamma' - 2\gamma'^3)\sqrt{1-\gamma^2}\sqrt{1-\gamma'^2}$	$2\tau = \theta$

	$+\frac{9}{4}e'^2 + \frac{7}{4}e'^4 + \ldots$	$- 2g'$
	$+\frac{3}{2}e' + \frac{27}{16}e'^3 + \ldots$	$- g'$
	$(1 - e'^2)^{-3/2}$	$0.g'$
	$+\frac{3}{2}e' + \frac{27}{16}e'^3 + \ldots$	$+ g'$
	$+\frac{9}{4}e'^2 + \frac{7}{4}e'^4 + \ldots$	$+ 2g'$
$-\frac{1}{4}e^2 + \frac{1}{12}e^4 + \ldots$		$- 2g + 2\tau$
$-e + \frac{1}{8}e^3 + \ldots$		$- g + 2\tau$
$1 + \frac{3}{2}e^2$ (exact)		$0.g + 2\tau$
$-e + \frac{1}{8}e^3 + \ldots$		$+ g + 2\tau$
$-\frac{1}{4}e^2 + \frac{1}{12}e^4 + \ldots$		$+ 2g + 2\tau$

Type $a\Omega_2$

Factors	*cos terms*
$+\frac{9}{2}(\gamma^2-\gamma^4)(\gamma'^2-\gamma'^4)$	$2\tau = 2\omega$
$+\frac{3}{4}(1-\gamma^2)^2(1-\gamma'^2)^2$	$2\tau = 2\omega + 2\theta$
$+\frac{3}{4}\gamma^4\gamma'^4$	$2\tau = 2\omega - 2\theta$
$+3(\gamma-\gamma^3)(\gamma'-\gamma'^3)\sqrt{1-\gamma^2}\sqrt{1-\gamma'^2}$	$2\tau = 2\omega + \theta$
$+3\gamma^3\gamma'^3\sqrt{1-\gamma^2}\sqrt{1-\gamma'^2}$	$2\tau = 2\omega - \theta$

	$+\frac{17}{2}e'^2 - \frac{115}{6}e'^4 + \ldots$	$-4g' - 2\omega'$
	$+\frac{7}{2}e' - \frac{123}{16}e'^3 + \ldots$	$-3g' - 2\omega'$
	$1 - \frac{5}{2}e'^2 + \frac{13}{16}e'^4 + \ldots$	$-2g' - 2\omega'$
	$-\frac{1}{2}e' + \frac{1}{16}e'^3 + \ldots$	$-g' - 2\omega'$
	0 (exact)	$0.g' - 2\omega'$
	$+\frac{1}{48}e'^3 + \ldots$	$+g' - 2\omega'$
	$+\frac{1}{24}e'^4 + \ldots$	$+2g' - 2\omega'$
$-\frac{1}{16}e^4 - \frac{11}{480}e^6$		$-2g + 2\tau$
$-\frac{7}{24}e^3 - \frac{47}{384}e^5 + \ldots$		$-g + 2\tau$
$+\frac{5}{2}e^2$ (exact)		$0.g + 2\tau$
$-3e + \frac{13}{8}e^3 + \ldots$		$+g + 2\tau$
$-\frac{5}{2}e^2 + \frac{23}{16}e^4 + \ldots$		$+2g + 2\tau$

Type $a\Omega_3$

Factors	*cos terms*
$+\frac{3}{2}(\gamma^2-\gamma^4)(1-6\gamma'^2+6'^4)$	$2\tau = 2\omega$
$+\frac{3}{2}(1-\gamma^2)^2(\gamma'^2-\gamma'^4)$	$2\tau = 2\omega + 2\theta$
$+\frac{3}{2}\gamma^4(\gamma'^2-\gamma'^4)$	$2\tau = 2\omega - 2\theta$
$+3\gamma^3(\gamma'-2\gamma'^3)\sqrt{1-\gamma^2}\sqrt{1-\gamma'^2}$	$2\tau = 2\omega - \theta$
$-3(\gamma-\gamma^3)(\gamma'-2\gamma'^3)\sqrt{1-\gamma^2}\sqrt{1-\gamma'^2}$	$2\tau = 2\omega + \theta$

	$+\frac{9}{4}e'^2+\frac{7}{4}e'^4+\ldots$	$-2g'$
	$+\frac{3}{2}e'+\frac{27}{16}e'^3+\ldots$	$-g'$
	$1+\frac{3}{2}e'^2+\frac{15}{8}e'^4+\ldots$	$0.g'$
	$+\frac{3}{2}e'+\frac{27}{16}e'^3+\ldots$	$+g'$
	$+\frac{9}{4}e'^2+\frac{7}{4}e'^4+\ldots$	$+2g'$
$-\frac{1}{16}e^4+\ldots$		$-2g+2\tau$
$-\frac{7}{24}e^3+\ldots$		$-g+2\tau$
$+\frac{5}{2}e^2$ (exact)		$0.g+2\tau$
$-3e+\frac{13}{8}e^3+\ldots$		$+g+2\tau$
$1-\frac{5}{2}e^2+\frac{23}{16}e^4+\ldots$		$+2g+2\tau$

Type $a\Omega_4$

Factors	*cos terms*
$+\frac{3}{2}(1-6\gamma^2+6\gamma^4)(\gamma'^2-\gamma'^4)$	$2\tau' = 2\omega'$
$+\frac{3}{2}(\gamma^2-\gamma^4)\gamma'^4$	$2\tau' = 2\omega' + 2\theta$
$+\frac{3}{2}(\gamma^2-\gamma^4)(1-\gamma'^2)^2$	$2\tau' = 2\omega' - 2\theta$
$+3(\gamma-2\gamma^3)\gamma'^3\sqrt{1-\gamma^2}\sqrt{1-\gamma'^2}$	$2\tau' = 2\omega' + \theta$
$-3(\gamma-2\gamma^3)(\gamma'-\gamma'^3)\sqrt{1-\gamma^2}\sqrt{1-\gamma'^2}$	$2\tau' = 2\omega' - \theta$

	$+\frac{1}{48}e'^3 + \ldots$	$-g' + 2\tau'$
	0 (exact)	$0.g' + 2\tau'$
	$-\frac{1}{2}e' + \frac{1}{16}e'^3 + \ldots$	$+g' + 2\tau'$
	$1 - \frac{5}{2}e'^2 + \frac{13}{16}e'^4 + \ldots$	$+2g' + 2\tau'$
	$+\frac{7}{2}e' - \frac{123}{16}e'^3 + \ldots$	$+3g' + 2\tau'$
	$+\frac{17}{2}e'^2 - \frac{115}{16}e'^4 + \ldots$	$+4g' + 2\tau'$
$-\frac{1}{4}e^2 + \frac{1}{12}e^4 + \ldots$		$-2g$
$-e + \frac{1}{8}e^3 + \ldots$		$-g$
$1 + \frac{3}{2}e^2$ (exact)		$0.g$
$-e + \frac{1}{8}e^3 + \ldots$		$+g$
$-\frac{1}{4}e^2 + \frac{1}{12}e^4 + \ldots$		$+2g$

Type $a\Omega_5$

Factors	*cos terms*
$+\frac{9}{2}(\gamma^2-\gamma^4)(\gamma'^2-\gamma'^4)$	$2\tau = 2\omega$
$+\frac{3}{4}(1-\gamma^2)^2\gamma'^4$	$2\tau = 2\omega + 2\theta$
$+\frac{3}{4}\gamma^4(1-\gamma'^2)^2$	$2\tau = 2\omega - 2\theta$
$-3(\gamma-\gamma^3)\gamma'^2\sqrt{1-\gamma^2}\sqrt{1-\gamma'^2}$	$2\tau = 2\omega + \theta$
$-3\gamma^3(\gamma'-\gamma'^3)\sqrt{1-\gamma^2}\sqrt{1-\gamma'^2}$	$2\tau = 2\omega - \theta$

	$+\frac{1}{48}e'^3 + \ldots$	$-g' + 2\omega'$
	0 (exact)	$0.g' + 2\omega'$
	$-\frac{1}{2}e' + \frac{1}{16}e'^3 + \ldots$	$+g' + 2\omega'$
	$1 - \frac{5}{2}e'^2 + \frac{13}{16}e'^4 + \ldots$	$+2g' + 2\omega'$
	$+\frac{7}{2}e' - \frac{123}{16}e'^3 + \ldots$	$+3g' + 2\omega'$
	$+\frac{17}{2}e'^2 - \frac{115}{6}e'^4 + \ldots$	$+4g' + 2\omega'$
$-\frac{7}{24}e + \ldots$		$-g + 2\tau$
$+\frac{5}{2}e^2$ (exact)		$0.g + 2\tau$
$-3e + \frac{13}{8}e^3 + \ldots$		$+g + 2\tau$
$1 - \frac{5}{2}e^2 + \frac{23}{16}e^4 + \ldots$		$+2g + 2\tau$
$+e - \frac{19}{8}e^3 + \ldots$		$+3g + 2\tau$
$+e^2 - \frac{5}{2}e^4 + \ldots$		$+4g + 2\tau$

Type $a\Omega_6$

Factors	*cos terms*
$-\frac{9}{2}(\gamma - 5\gamma^3 + 5\gamma^5)(\gamma' - 5\gamma'^3 + 5\gamma'^5)\sqrt{1-\gamma^2}\sqrt{1-\gamma'^2}$	$\tau = \omega$
$+\frac{3}{8}(1-\gamma^2)(1 - 10\gamma^2 + 15\gamma^4)(6\gamma'^2 - 20\gamma'^4 + 15\gamma'^6)$	$\tau = \omega + \theta$
$+\frac{3}{8}(6\gamma^2 - 20\gamma^4 + 15\gamma^6)(1-\gamma'^2)(1 - 10\gamma'^2 + 15\gamma'^4)$	$\tau = \omega - \theta$
$+\frac{15}{4}(\gamma - 4\gamma^3 + 3\gamma^5)(2\gamma'^3 - 3\gamma'^5)\sqrt{1-\gamma^2}\sqrt{1-\gamma'^2}$	$\tau = \omega + 2\theta$
$+\frac{15}{4}(2\gamma^3 - 3\gamma^5)(\gamma' - 4\gamma'^3 + 3\gamma'^5)\sqrt{1-\gamma^2}\sqrt{1-\gamma'^2}$	$\tau = \omega - 2\theta$
$+\frac{45}{8}(\gamma^2 - 2\gamma^4 + \gamma^6)(\gamma'^4 - \gamma'^6)$	$\tau = \omega + 3\theta$
$+\frac{45}{8}(\gamma^4 - \gamma^6)(\gamma'^2 - 2\gamma'^4 + \gamma'^6)$	$\tau = \omega - 3\theta$

	$+\frac{11}{8}e'^2 + \ldots$	$-g' + \omega'$
	$+e' + \ldots$	$0.g' + \omega'$
	$+1 + 2e'^2 + \ldots$	$+g' + \omega'$
	$+3e' + \ldots$	$+2g' + \omega'$
	$+\frac{53}{8}e'^2 + \ldots$	$+3g' + \omega'$
$+\frac{11}{8}e^2 + \ldots$		$-g + \tau$
$-\frac{5}{2}e - \frac{15}{8}e^3$ (exact)		$0.g + \tau$
$+1 + 2e^2 + \ldots$		$+g + \tau$
$-\frac{1}{2}e + \ldots$		$+2g + \tau$
$-\frac{3}{8}e^2 + \ldots$		$+3g + \tau$

Type $a\Omega_7$

Factors	*cos terms*
$+\frac{9}{2}(\gamma - 5\gamma^3 + 5\gamma^5)(\gamma' - 5\gamma'^3 + 5\gamma'^5)\sqrt{1-\gamma^2}\sqrt{1-\gamma'^2}$	$\tau = \omega$
$+\frac{3}{8}(1-\gamma^2)(1 - 10\gamma^2 + 15\gamma^4)(1-\gamma'^2)(1 - 10\gamma'^2 + 15\gamma'^4)$	$\tau = \omega + \theta$
$+\frac{3}{8}(6\gamma^2 - 20\gamma^4 + 15\gamma^6)(6\gamma'^2 - 20\gamma'^4 + 15\gamma'^6)$	$\tau = \omega - \theta$
$+\frac{15}{4}(\gamma - 4\gamma^3 + 3\gamma^5)(\gamma' - 4\gamma'^3 + 3\gamma'^5)\sqrt{1-\gamma^2}\sqrt{1-\gamma'^2}$	$\tau = \omega + 2\theta$
$+\frac{15}{4}(2\gamma^3 - 3\gamma^5)(2\gamma'^3 - 3\gamma'^5)\sqrt{1-\gamma^2}\sqrt{1-\gamma'^2}$	$\tau = \omega - 2\theta$
$+\frac{45}{8}(\gamma^2 - 2\gamma^4 + \gamma^6)(\gamma'^2 - 2\gamma'^4 + \gamma'^6)$	$\tau = \omega + 3\theta$
$+\frac{45}{8}(\gamma^4 - \gamma^6)(\gamma'^4 - \gamma'^6)$	$\tau = \omega - 3\theta$

	$+\frac{53}{8}e'^2 + \ldots$	$-3g' - \omega'$
	$+3e' + \ldots$	$-2g' - \omega'$
	$+1 + 2e'^2 + \ldots$	$-g' - \omega'$
	$+e' + \ldots$	$0.g' - \omega'$
	$+\frac{11}{8}e'^2 + \ldots$	$+g' - \omega'$
$+\frac{11}{8}e^2 + \ldots$		$-g + \tau$
$-\frac{5}{2}e - \frac{15}{8}e^3$ (exact)		$0.g + \tau$
$+1 + 2e^2 + \ldots$		$+g + \tau$
$-\frac{1}{2}e + \ldots$		$+2g + \tau$
$-\frac{3}{8}e^2 + \ldots$		$+3g + \tau$

Type $a\Omega_8$

Factors	*cos terms*
$-\frac{15}{2}(\gamma - 5\gamma^3 + 5\gamma^5)(\gamma'^3 - \gamma'^5)\sqrt{1-\gamma^2}\sqrt{1-\gamma'^2}$	$\tau = \omega$
$+\frac{15}{8}(1-\gamma^2)(1 - 10\gamma^2 + 15\gamma^4)(\gamma'^4 - \gamma'^6)$	$\tau = \omega + \theta$
$+\frac{15}{8}(6\gamma^2 - 20\gamma^4 + 15\gamma^6)(\gamma' - \gamma'^3)^2$	$\tau = \omega - \theta$
$+\frac{15}{4}(\gamma - 4\gamma^3 + 3\gamma^5)\gamma'^5\sqrt{1-\gamma^2}\sqrt{1-\gamma'^2}$	$\tau = \omega + 2\theta$
$-\frac{15}{4}(2\gamma^3 - 3\gamma^5)\gamma'(1-\gamma'^2)^2\sqrt{1-\gamma^2}\sqrt{1-\gamma'^2}$	$\tau = \omega - 2\theta$
$+\frac{15}{8}(\gamma - \gamma^3)^2\gamma'^6$	$\tau = \omega + 3\theta$
$+\frac{15}{8}(\gamma^4 - \gamma^6)(1-\gamma'^2)^3$	$\tau = \omega - 3\theta$

	0 (exact)	$0.g' + 3\omega'$
	$+\frac{1}{8}e'^2 + \ldots$	$+ g' + 3\omega'$
	$-e' + \ldots$	$+ 2g' + 3\omega'$
	$+ 1 - 6e'^2 + \ldots$	$+ 3g' + 3\omega'$
	$+ 5e' + \ldots$	$+ 4g' + 3\omega'$
	$+\frac{127}{8}e'^2 + \ldots$	$+ 5g' + 3\omega'$
$+\frac{11}{8}e^2 + \ldots$		$-g + \tau$
$-\frac{5}{2}e - \frac{15}{8}e^3$ (exact)		$0.g + \tau$
$+ 1 + 2e^2 + \ldots$		$+ g + \tau$
$-\frac{1}{2}e + \ldots$		$+ 2g + \tau$
$-\frac{3}{8}e^2 + \ldots$		$+ 3g + \tau$

Type $a\Omega_9$

Factors			*cos terms*
$+\frac{15}{2}(\gamma - 5\gamma^3 + 5\gamma^5)(\gamma'^3 - \gamma'^5)\sqrt{1-\gamma^2}\sqrt{1-\gamma'^2}$			$\tau = \omega$
$+\frac{15}{8}(1-\gamma^2)(1 - 10\gamma^2 + 15\gamma^4)(\gamma' - \gamma'^3)^2$			$\tau = \omega + \theta$
$+\frac{15}{8}(6\gamma^2 - 20\gamma^4 + 15\gamma^6)(\gamma'^4 - \gamma'^6)$			$\tau = \omega - \theta$
$-\frac{15}{4}(\gamma - 4\gamma^3 + 3\gamma^5)(\gamma' - 2\gamma'^3 + \gamma'^5)\sqrt{1-\gamma^2}\sqrt{1-\gamma'^2}$			$\tau = \omega + 2\theta$
$+\frac{15}{4}(2\gamma^3 - 3\gamma^5)\gamma'^5\sqrt{1-\gamma^2}\sqrt{1-\gamma'^2}$			$\tau = \omega - 2\theta$
$+\frac{15}{8}\gamma^2(1-\gamma^2)^2(1-\gamma'^2)^3$			$\tau = \omega + 3\theta$
$+\frac{15}{8}(\gamma^4 - \gamma^6)\gamma'^6$			$\tau = \omega - 3\theta$
	$+\frac{127}{8}e'^2 + \ldots$		$-5g' - 3\omega'$
	$+5e' + \ldots$		$-4g' - 3\omega'$
	$+1 - 6e'^2 + \ldots$		$-3g' - 3\omega'$
	$-e' + \ldots$		$-2g' - 3\omega'$
	$+\frac{1}{8}e'^2 + \ldots$		$-g' - 3\omega'$
	0 (exact)		$0.g' - 3\omega'$
$+\frac{11}{8}e^2 + \ldots$			$-g + \tau$
$-\frac{5}{2}e - \frac{15}{8}e^3$ (exact)			$0.g + \tau$
$+1 + 2e^2 + \ldots$			$+g + \tau$
$-\frac{1}{2}e + \ldots$			$+2g + \tau$
$-\frac{3}{8}e^2 + \ldots$			$+3g + \tau$

Type $a\Omega_{10}$

Factors	*cos terms*
$-\frac{15}{2}(\gamma^3-\gamma^5)(\gamma'-5\gamma'^3+5\gamma'^5)\sqrt{1-\gamma^2}\sqrt{1-\gamma'^2}$	$\tau = 3\omega$
$+\frac{15}{8}(\gamma-\gamma^3)^2(6\gamma'^2-20\gamma'^4+15\gamma'^6)$	$\tau = 3\omega+\theta$
$+\frac{15}{8}(\gamma^4-\gamma^6)(1-\gamma'^2)(1-10\gamma'^2+15\gamma'^4)$	$\tau = 3\omega-\theta$
$-\frac{15}{4}(\gamma-2\gamma^3+\gamma^5)(2\gamma'^3-3\gamma'^5)\sqrt{1-\gamma^2}\sqrt{1-\gamma'^2}$	$\tau = 3\omega+2\theta$
$+\frac{15}{4}\gamma^5(\gamma'-4\gamma'^3+3\gamma'^5)\sqrt{1-\gamma^2}\sqrt{1-\gamma'^2}$	$\tau = 3\omega-2\theta$
$+\frac{15}{8}(1-\gamma^2)^3(\gamma'^4-\gamma'^6)$	$\tau = 3\omega+3\theta$
$+\frac{15}{8}\gamma^6(\gamma'-\gamma'^3)^2$	$\tau = 3\omega-3\theta$

	$+\frac{11}{8}e'^2+\ldots$	$-g'+\omega'$
	$+e'+\ldots$	$0.g'+\omega'$
	$+1+2e'^2+\ldots$	$+g'+\omega'$
	$+3e'+\ldots$	$+2g'+\omega'$
	$+\frac{53}{8}e'^2+\ldots$	$+3g'+\omega'$
$-\frac{35}{8}e^3$ (exact)		$0.g+\tau$
$+\frac{57}{8}e^2+\ldots$		$+g+\tau$
$-\frac{9}{2}e+\ldots$		$+2g+\tau$
$+1-6e^2+\ldots$		$+3g+\tau$
$+\frac{3}{2}e+\ldots$		$+4g+\tau$
$+\frac{15}{8}e^2+\ldots$		$+5g+\tau$

Type $a\Omega_{11}$

Factors	*cos terms*
$+\frac{15}{2}(\gamma^3 - \gamma^5)(\gamma' - 5\gamma'^3 + 5\gamma'^5)\sqrt{1-\gamma^2}\sqrt{1-\gamma'^2}$	$\tau = 3\omega$
$+\frac{15}{8}(\gamma - \gamma^3)^2(1-\gamma'^2)(1 - 10\gamma'^2 + 15\gamma'^4)$	$\tau = 3\omega + \theta$
$+\frac{15}{8}(\gamma^4 - \gamma^6)(6\gamma'^2 - 20\gamma'^4 + 15\gamma'^6)$	$\tau = 3\omega - \theta$
$-\frac{15}{4}(\gamma - 2\gamma^3 + \gamma^5)(\gamma' - 4\gamma'^3 + 3\gamma'^5)\sqrt{1-\gamma^2}\sqrt{1-\gamma'^2}$	$\tau = 3\omega + 2\theta$
$+\frac{15}{4}\gamma^5(2\gamma'^3 - 3\gamma'^5)\sqrt{1-\gamma^2}\sqrt{1-\gamma'^2}$	$\tau = 3\omega - 2\theta$
$+\frac{15}{8}(1-\gamma^2)^3(\gamma' - \gamma'^3)^2$	$\tau = 3\omega + 3\theta$
$+\frac{15}{8}\gamma^6(\gamma'^4 - \gamma'^6)$	$\tau = 3\omega - 3\theta$

	$+\frac{53}{8}e'^2 + \ldots$	$-3g' - \omega'$
	$+3e' + \ldots$	$-2g' - \omega'$
	$+1 + 2e'^2 + \ldots$	$-g' - \omega'$
	$+e' + \ldots$	$0.g' - \omega'$
	$+\frac{11}{8}e'^2 + \ldots$	$+g' - \omega'$
$-\frac{35}{8}e^3$ (exact)		$0.g + \tau$
$+\frac{57}{8}e^2 + \ldots$		$+g + \tau$
$-\frac{9}{2}e + \ldots$		$+2g + \tau$
$+1 - 6e^2 + \ldots$		$+3g + \tau$
$+\frac{3}{2}e + \ldots$		$+4g + \tau$
$+\frac{15}{8}e^2 + \ldots$		$+5g + \tau$

Type $a\Omega_{12}$

Factors	*cos terms*
$-\frac{25}{2}(\gamma^3-\gamma^5)(\gamma'^3-\gamma'^5)\sqrt{1-\gamma^2}\sqrt{1-\gamma'^2}$	$\tau = 3\omega$
$+\frac{75}{8}(\gamma-\gamma^3)^2(\gamma'^4-\gamma'^6)$	$\tau = 3\omega+\theta$
$+\frac{75}{8}(\gamma^4-\gamma^6)(\gamma'-\gamma'^3)^2$	$\tau = 3\omega-\theta$
$-\frac{15}{4}(\gamma-2\gamma^3+\gamma^5)\gamma'^5\sqrt{1-\gamma^2}\sqrt{1-\gamma'^2}$	$\tau = 3\omega+2\theta$
$-\frac{15}{4}\gamma^5(\gamma'-2\gamma'^3+\gamma'^5)\sqrt{1-\gamma^2}\sqrt{1-\gamma'^2}$	$\tau = 3\omega-2\theta$
$+\frac{5}{8}(1-\gamma^2)^3\gamma'^6$	$\tau = 3\omega+3\theta$
$+\frac{5}{8}\gamma^6(1-\gamma'^2)^3$	$\tau = 3\omega-3\theta$

	0 (exact)	$0.g' + 3\omega'$
	$+\frac{1}{8}e'^2+\ldots$	$+g'+3\omega'$
	$-e'+\ldots$	$+2g'+3\omega'$
	$+1-6e'^2+\ldots$	$+3g'+3\omega'$
	$+5e'+\ldots$	$+4g'+3\omega'$
	$+\frac{127}{8}e'^2+\ldots$	$+5g'+3\omega'$
$-\frac{35}{8}e^3$ (exact)		$0.g+\tau$
$+\frac{57}{8}e^2+\ldots$		$+g+\tau$
$-\frac{9}{2}e+\ldots$		$+2g+\tau$
$+1-6e^2+\ldots$		$+3g+\tau$
$+\frac{3}{2}e+\ldots$		$+4g+\tau$
$+\frac{15}{8}e^2+\ldots$		$+5g+\tau$

Type $a\Omega_{13}$

Factors	*cos terms*
$+\frac{25}{2}(\gamma^3-\gamma^5)(\gamma'^3-\gamma'^5)\sqrt{1-\gamma^2}\sqrt{1-\gamma'^2}$	$\tau = 3\omega$
$+\frac{75}{8}(\gamma^2-2\gamma^4+\gamma^6)(\gamma'^2-2\gamma'^4+\gamma'^6)$	$\tau = 3\omega+\theta$
$+\frac{75}{8}(\gamma^4-\gamma^6)(\gamma'^4-\gamma'^6)$	$\tau = 3\omega-\theta$
$+\frac{15}{4}(\gamma-2\gamma^3+\gamma^5)(\gamma'-2\gamma'^3+\gamma'^5)\sqrt{1-\gamma^2}\sqrt{1-\gamma'^2}$	$\tau = 3\omega+2\theta$
$+\frac{15}{4}\gamma^5\gamma'^5\sqrt{1-\gamma^2}\sqrt{1-\gamma'^2}$	$\tau = 3\omega-2\theta$
$+\frac{5}{8}(1-\gamma^2)^3(1-\gamma'^2)^3$	$\tau = 3\omega+3\theta$
$+\frac{5}{8}\gamma^6\gamma'^6$	$\tau = 3\omega-3\theta$

	$+\frac{127}{8}e'^2+\ldots$	$-5g'-3\omega'$
	$+5e'+\ldots$	$-4g'-3\omega'$
	$+1-6e'^2+\ldots$	$-3g'-3\omega'$
	$-e'+\ldots$	$-2g'-3\omega'$
	$+\frac{1}{8}e'^2+\ldots$	$-g'-3\omega'$
	0 (exact)	$0.g'-3\omega'$
$-\frac{35}{8}e^3$ (exact)		$0.g+\tau$
$+\frac{57}{8}e^2+\ldots$		$+\varsigma+\tau$
$-\frac{9}{2}e+\ldots$		$+2g+\tau$
$+1-6e^2+\ldots$		$+3g+\tau$
$+\frac{3}{2}e+\ldots$		$+4g+\tau$
$+\frac{15}{8}e^2+\ldots$		$+5g+\tau$

However, in the case of the existing artificial satellites only the long-period terms are kept. The first power of e' is kept only in the second Legendre polynomial, because of the presence of the additional power of a/a' in the parallactic term. The accuracy of the coefficients of cos $(0.g + 2\tau)$ makes the resulting development of the disturbing function valid for all eccentricities and all inclinations, provided the ratio a/a' is small enough to secure fast convergence of the development of Equation 2. Thus we have the following:

Type $a[\Omega]_1$

Factors	*cos terms*
$+ \frac{1}{4}(1 - 6\gamma^2 + 6\gamma^4)(1 - 6\gamma'^2 + 6\gamma'^4)\left(1 + \frac{3}{2}e^2\right),$	$2\tau = 0$
$+ 3(\gamma^2 - \gamma^4)(\gamma'^2 - \gamma'^4)\left(1 + \frac{3}{2}e^2\right),$	$2\tau = 2\theta$
$+ 3(\gamma - 2\gamma^3)(\gamma' - 2\gamma'^3)\sqrt{1-\gamma^2}\sqrt{1-\gamma'^2}\left(1 + \frac{3}{2}e^2\right),$	$2\tau = \theta$

Multiplied by

$$+ \frac{3}{2}e' \cos(2\tau - g') + (1 - e'^2)^{-3/2}\cos 2\tau^{(*)} + \frac{3}{2}e' \cos(2\tau + g').$$

Type $a[\Omega]_2$

Factors	*cos terms*
$+ \frac{9}{2}(\gamma^2 - \gamma^4)(\gamma'^2 - \gamma'^4)\cdot\frac{5}{2}e^2,$	$2\tau = 2\omega$
$+ \frac{3}{4}(1 - \gamma^2)^2(1 - \gamma'^2)^2\cdot\frac{5}{2}e^2,$	$2\tau = 2\omega + 2\theta$
$+ \frac{3}{4}\gamma^4\gamma'^4\cdot\frac{5}{2}e^2,$	$2\tau = 2\omega - 2\theta$
$+ 3(\gamma - \gamma^3)(\gamma' - \gamma'^3)\sqrt{1-\gamma^2}\sqrt{1-\gamma'^2}\cdot\frac{5}{2}e^2,$	$2\tau = 2\omega + \theta$
$+ 3\gamma^3\gamma'^3\sqrt{1-\gamma^2}\sqrt{1-\gamma'^2}\cdot\frac{5}{2}e^2,$	$2\tau = 2\omega - \theta$

Multiplied by

$$+ \frac{7}{2}e' \cos(2\tau - 3g' - 2\omega') + \cos(2\tau - 2g' - 2\omega') - \frac{1}{2}e' \cos(2\tau - g' - 2\omega').$$

*The second term becomes a secular one for $2\tau = 0$.

Type $a[\Omega]_3$

Factors	*cos terms*
$+\frac{3}{2}(\gamma^2-\gamma^4)(1-6\gamma'^2+6\gamma'^4)\cdot\frac{5}{2}e^2,$	$2\tau = 2\omega$
$+\frac{3}{2}(1-\gamma^2)^2(\gamma'^2-\gamma'^4)\cdot\frac{5}{2}e^2,$	$2\tau = 2\omega + 2\theta$
$+\frac{3}{2}\gamma^4(\gamma'^2-\gamma'^4)\cdot\frac{5}{2}e^2,$	$2\tau = 2\omega - 2\theta$
$-3(\gamma-\gamma^3)(\gamma'-2\gamma'^3)\sqrt{1-\gamma^2}\sqrt{1-\gamma'^2}\cdot\frac{5}{2}e^2,$	$2\tau = 2\omega + \theta$
$+3\gamma^3(\gamma'-2\gamma'^3)\sqrt{1-\gamma^2}\sqrt{1-\gamma'^2}\cdot\frac{5}{2}e^2,$	$2\tau = 2\omega - \theta$

Multiplied by

$$+\frac{3}{2}e'\cos(2\tau - g') + \cos 2\tau + \frac{3}{2}e'\cos(2\tau + g').$$

Type $a[\Omega]_4$

Factors	*cos terms*
$+\frac{3}{2}(1-6\gamma^2+6\gamma^4)(\gamma'^2-\gamma'^4)\cdot\left(1+\frac{3}{2}e^2\right),$	$2\tau = 2\omega'$
$+\frac{3}{2}(\gamma^2-\gamma^4)\gamma'^4\cdot\left(1+\frac{3}{2}e^2\right),$	$2\tau = 2\omega' + 2\theta$
$+\frac{3}{2}(\gamma^2-\gamma^4)(1-\gamma'^2)^2\cdot\left(1+\frac{3}{2}e^2\right),$	$2\tau = 2\omega' - 2\theta$
$+3(\gamma-2\gamma^3)\gamma'^3\sqrt{1-\gamma^2}\sqrt{1-\gamma'^2}\cdot\left(1+\frac{3}{2}e^2\right),$	$2\tau = 2\omega' + \theta$
$-3(\gamma-2\gamma^3)(\gamma'-\gamma'^3)\sqrt{1-\gamma^2}\cdot\sqrt{1-\gamma'^2}\cdot\left(1+\frac{3}{2}e^2\right),$	$2\tau = 2\omega' - \theta$

Multiplied by

$$-\frac{1}{2}e'\cos(2\tau + g') + \cos(2\tau + 2g') + \frac{7}{2}e'\cos(2\tau + 3g').$$

Type $a[\Omega]_5$

Factors	*cos terms*
$+\frac{9}{2}(\gamma^2-\gamma^4)(\gamma'^2-\gamma'^4)\cdot\frac{5}{2}e^2,$	$2\tau = 2\omega + 2\omega'$
$+\frac{3}{4}(1-\gamma^2)^2\gamma'^4\cdot\frac{5}{2}e^2,$	$2\tau = 2\omega + 2\theta + 2\omega'$
$+\frac{3}{4}\gamma^4(1-\gamma'^2)^2\cdot\frac{5}{2}e^2,$	$2\tau = 2\omega - 2\theta + 2\omega'$
$-3(\gamma-\gamma^3)\gamma'^3\sqrt{1-\gamma^2}\cdot\sqrt{1-\gamma'^2}\cdot\frac{5}{2}e^2,$	$2\tau = 2\omega + \theta + 2\omega'$
$-3\gamma^3(\gamma'-\gamma'^3)\sqrt{1-\gamma^2}\cdot\sqrt{1-\gamma'^2}\cdot\frac{5}{2}e^2,$	$2\tau = 2\omega - \theta + 2\omega'$

Multiplied by

$$-\frac{1}{2}e'\cos(2\tau + g') + \cos(2\tau + 2g') + \frac{7}{2}e'\cos(2\tau + 3g').$$

Type $a[\Omega]_6$

Factors	*cos terms*
$-\frac{9}{2}(\gamma - 5\gamma^3 + 5\gamma^5)(\gamma' - 5\gamma'^3 + 5\gamma'^5)\sqrt{1-\gamma^2}\sqrt{1-\gamma'^2}\cdot\left(-\frac{5}{2}e - \frac{15}{8}e^3\right)$,	$\tau = \omega$
$+\frac{3}{8}(1-\gamma^2)(1 - 10\gamma^2 + 15\gamma^4)(6\gamma'^2 - 20\gamma'^4 + 15\gamma'^6)\cdot\left(-\frac{5}{2}e - \frac{15}{8}e^3\right)$,	$\tau = \omega + \theta$
$+\frac{3}{8}(6\gamma^2 - 20\gamma^4 + 15\gamma^6)(1-\gamma'^2)(1 - 10\gamma'^2 + 15\gamma'^4)\cdot\left(-\frac{5}{2}e - \frac{15}{8}e^3\right)$,	$\tau = \omega - \theta$
$+\frac{15}{4}(\gamma - 4\gamma^3 + 3\gamma^5)(2\gamma'^3 - 3\gamma'^5)\sqrt{1-\gamma^2}\sqrt{1-\gamma'^2}\cdot\left(-\frac{5}{2}e - \frac{15}{8}e^3\right)$,	$\tau = \omega + 2\theta$
$+\frac{15}{4}(2\gamma^3 - 3\gamma^5)(\gamma' - 4\gamma'^3 + 3\gamma'^5)\sqrt{1-\gamma^2}\sqrt{1-\gamma'^2}\cdot\left(-\frac{5}{2}e - \frac{15}{8}e^3\right)$,	$\tau = \omega - 2\theta$
$+\frac{45}{8}(\gamma^2 - 2\gamma^4 + \gamma^6)(\gamma'^4 - \gamma'^6)\cdot\left(-\frac{5}{2}e - \frac{15}{8}e^3\right)$,	$\tau = \omega + 3\theta$
$+\frac{45}{8}(\gamma^4 - \gamma^6)(\gamma'^2 - 2\gamma'^4 + \gamma'^6)\cdot\left(-\frac{5}{2}e - \frac{15}{8}e^3\right)$,	$\tau = \omega - 3\theta$

Multiplied by

$$+\cos(\tau + g' + \omega').$$

Type $a[\Omega]_7$

Factors	*cos terms*
$+\frac{9}{2}(\gamma - 5\gamma^3 + 5\gamma^5)(\gamma' - 5\gamma'^3 + 5\gamma'^5)\sqrt{1-\gamma^2}\sqrt{1-\gamma'^2}\cdot\left(-\frac{5}{2}e - \frac{15}{8}e^3\right)$,	$\tau = \omega$
$+\frac{3}{8}(1-\gamma^2)(1 - 10\gamma^2 + 15\gamma^4)(1-\gamma'^2)(1 - 10\gamma'^2 + 15\gamma'^4)\cdot\left(-\frac{5}{2}e - \frac{15}{8}e^3\right)$,	$\tau = \omega + \theta$
$+\frac{3}{8}(6\gamma^2 - 20\gamma^4 + 15\gamma^6)(6\gamma'^2 - 20\gamma'^4 + 15\gamma'^6)\cdot\left(-\frac{5}{2}e - \frac{15}{8}e^3\right)$,	$\tau = \omega - \theta$
$+\frac{15}{4}(\gamma - 4\gamma^3 + 3\gamma^5)(\gamma' - 4\gamma'^3 + 3\gamma'^5)\sqrt{1-\gamma^2}\sqrt{1-\gamma'^2}\cdot\left(-\frac{5}{2}e - \frac{15}{8}e^3\right)$,	$\tau = \omega + 2\theta$
$+\frac{15}{4}(2\gamma^3 - 3\gamma^5)(2\gamma'^3 - 3\gamma'^5)\sqrt{1-\gamma^2}\sqrt{1-\gamma'^2}\cdot\left(-\frac{5}{2}e - \frac{15}{8}e^3\right)$,	$\tau = \omega - 2\theta$
$+\frac{45}{8}(\gamma^2 - 2\gamma^4 + \gamma^6)(\gamma'^2 - 2\gamma'^4 + \gamma'^6)\cdot\left(-\frac{5}{2}e - \frac{15}{8}e^3\right)$,	$\tau = \omega + 3\theta$
$+\frac{45}{8}(\gamma^4 - \gamma^6)(\gamma'^4 - \gamma'^6)\cdot\left(-\frac{5}{2}e - \frac{15}{8}e^3\right)$,	$\tau = \omega - 3\theta$

Multiplied by

$$+\cos(\tau - g' - \omega').$$

Type $a[\Omega]_8$

Factors	*cos terms*
$-\frac{15}{2}(\gamma - 5\gamma^3 + 5\gamma^5)(\gamma'^3 - \gamma'^5)\sqrt{1-\gamma^2}\sqrt{1-\gamma'^2}\cdot\left(-\frac{5}{2}e - \frac{15}{8}e^3\right),$	$\tau = \omega$
$+\frac{15}{8}(1-\gamma^2)(1 - 10\gamma^2 + 15\gamma^4)(\gamma'^4 - \gamma'^6)\cdot\left(-\frac{5}{2}e - \frac{15}{8}e^3\right),$	$\tau = \omega + \theta$
$+\frac{15}{8}(6\gamma^2 - 20\gamma^4 + 15\gamma^6)(\gamma' - \gamma'^3)^2\cdot\left(-\frac{5}{2}e - \frac{15}{8}e^3\right),$	$\tau = \omega - \theta$
$+\frac{15}{4}(\gamma - 4\gamma^3 + 3\gamma^5)\gamma'^5\sqrt{1-\gamma^2}\sqrt{1-\gamma'^2}\cdot\left(-\frac{5}{2}e - \frac{15}{8}e^3\right),$	$\tau = \omega + 2\theta$
$-\frac{15}{4}(2\gamma^3 - 3\gamma^5)\gamma'(1-\gamma'^2)^2\sqrt{1-\gamma^2}\sqrt{1-\gamma'^2}\cdot\left(-\frac{5}{2}e - \frac{15}{8}e^3\right),$	$\tau = \omega - 2\theta$
$+\frac{15}{8}(\gamma - \gamma^3)^2\gamma'^6\cdot\left(-\frac{5}{2}e - \frac{15}{8}e^3\right),$	$\tau = \omega + 3\theta$
$+\frac{15}{8}(\gamma^4 - \gamma^6)(1-\gamma'^2)^3\cdot\left(-\frac{5}{2}e - \frac{15}{8}e^3\right),$	$\tau = \omega - 3\theta$

Multiplied by

$$+\cos(\tau + 3g' + 3\omega').$$

Type $a[\Omega]_9$

Factors	*cos terms*
$+\frac{15}{2}(\gamma - 5\gamma^3 + 5\gamma^5)(\gamma'^3 - \gamma'^5)\sqrt{1-\gamma^2}\sqrt{1-\gamma'^2}\cdot\left(-\frac{5}{2}e - \frac{15}{8}e^3\right),$	$\tau = \omega$
$+\frac{15}{8}(1-\gamma^2)(1 - 10\gamma^2 + 15\gamma^4)(\gamma' - \gamma'^3)^2\cdot\left(-\frac{5}{2}e - \frac{15}{8}e^3\right),$	$\tau = \omega + \theta$
$+\frac{15}{8}(6\gamma^2 - 20\gamma^4 + 15\gamma^6)(\gamma'^4 - \gamma'^6)\cdot\left(-\frac{5}{2}e - \frac{15}{8}e^3\right),$	$\tau = \omega - \theta$
$-\frac{15}{4}(\gamma - 4\gamma^3 + 3\gamma^5)(\gamma' - 2\gamma'^3 + \gamma'^5)\sqrt{1-\gamma^2}\sqrt{1-\gamma'^2}\cdot\left(-\frac{5}{2}e - \frac{15}{8}e^3\right),$	$\tau = \omega + 2\theta$
$+\frac{15}{4}(2\gamma^3 - 3\gamma^5)\gamma'^5\sqrt{1-\gamma^2}\sqrt{1-\gamma'^2}\cdot\left(-\frac{5}{2}e - \frac{15}{8}e^3\right),$	$\tau = \omega - 2\theta$
$+\frac{15}{8}\gamma^2(1-\gamma^2)^2(1-\gamma'^2)^3\cdot\left(-\frac{5}{2}e - \frac{15}{8}e^3\right),$	$\tau = \omega + 3\theta$
$+\frac{15}{8}(\gamma^4 - \gamma^6)\gamma'^6\cdot\left(-\frac{5}{2}e - \frac{15}{8}e^3\right),$	$\tau = \omega - 3\theta$

Multiplied by

$$+\cos(\tau - 3g' - 3\omega').$$

Type $a[\Omega]_{10}$

Factors	*cos terms*
$-\frac{15}{2}(\gamma^3-\gamma^5)(\gamma'-5\gamma'^3+5\gamma'^5)\sqrt{1-\gamma^2}\sqrt{1-\gamma'^2}\cdot\left(-\frac{35}{8}e^3\right),$	$\tau=3\omega$
$+\frac{15}{8}(\gamma-\gamma^3)^2(6\gamma'^2-20\gamma'^4+15\gamma'^6)\cdot\left(-\frac{35}{8}e^3\right),$	$\tau=3\omega+\theta$
$+\frac{15}{8}(\gamma^4-\gamma^6)(1-\gamma'^2)(1-10\gamma'^2+15\gamma'^4)\cdot\left(-\frac{35}{8}e^3\right),$	$\tau=3\omega-\theta$
$-\frac{15}{4}(\gamma-2\gamma^3+\gamma^5)(2\gamma'^3-3\gamma'^5)\sqrt{1-\gamma^2}\sqrt{1-\gamma'^2}\cdot\left(-\frac{35}{8}e^3\right),$	$\tau=3\omega+2\theta$
$+\frac{15}{4}\gamma^5(\gamma'-4\gamma'^3+3\gamma'^5)\sqrt{1-\gamma^2}\sqrt{1-\gamma'^2}\cdot\left(-\frac{35}{8}e^3\right),$	$\tau=3\omega-2\theta$
$+\frac{15}{8}(1-\gamma^2)^3(\gamma'^4-\gamma'^6)\cdot\left(-\frac{35}{8}e^3\right),$	$\tau=3\omega+3\theta$
$+\frac{15}{8}\gamma^6(\gamma'-\gamma'^3)^2\cdot\left(-\frac{35}{8}e^3\right),$	$\tau=3\omega-3\theta$

Multiplied by

$$+\cos(\tau+g'+\omega').$$

Type $a[\Omega]_{11}$

Factors	*cos terms*
$+\frac{15}{2}(\gamma^3-\gamma^5)(\gamma'-5\gamma'^3+5\gamma'^5)\sqrt{1-\gamma^2}\sqrt{1-\gamma'^2}\cdot\left(-\frac{35}{8}e^3\right),$	$\tau=3\omega$
$+\frac{15}{8}(\gamma-\gamma^3)^2(1-\gamma'^2)(1-10\gamma'^2+15\gamma'^4)\cdot\left(-\frac{35}{8}e^3\right),$	$\tau=3\omega+\theta$
$+\frac{15}{8}(\gamma^4-\gamma^6)(6\gamma'^2-20\gamma'^4+15\gamma'^6)\cdot\left(-\frac{35}{8}e^3\right),$	$\tau=3\omega-\theta$
$-\frac{15}{4}(\gamma-2\gamma^3+\gamma^5)(\gamma'-4\gamma'^3+3\gamma'^5)\sqrt{1-\gamma^2}\sqrt{1-\gamma'^2}\cdot\left(-\frac{35}{8}e^3\right),$	$\tau=3\omega+2\theta$
$+\frac{15}{4}\gamma^5(2\gamma'^3-3\gamma'^5)\sqrt{1-\gamma^2}\sqrt{1-\gamma'^2}\cdot\left(-\frac{35}{8}e^3\right),$	$\tau=3\omega-2\theta$
$+\frac{15}{8}(1-\gamma^2)^3(\gamma'-\gamma'^3)^2\cdot\left(-\frac{35}{8}e^3\right),$	$\tau=3\omega+3\theta$
$+\frac{15}{8}\gamma^6(\gamma'^4-\gamma'^6)\cdot\left(-\frac{35}{8}e^3\right),$	$\tau=3\omega-3\theta$

Multiplied by

$$+\cos(\tau-g'-\omega').$$

Type $a[\Omega]_{12}$

Factors	*cos terms*
$-\frac{25}{2}(\gamma^3-\gamma^5)(\gamma'^3-\gamma'^5)\sqrt{1-\gamma^2}\sqrt{1-\gamma'^2}\cdot\left(-\frac{35}{8}e^3\right),$	$\tau = 3\omega$
$+\frac{75}{8}(\gamma-\gamma^3)^2(\gamma'^4-\gamma'^6)\cdot\left(-\frac{35}{8}e^3\right),$	$\tau = 3\omega+\theta$
$+\frac{75}{8}(\gamma^4-\gamma^6)(\gamma'-\gamma'^3)^2\cdot\left(-\frac{35}{8}e^3\right),$	$\tau = 3\omega-\theta$
$-\frac{15}{4}(\gamma-2\gamma^3+\gamma^5)\gamma'^5\sqrt{1-\gamma^2}\sqrt{1-\gamma'^2}\cdot\left(-\frac{35}{8}e^3\right),$	$\tau = 3\omega+2\theta$
$-\frac{15}{4}\gamma^5(\gamma'-2\gamma'^3+\gamma'^5)\sqrt{1-\gamma^2}\sqrt{1-\gamma'^2}\cdot\left(-\frac{35}{8}e^3\right),$	$\tau = 3\omega-2\theta$
$+\frac{5}{8}(1-\gamma^2)^3\gamma'^6\cdot\left(-\frac{35}{8}e^3\right),$	$\tau = 3\omega+3\theta$
$+\frac{5}{8}\gamma^6(1-\gamma'^2)^3\cdot\left(-\frac{35}{8}e^3\right),$	$\tau = 3\omega-3\theta$

Multiplied by

$$+\cos(\tau+3g'+3\omega').$$

Type $a[\Omega]_{13}$

Factors	*cos terms*
$+\frac{25}{2}(\gamma^3-\gamma^5)(\gamma'^3-\gamma'^5)\sqrt{1-\gamma^2}\sqrt{1-\gamma'^2}\cdot\left(-\frac{35}{8}e^3\right),$	$\tau = 3\omega$
$+\frac{75}{8}(\gamma^2-2\gamma^4+\gamma^6)(\gamma'^2-2\gamma'^4+\gamma'^6)\cdot\left(-\frac{35}{8}e^3\right),$	$\tau = 3\omega+\theta$
$+\frac{75}{8}(\gamma^4-\gamma^6)(\gamma'^4-\gamma'^6)\cdot\left(-\frac{35}{8}e^3\right),$	$\tau = 3\omega-\theta$
$+\frac{15}{4}(\gamma-2\gamma^3+\gamma^5)(\gamma'-2\gamma'^3+\gamma'^5)\sqrt{1-\gamma^2}\sqrt{1-\gamma'^2}\cdot\left(-\frac{35}{8}e^3\right),$	$\tau = 3\omega+2\theta$
$+\frac{15}{4}\gamma^5\gamma'^5\sqrt{1-\gamma^2}\sqrt{1-\gamma'^2}\cdot\left(-\frac{35}{8}e^3\right),$	$\tau = 3\omega-2\theta$
$+\frac{5}{8}(1-\gamma^2)^3(1-\gamma'^2)^3\cdot\left(-\frac{35}{8}e^3\right),$	$\tau = 3\omega+3\theta$
$+\frac{5}{8}\gamma^6\gamma'^6\cdot\left(-\frac{35}{8}e^3\right),$	$\tau = 3\omega-3\theta$

Multiplied by

$$+\cos(\tau-3g'-3\omega').$$

The standard equations for variations of elliptic elements may be used in connection with this development. In particular, for the variation of the perigee height the equation is

$$\frac{d\delta q}{dt} = \frac{\sqrt{1-e^2}}{na^2e}\frac{\partial a\Omega}{\partial \omega}.$$

The proposed scheme leads to a form of the development which is standard in celestial mechanics. It differs from Kozai's scheme only by arrangement. The following method was used to obtain the development on the automatic computing machine:

$$\begin{aligned} G = {} & \cos^2\frac{i}{2}\ \cos^2\frac{i'}{2}\cos(\omega+\theta-g'-\omega') \\ & + \sin^2\frac{i}{2}\ \cos^2\frac{i'}{2}\cos(\omega-\theta+g'+\omega') \\ & + \cos^2\frac{i}{2}\ \sin^2\frac{i'}{2}\cos(\omega+\theta+g'+\omega') \\ & + \sin^2\frac{i}{2}\ \sin^2\frac{i'}{2}\cos(\omega-\theta-g'-\omega') \\ & + \frac{1}{2}\sin i\cdot\sin i'\ \cos(\omega-g'-\omega') \\ & - \frac{1}{2}\sin i\cdot\sin i'\ \cos(\omega+g'+\omega'). \end{aligned}$$

Then,

$$H = G + 2\frac{\partial G}{\partial g'}e'\sin g' = G + \frac{\partial G}{\partial g'}(f'-g'),$$

$$\begin{aligned} K &= \left(\frac{3}{2}H^2-\frac{1}{2}\right)(1+3e'\cos g') + \left(\frac{5}{2}H^3-\frac{3}{2}H\right)(1+4e'\cos g') \\ &= \left(\frac{3}{2}H^2-\frac{1}{2}\right)\left(\frac{a'}{r'}\right)^3 + \left(\frac{5}{2}H^3-\frac{3}{2}H\right)\left(\frac{a'}{r'}\right)^4. \end{aligned}$$

The terms of K are then sorted into four groups according to the coefficient of ω in their arguments: the 2ω terms are multiplied by $\left(+\frac{5}{2}e^2\right)$; the $0\cdot\omega$ terms are multiplied by $\left(1+\frac{3}{2}e^2\right)$; the $1\cdot\omega$ terms are multiplied by $\left(-\frac{5}{2}e-\frac{15}{8}e^3\right)$; and the 3ω terms are multiplied by $\left(-\frac{35}{8}e^3\right)$.

In order to include the main effect of the lunar and solar perturbations in the method used at the NASA Space Computing Center (Reference 6), the development of the disturbing function must be obtained in terms of the eccentric anomaly ξ of the satellite. By keeping the second harmonic only and using the formula

$$\begin{aligned} \left(\frac{r}{a}\right)^2\cos(2f+2\tau) = {} & (1+\beta^2)^{-2}\{\beta^4\cos(-2\xi+2\tau) \\ & - 4\beta^3\cos(-\xi+2\tau) + 6\beta^2\cos 2\tau \\ & - 4\beta\cos(+\xi+2\tau) + \cos(+2\xi+2\tau)\}, \end{aligned}$$

the following computational scheme is obtained. This scheme is valid for all eccentricities and all inclinations. The common factor $(m'a^3/a'^3)(1+\beta^2)^{-2}$ is omitted.

Type $a\Omega_1$

Factors	*cos terms*
$+\frac{1}{4}(1-6\gamma^2+6\gamma^4)(1-6\gamma'^2+6\gamma'^4),$	$2\tau = 0$
$+3(\gamma^2-\gamma^4)(\gamma'^2-\gamma'^4),$	$2\tau = 2\theta$
$+3(\gamma-2\gamma^3)(\gamma'-2\gamma'^3)\sqrt{1-\gamma^2}\sqrt{1-\gamma'^2}$	$2\tau = \theta$

	$+\frac{3}{2}e' + \ldots$ $(1-e'^2)^{-3/2}$ $+\frac{3}{2}e'$	$-g'$ $0.g'$ $+g'$
$+\beta^2$		$-2\xi+2\tau$
$-2\beta-2\beta^3$		$-\xi+2\tau$
$1+4\beta^2+\beta^4$		$0.\xi+2\tau$
$-2\beta-2\beta^3$		$+\xi+2\tau$
$+\beta^2$		$+2\xi+2\tau$

Type $a\Omega_2$

Factors	*cos terms*
$+\frac{9}{2}(\gamma^2-\gamma^4)(\gamma'^2-\gamma'^4),$	$2\tau = 2\omega$
$+\frac{3}{4}(1-\gamma^2)^2(1-\gamma'^2)^2,$	$2\tau = 2\omega + 2\theta$
$+\frac{3}{4}\gamma^4\gamma'^4,$	$2\tau = 2\omega - 2\theta$
$+3(\gamma-\gamma^3)(\gamma'-\gamma'^3)\sqrt{1-\gamma^2}\sqrt{1-\gamma'^2},$	$2\tau = 2\omega + \theta$
$+3\gamma^3\gamma'^3\sqrt{1-\gamma^2}\sqrt{1-\gamma'^2},$	$2\tau = 2\omega - \theta$

	$+\frac{7}{2}e' + \ldots$ $1-\frac{5}{2}e'^2 + \ldots$ $-\frac{1}{2}e' + \ldots$	$-3g'-2\omega'$ $-2g'-2\omega'$ $-g'-2\omega'$
$+\beta^4$		$-2\xi+2\tau$
$-4\beta^3$		$-\xi+2\tau$
$+6\beta^2$		$0.\xi+2\tau$
-4β		$+\xi+2\tau$
$+1$		$+2\xi+2\tau$

Type $a\Omega_3$

Factors	*cos terms*
$+\frac{3}{2}(\gamma^2 - \gamma^4)(1 - 6\gamma'^2 + 6\gamma'^4),$	$2\tau = 2\omega$
$+\frac{3}{2}(1 - \gamma^2)^2(\gamma'^2 - \gamma'^4),$	$2\tau = 2\omega + 2\theta$
$+\frac{3}{2}\gamma^4(\gamma'^2 - \gamma'^4),$	$2\tau = 2\omega - 2\theta$
$-3(\gamma - \gamma^3)(\gamma' - 2\gamma'^3)\sqrt{1-\gamma^2}\sqrt{1-\gamma'^2},$	$2\tau = 2\omega + \theta$
$+3\gamma^3(\gamma' - 2\gamma'^3)\sqrt{1-\gamma^2}\sqrt{1-\gamma'^2},$	$2\tau = 2\omega - \theta$

	$+\frac{3}{2}e' + \ldots$	$-g'$
	$1 + \frac{3}{2}e'^2 + \ldots$	$0.g'$
	$+\frac{3}{2}e' + \ldots$	$+g'$
$+\beta^4$		$-2\xi + 2\tau$
$-4\beta^3$		$-\xi + 2\tau$
$+6\beta^2$		$0.\xi + 2\tau$
-4β		$+\xi + 2\tau$
$+1$		$+2\xi + 2\tau$

Type $a\Omega_4$

Factors	*cos terms*
$+\frac{3}{2}(1-6\gamma^2+6\gamma^4)(\gamma'^2-\gamma'^4),$	$2\tau = 2\omega'$
$+\frac{3}{2}(\gamma^2-\gamma^4)\gamma'^4,$	$2\tau = 2\omega' + 2\theta$
$+\frac{3}{2}(\gamma^2-\gamma^4)(1-\gamma'^2)^2,$	$2\tau = 2\omega' - 2\theta$
$+3(\gamma-2\gamma^3)\gamma'^3\sqrt{1-\gamma^2}\sqrt{1-\gamma'^2},$	$2\tau = 2\omega' + \theta$
$-3(\gamma-2\gamma^3)(\gamma'-\gamma'^3)\sqrt{1-\gamma^2}\sqrt{1-\gamma'^2},$	$2\tau = 2\omega' - \theta$

	0 (exact)	$0.g'$
	$-\frac{1}{2}e' + \ldots$	$+ g'$
	$1-\frac{5}{2}e'^2 + \ldots$	$+ 2g'$
	$+\frac{7}{2}e' + \ldots$	$+ 3g'$
$+\beta^2$		$-2\xi + 2\tau$
$-2\beta - 2\beta^3$		$-\xi + 2\tau$
$1 + 4\beta^2 + \beta^4$		$0.\xi + 2\tau$
$-2\beta - 2\beta^3$		$+\xi + 2\tau$
$+\beta^2$		$+2\xi + 2\tau$

Type $a\Omega_5$

Factors	*cos terms*
$+\frac{9}{2}(\gamma^2 - \gamma^4)(\gamma'^2 - \gamma'^4)$,	$2\tau = 2\omega + 2\omega'$
$+\frac{3}{4}(1 - \gamma^2)^2\gamma'^4$,	$2\tau = 2\omega + 2\theta + 2\omega'$
$+\frac{3}{4}\gamma^4(1 - \gamma'^2)^2$,	$2\tau = 2\omega - 2\theta + 2\omega'$
$-3(\gamma - \gamma^3)\gamma'^3\sqrt{1-\gamma^2}\sqrt{1-\gamma'^2}$,	$2\tau = 2\omega + \theta + 2\omega'$
$-3\gamma^3(\gamma' - \gamma'^3)\sqrt{1-\gamma^2}\sqrt{1-\gamma'^2}$,	$2\tau = 2\omega - \theta + 2\omega'$

	0 (exact)	$0.g'$
	$-\frac{1}{2}e' + \ldots$	$+ g'$
	$1 - \frac{5}{2}e'^2 + \ldots$	$+ 2g'$
	$+\frac{7}{2}e' + \ldots$	$+ 3g'$
$+\beta^4$		$-2\xi + 2\tau$
$-4\beta^3$		$-\xi + 2\tau$
$+6\beta^2$		$0.\xi + 2\tau$
-4β		$+\xi + 2\tau$
$+1$		$+2\xi + 2\tau$

THE INTEGRATION PROBLEM

The method used at the NASA Space Computing Center is based on Hansen's idea of separating the perturbations *in* the orbit plane from the perturbations *of* the orbit plane. A typical differential equation of the method takes the form

$$\frac{dQ}{dE} = \sum A^{\cos}_{\sin}\,\alpha,$$

$$\alpha = iE + j\omega + k\Omega + i'g' + j'\omega' + k'\Omega' + pF,$$

where F is considered as a constant and

$$\omega = \omega_0 + \omega_1(E - E_0), \qquad g' = g_0' + n'(t - t_0),$$
$$\Omega = \Omega_0 + \Omega_1(E - E_0), \qquad \omega' = \omega_0' + n'\omega_1'(t - t_0),$$
$$\Omega' = \Omega_0' + n'\Omega_1'(t - t_0).$$

The time t can be eliminated by means of Kepler's equation,

$$E - e \sin E = g = g_0 + n(t - t_0);$$

and, after several transformations involving Bessel functions, the right-hand side can be reduced to an integrable form. However, instead of this complicated method, the integration can be performed in such a way that E and g' are both kept in the argument. A similar method was used by Hansen (Reference 7) in his development of the perturbations of Encke's comet by Saturn.

From Kepler's equation and from

$$g' = g_0' + n'(t - t_0)$$

it can be deduced that

$$\frac{dg'}{d\xi} = m(1 - e\cos\xi) \left(\text{where } m = \frac{n'}{n}\right),$$

and

$$\frac{dQ}{d\xi} = \frac{\partial Q}{\partial \xi} + \frac{\partial Q}{\partial g'} \cdot \frac{dg'}{dt} = \frac{\partial Q}{\partial \xi} + m\frac{\partial Q}{\partial g'}(1 - e\cos\xi).$$

Thus the problem is reduced to the integration of the linear partial differential equation

$$\frac{\partial Q}{\partial \xi} + m(1 - e\cos\xi)\frac{\partial Q}{\partial g'} = \sum A^{\cos}_{\sin}\,\alpha = X.$$

We can consider the equation

$$\frac{\partial Q}{\partial \xi} + m\frac{\partial Q}{\partial g'} = X + m_1 e\frac{\partial Q}{\partial g'}\cos\xi,$$

and replace m_1 by m after the integration is completed. By assuming that me is small (at the present time it does not exceed 0.02), the solution can be developed in powers of the small parameter. Putting

$$Q = Q_0 + m_1 Q_1 + m_1^2 Q_2 + \ldots$$

gives

$$\frac{\partial Q_0}{\partial \xi} + m\frac{\partial Q_0}{\partial g'} = X$$

and

$$\frac{\partial Q_i}{\partial \xi} + m\frac{\partial Q_i}{\partial g'} = \frac{\partial Q_{i-1}}{\partial g'}\cos\xi, \qquad (i = 1, 2, 3, \ldots).$$

Evidently

$$Q_0 = \sum \frac{\pm A^{\sin}_{\cos}\,\alpha}{(i + j\omega_1 + k\Omega_1) + m(i' + j'\omega_1 + k\Omega_1')}. \qquad (8)$$

At any step an equation will be obtained that is of the same general form as for Q_0, and Equation 8 can be applied to obtain the corresponding Q_i.

The same method can serve to develop the Hansen-type theory of natural planetary satellites, provided me is small enough to secure reasonably rapid convergence. For example, for the X^{th} satellite of Jupiter the value is 0.004. In developing the theory of the planetary satellites, the orbit plane of the planet can be taken as a basic reference plane and expressed as $\gamma' = 0$. This circumstance requires a change only in the lower part of Cayley's development (Reference 5), namely, replacing the development in terms of g by the development in terms of E. The remaining part of the theory will be similar to that given in the first part of this report.

By using the described methods, the analytical or numerical extension of the development can be done easily by modifying Cayley's scheme or by taking a numerical development of $r \cdot r'$ in an adequate form.

APPLICATION OF THE THEORY TO VANGUARD I AND EXPLORER VI

An abbreviated version of the terms $a\Omega_1$ to $a\Omega_5$ was programed for the IBM 704. This program was used to compute the perturbations of the perigee height for the satellites Vanguard I and Explorer VI. The results for Explorer VI give general qualitative information about the variations in perigee height for at least half of the satellite's orbital lifetime. Table 1 shows the main terms for each satellite.

TABLE 1.—*Lunar-Solar Perturbations in Perigee Height of Satellites*

1958 β_2, Vanguard I							1959 δ, Explorer VI						
Perigee (km)	cos						Perigee (km)	cos					
	ω	θ	$\lambda_\odot$	$\omega_\odot$	$\lambda_\mathbb{C}$	$\omega_\mathbb{C}$		ω	θ	$\lambda_\odot$	$\omega_\odot$	$\lambda_\mathbb{C}$	$\omega_\mathbb{C}$
−0.457	0	0	0	0	0	0	−1097.14	0	0	0	0	0	0
+0.067	+2	0	0	0	0	0	+110.51	+2	0	0	0	0	0
+0.115	+2	+2	0	0	0	0	−892.67	+2	+2	0	0	0	0
−0.157	+2	+1	0	0	0	0	−251.23	+2	+1	0	0	0	0
+1.458	+2	+2	−2	0	0	0	+15.20	+2	−1	0	0	0	0
+0.079	+2	+1	−2	0	0	0	−1.53	+2	0	−2	0	0	0
−0.389	+2	+2	−3	+1	0	0	−24.11	+2	+2	−2	0	0	0
−0.108	+2	+2	0	0	−2	0	−1.68	+2	+1	+2	0	0	0
−0.032	+2	+1	0	0	−2	0	−9.83	+2	+1	−2	0	0	0
							−1.25	+2	−1	+2	0	0	0
							−3.93	+2	+2	0	0	−2	0
							−1.43	+2	+1	0	0	−2	0

The comparison with the observed perigee height is shown in Figure 1. The observed values were obtained from the NASA Space Computing Center after removal of the third harmonic. Figure 2 shows the lunar and solar perturbations in the perigee height of Explorer VI. The effect on the Explorer satellite is much larger than that on the Vanguard because of the higher eccentricity of the Explorer orbit. Further investigations have been carried out on the basis of these results (Reference 8).

A refinement of earlier computations of the Vanguard I orbit revealed a very slow variation in perigee height, with a period of 449 days and an amplitude of 2 kilometers. Kozai suggested (in a private communication) that a term of this period and amplitude will result from a combination of lunar and solar perturbations. Kozai and Whitney then extended their calculations to the case of the paddle-wheel satellite, Explorer VI (Reference 1). Explorer VI has an apogee of 48,700 kilometers, a perigee of 6640 kilometers, and an orbital inclination of 47.3 degrees; it was found that this highly

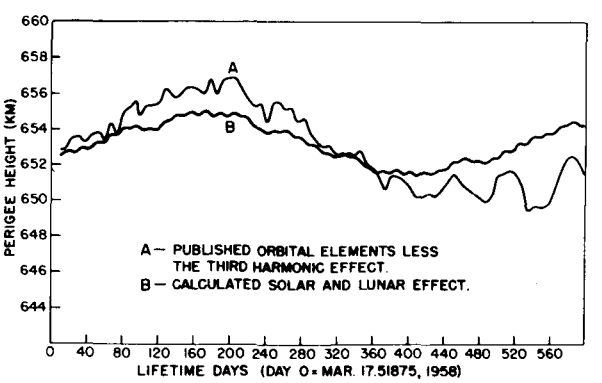

FIGURE 1.—*Solar and lunar perturbations on the perigee height of Vanguard I (1958 β_2).*

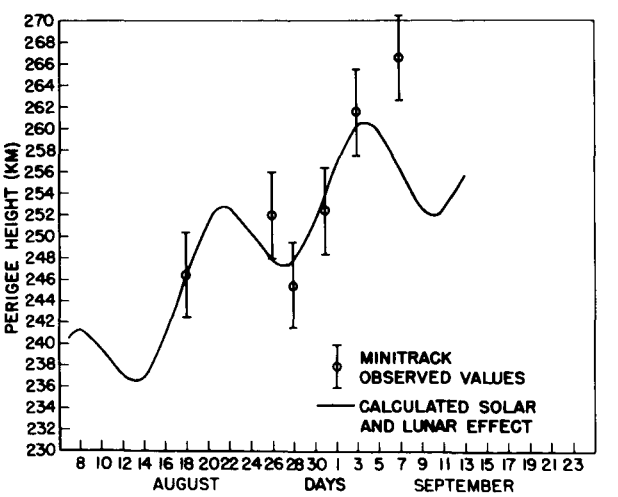

FIGURE 2.—*Solar and lunar perturbations on the perigee height of Explorer VI (1959 δ).*

eccentric orbit produces substantial lunar and solar perturbations which decrease the perigee altitude rapidly and shorten the orbital lifetime from several decades to a probable value of two years.

The interesting work of Kozai and Whitney encouraged further exploration of the possible lunar and solar effects on perigee height for satellite orbits of large eccentricity. In general, both the eccentricity and the perigee height vary with time as a result of these effects. The amplitudes, frequencies, and relative phases of the variations are determined by the orbit parameters, among which the hour of launch is of considerable importance. *For a special set of launch conditions, and for representative orbit parameters, the perigee height may be made to rise steadily over the course of several years at a rate of 1 kilometer per day. Thus, the sun and the moon may provide a substantial perigee boost for the satellite under properly chosen circumstances. For other conditions the perturbations may be minimized to obtain a relatively stable orbit.* These considerations may be of importance in deciding the launch programs for future satellites with highly eccentric orbits.

From the perturbing function developed herein, the rate of change of perigee height was found by the method of variation of constants. Letting q be the perigee height,

$$\frac{dq}{dt} = -\frac{(1-e)^2}{nae}\frac{\partial\Omega}{\partial\sigma} + \frac{\sqrt{1-e^2}}{nae}\frac{\partial\Omega}{\partial\omega}$$

where σ is essentially the mean anomaly g of the satellite, ω is the argument of perigee of the satellite, and Ω is the perturbing function.

The first-order perturbations of the gravitational effect of the sun and moon were developed, and several assumptions which considerably simplified the expression for the potential were made. It was assumed that the moon's orbital plane is coincident with the sun's. Only the long-duration effects on perigee altitude were considered; this eliminated terms with periods of the mean anomaly (and fractional parts thereof) of the satellite and, for the most part, of the moon (i.e., g and $g'_{\mathbb{C}}$).

Hence, the expression dq/dt becomes

$$\frac{dq}{dt} = +\frac{\sqrt{1-e^2}}{nae}\frac{\partial\Omega}{\partial\omega},$$

which is a trigonometric series whose arguments depend on various combinations of 2ω, θ, $\lambda_\odot$, $\lambda_{\mathbb{C}}$, $\omega_\odot$, $\omega_{\mathbb{C}}$. In terms of these elements several possible resonance effects can be recognized, two of which are associated with the following conditions:

$$2\dot{\omega} - 2(\dot{\lambda}_\odot - \dot{\theta}) = 0, \qquad (10a)$$

$$2\dot{\omega} + 2(\dot{\lambda}_\odot - \dot{\theta}) = 0, \qquad (10b)$$

where $\dot{\omega}$, $\dot{\lambda}$, $\dot{\theta}$ are the average angular velocities of ω, λ, θ, respectively.

These resonance conditions have a simple interpretation. For example, in Equation 10a, $\lambda_\odot - \theta$ represents the longitude of the sun relative to the line of nodes; and ω, the position of the perigee in the orbital plane, is also defined relative to the line of nodes. Therefore, in a system in which the line of nodes is fixed, the satisfaction of the resonance condition (case 10a) signifies that the mean angular velocities of the sun and perigee are equal; that is, the line of apsides follows the sun. In this case the orbital perturbations produced by the sun are clearly maximized. In Equation 10b, the sun and the line of apsides have the same period of revolution but in opposite directions. Again, it is clear that the solar perturbations will be maximized.

It was found that the effects on perigee height may be maximized or minimized by choosing suitable values of the orbital inclination and the time of launch. A long-period effect occurs when the inclination to the equator is near 63.4 degrees—the critical angle at which the motion of the argument of perigee is small. There is a 2ω term in dq/dt which at this inclination produces a near-resonance effect, causing the perigee height to change almost secularly. For an orbit with an apogee of 46,550 kilometers and a perigee of 6650 kilometers, the rate of change of perigee is about 1 kilometer per day, as shown in Figure 3. The precise magnitude of the rate of change depends on the initial argument of perigee. The hour of launch does not affect this result.

At angles of inclination other than 63.4 degrees, a variety of effects may be obtained by a suitable choice of the hour of launch. Selecting the hour of launch is equivalent to selecting the longitude of the ascending node,

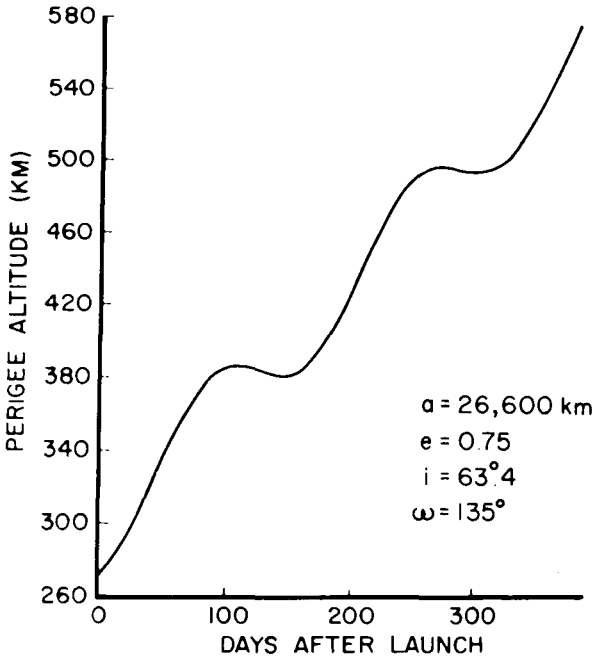

FIGURE 3.—*Rate of change of perigee for orbital inclination near 63.4 degrees.*

with any value available once in 24 sidereal hours. The results of three different launch times are shown in Figure 4, employing the same apogee and perigee as in Figure 3 with an argument of perigee equal to 135 degrees and an equatorial inclination of 28 degrees for February 1, 1960. Curve A corresponds to a launch time of 7 hours U.T. on February 1, curve B to 23 hours U.T., and curve C to 13 hours U.T. Cases A and C show rapid initial variations of perigee height—advantageous and disadvantageous. Case B represents a relatively stable orbit.

Curve C′ represents the addition of drag to case C. It rises initially above the solar and lunar perturbation curve because the drag decreases the period and the eccentricity, and these changes in turn decrease the solar and lunar perturbations. It is interesting to note that the lifetime for a satellite with the parameters of Figure 4 is 25 years in the absence of lunar and solar perturbations and approximately 1 year with these perturbations.

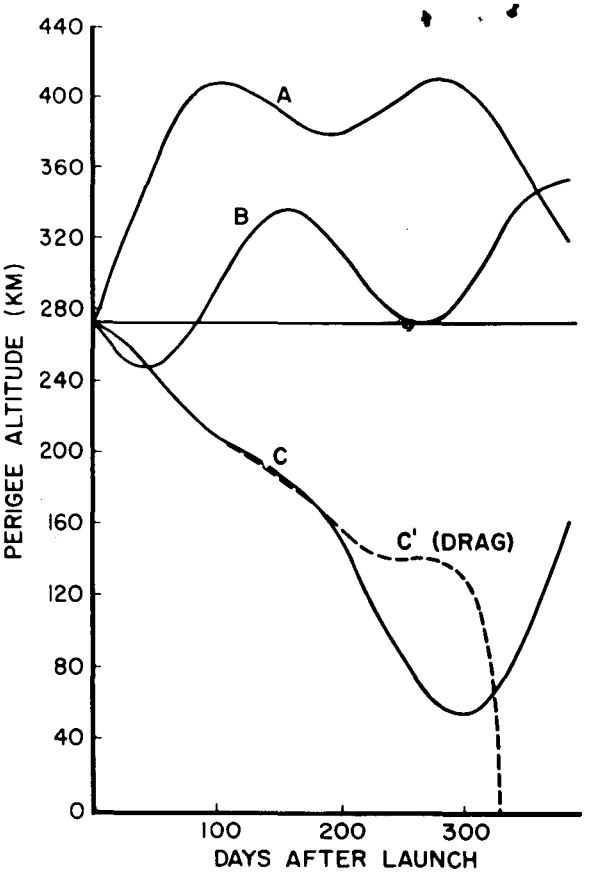

FIGURE 4.—*Results of three different choices of launch time on February 1, 1960: (A) 7h U.T., (B) 23h U.T., (C) 13h U.T.; (C1) shows the addition of drag to (C).*

ACKNOWLEDGMENTS

The authors take the opportunity to express their gratitude to their colleagues, C. Parks, J. Burley, E. Monasterski, and A. Smith, who programed this development and performed the actual computations; and P. Meyers, who checked the theoretical development of the disturbing function.

REFERENCES

1. Kozai, Y., "On the Effects of the Sun and the Moon upon the Motion of a Close Earth Satellite," Smithsonian Inst. Astrophys. Observ. Research in Space Science Spec. Report No. 22, Cambridge, Massachusetts, March 20, 1959, pp. 7–10.

2. Cayley, A., "On the Development of the Disturbing Function in the Lunar Theory," Mem. Roy. Astron. Soc. 27:69–95, 1859.
3. Musen, P., "Contributions to the Theory of Satellite Orbits," in: Space Research, Proceedings of the First International Space Symposium, U.S. National Academy of Sciences (in publication).
4. Radau, M. R., "Recherches Concernant les Inégalités Planétaires du Mouvement de la Lune," Annales de l'Observatoire de Paris, Memoires, vol. 21, p. B1–B114, 1895.
5. Cayley, A., "Tables of the Developments of Functions in the Theory of Elliptic Motion," Mem. Roy. Astron. Soc. 29:191–306, 1861.
6. Musen, P., "Application of Hansen's Theory to the Motion of an Artificial Satellite in the Gravitational Field of the Earth," J. Geophys. Res. 64(12): 2271–2279, December 1959.
7. Hansen, P. A., "Ermittlung der absoluten Störungen in Ellipse von beliebiger Exzentrizität und Neigung," Gotha: G. Gläser, 1843.
8. Upton, E., Bailie, A., and Musen, P., "Lunar and Solar Perturbations on Satellite Orbits," Science 130(3390):1710–1711, December 18, 1959.

On the Long-Period Lunisolar Effect in the Motion of the Artificial Satellite[1]

BY P. MUSEN
Theoretical Division
NASA Goddard Space Flight Center

This article contains two systems of formulas for the determination of the long-period perturbations caused by the sun and the moon in the motion of an artificial satellite. The first system can be used for the determination of the lunar effect for all satellites. The second method is more convenient for finding the lunar effect for close satellites and the solar effect for all satellites.

The knowledge of these effects is essential for the determination of the stability of the orbit of the satellite. The basic equations of both systems are arranged in a form that permits the use of numerical integration. The two theories are more accurate and more adaptable to the use of electronic machines than are the analytical developments obtained previously.

This article contains two systems of formulas for the determination of lunar and solar long-period effects of the first order in the motion of an artificial satellite. The first method is based on the theory originally developed by *Gauss* [1818] for a numerical treatment of the very long period effects in planetary motion. It is also applicable to artificial satellites. The second method is valid for close satellites and is based on the development of the disturbing function in terms of Legendre polynomials.

The knowledge of these long-period effects is essential for determining the stability of the orbit and the lifetime of the satellite. As an example, *Kozai* [1959] found that the solar and lunar perturbations have shortened the lifetime of Explorer VI by a factor of 10. The long-period lunar effect can be deduced by averaging the perturbations with respect to the mean anomaly of the moon and that of the satellite. The first averaging process is performed analytically; the second process, numerically. The long-period solar effect is obtained by averaging the perturbations with respect to the mean anomaly of the satellite only. Both methods result in the numerical integration of the equations for the variation of elements.

The interval of integration depends upon the proximity of the satellite to the earth and upon the secular changes of the node and perigee produced by earth's oblateness. In a normal case, the interval of integration will be of the order of several days. For more distant satellites it can be of the order of 1 month or even more. The choice of such a large interval is impossible if Cowell's method of integration in the rectangular coordinates is used.

It was found that for more distant satellites the development of the disturbing function into a series of Legendre polynomials converges so slowly that it is impossible to include all important long-period terms into an analytical development. A large orbital inclination might also contribute substantially to the slowness of the convergence. For such a case as, for example, $a = 10$ earth radii, $e = 0.8$, the analytical de-

[1] Published in the June 1961 issue of *Journal of Geophysical Research*. Reprinted by permission.

velopment obtained by *Musen, Bailie, and Upton* [1961] becomes incomplete. These circumstances caused the author to investigate the possibility of using the Gaussian method for the determination of the lunar long-period effects in the motion of an artificial satellite.

Halphen's [1888] form (with corrections by *Goriachev* [1937]) of the Gaussian method was found to be the most convenient, partly because of its mathematical simplicity and elegance and, partly, because it was found to be very adaptable to the use of electronic computers. Some necessary modifications were made in order to include the basic perturbations of the motion of the moon. Also, the *Goursat* [1881] transformation and the Euler summability process were used to speed up the convergence of the hypergeometric series. This method is valid for all values of e, i, and a/a'.

The development in terms of Legendre polynomials is permissible if the lunar or the solar perturbations for close satellites are to be determined. The basic equations of these two cases are arranged in the form that permits the use of the numerical integration and includes all the significant long-period terms. Theoretically, these equations are completely equivalent to the extensive analytical developments obtained by *Kozai* [1959] and by *Musen, Bailie, and Upton* [1961], but they have a more compact and symmetrical form and are more adaptable to the use of electronic machines. Thus the formulas given here represent, from a practical point of view, a substantial improvement over the previous methods.

LUNAR DISTURBING FORCE IN THE MOTION OF A DISTANT ARTIFICIAL SATELLITE

Let

$$g_0,\ \omega,\ \Omega,\ i,\ e,\ a,\ n$$

be the osculating elements of the artificial satellite referred to the earth's equator, and let

$$g_0',\ \omega',\ \Omega',\ i',\ e',\ a',\ n'$$

be the elements of the moon referred to the fixed ecliptic. We assume that there is no sharp commensurability between the mean motions n and n'. It is sufficient to take into account the secular changes in the ω', Ω', neglecting the periodic effects and the influence of the precession. Let $\mathbf{P}$ be the unit vector directed from the center of the earth to the perigee of the orbit of the satellite, $\mathbf{R}$ be the unit vector standing normally to the orbit plane, and

$$\mathbf{Q} = \mathbf{R} \times \mathbf{P}$$

Let $\mathbf{P}'$, $\mathbf{Q}'$, $\mathbf{R}'$ be the corresponding vectors connected with the orbit of the moon. Putting

$$A_1(\alpha) = \begin{bmatrix} +1 & 0 & 0 \\ 0 & +\cos\alpha & -\sin\alpha \\ 0 & +\sin\alpha & +\cos\alpha \end{bmatrix}$$

$$A_3(\alpha) = \begin{bmatrix} +\cos\alpha & -\sin\alpha & 0 \\ +\sin\alpha & +\cos\alpha & 0 \\ 0 & 0 & +1 \end{bmatrix}$$

we have for the components of $\mathbf{P}$, $\mathbf{Q}$, $\mathbf{R}$ and $\mathbf{P}'$, $\mathbf{Q}'$, $\mathbf{R}'$ in the equatorial system

$$[\mathbf{P}, \mathbf{Q}, \mathbf{R}] = A_3(\Omega) \cdot A_1(i) \cdot A_3(\omega) \tag{1}$$

$$[\mathbf{P}', \mathbf{Q}', \mathbf{R}'] = A_1(\epsilon) \cdot A_3(\Omega') \cdot A_1(i') \cdot A_3(\omega') \tag{2}$$

ϵ is the angle between the equator and the ecliptic. Designating u as the eccentric anomaly of the satellite, we have for the position vector

$$\mathbf{r} = \mathbf{P}a(\cos u - e) + \mathbf{Q}a\sqrt{1 - e^2}\sin u \tag{3}$$

Put

$$\begin{aligned} \varrho &= \frac{\mathbf{r}}{a}s + e'\mathbf{P}' \\ &= \mathbf{P}s(\cos u - e) \\ &\quad + \mathbf{Q}s\sqrt{1 - e^2}\sin u + e'\mathbf{P}, \end{aligned} \tag{4}$$

where s is the parallax

$$s = a/a'$$

Put

$$\alpha = \rho \cdot \mathbf{P}',\ \beta = \rho \cdot \mathbf{Q}',\ \gamma = \rho \cdot \mathbf{R}'$$

The system of *Halphen's* [1888] formulas for the

computation of auxiliary quantities can be slightly modified and rewritten in our notations in the following way

$$K_1 = \rho^2 - 2 + e'^2 \tag{5}$$

$$K_2 = (1 - e'^2)(1 - \alpha^2) - \beta^2 - (2 - e'^2)\gamma^2 \tag{6}$$

$$K_3 = \gamma^2(1 - e'^2) \tag{7}$$

$$g_2 = \tfrac{4}{3}(K_1^2 - 3K_2) \tag{8}$$

$$g_3 = \tfrac{4}{27}(2K_1^3 - 9K_1K_2 + 27K_3) \tag{9}$$

$$\xi = \frac{27g_3^2}{g_2^3} \tag{10}$$

The next step in Halphen's method is the computation of

$$\psi(\xi) = \frac{\pi}{\sqrt[4]{3}} F\left(\frac{1}{12}, \frac{5}{12}, 1, 1 - \xi\right) \tag{11}$$

$$\psi'(\xi) = -\frac{5}{144}\frac{\pi}{\sqrt[4]{3}} F\left(\frac{13}{12}, \frac{17}{12}, 2, 1 - \xi\right) \tag{12}$$

and of

$$A = \frac{\sqrt{6}\sqrt[4]{g_2}}{9g_2^3} \cdot \frac{144}{\pi}\sqrt{\xi}\,\psi'(\xi) \tag{13}$$

$$B = \frac{\sqrt{2}}{\pi g_2 \sqrt[4]{g_2}}\psi(\xi) \tag{14}$$

The values of ξ will be proper fractions. The series 11 and 12 possess an algebraic branch point at $\xi = 0$, and the convergence in the neighborhood of this singularity is slow. In order to obtain more convenient formulas representing our series in the interval $0 \leqq \xi \leqq 1$ rather uniformly, with the accuracy at least up to 10^{-6}, we apply the *Goursat* [1881] transformations and then the E summability process.

Putting

$$a = \tfrac{1}{12}, \qquad b = \tfrac{5}{12}, \qquad z = 1 - \xi$$

in

$$F(a, b, a + b + \tfrac{1}{2}, z) = \left(\frac{1 + \sqrt{1 - z}}{2}\right)^{-2a} F\left(2a, a - b + \tfrac{1}{2}, a + b + \tfrac{1}{2}, -\frac{1 - \sqrt{1 - z}}{1 + \sqrt{1 - z}}\right)$$

we deduce

$$\psi(\xi) = \frac{\pi}{\sqrt[4]{3}}\sqrt[6]{\frac{2}{1 + \sqrt{\xi}}} \cdot F(\tfrac{1}{6}, \tfrac{1}{6}, 1, -w) \tag{15}$$

Putting

$$a = \tfrac{13}{12}, \qquad b = \tfrac{17}{12}, \qquad z = 1 - \xi$$

in

$$F(a, b, a + b - \tfrac{1}{2}, z) = (1 - z)^{-1/2}\left(\frac{1 + \sqrt{1 - z}}{2}\right)^{1-2a} \cdot F\left(2a - 1, a - b + \tfrac{1}{2}, a + b - \frac{1}{2}, -\frac{1 - \sqrt{1 - z}}{1 + \sqrt{1 - z}}\right)$$

we have

$$\sqrt{\xi}\,\psi'(\xi) = -\frac{5}{144}\frac{\pi}{\sqrt[4]{3}}\left(\frac{2}{1 + \sqrt{\xi}}\right)^{7/6} \cdot F\left(\frac{1}{6}, \frac{7}{6}, 2, -w\right) \tag{16}$$

where

$$w = \frac{1 - \sqrt{\xi}}{1 + \sqrt{\xi}}$$

The series 15 and 16 are alternating and the E-process can be applied to speed up their convergence. The formula of the E-process for hypergeometric series takes the form

$$F(a, b, c, -x) = \sum_{k=0}^{N}(-1)^k \frac{(a, k)(b, k)}{(1, k)(c, k)} x^k + \lim_{m\to\infty}\sum_{j=0}^{m}(-1)^{N+j} \cdot \frac{(a, N + j)(b, N + j)}{(1, N + j)(c, N + j)} x^{N+j} \cdot \sum_{p=j}^{m}\frac{1}{2^{p+1}}\binom{p}{j} \tag{17}$$

where

$$(q, k) = q(q + 1) \ldots (q + k - 1)$$

Applying formula 17 to the series 15 and 16, and putting $N = 3$, $m = 19$, we deduce the two

following expressions whose coefficients are rapidly decreasing as the power of w increases.

$$\frac{144}{\pi}\sqrt{\xi}\,\psi'(\xi)$$

$$\psi(\xi) = \left(\frac{2}{1+\sqrt{\xi}}\right)^{1/6} \qquad = \left(\frac{2}{1+\sqrt{\xi}}\right)^{7/6}$$

$(+2.3870942$	$(-3.7991784$
$-0.0663082\,w$	$+0.3693646\,w$
$+0.0225632\,w^2$	$-0.1556119\,w^2$
$-0.0117691\,w^3$	$+0.0889726\,w^3$
$+0.0073743\,w^4$	$-0.0586828\,w^4$
$-0.0051060\,w^5$	$+0.0419870\,w^5$
$+0.0037250\,w^6$	$-0.0313364\,w^6$
$-0.0027325\,w^7$	$+0.0233758\,w^7$
$+0.0019070\,w^8$	$-0.0165247\,w^8$
$-0.0011936\,w^9$	$+0.0104483\,w^9$
$+0.0006337\,w^{10}$	$-0.0055933\,w^{10}$
$-0.0002710\,w^{11}$	$+0.0024083\,w^{11}$
$+0.0000884\,w^{12}$	$-0.0007898\,w^{12}$
$-0.0000205\,w^{13}$	$+0.0001837\,w^{13}$
$+0.0000030\,w^{14}$	$-0.0000268\,w^{14}$
$-0.0000002\,w^{15})$	$+0.0000018\,w^{15})$

The next step is to compute

$$K_4 = 9K_3 - K_1K_2$$

$$K_5 = K_1(K_1K_2 - 3K_3) - 2K_2^2$$

and

$$a_{11} = K_4(\alpha^2 - 1) + K_5 + \frac{3}{2}g_2K_3$$

$$a_{22} = K_4(\beta^2 - 1 + e'^2) + K_5 + \frac{3}{2}\frac{g_2K_3}{1-e'^2}$$

$$a_{33} = K_4\gamma^2 + K_5 + \tfrac{3}{2}g_2[\alpha^2(1-e'^2) + \beta^2 - (1-e'^2)]$$

$$a_{12} = a_{21} = K_4\alpha\beta$$

$$a_{23} = a_{32} = (K_4 - \tfrac{3}{2}g_2)\beta\gamma$$

$$a_{31} = a_{13} = [K_4 - \tfrac{3}{2}g_2(1-e'^2)]\gamma\alpha$$

$$a'_{11} = \alpha^2 - 1 - \tfrac{1}{3}K_1$$

$$a'_{22} = \beta^2 - 1 + e'^2 - \tfrac{1}{3}K_1$$

$$a'_{33} = \gamma^2 - \tfrac{1}{3}K_1$$

$$a'_{12} = a'_{21} = \alpha\beta$$

$$a'_{23} = a'_{32} = \beta\gamma$$

$$a'_{31} = a'_{13} = \gamma\alpha$$

Then the matrix is formed with the elements

$$A_{ij} = a_{ij}A + a'_{ij}B$$

introducing the dyadic (a matrix)

$$\Phi = \begin{Bmatrix} +A_{11}\mathbf{P}'\mathbf{P}' + A_{12}\mathbf{P}'\mathbf{Q}' + A_{13}\mathbf{P}'\mathbf{R}' \\ +A_{21}\mathbf{Q}'\mathbf{P}' + A_{22}\mathbf{Q}'\mathbf{Q}' + A_{23}\mathbf{Q}'\mathbf{R}' \\ +A_{31}\mathbf{R}'\mathbf{P}' + A_{32}\mathbf{R}'\mathbf{Q}' + A_{33}\mathbf{R}'\mathbf{R}' \end{Bmatrix} \tag{18}$$

we can represent the "disturbing," force averaged with respect to the mean anomaly of the moon, in the form

$$\mathbf{F}_0 = -\frac{2km'}{a'^3}\,\Phi\cdot\mathbf{r} \tag{19}$$

and the averaged momentum is

$$\mathbf{M}_0 = -\frac{2km'}{a'^3}\,\mathbf{r}\times\Phi\cdot\mathbf{r} \tag{20}$$

In addition, in the system adopted in this article, we have to compute the vector [*Musen*, 1954]

$$\mathbf{K}_0 = \left(1+\frac{r}{p}\right)\mathbf{F}_0 - \frac{1}{rp}\,\mathbf{r}\mathbf{r}\cdot\mathbf{F}_0 \tag{21}$$

The vectors $\mathbf{M}_0$ and $\mathbf{K}_0$ must be averaged along the orbit of the satellite. We have to obtain

$$(\mathbf{M}_{00}) = \frac{1}{2\pi}\int_0^{2\pi}\mathbf{M}_0 dg = \frac{1}{2\pi}\int_0^{2\pi}\mathbf{M}_0\frac{r}{a}\,du \tag{22}$$

$$(\mathbf{K}_{00}) = \frac{1}{2\pi}\int_0^{2\pi}\mathbf{K}_0 dg = \frac{1}{2\pi}\int_0^{2\pi}\mathbf{K}_0\frac{r}{a}\,du \tag{23}$$

This averaging is done numerically, by giving the values 0°, 30°, 60°, . . ., 330° to u, computing values of $\mathbf{M}_0(r/a)$ and $\mathbf{K}_0(r/a)$ for each of these angles, and then forming the arithmetical means.

The form of variation of constants for the long-period lunar effects. Designating the area "constant" by $\mathbf{c}$, we have

$$\mathbf{c} = \sqrt{p}\mathbf{R} \tag{24}$$

$$p = a(1-e^2) \tag{25}$$

and

$$\frac{d\mathbf{c}}{dt} = \mathbf{r}\times\mathbf{F} \tag{26}$$

Let $\mathbf{h}$ be the unit vector along the line of nodes

and let (**i**, **j**, **k**) be the unit vectors of the equatorial system. We have

$$\mathbf{h} = \mathbf{i}\cos\Omega + \mathbf{j}\sin\Omega \tag{27}$$

$$\mathbf{R} = \mathbf{h}\times\mathbf{k}\sin i + \mathbf{k}\cos i \tag{28}$$

It follows from (27) and (28)

$$\frac{d\mathbf{R}}{dt} = \mathbf{h}\sin i\,\frac{d\Omega}{dt} + \mathbf{h}\times\mathbf{R}\,\frac{di}{dt} \tag{29}$$

and from (26)

$$\mathbf{h}\sin i\,\frac{d\Omega}{dt} + \mathbf{h}\times\mathbf{R}\,\frac{di}{dt} - \frac{e}{1-e^2}\,\mathbf{R}\,\frac{de}{dt} + \frac{1}{\sqrt{a}}\,\mathbf{R}\,\frac{d\sqrt{a}}{dt} = \frac{1}{\sqrt{p}}\,\mathbf{r}\times\mathbf{F} \tag{30}$$

We deduce from the last equation the long-period effects by applying the double process of averaging and taking $da/dt = 0$ into account

$$\sin i\,\frac{d\Omega}{dt} = \frac{1}{\sqrt{p}}\,\mathbf{h}\cdot\mathbf{M}_{00} \tag{31}$$

$$\frac{di}{dt} = \frac{1}{\sqrt{p}}\,\mathbf{M}_{00}\cdot\mathbf{h}\times\mathbf{R} \tag{32}$$

$$\frac{de}{dt} = -\frac{\sqrt{1-e^2}}{e\sqrt{a}}\,\mathbf{R}\cdot\mathbf{M}_{00} \tag{33}$$

It is interesting to note that for long-period effects only the averaged momentum and not any other function of the disturbing force is contained in the equations 31–33. Equations 31 and 32 represent a particular case of equations deduced by *Makarova* [1958] for the computation of the special perturbations of minor planets. We have [*Musen*, 1954]

$$\mathbf{h}\,\frac{di}{dt} + \mathbf{k}\,\frac{d\Omega}{dt} + \mathbf{R}\,\frac{d\omega}{dt} = \frac{1}{\sqrt{p}}\,\mathbf{r}\mathbf{R}\cdot\mathbf{F} - \frac{\sqrt{p}}{e}\,\mathbf{R}\mathbf{P}\cdot\mathbf{K} \tag{34}$$

where

$$\mathbf{K} = \left(1 + \frac{r}{p}\right)\mathbf{F} - \frac{1}{rp}\,\mathbf{r}\mathbf{r}\cdot\mathbf{F} \tag{35}$$

We deduce from (34) the long period effect in ω, and by taking (31) into consideration we have

$$\frac{d\omega}{dt} = -\frac{\sqrt{p}}{e}\,\mathbf{P}\cdot\mathbf{K}_{00} - \frac{\cot i}{\sqrt{p}}\,\mathbf{h}\cdot\mathbf{M}_{00} \tag{36}$$

where

$$\mathbf{P}\cdot\mathbf{K}_{00} = \frac{1}{2\pi}\int_0^{2\pi}\mathbf{P}\cdot\mathbf{K}_0\,\frac{r}{a}\,du$$

Equation 36 is identical in form to the equation for planetary perturbations, deduced by Makarova on the basis of different considerations from *Musen*'s [1954] theory. The system 31, 32, 33, and 36 is to be integrated numerically. As we said before the interval of integration can be of the order of several days.

LUNAR PERTURBATIONS OF A CLOSE SATELLITE AND THE SOLAR PERTURBATIONS

The computation of the lunar perturbations of a close satellite and the computation of the solar perturbations for all satellites can be done by developing the disturbing function into series of Legendre polynomials. For our purpose, we can limit ourselves to the second Legendre polynomial, and the disturbing function takes the form

$$R = \frac{km'r^2}{r'^3}\left(\frac{3}{2}\cos^2 H - \frac{1}{2}\right) \tag{37}$$

where H is the angle between $\mathbf{r}$ and $\mathbf{r}'$. Let $\mathbf{u}^0$ be the unit vector in the direction of $\mathbf{r}'$. We have $\mathbf{u}^0$ with the accuracy up to e' in the periodic terms

$$\mathbf{u}^0 = \mathbf{P}'(-e' + \cos g' + e'\cos 2g') + \mathbf{Q}'(\sin g' + e'\sin 2g') \tag{38}$$

and (37) becomes

$$R = \frac{km'}{2r'^3}\,(3\mathbf{r}\cdot\mathbf{u}^0\mathbf{u}^0\cdot\mathbf{r} - r^2) \tag{39}$$

The "disturbing force" to be used in connection with the variation of elements will be

$$\mathbf{F} = \text{grad}\,R = \frac{km'}{a'^3}\left(\frac{a'}{r'}\right)^3(3\mathbf{u}^0\mathbf{u}^0\cdot\mathbf{r} - \mathbf{r}) \tag{40}$$

and the momentum of **F** takes the form

$$\mathbf{M} = \frac{3km'}{a'^3}\left(\frac{a'}{r'}\right)^3\mathbf{r}\times\mathbf{u}^0\mathbf{u}^0\cdot\mathbf{r} \tag{41}$$

Substituting

$$\mathbf{r} = \mathbf{P}r\cos f + \mathbf{Q}r\sin f$$

into (41), we obtain

$$\mathbf{M} = \frac{3km'a^2}{2a'^3}\left(\frac{a'}{r'}\right)^3 \cdot\Big[\mathbf{P}\times\mathbf{u}^0\mathbf{u}^0\cdot\mathbf{P}\,\frac{r^2}{a^2}(1+\cos 2f) + \mathbf{P}\times\mathbf{u}^0\mathbf{u}^0\cdot\mathbf{Q}\,\frac{r^2}{a^2}\sin 2f + \mathbf{Q}\times\mathbf{u}^0\mathbf{u}^0\cdot\mathbf{P}\,\frac{r^2}{a^2}\sin 2f + \mathbf{Q}\times\mathbf{u}^0\mathbf{u}^0\cdot\mathbf{Q}\,\frac{r^2}{a^2}(1-\cos 2f)\Big] \quad (42)$$

Taking

$$\frac{1}{2\pi}\int_0^{2\pi}\frac{r^2}{a^2}\,dg = 1+\tfrac{3}{2}e^2$$

$$\frac{1}{2\pi}\int_0^{2\pi}\frac{r^2}{a^2}\cos 2f\,dg = +\tfrac{5}{2}e^2$$

we deduce for the averaged value of $\mathbf{M}_0$,

$$\mathbf{M}_0 = \frac{3km'a^2}{2a'^3}\left(\frac{a'}{r'}\right)^3[(1+4e^2)\mathbf{P}\times\mathbf{u}^0\mathbf{u}^0\cdot\mathbf{P} + (1-e^2)\mathbf{Q}\times\mathbf{u}^0\mathbf{u}^0\cdot\mathbf{Q}] \quad (43)$$

Let φ, ψ, and ϑ be angles which the basic vectors $\mathbf{P}$, $\mathbf{Q}$, and $\mathbf{R}$ form with the direction to the moon,

$$\cos\varphi = \mathbf{P}\cdot\mathbf{u}^0,\ \cos\psi = \mathbf{Q}\cdot\mathbf{u}^0,\ \cos\vartheta = \mathbf{R}\cdot\mathbf{u}^0 \quad (44)$$

Replacing $\mathbf{M}_{00}$ in (31), (32), and (33), by (43), and taking

$$\begin{aligned}
\mathbf{h}\cdot\mathbf{P}\times\mathbf{u}^0 &= +\cos\vartheta\sin\omega\\
\mathbf{h}\cdot\mathbf{Q}\times\mathbf{u}^0 &= +\cos\vartheta\cos\omega\\
(\mathbf{h}\times\mathbf{R})\cdot(\mathbf{P}\times\mathbf{u}^0) &= +\cos\vartheta\cos\omega\\
(\mathbf{h}\times\mathbf{R})\cdot(\mathbf{Q}\times\mathbf{u}^0) &= -\cos\vartheta\sin\omega\\
\mathbf{R}\cdot\mathbf{P}\times\mathbf{u}^0 &= +\cos\psi\\
\mathbf{R}\cdot\mathbf{Q}\times\mathbf{u}^0 &= -\cos\varphi\\
\mathbf{h} &= \mathbf{P}\cos\omega - \mathbf{Q}\sin\omega
\end{aligned}$$

into account, we obtain

$$\sin i\,\frac{d\Omega}{dt} = \frac{3km'a^2}{2a'^3}\left(\frac{a'}{r'}\right)^3\frac{\cos\vartheta}{\sqrt{p}}\cdot[(1+4e^2)\cos\varphi\sin\omega + (1-e^2)\cos\psi\cos\omega] \quad (45)$$

$$\frac{di}{dt} = \frac{3km'a^2}{2a'^3}\left(\frac{a'}{r'}\right)^3\frac{\cos\vartheta}{\sqrt{p}}\cdot[(1+4e^2)\cos\varphi\cos\omega - (1-e^2)\cos\psi\sin\omega] \quad (46)$$

$$\frac{de}{dt} = -\frac{15}{2}e\sqrt{1-e^2}\,\frac{k}{\sqrt{a}}\cdot\frac{m'a^2}{a'^3}\left(\frac{a'}{r'}\right)^3\cos\varphi\cos\psi \quad (47)$$

Putting the mass of the earth equal to one, we have

$$\frac{k}{\sqrt{a}} = na$$

and the system 45–47 becomes

$$\sin i\,\frac{d\Omega}{dt} = \frac{3m'n}{2\sqrt{1-e^2}}\left(\frac{a}{a'}\right)^3\left(\frac{a'}{r'}\right)^3\cdot[(1+4e^2)\cos\varphi\sin\omega + (1-e^2)\cos\psi\cos\omega]\cos\vartheta \quad (45')$$

$$\frac{di}{dt} = \frac{3m'n}{2\sqrt{1-e^2}}\left(\frac{a}{a'}\right)^3\left(\frac{a'}{r'}\right)^3\cdot[(1+4e^2)\cos\varphi\cos\omega - (1-e^2)\cos\psi\sin\omega]\cos\vartheta \quad (46')$$

$$\frac{de}{dt} = -\frac{15m'ne\sqrt{1-e^2}}{2}\cdot\left(\frac{a}{a'}\right)^3\left(\frac{a'}{r'}\right)^3\cos\varphi\cos\psi \quad (47')$$

In addition we have with sufficient accuracy

$$\left(\frac{a'}{r'}\right)^3 = (1-e'^2)^{-3/2} + 3e'\cos g'$$

We have for $d\omega/dt$ an equation analogous to (36)

$$\frac{d\omega}{dt} = -\frac{\sqrt{p}}{e}\,\mathbf{P}\cdot\mathbf{K}_0 - \cos i\,\frac{d\Omega}{dt} \quad (48)$$

where

$$\mathbf{K}_0 = \frac{1}{2\pi}\int_0^{2\pi}\left[\left(1+\frac{r}{p}\right)\mathbf{F} - \frac{1}{rp}\,\mathbf{F}\cdot\mathbf{rr}\right]dg \quad (49)$$

Substituting

$$\mathbf{F} = \frac{km'}{r'^3}(3\mathbf{u}^0\mathbf{u}^0\cdot\mathbf{r} - \mathbf{r})$$

into (49) and taking

$$\mathbf{u}^0 \cdot \mathbf{r} = r \cos f \cos \varphi + r \sin f \cos \psi \qquad (49')$$

into account, we obtain

$$\frac{1}{2\pi}\int_0^{2\pi} \mathbf{P}\cdot\mathbf{F}\, dg = \frac{km'a}{r'^3}\frac{1}{2\pi} \cdot\int_0^{2\pi}\left[(3\cos^2\varphi - 1)\frac{r}{a}\cos f + 3\frac{r}{a}\sin f \cos\varphi\cos\psi\right] dg \qquad (50)$$

It follows from Cayley's tables

$$\frac{1}{2\pi}\int_0^{2\pi}\frac{r}{a}\cos f\, dg = -\tfrac{3}{2}e$$

$$\frac{1}{2\pi}\int_0^{2\pi}\frac{r}{a}\sin f\, dg = 0$$

and equation 50 becomes

$$\frac{1}{2\pi}\int_0^{2\pi}\mathbf{P}\cdot\mathbf{F}dg = \frac{3km'ae}{2r'^3}(1 - 3\cos^2\varphi) \qquad (51)$$

In a similar way we obtain

$$\frac{1}{2\pi}\int_0^{2\pi}\frac{r}{p}\mathbf{P}\cdot\mathbf{F}\, dg = \frac{km'a}{(1-e^2)r'^3} \cdot(1 - 3\cos^2\varphi)(2e + \tfrac{1}{2}e^3) \qquad (52)$$

by taking

$$\frac{1}{2\pi}\int_0^{2\pi}\frac{r^2}{a^2}\cos f\, dg = -2e - \tfrac{1}{2}e^3 \qquad (53)$$

$$\frac{1}{2\pi}\int_0^{2\pi}\frac{r^2}{a^2}\sin f\, dg = 0 \qquad (53')$$

into consideration. It follows from (51) and (52)

$$\frac{1}{2\pi}\int_0^{2\pi}\left(1 + \frac{r}{p}\right)\mathbf{P}\cdot\mathbf{F}\, dg = \frac{km'a}{r'^3} \cdot(1 - 3\cos^2\varphi)\frac{7e - 2e^3}{2(1-e^2)} \qquad (54)$$

The next step is to compute the integral

$$\frac{1}{2\pi}\int_0^{2\pi}\frac{1}{rp}\mathbf{P}\cdot\boldsymbol{\pi}\cdot\mathbf{F}\, dg$$

We have

$$\frac{1}{2\pi}\int_0^{2\pi}\frac{1}{rp}\mathbf{P}\cdot\boldsymbol{\pi}\cdot\mathbf{F}\, dg = \frac{km'a}{(1-e^2)r'^3}\frac{1}{2\pi a^2} \cdot\int_0^{2\pi}[3(\mathbf{u}^0\cdot\mathbf{r})^2 - \mathbf{r}^2]\cos f\, dg$$

or, after some transformations and taking (49′) into account

$$\frac{1}{2\pi}\int_0^{2\pi}\frac{1}{rp}\mathbf{P}\cdot\boldsymbol{\pi}\cdot\mathbf{F}\, dg = \frac{km'a}{(1-e^2)r'^3} \cdot\left[(\tfrac{9}{4}\cos^2\varphi + \tfrac{3}{4}\cos^2\psi - 1) \cdot\frac{1}{2\pi}\int_0^{2\pi}\frac{r^2}{a^2}\cos f\, dg + (\tfrac{3}{4}\cos^2\varphi - \tfrac{3}{4}\cos^2\psi)\frac{1}{2\pi}\int_0^{2\pi}\frac{r^2}{a^2}\cos 3f\, dg\right] \qquad (55)$$

From (53) and from

$$\frac{1}{2\pi}\int_0^{2\pi}\frac{r^2}{a^2}\cos 3f\, dg = -\tfrac{5}{2}e^3$$

we deduce a final result

$$\frac{1}{2\pi}\int_0^{2\pi}\frac{1}{rp}\mathbf{P}\cdot\boldsymbol{\pi}\cdot\mathbf{F}\, dg = \frac{km'a}{(1-e^2)r'^3} \cdot[(-\tfrac{9}{2}\cos^2\varphi - \tfrac{3}{2}\cos^2\psi + 2)e + (\tfrac{1}{2} - 3\cos^2\varphi + \tfrac{3}{2}\cos^2\psi)e^3]. \qquad (56)$$

Substituting (54) and (56) into (48), and eliminating k in favor of a and n, we obtain

$$\frac{d\omega}{dt} = \frac{3m'na^3}{2a'^3}\left(\frac{a'}{r'}\right)^3(4\cos^2\varphi - \cos^2\psi - 1) \cdot\sqrt{1-e^2} - \cos i\frac{d\Omega}{dt} \qquad (57)$$

The system of equations 45′–47′ and 57 should be used in the investigations connected with the lunar perturbations for close satellites and with the solar perturbations. They contain all the significant long period terms. In addition, the lunar part also contains the terms having periods of the order of one month. The interval of integration for the solar perturbations can be taken to be approximately 1 month.

However, for the lunar perturbations it would be preferable to take the interval to be of the order of days, to obtain a smoother curve and to avoid ambiguity in interpreting the results.

CONCLUSION

The methods described in this article are more accurate and more adaptable to the use of electronic computers than the analytical development obtained previously. They can be used in the investigations connected with the stability of orbits and for the separation of known and unknown long period effects in the observations. It is recommended that, in practical use, the analytical development be replaced by the semi-analytical solution given in this article.

ACKNOWLEDGMENTS

I should like to express my gratitude to my colleagues Mrs. Ann Bailie and Miss Maxine Goldstein for the careful preparation of the manuscript for print, and to Mr. Arthur Smith for programming the methods described in this paper.

REFERENCES

Gauss, K. F., Determinatio attractionis quam in punctum quodvis positionis data exerceret planeta, si eius massa, etc., *Coll. Works, III*, 331, 1818.

Goriachev, N. N., On the method of Halphen of the computation of secular perturbations, (Russ.), University of Tomsk., 1–115, 1937.

Goursat, E., *Ann. Scient. Ecole Norm. Sup.* (2), *10*, 3–142, 1881.

Halphen, G. H., *Traite des fonction élliptiques, II*, Paris, 1888.

Kozai, Y., On the effects of the sun and the moon upon the motion of a close earth satellite, Smithsonian Astrophys. Obs., *Special Report No. 22*, Cambridge, 1959.

Makarova, E. N., On the simultaneous determination of systematic errors of stellar catalogues and of masses of planets from the observations of asteroides, *Bull. Inst. Theoret. Astr., VII* (84), 1–18, Leningrad, 1958.

Musen, P., Special perturbations of the vectorial elements, *Astron. J., 59*, 262, 1954.

Musen, P., A. Bailie, and E. Upton, Development of the lunar and solar perturbations in the motion of an Artificial satellite, *NASA Technical Note, D–494*, 1961.

(Manuscript received March 6, 1961.)

On the Long-Period Lunar and Solar Effects on the Motion of an Artificial Satellite, 2 [1]

BY PETER MUSEN

Theoretical Division
NASA Goddard Space Flight Center

The disturbing function for the long-period lunisolar effects is developed into a series of polynomials in the components of the vectorial elements in the direction to the disturbing body. This development is convergent for all eccentricities and all inclinations. The equations are established for the variation of elements in a form suitable for the use of numerical integration and for the development of the perturbations into trigonometric series with numerical coefficients. An application of Milankovich's theory of perturbations leads to the equations for perturbed elements in which the small numerical divisors, the sine of the inclination and the eccentricity, are not present. These new equations, like the equations for canonical elements, have a symmetrical form and a wider range of applicability than the equations for elliptic elements.

SYMBOLS

M, the mean anomaly of the satellite for the moment t.
ω, the argument of the perigee of the satellite.
Ω, the longitude of the ascending node of the satellite.
i, the inclination of the orbit of the satellite with respect to the equator.
e, the eccentricity of the orbit of the satellite.
a, the semimajor axis of the orbit of the satellite.
n, the mean motion of the satellite.
p, $a(1-e^2)$.
M', the mean anomaly of the disturbing body at the moment t.
ω', the argument of the perigee of the orbit of the disturbing body, but with respect to the ecliptic of the fixed epoch.
Ω', the longitude of the ascending node of the orbit of the disturbing body with respect to ecliptic.
i', the inclination of the orbit of the disturbing body toward ecliptic.
e', the eccentricity of the orbit of the disturbing body.
a', the semimajor axis of the orbit of the disturbing body.
n', the mean motion of the disturbing body.
Ω, the disturbing function.
$\mathbf{r}$, the position vector of the satellite.
$\mathbf{r}^0$, the unit vector in the direction of $\mathbf{r}$.
$\mathbf{u}^0$, the unit vector directed from the center of the earth to the disturbing body.
$\mathbf{i}, \mathbf{j}, \mathbf{k}$, the basic system of unit vectors in the equatorial system of coordinates.
$\mathbf{P}$, the unit vector directed from the center of the earth toward the perigee of the satellite.
$\mathbf{R}$, the unit vector standing normally to the orbit plane of the satellite.
$\mathbf{Q}$, the unit vector standing normally to $\mathbf{P}$ and $\mathbf{R}$; $\mathbf{Q} = \mathbf{R} \times \mathbf{P}$.

[1] Published in the September 1961 issue of *Journal of Geophysical Research*. Reprinted by permission.

$\mathbf{P}'$, the unit vector directed from the center of the earth toward the perigee of the disturbing body.

$\mathbf{R}'$, the unit vector standing normally to the orbit plane of the disturbing body.

$\mathbf{Q}'$, a unit vector standing normally to $\mathbf{P}'$ and $\mathbf{R}'$, $\mathbf{Q}' = \mathbf{R}' \times \mathbf{P}'$.

α, the projection of $\mathbf{P}$ on $\mathbf{u}^0$.

β, the projection of $\mathbf{Q}$ on $\mathbf{u}^0$.

γ, the projection of $\mathbf{R}$ on $\mathbf{u}^0$.

$\mathbf{c} = \sqrt{1-e^2}\mathbf{R}$.

$\mathbf{g} = c\mathbf{P}$.

$\nabla_a = \mathbf{i}\partial/\partial a_1 + \mathbf{j}\partial/\partial a_2 + \mathbf{k}\partial/\partial a_3$; the partial del operator with respect to vector $\mathbf{a} = \mathbf{i}a_1 + \mathbf{j}a_2 + \mathbf{k}a_3$.

INTRODUCTION

The object of this paper is the presentation of a theory of lunisolar effects on the motion of an artificial satellite in a form suitable for the use of the numerical integration procedure and for the development of the perturbations into Fourier series with numerical coefficients. The numerical integration procedure is less laborious than the development into series, and the interval of integration can be of the order of several days. However, it is sometimes of interest to have the perturbations in the form of series, in particular, if a near-resonance effect occurs.

For satellites with a large ratio a/a' of semi-major axes the higher Legendre polynomials have to be included in the development of the disturbing function. The parallactic factor for a satellite with a period of 24 hours is about 0.1, and in considering the long-range stability it is advisable to take the parallactic term into consideration.

The problem of the development of perturbations into series can be solved either in an analytical or a semianalytical way. The purely analytical way is theoretically possible, but it presents considerable technical difficulties if the inclination of the orbit is not small.

Attempts made by *Musen, Bailie, and Upton* [1961] show that the technical difficulties become almost insurmountable with the inclusion of the fourth Legendre polynomial into the development of the disturbing function.

The use of a semianalytical procedure, valid for all inclinations and all eccentricities, is proposed in this paper. This method is adaptable to the use of electronic machines. The multiplication of Fourier series is performed automatically following the method developed at the National Aeronautics and Space Administration, Theoretical Division.

DEVELOPMENT OF THE DISTURBING FUNCTION

All notations in this article are the same as in the author's previous article [*Musen*, 1961] with the exception of the mean anomalies, which are designated in this paper by M and M'. The disturbing function Ω is taken in the form

$$\Omega = m'n \sum_{n=2}^{+\infty} p^{n+1} \left(\frac{a'}{r'}\right)^{n+1} \cdot \frac{1}{2\pi} \int_0^{2\pi} \left(\frac{r}{a}\right)^n P_n(\cos H)\, dM \qquad (1)$$

p is the parallactic factor a/a'. Let $\mathbf{r}^0$ be the unit vector directed from the center of the earth to the satellite. We have

$$\mathbf{r}^0 = \mathbf{P}\cos f + \mathbf{Q}\sin f \qquad (2)$$

and a corresponding unit vector for the moon (or the sun)

$$\mathbf{u}^0 = \mathbf{P}'\cos f' + \mathbf{Q}'\sin f' \qquad (3)$$

where $(\mathbf{P}, \mathbf{Q}, \mathbf{R})$ and $(\mathbf{P}', \mathbf{Q}', \mathbf{R}')$ are the basic unit vectors connected with the osculating orbit planes. We have in the equatorial system

$$\mathbf{P} = \begin{bmatrix} +\cos^2\frac{i}{2}\cos(\omega+\Omega) + \sin^2\frac{i}{2}\cos(\omega-\Omega) \\ +\cos^2\frac{i}{2}\sin(\omega+\Omega) - \sin^2\frac{i}{2}\sin(\omega-\Omega) \\ +\sin i \sin\omega \end{bmatrix} \tag{4}$$

$$\mathbf{Q} = \begin{bmatrix} -\cos^2\frac{i}{2}\sin(\omega+\Omega) - \sin^2\frac{i}{2}\sin(\omega-\Omega) \\ +\cos^2\frac{i}{2}\cos(\omega+\Omega) - \sin^2\frac{i}{2}\cos(\omega-\Omega) \\ +\sin i \cos\omega \end{bmatrix} \tag{5}$$

$$\mathbf{R} = \begin{bmatrix} +\sin i \sin\Omega \\ -\sin i \cos\Omega \\ +\cos i \end{bmatrix} \tag{6}$$

$$\mathbf{P}' = \begin{bmatrix} +\cos^2\frac{i'}{2}\cos(\omega'+\Omega') + \sin^2\frac{i'}{2}\cos(\omega'-\Omega') \\ +\cos^2\frac{i'}{2}\cos\epsilon\sin(\omega'+\Omega') - \sin^2\frac{i'}{2}\cos\epsilon\sin(\omega'-\Omega') - \sin i'\sin\epsilon\sin\omega' \\ +\cos^2\frac{i'}{2}\sin\epsilon\sin(\omega'+\Omega') - \sin^2\frac{i'}{2}\sin\epsilon\sin(\omega'-\Omega') + \sin i'\cos\epsilon\sin\omega' \end{bmatrix} \tag{7}$$

$$\mathbf{Q}' = \begin{bmatrix} -\cos^2\frac{i'}{2}\sin(\omega'+\Omega') - \sin^2\frac{i'}{2}\sin(\omega'-\Omega') \\ +\cos^2\frac{i'}{2}\cos\epsilon\cos(\omega'+\Omega') - \sin^2\frac{i'}{2}\cos\epsilon\cos(\omega'-\Omega') - \sin i'\sin\epsilon\cos\omega' \\ +\cos^2\frac{i'}{2}\sin\epsilon\cos(\omega'+\Omega') - \sin^2\frac{i'}{2}\sin\epsilon\cos(\omega'-\Omega') + \sin i'\cos\epsilon\cos\omega' \end{bmatrix} \tag{8}$$

The elements of the satellite ω, Ω, i are referred to the equator, but the elements ω', Ω', i' of the disturbing body are referred to the ecliptic of some fixed epoch. Such a choice of reference planes permits us to consider i' as a constant and ω' and Ω' as linear functions of time, provided that we are interested in determining perturbations of the first order only.

We have from (2) and (3)

$$\cos H = \mathbf{r}^0 \cdot \mathbf{u}^0 = \alpha \cos f + \beta \sin f \tag{9}$$

$$\alpha = \mathbf{P} \cdot \mathbf{u}^0 = \mathbf{P} \cdot \mathbf{P}' \cos f' + \mathbf{P} \cdot \mathbf{Q}' \sin f' \tag{10}$$

$$\beta = \mathbf{Q} \cdot \mathbf{u}^0 = \mathbf{Q} \cdot \mathbf{P}' \cos f' + \mathbf{Q} \cdot \mathbf{Q}' \sin f' \tag{11}$$

$$f' = M' + 2e' \sin M' + \ldots \tag{12}$$

In addition, we put

$$\gamma = \mathbf{R} \cdot \mathbf{u}^0 = \mathbf{R} \cdot \mathbf{P}' \cos f' + \mathbf{R} \cdot \mathbf{Q}' \sin f' \tag{13}$$

We deduce from (4)–(8)

(14) (15)

coeff.	α	β
$\cos^2 \frac{i}{2} \cos^2 \frac{i'}{2} \sin^2 \frac{\epsilon}{2}$	$+\cos(\omega + \omega' + \Omega + \Omega' + f')$	$-\sin(\omega + \omega' + \Omega + \Omega' + f')$
$\cos^2 \frac{i}{2} \cos^2 \frac{i'}{2} \cos^2 \frac{\epsilon}{2}$	$+\cos(\omega - \omega' + \Omega - \Omega' - f')$	$-\sin(\omega - \omega' + \Omega - \Omega' - f')$
$\sin^2 \frac{i}{2} \cos^2 \frac{i'}{2} \cos^2 \frac{\epsilon}{2}$	$+\cos(\omega + \omega' - \Omega + \Omega' + f')$	$-\sin(\omega + \omega' - \Omega + \Omega' + f')$
$\sin^2 \frac{i}{2} \cos^2 \frac{i'}{2} \sin^2 \frac{\epsilon}{2}$	$+\cos(\omega - \omega' - \Omega - \Omega' - f')$	$-\sin(\omega - \omega' - \Omega - \Omega' - f')$
$\cos^2 \frac{i}{2} \sin^2 \frac{i'}{2} \cos^2 \frac{\epsilon}{2}$	$+\cos(\omega + \omega' + \Omega - \Omega' + f')$	$-\sin(\omega + \omega' + \Omega - \Omega' + f')$
$\cos^2 \frac{i}{2} \sin^2 \frac{i'}{2} \sin^2 \frac{\epsilon}{2}$	$+\cos(\omega - \omega' + \Omega + \Omega' - f')$	$-\sin(\omega - \omega' + \Omega + \Omega' - f')$
$\sin^2 \frac{i}{2} \sin^2 \frac{i'}{2} \sin^2 \frac{\epsilon}{2}$	$+\cos(\omega + \omega' - \Omega - \Omega' + f')$	$-\sin(\omega + \omega' - \Omega - \Omega' + f')$
$\sin^2 \frac{i}{2} \sin^2 \frac{i'}{2} \cos^2 \frac{\epsilon}{2}$	$+\cos(\omega - \omega' - \Omega + \Omega' - f')$	$-\sin(\omega - \omega' - \Omega + \Omega' - f')$

coeff.	α	β
$\frac{1}{2}\cos^2\frac{i}{2}\sin i'\sin\epsilon$	$+\cos(\omega+\omega'+\Omega+f')$	$-\sin(\omega+\omega'+\Omega+f')$
$\frac{1}{2}\cos^2\frac{i}{2}\sin i'\sin\epsilon$	$-\cos(\omega-\omega'+\Omega-f')$	$+\sin(\omega-\omega'+\Omega-f')$
$\frac{1}{2}\sin^2\frac{i}{2}\sin i'\sin\epsilon$	$-\cos(\omega+\omega'-\Omega+f')$	$+\sin(\omega+\omega'-\Omega+f')$
$\frac{1}{2}\sin^2\frac{i}{2}\sin i'\sin\epsilon$	$+\cos(\omega-\omega'-\Omega-f')$	$-\sin(\omega-\omega'-\Omega-f')$
$\frac{1}{2}\sin i\cos^2\frac{i'}{2}\sin\epsilon$	$-\cos(\omega+\omega'+\Omega'+f')$	$+\sin(\omega+\omega'+\Omega'+f')$
$\frac{1}{2}\sin i\cos^2\frac{i'}{2}\sin\epsilon$	$+\cos(\omega-\omega'-\Omega'-f')$	$-\sin(\omega-\omega'-\Omega'-f')$
$\frac{1}{2}\sin i\sin^2\frac{i'}{2}\sin\epsilon$	$+\cos(\omega+\omega'-\Omega'+f')$	$-\sin(\omega+\omega'-\Omega'+f')$
$\frac{1}{2}\sin i\sin^2\frac{i'}{2}\sin\epsilon$	$-\cos(\omega-\omega'+\Omega'-f')$	$+\sin(\omega-\omega'+\Omega'-f')$
$\frac{1}{2}\sin i\sin i'\cos\epsilon$	$+\cos(\omega-\omega'-f')$	$-\sin(\omega-\omega'-f')$
$\frac{1}{2}\sin i\sin i'\cos\epsilon$	$-\cos(\omega+\omega'+f')$	$+\sin(\omega+\omega'+f')$

and

$$
\begin{aligned}
\gamma = {} & + \sin i\cos^2\frac{i'}{2}\sin^2\frac{\epsilon}{2}\sin(\Omega+\omega'+\Omega'+f') \\
& + \sin i\cos^2\frac{i'}{2}\cos^2\frac{\epsilon}{2}\sin(\Omega-\omega'-\Omega'-f') \\
& + \sin i\sin^2\frac{i'}{2}\cos^2\frac{\epsilon}{2}\sin(\Omega+\omega'-\Omega'+f') \\
& + \sin i\sin^2\frac{i'}{2}\sin^2\frac{\epsilon}{2}\sin(\Omega-\omega'+\Omega'-f') \\
& + \tfrac{1}{2}\sin i\sin i'\sin\epsilon\sin(\Omega+\omega'+f') \\
& - \tfrac{1}{2}\sin i\sin i'\sin\epsilon\sin(\Omega-\omega'-f') \\
& + \cos i\cos^2\frac{i'}{2}\sin\epsilon\sin(\omega'+\Omega'+f') \\
& - \cos i\sin^2\frac{i'}{2}\sin\epsilon\sin(\omega'-\Omega'+f') \\
& + \cos i\sin i'\cos\epsilon\sin(\omega'+f')
\end{aligned}
\tag{16}
$$

The expressions 14–16 for α, β, and γ are to be used if the development of the perturbations into series is required. If numerical integration is preferred, it is simpler to obtain α, β, and γ by computing independently expressions 4–6, 7–8, 12, and 10–13.

Following an idea suggested by the author in the previous article [*Musen*, 1961], the disturbing function will be developed in powers of α and β instead of using the standard procedure of developing in powers of the inclination. This procedure leads to a more compact form of the disturbing function, and in the development into series the numerical values of the inclinations can be substituted into α, β, and γ from the outset. We have from (9)

$$\cos H = \alpha \cos f + \text{sine term} \tag{17}$$

$$\cos^2 H = \tfrac{1}{2}(\alpha^2 + \beta^2) + \tfrac{1}{2}(\alpha^2 - \beta^2)\cos 2f + \text{sine terms} \tag{18}$$

$$\cos^3 H = \tfrac{3}{4}\alpha(\alpha^2 + \beta^2)\cos f + \tfrac{1}{4}(\alpha^3 - 3\alpha\beta^2)\cos 3f + \text{sine terms} \tag{19}$$

$$\cos^4 H = \tfrac{3}{8}(\alpha^2 + \beta^2)^2 + \tfrac{1}{2}(\alpha^4 - \beta^4)\cos 2f + \tfrac{1}{8}(\alpha^4 - 6\alpha^2\beta^2 + \beta^4)\cos 4f + \text{sine terms} \tag{20}$$

Only the cosine terms are retained, because the sine terms do not contribute any long-period terms in (1). Substituting 17–20 into 1, and taking the following accurate expressions,

$$\frac{1}{2\pi}\int_0^{2\pi}\frac{r^2}{a^2}\cos 2f\,dM = +\frac{5}{2}e^2$$

$$\frac{1}{2\pi}\int_0^{2\pi}\frac{r^2}{a^2}\,dM = 1 + \frac{3}{2}e^2$$

$$\frac{1}{2\pi}\int_0^{2\pi}\frac{r^3}{a^3}\cos 3f\,dM = -\frac{35}{8}e^3$$

$$\frac{1}{2\pi}\int_0^{2\pi}\frac{r^3}{a^3}\cos f\,dM = -\frac{5}{2}e - \frac{15}{8}e^3$$

$$\frac{1}{2\pi}\int_0^{2\pi}\frac{r^4}{a^4}\cos 4f\,dM = +\frac{63}{8}e^4$$

$$\frac{1}{2\pi}\int_0^{2\pi}\frac{r^4}{a^4}\cos 2f\,dM = \frac{21}{4}e^2 + \frac{21}{8}e^4$$

$$\frac{1}{2\pi}\int_0^{2\pi}\frac{r^4}{a^4}\,dM = 1 + 5e^2 + \frac{15}{8}e^4$$

into account, we deduce a compact form of the disturbing function convergent for all eccentricities and all inclinations.

We have

$$\begin{aligned}\Omega = {} & m'np^3\left(\frac{a'}{r'}\right)^3\left[\left(+\tfrac{3}{4}\alpha^2 + \tfrac{3}{4}\beta^2 - \tfrac{1}{2}\right)\right. \\ & \left. + (3\alpha^2 - \tfrac{3}{4}\beta^2 - \tfrac{3}{4})e^2\right] \\ & + m'np^4\left(\frac{a'}{r'}\right)^4\left[\left(-\frac{75}{16}\alpha^3 - \frac{75}{16}\alpha\beta^2 + \frac{15}{4}\alpha\right)e\right. \\ & \left. + \left(-\frac{25}{4}\alpha^3 + \frac{75}{16}\alpha\beta^2 + \frac{45}{16}\alpha\right)e^3\right] \\ & + m'np^5\left(\frac{a'}{r'}\right)^5\left[\left(+\frac{105}{64}\alpha^4 + \frac{105}{32}\alpha^2\beta^2\right.\right. \\ & \left. + \frac{105}{64}\beta^4 - \frac{15}{8}\alpha^2 - \frac{15}{8}\beta^2 + \frac{3}{8}\right) \\ & + \left(+\frac{315}{16}\alpha^4 + \frac{525}{32}\alpha^2\beta^2 - \frac{105}{32}\beta^4\right. \\ & \left. - \frac{615}{32}\alpha^2 + \frac{15}{32}\beta^2 + \frac{15}{8}\right)e^2 \\ & + \left(+\frac{105}{8}\alpha^4 - \frac{315}{16}\alpha^2\beta^2 + \frac{105}{64}\beta^4\right. \\ & \left.\left. - \frac{135}{16}\alpha^2 + \frac{45}{32}\beta^2 + \frac{45}{64}\right)e^4\right] + \cdots\end{aligned} \tag{21}$$

A second concise form of the disturbing function can be obtained, if we eliminate α, β, and e from (21) in favor of vectors

$$\mathbf{c} = \sqrt{1 - e^2}\,\mathbf{R} \tag{22}$$

$$\mathbf{g} = e\mathbf{P} \tag{23}$$

These vectors are closely related to the constants of the area integral and to the constant of the Laplacian integral. Substituting

$$\alpha = \frac{\mathbf{g}\cdot\mathbf{u}^0}{e},\quad \beta^2 = 1 - \alpha^2 - \gamma^2,\quad \gamma = \frac{\mathbf{c}\cdot\mathbf{u}^0}{\sqrt{1 - e^2}}$$

into (21), we deduce

$$\begin{aligned}\Omega = {} & \tfrac{3}{4}m'np^3\left(\frac{a'}{r'}\right)^3[5(\mathbf{g}\cdot\mathbf{u}^0)^2 + (\mathbf{c}\times\mathbf{u}^0)^2 - \mathbf{g}^2] \\ & + \frac{5}{16}m'np^4\left(\frac{a'}{r'}\right)^4[-35(\mathbf{g}\cdot\mathbf{u}^0)^2 \\ & - 15(\mathbf{c}\times\mathbf{u}^0)^2 + 9\mathbf{g}^2 + 12]\mathbf{g}\cdot\mathbf{u}^0 + \cdots\end{aligned} \tag{24}$$

The expressions 21 and 24 are suitable for the application of numerical integration, and in a

hidden form they contain all the long-period terms of the first order.

THE VARIATION OF CONSTANTS

Two systems of differential equations will be established. The first system will be for the classical elliptic elements, but the derivatives of Ω with respect to the elements will be eliminated in favor of derivatives with respect to α and β. This makes the actual computations easier. The second system of equations gives the vectors g and c in a direct way, and the derivation is based on the application of *Milankovich's* [1939] form of variation of constants. This theory is not widely used in celestial mechanics. Its mathematical apparatus belongs, possibly, more to the domain of theoretical physics than to the domain of classical celestial mechanics, but some recent investigations by *Popovich* [1960] show that the application of this theory to the secular perturbations of planets might be of great interest. The application of Milankovich's theory to the determination of the lunisolar effect leads to the equations that are free from the "small divisors," sin i or e, and consequently have a wider domain of validity than the equations for variations of elliptic elements.

We have from (4), (5), (10), and (11)

$$\frac{\partial\alpha}{\partial\omega} = +\beta$$

$$\frac{\partial\beta}{\partial\omega} = -\alpha$$

$$\frac{\partial\alpha}{\partial i} = +\gamma \sin\omega$$

$$\frac{\partial\beta}{\partial i} = +\gamma \cos\omega$$

and

$$\frac{\partial\alpha}{\partial\Omega} = \mathbf{u}^0\cdot\mathbf{k}\times\mathbf{P} = \mathbf{u}^0\cdot(\mathbf{k}\times(\mathbf{Q}\times\mathbf{R}))$$

$$= \mathbf{u}^0\cdot(\mathbf{Q}\cos i - \mathbf{R}\sin i\cos\omega)$$

$$\frac{\partial\beta}{\partial\Omega} = \mathbf{u}^0\cdot\mathbf{k}\times\mathbf{Q} = \mathbf{u}^0\cdot(\mathbf{k}\times(\mathbf{R}\times\mathbf{P}))$$

$$= \mathbf{u}^0\cdot(\mathbf{R}\sin i\sin\omega - \mathbf{P}\cos i)$$

or, in a final form,

$$\frac{\partial\alpha}{\partial\Omega} = \beta\cos i - \gamma\sin i\cos\omega$$

$$\frac{\partial\beta}{\partial\Omega} = \gamma\sin i\sin\omega - \alpha\cos i$$

Substituting

$$\frac{\partial\Omega}{\partial i} = \frac{\partial\Omega}{\partial\alpha}\gamma\sin\omega + \frac{\partial\Omega}{\partial\beta}\gamma\cos\omega$$

$$\frac{\partial\Omega}{\partial\omega} = \beta\frac{\partial\Omega}{\partial\alpha} - \alpha\frac{\partial\Omega}{\partial\beta}$$

$$\frac{\partial\Omega}{\partial\Omega} = \frac{\partial\Omega}{\partial\alpha}(\beta\cos i - \gamma\sin i\cos\omega) + \frac{\partial\Omega}{\partial\beta}(\gamma\sin i\sin\omega - \alpha\cos i)$$

into the equations

$$\begin{aligned}
\frac{d\Delta M}{dt} &= -\frac{1-e^2}{e}\frac{\partial\Omega}{\partial e} - 2a\frac{\partial\Omega}{\partial a}\\
\frac{di}{dt} &= \frac{\cos i}{\sin i\sqrt{1-e^2}}\frac{\partial\Omega}{\partial\omega} - \frac{1}{\sin i\sqrt{1-e^2}}\frac{\partial\Omega}{\partial\Omega}\\
\frac{d\Omega}{dt} &= \frac{1}{\sin i\sqrt{1-e^2}}\frac{\partial\Omega}{\partial i}\\
\frac{d\omega}{dt} &= +\frac{\sqrt{1-e^2}}{e}\frac{\partial\Omega}{\partial e} - \cos i\frac{d\Omega}{dt}\\
\frac{de}{dt} &= -\frac{\sqrt{1-e^2}}{e}\frac{\partial\Omega}{\partial\omega}
\end{aligned} \tag{25}$$

we deduce for the long-period lunisolar effects

$$\begin{aligned}
\frac{d\Delta M}{dt} &= -\frac{1-e^2}{e}\frac{\partial\Omega}{\partial e} - 2p\frac{2\partial}{\partial p}\left(\frac{\Omega}{p}\right)\\
\frac{di}{dt} &= \frac{\gamma}{\sqrt{1-e^2}}\cdot\left(\frac{\partial\Omega}{\partial\alpha}\cos\omega - \frac{\partial\Omega}{\partial\beta}\sin\omega\right)\\
\frac{d\Omega}{dt} &= \frac{\gamma}{\sin i\sqrt{1-e^2}}\cdot\left(\frac{\partial\Omega}{\partial\alpha}\sin\omega + \frac{\partial\Omega}{\partial\beta}\cos\omega\right)\\
\frac{d\omega}{dt} &= \frac{\sqrt{1-e^2}}{e}\frac{\partial\Omega}{\partial e} - \cos i\frac{d\Omega}{dt}\\
\frac{de}{dt} &= -\frac{\sqrt{1-e^2}}{e}\left(\beta\frac{\partial\Omega}{\partial\alpha} - \alpha\frac{\partial\Omega}{\partial\beta}\right)
\end{aligned} \tag{26}$$

in addition, we have

$$da/dt = 0$$

If the development into series is required, we compute (26) in terms of ω, ω', Ω, Ω', f' using (14)–(16). In the process of computation several small terms with the factors of the form $p^k \sin^l i'/2$ can be neglected. The transition from f' to M' is performed using the standard formulas and therefore is not presented in detail. Because of the smallness of e', only the first two or three powers of e' should be retained.

As an application and for a check we will develop the equations for variation of constants for the case of a close satellite. We put

$$\Omega = m'np^3\left(\frac{a'}{r'}\right)^3\left[\left(\frac{3}{4}\alpha^2 + \frac{3}{4}\beta^2 - \frac{1}{2}\right) + \left(3\alpha^2 - \frac{3}{4}\beta^2 - \frac{3}{4}\right)e^2\right]$$

Substituting this value into (26), we deduce

$$\begin{aligned}
\frac{di}{dt} &= \frac{3m'n\gamma}{2\sqrt{1-e^2}}\,p^3\left(\frac{a'}{r'}\right)^3 \\
&\cdot[(1+4e^2)\alpha\cos\omega - (1-e^2)\beta\sin\omega] \\
\sin i\,\frac{d\Omega}{dt} &= \frac{3m'n\gamma}{2\sqrt{1-e^2}}\,p^3\left(\frac{a'}{r'}\right)^3 \\
&\cdot[(1+4e^2)\alpha\sin\omega + (1-e^2)\beta\cos\omega] \qquad (27) \\
\frac{d\omega}{dt} &= \frac{3m'n}{2}\,p^3\left(\frac{a'}{r'}\right)^3(4\alpha^2 - \beta^2 - 1) \\
&\cdot\sqrt{1-e^2} - \cos i\,\frac{d\Omega}{dt} \\
\frac{de}{dt} &= -\frac{15m'ne}{2}\,p^3\left(\frac{a'}{r'}\right)^3\alpha\beta\sqrt{1-e^2}
\end{aligned}$$

This system is identical with the system deduced by the author in his previous article [*Musen*, 1961] using a less direct method.

The equations of Milankovich for the disturbed motion

$$\frac{d^2\mathbf{r}}{dt^2} = -\frac{\mu^2\mathbf{r}}{r^3} + \operatorname{grad} R$$

are

$$\begin{aligned}
\frac{d\mathbf{c}}{dt} &= \mathbf{c}\times\nabla_{\mathbf{c}}R + \mathbf{g}\times\nabla_{\mathbf{g}}R \\
\frac{d\mathbf{g}}{dt} &= \mathbf{g}\times\nabla_{\mathbf{c}}R + \frac{\mu^2 - \mathbf{g}^2}{\mathbf{c}^2}\,\mathbf{c} \\
&\quad\times\nabla_{\mathbf{g}}R - \frac{\mathbf{c}^2}{\mathbf{g}^2}\,\frac{\partial R}{\partial\tau}\,\mathbf{g}
\end{aligned}$$

with

$$\begin{aligned}
\mathbf{c} &= \mu\sqrt{a(1-e^2)}\,\mathbf{R} \\
\mathbf{g} &= \mu^2 e\mathbf{P}
\end{aligned}$$

and the symbols $\nabla_{\mathbf{c}}$ and $\nabla_{\mathbf{g}}$ designate the partial del operators

$$\begin{aligned}
\nabla_{\mathbf{c}} &= \mathbf{i}\frac{\partial}{\partial c_1} + \mathbf{j}\frac{\partial}{\partial c_2} + \mathbf{k}\frac{\partial}{\partial c_2} \\
\nabla_{\mathbf{g}} &= \mathbf{i}\frac{\partial}{\partial g_1} + \mathbf{j}\frac{\partial}{\partial g_2} + \mathbf{k}\frac{\partial}{\partial g_2}
\end{aligned}$$

For long-period lunisolar effects in the motion of an artificial satellite, the equations of Milankovich take a simpler form

$$\begin{aligned}
\frac{d\mathbf{c}}{dt} &= \mathbf{c}\times\nabla_{\mathbf{c}}\Omega + \mathbf{g}\times\nabla_{\mathbf{g}}\Omega \\
\frac{d\mathbf{g}}{dt} &= \mathbf{g}\times\nabla_{\mathbf{c}}\Omega + \mathbf{c}\times\nabla_{\mathbf{g}}\Omega
\end{aligned} \qquad (28)$$

with $\mathbf{c}$ and $\mathbf{g}$ defined by (22) and (23) and Ω defined by (24). The system (28) admits two particular integrals

$$\begin{aligned}
\mathbf{c}^2 + \mathbf{g}^2 &= 1 \\
\mathbf{c}\cdot\mathbf{g} &= 0
\end{aligned}$$

These integrals can be used either for a check or to reduce the computation to four components instead of six. As an application we give here the explicit form of the equations for the perturbations of a close satellite. It is not difficult to write these equations for more general cases. We have

$$\Omega = \tfrac{3}{4}m'np^3\left(\frac{a'}{r'}\right)^3[5(\mathbf{g}\cdot\mathbf{u}^0)^2 + (\mathbf{c}\times\mathbf{u}^0)^2 - \mathbf{g}^2]$$

Taking

$$\nabla_{\mathbf{g}}(\mathbf{g}\cdot\mathbf{u}^0)^2 = 2\mathbf{g}\cdot\mathbf{u}^0\mathbf{u}^0$$

$$\nabla_{\mathbf{g}}\mathbf{g}^2 = 2\mathbf{g}$$

$$\nabla_{\mathbf{c}}(\mathbf{c}\times\mathbf{u}^0)^2 = \nabla_{\mathbf{c}}(\mathbf{c}^2 - \mathbf{c}\cdot\mathbf{u}^0\mathbf{u}^0\cdot\mathbf{c}) = 2(\mathbf{c} - \mathbf{c}\cdot\mathbf{u}^0\mathbf{u}^0)$$

$$\nabla_{\mathbf{g}}\Omega = \frac{3m'n}{2}p^3\left(\frac{a'}{r'}\right)^3(5\mathbf{g}\cdot\mathbf{u}^0\mathbf{u}^0 - \mathbf{g})$$

$$\nabla_{\mathbf{c}}\Omega = \frac{3m'n}{2}p^3\left(\frac{a'}{r'}\right)^3(\mathbf{c} - \mathbf{c}\cdot\mathbf{u}^0\mathbf{u}^0)$$

into consideration, we deduce a system with no 'small divisors.'

$$\frac{d\mathbf{c}}{dt} = \tfrac{3}{2}m'np^3\left(\frac{a'}{r'}\right)^3(5\mathbf{g}\times\mathbf{u}^0\mathbf{u}^0\cdot\mathbf{g} - \mathbf{c}\times\mathbf{u}^0\mathbf{u}^0\cdot\mathbf{c}) \qquad (29)$$

$$\frac{d\mathbf{g}}{dt} = \tfrac{3}{2}m'np^3\left(\frac{a'}{r'}\right)^3(2\mathbf{g}\times\mathbf{c} - \mathbf{g}\times\mathbf{u}^0\mathbf{u}^0\cdot\mathbf{c} + 5\mathbf{c}\times\mathbf{u}^0\mathbf{u}^0\cdot\mathbf{g}) \qquad (30)$$

This form for equations is suitable for the determination of the influence of the sun on a close satellite. As is seen from (29) and (30), the change of $\mathbf{c}$ is always in the plane normal to $\mathbf{u}^0$ and the change of $\mathbf{g}$ can be decomposed into two components, the first one in the direction of $\mathbf{Q}$ and the second normal to $\mathbf{u}^0$.

In order to deduce the long-period perturbations caused by the moon, the process of averaging with respect to M', the mean anomaly of the moon, must be applied to (29) and (30). We have

$$\frac{1}{2\pi}\int_0^{2\pi}\left(\frac{a'}{r'}\right)^3\mathbf{u}^0\mathbf{u}^0\,dM' = \frac{1}{2\pi}\int_0^{2\pi}\left(\frac{a'}{r'}\right)^3(\mathbf{P}'\cos f' + \mathbf{Q}'\sin f')\cdot(\mathbf{P}'\cos f' + \mathbf{Q}'\sin f')\,dM'$$

$$= \frac{1}{2\pi}\int_0^{2\pi}\left(\frac{a'}{r'}\right)^3\{\tfrac{1}{2}(\mathbf{P}'\mathbf{P}' + \mathbf{Q}'\mathbf{Q}') + \tfrac{1}{2}(\mathbf{P}'\mathbf{P}' - \mathbf{Q}'\mathbf{Q}')\cos 2f\}\,dM'$$

Taking

$$\mathbf{P}'\mathbf{P}' + \mathbf{Q}'\mathbf{Q}' = I - \mathbf{R}'\mathbf{R}'$$

where I is the idemfactor, and

$$\frac{1}{2\pi}\int_0^{2\pi}\left(\frac{a'}{r'}\right)^3 dM' = (1 - e'^2)^{-3/2}$$

$$\frac{1}{2\pi}\int_0^{2\pi}\left(\frac{a'}{r'}\right)^3\cos 2f'\,dM' = 0$$

into account, we have

$$\frac{1}{2\pi}\int_0^{2\pi}\left(\frac{a'}{r'}\right)^3\mathbf{u}^0\mathbf{u}^0\,dM' = \tfrac{1}{2}(1 - e'^2)^{-3/2}(I - \mathbf{R}'\mathbf{R}')$$

Substituting this result into (29) and (30), we deduce for the long-period lunar effect

$$\frac{d\mathbf{c}}{dt} = \tfrac{3}{4}m'np^3(1 - e'^2)^{-3/2}(\mathbf{c}\times\mathbf{R}'\mathbf{R}'\cdot\mathbf{c} - 5\mathbf{g}\times\mathbf{R}'\mathbf{R}'\cdot\mathbf{g}) \qquad (29')$$

$$\frac{d\mathbf{g}}{dt} = \tfrac{3}{4}m'np^3(1 - e'^2)^{-3/2}[2\mathbf{c}\times\mathbf{g} + \mathbf{g}\times\mathbf{R}'\mathbf{R}'\cdot\mathbf{c} - 5\mathbf{c}\times\mathbf{R}'\mathbf{R}'\cdot\mathbf{g}]$$

By forming the dot product of (29′) and $\mathbf{R}$ we deduce for the long-period lunar effect in the eccentricity a formula analogous to the last equation of (27)

$$\frac{de}{dt} = +\frac{15m'ne\sqrt{1 - e^2}}{4}p^3\mathbf{P}\cdot\mathbf{R}'\mathbf{R}'\cdot\mathbf{Q}(1 - e'^2)^{-3/2}$$

It is of interest to note that the long-period lunar effect on close satellites depends only upon the position of the orbital plane of the moon and is not influenced by the position of the lunar perigee. In addition, the change of the areal velocity $\mathbf{c}$ is always parallel to the orbit of the moon. The form of the perturbations is not so simple for more distant satellites, because the terms depending upon the position of the lunar perigee will appear in the parallactic term.

CONCLUSION

This article contains two forms of the development of the averaged disturbing function to be used in the determination of long-period lunar and solar effects in the motion of an artificial satellite. The first form represents a development into series of polynomials with respect to cosines of the angles between the vectorial elements **P**, **Q** of the satellite and the position vector of the disturbing body. The second, more compact form utilizes the areal velocity and the Laplacian vector of the satellite to eliminate 'small divisors,' sin i and e, from the equations for perturbations. The perturbations can either be developed into trigonometric series with numerical coefficients or they can be obtained by the method of numerical integration. The form of equations established here permits the interval of integration to be of the order of 10 days or even more.

The development of the perturbations into trigonometric series is of interest if the near-resonance condition occurs. The main types of near-resonance conditions were listed by *Cook* [1961]. Cook and *Musen* [1961] arrived quite independently at similar equations for lunisolar perturbations for close satellites. Cook's equations are similar to equations 27 of this article.

ACKNOWLEDGMENTS

I should like to take this opportunity to express my gratitude to my colleagues, Mrs. Ann Bailie and Miss Maxine Goldstein, for the careful preparation of the manuscript for print.

REFERENCES

Cook, G. E., Luni-solar perturbations of the orbit of an earth satellite, Report published by Royal Aircraft Establishment Farnborough, 1961.

Milankovich, M., *Bull. Acad. Math. Natur.* (*A*) *Sci. Math. Phys.*, no. 6, Belgrade, 1939.

Musen, P., On the long-period lunisolar effect in the motion of the artificial satellite, *J. Geophys. Research*, *66*(6) 1659–1665, 1961.

Musen, P., A. Bailie, and E. Upton, Development of the lunar and solar perturbations in the motion of an artificial satellite, *NASA Tech. Note, D–494*, 1961.

Popovich, B., Secular perturbations of vectorial elements of planetary orbits, (Serb.), *Sci. Soc. Bosnia*, *14*, ser. 3, pp. 1–50, 1960.

(Manuscript received June 8, 1961.)

On the Long-Period Effects in the Motion of an Artificial Satellite Caused by the Ellipticity of the Equator of the Earth[1]

BY PETER MUSEN

Theoretical Division
NASA Goddard Space Flight Center

If a satellite has a mean daily motion nearly commensurable with the angular velocity of rotation of the earth, long-period perturbations will influence its motion. The eccentricity of such a commensurable orbit is not necessarily small, as the orbit of Explorer VI shows. This circumstance caused the author to develop a semianalytical method of treating these perturbations, which avoids the development of the disturbing function into powers of the eccentricity and consequently includes the cases of elongated orbits and orbits with moderate eccentricities.

SYMBOLS

l, the mean anomaly of the satellite.
f, the true anomaly of the satellite.
g, the argument of the perigee of the satellite.
h, the longitude of the ascending node of the satellite.
i, the inclination of the satellite orbit with respect to the equator.
e, the eccentricity of the orbit of the satellite.
a, the semimajor axis of the orbit of the satellite.
n, the mean motion of the satellite.
n', the angular velocity of rotation of the earth.
ϵ, the eccentric anomaly of the satellite.
r, the radius vector of the satellite.
x, y, z, the coordinates of the satellite with respect to the rotating system.
Ω, the disturbing function.
R, the averaged disturbing function.

INTRODUCTION

This article considers the long-period perturbations in the motion of a satellite produced by the ellipticity of the earth's equator.

If the mean daily motion of the satellite is nearly commensurable with the angular velocity of rotation of the earth, long-period (critical) terms appear in the development of the disturbing function. Methods developed by *O'Keefe and Batchlor* [1957], *Sehnal* [1960], and *Cook* [1961] are applicable to the cases when the eccentricity is small and the coefficients of the critical terms can be developed into rapidly convergent power series in the eccentricity. However, the eccentricities of the commensurable orbits are not necessarily small, as the example of Explorer VI shows. Moreover, in many cases of the commensurability, like $n'/n=\frac{2}{3}$ or $\frac{2}{5}$, the influence of the ellipticity of the equator can be found more easily from observations when the eccentricity is not small. All these circumstances caused the author to develop a theory applicable to moderate and large eccentricities indiscriminately, up to $e=0.8$, approximately. This value can be considered the upper limit to practical application of the theory, because for larger e the basic series of this theory begin to converge more slowly. The basic idea of the described method is similar to that of *Brouwer* [1947] in treating the secular perturbations of eccentric orbits.

[1] Published in the January 1962 issue of *Journal of Geophysical Research*. Reprinted by permission.

DEVELOPMENT OF THE DISTURBING FUNCTION

Instead of developing the coefficients of the critical terms in the disturbing function and its derivatives into series in powers of the eccentricity, the numerical value of e is substituted from the outset and the values of the coefficients are computed by means of numerical integration. Thus the development set forth in this article is numerical with respect to the eccentricity but literal with respect to all remaining elements. The motion of the satellite is referred to the system of coordinates rigidly connected with the rotating earth. The coordinates of the satellite are given with respect to this system, but the elliptic elements of satellite's orbit are given with respect to the inertial system having its origin in the center of the earth, the x and y axes lying in the equator and the z axis being directed toward the north pole. With the proper choice of the moving axes [*O'Keefe and Batchlor*, 1957] the disturbing function Ω can be represented in the form

$$\Omega = (A_{22}/r^3)(x^2 - y^2)/r^2 \tag{1}$$

where

$$\begin{aligned} x &= r\cos(f+g)\cos(h-n't) \\ &\quad - r\sin(f+g)\sin(h-n't)\cos i \\ y &= r\cos(f+g)\sin(h-n't) \\ &\quad + r\sin(f+g)\cos(h-n't)\cos i \\ z &= r\sin(f+g)\sin i \end{aligned} \tag{2}$$

Substituting (2) into (1), we deduce

$$\begin{aligned} \Omega &= \frac{A_{22}}{4a^3}(1+\cos i)^2\left(\frac{a}{r}\right)^3 \\ &\quad \cdot\cos(2f+2g+2h-2n't) \\ &\quad + \frac{A_{22}}{4a^3}(1-\cos i)^2\left(\frac{a}{r}\right)^3 \\ &\quad \cdot\cos(2f+2g-2h+2n't) \\ &\quad + \frac{A_{22}}{2a^3}\sin^2 i\left(\frac{a}{r}\right)^3\cos(2h-2n't) \end{aligned} \tag{3}$$

Introducing the critical argument

$$w = sl - 2n't$$

we have

$$\begin{aligned} \Omega &= \frac{A_{22}}{4a^3}(1+\cos i)^2\left(\frac{a}{r}\right)^3 \\ &\quad \cdot\cos(2f - sl + w + 2g + 2h) \\ &\quad + \frac{A_{22}}{4a^3}(1-\cos i)^2\left(\frac{a}{r}\right)^3 \\ &\quad \cdot\cos(2f + sl - w + 2g - 2h) \\ &\quad + \frac{A_{22}}{2a^3}\sin^2 i\left(\frac{a}{r}\right)^3\cos(-sl + w + 2h) \end{aligned} \tag{4}$$

Using (4) we can write the long-period part of the disturbing functions as

$$R = \frac{1}{2\pi}\int_0^{2\pi}\Omega\, dl \tag{5}$$

Taking

$$\frac{1}{2\pi}\int_0^{2\pi}\left(\frac{a}{r}\right)^p\sin(qf - sl)\, dl = 0$$

into consideration, and putting

$$Q_s^{p,q} = \frac{1}{\pi}\int_0^{\pi}\left(\frac{a}{r}\right)^p\cos(qf - sl)\cdot dl \tag{6}$$

we deduce

$$\begin{aligned} R &= \frac{A_{22}}{4a^3}(1+\cos i)^2 Q_s^{3,2} \\ &\quad \cdot\cos(sl + 2g + 2h - 2n't) \\ &\quad + \frac{A_{22}}{4a^3}(1-\cos i)^2 Q_{-s}^{3,2} \\ &\quad \cdot\cos(sl - 2g + 2h - 2n't) \\ &\quad + \frac{A_{22}}{2a^3}\sin^2 i\, Q_s^{3,0}\cos(sl + 2h - 2n't) \end{aligned} \tag{7}$$

The coefficients $Q_s^{p,q}$ are functions of the eccentricity only, and they are to be computed by taking the quadrature (6) numerically for the given value of e. If the eccentricity is large, neither the mean nor the eccentric nor the true anomaly is convenient for use as the basic variable in the process of integration along the whole orbit. In some part of the orbit one of the anomalies might be more convenient than

another, but the use of any of these anomalies along the complete orbit leads to the multiplication of a large number by a small one and in addition the use of Kepler's equation becomes inconvenient. For these reasons a new anomaly is introduced by means of the equation

$$\tfrac{1}{2} f = am(u, k) \tag{8}$$

with

$$k^2 = 2e/(1 + e) \tag{9}$$

and

$$k'^2 = (1 - e)/(1 + e) \tag{10}$$

The introduction of u leads to the representation of the integrand by means of rapidly convergent series even for large eccentricities, and the troublesome divisor $1 - e$ will appear in front of the integral. Basically, the anomaly u does not differ from the anomaly introduced by *Gravelius* [1889] in treating the planetary perturbations in the case of highly eccentric orbits. The transformation of Gravelius is a special case of *Gylden*'s [1869] transformation.

We deduce from (8)

$$\frac{a}{r} = \frac{1 + e\cos f}{1 - e^2} = \frac{1 + k'^2}{2k'^2}\, dn^2 u \tag{11}$$

and from (8) and the last equation

$$d\epsilon = \frac{1}{\sqrt{1 - e^2}} \cdot \frac{r}{a}\, df = \frac{2k'}{dnu}\, du \tag{12}$$

$$dl = 2\frac{r}{a} \cdot \frac{k'}{dnu}\, du \tag{13}$$

It follows from (11) and (13)

$$dl = \frac{4k'^3}{1 + k'^2} \cdot \frac{du}{dn^3 u} \tag{14}$$

Taking

$$\frac{k'}{dnu} = dn(u + K)$$

and

$$dn^3 u = \frac{1 + k'^2}{2}\, dnu - \frac{1}{2}\frac{d^2}{du^2}(dnu)$$

into account, we have from (14)

$$dl = 2\, dn(u + K)\, du - \frac{2}{1 + k'^2}\frac{d^2}{du^2}\, dn(u + K)\, du$$

and

$$l = 2am(u + K) - \pi - \frac{2}{1 + k'^2}\frac{d}{du}\frac{k'}{dnu} \tag{15}$$

The half of the period $2K$ is computed using the formulas

$$P = (1 - \sqrt{k'})/(1 + \sqrt{k'})$$

$$\lambda = \left(\frac{P}{2}\right) + 2\left(\frac{P}{2}\right)^5 + 15\left(\frac{P}{2}\right)^9 + \cdots$$

$$\sqrt{\frac{2K}{\pi}} = 1 + 2\lambda + 2\lambda^4 + 2\lambda^9 + \cdots$$

We obtain from (6), (8), (11), (13), and (15)

$$Q^{p,q}_{s} = \frac{1}{2^{p-2}} \frac{(1 + k'^2)^{p-1}}{k'^{2p-3}} \frac{1}{\pi} \cdot \int_0^K \cos(qf - sl) \cdot dn^{2p-3} u\, du \tag{16}$$

and

$$qf - sl = 2qamu - 2s \cdot am(u + K) + s\pi + \frac{2s}{1 + k'^2}\frac{d}{du}\frac{k'}{dnu} \tag{17}$$

The argument $qf - sl$ and $dn^{2p-3}\, u$ can be developed into fast convergent Fourier series, and for the purpose of computing the perturbations only the first few terms of these series need be taken into consideration. Taking the developments

$$amu = \frac{\pi u}{2K} + \sum_{n=1}^{\infty} \frac{2\lambda^n}{n(1 + \lambda^{2n})} \sin\frac{n\pi u}{K} \tag{18}$$

and $$\frac{k'}{dnu} = \frac{\pi}{2K} + \frac{\pi}{K}\sum_{n=1}^{\infty} (-1)^n \frac{2\lambda^n}{1 + \lambda^{2n}} \cos\frac{n\pi u}{K} \tag{18'}$$

into consideration, we deduce from (15) and (17) the following rapidly convergent series

$$l = \frac{\pi u}{K} + 4\sum_{n=1}^{\infty}(-1)^n\left(\frac{1}{n} + \frac{\pi^2}{K^2}\frac{n}{1+k'^2}\right) \cdot \frac{\lambda^n}{1+\lambda^{2n}}\sin\frac{n\pi u}{K} \qquad (19)$$

$$qf - sl = \frac{\pi(q-s)}{K}u + 4\sum_{n=1}^{\infty}\left\{\frac{q+s(-1)^{n+1}}{n} + \frac{\pi^2}{K^2}\frac{ns(-1)^{n+1}}{1+k'^2}\right\}\frac{\lambda^n}{1+\lambda^{2n}}\cdot\sin\frac{n\pi u}{K} \qquad (20)$$

In addition we have

$$dnu = \frac{\pi}{2K} + \frac{\pi}{K}\sum_{n=1}^{\infty}\frac{2\lambda^n}{1+\lambda^{2n}}\cos\frac{n\pi u}{K} \qquad (21)$$

Using the system of formulas 20 and 21 we can easily obtain the values of $Q_s^{p,q}$ by means of a numerical quadrature. The value of λ is small even for large eccentricities; for example, for $e=0.8$ we have $\lambda=0.134$.

In order to compute the perturbations of the elements we have to form the derivatives of R with respect to the elements. All the derivatives can be easily computed analytically except the derivative with respect to the eccentricity, which must be computed numerically. Differentiating (6) with respect to e, and taking

$$\frac{\partial}{\partial e}\frac{a}{r} = \frac{a^2}{r^2}\cos f$$

$$\frac{\partial f}{\partial e} = \left(\frac{a}{r} + \frac{1}{1-e^2}\right)\sin f$$

into consideration, we obtain a general formula for the numerical computation of the derivative $Q_s^{p,q}$ with respect to e

$$\frac{\partial}{\partial e}Q_s^{p,q} = \frac{p+q}{2}Q_s^{p+1,q+1} + \frac{p-q}{2}Q_s^{p+1,q-1} + \frac{q}{2}\frac{1}{1-e^2}(Q_s^{p,q+1} - Q_s^{p,q-1})$$

In our particular case we have, taking $Q_s^{p,q} = Q_{-s}^{p,-q}$ into consideration,

$$\frac{\partial}{\partial e}Q_s^{3,2} = \frac{5}{2}Q_s^{4,3} + \tfrac{1}{2}Q_s^{4,1} + \frac{1}{1-e^2}(Q_s^{3,3} - Q_s^{3,1})$$

and

$$\frac{\partial}{\partial e}Q_s^{3,0} = \tfrac{3}{2}(Q_s^{4,1} + Q_{-s}^{4,1})$$

The coefficients $Q_s^{p,q}$ are identical with the coefficients $X_s^{-p,q}$ of *Hansen* [1855], and if e is small either Hansen's development of these coefficients into series or Cayley's tables can be used if an analytic representation is desired.

THE PROBLEM OF INTEGRATION

In performing the integration the canonical elements of Delaunay are used. This choice is justified by the simplicity of the process by which the perturbations of higher orders can be obtained, if necessary [*von Zeipel*, 1916; *Brown and Shook*, 1933]. We assume that the commensurability is not extremely sharp and that the integrals can be represented in the trigonometrical form. In a case of a sharp commensurability the theory of resonance should be applied. In terms of Delaunay canonical variables

$$L = \sqrt{a} \qquad l$$
$$G = \sqrt{a(1-e^2)} \qquad g$$
$$H = \sqrt{a(1-e^2)}\cdot\cos i \qquad h$$

the disturbing function can be expressed in the form

$$R = \frac{1}{4}\frac{A_{22}}{L^6}\left(1+\frac{H}{G}\right)^2 Q_s^{3,2}\cdot\cos(sl + 2g + 2h - 2n't) + \frac{1}{4}\frac{A_{22}}{L^6}\left(1-\frac{H}{G}\right)^2 Q_{-s}^{3,2}\cdot\cos(sl - 2g + 2h - 2n't) + \frac{1}{2}\frac{A_{22}}{L^6}\left(1-\frac{H^2}{G^2}\right)Q_s^{3,0}\cdot\cos(sl + 2h - 2n't) \qquad (22)$$

The gravitational constant is set equal to 1. The value of A_{22} is comparable to the value of the coefficient of the fourth harmonic, and we will limit ourselves to the perturbations of the first order with respect to A_{22}. We can assume in performing the integration that the arguments are linear functions of time, if only the perturbations of the first order with respect to A_{22} are to be determined. The mean motions of l, g, and h can be taken from *Brouwer*'s [1959] work, and for L, G, H we substitute their mean values in the right-hand side of the equations.

We deduce from

$$\frac{dL}{dt} = +\frac{\partial R}{\partial l} \qquad \frac{dl}{dt} = -\frac{\partial R}{\partial L}$$

$$\frac{dG}{dt} = +\frac{\partial R}{\partial g} \qquad \frac{dg}{dt} = -\frac{\partial R}{\partial G}$$

$$\frac{dH}{dt} = +\frac{\partial R}{\partial h} \qquad \frac{dh}{dt} = -\frac{\partial R}{\partial H}$$

the following equations:

$$\begin{aligned}\frac{dL}{dt} = &-\frac{1}{4}\frac{A_{22}}{L^6}s\left(1+\frac{H}{G}\right)^2 Q_s^{3,2}\\ &\cdot\sin(sl+2g+2h-2n't)\\ &-\frac{1}{4}\frac{A_{22}}{L^6}s\left(1-\frac{H}{G}\right)^2 Q_{-s}^{3,2}\\ &\cdot\sin(sl-2g+2h-2n't)\\ &-\frac{1}{2}\frac{A_{22}}{L^6}s\left(1-\frac{H^2}{G^2}\right) Q_s^{3,0}\\ &\cdot\sin(sl+2h-2n't)\end{aligned} \tag{23}$$

$$\begin{aligned}\frac{dG}{dt} = &-\frac{1}{2}\frac{A_{22}}{L^6}\left(1+\frac{H}{G}\right)^2 Q_s^{3,2}\\ &\cdot\sin(sl+2g+2h-2n't)\\ &+\frac{1}{2}\frac{A_{22}}{L^6}\left(1-\frac{H}{G}\right)^2 Q_{-s}^{3,2}\\ &\cdot\sin(sl-2g+2h-2n't)\end{aligned} \tag{24}$$

$$\begin{aligned}\frac{dH}{dt} = &-\frac{1}{2}\frac{A_{22}}{L^6}\left(1+\frac{H}{G}\right)^2 Q_s^{3,2}\\ &\cdot\sin(sl+2g+2h-2n't)\\ &-\frac{1}{2}\frac{A_{22}}{L^6}\left(1-\frac{H}{G}\right)^2 Q_{-s}^{3,2}\\ &\cdot\sin(sl-2g+2h-2n't)\\ &-\frac{A_{22}}{L^6}\left(1-\frac{H^2}{G^2}\right) Q_s^{3,0}\\ &\cdot\sin(sl+2h-2n't)\end{aligned} \tag{25}$$

and, taking

$$\frac{\partial Q_s^{p,q}}{\partial L} = \frac{1}{e}\frac{\partial Q_s^{p,q}}{\partial e}\frac{G^2}{L^3}$$

$$\frac{\partial Q_s^{p,q}}{\partial G} = -\frac{1}{e}\frac{\partial Q_s^{p,q}}{\partial e}\frac{G}{L^2}$$

into account, we have

$$\begin{aligned}\frac{dl}{dt} &= -\frac{\partial R}{\partial L} - \frac{1}{e}\frac{\partial R}{\partial e}\frac{G^2}{L^3}\\ &= \frac{A_{22}}{L^7}\left(\frac{3}{2}\cdot Q_s^{3,2} - \frac{1}{4e}\frac{G^2}{L^2}\frac{\partial Q_s^{3,2}}{\partial e}\right)\\ &\quad\cdot\left(1+\frac{H}{G}\right)^2\cos(sl+2g+2h-2n't)\\ &\quad+\frac{A_{22}}{L^7}\left(\frac{3}{2}\cdot Q_{-s}^{3,2} - \frac{1}{4e}\frac{G^2}{L^2}\frac{\partial Q_{-s}^{3,2}}{\partial e}\right)\\ &\quad\cdot\left(1-\frac{H}{G}\right)^2\cos(sl-2g+2h-2n't)\\ &\quad+\frac{A_{22}}{L^7}\left(3\,Q_s^{3,0} - \frac{1}{2e}\frac{G^2}{L^2}\frac{\partial Q_s^{3,0}}{\partial e}\right)\\ &\quad\cdot\left(1-\frac{H^2}{G^2}\right)\cos(sl+2h-2n't)\end{aligned} \tag{26}$$

$$\begin{aligned}\frac{dg}{dt} &= -\frac{\partial R}{\partial G} + \frac{1}{e}\frac{\partial R}{\partial e}\cdot\frac{G}{L^2}\\ &= \frac{1}{4}\frac{A_{22}}{L^7}\left[2\frac{H}{L}\cdot\frac{L^2}{G^2}\left(1+\frac{H}{G}\right)Q_s^{3,2}\right.\\ &\quad\left.+\left(1+\frac{H}{G}\right)^2\frac{1}{e}\frac{\partial Q_s^{3,2}}{\partial e}\frac{G}{L}\right]\end{aligned}$$

$$\cdot\cos(sl+2g+2h-2n't)$$
$$-\frac{1}{4}\frac{A_{22}}{L^7}\left[2\frac{H}{L}\cdot\frac{L^2}{G^2}\left(1-\frac{H}{G}\right)Q^{3,2}_{-s}\right.$$
$$\left.-\left(1-\frac{H}{G}\right)^2\frac{1}{e}\frac{\partial Q^{3,2}_{-s}}{\partial e}\frac{G}{L}\right]$$
$$\cdot\cos(sl-2g+2h-2n't)$$
$$-\frac{1}{2}\frac{A_{22}}{L^7}\left[2\frac{H^2}{L^2}\cdot\frac{L^3}{G^3}Q^{3,0}_{s}\right.$$
$$\left.-\left(1-\frac{H^2}{G^2}\right)\frac{1}{e}\frac{\partial Q^{3,0}_{s}}{\partial e}\frac{G}{L}\right]$$
$$\cdot\cos(sl+2h-2n't) \qquad (27)$$

$$\frac{dh}{dt}=-\frac{1}{2}\frac{A_{22}}{L^7}\left(1+\frac{H}{G}\right)\frac{L}{G}Q^{3,2}_{s}$$
$$\cdot\cos(sl+2g+2h-2n't)$$
$$+\frac{1}{2}\frac{A_{22}}{L^7}\left(1-\frac{H}{G}\right)\frac{L}{G}Q^{3,2}_{-s}$$
$$\cdot\cos(sl-2g+2h-2n't)$$
$$+\frac{A_{22}}{L^7}\cdot\frac{H}{L}\cdot\frac{L^2}{G^2}Q^{3,0}_{s}$$
$$\cdot\cos(sl+2h-2n't) \qquad (28)$$

Putting

$$\gamma_{22}=A_{22}/L^4$$

and designating the mean motions of the arguments

$$sl+2g+2h-2n't,\ sl-2g+2h-2n't,\ sl+2h-2n't$$

by

$$W_1/L^3,\ W_2/L^3,\ W_3/L^3$$

we deduce the following expressions for perturbations:

$$\frac{\delta L}{L}=\frac{1}{4}\frac{s\gamma_{22}}{W_1}\left(1+\frac{H}{G}\right)^2Q^{3,2}_{s}$$
$$\cdot\cos(sl+2g+2h-2n't)$$
$$+\frac{1}{4}\frac{s\gamma_{22}}{W_2}\left(1-\frac{H}{G}\right)^2Q^{3,2}_{-s}$$
$$\cdot\cos(sl-2g+2h-2n't)$$
$$+\frac{1}{2}\frac{s\gamma_{22}}{W_3}\left(1-\frac{H^2}{G^2}\right)Q^{3,0}_{s}$$
$$\cdot\cos(sl+2h-2n't) \qquad (29)$$

$$\frac{\delta G}{L}=\frac{\gamma_{22}}{2W_1}\left(1+\frac{H}{G}\right)^2Q^{3,2}_{s}$$
$$\cdot\cos(sl+2g+2h-2n't)$$
$$-\frac{\gamma_{22}}{2W_2}\left(1-\frac{H}{G}\right)^2Q^{3,2}_{-s}$$
$$\cdot\cos(sl-2g+2h-2n't) \qquad (30)$$

$$\frac{\delta H}{L}=\frac{\gamma_{22}}{2W_1}\left(1+\frac{H}{G}\right)^2Q^{3,2}_{s}$$
$$\cdot\cos(sl+2g+2h-2n't)$$
$$+\frac{\gamma_{22}}{2W_2}\left(1-\frac{H}{G}\right)^2Q^{3,2}_{-s}$$
$$\cdot\cos(sl-2g+2h-2n't)$$
$$+\frac{\gamma_{22}}{W_3}\left(1-\frac{H^2}{G^2}\right)\cos(sl+2h-2n't) \qquad (31)$$

$$\delta l=\frac{\gamma_{22}}{W_1}\left(\tfrac{3}{2}Q^{3,2}_{s}-\frac{1}{4e}\frac{G^2}{L^2}\frac{\partial Q^{3,2}_{s}}{\partial e}\right)$$
$$\cdot\left(1+\frac{H}{G}\right)^2\cos(sl+2g+2h-2n't)$$
$$+\frac{\gamma_{22}}{W_2}\left(\tfrac{3}{2}Q^{3,2}_{-s}-\frac{1}{4e}\frac{G^2}{L^2}\frac{\partial Q^{3,2}_{-s}}{\partial e}\right)$$
$$\cdot\left(1-\frac{H}{G}\right)^2\cos(sl-2g+2h-2n't)$$
$$+\frac{\gamma_{22}}{W_3}\left(3Q^{3,0}_{s}-\frac{1}{2e}\frac{G^2}{L^2}\frac{\partial Q^{3,0}_{s}}{\partial e}\right)$$
$$\cdot\left(1-\frac{H^2}{G^2}\right)\cos(sl+2h-2n't) \qquad (32)$$

$$\delta g=\frac{1}{4}\frac{\gamma_{22}}{W_1}\left[2\frac{H}{L}\cdot\frac{L^2}{G^2}\left(1+\frac{H}{G}\right)Q^{3,2}_{s}\right.$$
$$\left.+\frac{1}{e}\left(1+\frac{H}{G}\right)^2\frac{\partial Q^{3,2}_{s}}{\partial e}\frac{G}{L}\right]$$
$$\cdot\sin(sl+2g+2h-2n't)$$
$$-\frac{1}{4}\frac{\gamma_{22}}{W_2}\left[2\frac{H}{L}\cdot\frac{L^2}{G^2}\left(1-\frac{H}{G}\right)Q^{3,2}_{-s}\right.$$
$$\left.-\frac{1}{e}\left(1-\frac{H}{G}\right)^2\frac{\partial Q^{3,2}_{-s}}{\partial e}\frac{G}{L}\right]$$
$$\cdot\sin(sl-2g+2h-2n't)$$
$$-\frac{1}{2}\frac{\gamma_{22}}{W_3}\left[2\frac{H^2}{L^2}\cdot\frac{L^3}{G^3}Q^{3,0}_{s}\right.$$

$$- \left(1 - \frac{H^2}{G^2}\right) \frac{1}{e} \frac{\partial Q_*^{3,0}}{\partial e} \frac{G}{L}\Bigg]$$

$$\cdot \sin (sl + 2h - 2n't) \qquad (33)$$

$$\delta h = -\frac{\gamma_{22}}{2W_1}\left(1 + \frac{H}{G}\right)\frac{L}{G} Q_*^{3,2}$$

$$\cdot \sin (sl + 2g + 2h - 2n't)$$

$$+ \frac{\gamma_{22}}{2W_2}\left(1 - \frac{H}{G}\right)\frac{L}{G} Q_{-*}^{3,2}$$

$$\cdot \sin (sl - 2g + 2h - 2n't)$$

$$+ \frac{\gamma_{22}}{W_3}\frac{H}{L}\cdot\frac{L^2}{G^2} Q_*^{3,0} \sin (sl + 2h - 2n't) \qquad (34)$$

CONCLUSION

The semianalytical method of treating the influence of the ellipticity of the equator on the motion of a satellite is presented in this article. This method does not require a development of the disturbing function into powers of the eccentricity and, consequently, is valid for highly eccentric orbits. Its validity for orbits with a small eccentricity depends on the type of programing used. Programing with a floating decimal point would permit its use for small eccentricities also.

Long-period terms appear in the development of the perturbations if the mean daily motion of the satellite is commensurable with the angular velocity of the earth's rotation. It must be remarked that the influence of the ellipticity of the earth's equator is larger for a satellite with a direct motion than for a satellite with a retrograde motion, providing that i and e are small, as could easily be seen from an analytic development of the disturbing function. The order of the coefficients of the long-period terms is higher if the motion is retrograde. Thus, if it is planned to launch a satellite with a mean motion commensurable with the earth's rotational velocity and at the same time it is wished to diminish or eliminate the influence of the ellipticity of the equator, the satellites must be launched into a retrograde orbit.

ACKNOWLEDGMENT

I wish to express my gratitude to my colleague, Mrs. Ann Bailie, for her valuable assistance in checking the manuscript.

REFERENCES

Brouwer, D., Secular variations of the elements of Encke's comet, *Astron. J.*, *52*, 190–198, 1947.

Brouwer, D., Solution of the problem of artificial satellite theory, *Astron. J.*, *64*, 379–397, 1959.

Brown, E. W., and C. A. Shook, *Planetary Theory*, Cambridge, 1933.

Cook, A. H., Resonant orbits of artificial satellites and longitudinal terms in the earth external potential, *Geophys. J.*, *4*, 53–72, 1961.

Gravelius, H., Notices préliminaires sur une application des fonctions elliptiques au calcul des perturbations planétaires, *Bull. Astron.*, *6*, 141–151, 1889.

Gylden, H., *Über eine Methode die Störungen eines Cometen vermittelst rasch convergierender Ausdrücke darzustellen*, St. Petersburg, 1869.

Hansen, P. A., Entwickelungen der negativen und ungeraden Potenzen usw., *Abhandl. ABH. Königl. sächs. Ges. Wiss.*, *IV*, 283–376, 1855.

O'Keefe, J. A., and C. D. Batchlor, Perturbations of a close satellite by the equatorial ellipticity of the earth, *Astron. J.*, *62*, 183, 1957.

Sehnal, L., The influence of the equatorial ellipticity of the earth gravitational field on the motion of a close satellite, *Bull. Astron. Inst. Czechoslovakia*, *11*(3), 90–93, 1960.

Von Zeipel, H., *Arkiv Astron., Mat., Fys.*, *11*(1), 1916.

(Manuscript received September 27, 1961; revised October 19, 1961.)

Page intentionally left blank

PART II: IONOSPHERIC PHYSICS

Page intentionally left blank

Radio Propagation Measurements Using the Explorer VI Satellite[1]

BY CARL D. GRAVES
Space Technology Laboratories, Inc.

This paper presents the results of an experiment to measure the electron density above the ionosphere. The experiment utilized two coherent signals, one VHF and one UHF, transmitted from the Explorer VI satellite. The evidence of our data is that the electron concentration in the vicinity of the satellite, 18,000 km above the earth, was unusually high, of the order of 10^4 electrons/cm^3. However, the results were influenced by unexpectedly high correction factors and possibly by an intense world-wide magnetic storm that occurred during the measurement period.

This paper presents the results of an experiment to measure the electron density above the ionosphere. The experiment utilized two coherent signals, one VHF (approximately 108 Mc/s) and one UHF (approximately 378 Mc/s), transmitted from the Explorer VI satellite. This satellite had a perigee of 136 miles and an apogee of 23,000 miles. Eight separate measurements were made at a receiving station in Hawaii before one of the coherent transmitters failed. To determine the electron density at the satellite, measurements were made of the Doppler difference frequency and the rate of change of the Faraday polarization rotation. Five of the records were of good quality and have been analyzed. Although suggestive results were obtained, not enough data are available to make definite assertions. However, these preliminary measurements indicated that the electron density appeared to be much higher than had been expected. It should be noted that the results were obtained after a large magnetic storm and also that they are contingent upon estimated corrections made for ray bending and for the effects of a nonstatic ionosphere.

When these corrections are small the simultaneous measurement of the difference between the Doppler shift at two frequencies and the change of the Faraday rotation can be used to obtain an accurate measurement of the electron density in the vicinity of the satellite. This comes about in the following way. The time rate of change of the phase of a high-frequency transmission from a satellite is

$$\frac{dP}{dt} = [\mathbf{V}\cdot\mathbf{k}], + \int d\mathbf{l}\cdot\frac{\partial \mathbf{k}}{\partial t} \qquad (1)$$

where $\mathbf{V}$ is the velocity of the satellite relative to the receiving station, $\mathbf{k}$ is the propagation vector normal to the phase front with a magnitude of $\omega n/c$, n is the index of refraction, c is the velocity of light in a vacuum, and ω is the angular frequency of the transmission. The term $\mathbf{V}\cdot\mathbf{k}$ is evaluated at the satellite, and the integral is evaluated along the path that the

[1] This paper was presented at the Symposium on the Exosphere and Upper *F* Region sponsored by Commission III of the United States National Committee of the International Scientific Radio Union (URSI), held on May 4, 1960, in Washington, D.C. Published in the September 1960 issue of *Journal of Geophysical Research*. Reprinted by permission.

energy propagates. This equation holds for either polarization propagation mode. If two coherent frequencies, f_1 and $f_2 = qf_1$, are transmitted from the satellite, the difference between them, when compared at the same frequency, that is, f_1 and qf_1, is

$$W = [\mathbf{V} \cdot (q\mathbf{k}_1 - \mathbf{k}_2)]_s + \int d\mathbf{l} \cdot \frac{\partial}{\partial t} (q\mathbf{k}_1 - \mathbf{k}_2) \quad (2)$$

where the difference between the two propagation paths can be neglected. The first term in equation 2, the usual *Seddon* [1953] type difference frequency term, is proportional to the electron density at the satellite. When electron-density measurements are made in the exosphere it is necessary to include the effect of time changes in electron density in the ionosphere. In the exosphere the electron densities to be measured are small, and changes in electron density throughout the ionosphere can have an appreciable effect on the Doppler difference frequency. Therefore a part of the present experiment [*Kelso*, 1958] involved measuring the value of the integral appearing in equation 2. This was accomplished by recording the rate of Faraday rotation, ϕ, which can be expressed using the quasi-longitudinal approximation as

$$\phi = [\mathbf{V} \cdot (\mathbf{k} - \mathbf{k}')]_s + \int d\mathbf{l} \cdot \frac{\partial}{\partial t} (\mathbf{k} - \mathbf{k}') \quad (3)$$

where the primes distinguish one circular propagation mode from the other.[2]

Thus, to determine the electron density at the satellite, equations 2 and 3 are combined. But it should be noted that in equation 3 the term evaluated at the satellite is proportional to the product of the magnetic field and the electron density. Since the magnetic field at the satellite at the ranges involved in the Explorer VI measurements (12,000 to 26,000 miles above the earth) is much smaller than the magnetic field through the ionosphere, the correction to the electron density contributed by this term is negligible. Hence, at the usual high-frequency approximation for the index of refraction and quasi-longitudinal propagation [*Mitra*, 1952], equation 3 becomes

$$\int \frac{\partial N}{\partial t} dl = \frac{C_1 \phi}{\overline{H}_L} \quad (4)$$

where $\overline{H}_L$ is an average value of the longitudinal component of the magnetic field through the ionosphere and C_1 is a constant for any frequency. Equation 2 is most easily solved for the electron density, N, expressing $\mathbf{V}$ in polar coordinates with respect to the receiving station; then

$$N = \frac{1}{V_R} \left[C_2 W - \int \frac{\partial N}{\partial t} dl - C_3 V_\theta \delta \right] \quad (5)$$

where V_R and V_θ are the radial and zenith angle polar components, respectively, of $\mathbf{V}$, and δ is the angle between the propagation vectors of the two frequencies at the satellite as a result of their different ray bending. The small amount of refraction for these high frequencies allowed the neglect of higher-order terms in δ. Combining equations 4 and 5 yields for the electron density

$$N = [1/V_R][C_2 W - (C_1 \phi / \overline{H}_L) - C_3 V_\theta \delta] \quad (6)$$

This expression for N contains the two measured quantities W and ϕ, the polar components of velocity known from orbit data, and the unknown average magnetic field $\overline{H}_L$ and ray-bending difference angle δ. Hence, to obtain a value for the electron density it is necessary to make an estimate of $\overline{H}_L$ and δ. Because of the uncertainty associated with these estimates, however, it is desirable that they be small corrections to W, the precisely determined Doppler term. This problem, inherent in the radio propagation method for determining electron densities in the exosphere, necessitates the accumulation of considerable data at well-chosen orbit positions and times. For example, temporal changes within the ionosphere are relatively small later at night. Also, for example, the refraction correction is small when elevation angles are close to 90°. Unfortunately in the short time that electron-density measurements were taken from Explorer

[2] The integral in equation 3 is evaluated along the energy propagation path of the VHF signal. In an exact treatment the two modes of propagation have slightly different propagation paths. However, to order $1/\omega^5$ the propagation paths are identical and hence this effect can be neglected.

VI it was not possible to obtain data when both the correction terms were small.

Eight separate electron-density measurements were made at our Hawaiian tracking station in the period August 13 through 23, 1959, for periods varying from 20 to 70 minutes. After the latter date one of the two coherent transmitters on board the satellite failed and the electron-density measurements had to be discontinued. On three occasions, August 13, 15, and 19, severe fading of the VHF signal made the data unanalyzable.[3] For the other five measurements, an attempt was made to estimate the ray-bending correction using ionospheric electron-density profiles obtained from the Bureau of Standards sounding station at Hawaii and a model electron-density profile[4] above the peak of the F layer. Unfortunately, owing to ionospheric abnormalities, electron profiles were available only for the last two days, August 22 and 23.

On August 23 the ray-bending correction was estimated to be small, approximately 10 per cent of W, the Doppler term in equation 6. The Doppler measurement yielded an uncorrected electron density of 10^4 electrons/cm^3. The Faraday measurement yielded an equivalent electron density due to the 'growing' 3×10^4 electrons/cm^3. This value was obtained using the measured ϕ and the earth's magnetic field component along the ray path at 300 km for $\overline{H}_L$. The net electron density is the difference[5] between these values (equation 6), or approximately 2×10^4 electrons/cm^3. The height of the satellite above the earth at this time was 18,000 km, and its position was 5°N latitude and 120°W longitude. This result is considerably higher than would be expected from the interpretation of whistler propagation studies. On August 22 data were taken while the satellite was passing through apogee, and, hence, the radial component of the satellite velocity was essentially zero. This was done to provide a check on the procedure, since under these conditions the Doppler difference frequency depends only on the ray-bending correction and the changing electron content of the ionosphere which is measured by the Faraday rotation. Using the ionospheric sounding data to calculate the ray-bending effect and the earth's magnetic field at 300 km with the measured Faraday rotation to calculate the ionospheric effect, results were obtained which checked with the measured value of the Doppler difference frequency to within a few per cent. Even though ionospheric sounding data were lacking for the other three times of measurement, an effort was made to analyze the data by calculating ray-bending corrections using a typical ionosphere. On August 16 this correction was estimated to be sufficiently small to allow a calculation of electron density. Again the data yielded electron densities of the order of 10^4 electrons/cm^3 at a height above the earth of about 20,000 km.

The evidence of our data is that the electron concentration in the vicinity of the satellite was unusually high, but in view of the small amount of data acquired and the occurrence of unexpectedly high correction factors these results can only be regarded as having order-of-magnitude validity. An event that may have influenced the results presented here was the intense worldwide magnetic storm and the abrupt increase in solar flare activity recorded on August 16 and 17. During the storm and increased activity period the low-energy scintillation counter on Explorer VI (200-kev to 1-Mev electrons) gradually increased its counting rate. By August 18 it had increased by a factor of 30, and it remained abnormally high for many days thereafter. Also, data reported on at this symposium by Farmer and Robinson indicate that electron densities have increased by an order of magnitude at heights 800 km above the earth shortly after a large solar flare. In conclusion, because of the difficulties encountered, inherent in this type of propagation measurement of electron densities in the

[3] The unusual fading of the VHF signal occurred almost every evening at Hawaii and will be the subject of a forthcoming publication.

[4] The model of the exosphere used was based upon the data presented by *Townsend* [1959].

[5] Note that only the absolute value of the two measured terms in equation 6 is measured in this experiment. Consequently, whether these terms should be added or subtracted depends on whether the ionospheric electron content is increasing or decreasing.

exosphere, it seems desirable to use a more direct means for these measurements in the future.

ACKNOWLEDGMENT

I should like to thank Dr. Saul Altshuler and Dr. Richard Wagner for many helpful discussions of these measurements, and Dr. John Kelso who was a collaborator in the initial phases of the experiment.

REFERENCES

Kelso, J. M., The measurement of electron densities in the outer ionosphere, *Proc. Conf. Propagation of Radio Waves, Liège, October 1958.*

Mitra, S. K., *The Upper Atmosphere,* Asiatic Society Monograph Series, vol. 5, Calcutta, India, 2nd edition, 1952.

Seddon, J. C., *J. Geophys. Research, 58,* 323, 1953.

Townsend, J. W., Jr., Soviet papers presented at the rocket and satellite symposium, *Science, 129,* 80–84, 1959.

Daytime Whistler-Mode Attenuation through the Lower Ionosphere at 15.5 Kc as Measured on Explorer VI during Launch Trajectory[1]

BY R. F. MLODNOSKY[2]
Radioscience Laboratory
Stanford University

BY R. A. HELLIWELL AND L. H. RORDEN
Stanford Research Institute

Signals from the U.S. Navy Station NSS (15.5 kc) were detected over the altitude range of zero to about 160 km by a satellite-borne VLF receiver during the daytime launch phase of the Explorer VI Satellite. The signals were received on a small electric antenna which was also used simultaneously to transmit VHF telemetry. During the launch phase, the antenna was confined between the third-stage rocket case and the folded solar paddles, with an epoxy shroud covering the satellite and the third-stage rocket. Nevertheless, signals were clearly visible in amplitude-time chart recordings (50-cps bandwidth) up to 67 km altitude. The signal variations between 67 km and 160 km were obtained by narrow-band cross-correlating filter techniques. The receiver output was interpreted in terms of incident electric field strength, and the total measured attenuation through the lower ionosphere up to 150 km was estimated to be 43 db. A predicted total attenuation was computed including the effects of absorption, the change in antenna impedance within the ionosphere, reflection losses and antenna polarization. The predicted and measured attenuations are in good agreement. The measurements are compared with those of relevant rocket and satellite experiments. It is concluded that the launching of the whistler mode, at least in daytime, can be described by utilizing a sharply-bounded model of the ionosphere to account for the reflection-transmission phenomenon, and a slowly-varying model to account for the absorption experienced by the transmitted wave.

INTRODUCTION

The Explorer VI Satellite was launched from Cape Canaveral at about 0930 Eastern Standard time on 7 August 1959. Among the scientific instruments aboard this satellite was a calibrated VLF receiver designed to study whistler-mode propagation and ionospheric noise.[1,3] The receiver was designed to receive transmissions from the U.S. Navy Station NSS (15.5 kc) at Annapolis, and had a dynamic range of about 80 db and a 3-db bandwidth of 100 cps.[2]

Signals were to be received on a small electric antenna which was used simultaneously to transmit VHF Telemetry. The antenna consisted of two lineal elements, about three-fourths of a meter long, approximately parallel to the satellite spin axis (and the rocket longitudinal axis before rocket-satellite separation). The

[1] This manuscript was submitted for publication, but the untimely death of the principal author has prevented final revision.
[2] Deceased June 24, 1963.
[3] Superior numbers in text designate References.

elements were electrically connected and functioned at VHF as a monopole relative to the satellite body. The undetected receiver intermediate-frequency output was telemetered in analog form beginning before lift-off and continuing throughout the launch until the rocket went over the horizon from Cape Canaveral. The data were obtained during undisturbed ionospheric conditions and thus afforded the opportunity to study the propagation of VLF radio waves through the lowest layers of the "quiet" ionosphere.

In order to interpret the data, it is essential to have a clear understanding of the satellite environment during the launch period. The satellite proper was mounted so that the forward end of the third-stage rocket was located between the antenna elements. The solar paddles were folded over the antenna, reducing the sensitivity by an estimated 30 db. (This sensitivity change was estimated by comparing measurements made on a model of the satellite with paddles erected, with measurements made on the actual satellite mounted on a floor-stand pedestal with paddles folded.) In addition, an epoxy shroud covered the entire satellite and third-stage rocket. The above conditions apply to all data that will be utilized here. The small amount of data obtained after the epoxy shroud was jettisoned could not be meaningfully interpreted.

An initial examination of chart recordings of the data in a 50-cps bandwidth revealed that, in spite of the above shielding of the antenna, NSS signals were detected up to an altitude of about 67 km. The signal disappeared into the noise background at the most interesting altitudes; namely just as the vehicle entered the D-region. The data were extended in altitude with the aid of cross-correlating, narrow-band filtering techniques.

The receiver output variations were referred to the receiver input and interpreted in terms of incident relative electric field strength. Calculations of whistler-mode absorption were made for various electron density and collision frequency models of the lower ionosphere. Absorption and other attenuating effects were combined to estimate a predicted total attenuation. The predicted attenuation was found to be in good agreement with the measured value.

DATA ANALYSIS

The undetected output of the VLF receiver was heterodyned down to 2.932 kc in the satellite and added to the telemetry baseband. At the ground station, VLF receivers also monitored station NSS. The NSS signal received on the ground was heterodyned down to 0.884 kc and recorded without rectification together with the telemetry baseband. Thus, the magnetic tape data recordings contained both the output of the satellite VLF receiver and the output of the ground VLF receiver.

The satellite and ground receiver outputs were selected (by filtering—50 cps bandwidth), then rectified and presented in amplitude-time chart recordings. An important section of the launch chart-recording is shown in figure 1. The top channel is the rectified ground receiver output, and shows a normal sequence of dots and dashes in the Morse code. The bottom channel is the rectified satellite receiver output. Timing marks are shown on the upper event-marker channel. Amplitude calibration pulses appear about every 30 seconds in the satellite channel. A good quality calibration pulse is shown between the sections labeled loop 19 and loop 24. Each calibration pulse consists of two levels, the first of which calibrates the receiver and the second of which measures the magnitude of the antenna impedance.

In the satellite channel, the NSS signal amplitude decreases quickly, disappearing into the increasing noise background at about 67 km (within the portion labeled loop 11). The increasing telemetry noise level at just above this altitude is believed to be associated with the interaction of the vehicle and the ionosphere and its discussion is outside the scope of this paper. Before the signal disappeared into the noise, as shown in figure 1, its amplitude was determined by comparison with the calibration pulse amplitudes. The amplitude variations of receiver output below 67 km were scaled directly from the chart recordings and are given in figure 2. Sufficient points are plotted to represent the detailed variations exhibited by the data.

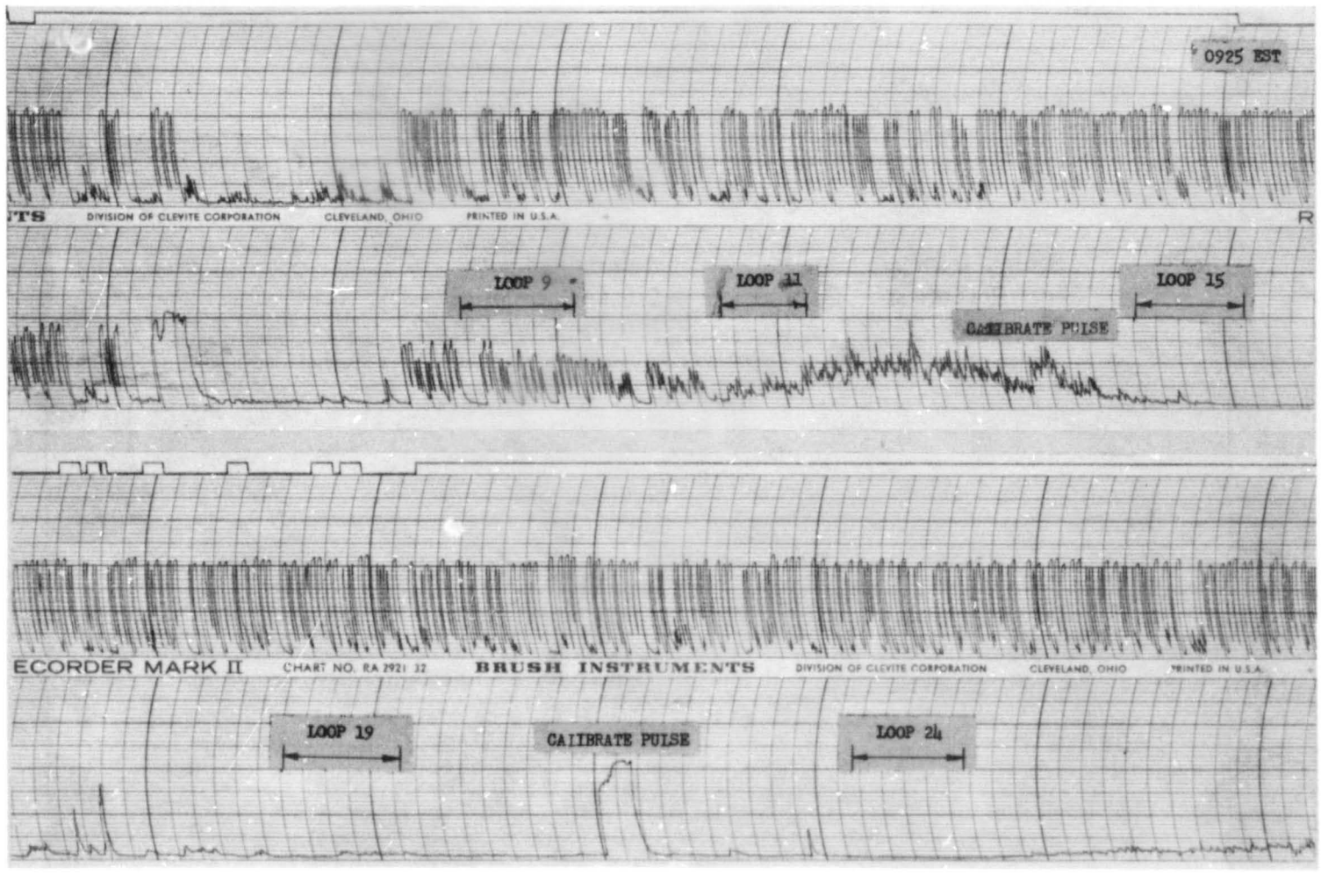

FIGURE 1.—*Section of chart recording of the launch data. Upper channel is detected ground receiver output. Bottom channel is detected satellite receiver output.*

The receiver output variations after the signal disappeared into the noise were measured with the aid of cross-correlating, narrow-band filtering techniques. A block diagram of the device used is shown in figure 3. The basic principle is bandwidth reduction, achieved by the heterodyning of the satellite receiver output f_s to a center frequency of 100 cps where narrow bandwidths are easily realized. Post-detection filtering was also employed. Referring to figure 3, it can be seen that the satellite receiver output is heterodyned in Mixer No. 3. The portion of the satellite receiver output spectrum to be examined was selected by adjustment of the mixing frequency $(3\frac{1}{2}f_g - f_v)$. The fixed component of the mixing frequency $3\frac{1}{2}f_g$ was generated by the frequency multiplying circuitry from either an audio oscillator f_g', or the ground receiver output f_g. The variable frequency component f_v was generated by a voltage controlled oscillator (VCO). Provisions were made for the manual adjustment or periodic control of the VCO with a function generator. The filtering operations indicated in the block diagram were performed by switch-selected components to provide for faster-than-real-time data processing.

When the audio oscillator was used, the mixing frequency signal was continuous and the device operated solely as a narrow-band filter. When the ground receiver output was used, the mixing frequency signal was present only when NSS was keyed on. This mode of operation is equivalent to cross-correlation between the satellite signal and the essentially noiseless ground-channel information. Cross-correlation in this case reduces the average noise power relative to the average signal power. No provisions were made for adjusting the time delay, and thus the cross-correlation mode was useful only when the delay between the satellite and ground receiver signals was negli-

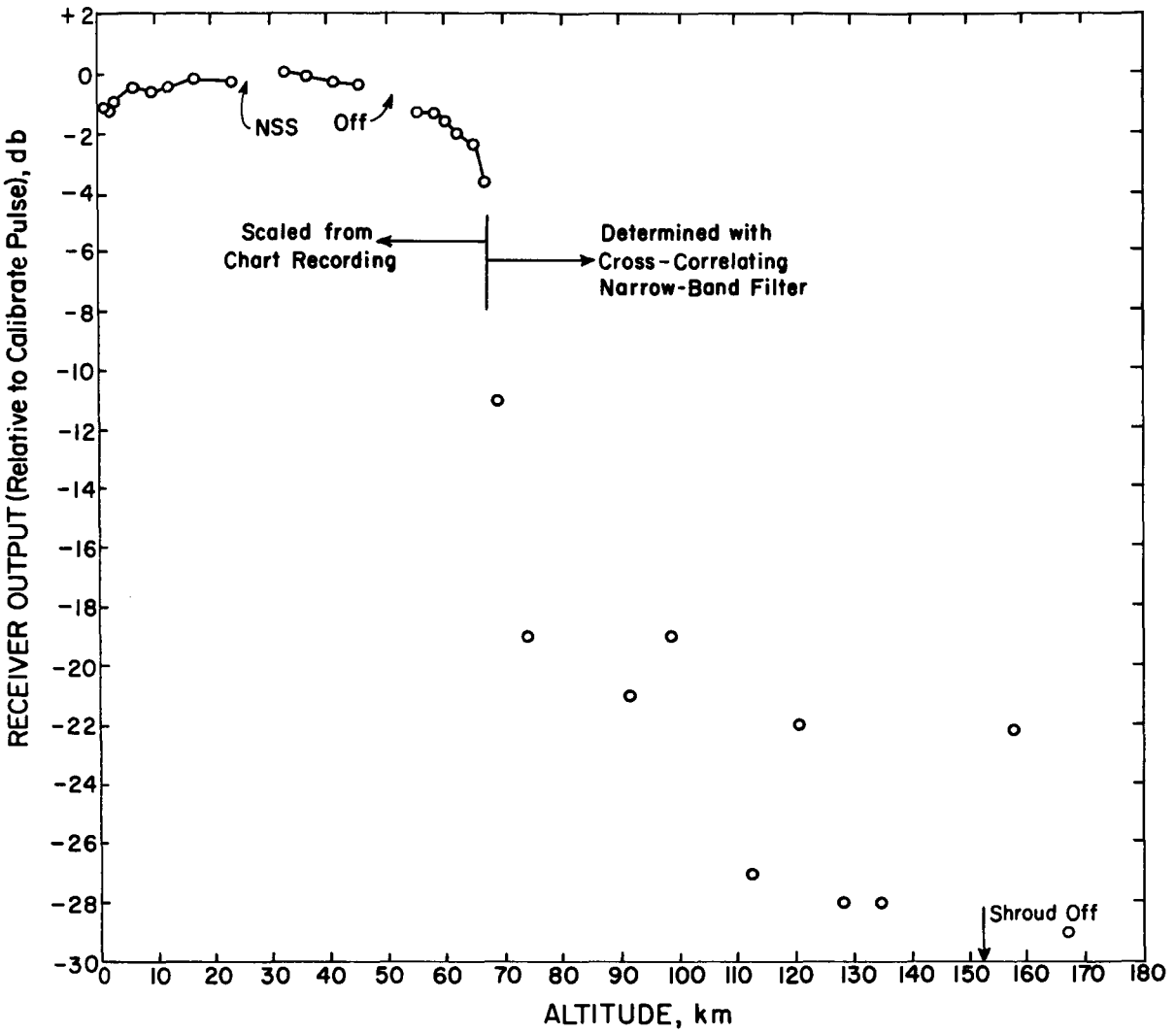

FIGURE 2.—*Satellite receiver output level relative to calibrate pulse plotted vs. altitude.*

gible with respect to the time scale of NSS traffic. During launch the time delay was assumed to be negligible.

The device described above was used with the launch data in the cross-correlation mode at twice normal tape-playback speed. A predetection bandwidth of 1.7 cps and a 12.0-second post-detection time constant were used. The ground receiver output supplied the fixed frequency component of the mixing frequency. It was found that with the above equipment adjustments, maximum spectral detail was obtained and the measurements were repeatable. Smaller predetection bandwidths were not useful because of tape recorder limitations. Sections of records to be analyzed were rerecorded on magnetic tape loops which contained 4 seconds of real-time data. While a tape loop was circulating, the VCO was manually advanced and the loop allowed to circulate until a steady output was achieved. The result was a spectrum for each 4-second section of the receiver output data.

Selected examples of the spectra obtained are shown in figure 4. The corresponding sections of the chart recording are labeled with the appropriate tape-loop numbers in figure 1. Although 25 loops were made,

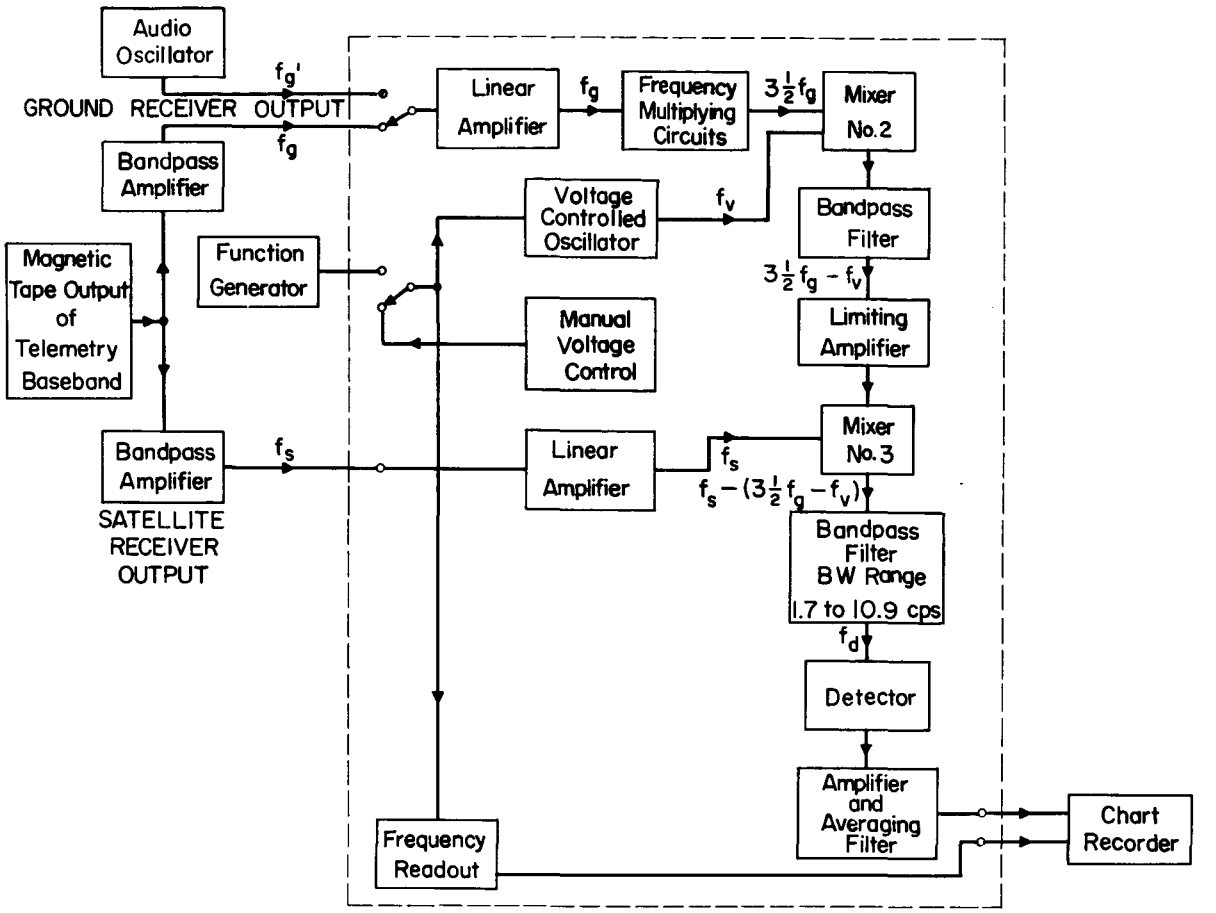

FIGURE 3.—*Block diagram of cross-correlating narrow-band filter.*

certain loops were discarded because they contained impulsive noise or calibration pulses. It should be noted that the frequency scale in figure 4 is slightly nonlinear. No absolute frequency scale is given because of slow (order of hours) frequency drifts in the system. The limits of the 50 cps noise bandwidth were relied upon for approximate frequency identification within any given spectrum.

The spectrum of loop 9 is in a portion of the data where the NSS signal is readily visible in the chart-recording, and the spectrum of NSS traffic is clearly defined. The succeeding loops exhibit less signal as can be seen in figure 4, and the spectra are more complex. Loop 15 shows small secondary peaks on either side of the central spectrum. This phenomenon is enhanced in loop 19. The exact cause of these secondary peaks is not known, but may be some form of interference. The appearance of these spectra suggests some form of amplitude modulation of the NSS signal as received at the satellite, although the mechanism for such modulation is not obvious. It was assumed, a priori, that the level of NSS signal is measured by the central peaks in these spectra. The most convincing support for this assumption lies in the systematic and meaningful variation of the electric field strength with altitude which is ultimately deduced. The probability that various random noise or interference sources could produce the systematic variation obtained must be exceedingly small.

The relative level of the signals in the spectra was determined by comparing the central peaks in the spectra to the peak in a reference spectrum where the signal was scalable on the chart recording (loop 9 in this case) and then account-

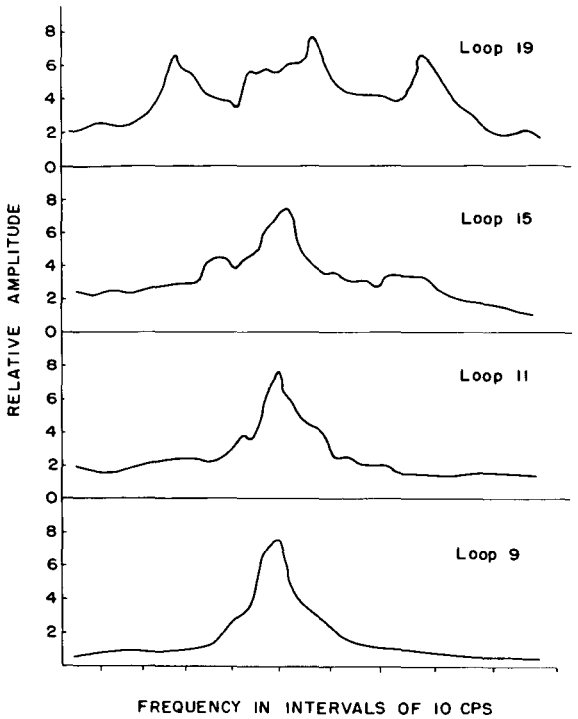

FIGURE 4.—*Selected spectra obtained with the cross-correlating narrow-band filter. Corresponding sections of the chart-recording are labeled in figure 1.*

ing for the noise power contained in the peaks of the spectra. The data so obtained are plotted in figure 2 for altitudes above 67 km. It can be seen that there is considerable scatter in the data.

It will be noted that the cross-correlating, narrow-band filter extended the receiver output measurements to 167 km altitude and to a level 25 db below that possible using the chart recordings. The sensitivity improvement that might have been expected is 24 db. This is based on an 18 db gain from a reduction in the predetection bandwidth from 50 to 0.85 cps, a 3 db gain from reduction of average noise power by the cross-correlation technique for an estimated duty cycle of 50% for NSS traffic, a 5 db gain from the post-detection averaging of each 4-second sample, and an estimated 2 db loss because of detector SNR reduction. This agreement between the observed and predicted performance of the correlating filter is surprisingly good.

The receiver output was referred to the receiver input through the receiver gain characteristic which was approximately logarithmic. For the data below 67 km, the receiver gain was set by NSS signal amplitude. For the data above 67 km, the receiver gain was set primarily by the noise in the receiver passband. The resulting curve of receiver input vs altitude is shown in figure 5. It can be noted that there is considerably less scatter in figure 5 than was present in the receiver output curve as shown in figure 2. This fact is the principal justification for the interpretation of the spectra of figure 4 as described above.

MEASURED TOTAL ATTENUATION

In order to determine the variation of electric field strength with altitude, it was necessary to consider the antenna orientation and changes in the terminal impedance of the antenna. The antenna elements made an angle with the vertical of 70° and greater after the rocket entered the D-region. On the assumption that the wave normal in the whistler mode was vertical, the correction for antenna orientation was no more than 1 db and can be considered negligible. Measurements of the magnitude of antenna impedance during launch showed no significant variations until the shroud was jettisoned, although the impedance was different from that in free space because of the proximity of the third-stage rocket, solar paddles and epoxy shroud. The lack of significant variation in antenna terminal impedance before shroud ejection is believed to be due to the fact that the epoxy shroud shielded the antenna elements from electron and ion currents from the ionosphere.[3] With the effects of both antenna orientation and the change in antenna impedance being negligible, the curve of receiver input can be considered to represent the variation of relative electric field strength between about 60 and 152 km altitude.

Absorption calculations, described later, indicate that absorption begins about 10 km below the inflection point of the field strength curve, or about 60 km in this case. Assuming that the whistler-mode signal is launched into the ionosphere at this height, the measured

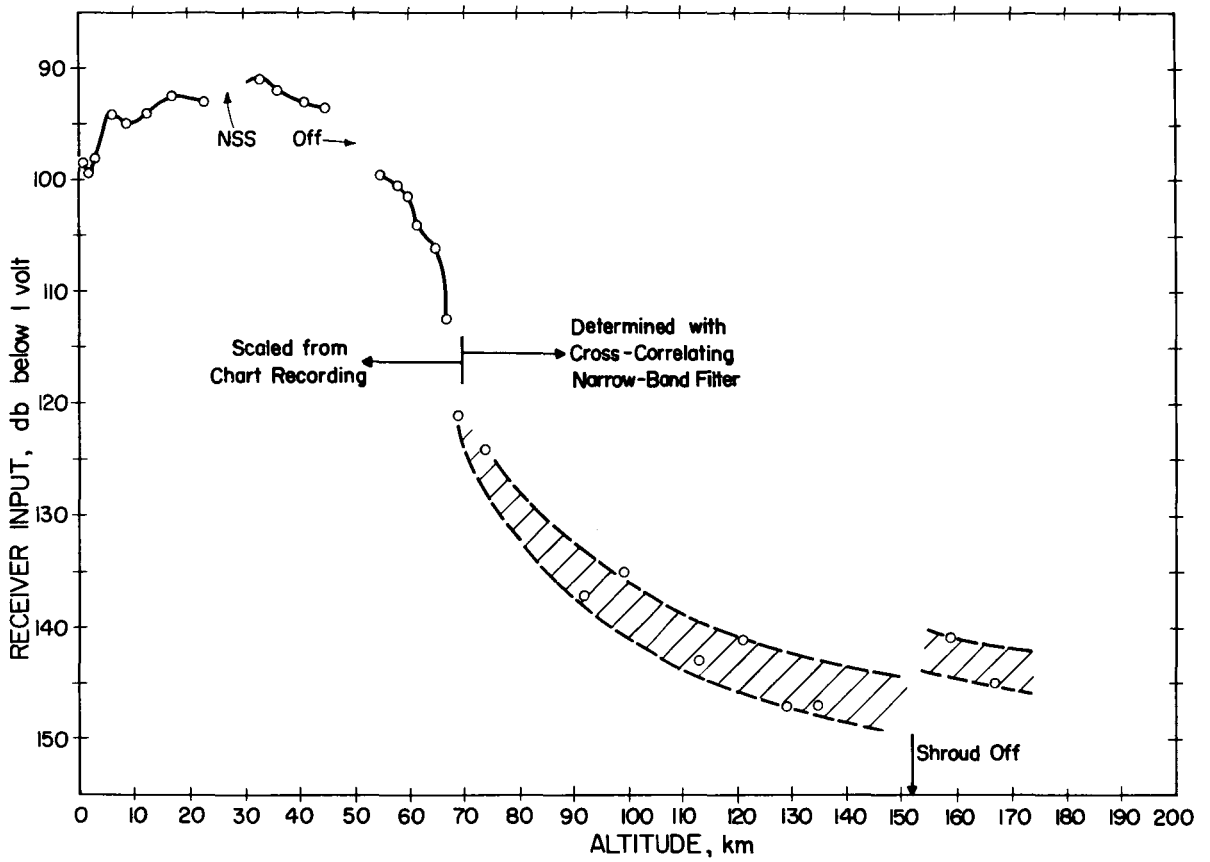

FIGURE 5.—*Satellite receiver input level below 1 volt plotted vs. altitude. Data between about 60 and 152 km may be interpreted as relative variation of electric field strength within the ionosphere.*

total attenuation through the lower ionosphere up to about 150 km is 43 db ± 4 db for daytime.

At heights below 60 km, the observed variation in signal strength appears to be explained by the waveguide-mode theory of VLF propagation.[4] Recent calculations of the height-gain effect by Wait and Spies[5] show that as altitude increases the intensity first increases, reaches a maximum, and then decreases to some fraction of the ground intensity at the ionosphere boundary. For parameters appropriate to this situation, these calculations do not show as great an increase in intensity for the low altitudes as the measurements show, and it must be taken into account that the distance to NSS decreased and that the relative amount of seawater path increased as the rocket ascended.

Whatever the influence of the last-mentioned factors, the variation near the ionosphere is predominantly due to the height-gain effect since there is little change in the path or distance for this altitude increment. And a priori choice of 70 km for an effective height of the lower edge of the ionosphere would be in agreement with that adopted by most workers who assume a homogeneous sharply-bounded ionosphere model for VLF calculations. The height-gain calculations[5] for an assumed ionosphere height of 70 km show a 6 db loss between 60 and 70 km. However, the measured loss between 60 and 70 km, as shown in figure 5, is about 17 db. This significant discrepancy further suggests that the effective height of the ionosphere and the beginning of absorption was more nearly 60 km at the time the measurements reported here were made.

PREDICTED TOTAL ATTENUATION

Some preliminary calculations of whistler-mode absorption have been made at Stanford for various electron-density and collision-frequency models of the lowest ionosphere.[6] The daytime models are applicable to this experiment since the launch took place at about 0930 EST and the trajectory carried the satellite into longitudes of even later local time. The calculations show that almost all of the D- and E-region absorption occurs below about 130 km. Hence, the calculations can be considered to predict all the absorption up to 150 km. The first calculation utilized the electron-density profile deduced by Nertney[7] and the collision-frequency profile deduced by Nicolet,[8] and yielded a total absorption of 17 db. A second calculation utilized profiles of electron density and collision frequency which can be considered composite models deduced from the data given in the survey of Waynick,[9] and yielded a total absorption of 23 db.

Before the calculations can be compared with the measurements, there are several other sources of attenuation that must be considered. These include reflection losses and the effects of antenna polarization and changing wave impedance within the ionosphere. The loss due to reflection at the lower boundary of the ionosphere will be accounted for by considering only the direct ray. The higher-order reflected rays should be considerably attenuated by reflection from a daytime ionosphere. In this case, the subrocket point at the boundary of the lower ionosphere is just below the horizon. However, a consideration of diffractive effects in low frequency propagation by Wait[10] shows that the "cut-back factor" for this case is negligible. A computation of the transmission coefficient based on the work of Budden[11] shows that for the ordinary ray (whistler-mode) a reflection loss of 19 db occurs for a sharply-bounded, summer-daytime ionosphere model ($\omega/\omega_\tau=0.6$, $\tau=60°$). The extraordinary ray which is transmitted into the ionosphere is completely absorbed well below 150 km.

The change in wave impedance in the ionosphere results in attenuation since, for a given power density, the electric field strength varies directly with the square-root of the wave impedance, and the wave impedance in the ionosphere is less than that of free space. This attenuation, assuming longitudinal propagation, is found to be 11 db between the lower boundary of the ionosphere ($\omega/\omega\tau=0.6$, $\tau=60°$) and 150 km where the electron gyrofrequency and plasma frequency are estimated to be about 1.2 and 3.0 Mcps, respectively.

Just below the ionosphere, the incident electric field, consisting primarily of the direct ray, can be assumed to be vertical, while just within the ionosphere the field can be assumed to be circularly polarized in the horizontal plane.[12] Thus the antenna made an angle of 70° with the electric field just below the ionosphere, while making an angle of 20° or less with the horizontal field within the ionosphere. Polarization corrections based on these relative orientations amount to a gain of about 9 db. In addition, a loss of about 3 db is incurred because of the spatial averaging of the approximately circularly polarized whistler-mode component within the ionosphere by the linear satellite antenna.

Adding the above factors to the absorption gives the following tabulation for the estimated total attenuation through the summer-daytime ionosphere up to 150 km altitude:

Day Model	*Total Absorption*	*Total Attenuation*
Nicolet and Nertney	17 db	41 db
Composite	23 db	47 db

DISCUSSION

It should be noted that the predictions outlined in the previous section were prepared assuming whistler-mode propagation along the magnetic field (assumed to be vertical here) for a constant incident electric field intensity at the lower ionosphere. The propagation path from Station NSS to the satellite did not quite provide constant field intensity in the ionosphere below the satellite. The course of the launch trajectory was in a north-easterly direction from Cape Canaveral and the average distance from Station NSS to the sub-satellite point for the altitude increment of 60 to 150 km was about 1,000 km and changed about 15%. Calculation for a comparable situation suggest

that the field strength just within the ionosphere would probably vary by about 3 db over this distance change.[13] This will be considered negligible here, and the predictions as given can be considered to apply to the measurements.

It can be seen that the total attenuation measurement of 43 db ± 4 db compares quite well with the calculated total attenuations of 41 and 47 db. The discrepancy is within the experimental errors and the magnitudes of the various effects which have been neglected in this analysis. It should be obvious that the calculations are only approximate since several 1 to 3 db effects have been neglected. However, the measurements also were only approximate since a rough estimate was used to select the altitude at which absorption began. Nonetheless, it appears that no unusual attenuation phenomena were observed and that the measured total attenuation can be accounted for by the analysis presented above.

Since the measurements which are reported here were made, the results of two relevant experiments have been reported. In the first experiment, the variation of Station NBA located at Summit, Panama Canal Zone (18.0 kc) signal strength with altitude up to about 115 km was measured at about 1700 local time on 14 March 1961 using a split-rocket electric dipole antenna.[14] Aspect data was not available for these measurements. Allowing for uncertainties in antenna orientation and such factors as diurnal and seasonal effects, these rocket measurements are quite consistent with those reported here.

The second relevant measurements were those made in the LOFTI I Satellite experiment.[15, 16] The total attenuation deduced from the LOFTI I measurements is somewhat different in that the detailed variation of signal strength with altitude was not obtained, although much more data on total attenuation was, of course, obtained. The measurements reported (ratio of apparent electric field intensity at the satellite to computed field intensity on the ground)[15] are also consistent with the measurements reported here when proper allowances are made for different measurement frequencies, the attenuation through the F-region and the different geometric factors for each case.

In conclusion, it appears that the launching of the whistler mode, at least in daytime, can be described to a first order by utilizing a sharply-bounded model of the ionosphere to account for the reflection-transmission phenomenon, and a slowly-varying model to account for the absorption experienced by the transmitted wave.

REFERENCES

1. Space Technology Laboratories, Project Able-3 Final Mission Report Volume 2, August 1960.
2. Rorden, L. H., and Wolfram, R. T., VLF Instrumentation for the Able-3 and Able-4 Satellite Programs, SRI Final Report Proj. 2765, Stanford Res. Inst., February 1961.
3. Mlodnosky, R. F., and Garriott, O. K., The v.l.f Admittance of a Dipole in the Lower Ionsphere, Proc. Internat. Conf. on the Ionosphere, London, July 1962, pp. 484–491, The Institute of Physics and the Physical Soc., 1963.
4. Budden, K. G., The Waveguide Mode Theory of Wave Propagation, Prentice-Hall, New York, 1962.
5. Wait, J. R., and Spies, K. P., Height-Gain for VLF Radio Waves, J. Res. NBS, Vol. 67D, No. 2, pp. 183–188, March–April 1963.
6. Shih, K. K., Unpublished work.
7. Nertney, R. J., The Lower E and E Region of the Ionosphere as Deduced from Long Radio Wave Measurements, J. Atmos. Terr. Phys., Vol. 3, No. 2, pp. 92–107, 1953.
8. Nicolet, M., Collision Frequency of Electrons in the Terrestrial Atmosphere, Phys. of Fluids, Vol. 2, No. 2, pp. 95–99, March–April 1959.
9. Waynick, A. H., The Present State of Knowledge Concerning the Lower Ionosphere, Proc. IRE, Vol. 45, No. 6, June 1957.
10. Wait, J. R., Diffractive Corrections to the Geometrical Optics of Low Frequency Propagation, NBS Rept. 5572, U.S. Dept. of Comm., Natnl. Bureau Stds., June 1958.
11. Budden, K. G., Radio Waves in the Ionosphere, Cambridge University Press, 1961.
12. Storey, L. R. O., An Investigation of Whistling Atmospherics, Phil. Trans. Roy. Soc. A, Vol. 246, pp. 113–141, 1953.
13. Bell, T. F., Helliwell, R. A., Mlodnosky, R. F., and Smith, R. L., Geocyclotron Feasibility Study Radioscience Lab., Stanford Univ., Final Rept. Contract AF29(601)–4506, Chap. III, pp. 97–114, Jan. 1963.
14. Lomax, J. B., Measurement of VLF–Transmission Characteristics of the Ionosphere with Instrumented Nike-Cajun Rockets, Stanford Res. Inst. Final Rept. Contract NOw 60–0405(FBM), June 1961.
15. Leiphart, J. P., Zeek, R. W., Bearce, L. S., and

Toth, E., Penetration of the Ionosphere by Very-Low-Frequency-Radio Signals—Interim Results of the LOFTI I Experiment, Proc. IRE, Vol. 50, No. 1, pp. 6–17, Jan. 1962.

16. Rorden, L. H., Helliwell, R. A., and Smith, R. L., An Interpretation of LOFTI–I VLF Observations, Presented at AGARD Meeting, Munich, Germany 17–21 September 1962.

PART III: ENERGETIC PARTICLES IN MAGNETIC FIELDS

1. Ion Chamber and Geiger Counter Experiments Designed by the University of Minnesota
2. Cosmic and Trapped Radiation Studies Designed by the University of Chicago
3. Scintillation Counter Experiments Designed by Space Technology Laboratories, Inc.
4. Magnetic Field Experiments Designed by Space Technology Laboratories, Inc.

Page intentionally left blank

Section 1. Ion Chamber and Geiger Counter Experiments Designed by the University of Minnesota

765-698 O-65—8

Page intentionally left blank

Introduction to the Ion Chamber and Geiger Counter Experiments Designed by the University of Minnesota

BY J. R. WINCKLER

School of Physics
University of Minnesota

The Explorer VI observations in 1959 were the first extensive ones made throughout the volume of the trapping region, and they remain unique in giving its state at a particular time in the solar cycle.

Since Explorer VI was placed in a very elliptical orbit, and because of the inclination of the earth's magnetic axis to its spin axis, the satellite swept through a considerable part of the trapping region, making possible the construction of rather complete contours of constant counting rate and radiation dosages as measured by the Geiger counter and ionization chamber, respectively. Such contours necessarily depend strongly on the shielding surrounding the detectors and are thus peculiar to the spacecraft. Nevertheless, the Explorer VI rate contours displayed a shape quite different from those derived by Van Allen using a similar Geiger counter which was mounted aboard several previous spacecraft.

The rates of the ionization chamber and Geiger counter displayed a minimum in the outer zone. According to the present magnetic data, the minimum in detector rates does not lie on a particle shell connecting the Capetown magnetic anomaly and, hence, cannot be attributed to a scattering of radiation out of the trapping region by the anomaly. A spectral study of the outer zone suggests that the minimum has a spectral-detector origin.

The proton differential energy spectrum, fit to the data in the inner zone at a geomagnetic latitude of $-28°$, has the form $E^{-1.65}$ above 30 Mev. Electron fluxes in the inner zone are inferred to be greater than 10^7 electrons/cm^2 sec above 200 Kev.

In fitting trial spectrums to the outer-zone data it is seen that flat spectrums with electron energies up to 5 Mev must prevail at the inner edge of small ranges. The flux of electrons of energies between 1 and 5 Mev here is of the order of 10^6 electrons/cm^2 sec. With increasing range, the spectrums steepen until at the outer edge the ionization chamber and Geiger counter are detecting the electrons only through the intermediate bremsstrahlung process.

As is indicated by the nearly constant ratio of ionization chamber to Geiger counter rates, the spectrum of trapped particles in the outer zone to which the detectors are sensitive does not change appreciably down magnetic lines of force except at low altitudes. The counting rates of the Geiger counter were then used to determine the pitch-angle distributions of the trapped particles by studying the intensity down force lines. Such distributions in the outer zone show that beyond the line of force crossing the equator at 25,000 km there is an increasing number of particles turning near the equatorial plane. The pitch-angle distributions of the particles in the outer zone are inconsistent with those resulting from albedo neutron decay.

Large rate changes are observed in the outer radiation region, and are correlated with solar activity having a time delay indicating that the coupling is by means of solar plasma streams. The percentage of decreases are greater for lines of force at large radial distances. The data place an upper limit of about 10 percent for time variations in the inner zone caused by solar activity during the lifetime of Explorer VI.

Evidence of the lowering of mirror points in the outer zone during magnetically disturbed periods has been obtained. The pitch-angle distributions of "new particles" in the outer zone after a magnetic disturbance show that they mirror nearer the equatorial plane.

The simultaneous measurement of low-energy radiation at 42,000 km on an electron shell connecting an aurora suggests that the aurora is associated with a disturbance extending over many degrees of longitude and out to large ranges. During a strong low-latitude aurora a rapid decrease in count rate was observed in the outer zone time coincident with the break-up of the aurora, indicating either the precipitation or deceleration of the trapped particles at this time.

Observations of the Van Allen Radiation Regions during August and September 1959, Part 1[1]

BY R. L. ARNOLDY,[2] R. A. HOFFMAN,[3] AND J. R. WINCKLER

School of Physics
University of Minnesota

An integrating ionization chamber and a single Geiger counter were flown on United States satellite Explorer VI in an elliptical orbit extending to 48,000 km. In addition to the Van Allen inner zone and the great outer zone, a stable and distinct intermediate zone was detected throughout August and September 1959. The outer-zone intensity showed a large decrease following the sudden commencement of a geomagnetic storm. Later in the storm the outer zone increased to much in excess of its prestorm level. During stable periods the outer zone was fairly constant and less intense than it had been observed to be with Pioneer III or Pioneer IV or the first Soviet cosmic rocket. Cosmic-ray background counting rates were reached on most passes in August and September near apogee of the satellite. The radiation 'dumped' from the outer zone during the geomagnetic storm fits very well with the intensity and latitude distribution required to account for balloon observations of auroral X rays made during the IGY period. This paper is based on preliminary analysis of Explorer VI data.

INTRODUCTION AND DESCRIPTION OF APPARATUS

The University of Minnesota provided a radiation-detection experiment for the payload of Explorer VI satellite, launched August 7, 1959, from Cape Canaveral, Florida. The program was under the auspices of the National Aeronautics and Space Administration, and the payload was engineered by the Space Technology Laboratories of Los Angeles. This paper is based on a preliminary analysis of data now available. Additional data may be available from magnetic tape playback during the period under discussion in this paper. The present paper is an extension of an earlier version presented at the first international space symposium at Nice, France, in January 1960 [*Arnoldy, Hoffman, and Winckler*, 1960].

Figure 1 shows the University of Minnesota package before the potting compound was inserted to fill the container. The instruments are an integrating ionization chamber and a Geiger counter. The ionization chamber operates on the pulsing electrometer principle, which has been extensively used by the balloon projects at the University of Minnesota and was developed for cosmic-ray purposes by Neher and Millikan [*Winckler, Peterson, Arnoldy, and Hoffman*, 1958]. The specifications of the two instruments are given in Table 1.

The ionization chamber and counter are sensitive to all types of radiation, but in addition, the ratio of the counting rates of the two instruments gives a measure of the mean particle ionization and accordingly particle energies if the type of particle is known. For X rays,

[1] This work was supported by the National Aeronautics and Space Administration under contract NASw-56. Published in the May 1960 issue of *Journal of Geophysical Research*. Reprinted by permission.

[2] Now at Honeywell Co.

[3] Now at NASA Goddard Space Flight Center.

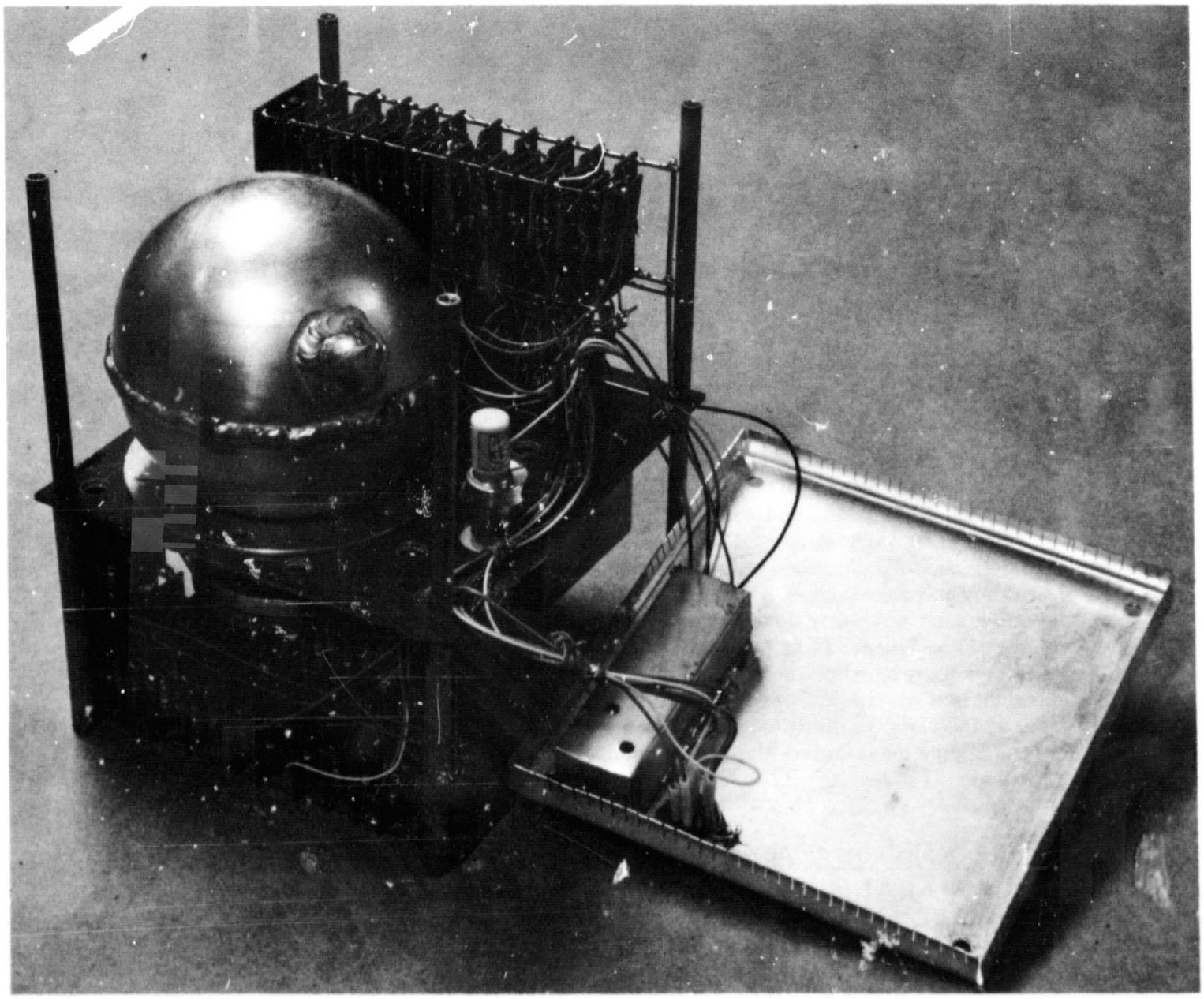

FIGURE 1.—*View of the University of Minnesota radiation experiment containing the 3-inch-diameter aluminum ion chamber, left, and the small Anton infinite-life Geiger counter on the right side of the package. Note transistor scaling circuits and radio-frequency filter box on the cover of the package. This unit is completely filled with a polyurethane foaming plastic in its case.*

which are an important contribution to the radiation detected inside the satellite, the relative response of the two instruments is sensitive to the energy of the X rays encountered, and suitable calibrations have been carried out with X-ray machines. Table 2 lists the rms plate voltage of the a-c X-ray machine versus the ionizing power ratio expressed as number of times the ratio for minimum ionizing particles. The unit has also been exposed to protons in the energy range 10 to 30 Mev from the Minnesota linear accelerator. Using the observed ratio for protons, and the ratio for Co^{60} γ rays given in Table 2 as characteristic of minimum ionizing particles, very reasonable agreement is obtained with the known specific ionization of the Linac protons. We give in figure 2 the response of the ion chamber and counter to known amounts of Co^{60} γ radiation supplied by the high-intensity γ-ray facility at the University of Minnesota. The radiation dosage in roentgens is obtained from carefully calibrated Victoreen R meters exposed, along with the satellite package, to the cobalt radiation source.

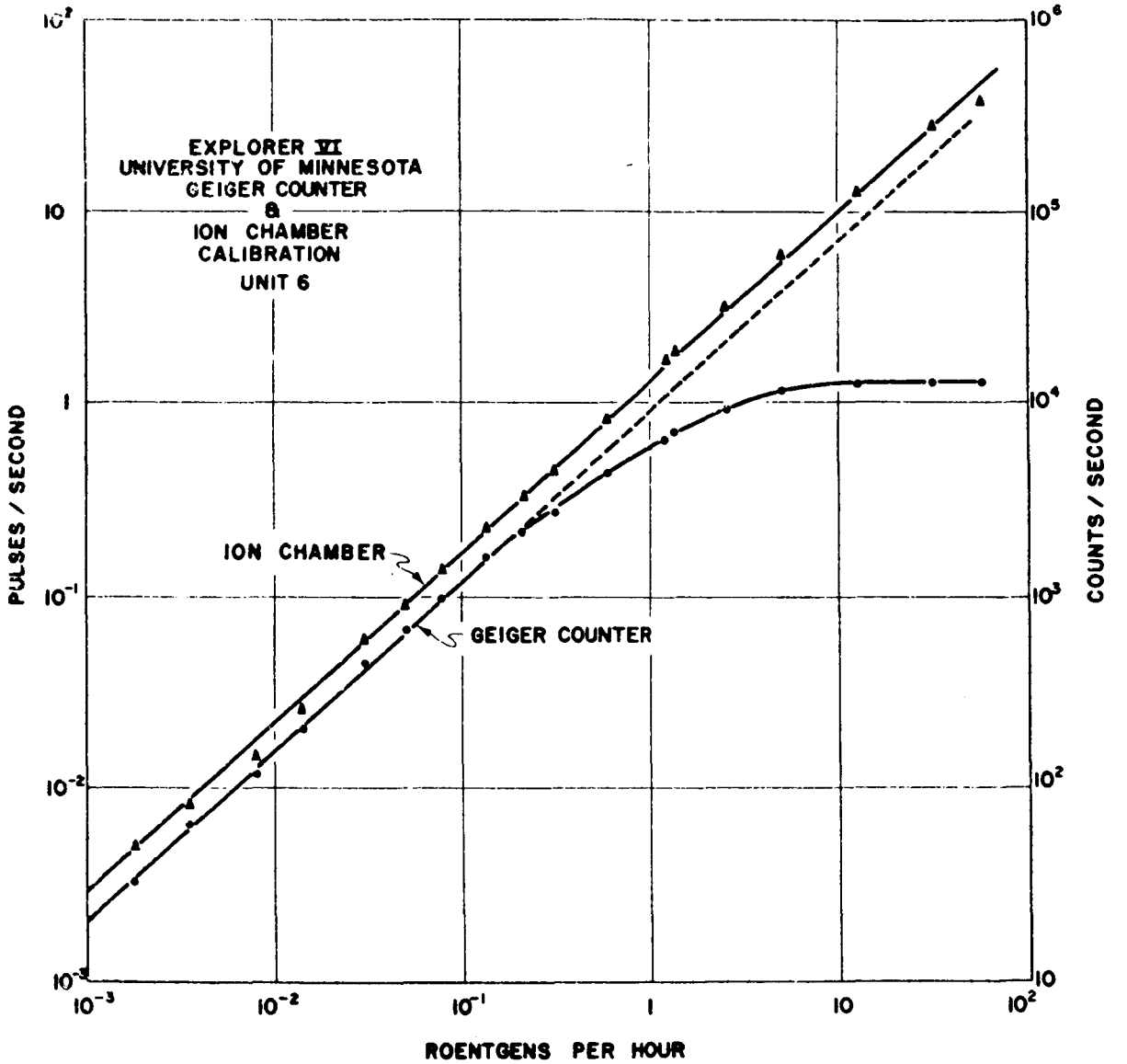

FIGURE 2.—*Calibration curve for the ion chamber and Geiger counter used in the University of Minnesota Explorer VI experiment. The rates for the two instruments are plotted against the radiation in roentgens per hour as measured by calibrated Victoreen R. meters. The source of radiation was cobalt 60.*

The ion chamber shows essentially a straight-line log-log plot with a slope differing slightly from unity. The Geiger counter shows a dropping off at high rates which occurs because of the dead time of the counter and circuitry. With the aid of this calibration curve, true counting rates can be inferred from the observed counting rate of the counter at high rates.

Both analog and digital telemetry were used, but only the former was analyzed for this report. The Geiger counter fed 17 binaries in series, samples being taken after the 8th and 17th. These were mixed, with different amplitudes, with the output of the 5th binary after the ionization chamber. The record could be read without difficulty, since usually only one of the

TABLE 1.—*Specifications of Radiation Detectors*

Ionization chamber	
Diameter	3.0 in.
Wall thickness of aluminum	0.020 in.
Filling pressure of argon	94 lb/in.² absolute.
Charge collected/pulse	2.14×10^{-10} coulomb/pulse.
Geiger counter	
Anton type 302:	
Wall thickness of stainless steel	0.020 in.
Efficiency for charged particles	80 percent.*
Omnidirectional factor	0.55–0.75 cm.²†

*As given by manufacturer.

†Computed from direct measurements on samples and from manufacturer's dimensions. A more accurate value for the flight unit will be reported later.

TABLE 2.—*Relative Photon Response of University of Minnesota Radiation Detectors*

[Exposure was made with experiment removed from satellite]

X-Ray Tube RMS Plate Voltage, kv	Approximate X-Ray Ratio/Minimum Ionizing Ratio
35	844
38	76
43	34
50	30
57	10
Isotropic Co^{60} γ Rays	1.33×10^{-4}

scaling rates of the counter and the ion chamber was observed at the same time, owing to the action of a 3-cps filter network.

The radiation unit in the payload was surrounded by considerable material located mostly in the plane of the figure. A preliminary evaluation has been made of the complex shielding experienced in different directions by the unit, and in a simple way this may be expressed by the values in Table 3 covering different ranges of absorption. In general, the lower limit of detectability is about 16 Mev for protons and about 2 Mev for electrons directly. Low-energy electrons may be detected indirectly by the X rays generated when collisions occur with the skin and other parts of the payload. For such X rays the limit of detectability is approximately 30 kv, where the sensitivity of the detectors drops off to a negligible value. The efficiency of detection of such electrons is of course low on account of the intermediate bremsstrahlung process.

The payload was injected into an elliptical orbit positioned in space as shown in figure 3 with the plane of the orbit making an angle of 38° with the ecliptic plane. The period of the satellite was about 12 hours and 42 minutes, and the payload was spun about its axis of greatest moment at a rate of 2½ revolutions per second. Perigee was 6615 km and apogee 48,616 km from earth center. Successful telemetry of the channel carrying the University of Minnesota experiment was maintained for approximately 2 months, between August 7 and October 6, 1959. During this period a strong geomagnetic storm occured on August 16–17 which will be discussed in detail below. A great solar radio noise storm took place at the end of August, and on September 4 and 23 disturbances that may be of the recurrent *M*-region type were also observed. These latter storms will be discussed in full detail in a later communication when more data have been read.

PROFILE OF THE VAN ALLEN REGIONS DURING THE FIRST WEEK OF THE SATELLITE

Because the Explorer VI satellite was placed into a high-ellipticity orbit, and because with respect to the geomagnetic axis of the earth the orbits swing northward and southward in latitude, a large part of the radiation belts is swept out in a period of several days, affording an unusual opportunity to plot the details of the distribution of particles that are accessible to the instruments in this experiment. Figure 4 shows a series of typical orbits plotted in rectilinear form, in which the geomagnetic latitude appears as the vertical coordinate and the range as the horizontal coordinate. These orbits were obtained from an ephemeris

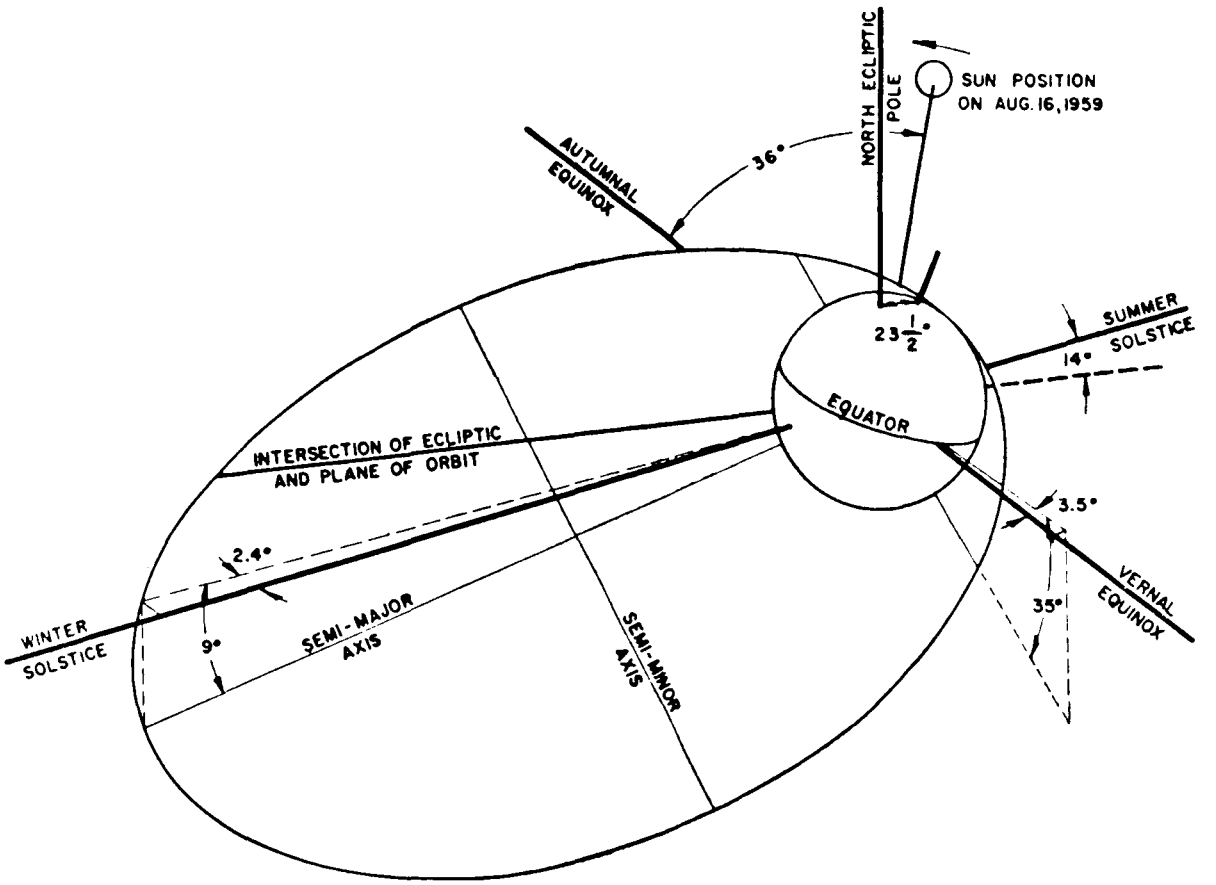

FIGURE 3.—*The orbit of Explorer VI in space. The angle between the plane of the orbit and the earth's equatorial plane is 47°. The orbital plane is tipped 38° to the plane of the ecliptic. On August 16 during the geomagnetic storm the major axis was directed about 125° away from the sun.*

TABLE 3.—*Shielding Effect of Material in Satellite Around Minnesota Package*

Range Interval, g/cm²	Percentage of Total Solid Angle	
	Counter	Chamber
0–0.5	16	26
0.5–5	54	46
>5	30	28

furnished by the Space Technology Laboratories. The geographic latitude, longitude, and range have been converted to geomagnetic latitude and range with the aid of the earth-centered dipole approximation of *Vestine* [1948]. Recently the orbits in geomagnetic coordinates from Vestine's analysis have also been furnished directly by the Space Technology Laboratories, in 1-minute intervals. In addition, the NASA, on the basis of data obtained by the minitrack net and analyzed under the Vanguard program, has furnished orbital data in 1-minute intervals. These various measurements are in good agreement. Figure 4 also includes lines of force of the earth's centered dipole field in the rectilinear form of plotting.

From the Geiger counter rate during the first 14 passes of Explorer VI, a contour plot of the radiation regions has been constructed, which appears in figure 5 in rectilinear form. This period, the first week after launch, was fairly quiet magnetically, and the radiation regions

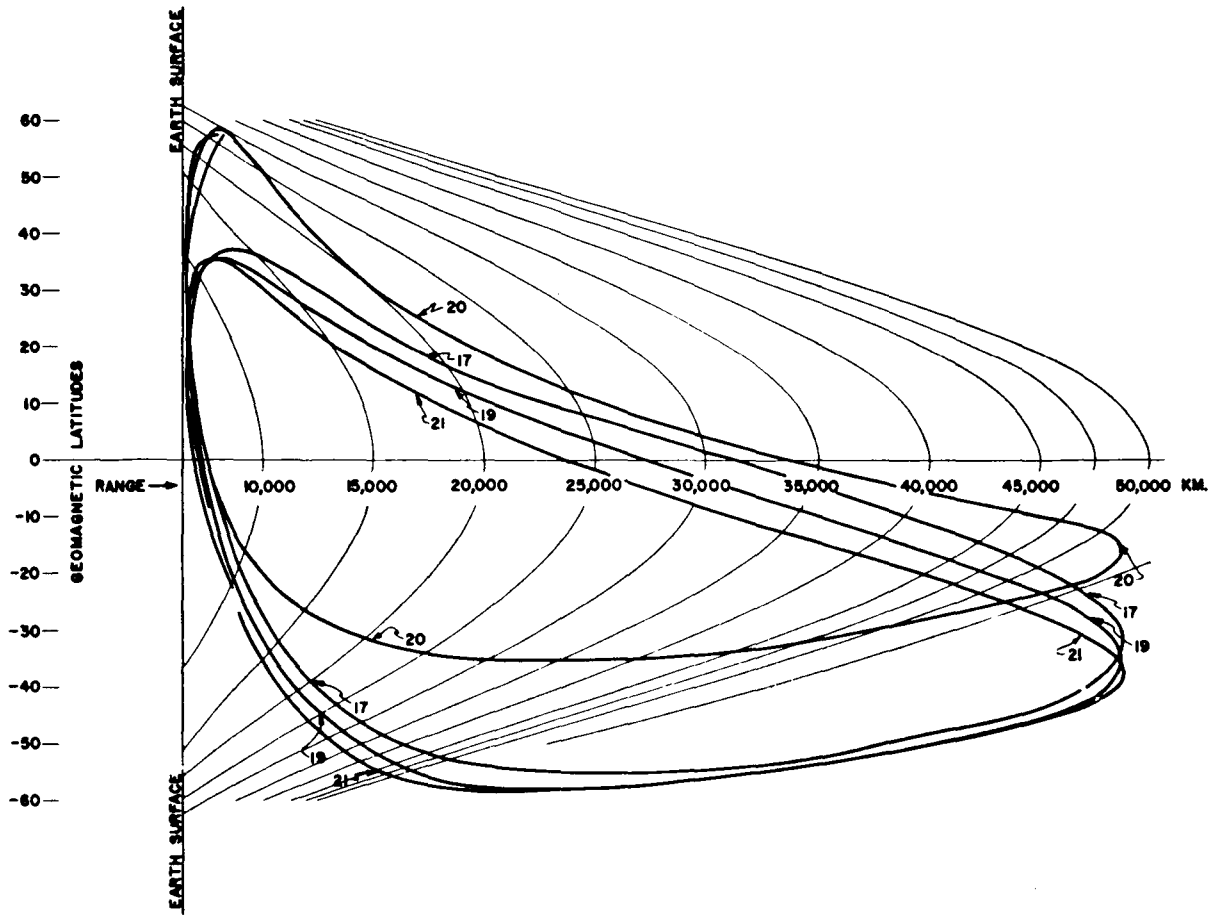

FIGURE 4.—*Typical orbits of Explorer VI plotted in the geomagnetic meridian with the lines of force of the earth's field shown for comparison. A rectilinear plot is used, the earth's surface being represented by the* Y *coordinate and the range by the* X *coordinate. The particular passes shown are those occurring during the geomagnetic storm beginning August 16.*

were stable. The dotted parts of contour lines are extrapolations between regions where data are available. A more recent contour plot, making use of the geomagnetic data at 1-minute intervals and additional data from the counter, shows considerably more detail at low altitudes, for example, the 'horns' derived from Explorer IV data by *Van Allen* [1959*a*].

In figure 6, on a polar-type diagram which is more familiar to most readers, the extent and intensity of the radiation zones as given by Van Allen, upper [*Van Allen*, 1959*a*], and as derived from Explorer VI measurements, lower, are compared. The comparison is made on the basis of the same instrument, namely an Anton type 302 counter. Although the shielding of the surroundings of Explorer VI may not be quite the same as for the Explorer IV and Pioneer III and IV rockets used by Van Allen, they are not too dissimilar for the present purpose. It is apparent that since the time of the construction of the radiation zone figure by Van Allen the zones have shrunk considerably in intensity and extent. It is seen that during the first week of August the counting rate reached the cosmic-ray background of 1.5 counts/sec at the outer extremity of the orbit of Expolrer VI, whereas earlier in the year the radiation intensity as deduced from

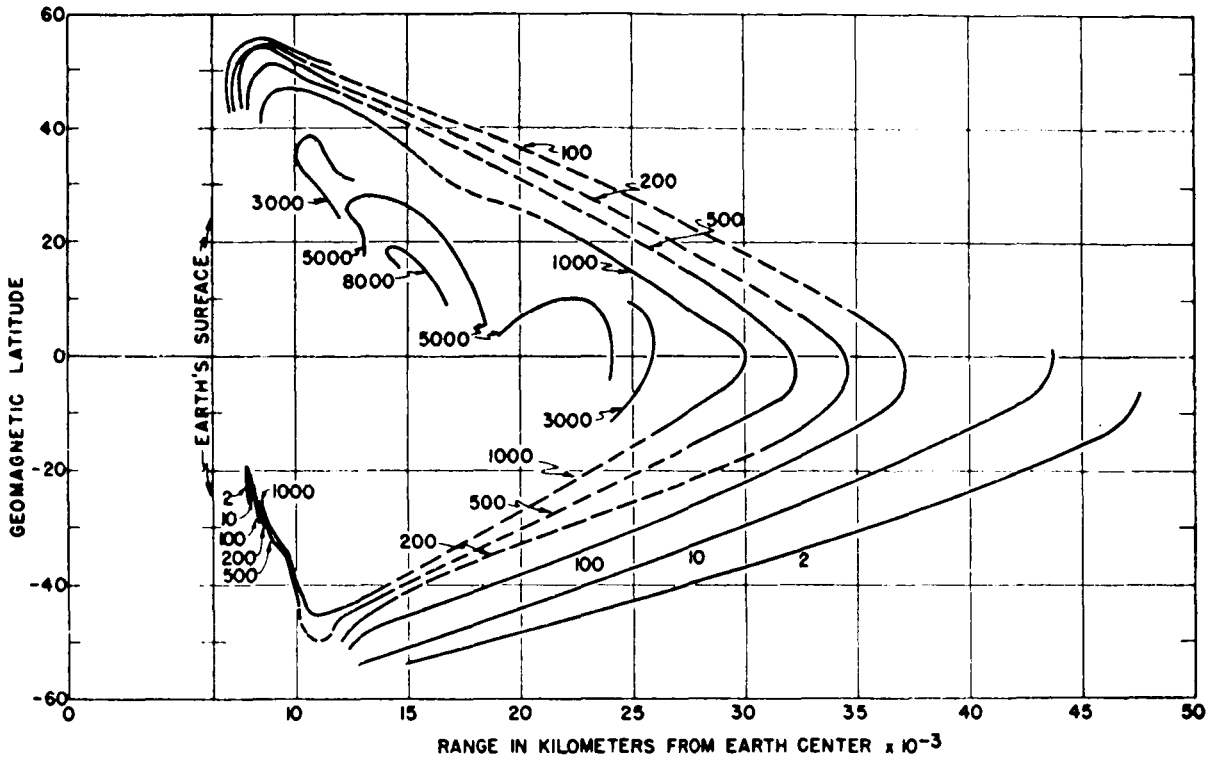

FIGURE 5.—*Rectilinear plot of contours of equal counting rate for the Anton counter as obtained from the first week of Explorer VI.*

the Pioneer shots was still considerably above this value.

Throughout the time of observation, three distinct maxima in the trapped radiation region were measured by both detectors. The first of these three regions can be identified with the Van Allen inner zone and is closest to the earth. The second and third regions are seen at 17,000 and 23,000 km, respectively, near the equator. Only these last two are measured on outgoing passes, owing to the high latitude of the orbit. Many incoming passes display all three regions as they exist at southerly magnetic latitudes between 20° and 50°. Maxima observed on outgoing and incoming passes lie on connecting lines of force in the dipole field. An example of such an incoming pass is shown in figure 7 for pass 27, which has an incoming trajectory similar at low latitudes to that for pass 21 (see fig. 4). The maximum rates for the two outer regions are somewhat larger than normal, since the pass occurred during a rising intensity following a magnetic storm. The two innermost maxima have average ionizing power as observed by the two instruments 5 to 6 times that for minimum ionizing particles. The outermost maximum has a ratio of approximately 16 times that for minimum ionizing particles. Such a large ratio is consistent with soft X rays produced by electrons bombarding the outer shell of the payload. Protons with this specific ionization would be stopped by the material surrounding the instruments.

Assuming that the soft outermost maximum is due to electrons, it is possible to estimate the flux incident upon the payload shell. Comparing the ratio of the ion-chamber rate to counter rate at this point with that from the X-ray calibration of the unit yields a value of 50 kev for the mean energy of the X rays. For the maximum value, observed during the first week, of 10 r/hr (1.9×10^8 ev/cm^3·sec in air), the X-ray

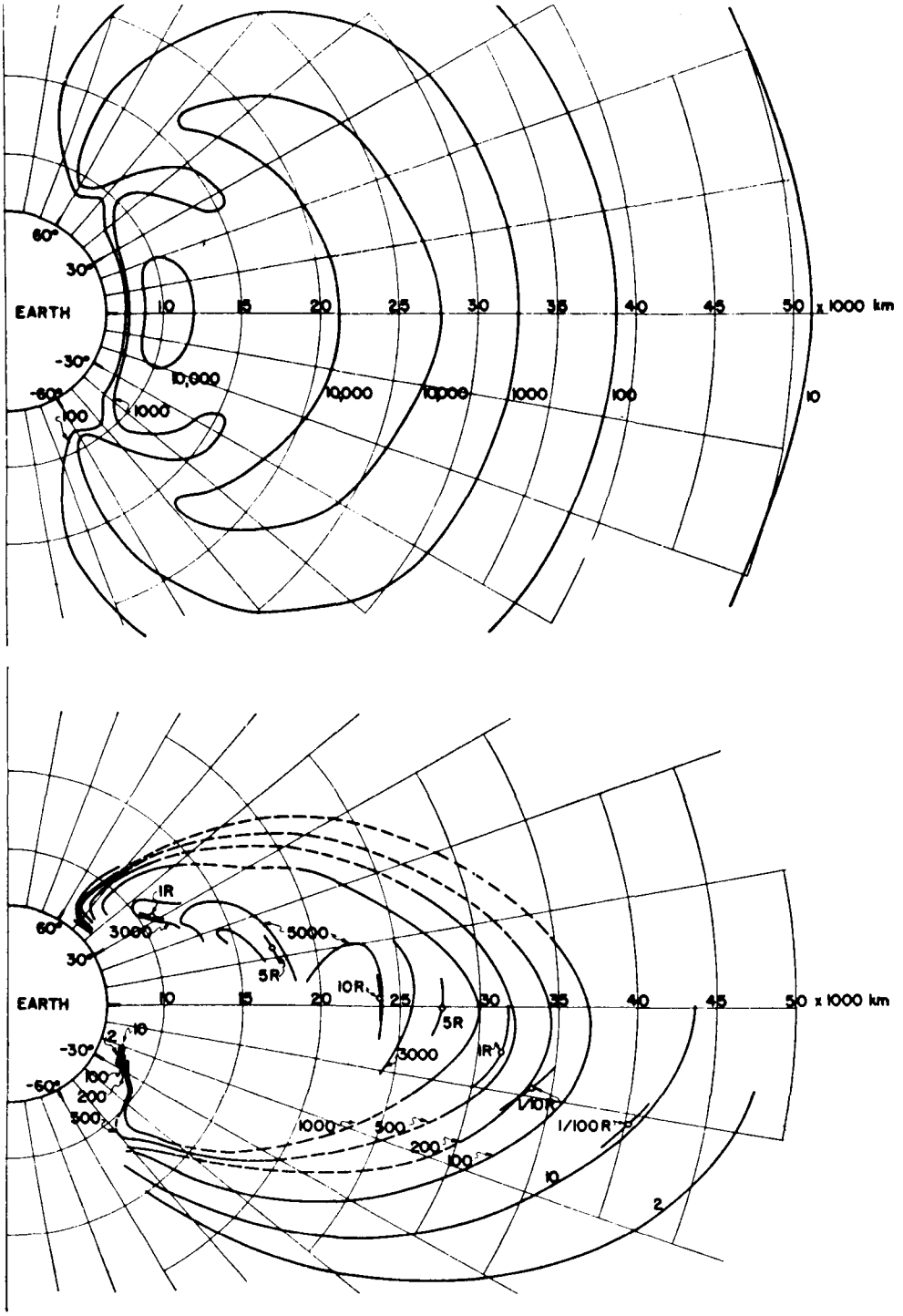

FIGURE 6.—*Comparison of the counting-rate contours in the radiation zone as given by Van Allen* (upper) *and as given by analysis of Explorer VI* (lower) *shown on a polar plot. It is apparent that the radiation zones during the time of Explorer VI have shrunk considerably and changed form since those inferred from the Explorer IV and Pioneer III and IV data.*

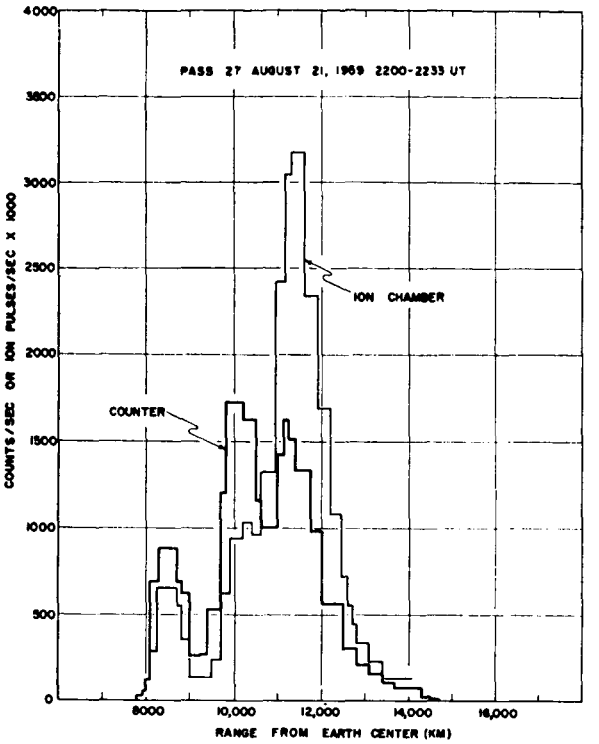

FIGURE 7.—*Radiation levels on the incoming part of pass 27, which show three distinct radiation regions. The Van Allen inner zone appears at 8500 km, the outer zone at 11,500 km, and the new intermediate zone close to 10,000 km. The trajectory is closely similar to that for pass 21, figure 4. The relative intensities are meaningful only when the position along the magnetic line of force is considered.*

energy flux is given by

$$N = \frac{dN}{\lambda dx} = \frac{1.9 \times 10^8 \text{ ev/cm}^3 \cdot \text{sec}}{0.23 \text{ cm}^2/\text{g} \times 0.0013 \text{ g/cm}^3}$$

$$= 6.3 \times 10^{11} \text{ ev/cm}^2 \cdot \text{sec} \qquad (1)$$

The mass absorption coefficient, λ, in the argon gas of the chamber is chosen for 50-kev X rays. The electron energy flux is about 10^4 times greater than the X-ray energy flux at 50 kev, owing to the inefficiency of the bremsstrahlung process. The electron particle flux is then found to be

$$\frac{6.3 \times 10^{11} \times 10^4 \text{ ev/cm}^2 \cdot \text{sec}}{50 \times 10^3 \text{ ev}} = 1.2 \times 10^{11}/\text{cm}^2 \cdot \text{sec} \qquad (2)$$

Another way to compare the various measurements of the radiation zones is shown in figure 8, in which the counting rate of the Geiger counter is plotted as a function of range in kilometers for passes of the Pioneer III and IV, the Russian Mechta rocket [*Vernov, Chudakov, Vakulov, and Logachev,* 1959] and a typical pass (no. 6, August 10, 1959) of Explorer VI. It is seen in figure 8 that the highest over-all intensity was that recorded by the space probe Pioneer IV launched March 3, 1959, in which the intensity in the central part of the outer region went off sale but was perhaps as much as 10^6 counts/sec. The Russian Mechta rocket, launched January 2, 1959, recorded intensities one to two orders of magnitude less intense. The Pioneer III data in December of 1958 are still lower, and the closest in intensity to the Explorer VI results. Explorer VI reached the cosmic-ray background rate of about 1.5 counts/sec at approximately 42,000 km, and at that point had a rate 10^{-4} of the Pioneer IV rate. The intensity measured is strongly a function of the position of the trajectory. Figure 9 compares the trajectories of Pioneer III, Pioneer IV, and Mechta plotted on the same rectilinear scale on which the typical passes of Explorer VI are shown in figure 4. These trajectories are roughly similar, but the Mechta probe crossed the equator at larger distances. It is clear that large temporal changes occur in at least the outer radiation regions surrounding the earth. The Iowa group reports that the enormous filling-up of the regions shown on the March 3 pass of Pioneer IV is associated with an *M*-region solar-type disturbance [*Van Allen,* 1959*b*]. It will be shown that an analysis of Explorer VI data likewise shows strong dependence on solar activity but not in a simple manner.

To illustrate some of the time variations observed on Explorer VI, Table 4 lists the Geiger counter rates along the trajectories at the maximum of the soft outer region for magnetic latitudes within 8° of the equator. Also tabulated are the planetary magnetic indices A_p and the ionizing power of the trapped radiation expressed as number of times that for minimum ionizing particles (i.e., Co^{60} γ rays). No data were received from the ion chamber after August 21, and hence the ratios are missing during

TABLE 4.—*Preliminary Summary of Measurements of Outer Zone Maximum during August and September 1959*

Date	Time UT	Pass No.	Counts (Sec)	X Minimum Ionizing	A_p Planetary Indices	Magnetic Latitude, degrees	Range from Earth Center, km
Aug 7	1538	1	5, 050	15. 5	14	7. 5	22, 000
Aug 9	0559	4	5, 400	14. 3	22	7	23, 500
Aug 10	0727	6	4, 700	14. 5	14	2	22, 600
Aug 11	0859	8	5, 650	13. 9	8	−1	22, 500
Aug 12	1028	10	6, 100	13. 9	5	0	23, 500
Aug 13	1200	12	5, 500	14. 3	6	−2	22, 500
Aug 14	1330	14	6, 250	----------	6	1	22, 600
Aug 17	0509	19	1, 900	7. 6	114	7	21, 700
Aug 18	0645	21	8, 150	15. 7	28	0	23, 500
Aug 19	0817	23	10, 000	15. 7	21	−3	23, 500
Aug 20	0900	25	28, 000	10. 3	38	−1	21, 700
Aug 21	1000	27	27, 000	11. 1	34	−1	21, 500
Aug 22	1232	29	28, 500	----------	27	3	20, 500
Aug 26	0542	36	27, 000	----------	8	4	21, 000
Aug 27	0710	38	28, 300	----------	5	0	20, 700
Aug 29	1005	42	27, 500	----------	13	0. 5	20, 500
Aug 30	1130	44	22, 300	----------	9	3	19, 800
Aug 31	1302	46	17, 200	----------	9	3. 5	20, 500
Sep 2	0312	49	16, 000	----------	34	7. 5	20, 700
Sep 3	0438	51	16, 000	----------	33	6	20, 000
Sep 4	0600	53	5, 100	----------	103	4	19, 000
Sep 5	0730	55	7, 600	----------	34	2. 5	18, 500
Sep 12	0446	68	8, 100	----------	14	7. 8	17, 200
Sep 27	0116	96	3, 800	----------	21	−2	26, 300
Sep 28	1524	99	4, 100	----------	18	2	25, 500
Sep 29	0400	100	4, 000	----------	9	4	25, 500

the high intensity and the subsequent decrease. This table will be discussed further in connection with the magnetic storm of August 16–18, 1959. The table is incomplete but represents the present state of analysis of the data.

OBSERVATIONS DURING THE GEOMAGNETIC STORM OF AUGUST 16–18, 1959

We shall now consider in detail the changes observed in the trapped radiation associated with a strong geomagnetic storm having a sudden commencement at about 0414 UT on August 16. The remarkable effect observed during the first 24 hours of this storm was a large loss of radiation from the outer region. It is shown in figure 10, where pass 17, which occurred early in the disturbance, is compared with pass 19, which occurred 1 day later. In figure 10 the ion-chamber rate and the corrected or true counter rate are plotted in pulses per second multiplied by 1,000 and in counts per second, respectively. The ion-chamber rate dropped from a maximum of 9 to about 2 pulses/sec, and the counting rate from 4800 to about 1800 counts/sec. This means that about two-thirds of the detectable radiation existing in the outer zone during the first week of Explorer VI was lost during the first day of this geomagnetic storm. As is seen from Table 4, the trapped radiation remaining after the dumping was considerably harder than before the storm. Changes were also observed in the intermediate maximum occurring at around 13,000 km, but they have not yet been analyzed in detail.

If the change in the ion-chamber rates at different ranges as shown in figure 10 is considered, and the location on the surface of the

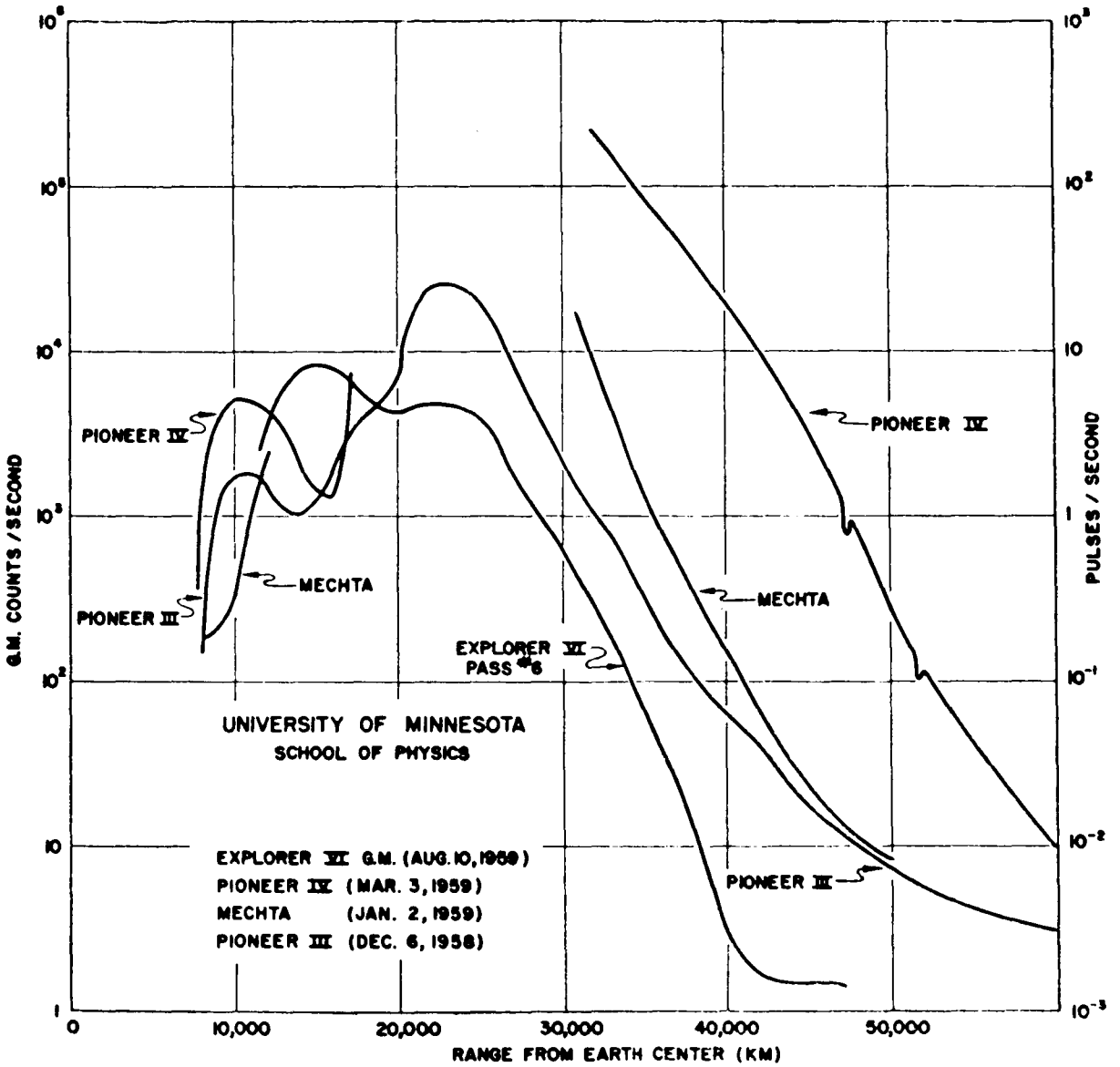

FIGURE 8.—*Comparison of Geiger counter rates for Explorer VI, Pioneer III, Pioneer IV, and the Russian Mechta space probe. The various counting rates are on a comparable basis within approximately 25 percent. To compare orbits, see figures 5 and 8. Explorer VI shows the lowest intensity of trapped radiation, and Pioneer IV the greatest enhancement of the radiation regions. These curves illustrate the time variability of the outer regions over long periods.*

earth where this radiation must be precipitated is computed, on the assumption that it is discharged down along the corresponding lines of force, the precipitation or 'dumping' profile shown in figure 11 is obtained. The radiation intensities have been corrected, because of the convergence of the magnetic lines of force, by the ratio of the surface field to the field along the orbit at the point from which the radiation disappeared. The radiation lost from the outer region is dumped between geomagnetic latitudes 52° and 62° with a peak intensity around 57° or 58°. This profile of precipitation lies definitely below the usual latitude of the auroral zone.

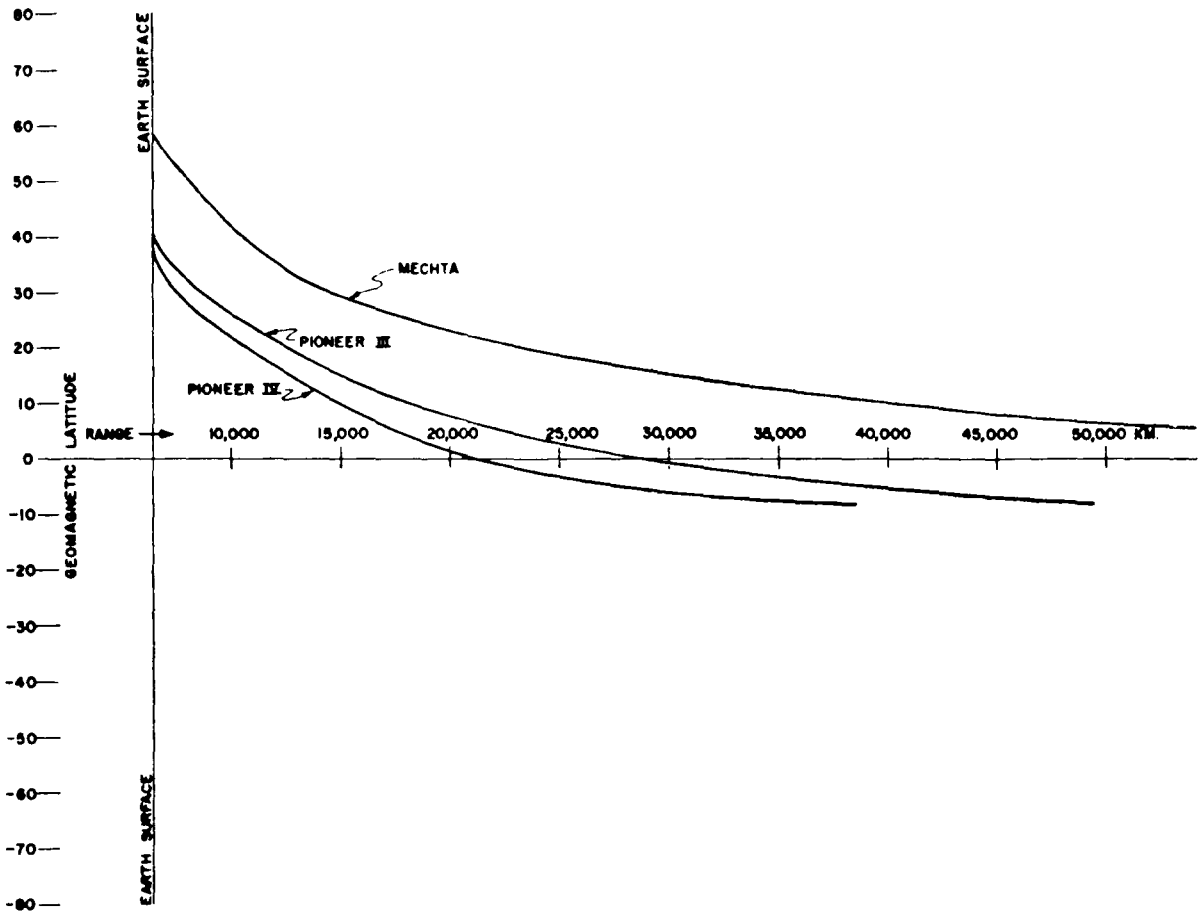

FIGURE 9.—*Comparison of the outgoing trajectories of Pioneer III, Pioneer IV, and Mechta.*

The ratio of the ion chamber and counter for the dumped radiation suggests that the particles are electrons of approximately 50-kev energy. We conclude that this source of electrons could well provide the auroral X rays seen on numerous occasions in balloon flights flown near the latitude of Minneapolis, which is about 56° geomagnetic [*Winckler, Peterson, Arnoldy, and Hoffman*, 1958]. In fact, a semiquantitative comparison can be made between the ion chambers flown on balloons measuring the X rays generated by the impact of the electrons on the atmosphere, and the ion chamber contained in the satellite measuring the X rays from the electrons bombarding the outer shell of the satellite. We estimate that for a typical strong balloon X-ray event, considered as extrapolated above the atmosphere, in a 24-hour period a dosage R_s of approximately 24 mr of X radiation would be produced. From the change in the satellite ion-chamber reading shown in figure 10, it is estimated that 7 r/hr of radiation dosage rate was lost from the radiation belts at the place of maximum intensity at about 21,000 km. The change in the number of electrons in the radiation zone at 21,000 km may be expressed by

$$\Delta N_{\text{loss}} = (\Delta \text{r/hr})/K \cdot T \tag{3}$$

The number of electrons required to produce the observed auroral X rays at balloon levels may also be expressed

$$\Delta N_{\text{precip}} = (R_s/K)(B/B_s) \tag{4}$$

where the constant K is the number of roentgens delivered in the form of X rays to the ioniza-

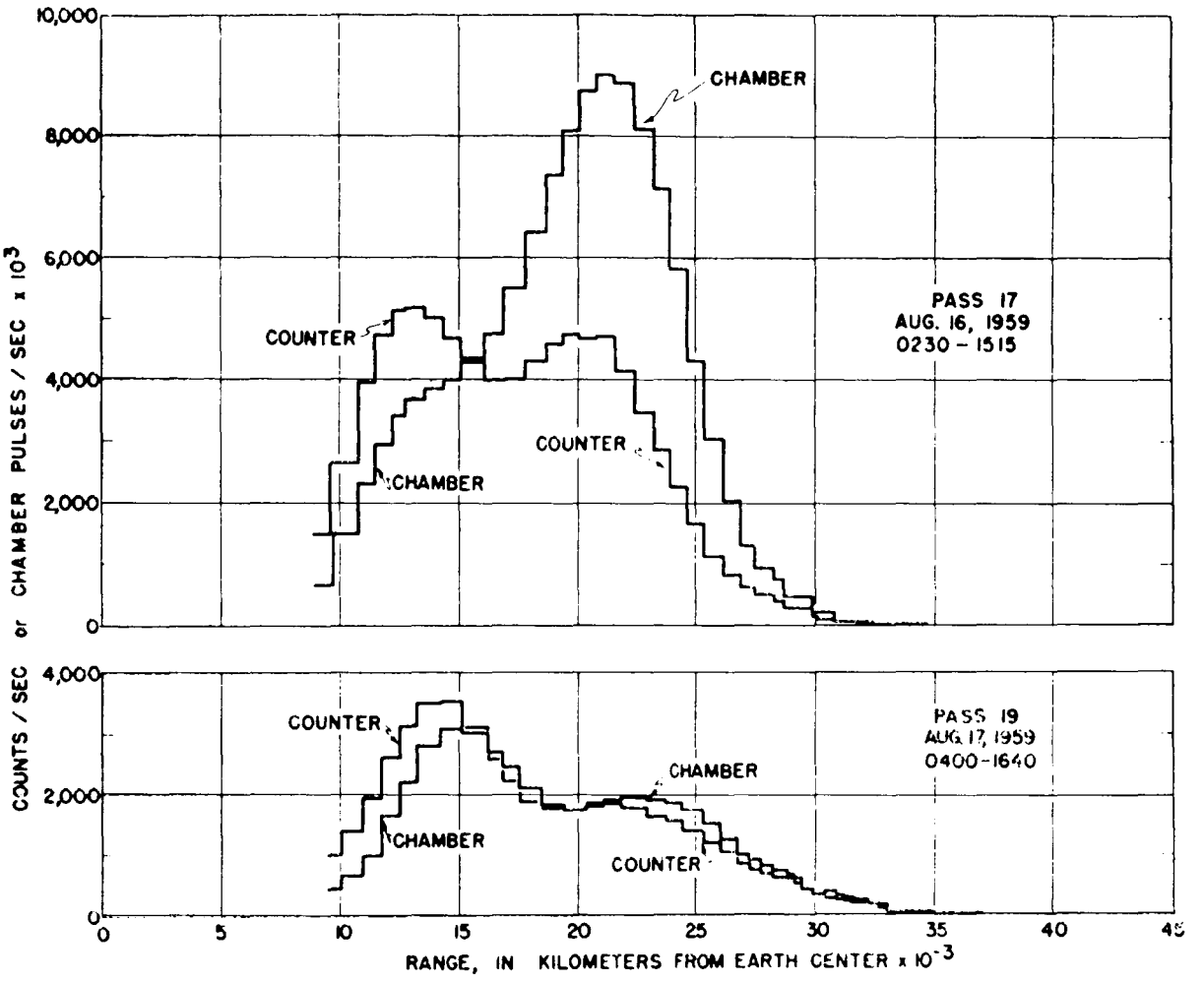

FIGURE 10.—*Comparison of a pass at the very beginning of the geomagnetic storm and a pass 24 hours after the beginning of the geomagnetic storm. Note the large decrease in the radiation content of the outer region. From this disappearance of net radiation, it can be computed that the electrons discharged are sufficient to produce the auroral X rays observed at balloon altitudes in subauroral zone auroras.*

tion chamber, either in balloon or satellite, by one electron, T is the period of an electron trapped in the radiation region and oscillating back and forth between the mirror points (approximately 1 second), B_s, is the surface value of the geomagnetic field, and B is the value of the field at 21,000 km. The ratio of ΔN_{loss} to $\Delta N_{\text{precipitated}}$ is equal to approximately 4, which means that enough radiation is lost from the outer zone to account completely for the bursts of X rays observed at balloon levels. A further remarkable observation is that on the night of August 16–17 a very strong aurora was observed by one of us (JRW) at approximately 57° geomagnetic latitude over the state of Minnesota. The aurora was a typical strong storm aurora with ray structure and visible forms extending as far south as 54° or 55° geomagnetic latitude. The visual observations indicated that this was the type of aurora, when observed with balloons at this latitude, which would produce strong X-ray bursts. A bright corona was observed, which has always been correlated with the

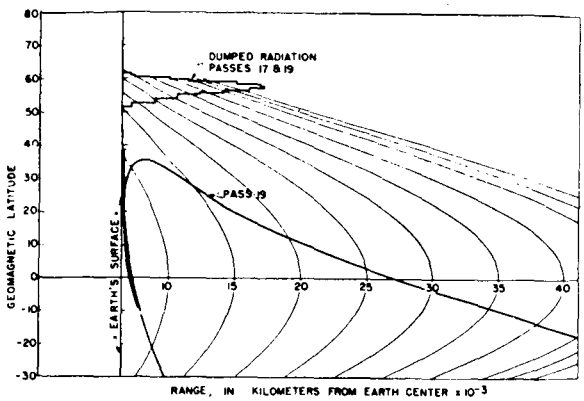

FIGURE 11.—*Estimate of the precipitation of electronic radiation from the outer regions of the trapped radiation onto the surface of the earth inferred from the measurements before and during the geomagnetic storm of August 16–17. Note that the electrons strike the earth's surface at about 57° geomagnetic latitude, and that, at least with the profile of radiation intensity observed in August and September 1959, they are not discharged into the auroral zone.*

presence of balloon X rays if the corona is seen near the balloon at these latitudes. It thus seems very reasonable that the balloon X rays can be due to the direct discharge of the soft radiation from the outer radiation zone.

This observation also may account for conclusions reached by *Anderson* [1959] that, although strong X-ray bursts are observed under visible auroras in latitudes below that of the auroral zone, balloon observations of auroras in the auroral zone show only weak X rays. The line of force connecting to the auroral zone at approximately 65° geomagnetic latitude leads into the trapped radiation at a region where the soft radiation is at a very low intensity, at least as seen during August and September 1959. There is some evidence also from examination of figure 8 that the radiation regions tend to return to a configuration similar to that observed in Explorer VI except for times when there is a large acceleration or injection from outside, and so the normal situation might be similar to that seen in August and September.

These observations are concerned with only one component of the aurora, namely electrons around 50 kev of energy. It is not certain what fraction of the total auroral energy is contained in these electrons. We have estimated from balloon X-ray data that some times sufficient energy is present in the X-ray electrons to supply all the energy of an auroral display. It is probable, however, that the solar plasma, which is presumably present but inaccessible to measurements with our instruments, or a similar type of low-energy radiation normally in the radiation regions, discharges to the surface and produces a large fraction of the visible auroral luminosity, both in the auroral zone and at latitudes below it. The association of the auroral X rays with the visible aurora occurs only in very strong auroras which sweep southward from the auroral zone and are characterized by magnetic indices of $K7$ to $K9$.

The exact mechanism of dumping in this case is not clear, but it seems certain that the increase in altitude of the atmosphere due to heating cannot remove enough particles. By following down the line of force with passes through the outer zone maximum, it is found that too large a fraction of the particles have turning points near the equator and hence at too high an altitude to be removed by scattering from a rising atmosphere. Therefore some other mechanism besides atmospheric heating must be invoked to explain the great loss of particle fluxes from the trapped radiation. Possibly perturbations of the magnetic field by the solar plasma exciting the geomagnetic storm may account for this, and the accompanying discharge of the particles into the atmosphere may perhaps cause the atmospheric warming and the scattering-out of trapped particles with low mirror points. Evidence for this latter phenomenon has been obtained by the Iowa group [*Rothwell and McIlwain*, 1959] as the result of extensive observations with the Explorer IV satellite, which penetrates the outer zone at low altitudes up to 1,000 km above the surface.

Another surprising observation is that, near the end of the storm on August 18, pass 21, as shown in figure 12, recorded an increase in the intensity of radiation in the outer region to a

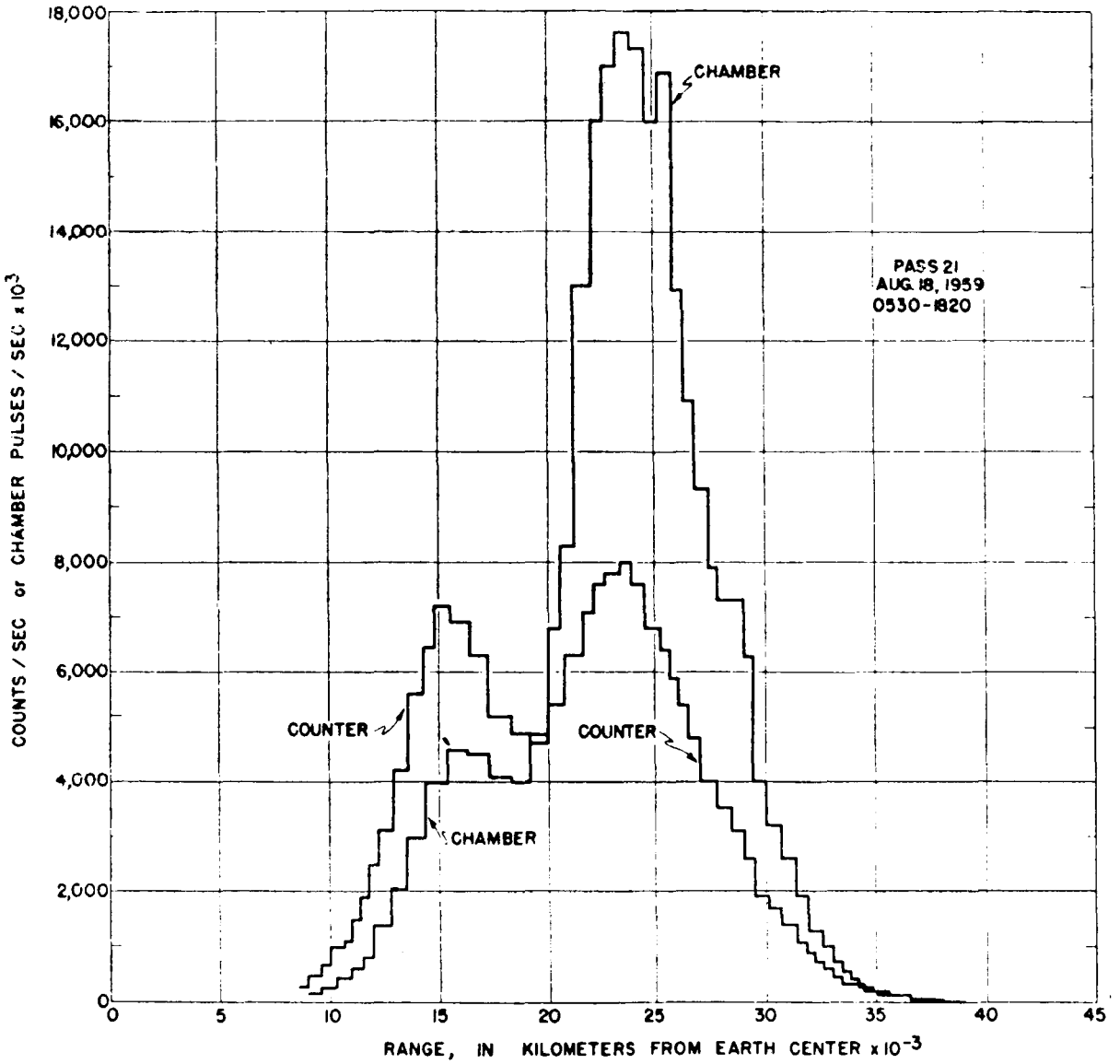

FIGURE 12.—*Pass 21 occurring at the end of the second day of the strong geomagnetic storm on August 16. Note the great increase in intensity of the radiation regions following the dumping shown in the previous figure. This pass went out from the earth at a quite low latitude. The maximum at 15,000 km is the new intermediate zone, also shown on figure 10.*

value very much higher than that we have called normal, characteristic of prestorm conditions. Pass 22, as shown in figure 13, showed a similar increase above normal, although the pass went through the trapped radiation at a very high latitude. Table 4 shows that the intensity in the soft outer maximum following the storm rapidly increased on August 20 to about 5 times prestorm levels, and remained at this value until August 30, when it began to decrease. While at peak intensity the radiation appeared harder than before the storm as given by the ratios on August 20 and 21. The magnetic storm of September 3–4 likewise diminishes the radiation in the soft maximum with a small intensity increase following it. The data for this storm are

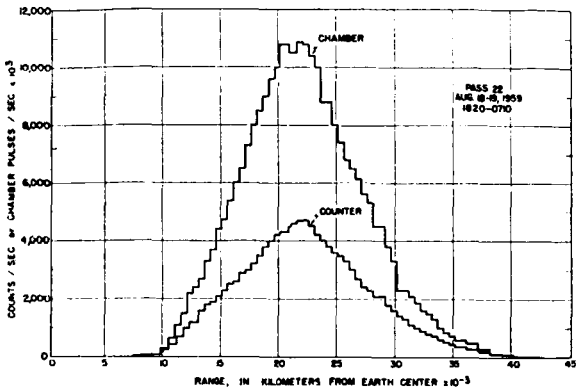

FIGURE 13.—*Pass 22, showing the increase following the geomagnetic storm of August 16–17. This pass went out at high latitude and missed the new intermediate zone.*

incomplete and will not be discussed further here.

During the peak intensity in the outermost maximum, a great long-lasting solar radio noise storm was observed. A plot of the intensity of radio emission at 169 Mc/s as determined by the Meudon Observatory group from the solar radio station at Nançay, France, is shown in figure 14, which is taken from the Boulder reports [*National Bureau of Standards*, 1959]. The sun is scanned every day, and the intensities are plotted across the disk. Regions of moderate activity appear frequently, as shown by the small black and white spots, but on August 22 a region developed which on succeeding days reached very high intensity. The radio emission from this region extended beyond the limits of the disk (shown by the horizontal lines labeled W and E on the left margin). This long-lasting solar noise storm has been observed at several other stations, for example by Warwick (private communication, 1959) at Boulder and by Erickson (private communication, 1959), at the Convair radio astronomy station in California. Warwick's sweep frequency interferometer covering the approximate range 15 to 100 Mc/s showed that the emission was continuum radiation, definitely not thermal, and attributable to synchrotron radiation from electrons in a region that appeared to be at a very great distance from the surface of the sun.

The unusual nature of this noise storm is also made clear by observations of the Fraunhofer Institute, which showed numerous wide-band rapid intensity fluctuations during the period. Similar observations were reported by the Nera Observatory [*Information Bulletin*, 1960].

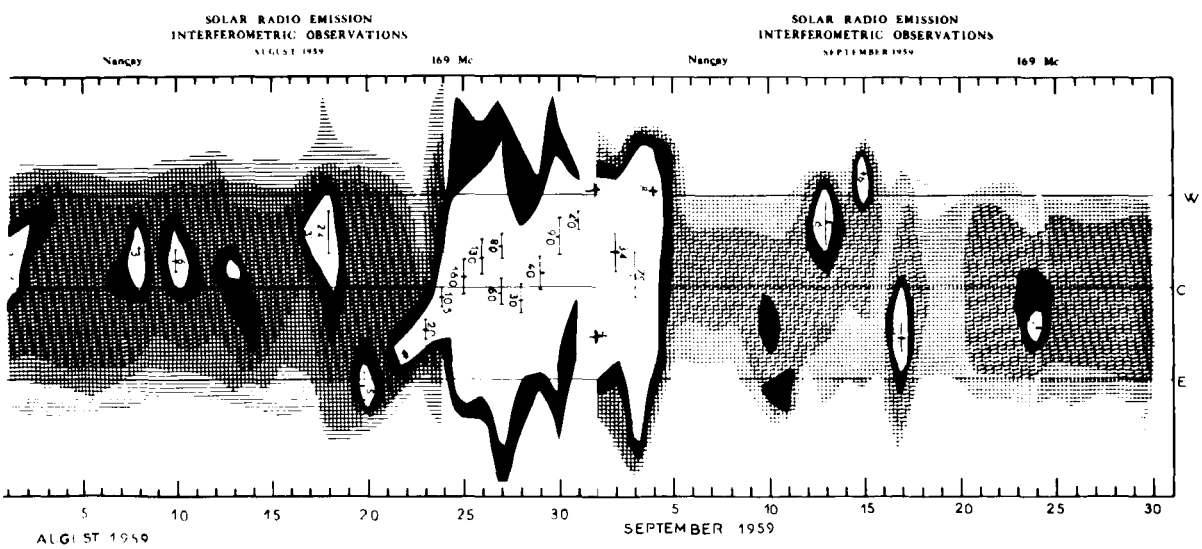

FIGURE 14.—*Solar radio noise intensity measured in Nancay on 169 Mc/s during August and September 1959, showing the great long-lasting noise storm beginning on August 22. Between August 24 and 30 the outer radiation zone stabilized at a high intensity.*

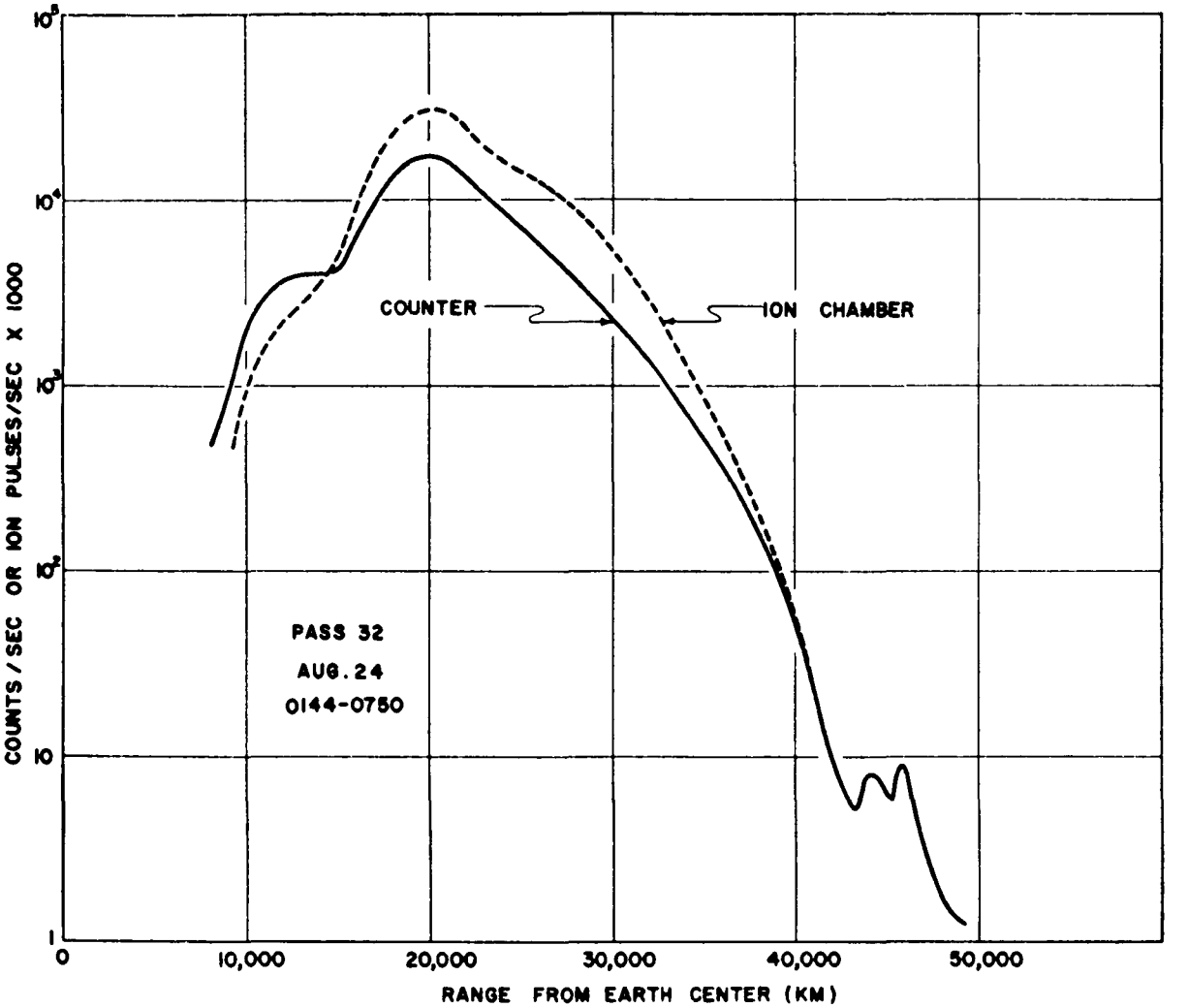

FIGURE 15.—*Pass 32 on August 24 during the high-intensity period of the outer zone. Note the structure at 45,000 km and the enhanced ion chamber and counter at the maximum at 20,000-km range. The structure is soft radiation similar to the maximum outer zone.*

On the basis of incomplete data used in our earlier report [*Arnoldy, Hoffman, and Winckler*, 1960], a close association seemed to exist between the beginning of the intense part of this noise storm and the increase in the outer zone. The acquisition of additional data makes this association less certain.

During the time of observations of the first half of this radio noise storm, the trapped radiation was extremely stable and the magnetic indices were low. Whether the build-up of the radiation is related to an unobserved initial phase of the solar radio noise storm or is an after-effect of the magnetic storm starting August 16 cannot be determined. Nevertheless, the injection of some particles into the trapped-radiation region during this period is suggested by figure 15, which shows a pass during the high intensity in the outermost maximum. This pass has structure at apogee and a counting rate there about 5 times that observed for cosmic rays during undisturbed periods. A pass during the intensity build-up just after the magnetic storm displayed similar structure, as

did several other passes during the enhanced intensity.

If the increase of electron flux is associated only with the geomagnetic storm beginning August 16, shown in figure 12, a tentative conclusion is that somehow in the wake of the storm part of the low-energy matter that is normally undetectable was elevated in energy and passed across the energy threshold of the ion chamber and counter carried in the Explorer VI satellite, appearing as an increase in the electronic component. Further studies of the details of the magnetic field during this storm and similar ones will be needed to decide on the exact mechanism of this acceleration process, if, in fact, it does exist.

Professor Sydney Chapman and his collaborator, S. Akasofu, have kindly furnished us with a preliminary D_{st} curve for the storm of August 16, obtained from eight selected equatorial stations. This curve, shown in figure 16, has been corrected for the regular diurnal magnetic variation S_q, and for the effect of the underground current system (by taking ⅔ of the total H variation after S_q correction). With relation to this storm time field variation, which seems to be a more or less typical example of a strong storm, the behavior of the energetic trapped electrons in the outer zone may be described by the observations of Explorer VI. We show the times of the appropriate passes by the indicated bars on figure 16. Data so far have been analyzed only for the outgoing parts of the passes.

The sudden commencement occurred during the outgoing part of pass 17, at about 25,600-km range from earth center (see fig. 10). No appreciable changes from prestorm conditions are observed during this pass. The 'dumping' effect is observed after about 24 hours of the main phase have elapsed. The replacement or local acceleration effect coincides with the recovery of the field to its normal value. These relationships are probably extremely significant for understanding the morphology of the storm, but we will defer detailed discussion until a more complete analysis of the data has been made.

In conclusion, it must be emphasized that the data reported herein are preliminary, as a great amount of unanalyzed records yet remains. We think that the essential features of this

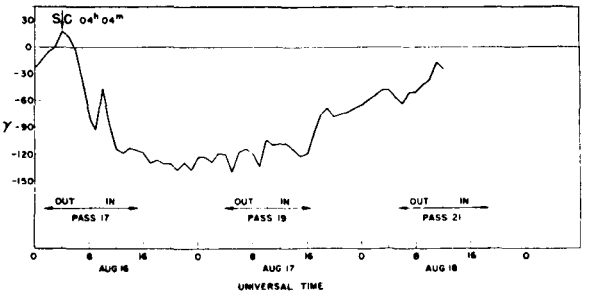

FIGURE 16.—*The* Dst(H) *curve for the August 16 storm as analyzed by Chapman and Akasofu. This analysis is based on 12 observatories well distributed in latitude and longitude between geomagnetic latitudes 30° N and S. Each record was corrected to remove the quiet-day solar daily variation of* H. *About 2/3 of the* Dst(H) *variation is supposed to be of external origin. From figures 10 and 12, on the outgoing portions pass 17 showed normal, pass 19 showed a large decrease, and pass 21 a large increase in the outer-zone intensity.*

discussion will, however, be preserved. It should also be noted that Explorer VI carried a variety of detectors from various laboratories, including a scintillation counter, a magnetometer, a coincidence telescope train, a lead-shielded counter, and the present ion chamber and unshielded counter. A comparison of these instruments, when more complete data are available, is certain to yield a more definitive account of the types and intensities of particles in the radiation regions surrounding the earth.

ACKNOWLEDGMENTS

We wish to acknowledge the coordinated efforts of the NASA and Space Technology Laboratories in successfully executing this complex experiment. The University of Minnesota effort was financed by a direct grant from the NASA, and the understanding support of Dr. John Lindsay of NASA is appreciated. The excellent work of Mr. Robert Howard of the University of Minnesota in the design of the electronic circuitry is also acknowledged. We have had numerous enlightening discussions about the interpretation of the results with Professor Paul Kellog of the University of Minnesota.

REFERENCES

Anderson, K. A., Balloon observations of X rays in the auroral zone, I, *Preprint SUI–59–22*, Department of Physics and Astronomy, State University of Iowa, 1959.

Arnoldy, R., R. Hoffman, and J. R. Winckler, Observations of Van Allen radiation regions during geomagnetic storms, *Proc. COSPAR 1st Intern. Space Sci. Symposium*, Nice, January 1960.

Information Bulletin of Solar Radio Observations in Europe, no. 1, Section Ionosphere and Radio Astronomy, Netherlands PTT, The Hague, January 1960.

National Bureau of Standards, *Solar and Geophysical Data*, September and October 1959, Central Radio Propagation Laboratory, Boulder, Colorado.

Rothwell, P., and C. E. McIlwain, Magnetic storms and the Van Allen radiation belts: Observations from satellite 1958 epsilon (Explorer IV), *Preprint SUI–59–25*, Department of Physics and Astronomy State University of Iowa, 1959.

Van Allen, J. *A.*, The geomagnetically trapped corpuscular radiation, *J. Geophys. Research, 64*, 1683–1689, 1959*a*.

Van Allen, J. A., Radiation measurements to 658,300 kilometers with Pioneer IV, *Bull. Am. Phys. Soc., 4*, 402,1959*b*.

Vernov, S. N., *A.* E. Chudakov, P. V. Vakulov, and Yu. I. Logachev, The study of the terrestrial corpuscular radiation and cosmic rays during the flight of a cosmic rocket, *Soviet Phys. JETP, 4*, 338, 1959.

Vestine, E. H., L. Laporte, C. Cooper, I. Lange, and W. C. Hendrix, Description of the earth's main magnetic field and its secular change, 1905–1945, *Carnegie Inst. Washington Publ. 578*, pp. 23–39, 1918.

Winckler, J. R., Balloon study of high-altitude radiation during the International Geophysical Year, *J. Geophys. Research, 65*, 1331–1359, 1960.

Winckler, J. R., L. Petersoon, R. Arnoldy, and R. Hoffman, X rays from visible aurorae at Minneapolis, *Phys. Rev., 110*, 1221–1231, 1958.

(Manuscript received March 16, 1960.)

Observations of the Van Allen Radiation Regions during August and September 1959[1]

2. The Capetown Anomaly and the Shape of the Outer Belt

BY ROBERT A. HOFFMAN[2]

School of Physics
University of Minnesota

This paper shows that any particles affected by the Capetown magnetic anomaly do not have trajectories that would pass through the position of the experimentally observed minimum in the outer belt. Therefore, the minimum cannot be taken as evidence either for the effect of the anomaly on the trapped radiation or for support of the neutron albedo source for the outer zone electrons.

Dessler and Karplus [1960] and *Hess* [1960] have proposed that the relative minimum in the outer belt as measured by radiation detectors aboard Explorer VI earth satellite is caused by a predominantly low-altitude injection from neutron albedo decays and a local loss of particles when those with low mirror points drift through the Capetown magnetic anomaly. To the contrary, this note will show, assuming the validity of present magnetic data, that any particles affected by the Capetown anomaly do not have trajectories that would pass through the position of the observed minimum in the outer belt.

EXPERIMENTAL OBSERVATIONS

The experimental observations to which the anomaly theory is here applied occurred from August 7 to 13, 1959, when the Explorer VI earth satellite passed twice a day through the heart of the outer zone at latitudes near the magnetic equator. Every even-numbered pass showed two maxima and the minimum in the counting rates of the ion chamber and Geiger counter which the University of Minnesota had aboard [*Arnoldy, Hoffman, and Winckler,* 1960]. The odd-numbered passes were too far north magnetically to exhibit the innermost maximum. This period of time was reasonably quiet magnetically.

Table 1 shows for the even-numbered passes the position of the minimum counting rate of the Geiger counter and the small extrapolation to the magnetic equator by use of the dipole approximation to the earth's field, $R=R_0 \cos^2\Lambda$. The average equatorial range of the minimum for the six passes is 19,700 km from the center of the earth at a geographic longitude of 148° E, or 13,300 km from the surface of the earth. Figure 1 is a profile for the outer belt of the Geiger counter counting rate as it would be if a pass went directly out the magnetic equator, and shows the two maxima and relative minimum.

CAPETOWN MAGNETIC ANOMALY AND PARTICLE TRAJECTORIES

The effect of the Capetown magnetic anomaly on the motion of trapped particles has been

[1] Published in the December 1961 issue of *Journal of Geophysical Research.* Reprinted by permission.

[2] Now at NASA Goddard Space Flight Center.

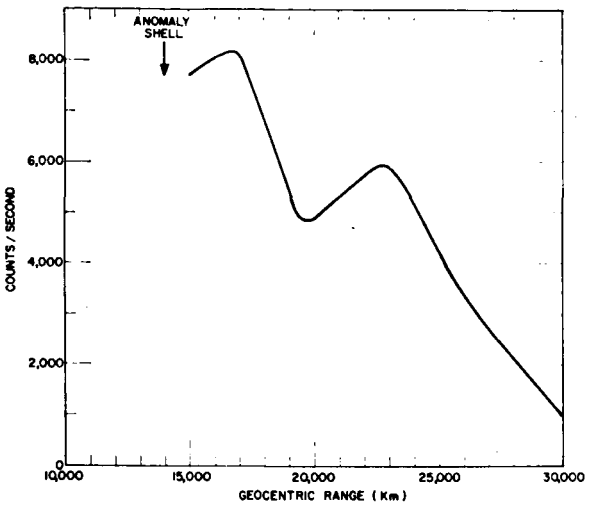

FIGURE 1.—*Profile for the outer belt of the Geiger counter counting rate as if a pass went directly out the magnetic equator. The position of the anomaly affected trajectories is indicated.*

thoroughly discussed by *Dessler* [1959] and *Dessler and Karplus* [1960], and therefore will not be repeated here. *Hess* [1960] and *Hess and Killeen* [1960] have calculated that the depth of the gap as it would be seen by radiation detectors, assuming a neutron source injection, to be about a 10-percent decrease at the equator, approximately half the value observed. However, it has never been proven that the particles affected by the anomaly, assuming they had drifted on their magnetic shell to the longitude at which the experimental observations have been made, actually would pass through the position near the magnetic equator at which the minimum is observed. Such a construction can be made as follows:

The particles that would have mirror points below about 1300 km over the anomaly are of interest because at this altitude they begin to be rapidly scattered into the atmosphere. The locus of the mirror points of these particles must be followed as they drift in longitude around the earth to 148° E longitude. This gives the location of the affected mirror points at the longitude of experimental observation. Then the trajectories of the guiding centers must be found as the particles spiral out away from the earth to the place where they would

TABLE 1

Pass No.	Date	Geographic Longitude E	Range R, km	Magnetic Latitude	R_0, km
2	Aug. 8	206.7	18,030	19.8	20,400
4	9	183.4	18,630	13.9	19,800
6	10	160.7	19,940	7.3	20,300
8	11	136.0	19,020	6.1	19,200
10	12	111.7	18,590	5.7	18,800
12	13	89.0	19,580	4.4	19,700
Averages		148.0			19,700

cross the magnetic equator. This equatorial range is finally compared to the range at which the minimum in the outer belt is actually observed.

Mirror Point Loci

The locus of the mirror points of a trapped particle has been shown to be defined by two adiabatic invariants: (*a*) the magnetic moment, which defines the magnetic field strength B_m of the mirror point, and (*b*) the action integral,

$$I = \int_{B_m}^{B_{m'}} \frac{V_{||}}{V}\, dl = \int_{B_m}^{B_{m'}} \left(1 - \frac{B}{B_m}\right)^{1/2} dl$$

which defines the magnetic line of force followed by the guiding center of the particle as it spirals out from B_m, across the magnetic equator, and back toward the earth to the field strength $B_{m'}$ [*Welch and Whitaker*, 1959]. Here V and $V_{||}$ are the total velocity and velocity component parallel to the field for the particle; dl is the arc length along the path of integration; B_m, $B_{m'}$ are the conjugate mirror points; and B is the scalar field along the path of integration.

Jensen, Murray, and Welch [1960] have published tables of the geographic latitude, longitude, and altitude of the loci of mirror points as defined by various values of B_m and ln I, using a 512 coefficient expansion of the earth's field in order to obtain a good fit near the Capetown anomaly.

In figures 2*a* and 2*b* are plotted the loci of mirror points in the southern hemisphere defined by several values of B_m and ln I. The particles having mirror points at the Capetown

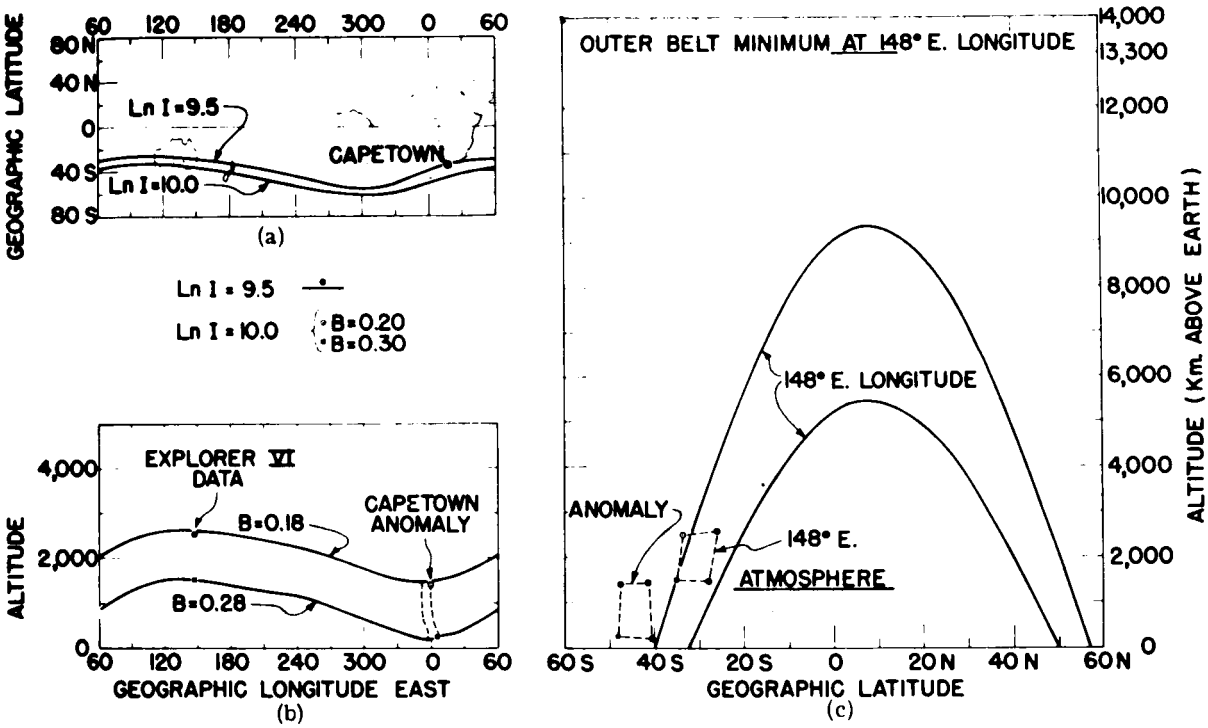

FIGURE 2*a*, *b*, *and c*.—*Construction to prove that any particles affected by the Capetown anomaly do not have trajectories that pass through the position of the outer belt minimum.*

anomaly are slightly south of the ln $I = 9.5$ line in figure 2*a*, but not nearly as far south as ln $I = 10.0$. The tables of *Jensen, Murray, and Welch* [1960] do not have the locus of mirror points which pass directly through the anomaly. Figure 2*b* shows the altitude dependence of the mirror points as a function of longitude. The particles affected by the anomaly lie between the two lines. Any particle above the upper line never dips below 1300 km as it drifts around the earth. Any particle injected below the lower line, even at the maximum altitude of the line at 125° E will be almost immediately scattered into the atmosphere. The lines are for ln $I = 9.5$; the circled dots and squared dots give the minimum altitude of mirror points for ln $I = 10.0$ at the anomaly and the altitude at 148° E. Hence the four loci (ln $I = 9.5$, $B_m = 0.18$ and 0.28; and ln $I = 10.0$, $B_m = 0.20$ and 0.30) bracket the particles having mirror points affected by the anomaly. These four bracketing loci are shown in figure 2*c* as the lower altitude and more southern latitude set of points when at the anomaly, and the higher altitude and more equatorial set when at 148° E longitude.

Hence we have found the approximate position of the particles having mirror points that would be affected by the anomaly when thay had drifted to the longitude where the experimental observations have occurred. A typical particle has its mirror point at 148° E longitude at about 29° south and 2,000 km altitude.

Guiding Center Trajectory

The next step is to determine the altitude at which these affected particles will cross the magnetic equator at the longitude of experimental observations. *Vestine* [1959] has published tables of coordinates (ϕ, λ, h) of points defining the geomagnetic field lines intersecting the earth's surface at latitude ϕ and longitude λ, appropriate at height $h = 0$, using the 48 coefficient expansion. However, a line having $\phi = 29°$ S, $\lambda = 148°$ E, and $h = 2{,}000$ km is required for the construction

for a particle which has drifted from the anomaly. Such a line has not been published, so it is again necessary to bracket the point of interest. Two such bracketing lines are plotted in figure 2*c*, the lower one leaving the earth at $\phi = 32°$ 20′ S, and $\lambda = 143°$ 57′ E, and the upper one leaving at $\phi = 40°$ 00′ S, and $\lambda = 150°$ 00′ E.

Hence it is seen from figure 2*c* that particles having mirror points affected by the anomaly cross the magnetic equator at about 148° E longitude somewhere between the altitudes of 9,370 km and 5,450 km, perhaps at about 7,500 km altitude (14,000 km geocentric range). The minimum as experimentally observed has an altitude of 13,300 km, well above any anomaly-affected particles (see fig. 1).

DISCUSSION

The first conclusion resulting directly from the above discussion is that the Capetown anomaly is not an explanation for the minimum in the outer belt. This conclusion is based on the assumption that the primary magnetic data upon which *Jensen, Murray, and Welch* [1960] have based their analysis are correct. However, a comparison between the current United States' charts of total magnetic field and a recent magnetic survey of the area west of Capetown indicates that the field contours for 1955 could be moved east by as much as 17° [*Heirtzler and Hirshman*, 1960]. However, even such a large shift of the anomaly to the east would probably not move the anomaly-affected particles out of the four bracketing loci of mirror points, that is, south of the ln $I = 10.0$ line in figure 2*a*. Therefore it is not likely that agreement can be reached between the actual position of the minimum and the equatorial range of the trajectories through the anomaly.

Dessler and Karplus [1960] and *Hess* [1960] have also used the theory of the anomaly causing the minimum as supporting evidence for the neutron albedo decay source of the outer belt. In order to cause the minimum in the equilibrium population of the particles, the local decrease in magnetic field strength at the anomaly would require an injection of particles that is strongly weighted toward the surface of the earth. Such a source is found in albedo neutrons, whose decay density falls off rather like R^{-4} [*Hess*, 1960]. A corollary to the first conclusion is that the minimum can no longer be considered as a piece of evidence in favor of the neutron source.

ACKNOWLEDGMENTS

This work was supported by the National Aeronautics and Space Administration under contract NASw–56. I wish to thank my adviser, Dr. John R. Winckler, and my coworker, Mr. Roger L. Arnoldy, for helpful discussions during the preparation of this paper.

REFERENCES

Arnoldy, R. L., R. A. Hoffman, and J. R. Winckler, Observations of the Van Allen radiation regions during August and September 1959, Part 1, *J. Geophys. Research, 65*, 1361–1376, 1960.

Dessler, A. J., Effect of magnetic anomaly on particle radiation trapped in geomagnetic field, *J. Geophys. Research, 64*, 713–715, 1959.

Dessler, A. J., and R. Karplus, Some properties of the Van Allen radiation, *Phys. Rev. Letters, 4*, 271–274, 1960.

Heirtzler, J. R., and J. Hirshman, Measurements of the geomagnetic field near Capetown, *J. Geophys. Research, 65*, 3016–3018, 1960.

Hess, W. N., The radiation belt produced by neutrons leaking out of the atmosphere of the earth, *J. Geophys. Research, 65*, 3107–3115, 1960.

Hess, W. N., and J. Killeen, Densities of electrons from neutron decay trapped by the geomagnetic field, *Bull. Am. Phys. Soc., 5*, 260, 1960.

Jensen, D. C., W. Murray, and J. A. Welch, Table of adiabatic invariants for the geomagnetic field 1955, *Air Force Spec. Weapons Center Albuquerque Rept. TN 60–8*, April 1960.

Vestine, E. H., Geomagnetic field in space, *Rand Corporation, Rept. L–4970*, 1959.

Welch, J. A., and W. A. Whitaker, Theory of geomagnetically trapped electrons from an artificial source, *J. Geophys. Research, 64*, 909–922, 1959.

(Manuscript received August 11, 1961; revised August 31, 1961.)

Observations of the Van Allen Radiation Regions during August and September 1959[1]

3. The Inner Belt

BY R. A. HOFFMAN,[2] R. L. ARNOLDY,[3] AND J. R. WINCKLER

School of Physics
University of Minnesota

The differential energy spectrum of an assumed power law form for trapped protons in the inner belt has been determined from data received from the ion chamber and Geiger counter aboard the earth satellite Explorer VI. Above an energy of 30 Mev, the spectrum has the form of $E^{-1.65}$ at about $-28°$ geomagnetic latitude. The spectrum has been checked by comparison of the actual proton counting rate of the triple coincidence telescope aboard Explorer VI in the inner belt with the rate calculated from such a spectrum. It is then shown that the counting rate from the scintillation counter aboard Explorer VI is probably due primarily to electrons. Electron fluxes at the maximum of the inner belt are given as about 2×10^9 electrons/cm² sec from 200 to 500 kev, or about 1×10^7 electrons/cm² sec greater than 500 kev at $-28°$ geomagnetic latitude. The spectra obtained are shown to be in agreement with those previously published, and not in conflict with the spectrum calculated from neutron albedo decay. The data also place an upper limit of about 10 percent for time variations caused by magnetic storms, although they are probably consistent with no variations at all.

During twelve passes of the earth satellite Explorer VI between August 7 and October 2, 1959, telemetry was received while the satellite was passing through the maximum of the inner belt on the inward part of the orbit. This paper presents an analysis of the data received from the four radiation detectors aboard the satellite. With the assumption that the proton component has a differential energy spectrum of the power law form, one such spectrum is found to be compatible with the counting rates and calibrations of the ion chamber and Geiger counter which the University of Minnesota had aboard [*Arnoldy, Hoffman, and Winckler*, 1960] and also the triple coincidence telescope from the University of Chicago [*Fan, Meyer, and Simpson*, 1961]. From calibrations of the Space Technology Laboratories' scintillator [*Rosen and Farley*, 1961] it will be shown that it probably measures predominantly the electron flux in the inner belt, and so estimates of this flux at the maximum of the belt will be given.

Comparisons with previous emulsion and counter experiments flown into the inner belt will be made, and the data will be analyzed in such a manner as to place an upper limit for time variations of the proton component due to magnetic storms.

CALIBRATION OF THE DECTECTORS TO PROTONS

The interpretation of the data received from the radiation detectors, when situated inside the

[1] Published in the January 1961 issue of *Journal of Geophysical Research*. Reprinted by permission.

[2] Now at NASA Goddard Space Flight Center.

[3] Now at Honeywell Co.

complex payload passing through the unknown radiation flux of the inner belt, requires a knowledge of the probability of causing a count in the detector for a proton of a given energy incident upon the payload. These numbers are a function of the impact point on the payload, because the particle will lose a varying amount of energy along its trajectory to the detector, depending on the thickness and kind of material through which it must pass. Therefore, the counting rates will be expressed as an average over the entire payload, or the rate in an isotropic flux. Such numbers will be termed the efficiency of the detector and will be expressed as the actual counting rate of a detector situated inside the payload to an isotropic flux outside the payload of 1 proton/cm^2 sec at an energy E, where E is in Mev.

The efficiencies of the four radiation detectors to protons were determined in three steps: (1) The responses of the detectors were first ascertained for the detectors outside the payload experimentally, theoretically, or both. (2) The distribution of matter around the detector inside the payload was determined. It was necessary to know the fraction of the total solid angle (4π) about each detector having a certain thickness of absorbing material ρ_i: $\Omega(\rho_i)/4\pi$. (3) Then a monoenergetic, isotropic proton flux of energy E_0 was assumed incident upon the payload. For the various fractions of the total solid angle having known thicknesses of absorption, the energy loss by the protons was calculated, so that the remaining energy for the protons (E_i) incident upon the detector for each element of solid angle was known. Then, from the response curves of step 1, the counting rates of the detectors for protons from each element of solid angle were found, $R_i(E_i)$. The total efficiency for the entire 4π solid angle was just the sum of the products of these responses with the fraction of the 4π having the given absorption:

$$\text{Efficiency} = \sum_i R_i(E_i) \frac{\Omega(\rho_i)}{4\pi}$$

CALIBRATION OF THE ION CHAMBER AND GEIGER COUNTER

The ion chamber and Geiger counter and associated electronics have been described previously [*Arnoldy, Hoffman, and Winckler*, 1960]. These two detectors were exposed to a beam of protons in the energy range zero to 36.8 Mev at the University of Minnesota linear accelerator. To obtain the low fluxes capable of being counted by the detectors, the protons were elastically scattered from helium, and the energy of the scattered beam was varied by inserting aluminum absorbers into the beam path. The scattered beam flux was measured with a NaI(TI) scintillator, whose output was monitored with a twenty-channel pulse height analyzer.

Table 1 is a summary of the experimental results and also includes the calculated response of the chamber. Since there is excellent agreement between the calculated response of the chamber and its experimental measured response, the energy range of the calibration was extended to higher energies by accepting the calculated values. From table 1 it is seen that the Geiger counter response increases with energy, reaching its full cross section of 0.710 cm^2 at 36.8 Mev for radiation incident normal to its axis. Above this energy the response is constant.

The mass distribution around the detectors was determined by three methods: a knowledge of the weights, sizes, and positions of the packages inside the payload; the measurement of the absorption of Co^{60} γ rays; and, for the regions where the thicknesses were less than about 1 g/cm^2, by the absorption of β rays.

The matter around the ion chamber was divided into nine different absorption thicknesses, each with a chosen average thickness; the matter about the Geiger counter was divided into seven regions. These are listed in table 2 along with the fraction of the total solid angle subtended by each region about the specific detector.

Using the knowledge of the responses of the detectors outside the payload to protons and the mass distributions, the efficiencies of the chamber and Geiger counter were calculated; they are plotted in figures 1 and 2.

Whenever a new fraction of solid angle opens up, allowing protons with high specific ionization to penetrate to the chamber gas, the computed efficiency undergoes a sudden increase.

TABLE 1.—*Experimental Results from Calibration of Ion Chamber and Geiger Counter to Protons from University of Minnesota Linear Accelerator*

[The calculated response of the ion chamber is included to demonstrate the agreement with experiment, justifying the use of the calculated response at higher energies.]

E, Mev	Ion Chamber, pulses (proton/cm²)		Geiger Counter, counts (proton/cm²)
	Experimental Response	Calculated Response	Experimental Response
18. 7	4.98×10^{-5}	5.12×10^{-5}	0. 000
28. 1	3.30×10^{-5}	3.50×10^{-5}	0. 334
33. 3	2.89×10^{-5}	2.86×10^{-5}	0. 595
36. 8	2.72×10^{-5}	2.62×10^{-5}	0. 710

TABLE 2.—*Various Average Absorption Thicknesses for Which the Matter Surrounding the Ion Chamber and Geiger Counter in the Explorer VI Payload Was Divided, along with the Fraction of the Total Solid Angle Subtended by Each Region about the Specific Detectors*

Region	Avg. Thickness, ρ_i g/cm²	$\Omega_i(\rho_i)$ / 4π
Ion chamber:		
1	0. 574	0. 0349
2	0. 915	0. 0659
3	1. 10	0. 0143
4	1. 50	0. 1315
5	2. 00	0. 0434
6	2. 70	0. 160
7	3. 75	0. 142
8	7. 30	0. 184
9	18	0. 224
Geiger counter:		
1	1. 10	0. 027
2	1. 78	0. 097
3	1. 97	0. 267
4	2. 65	0. 033
5	3. 92	0. 135
6	7. 50	0. 190
7	18	0. 251

In reality, of course, such jumps would not occur, because $\Omega(\rho)/4\pi$ would be a rather smooth function; therefore, the efficiency must be smoothed out as shown by the straight lines in the figure. This straight-line approximation will be used in the calculations, because straight lines on the log-log plot transform to power law efficiencies of the form $\epsilon_{IC}(E) = KE^a$, which are easy to use with power law spectra. The equations of the three lines are given in table 3.

Similarly for the counter, the calculated curve has been approximated by the straight lines on the log-log plot, the equations of the lines being given in table 3. For energies greater than 180 Mev, the protons enter the Geiger counter from all directions, so that the efficiency is the omnidirectional geometric factor of 0.722 cm².

CALIBRATION OF THE TRIPLE COINCIDENCE TELESCOPE

The University of Chicago triple coincidence telescope has been calibrated outside the payload to protons at the Chicago synchrocyclotron [*Fan, Meyer, and Simpson*, 1961, fig. 3]. The calibration curve given in their figure for the triples was normalized to its omnidirectional geometric factor of 2.82 cm² at an energy of 1,000 Mev. To obtain the efficiency of the telescope inside the payload, the assumption is made here that the mass distribution about the detector was not too different from that around the ion chamber, and the efficiency was calculated in the same manner as for the chamber. This calculated efficiency is plotted in figure 3, and the equations of the straight-line approximations are given in table 3.

CALIBRATION OF THE SCINTILLATOR

The efficiencies of the Space Technology Laboratories scintillator have been given for protons and electrons [*Rosen and Farley*, 1961]. From this reference we have constructed figure 4, and the equations of the approximating lines are given in table 3.

TABLE 3.—*Power Law Lines Approximating the Efficiencies of the Four Radiation Detectors Inside the Explorer VI Payload to Protons*

[Efficiency is expressed as the actual counting rate of the detector situated inside the payload to an isotropic flux outside the payload of 1 proton/cm² sec at an energy E, where E is expressed in Mev.]

Detector Efficiencies	
Energy Range, Mev	Efficiency
Ion Chamber	
< 23.6	0.00
23.6 — 33.	$9.69 \times 10^{-13} E^{5.56}$
33. — 60.	$4.87 \times 10^{-6} E^{1.16}$
60. — 1,000.	$5.87 \times 10^{-3} E^{-0.58}$
$>1,000.$	1.26×10^{-4}
Geiger-Müller Counter	
<36.4	0.00
36.4 — 50.	$3.73 \times 10^{-24} E^{13.9}$
50. — 67.	$2.64 \times 10^{-6} E^{2.82}$
67. — 180.	$2.18 \times 10^{-2} E^{0.673}$
$> 180.$	0.722
Proportional Counter Telescope	
$< 68.$	0.00
68. — 92.	$9.73 \times 10^{-23} E^{10.88}$
92. — 140.	$2.92 \times 10^{-11} E^{5.03}$
140. — 200.	$5.43 \times 10^{-3} E^{1.18}$
$> 200.$	2.82
Scintillation Counter	
$<2.$	0.00
2. — 10.	2.1×10^{-4}
10. — 180.	$1.0 \times 10^{-3} E^{1.57}$
$> 180.$	3.5

ION CHAMBER AND GEIGER COUNTER DATA

The time resolution of the data received from the detectors while the satellite was passing through the inner belt was often quite coarse, for two reasons: the satellite was moving very fast during this part of the orbit where it was approaching perigee; and the counting rate of the Geiger counter was high enough so that the rate sampled from the eighth binary was filtered out, leaving only the sampling from the seventeenth binary, which switched only a few times while in the belt. Also, the chamber pulsing rate was scaled down by 32, making the chamber cycles quite long.

Figure 5 shows the data from one of the more completely recorded passes through the inner belt. Figure 6 is a map showing contours of constant counting rate for the counter from data obtained from five passes between August 11 and August 21, 1959. Although inner-belt data were received through October 2, the present trajectory data after August 26 are not sufficiently accurate to allow the data to be incorporated into a contour map. The dipole approximation has been used, but, since all the telemetry was received at the Singapore station, the longitude interval spanned by the data runs only from 62° to 139° E. In this region the dipole shells are very nearly parallel to the actual magnetic field shells, and so the longitude effect does not introduce errors in plotting the data on a common meridian plane. The contour plot also indicates the position of the maximum counting rate for each of the five passes (shown by X's). The only measurement indicating the locus of the maximum of the inner belt near the geomagnetic equator was that obtained from the inbound part of the Pioneer III flight, for which the counting rate of the Anton 302 counter aboard was still increasing at about 10,500 km geocentric range, only a few degrees from the geomagnetic equator [*Van Allen and Frank*, 1959*a*]. Therefore, the maximum of the inner belt is apparently at a geocentric range of about 10,000 km at the equator, and follows down this line of force to a magnetic latitude of about 25°, where it turns outward.

In figure 7 is plotted the ratio of the ion chamber rate to the Geiger counter rate divided by this ratio for minimum ionizing protons (1.57×10^{-4} pulse/count). Since the pulsing rate of the chamber is proportional to the rate of ionization in the chamber, the ratio is a measure of the average ionizing power, or the average energy of the incident radiation. Although there

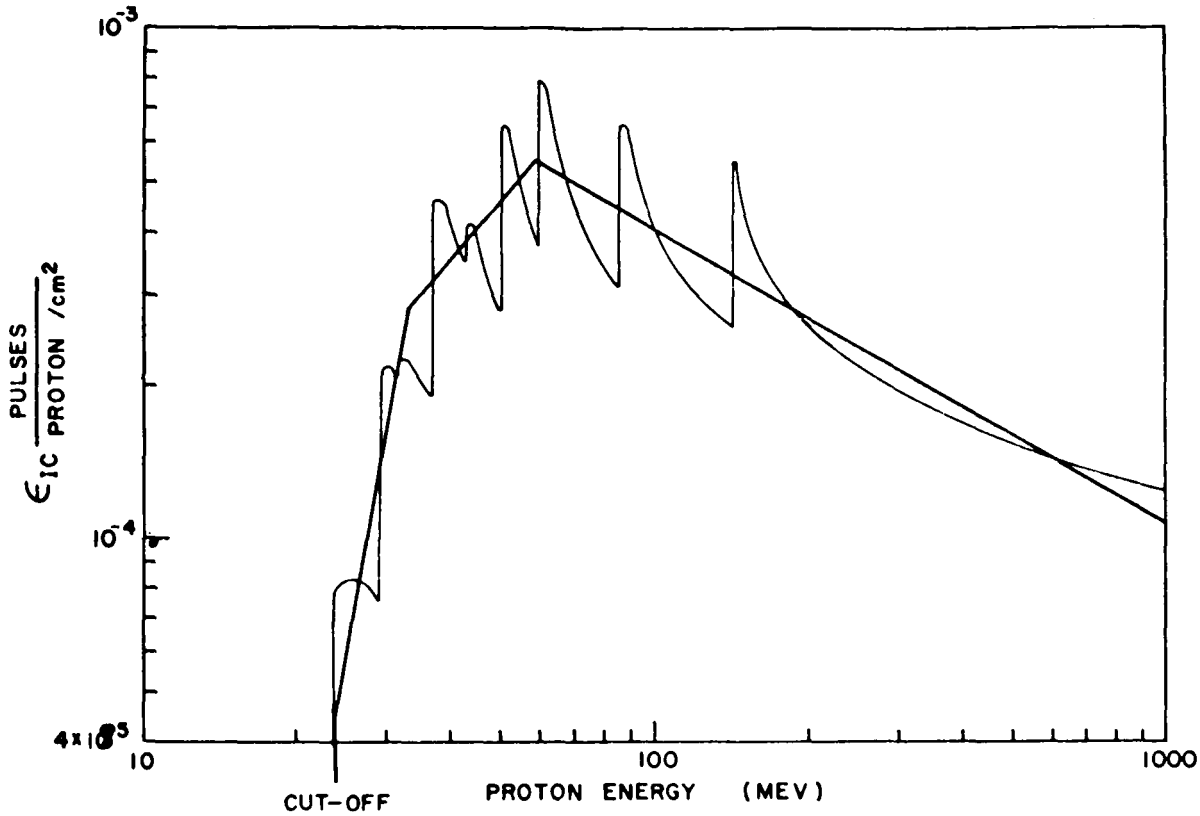

FIGURE 1.—*Efficiency of ionization chamber (inside Explorer VI payload) to protons.*

does not seem to be any large variation in average energy in the belt, there is a tendency to hardening toward the low-altitude side of the belt, and perhaps a slight hardening toward lower latitudes. *Van Allen and Frank* [1959*b*] report a similar observation by the two counters aboard Pioneer IV. It is also noticed from figure 5 that the radiation is hardest in the slot between the two belts, at a time 2315:30 UT for pass 12, probably indicating high-energy electrons (above 2.86 Mev) from the inner side of the outer belt.

PROTON SPECTRA

Since the discovery of the inner radiation belt by satellite 1958*a*, a number of workers have flown emulsions and counters into the radiation to determine its nature and energy spectrum. Both protons and electrons have been found, and the energy spectrum of the protons has been measured a number of times at different positions. The electron flux is known to be much larger but not nearly so penetrating as that of the protons.

From the ratio of chamber to Geiger counter rates, it is possible to determine the energy spectrum of the protons in the inner belt; then from the rate of either detector the flux can be calculated. However, it must be shown that the detectors are counting only protons; that is, the maximum energy of the electrons must be below the threshold energy for direct detection by the instruments (1.50 Mev for the chamber and 2.86 Mev for the counter). Also the contribution to the count rate from bremsstrahlung must be small. Unfortunately, the maximum electron energy has so far evaded accurate measurement. *Freden and White* [1959] place an upper limit of one percent on the ratio of the number of electrons to protons that can penetrate 6 g/cm² of material (75 Mev for protons, 12 Mev for electrons). *Armstrong,*

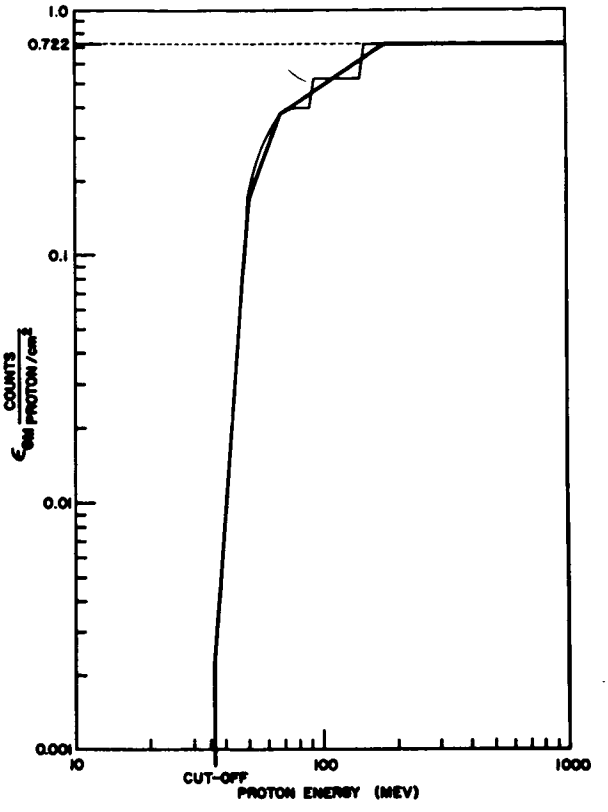

FIGURE 2.—*Efficiency of Geiger counter (inside Explorer VI payload) to protons.*

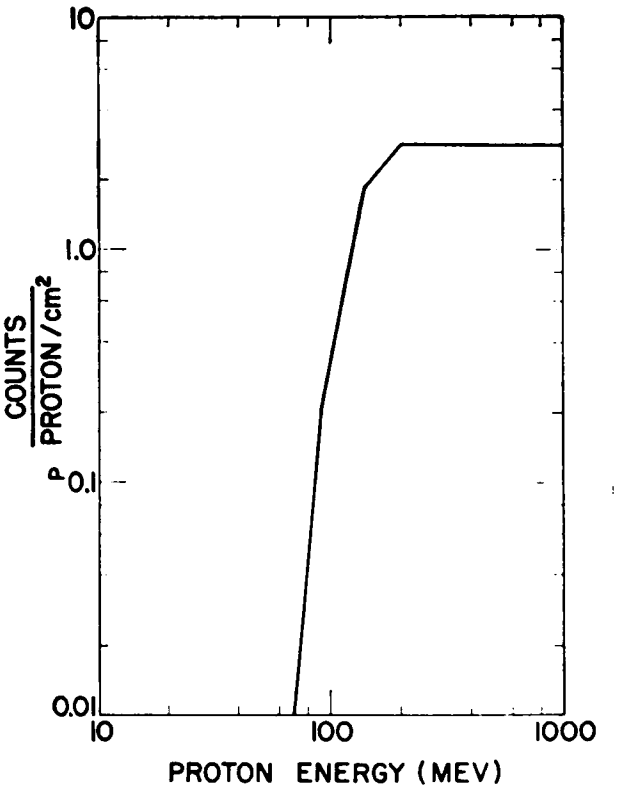

FIGURE 3.—*Approximate efficiency of proportional counter telescope (inside Explorer VI payload) to protons.*

Harrison, and Rosen [1959] report that electrons greater than 11 Mev exist in an abundance of less than 5 percent of protons having energy over 70 Mev. *Holly, Allen and Johnson* [1961] flew packages of eight Geiger tubes shielded by various amounts of metal absorbers into the inner belt to obtain range spectra. The data are consistent with an end point electron energy between 700 and 800 kev, although it could run to higher energies. *Van Allen and Frank* [1959*b*] believe that the electrons have energies ranging up to about 1 Mev, with a spectrum rising strongly toward lower energies. They give a flux in the heart of the inner zone at an altitude of 3,600 km on the geomagnetic equator of about 10^7 electrons/cm² sec sr with energy greater than 600 kev.

With the above measurements as evidence, the assumption will be made here that the electron flux entering the ion chamber and Geiger counter while Explorer VI was passing through the inner belt was small compared with the proton flux. This assumption places an upper limit in energy of 1.5 Mev for electrons. Although it has been demonstrated by *Freden and White* [1960] that the proton component above 40 Mev is due to albedo neutrons produced in the atmosphere by cosmic rays, it is doubtful that such a source is strong enough to account for the electron flux [*Kellogg*, 1960]. Since another electron source is apparently necessary, it is not justifiable to assume that the maximum electron energy is that from β decay of neutrons, about 800 kev.

Because the ion chamber and counter have different efficiency curves to protons, it is possible to solve for two parameters in any analytically expressed spectrum of particles. Since it is known that the protons of the inner belt follow closely a power law energy spectrum $dN/dE = N_0E^{-\gamma}$ [*Freden and White*, 1959], the determination of N_0 and γ will be exhibited.

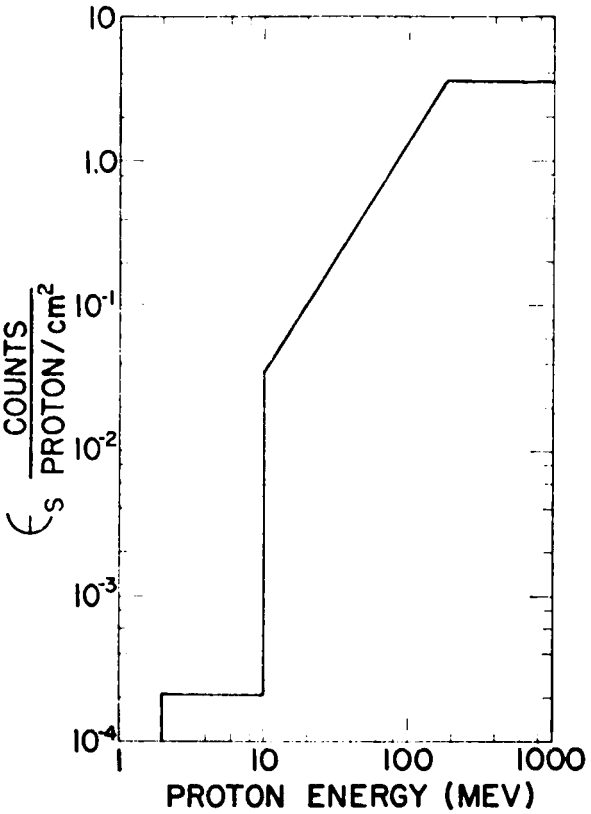

FIGURE 4.—*Approximate efficiency of scintillation counter (inside Explorer VI payload) to protons.*

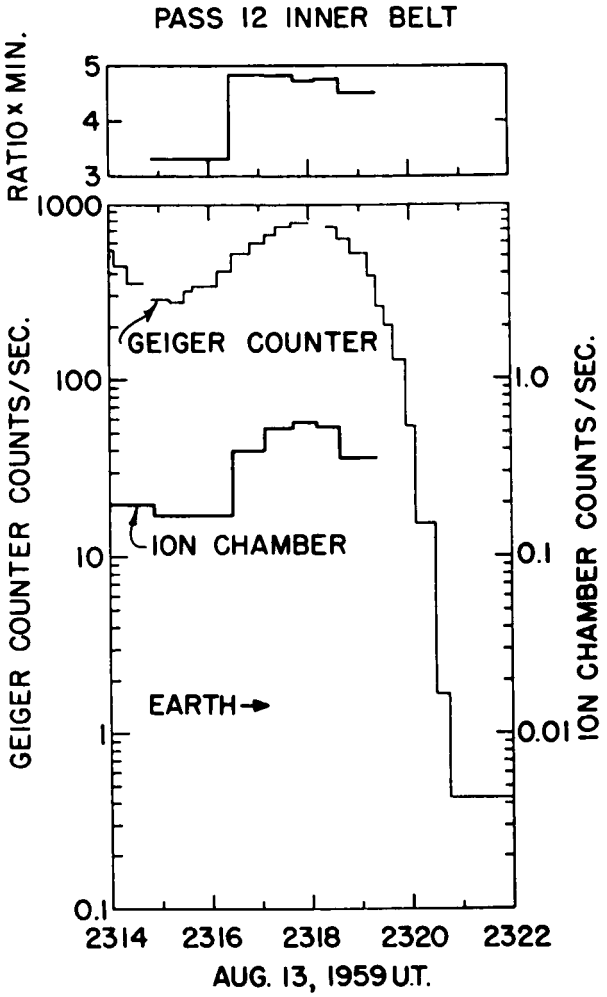

FIGURE 5.—*Data from ion chamber and Geiger counter for a typical pass of Explorer VI through the inner belt.*

From the efficiencies of the detectors, as expressed in the power law form in table 3, the pulsing rate of the chamber to a differential energy spectrum $dN/dE = N_0E^{-\gamma}$ is

$$R_{IC} = \int_0^\infty \frac{dN}{dE}\epsilon_{IC}(E)dE = N_0F_{IC}(\gamma)$$

or N_0 times a function of γ; and the counting rate of the counter is

$$R_{GM} = \int_0^\infty \frac{dN}{dE}\epsilon_{GM}(E)dE = N_0F_{GM}(\gamma)$$

Hence the ratio of the ion chamber rate to Geiger counter rate is a function of γ only:

$$\frac{R_{IC}}{R_{GM}} = \frac{N_0F_{IC}(\gamma)}{N_0F_{GM}(\gamma)} = F(\gamma)$$

By placing various values of γ into the counting rate integrals, and carrying out the integrations, a curve of the ratio versus γ is obtained, and is plotted in the upper part of figure 8. After γ has been determined for an incident flux of protons, N_0 can be calculated from the counting rate of either detector:

$$N_0 = R_{GM}/F_{GM}(\gamma)$$

$N_0/R_{GM} = 1/F_{GM}(\gamma)$ is also plotted versus γ in figure 8.

The above procedure will now be applied to data obtained in the inner belt. As an example, from figure 8 or from table 4, the summary

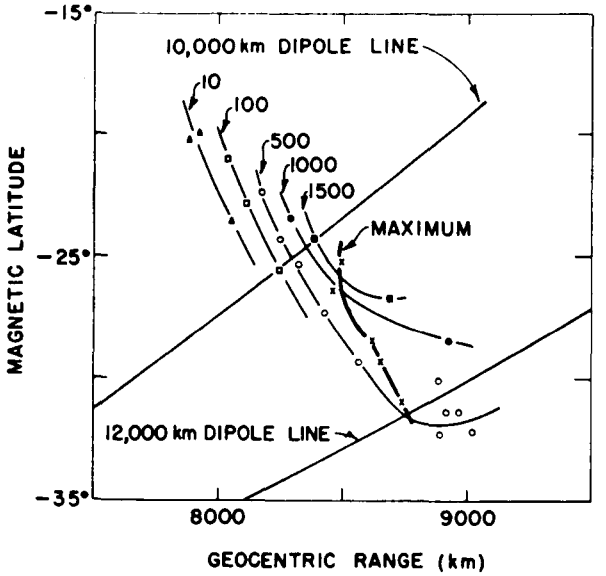

FIGURE 6.—*Contours of constant counting rate of Geiger counter in the inner belt.*

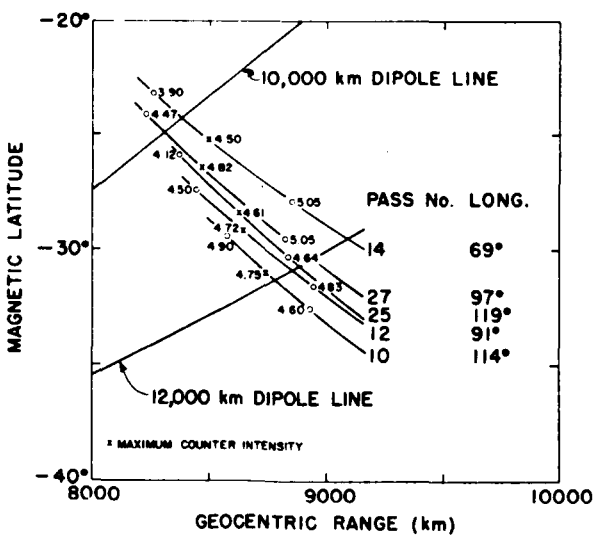

FIGURE 7.—*Ratio of ion chamber rate to Geiger counter rate divided by ratio for minimum ionizing protons. The ratio is given at the position of the maximum Geiger counter rate for a pass, marked by an X, and for one point on either side of the maximum, marked by a circle.*

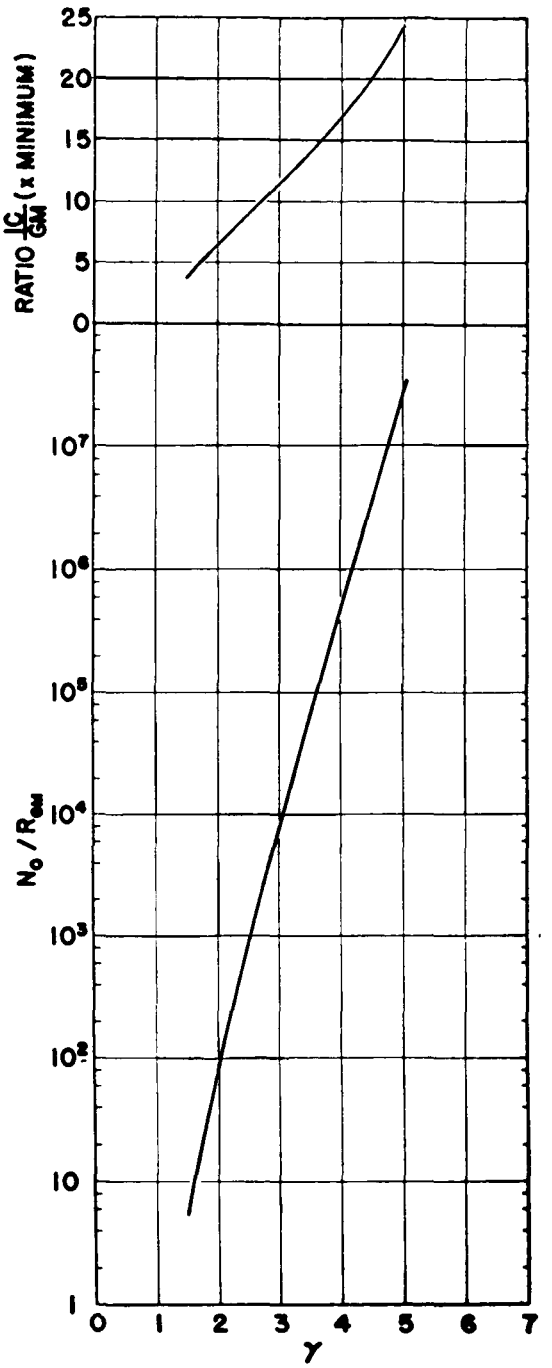

FIGURE 8.—*Assuming a power law spectrum of protons, the top part of the figure shows the relationship between the ratio of ion chamber to Geiger counter (times minimum), calculated from their respective efficiencies, and the exponent γ. The bottom part of the figure shows the relationship between γ and N_0/R_{GM}.*

TABLE 4.—*Summary of Inner-Belt Data and Calculations*

Pass No.	Date	Mag. Lat.	Range	Counter Rate	Ratio × Minimum	γ	N_0/R	Spectrum	Protons (cm^2 sec Mev)
10	Aug. 12	−31.8°	8740	~600	4.75	1.67	15.0	0.90×10^4	$E^{-1.67}$
12	Aug. 13	−29.2°	8660	790	4.72	1.66	14.5	1.14×10^4	$E^{-1.66}$
25	Aug. 20	−28.4°	8625	880	4.61	1.64	13.0	1.14×10^4	$E^{-1.64}$
27	Aug. 21	−26.5°	8460	~900	4.82	1.68	16.0	1.44×10^4	$E^{-1.68}$
14	Aug. 15	−25.3°	8490	1730	4.50	1.62	11.5	1.99×10^4	$E^{-1.62}$
						[1]1.65	[1]14.0	$14.0\times R\times$	$E^{-1.65}$
57	Sept. 6	−24.5°		1900				2.66×10^4	$E^{-1.65}$
72	Sept. 14	−23.5°		1850				2.59×10^4	$E^{-1.65}$
89	Sept. 23	−23.0°		2200				3.08×10^4	$E^{-1.65}$
104	Oct. 1	−22.0°		2840				3.98×10^4	$E^{-1.65}$
106	Oct. 2	−22.0°		3100				4.34×10^4	$E^{-1.65}$
85	Sept. 21	−21.5°		1450				2.03×10^4	$E^{-1.65}$
102	Sept. 30	−21.0°		~3300				4.62×10^4	$E^{-1.65}$

[1] Average.

table for the inner belt, the ratio of chamber to counter at the maximum Geiger counter rate of 790 counts/sec in the inner belt for pass 12 is 4.72 times minimum ionizing protons. From figure 8, a ratio of 4.72 corresponds to a γ of 1.66, and for a γ of 1.66, $N_0/R=14.5$. Therefore the proton spectrum at the maximum of the inner belt at −29.2° latitude is $dN/dE=1.14\times10^4E^{-1.66}$ protons/cm^2 sec Mev. Table 4 summarizes, in order of decreasing magnetic latitude, the proton spectra obtained in this manner up through pass 27. After pass 35, on August 25, no ion chamber data were received, and so the spectra could not be calculated. However, over a change in magnetic latitude of 6½°, the spectrum remained quite constant with the average value of γ equal to 1.65. Hence, assuming that such a spectrum continues down to a latitude of −21.0°, the table summarizes the spectra for the remaining passes on which usable data were obtained.

The remainder of table 4 beyond pass 27 requires an explanation. It was mentioned that the trajectory data beyond pass 36 were not sufficiently accurate to be incorporated into the contour plot, figure 6. The assumption is here made that the error in trajectory is not one in spatial position, but one of time along the orbit, as evidenced by comparison of the newly compiled trajectory through pass 36 with the original trajectory data. Consequently, the latitude of the maximum was determined by finding the intersection of the orbit with the 10,000-km line of force. The time shifts to bring the observed maximum counting rates into coincidence with the line of force are reasonable except for passes 72 and 85, which require shifts of 9 minutes. The orbits of all the passes used later than pass 36 were north of those before pass 36.

It was mentioned above that there was no large variation in average energy during passage through the belt. It is seen from figure 7 that the ratio at ranges beyond the maximum intensity is usually slightly larger than at the maximum, the largest being 5.05 times minimum, whereas those on the inner side of the maximum are slightly lower, the smallest being 3.90. These ratios correspond to γ's of 1.72 and 1.53, respectively, a rather small change in slope of the spectrum.

It is also noticed from table 4 that there is a progressive hardening of the radiation (lowering in exponent) with decrease in latitude, except for pass 27. However, the Geiger counter rate at maximum intensity for this pass is not accu-

rately known, and could be somewhat higher, causing a lower ratio, and therefore smaller γ.

It is of interest to check the spectrum obtained from the chamber and counter rates by calculating from it the counting rate that should have occurred in the triple coincidence telescope, and comparing this with the actual rate for a particular pass. Since the counting rate of the telescope in the inner belt has been published for pass 27 [*Fan, Meyer, and Simpson*, 1960], the spectrum used is $dN/dE = 1.44 \times 10^4 E^{-1.68}$. This spectrum and the efficiencies listed in table 3 are inserted into the counting-rate formula,

$$\text{Rate} = \int_0^\infty \frac{dN}{dE} \epsilon_{\text{prop}}(E) dE$$

and the rate of 2185 counts/sec is obtained. The maximum actual counting rate for the inward portion of pass 27 is about 1850 counts/sec, only 18 percent lower. Assuming the accuracy of the efficiency curves, such a reduction over the calculated value of triples counting rate indicates that the spectrum falls off more steeply than $E^{-1.68}$ at high energies since the major contribution to the above integral comes from energies above 200 Mev. Such an increase in exponent with energy has been observed by *Freden and White* [1960] with emulsions.

ELECTRON FLUXES

For the Space Technology Laboratories' scintillation counter, the assumption that the counting rate in the inner belt is due solely to protons cannot be applied, because the low-energy cutoff for electrons is about 200 kev [*Rosen and Farley*, 1961]. It is of interest, however, to determine what fraction of the scintillator counting rate could possibly be due to protons. The spectrum given in table 4 for pass 25 and the scintillator efficiencies from table 3 are placed in the counting-rate equation, which gives a scintillator rate of 3680 counts/sec. The assumption is made in this equation that the proton spectrum determined from the chamber and counter extends down to an energy of 2 Mev, the low-energy cutoff for the scintillator. This rate of 3680 counts/sec is negligible in comparison with an actual rate of 4.5×10^5 counts/sec, which, after correction for binary failure and saturation effects, gives a true rate of 4×10^5 counts/sec [*Rosen and Farley*, 1961].

Naugle and Kniffen [1961] have recently published the results of their study of the proton spectrum as a function of position in the inner belt, down to energies of 8 Mev. They found that, at higher latitudes, the slope of the spectrum below 30 Mev steepens considerably. At about 33° magnetic latitude the spectrum is given by

$$J(E) = \frac{3.2 \pm 0.6 \times 10^6}{E^{4.5 \pm 0.5}} \text{ protons/cm}^2 \text{ sec sr Mev}$$

Such a steepening would increase the calculated counting rate of the scintillator over that given above. Hence, a proton spectrum incorporating these results below 30 Mev will be determined for use in the scintillator rate calculation. The emulsion data were gathered at the lower-altitude side of the belt, where the intensity is less than at the maximum. Therefore, below 30 Mev, the spectrum will be taken as $dN/dE = KE^{-4.5}$, and K is determined by normalizing this spectrum at 30 Mev to the one used above 30 Mev:

$$dN/dE = 1.44 \times 10^4 E^{-1.68}$$

K is then found to be 1.90×10^8.

Putting this double-sloped spectrum into the counting-rate equation, along with the efficiencies in table 3, gives a counting rate for the scintillator of 5,490 counts/sec, again well below the actual rate. Therefore, the scintillator counting rate in the inner belt must be ascribed principally to electrons. The efficiency for electrons between 200 and 500 kev is 2.1×10^{-4}, and at slightly above 500 kev, 3.7×10^{-2} [*Rosen and Farley*, 1961]. These factors would yield fluxes in the inner belt of about 2×10^9 electrons/cm^2 sec between 200 and 500 kev, or 1×10^7 electrons/cm^2 sec above 500 kev for the true counting rate of 4.0×10^5 counts/sec. The measurements are for pass 25 at about $-28.4°$ magnetic latitude.

The interpretation of the scintillator counting rate in the inner belt as due to electrons explains the noncoincidence of peak counting rates of the scintillator and proportional counter telescope while passing through the inner belt.

TABLE 5.—*Comparison of Exponents to Power Law Spectra for Protons from Data in Inner Belt*

Experiment	Altitude, km	Mag. Lat.	γ	Energy Range, Mev
Emulsions				
Freden and White [1959].	1,230 max 1,200 av	25°	1.84	75–700
Armstrong and Heckman [1961].	1,170 max 1,080 av	22°	1.80	80–600
Naugle and Kniffen [1961].	1,600	27½°	1.7	40–100
Counters, etc.				
Holly, Allen, and Johnson [1961].				
Flight 4	940	26°	1.42	>17.5
Flight 5	1,100	19°	1.68	>23
Explorer VI chamber and counter.	2,225 av	−28.2° av	1.65	>23.6

This is shown in Figure 11 of *Rosen and Farley* [1961], where the scintillator peak is at a range 250 km larger than the telescope peak.

The good agreement between the calculated counting rate of the telescope and the actual rate adds a justification to the assumption that the electron flux entering the ion chamber and Geiger counter in the inner belt was small compared with the proton flux, placing an upper limit of about 1.5 Mev for electrons in the inner belt.

COMPARISONS WITH OTHER EXPERIMENTS

Besides the satellite measurements, there have been several emulsion flights and two counter flights into the lower side of the inner belt. Since they have occurred at different geographic locations, it is difficult to compare their relative intensity measurements, but the exponents (γ) to the power law energy spectra determined from the various data are of interest. Table 5 summarizes the results.

Above about 100 Mev, the proton spectrum obtained from emulsions is in good agreement with that expected from neutron albedo decay [*Freden and White*, 1960]. Below 80 Mev, the calculated neutron decay spectrum falls off to an exponent of only 0.72.

The spectra derived from both Geiger counter experiments and the chamber and counter combination are somewhat less than the spectrum from emulsions, probably for two reasons. First, the exponent decreases with decreasing energy. Since the spectra derived from the counters and chamber are average spectra valid to lower energies than those quoted for the emulsions, the exponent would be expected to be smaller. Recent emulsion work to low proton energies has also shown that there is a small maximum at 30 to 40 Mev, and a minimum at about 20 Mev at latitudes lower than Naugle and Kniffen's flight [*Freden and White*, 1961; *Armstrong and Heckman*, 1961]. This falloff in intensity from a power law at low energies would also tend to lower the exponent derived from Geiger counter experiments. The sharp rise in spectrum at energies below 30 Mev found by *Naugle and Kniffen* [1961] would probably not affect the chamber and counter combination, because the low-energy proton cutoffs are at 23.6 and 36.4 Mev, respectively. Therefore, we can conclude that the spectra at the inner belt maximum derived from the chamber and counter are not in disagreement with the spectrum from neutron albedo decays.

No other electron fluxes have been measured at the latitude where Explorer VI crossed the maximum of the belt. Van Allen, on the basis of observations from Explorer IV and Pioneer III, has suggested tentative fluxes at the heart of the inner zone on the geomagnetic equator [*Van Allen and Frank*, 1959*a*]:

Electrons
>20 kev $\sim 2 \times 10^{10}$/cm² sec
>600 kev $\sim 2 \times 10^{8}$/cm² sec

To these estimates are now added the scintil-

lator measurements at −28.4° geomagnetic latitude:

Electrons
200–500 kev ~2 × 10^9/cm² sec
or
500 kev ~1 × 10^7/cm² sec

TIME VARIATIONS

The contour plot of figure 6 contains three passes, 10, 12, and 14, during a quiet time before the magnetic storm of August 16, 1959, and two passes during and after considerable magnetic activity, passes 25 and 27. Between passes 14 and 27, the outer belt underwent large changes in intensity. The Geiger counter first showed a decrease to an intensity one-third that of the prestorm value, and then an increase by a factor of 5 above the prestorm value [*Arnoldy, Hoffman, and Winckler*, 1960]. The inclusion of passes 25 and 27 in the plot produces smooth contour lines, especially on the low-altitude side of the maximum. From this analysis, the data are consistent with no time variations due to magnetic activity.

Figure 9 is a plot of the maximum counting rate for each pass versus geomagnetic latitude, as listed in table 4. Except for passes 27 and 85 the points fall reasonably near a smooth curve. There were magnetic storms between almost all the passes beyond pass 72. Hence, if proximity to the smooth curve is taken as the criterion for stability, the inner belt does not change more than about 10 percent.

Passes 72 and 85 can possibly be accounted for by trajectory error, as was previously mentioned. Pass 27 remains somewhat troublesome. Even though the maximum rate could not be read accurately, it is most likely not higher than 1,000 counts/sec. It is noticed from figures 6 and 7, however, that the range of the maximum is slightly smaller than where the surrounding passes indicate that it might be. Moving the maximum to the intersection of the orbit with the line of maximum intensity shown in figure 6 displaces the latitude of the maximum almost one degree south. This displacement, coupled witn a true maximum rate of 1,000 counts/sec, brings the point within 10 percent of the line in figure 9. It should be pointed out that there is still a question about the accuracy

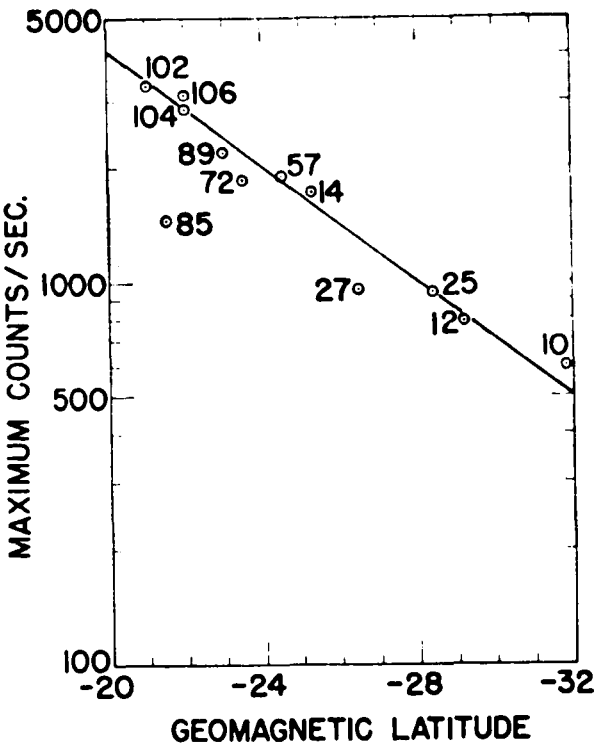

FIGURE 9.—*Maximum Geiger counter rate vs. magnetic latitude of the maximum for each pass through the inner belt from which data were received.*

of even the new trajectory data near perigee (J. A. Lindner, private communication). With this fact in mind, it seems possible that the data plotted in figure 9 might be consistent with no time variations in intensity of the inner belt due to magnetic storms for protons of energies greater than about 30 Mev.

SUMMARY

The principal results obtained from this investigation are: (1) For an assumed power law energy spectrum for the trapped protons, the spectrum has a form 1.14 × 10^4 $E^{-1.64}$ at the maximum intensity at about −28° magnetic latitude. Spectra for other latitudes are listed in table 4. (2) The radiation becomes slightly softer with increasing range through the belt, and with increasing latitude. (3) Electron fluxes at the maximum intensity at −28° magnetic latitude are about 2 × 10^9/cm² sec

from 200 to 500 kev, or about $1 \times 10^7/cm^2$ sec greater than 500 kev. (4) The proton spectra through the belt are not in disagreement either with those previously published or with the spectrum calculated from the neutron albedo decays. (5) An upper limit of about 10 percent is placed on time variations of the proton component due to magnetic storms, although the data are probably consistent with no variations at all.

ACKNOWLEDGMENTS

The assistance of Mr. Karl A. Pfitzer and Mr. Richard M. Brown in the reduction and analysis of the data is gratefully acknowledged.

The cooperation of Dr. Robert Eisberg and Dr. Lawrence Johnston in arranging time on the Minnesota proton linear accelerator is appreciated.

This work was supported by the National Aeronautics and Space Administration under contract NASw-56.

REFERENCES

Armstrong, A. H., F. B. Harrison, and L. Rosen, Flux and energy of charged particles at 300 and 600 mile altitude, *Bull. Am. Phys. Soc., 4*, 360, 1959.

Armstrong, A. H., and H. H. Heckman, Flux and spectrum of charged particles in the lower Van Allen belt, *Bull. Am. Phys. Soc., 6*, 361, 1961.

Arnoldy, R. L., R. A. Hoffman and J. R. Winckler, Observations of the Van Allen radiation regions during August and September 1959, 1, *J. Geophys. Research, 65*, 1361–1376, 1960.

Fan, C. Y., P. Meyer, and J. A. Simpson, Trapped and cosmic radiation measurements from Explorer VI, *Space Research: Proceedings of the First International Space Science Symposium*, North-Holland Publishing Company, Amsterdam, p. 951, 1960.

Fan, C. Y., P. Meyer, and J. A. Simpson, Dynamics and structure of the outer radiation belt, *Preprint EFINS, 61*, 34, Enrico Fermi Institute for Nuclear Studies, University of Chicago, 1961, and *J. Geophys. Research, 66*, 2607–2640, 1961.

Freden, S. C., and R. S. White, Protons in the earth's magnetic field, *Phys. Rev. Letters, 3*, 9, 1959.

Freden, S. C., and R. S. White, Particle fluxes in the inner radiation belt, *J. Geophys. Research, 65*, 1377–1383, 1960.

Freden, S. C., and R. S. White, Protons in the lower radiation belt, *Bull. Am. Phys. Soc., 6*, 361, 1961.

Holly, F. E., L. Allen, Jr., and R. G. Johnson, Radiation measurements to 1500 kilometers altitude at equatorial latitudes, *J. Geophys. Research, 66*, 1377–1383, 1960.

Kellogg, P. J., Electrons of the Van Allen radiation, *J. Geophys. Research, 65*, 2705–2713, 1960.

Naugle, J. E., and D. A. Kniffen, The flux and energy spectra of the protons in the inner Van Allen belt, *Phys. Rev. Letters, 7*, 3–6, 1961.

Rosen, A., and T. A. Farley, Characteristics of the Van Allen radiation zones as measured by the scintillation counter on Explorer VI, *J. Geophys. Research, 66*, 2013–2028, 1961.

Van Allen, J. A., and L. A. Frank, Radiation around the earth to a radial distance of 107,400 km, *Nature, 183*, 430–434, 1959*a*.

Van Allen, J. A., and L. A. Frank, Radiation measurements to 658,300 km with Pioneer IV, *Nature, 184*, 219–224, 1959*b*.

(Manuscript received October 10, 1961.)

Observation of the Van Allen Radiation Regions during August and September, 1959[1]

4. The Outer-Zone Electrons

BY R. L. ARNOLDY,[2] R. A. HOFFMAN,[3] AND J. R. WINCKLER

School of Physics
University of Minnesota

A study is reported of the data from the radiation detectors aboard the Explorer VI earth satellite (1959δ_1, launched August 7, 1959) as the spacecraft passed through the outer zone during a period when the count rate time variations and the geomagnetic activity were low. The radiation detectors aboard the satellite were an ionization chamber, a Geiger counter, a proportional counter telescope, and a scintillator. Extensive calibrations were made to determine the response of these detectors to monoenergetic electrons when inside a spare payload. In using these calibrations and fitting assumed power-law spectra of electrons to the data, it is seen that the spectrum is flat and must extend to several Mev at the small ranges, with the ion chamber and Geiger counter responses there due primarily to direct electron detection. The intensity of the energetic electrons is shown to decrease with increasing range as the spectra steepen and the radiation softens, resulting in an increasing contribution of bremsstrahlung to the rates of the chamber and Geiger counter. Any attempt to utilize the bremsstrahlung response of the Explorer VI detectors to determine fluxes is useless if an appreciable portion of their counting rate is produced by direct energetic particles. The spectral shape of the outer zone as suggested by this analysis allows us to interpret the minimum observed in the Geiger counter rate at an equatorial geocentric range of 19,000 km as having spectral-detector origin rather than as representing the removal of radiation by an anomaly in the earth's magnetic field. This analysis is only capable of fitting trial spectra to the data; the procedure does not eliminate the possibility of more complex spectra existing in the outer zone which would lead to different conclusions about the nature of the trapped radiation.

This paper reports a study of the energetic radiation trapped in the outer Van Allen zone, using data from the detectors aboard the Explorer VI satellite. The orbit of Explorer VI was very elliptical, with an apogee of 48,800 km and perigee of 6,600 km. Since the period of revolution was about 12 hours, the satellite passed twice a day nearly through the heart of the outer zone. Owing to the slow precession of the orbit and the inclination of the earth's magnetic axis to its spin axis, the satellite swept through a considerable part of the outer belt. The upper part of figure 1 shows the average Geiger counter rate in the geomagnetic equatorial plane versus range compiled from the first fifteen passes; the lower part is a plot of the orbit of a typical pass, pass 12, for a rectangular coordinate system.

[1] Published in the July 1962 issue of *Journal of Geophysical Research*. Reprinted by permission.

[2] Now at Honeywell Co.

[3] Now at NASA Goddard Space Flight Center.

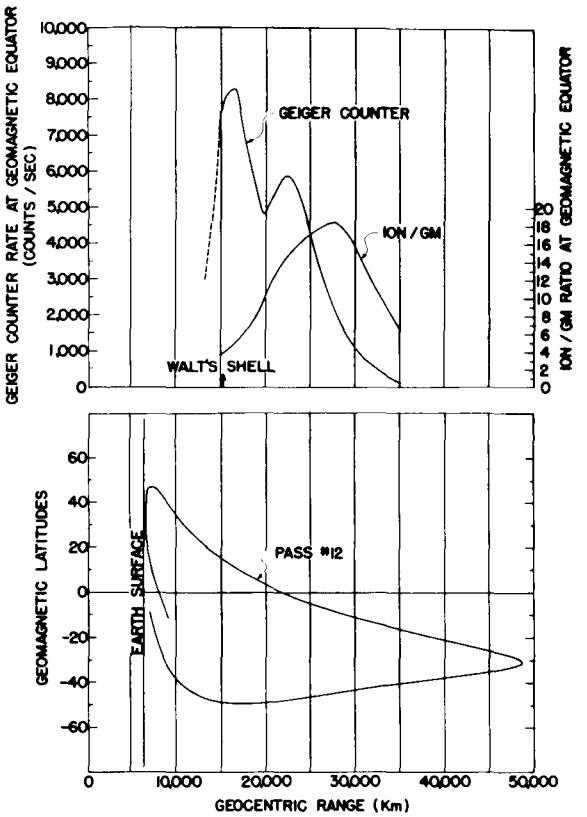

FIGURE 1.—Top: *Average Geiger counter rates and ratios of ion chamber to Geiger counter rates on the geomagnetic equatorial plane versus geocentric range compiled from the first fifteen passes. The dashed line in the Geiger counter curve represents an extrapolation to the equator made from a plot of contours of constant counting rate. The arrow marks the equatorial position of the shell upon which Walt and co-workers measured an electron spectrum.* Bottom: *A rectangular plot of the orbit of Explorer VI for pass 12.*

Data were obtained from Explorer VI for approximately two months, and time variations associated with geophysical events were recorded during this period. The first fifteen passes of the satellite will be considered the normal state or 'quiet time' representation of the trapped radiation in the outer zone as measured by Explorer VI, since no significant intensity variations occurred during this period. This paper will discuss the trapped radiation as measured along the orbit of a quiet time pass, pass 12, between geocentric ranges of 11,000 and 37,000 km. Within these ranges the satellite on the outgoing part of pass 12 did not move more than 30° off the geomagnetic equator, as can be seen in the lower part of figure 1. In figure 2 are plotted the ratios of the ion chamber to Geiger counter rate for the quiet time passes measured along the line of force that crosses the equator at a geocentric range of 17,000 km. This plot shows that the ratios remain constant along the line of force from the equator to at least 30° latitude, indicating that the spectrum of the radiation to which the ionization chamber and Geiger counter are sensitive does not change in this interval. Experimental ion chamber to Geiger counter ratios along other lines of force give similar results. Consequently, radiation measured along the orbit will be nearly identical to that in the equatorial plane when traced down appropriate lines of force to the equator. This is further indicated by the similarity in the shape of the curve for the average ratio of the ion chamber rate to the Geiger counter rate versus range in the equatorial plane in figure 1 (top) and the curve for the same ratio versus range along the orbit in figure 4.

However, from figure 2 it should be noticed that for latitudes greater than 30° the ratios increase, indicating that the spectrum does change

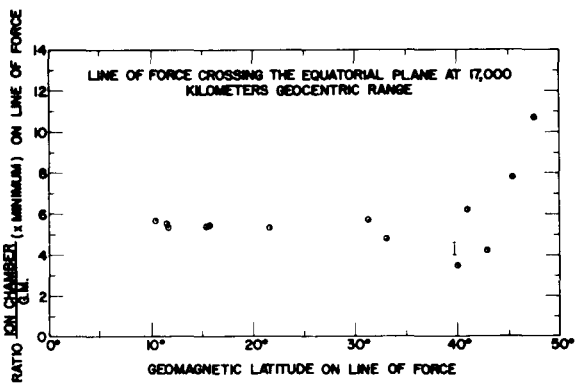

FIGURE 2.—*Ratio of the ion chamber rate to the Geiger counter rate along the dipole line of force crossing the equatorial plane at 17,000 km geocentric range plotted versus the geomagnetic latitude along the line of force.*

at large distances off the equatorial plane and near the earth. This point will be discussed further when the measurements along the orbit are compared with low-altitude outer-zone data.

Counters aboard the Pioneer III space probe, launched December 6, 1958, first measured the trapped radiation as having two distinct intensity peaks [*Van Allen and Frank*, 1959*a*], now commonly called the inner and outer zones. Since that time several space probes and satellites have passed through the outer zone, among them the Explorer VI satellite. The results obtained from this analysis of the Explorer VI data will be compared with the other measurements.

Unless otherwise stated, ranges used in this discussion will refer to geocentric distance to positions on the orbit.

EFFICIENCIES

Before we can study the outer zone it is necessary to know the radiation response characteristics of the detectors aboard Explorer VI. These detectors are the University of Minnesota ionization chamber and Geiger counter (*Arnoldy, Hoffman, and Winckler*, 1960*a*], the University of Chicago proportional counter [*Fan, Meyer, and Simpson*, 1960], and the scintillator furnished by Space Technology Laboratories [*Rosen and Farley*, 1961]. The counters of the University of Chicago experiment were operated in the semiproportional region with the circuitry simply counting all pulses above a fixed bias. Both the count rate from one of the counters and the triple coincidence rate were telemetered. In this study the single rate is used unless otherwise stated. The scintillator count rates used in this discussion are the observed rates corrected for a binary failure and saturation.

Because of electron bremsstrahlung and the complicated distribution of matter about the detectors in which it is produced, the detector responses to electrons from 30 kev to 1 Mev were obtained experimentally. To obtain these responses or efficiencies calibration experiments were performed jointly by the experimenters, with the detectors inside a spare payload. From zero to 90 kev a small d-c electron accelerator constructed at the University of Minnesota for this purpose was used. Electrons from several hundred kev to 1 Mev were obtained from a Van de Graaff generator (Hi Voltage Engineering, Inc.) and a Cockcroft-Walton electron accelerator (General Electric Co.).

For the calibration of the ionization chamber and Geiger counter, the surface area of the payload was divided into 86 approximately equal areas, many of which were further subdivided if they were close to the detectors. About 140 spots on the payload surface were bombarded with electrons at various energies and known currents while the detector rate inside the payload was monitored. The response from this bombardment at a given energy was integrated over the whole surface of the payload to obtain the efficiency of the detector. The efficiency is expressed as the actual counting rate of the detector inside the Explorer VI payload when the payload is immersed in an isotropic flux, J_0, of 1 electron/cm^2 sec at an energy E (kev). (J_0 has the usual definition ,that is, the counting rate of a spherical counter of 1 cm^2 cross section.)

To obtain the efficiency of the ionization chamber and Geiger counter beyond 1 Mev, β- and γ-ray measurements of the payload thicknesses for various directions of incidence were made. These absorption measurements were then used in conjunction with the positions in the payload, wall thicknesses of the detectors, and the sensitivity and gas pressure of the ionization chamber to calculate the efficiencies of the counter and chamber.

The efficiencies of the proportional counter and scintillator obtained from the calibrations have been published [*Fan, Meyer, and Simpson*, 1961; *Rosen and Farley*, 1961]. Figure 3 is a plot of the efficiency curves for the four detectors. The proportional counter efficiency curve is a factor of 4 lower than that given by *Fan, Meyer, and Simpson* [1961], because it is expressed in terms of the isotropic intensity in space. The scintillator efficiency curve was extended beyond the 1-Mev value given by *Rosen and Farley* [1961] by requiring it to approach the detector geometrical factor of 3.5 cm^2 at energies sufficient for electron penetration of the payload from every direction about the detector, taken as 50 Mev. Likewise, the pro-

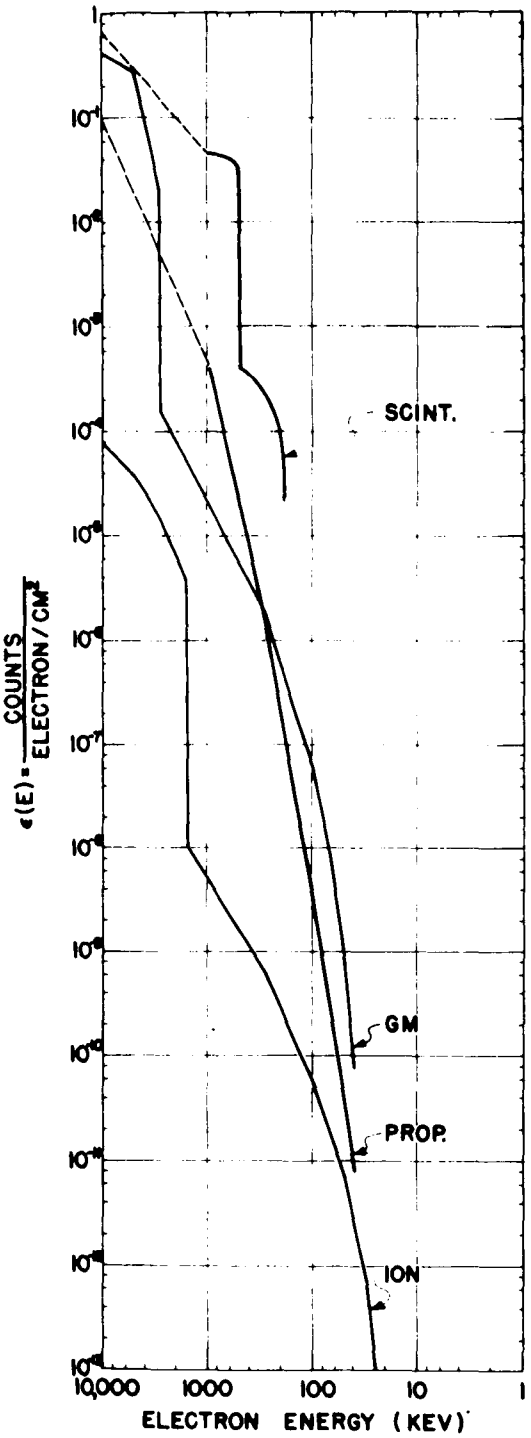

FIGURE 3.—*The efficiencies of the four detectors aboard Explorer VI versus electron energy. The dashed extensions to the scintillator and proportional counter curves are extrapolations.*

portional counter efficiency curve was extended to approach its omnidirectional geometrical factor of 5.5 cm² at 50 Mev.

TABLE 1

Proton Energy, Mev	$\frac{\text{Ion Chamber Rate}}{\text{GM Rate}} \times$ Minimum
36	∞
40	35
50	18
60	13
75	8

The discontinuity in the ion chamber efficiency curve at 1.55 Mev and in the Geiger counter curve at 2.86 Mev shows that some electrons above this energy were able to penetrate certain parts of the payload and reach the chamber and counter directly, instead of being detected through the less efficient bremsstrahlung process. The proportional single counter was surrounded by 5 g/cm² of lead, so that no electrons below 13 Mev could be detected directly. The scintillator had an electronic bias so that its theoretical threshold for photon detection was about 220 kev [*Rosen and Farley*, 1961]. From 200 to 500 kev electrons were detected through a thin aluminum window in the payload skin; above 500 kev the electrons could penetrate a significant fraction of the payload skin to produce the discontinuity in the efficiency curve.

The proton sensitivities of the ionization chamber and Geiger counter are presented in an article by *Hoffman, Arnoldy, and Winckler* [1962]. For the ionization chamber, the threshold for proton detection was 23.6 Mev, and for the Geiger counter it was 36.4 Mev. The proportional counter, being shielded by 5 g/cm² of lead, had a threshold when in the satellite of about 75 Mev [*Fan, Meyer, and Simpson*, 1961]. By detection of protons through the window in the satellite skin, the scintillator could measure protons above 2 Mev in energy with an omnidirectional factor of 2×10^{-4} cm² [*Rosen and Farley*, 1961]. For detection of protons penetrating the satellite skin the threshold of the

scintillator was 10 Mev, the omnidirectional factor increasing to 4×10^{-2} cm^2.

Measurements made by *Van Allen and Frank* [1959*b*] with detectors aboard Pioneer IV, launched March 3, 1959, gave an outer-zone proton flux for energies greater than 60 Mev of less than 100 particles/cm^2 sec. Instruments flown on the Cosmic Rocket II [*Vernov, Chudakov, Vakulov, Logachev, and Nikolayev,* 1960], launched September 12, 1959, detected less than 1 proton/cm^2 sec of energy greater than 30 Mev. The data from the proportional counter telescope aboard Explorer VI are consistent with these results in detecting no protons above 75 Mev energy in excess of the galactic cosmic-ray background [*Fan, Meyer, and Simpson,* 1960]. The large rate, then, of the proportional singles counter aboard Explorer VI can only be attributed to electrons.

For the ionization chamber and Geiger counter, protons of 75 Mev energy make their ratio of rates 8 times that for minimum ionizing radiation. This ratio rapidly increases to infinity for lower proton energies, as can be seen in table 1, because of the larger threshold of the Geiger counter. If a significant number of protons below 75 Mev are trapped in the outer zone, they would have to be concentrated between geocentric ranges of 19,000 and 33,000 km where the measured ratio of the ion chamber rate to the Geiger counter rate was above 8. Furthermore, there can be no significant contribution to the rates by protons of energy between 24 and 50 Mev, since this radiation would increase the measured ratio much beyond the maximum value of 18 times minimum ionizing that was observed. Thus, for an appreciable proton contribution to the ion chamber and Geiger counter rates in the outer zone, the protons would have to be trapped in a very narrow range interval and have energies between 50 and 75 Mev. In view of this and the results of the previous measurements, the analysis presented here will contend that only electrons were detected by the ion chamber and Geiger counter.

It is more difficult to understand the scintillator rates, but, if they are due entirely to protons, they require a steep spectrum of 10^8 to 10^{10} protons/cm^2 sec between energies of 2 to 75 Mev. But such a steep spectrum has a sufficient number of protons in the energy interval 24 to 36 Mev, that is, between the ion chamber and Geiger counter thresholds, so that the ratio of the rates of these two detectors would become very large and be inconsistent with the measured values. We cannot rule out the possibility that a large flux of protons between 2 and 24 Mev exists in the outer zone and was detected only by the scintillator. However, if the scintillator rate was due entirely to protons of 2-Mev energy, the energy density of the radiation would exceed that of the trapping field at the heart of the outer zone; similarly, a monoenergetic flux of 24-Mev protons producing the counting rate of the scintillator would nearly equal the field energy density. It will be assumed here that electrons, which produced the rates of the other detectors, rather than protons, contributed predominantly to the scintillator rate.

EXPERIMENTAL OBSERVATIONS

The Geiger counter rate along the orbit of pass 12 is plotted versus range in figure 4, along with the ratios ion chamber to Geiger counter (ion/GM), proportional singles rate to Geiger counter (prop/GM), and scintillator rate to Geiger counter (scint/GM). The major quiet time characteristics of the outer-zone electrons measured by the Explorer VI detectors are displayed in this plot. First, the Geiger counter shows two maxima in its counting rate. The proportional counter singles rate would likewise show these peaks in approximately the same spatial configuration, but the relative intensity of the two peaks is quite different for the two instruments. The scintillator detects three maxima in count rate [*Rosen and Farley,* 1961], the third being beyond the two seen by the Geiger counter. The spatial intensity distribution as detected by the ion chamber, proportional counter, and scintillator will be analyzed by studying their rates in ratio to the Geiger counter rate as plotted in figure 4.

The second characteristic of the outer zone is that the ion/GM ratio varies smoothly with radial distance and is quite closely followed by the prop/GM ratio. It is not clear whether the

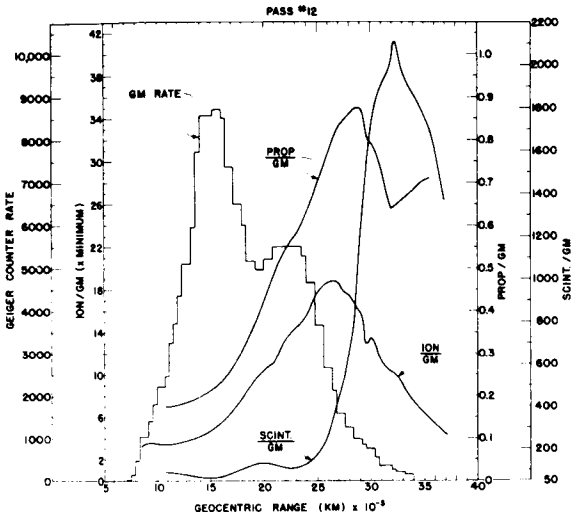

FIGURE 4.—*Geiger counter rate and the ratios of the rates of the detectors to the Geiger counter rate measured along the orbit of pass 12. The geocentric range is measured to points on the orbit.*

decrease in the prop/GM ratio beyond 29,000 km and its subsequent increase is a significant effect or a manifestation of the large fluctuations in the ratio at large distances as seen by *Fan, Meyer, and Simpson* [1961]. These fluctuations could arise from the slightly different time intervals over which the counting rates of the instruments in ratio are obtained. At high counting rates such time differences are negligibly small, but with decreasing intensity of the radiation the different scaling factors for the two instruments cause shifts in the time intervals over which the rates are taken.

Third, the ratio of ion/GM shows no maxima coincident with count rate maxima but rises steadily to reach a peak ratio at 26,500 km and then decreases rather slowly to the cosmic-ray ratio of about 3 times minimum ionizing. The last point to observe in figure 4 is the large increase in the ratio of scint/GM after the maximum in ion/GM ratio and when Geiger counter rate has diminished to 2 percent of its peak value.

RATIO CALCULATIONS

By using the efficiencies of the counters, the rates and ratios of detectors can be calculated for assumed spectral forms for the trapped electrons. Matching these calculated ratios with the experimental observations, we can solve for certain parameters of the assumed spectra, thus providing a spectral interpretation of the dominant outer-zone features displayed in figure 4.

If a differential energy spectrum of electrons, dN/dE, is assumed, the counting rate of a detector having a known efficiency dependence on electron energy, $\epsilon(E)$, can be calculated from the equation

$$\text{Rate} = \int_{E_{\min}}^{E_{\max}} \frac{dN}{dE}\,\epsilon(E)\,dE$$

The measured efficiencies of the detectors as a function of electron energy are approximated in figure 3 by a series of n straight lines, $A_i E^{b_i}$, where the subscript i refers to the energy interval, E_i to E_{i+1}, over which the straight-line approximation is made. There are seven such straight lines in the approximation for the ion chamber and six for the Geiger counter from 25 kev and 40 kev, respectively, up to 5000 kev. Hence the counting rate of a given detector for an assumed differential power-law spectrum of electrons, $dN/dE = N_0 E^{-\gamma}$, is then

$$R = \sum_{i=1}^{n} \int_{E_i}^{E_{i+1}} A_i E^{b_i} N_0 E^{-\gamma}\,dE$$

The energies E are always given in kev. The ratios of the detector rates have been calculated for a range of γ, with E_{n+1} variable. Figures 5 to 7 show the dependence of the various ratios on γ, and also the large dependence on the choice of the upper limit of integration, E_{n+1}. This sensitivity to the high-energy cutoff is due to the discontinuity in the Geiger counter efficiency resulting from direct electron detection. The prop/GM and scint/GM ratio curves become a double-valued function of γ for spectrum high-energy cutoffs greater than the Geiger counter cutoff for direct detection at 2.86 Mev, whereas the ion/GM ratios are double valued for high-energy cutoffs below this energy. The scintillator rates are obtained by integration of

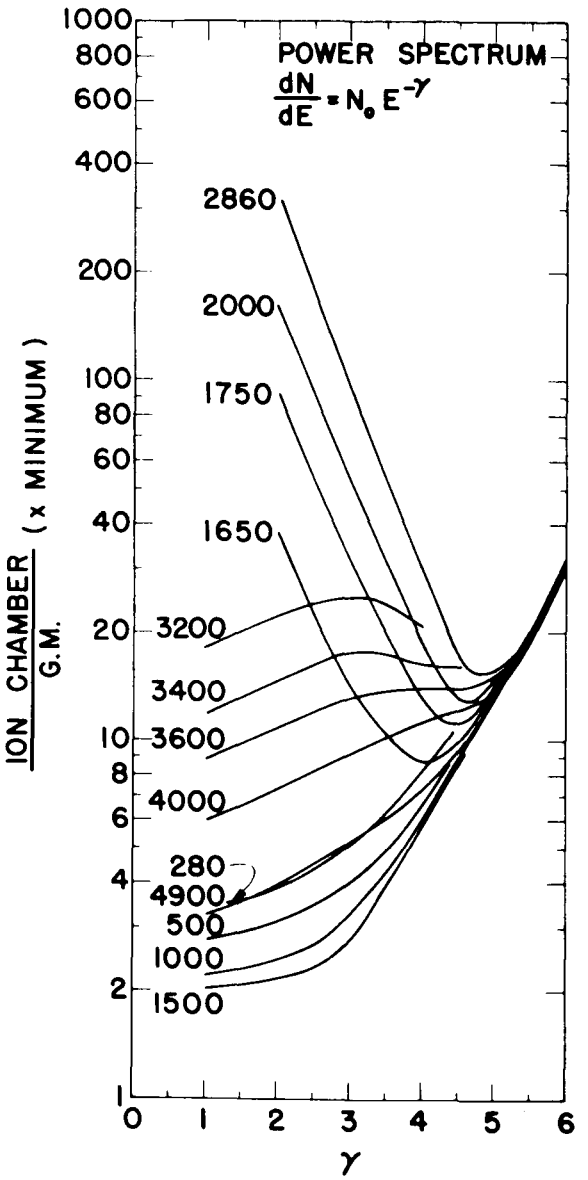

FIGURE 5.—*Ratios of the ion chamber to Geiger counter rates as a function of the exponent* γ, *for assumed power-law spectra of electrons. Ratios were obtained from calculations using the measured efficiencies of the detectors. The various curves are labeled according to the high-energy cutoff (in kev) imposed on the assumed spectra.*

(1) with a lower limit of 200 kev, whereas the Geiger counter, ion chamber, and proportional counter rates for figures 5 to 7 have zero as the lower limit. Zero can be used because the efficiency drops faster with decreasing energy than the number of electrons increases; i.e., b_1 is greater than γ for the range of γ considered.

We might think of figures 5 and 6 as containing two sets of curves, one set representing solely the bremsstrahlung response of the detectors (curves with high-energy cutoffs less than the thresholds for direct electron detection) and the other set the response for both bremsstrahlung from low-energy electrons and direct detection of energetic electrons. Figures 8 and 9 give the ion/GM and prop/GM ratios, respectively, for spectra of electrons above 1,000 kev energy and hence represent the detector responses for only energetic electrons.

It is of interest to introduce another parameter to the assumed power-law spectrum and study its influence on the ratio curves. If the power-law dependence is not continued down to very low energies, but the spectrum is made completely flat below some energy E_f, the ion/GM ratio curves will take a form as shown in figures 10 and 11. The rate of a detector for a power spectrum flat below E_f is given by

$$R_f = N_0 E_f^{-\gamma} \sum_{i=1}^{k} \int_{E_i}^{E_{i+1}} A_i E^{b_i}\, dE + \sum_{i=k+1}^{n} \int_{E_i}^{E_{i+1}} N_0 E^{-\gamma} A_i E^{b_i}\, dE$$

where E_f equals E_{k+1}. k is the number of straight-line approximations to the efficiency curve that are included in the energy interval E_1 to E_f. E_1 can be taken as zero in the calculation, because of the rapid drop in efficiencies toward low energies.

A power-law spectrum with a flat portion at low energies makes the ratio of ion/GM decrease when γ increases from 4 to 6. However, as can be seen in figure 13, the flattening of the spectrum at low energies greatly increases the scint/GM ratio for large γ because counts are removed from the Geiger counter rate and none or few (depending upon the extent of the flattened portion) from the scintillator rate because of its electronic bias. The same is true for the prop/GM ratios in figure 12, because the Geiger counter is more efficient at lower energies than the proportional counter.

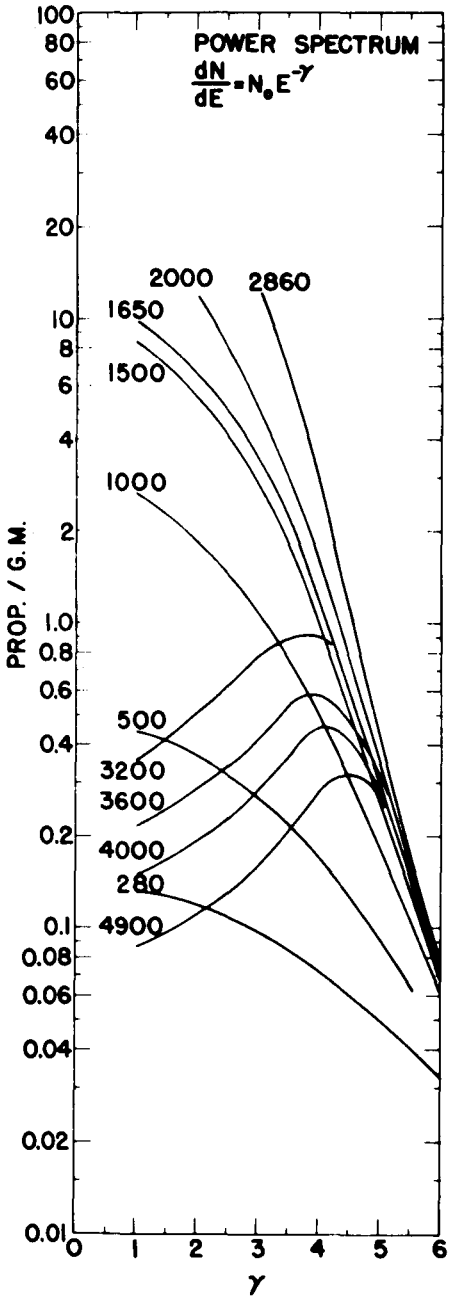

FIGURE 6.—*Ratios of the proportional counter to Geiger counter rates as a function of the exponent* γ, *for assumed power-law spectra of electrons. Ratios were obtained from calculations using the measured efficiencies of the detectors. The various curves are labeled according to the high-energy cutoff (in kev) imposed on the assumed spectra.*

In comparing figures 10 to 13 with figures 5 to 7, it is seen that, when the detectors are measuring both bremsstrahlung and energetic electrons directly, the introduction of a flat portion to the power-law spectrum at low energies has little or no effect on the ratio curves for a γ of 4 or less. Furthermore, by comparing figures 8 and 9 with figures 5 and 6, respectively, we observe that, even when all the low-energy radiation, i.e., less than 1,000 kev, is removed, the ratio curves for a γ less than 4 are quite similar to those for which the response to low-energy electrons is included. It thus becomes evident that, for not too steep a spectrum, i.e., γ less than 4, the ratios of the Explorer VI detectors become very insensitive to the low-energy radiation when the Geiger counter is directly detecting energetic electrons. As will be seen later, this behavior limits the extent of the analysis of the outer zone that can be made using the Explorer VI counters.

OUTER-ZONE RADIATION FOR RANGES LESS THAN 26,500 KM

In this section the experimental detector ratios in figure 4 from 11,000 to 26,500 km range will be investigated. In this region the ion/GM ratio steadily increases with increasing range from 3.5 times minimum ionizing to a maximum in the outer zone at 26,500 km of 18.8 times minimum ionizing. From an examination of figures 5 and 11 it is seen that the low ratio of 3.5 at 11,000 km can be obtained in several ways. These will be listed here and then studied in the light of the requirements of the experimental prop/GM and scint/GM ratios. The first possibility (*a*) is to have at small ranges a flat spectrum containing only low-energy electrons, i.e., have a high-energy cutoff less than 1,500 kev, and then steepen the spectra with increasing range to obtain the increasing ratios. A second alternative (*b*) is again to have flat spectra that steepen with range, but to have them contain energetic electrons that are detected directly, i.e., high-energy cutoffs greater than 2,860 kev. A final possibility (*c*) would be to have a steep spectrum at small ranges with a flat portion at low energies extending from zero to a couple

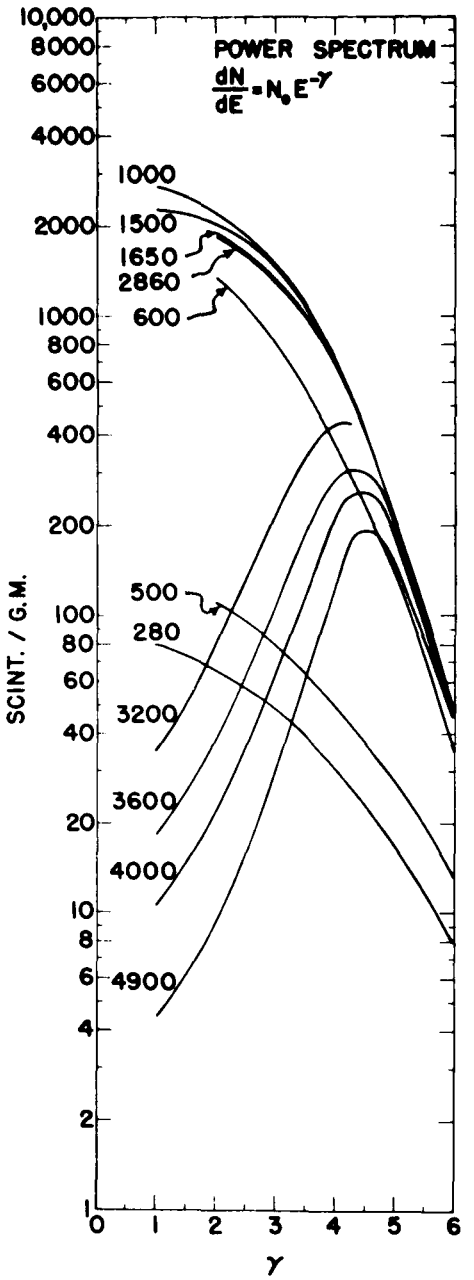

FIGURE 7.—*Ratios of the scintillator to Geiger counter rates as a function of the exponent γ, for assumed power-law spectra of electrons. Ratios were obtained from calculations using the measured efficiencies of the detectors. The various curves are labeled according to the high-energy cutoff (in kev) imposed on the assumed spectra.*

765-698 O-65—11

of hundred kev; we would obtain then the smoothly increasing ratios with increasing range by decreasing the exponent, i.e., by flattening the spectra.

The prop/GM ratio rises from a value of 0.18 at a geocentric range of 11,000 km to 0.80 at 26,500 km. The only two interpretations for this behavior that are consistent with the ion/GM ratios are (*a*) and (*b*) above. First, the flat spectra that steepen with range and contain only low-energy electrons fit both ratios. However, since the prop/GM ratio curves for high-energy cutoffs less than 1,500 kev have a slope opposite to those for the ion/GM ratio, an increasing prop/GM ratio that is consistent with the ion/GM ratio can be obtained only by steadily moving from a curve with a low cutoff at small ranges to curves with larger high-energy cutoffs. The second interpretation consistent with the two experimental ratios, (*b*), is to have flat spectra containing energetic electrons steepen with range.

Because the prop/GM and scint/GM ratio curves rise when flat portions at low energies are introduced to steep spectra (see figs. 12 and 13), the low experimental ratios at small ranges cannot be matched by such spectra, hence the last interpretation of the experimental ion/GM ratio, (*c*), must be incorrect.

Finally, the experimental scint/GM ratios limit us to just one interpretation of the measurements of the outer zone between 11,000 and 26,500 km that is consistent with all the detector rates. The analysis that attributes the detector rates to low-energy electrons, (*a*), must, according to the experimental prop/GM ratios, have the high-energy cutoffs smoothly increase from 500 to 600 kev with increasing range. However, the scint/GM ratio curves give a very rapid jump in ratio for a small change in γ in going from a cutoff of 500 to one of 600 kev. Such a sudden increase in the scint/GM ratio is not experimentally observed at small ranges; hence the interpretation is not consistent with the scintillator measurements. The large difference between the 500- and 600-kev ratio curves in figure 7 reflects the discontinuity in the scintillator efficiency at 500 kev due to electron penetration of the satellite skin.

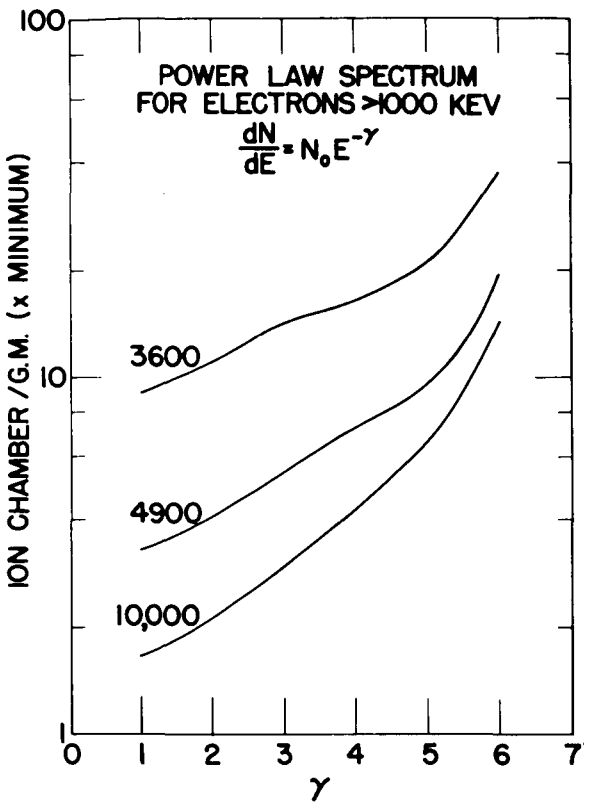

FIGURE 8.—*Ratios of the ion chamber to Geiger counter rates as a function of the exponent* γ, *for assumed power-law spectra of electrons. Ratios were obtained from calculations using the measured efficiencies of the detectors. The assumed spectra contain only electrons of energy greater than 1,000 kev. The various curves are labeled according to the high-energy cutoff imposed on the assumed spectra.*

The remaining interpretation is, then, the one that has energetic electrons trapped in the outer zone, namely (*b*). At 11,000 km the data require electrons of energy 5 Mev or larger. Using the curves of figures 5 and 7, the exponent of an assumed power-law spectrum fit to the data will be between 2 and 3 at 11,000 km and increase to between 3.5 and 4.5 at 22,500 km range, the position of the second count rate maximum. The high-energy cutoff must decrease with increasing range in order to obtain the large ratios measured at 22,500 km, with the best fit to the data giving a cutoff of 3.5 Mev at this range. We wish to emphasize here how the spectral parameters tend to change with range rather than their exact numerical values. This analysis was made by using curves that reflect the general behavior of the detector ratios for various spectra. Since the exact shape of the curves and the numerical spectral paramenters associated with them are the result of complicated calibrations, idealized calculations, and estimations of the scintillator and proportional counter response character-

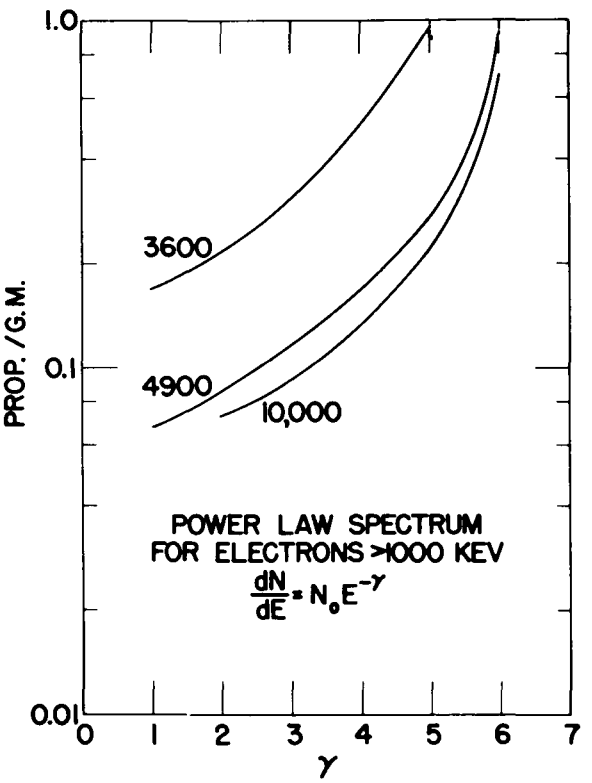

FIGURE 9.—*Ratios of the proportional counter to Geiger counter rates as a function of the exponent* γ, *for assumed power-law spectra of electrons. Ratios were obtained from calculations using the measured efficiencies of the detectors. The assumed spectra contain only electrons of energy greater than 1,000 kev. The various curves are labeled according to the high-energy cutoff imposed on the assumed spectra.*

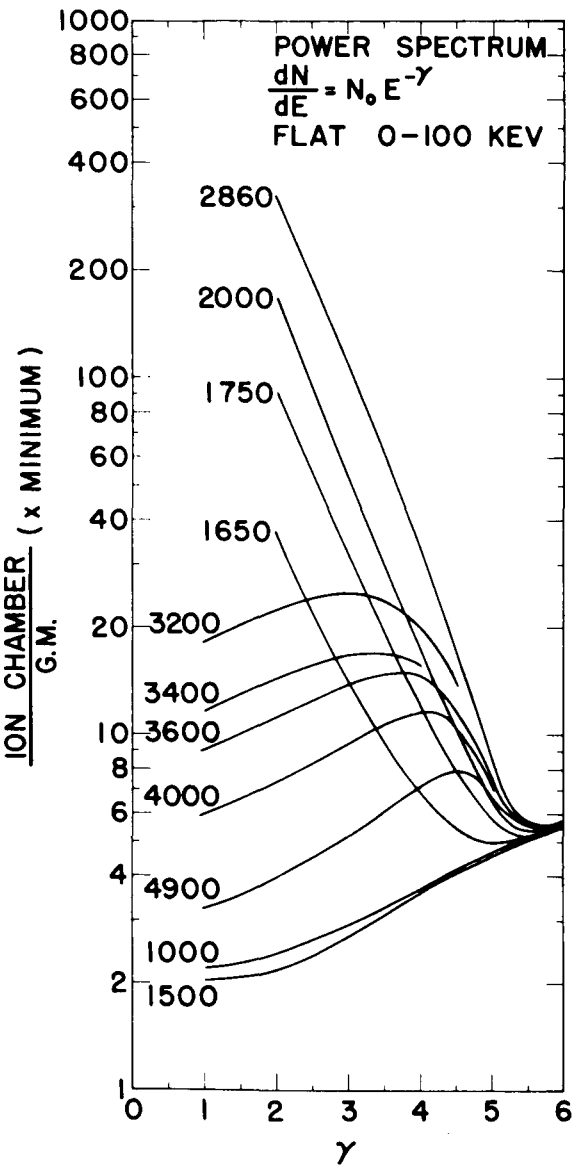

FIGURE 10.—*Ratios of the ion chamber to Geiger counter rates as a function of the exponent γ, for assumed power-law spectra of electrons. The power-law spectra have a flat portion from zero to 100 kev. The various curves are labeled according to high-energy cut-off imposed on the assumed spectra.*

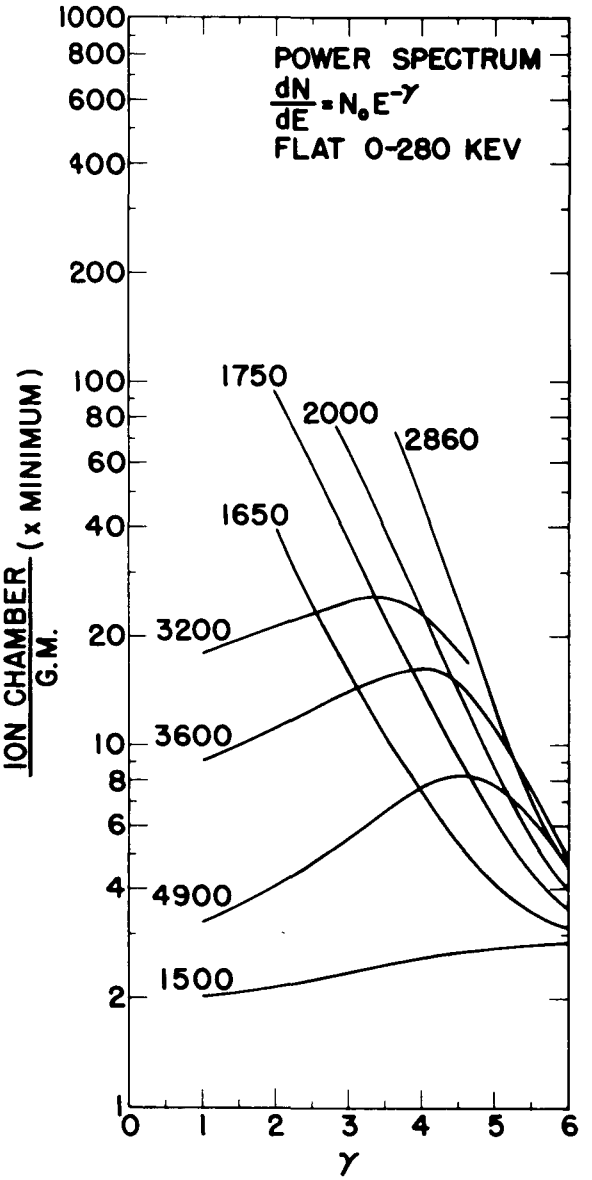

FIGURE 11.—*Ratios of the ion chamber to Geiger counter rates as a function of the exponent γ, for assumed power-law spectra of electrons. The power-law spectra have a flat portion from zero to 280 kev. The various curves are labeled according to the high-energy cutoff imposed on the assumed spectra.*

istics above 1 Mev, it is difficult to assign an estimate of error.

Because the detector ratios become insensitive to the low-energy radiation when energetic electrons are measured, it is not possible to investigate the low-energy electrons in the range interval 11,000 to 26,500 km by using the Explorer VI data. This fact is exemplified in fig-

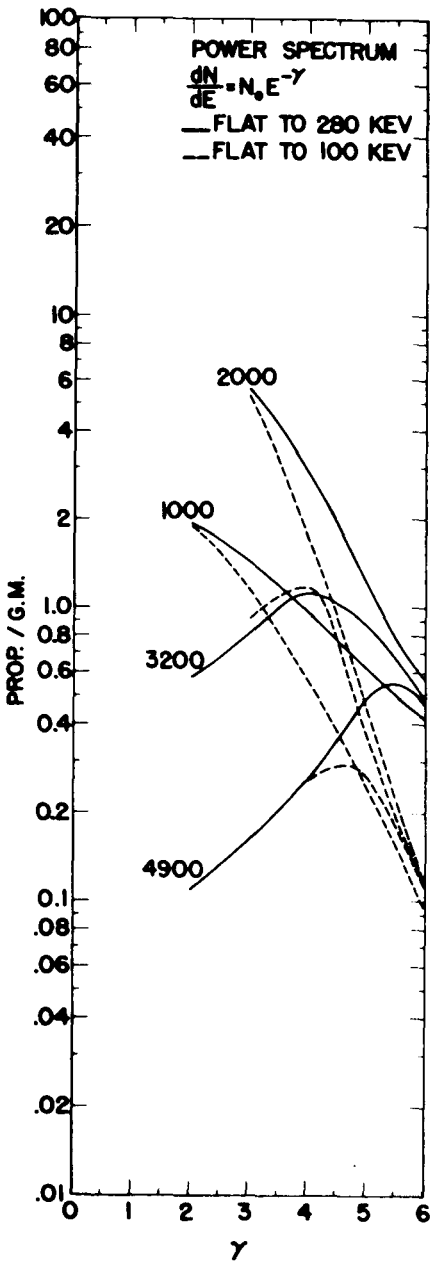

FIGURE 12.—*Ratios of the proportional counter to Geiger counter rates versus the exponent γ, for power-law spectra of electrons. The assumed power-law spectra have a flat portion from zero to 100 kev for the dashed curves and a flat portion from zero to 280 kev for solid curves. Various curves are labeled according to high-energy cut-off imposed on the assumed spectra.*

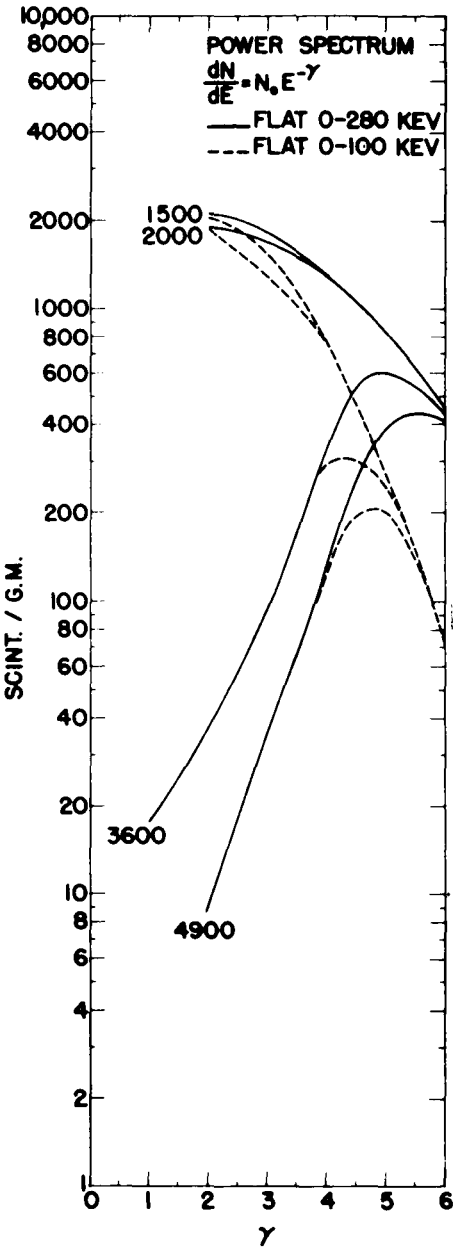

FIGURE 13.—*Ratios of the scintillator to Geiger counter rates versus the exponent γ, for power-law spectra of electrons. The assumed power-law spectra have a flat portion from zero to 100 kev for the dashed curves and a flat portion from zero to 280 kev for the solid curves. Various curves are labeled according to the high-energy cutoff imposed on the assumed spectra.*

ure 14, in which are plotted the ion/GM ratios versus γ for a fixed-high-energy cutoff and as a function of the extent of the low-energy flat portion. We see from this figure that even for an exponent as large as 4 the ion/GM ratio is insensitive to what is done to the low-energy end of the power spectrum. Without a unique spectral form for the low-energy radiation, flux estimates that include the low-energy electrons cannot be made.

The fact that an assumed power-law spectrum has been used for the electrons does not restrict the general conclusions arrived at in this paper about the trapped radiation between 11,000 and 26,500 km as being peculiar to the power-law spectrum. If we use an exponential energy dependence for the electrons of the form $dN/dE = N_0 e^{-kE}$, the existence of energetic electrons can be demonstrated as was done for the power-law spectra. The ion/GM and prop/GM ratio curves versus k of the exponential law are shown in figures 15 and 16. Note that it is only for k values between 0.00 and 0.01 that the effect of direct electron detection becomes significant. For k greater than 0.01 the ion/GM and prop/GM ratio curves have different slopes, hence the smooth rise in both experimental ratios from a range of 11,000 to 26,500 km can be obtained from these figures, as was true for the power-law spectra, only by introducing energetic electrons that give the curves the same slope for some range of k less than $k = 0.01$.

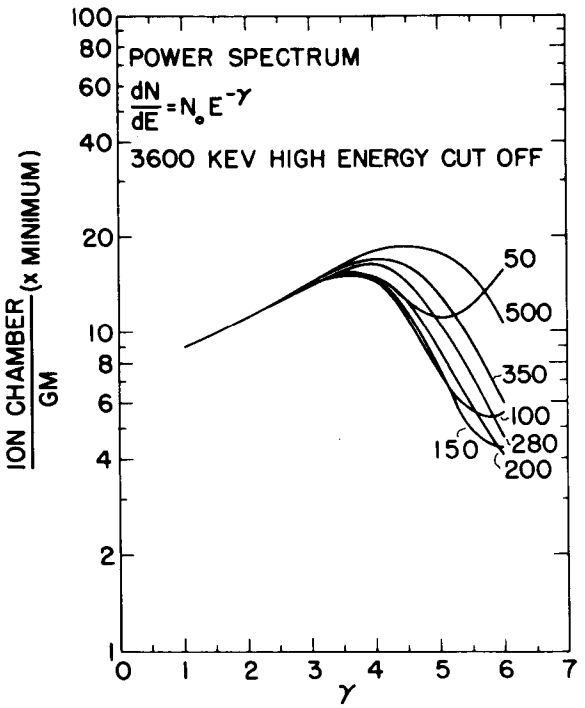

FIGURE 14.—*Ratios of the ion chamber to Geiger counter rates as a function of the exponent γ for assumed power-law spectra of electrons. The high-energy cutoff imposed on the spectra is fixed at 3,600 kev. The various curves are labeled according to the extent of the flat portion introduced in the spectra from zero to the energy in kev shown.*

TRAPPED RADIATION BEYOND 26,500 KM RANGE

As is shown in figure 4, beyond a range of 26,500 km the ion/GM ratio decreases, until at 37,000 km it is at nearly the same low value that prevailed at 11,000 km. The prop/GM ratio, however, continues to increase to reach a maximum at 29,000 km, and exhibits some fluctuation, but never returns to a value as low as measured at small ranges. The scint/GM ratio rises sharply beyond 26,500 km. This large increase in the ratio is due to a maximum in the scintillator count rate at 29,000 km, where the other three detectors are decreasing in rate with increasing range. *Rosen and Farley* [1961] interpret this maximum in count rate as due to efficient detection of radiation through the window, to which the other detectors respond inefficiently.

The flux of protons of energy between 2 and about 20 Mev necessary to produce the large rate maximum at 29,000 km would have a particle energy density exceeding the magnetic field energy density at this range. The fact that dipole lines maintain their identity in the trapped radiation indicates that this is not the situation [*Fan, Meyer, and Simpson*, 1961]. The only way the large prop/GM and scint/GM ratios can be consistent with the low ion/GM ratios at large ranges if the rates are due to electrons is to have steep spectra with flat portions at the low energies. By studying figures 11 to

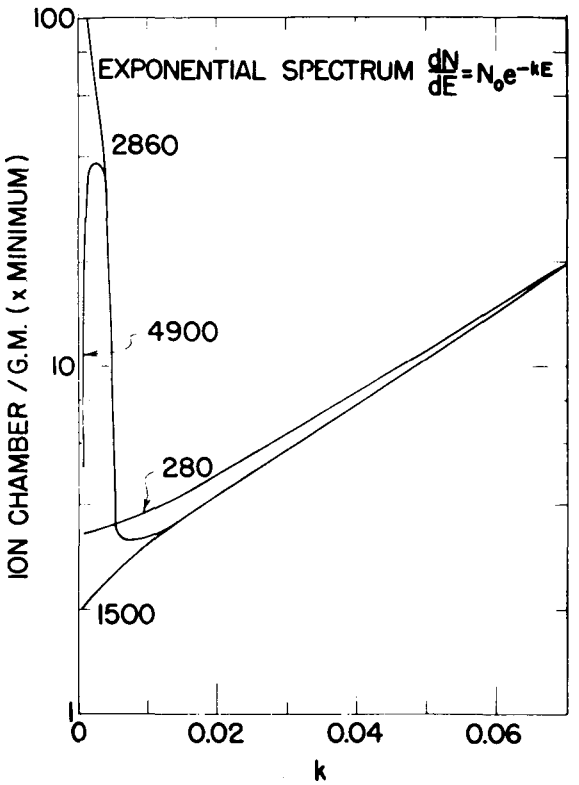

FIGURE 15.—*Ratios of the ion chamber to Geiger counter rates as a function of the parameter* k, *for assumed exponential spectra of electrons. Ratios were obtained from calculations using the measured efficiencies of the detectors. The various curves are labeled according to high-energy cutoff imposed on the assumed spectra.*

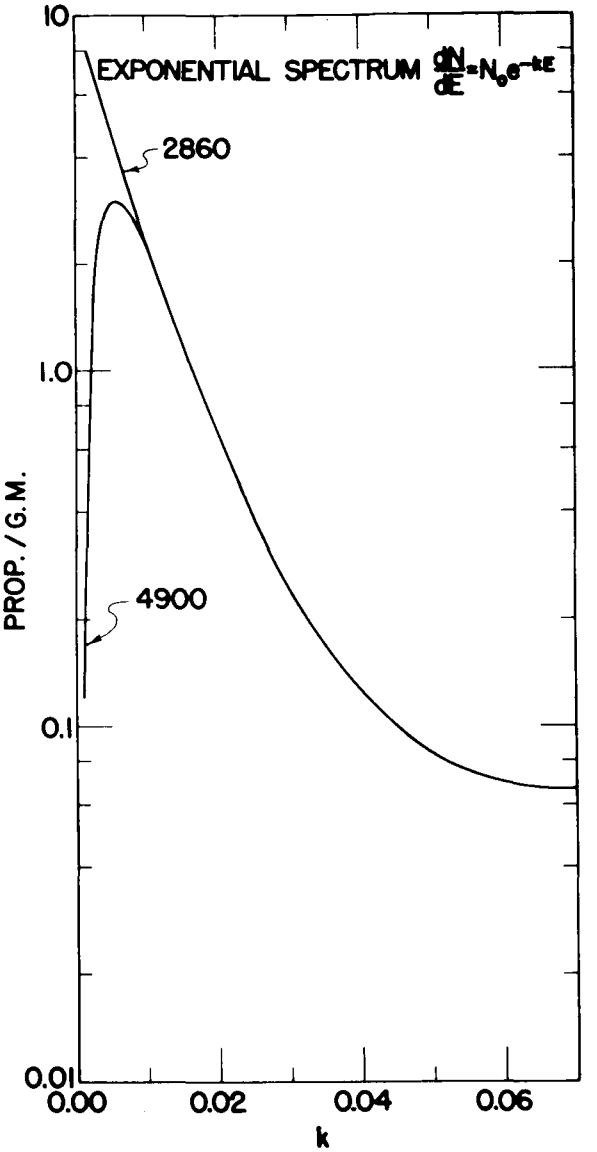

FIGURE 16.—*The ratio of proportional counter to Geiger counter rates as a function of the parameter* k *for assumed exponential spectra of electrons. The ratios are obtained from calculations using the measured efficiencies of the detectors. The various curves are labeled according to the high-energy cutoff imposed on the assumed spectra.*

13 we see that such spectra can produce the measured ion/GM and prop/GM ratios beyond a range of 26,500, km but cannot give the magnitude of the scint/GM ratios. We could suggest the possibility of an error in the scintillator saturation correction, but it seems more likely that we cannot compare the scintillator data beyond 26,500 km with that from the nearly omnidirectional Geiger counter by means of the ratio curves of figure 13.

Evidence for a change in the distribution of the trapped radiation along magnetic field lines for ranges beyond about 23,000 km is given in figure 17. In the figure are plotted the Geiger counter rates measured along lines of force labeled by their goecentric range. The abscissa is the field strength along the line of force in units of the equatorial field (B_0) for that par-

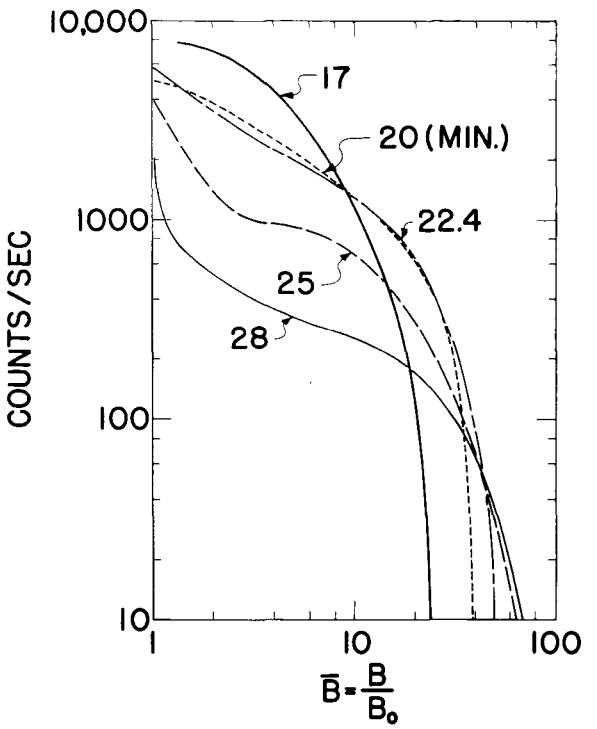

FIGURE 17.—*Geiger counter rates measured along magnetic dipole lines versus the field strength along the line. The different dipole lines are labeled according to the range where they cross the equatorial plane.*

ticular line. Lines of force beyond the 22,400 km line have an increasing Geiger counter rate near the equatorial plane, as is indicated by the upswing in the curves near $B/B_0 = 1$. This enhanced Geiger counter rate is not due to a spectral change for radiation trapped near the equator, since the ion/GM ratio along the line of force does not change significantly. The enhanced rate can only mean an increasing concentration of radiation near the equatorial plane having a spectrum similar to that for the radiation that turns further down the line of force. The 28,000-km line shows that about 50 percent of the intensity measured at the equator is due to trapped radiation having turning points near the equatorial plane. Orientation of the spin-stabilized satellite so that the look direction of the scintillator through the window is also perpendicular to the field lines would greatly increase the efficiency of the scintillator above that used in the calculation of the ratio curves for detection of this radiation if a significant fraction of it lies in the energy interval 200–500 kev. Hence, we could not expect under these circumstances to study the measured ratio with the curves of figure 13.

Regardless of whether the above interpretation of the scint/GM ratio is correct or not, we must conclude from the scintillator rates and the ion/GM and prop/GM ratios that the spectrum is steep at large ranges. To obtain the ion/GM ratio of 4.4. times minimum ionizing at 37,000 km, a flat portion of 200 to 300 kev in extent is necessary at the low-energy end of the steep spectrum. Whether such rounding of the spectra at low energies occurs at smaller ranges cannot be determined in this analysis because the detectors are insensitive to the low-energy radiation at the smaller ranges, as was pointed out above.

SHAPE OF THE OUTER ZONE

By means of the crude spectral analysis of the outer zone presented in the previous discussion, it is possible to interpret the minimum in detector rates at 19,000 km as having a spectral-detector origin rather than as representing a minimum in intensity. Relative to this second maximum, the first Geiger counter rate peak is larger; for the proportional counter, however, the first peak is much smaller than its second count rate maximum. This suggests that the two maxima can be looked upon as the result of the addition of two intensity curves folded in with the sensitivities of the detectors. One curve represents the decreasing number of energetic electrons caused by the steepening spectra and decreasing high-energy cutoff with increasing range; the other represents the large increase in the low-energy electrons resulting from the steepening spectra with range. The first maximum is thus due to the efficient detection of energetic electrons. Since the Geiger counter efficiency is greater than that of the proportional counter because of direct electron detection, its count rate relative to its second peak is much larger than that for the proportional counter. As the number of ener-

getic electrons decreases the rates go down, but they are soon increased again by the increasing number of low-energy electrons. The second peak is thus produced by the detection of a large number of these low-energy electrons. Because of the great difference in the efficiencies of the counters for measuring the two groups of electrons, the second peak, even though it is smaller for the Geiger counter rate than the first one, represents the maximum in intensity. Thus the intensity of the radiation increases steadily with range because of the increasing contribution of inefficient low-energy-electron detection to the total rate of the counters. The fact that different counters do not measure the minimum at the same range reflects the different sensitivities of the detectors. The shift of the minimum in range during disturbed periods when time variations occur in the outer zone indicates the changing spectral shape of the trapped radiation.

COMPARISON WITH OTHER MEASUREMENTS

The first suggestion of trapped energetic electrons in the outer zone was made by the Russian scientists [*Vernov and Chudakov*, 1960] in their analysis of data from Cosmic Rockets I and II launched on January 2, 1959, and September 12, 1959. A flux of 10^6 electrons/cm^2 sec with energies between 1 and 3 Mev was inferred from the detector rates of Cosmic Rocket II, with the scintillator measuring the flux of electrons of energy greater than 5 Mev to be less than 1 particle/cm^2 sec. Shielded Geiger counters aboard Cosmic Rocket II, sensitive to energetic electrons, reached their peak rate at smaller ranges than the maximum in ionization, the counter having the greater shielding being at a slightly smaller range than the less-shielded counter. The exponent of the integral power-law spectrum fit to these energetic particles observed at the edge of the outer zone was approximately 2. These results support the Explorer VI observations that have energetic electrons at small ranges with a high-energy cutoff of 5 Mev or more at an equatorial range of 15,000 km. A differential power-law spectrum fit to the Explorer VI data at this equatorial range can have an exponent as low as 2. For such a spectrum the flux of electrons from 1- to 5-Mev energy is of the order of 10^6 electrons/cm^2 sec.

Walt, Chase, Cladis, and Imhof [1960] measured the spectrum of the trapped radiation with an electron spectrometer aboard a rocket flight into the foot of the outer zone on July 7, 1959. The vehicle reached an altitude of 1,045 km, and measurements were made on a dipole line of force that crossed the equatorial plane at about 15,000 km. In figure 1 (top), the position at 125° east longitude of the electron shell upon which Walt's measurement was made is indicated with respect to the profile of the outer belt at this longitude. It is seen that the spectrometer measurements are on the inside edge of the first Geiger counter rate maximum.

The spectrum obtained from this measurement is quite steep, the exponent of a differential power-law spectrum fit to the data above a few hundred kev being about 5. The observed counting rates were not inconsistent with a spectrum having an end-point energy of 760 kev. An absolute upper limit to the number of electrons above 1.5 Mev is less than 1 per cent of the total flux observed, which is less the 10^4 electrons/cm^2 sec. However, since the background corrections were of this order of magnitude, the presence of electrons of energy greater than 1.5 Mev was not established by the measurement. The Explorer VI measurements suggest a flatter spectrum and definitely establish the existence of electrons above 1.5 Mev. The difference in spectral shape is probably due to the fact that the spectrometer spectrum was measured at a low altitude whereas the Explorer VI measurements were made nearer the equatorial plane.

By studying the prop/GM ratio at low altitudes and near the equatorial plane, the spectra in the two places can be compared. The proportional counter is used, since no ion chamber data are available at low altitudes, owing to the reduced intensity of the trapped radiation. The average prop/GM ratio for a time interval in which the satellite spanned an altitude from 700 to 1,900 km and moved northward in magnetic latitude from 40° to 49.5° was 0.63 for a quiet time pass. The ratios measured near the

equatorial plane as the satellite cut lines of force enclosing the geographic interval over which the low altitude ratio was obtained varied from 0.40 to 0.18 for a latitude interval of 28° to 5°. This indicates that the spectrum changes down the line of force when low altitudes are approached, and, to be consistent with the ion/GM ratios, the prop/GM ratios near the equatorial plane require high-energy electrons. The only explanation for the higher prop/GM ratio at large distances off the equator is to have the spectrum steepen, as, indeed, Walt's measurement indicates.

DISCUSSION

In an earlier draft of this paper (*Cosmic Ray Group Tech. Rept. CR–46*, University of Minnesota) we deduced electron energy spectra and fluxes in the range 30 to several hundred kev by fitting trial spectra to the measured instrument responses. It is now completely clear, however, that any attempt to utilize the bremsstrahlung response of Explorer VI instruments is useless if an appreciable portion of their counting rate is produced by direct energetic particles. This fact is evident in the calibration curves of figure 3, which show the nearly three orders of magnitude difference in efficiency between the bremsstrahlung and direct measurements of electrons.

The realization of the importance of this effect has come from the new measurements in the outer zone made by the Explorer XII satellite, which for the first time directly measured electrons below 100 kev [*O'Brien, Van Allen, Laughlin, and Frank*, 1962].

We therefore believe that total fluxes deduced in the heart of the outer zone by fitting trial spectra to the Explorer VI data are meaningless. This statement must include the preliminary flux value quoted by the Minnesota group in an earlier paper [*Arnoldy, Hoffman, and Winckler*, 1960*a*]. The inability to determine fluxes is in principle a result not of insufficient knowledge of the bremsstrahlung process as suggested by *Dessler* [1960] but rather of the presence of a much more powerful competing effect that dominates certain detectors. However, certain aspects of the kind of analysis presented herein appear to be on a firm basis and are useful.

In fitting assumed power-law spectra of electrons to the Explorer VI data, it has been seen in this discussion that the spectrum must extend to several Mev at the small ranges, with the ion chamber and counter responses there due primarily to direct electron detection. The intensity of the energetic electrons was shown to decrease with range as the spectra steepen and the radiation softens, resulting in an increasing contribution of bremsstrahlung to the rates of the chamber and Geiger counter. At the outer edge of the trapped radiation, bremsstrahlung is the dominant factor.

The spectral dependence of the trapped radiation on range might be attributed to the source of the radiation and (or) loss mechanisms that operate in the outer zone. Very little is known about the source of the radiation, although three general origins have been discussed. They are, first, the injection of electrons into the trapping region from the decay of cosmic-ray albedo neutrons [*Hess*, 1960]; second, the direct injection of electrons into the trapping region from solar gas clouds; and last, the local acceleration of low-energy electrons present in the exosphere or from the solar stream [*Van Allen and Frank*, 1959*b*; *Arnoldy, Hoffman, and Winckler*, 1960*b*]. It is possible that all the above-mentioned sources, and perhaps even some that have not been considered, contribute to the intensity of the radiation. Present data, which we must admit are meager, indicate that some unknown local acceleration mechanism is the dominant origin, only by reason of eliminating the other two possibilities as strong sources.

The existence of energetic electrons, i.e., electrons of energy greater than 1 Mev, poses a serious problem for the neutron albedo theory. The neutron decay electron is less than 1 Mev in energy, and the kinetic energy of a decaying neutron by conservation of momentum is given primarily to the decay proton. Hence, the electrons from neutron decay are too low in energy to account for the energetic outer-zone radiation. To raise the energy of the decay electrons an acceleration mechanism is needed. It is then no longer clear that, if acceleration is taking place in the outer zone, the decay electrons

remain as the dominant source, in view of the large quantity of low-energy electrons available for acceleration from the solar stream. Furthermore, the measured electron flux along a line of force in the outer zone is found to be inconsistent with the calculated distribution expected from a neutron decay source [*Hess, Killeen, Fan, Meyer, and Simpson*, 1961] (Hoffman, private communication, 1961), indicating that other processes, in addition to electron injection by neutron decay, are responsible for the distribution of the outer-zone electrons.

Simultaneous measurements of the trapped radiation by detectors aboard the Explorer VII satellite [*Van Allen and Lin*, 1960] and of the radiation in a solar cloud in transit to the earth by similar detectors aboard the Pioneer VI space probe [*Arnoldy, Hoffman, and Winckler*, 1960*b*] indicate that for the particular solar cloud encountered by the space probe the maximum flux of electrons present in the cloud of energies characteristic of the trapped particles was about three orders of magnitude too low to account for the subsequent electron intensity changes that the satellite observed in the outer zone. In fact, the space-probe data are consistent with no energetic electrons in the cloud, since the response of the detectors can be attributed to solar protons that were also in transit to the earth at the same time and were measured by balloon-borne detectors. This single observation suggests that direct solar injection is not a likely origin for the outer-zone electrons.

Although a local acceleration process has been generally conceded as fundamental in a source for the outer zone, the exact mechanism is not known. Loss of trapped radiation resulting from violation of one or more of the adiabatic invariants has been discussed [*Parker*, 1960; *Parker*, 1961; *Welch and Whitaker*, 1959]. However, the role of local acceleration and loss mechanisms in establishing the properties of the outer zone as discussed in this paper cannot be fully understood until more data on the dynamics of the magnetosphere are available.

ACKNOWLEDGMENTS

We are indebted to Mr. Richard M. Brown and Mr. Karl A. Pfitzer for their diligent readout of the raw data and calculation of the many ratios employed in this paper. The cooperation of the University of Chicago experimenters, C. Fan, P. Meyer, and J. Simpson, and the Space Technology Laboratories group of A. Rosen and T. Farley, in making the joint calibrations and exchanging data, is appreciated.

We wish to thank Dr. Robert Rochlin, Mr. Robert D. Downing, and Mr. W. R. Giard of the General Electric Company for the use of the Cockcroft-Walton accelerator. The services given by Mr. Eli Young of Hi Voltage Engineering Company in the use of the electron Van de Graaff are appreciated. We wish to extend our thanks to Dr. John Ryan of the Minnesota Mining and Manufacturing Company for making available to us the radioactive sources used in the calibrations.

This work was supported by the National Aeronautics and Space Administration under contract NASw–56.

REFERENCES

Arnoldy, R. L., R. A. Hoffman, and J. R. Winckler, Observations of the Van Allen radiation regions during August and September 1959, 1, *J. Geophys. Research*, *65*(5), 1361–1376, 1960*a*.

Arnoldy, R. L., R. A. Hoffman, and J. R. Winckler, Solar cosmic rays and soft radiation observed at 5,000,000 kilometers from earth, *J. Geophys. Research*, *65*(9), 3004–3007, 1960*b*.

Dessler, A. J., Discussion of paper by Arnoldy, Hoffman, and Winckler, "Observations of the Van Allen radiation regions during August and September 1959, 1," *J. Geophys. Research*, *65*(10) 3487–3490, 1960.

Fan, C. Y., P. Meyer, and J. A. Simpson, *Space Research*, Proc. First Intern. Space Sci. Symposium, North-Holland Publishing Company, Amsterdam, pp. 951–966, 1960.

Fan, C. Y., P. Meyer, and J. A. Simpson, Dynamics and structure of the outer radiation belt, *J. Geophys. Research*, *66*(8), 2607–2640, 1961.

Hess, W. N., The radiation belt produced by neutrons leaking out of the atmosphere of the earth, *J. Geophys. Research*, *65*(10), 3107–3115, 1960.

Hess, W. N., J. Killeen, C. Y. Fan, P. Meyer, and J. A. Simpson, The observed outer-belt electron distribution and the neutron decay hypothesis, *J. Geophys. Research*, *66*(9), 2313–2314, 1961.

Hoffman, R. A., R. L. Arnoldy, and J. R. Winckler, Observations of the Van Allen radiation regions during August and September 1959, 3, *J. Geophys. Research*, *67*(1), 1–12, 1962.

O'Brien, B. J., J. A. Van Allen, C. D. Laughlin, and L. A. Frank, Absolute electron intensities in the heart of the earth's outer radiation zone, *J. Geophys. Research, 67*(1), 397–403, 1962.

Parker, E. N., Geomagnetic fluctuations and the form of the outer zone of the Van Allen radiation belt, *J. Geophys. Research, 65*(10), 3117–3130, 1960.

Parker, E. N., Effect of hydromagnetic waves in a dipole field on the longitudinal invariant, *J. Geophys. Research, 66*(3), 693–708, 1961.

Rosen, A., and T. A. Farley, Characteristics of the Van Allen radiation zones as measured by the scintillation counter on Explorer VI, *J. Geophys. Research, 66*(7), 2013–2028, 1961.

Van Allen, J. A., and L. A. Frank, *Nature, 183*, 430–434, 1959*a*.

Van Allen, J. A., and L. A. Frank, *Nature, 184*, 219–224, 1959*b*.

Van Allen, J. A., and W. C. Lin, Outer radiation belt and solar proton observations with Explorer VI during March–April 1960, *J. Geophys. Research, 65*(9), 2998–3003, 1960.

Vernov, S. N., and A. E. Chudakov, *Space Research*, Proc. First Intern. Space Sci. Symposium, North-Holland Publishing Company, Amsterdam, pp. 751–796, 1960.

Vernov, S. N., A. E. Chudakov, P. V. Vakulov, Yu. I. Logachev, and A. G. Nikolayev, *Space Research*, Proc. First Intern. Space Sci. Symposium, North-Holland Publishing Company, Amsterdam, pp. 845–851, 1960.

Walt, M., L. F. Chase, Jr., J. B. Cladis, and W. L. Imhof, *Space Research*, Proc. First Intern. Space Sci. Symposium, North-Holland Publishing Company, Amsterdam, pp. 910–920, 1960.

Walt, M., and W. M. MacDonald, Energy spectrum of electrons trapped in the geomagnetic field, *J. Geophys. Research, 66*(7), 2047–2052, 1961.

Welch, J. A., Jr., and W. A. Whitaker, Theory of geomagnetically trapped electrons from an artificial source, *J. Geophys. Research, 64*(8), 909–922, 1959.

(Manuscript received April 16, 1962.)

Observations of the Van Allen Radiation Regions during August and September 1959[1]

5. Visual Auroras, High-Altitude X-Ray Bursts, and Simultaneous Satellite Observations

BY R. L. ARNOLDY,[2] R. A. HOFFMAN,[3] AND J. R. WINCKLER

School of Physics
University of Minnesota

S.-I. AKASOFU

Geophysical Institute
University of Alaska

The measurements made in the outer trapped radiation region by the University of Minnesota ionization chamber and Geiger counter and the scintillation counter furnished by Space Technology Laboratories, Inc., aboard the Explorer 6 earth satellite during the August 16, 1959, magnetic storm are studied. The variations in the detector rates are correlated with the visual aurora recorded by all-sky cameras and with high-altitude X-ray bursts observed by balloon-borne detectors. An increase in radiation observed at a geocentric range of 42,000 km simultaneously with the occurrence of a visual aurora on the electron shell connecting with the satellite measurements suggests that the aurora is associated with a disturbance extending over many degrees of longitude and out to large ranges. Furthermore, a rapid decrease in the Geiger counter rate coincident with a strong low-latitude aurora at Fargo, North Dakota, indicates that energetic radiation is either precipitated out of the outer zone during strong auroras or decelerated by a perturbation of the earth's magnetic field accompanying the aurora. Frequent observations of rate variations at the outer edge of the trapped radiation and at apogee point out the great instability there that results in the frequent discharge of radiation into the atmosphere observed by balloon-borne detectors at the high latitudes connecting with the region. The close correlation of outer-zone intensity variations and solar phenomena indicates that the energy involved in the dynamics of the trapping region has a solar origin.

INTRODUCTION

During the lifetime of the Explorer 6 earth satellite (August 7 to October 6, 1959) five magnetic storms occurred. Variations in the count rates of the detectors associated with these magnetic storms, while the satellite was in the trapped radiation, have been discussed in detail by *Arnoldy, Hoffman, and Winckler* [1960a], *Farley and Rosen* [1960], *Rosen and Farley* [1961], and *Fan, Meyer, and Simpson* [1961].

The maximum count rate of the Anton 302 Geiger counter while the satellite was in the outer zone and close to the equatorial plane (within $\pm$ 10° geomagnetic latitude) is shown in figure 1 to summarize the general features of the outer zone during the lifetime of the satellite. The intensity of the horizontal component of the earth's field at Honolulu (geomagnetic

[1] 1962 issue of *Journal of Geophysical Research*. Reprinted by permission.
[2] Now at Honeywell Co.
[3] Now at NASA Goddard Space Flight Center.

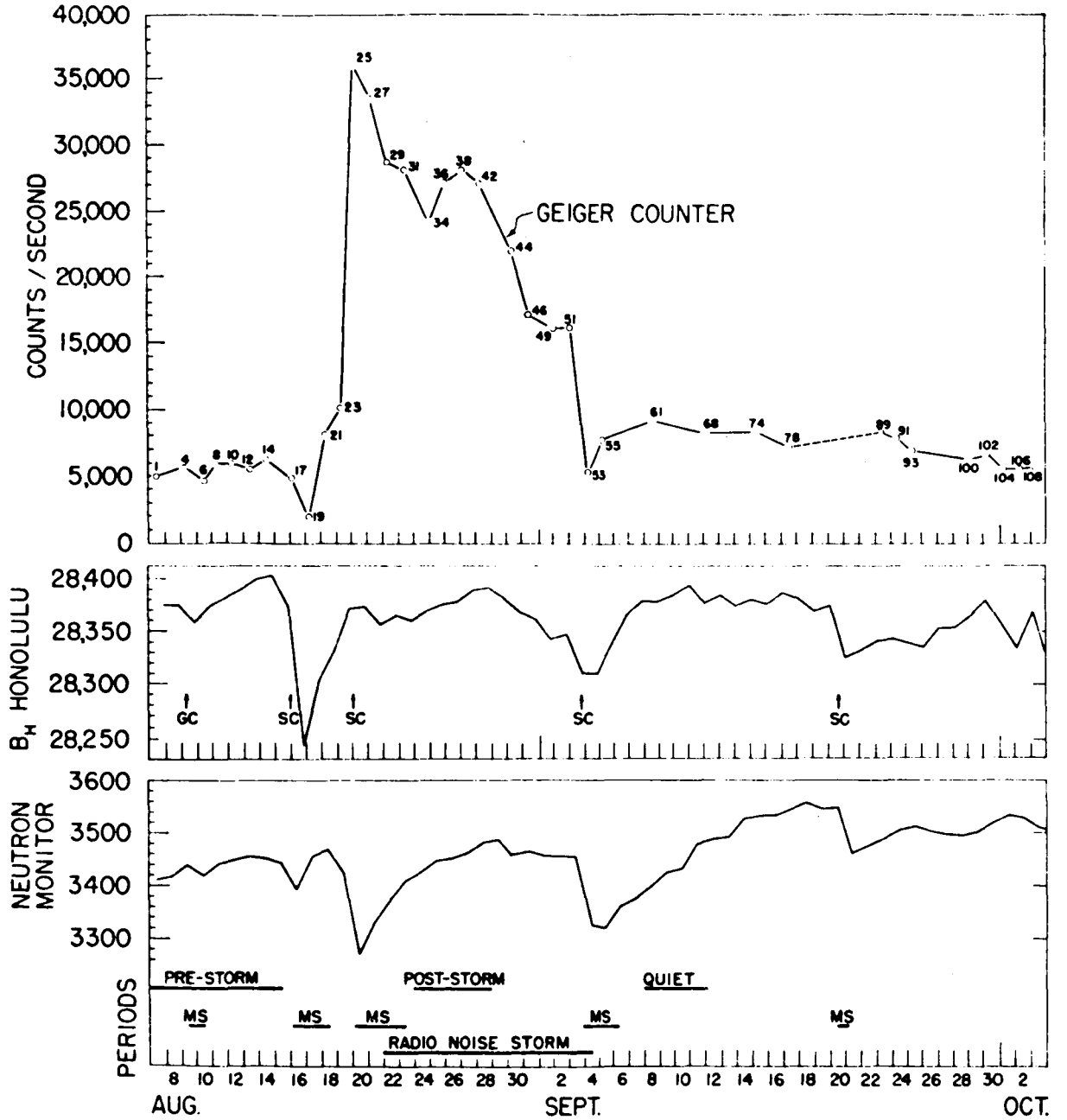

FIGURE 1.—*Time correlation of measurements during the lifetime of the Explorer 6 transmitters. The Geiger counter rate at the outermost maximum in the outer belt* (top), *the daily average of the earth's magnetic field* (middle), *and the daily average of the bihourly counting rate from the Deep River neutron monitor* (bottom).

latitude 21.0° N, data from the IGY Data Center A for Cosmic Rays) and the neutron monitor data from Deep River (courtesy of H. Carmichael through the IGY Data Center A for Cosmic Rays) for the same period are also shown in the figure. The August 16, 1959,

storm produced the largest rate variation as measured by the Explorer 6 Geiger counter; this is the period considered here.

In studying the rate changes of the Explorer 6 detectors, however, we must keep in mind the response characteristics of the instruments, since such changes reflect variations only for the part of the spectrum to which the detectors are sensitive. For example, a reduction in the Geiger counter rate does not necessarily mean that the over-all intensity of the trapped radiation is reduced. The Explorer 6 Geiger counter had a cutoff of 36.4 Mev for proton detection and a 2.9-Mev threshold for direct electron detection. Below 2.9 Mev, electrons were detected less efficiently through the intermediate bremsstrahlung process [*Arnoldy, Hoffman, and Winckler*, 1962]. The response characteristics of the scintillator will be discussed in the next section.

The state of the outer zone before, during, and after the August 16 storm is represented by the observations during passes 12, 16, 17, 19, 20, and 25 shown in figures 2*A* to 2*F*. In these figures the rates on the ion chamber and Geiger counter are plotted as a function of radial distance from the earth's center. The profile of the outer zone as the Geiger counter would have measured it if prestorm conditions had prevailed is sketched for each pass. This profile is obtained from curves giving the prestorm Geiger counter rate along dipole lines of force. The prestorm rates for a given pass are read from these plots at the position along a given force line where the orbit for the pass crossed the line. The important features of each of the passes may be summarized as follows:

Pass 12: represents the "normal state" of the trapped radiation as far as the Explorer 6 data are concerned.

Pass 16: observed the reduction in ion chamber and Geiger counter rates at large ranges before the sudden commencement of the August 16 magnetic storm.

Pass 17: the ssc of the magnetic storm occurred at 0404 UT August 16, when the satellite was at a range of 26,400 km. The rates were further reduced below prestorm levels at the large ranges.

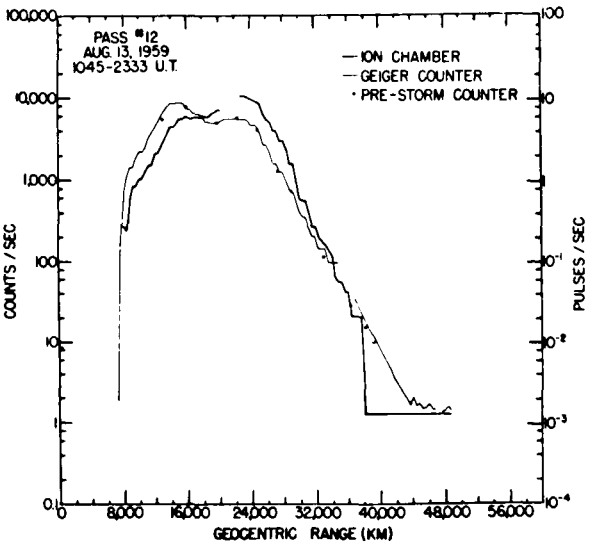

FIGURE 2A.—*The outer zone as measured during the outgoing part of pass 12.*

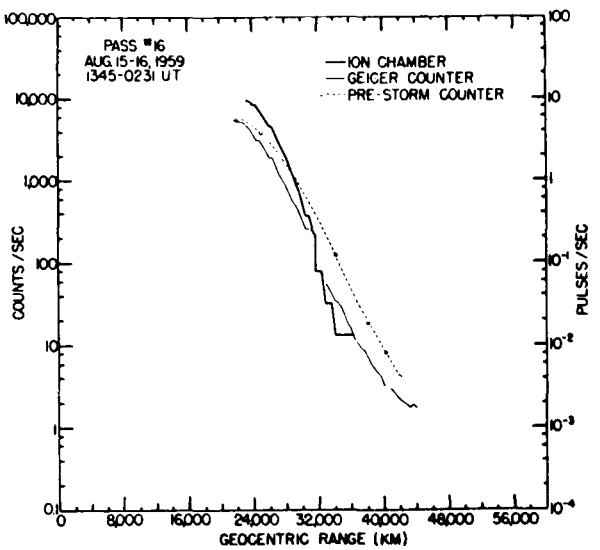

FIGURE 2B.—*The outer zone as measured during the outgoing part of pass 16.*

Pass 19: the minimum count rates in the outer zone for the ionization chamber and Geiger counter were observed on this pass.

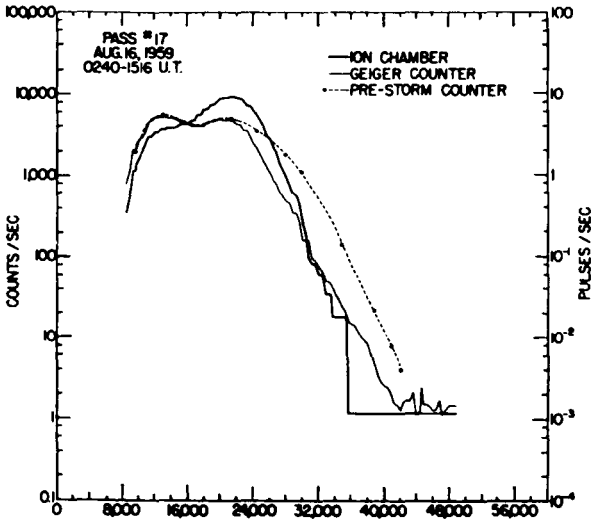

FIGURE 2C.—*The outer zone as measured during the outgoing part of pass 17.*

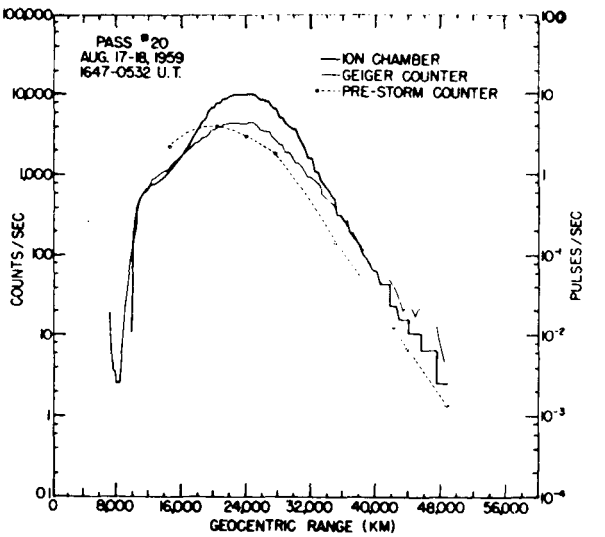

FIGURE 2E.—*The outer zone as measured during the outgoing part of pass 20.*

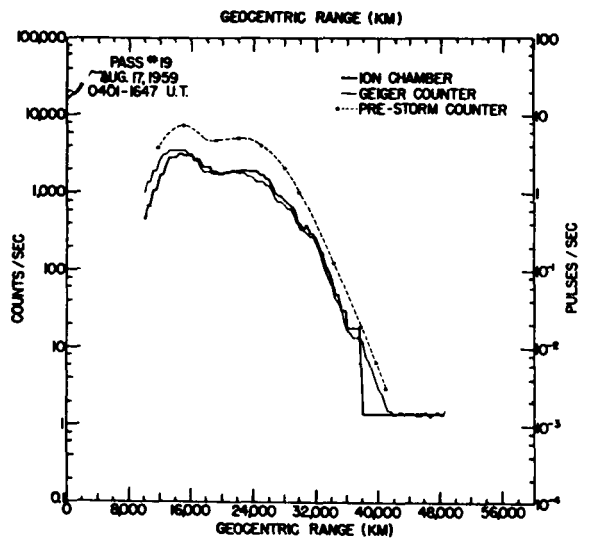

FIGURE 2D.—*The outer zone as measured during the outgoing part of pass 19.*

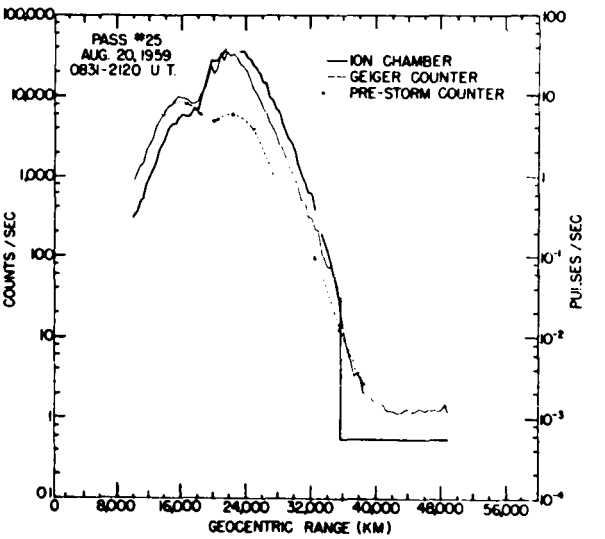

FIGURE 2F.—*The outer zone as measured during the outgoing part of pass 25.*

Pass 20: first measurement of the radiation built-up occurring after the minimum.

Pass 25: the maximum count rates in the outer zone were recorded by the Explorer 6 detectors during this pass.

The state of the heart of the outer zone following the sudden commencement as measured by the ion chamber and Geiger counter is uncertain because of the lack of data from these detectors for pass 18. Pass 19 measured the reduction in Geiger counter rate by a factor of 2½ some twenty hours after the sudden commencement.

In this paper our effort is concentrated on correlating the variations of the Explorer 6 detector count rates with simultaneous visual auroras recorded by all-sky cameras and with high-altitude X-ray bursts observed by balloon-borne instruments.

AURORAS
0440–0710 UT, August 16, 1959

During pass 17 the satellite detectors recorded their first large rate fluctuations, superimposed on the general reduction in the outer-zone rates at the large ranges. These rapid variations began at about 0550 UT, 1 hour and 46 min after the ssc and when the satellite was at ranges larger than 42,000 km. In figure 3*A* the Geiger counter and scintillator rates are plotted versus time as the satellite moved from a range of about 34,000 to 46,000 km and from the equatorial plane to about 20° S geomagnetic latitude. Also shown in the figure is the inferred prestorm rate curve of the Geiger counter obtained from the first 15 quiet-time passes. The prestorm curve for the scintillator, crudely obtained from the contour plot of the trapped radiation made from the first 15 passes, is given in the paper by *Rosen and Farley* [1960]. The decrease in the count rates from those that would have occurred if prestorm conditions had prevailed is evident. However, it is not clear whether the fluctuations represent new radiation added to the depleted intensity or whether the important feature is the selective removal of radiation from the prestorm intensity resulting in the observed structure. The evidence available, however, suggests that the structure represents new radiation added to the depleted trapping region. The Geiger counter peak at 0628 UT is about an 80 percent increase above

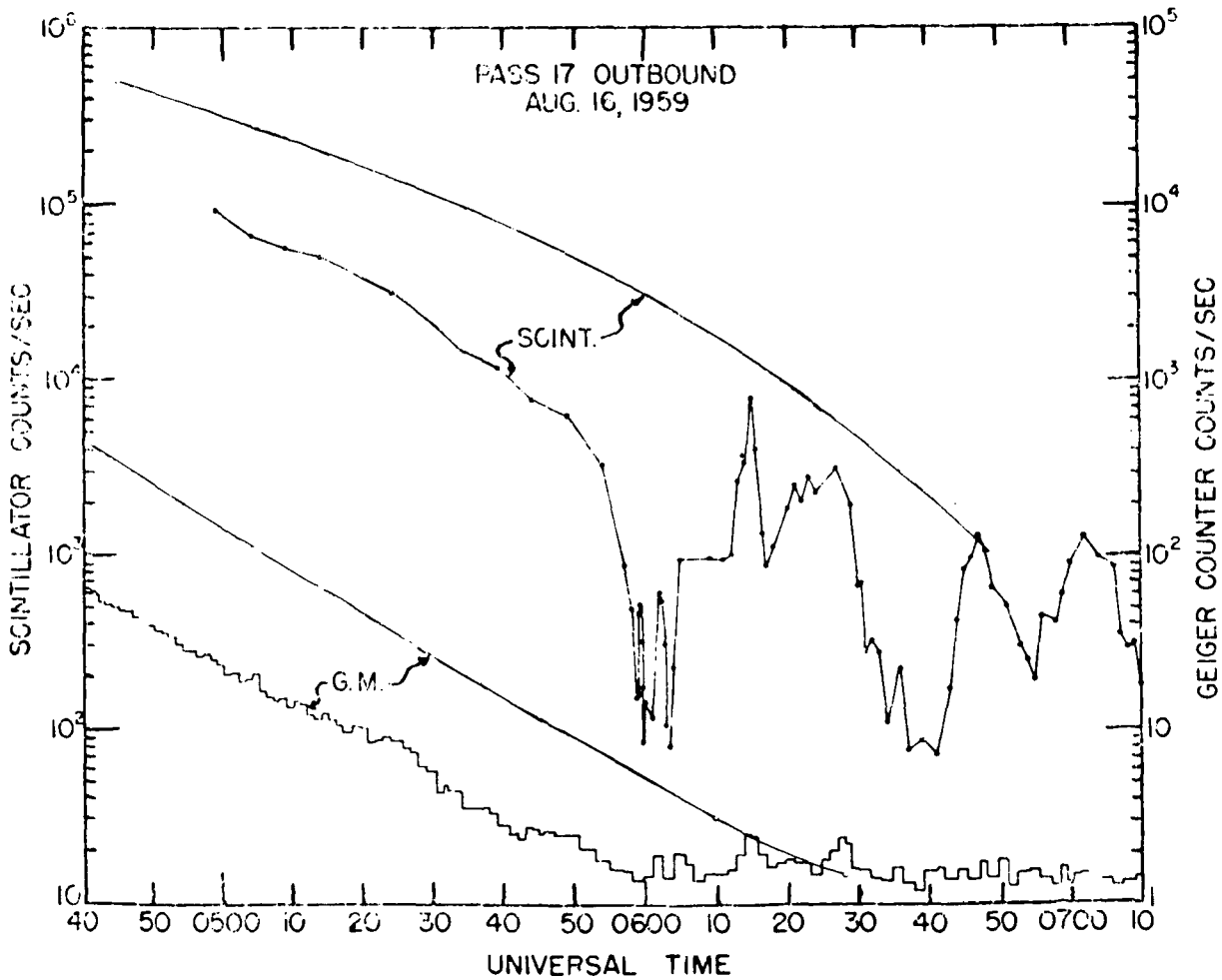

FIGURE 3A.—*Scintillator and Geiger counter data as the satellite moved from a range of 34,000 to 46,000 km on pass 17. Prestorm curves for these two detectors are given.*

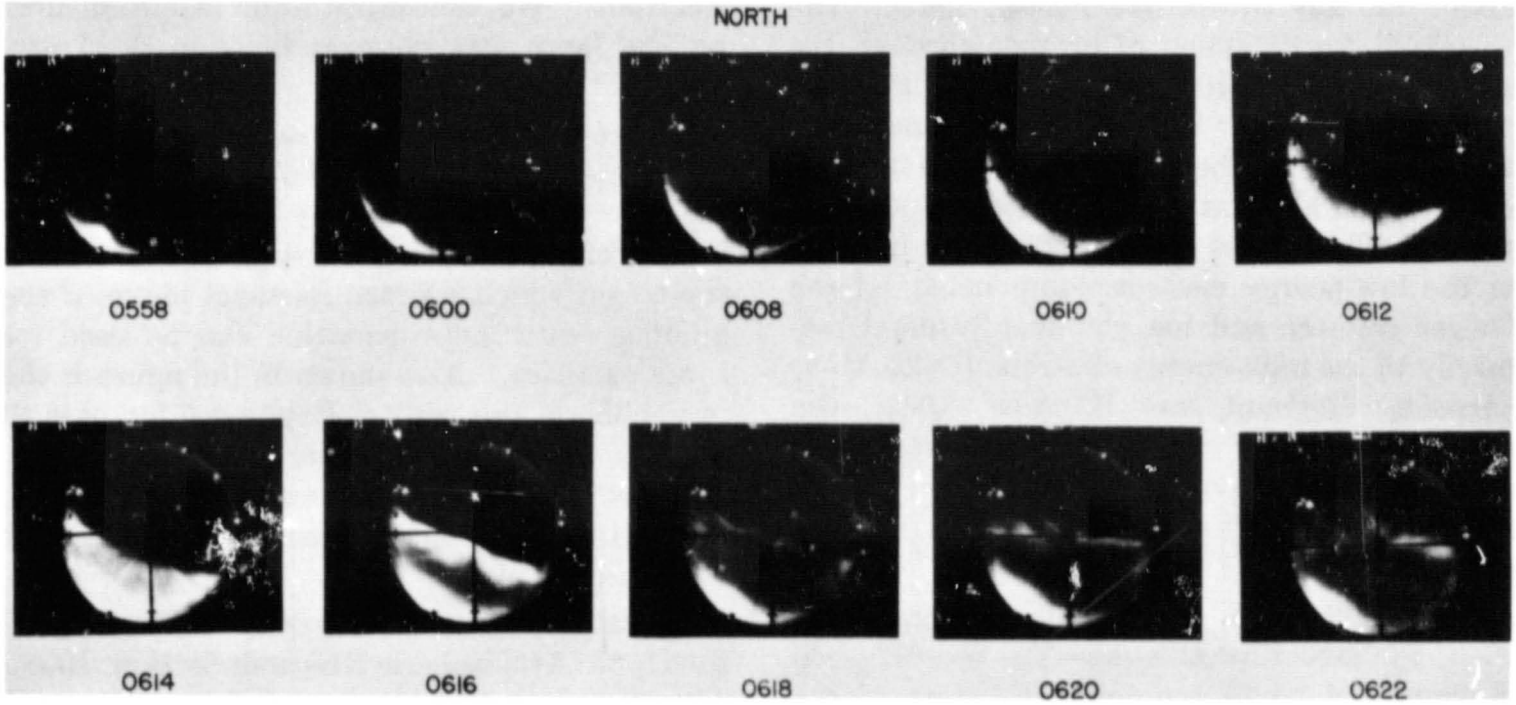

FIGURE 3B.—*Fort Churchill all-sky-camera pictures; positive prints.*

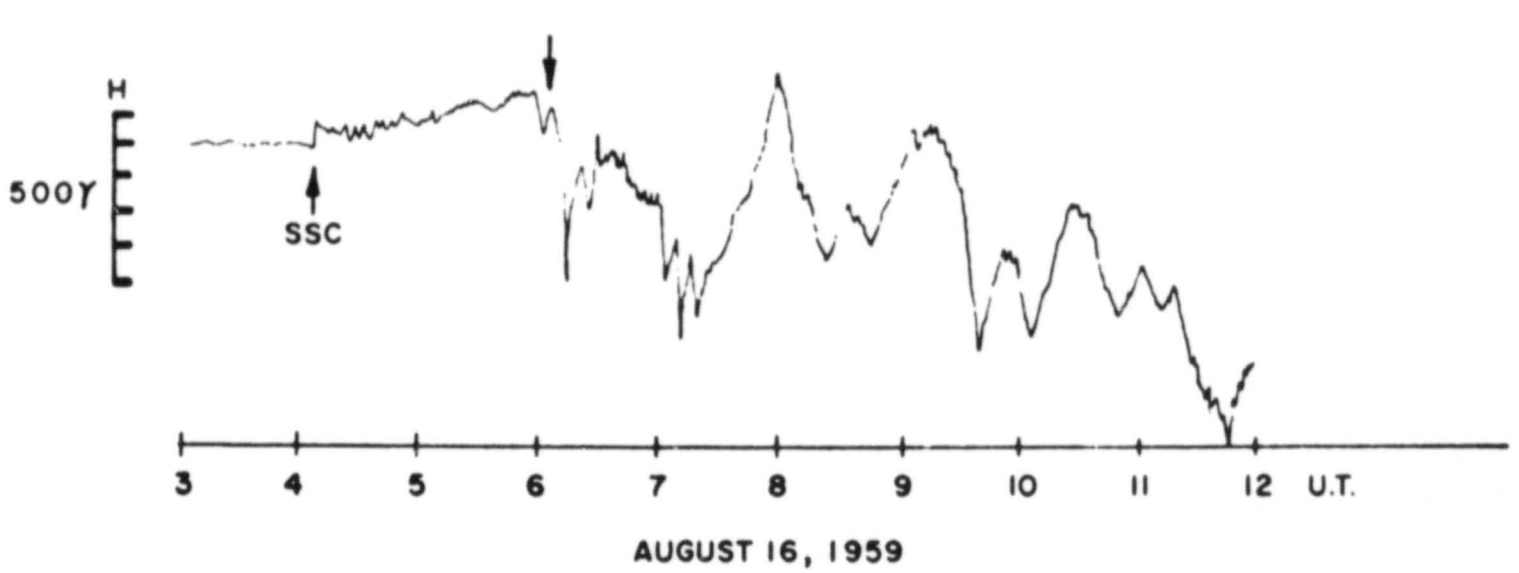

FIGURE 3C.—*The horizontal component of the earth's magnetic field as observed at Meanook, Canada.*

the prestorm curve and is outside the statistical fluctuations of the counter.

Moreover, we must not isolate these measurements made on pass 17 from the over-all picture in the outer belt of the rate variations associated with the August 16 magnetic storm. On pass 18 the scintillator rates increased above prestorm levels [*Farley and Rosen*, 1960], in contrast to the reduction seen during pass 17 and displayed a large amount of fluctuation. Unfortunately, no data are available from the ionization chamber and Geiger counter at the center of the outer zone for pass 18, but on pass 19 these detectors recorded a large reduction in rates (see fig. 2), in contrast to a further increase in the scintillator rates. Since the scintillator had a lower threshold for proton detection than the other detectors the rate increases of passes 18 and 19 have been attributed to low-energy protons [*Farley and Rosen*, 1960]. (The scintillator could detect radiation through a window in the satellite skin. The threshold for proton detection through the window was 2 Mev and for electron detection 200 kev. The detector had an electronic bias giving it a theoretical threshold for photon detection of

765-698 O-65—12

about 200 kev [*Rosen and Farley*, 1961]. The threshold for detection of protons through the satellite skin was 10 Mev and for electron detection 500 kev.) With an understanding of the response of the Explorer 6 detectors to electrons an alternative explanation is possible; the scintillator rates could be due to an increase in the low-energy electron component. If the Geiger counter and ion chamber respond primarily to the high-energy electrons (>1.5 Mev) [*Arnoldy, Hoffman, and Winckler*, 1962], the reduction in their rates would indicate a decrease in this component. All this amounts to a very large steepening of the spectrum of electrons.

Consistent with the above interpretation, then, the structure at apogee on pass 17 seen in figure 3*A* could represent the start of the enhancement of the low-energy electrons seen by the scintillator on passes 18 and 19. Evidence that the structure is due to low-energy electrons is that the Geiger counter barely responds to the radiation, whereas the scintillator measures it more efficiently. The ratio of the scintillator rate to the Geiger counter rate at 0614 UT is what would prevail for a monoenergetic beam of 500-kev electrons. Measurements with a low-energy laboratory accelerator have shown that, for a sufficiently large flux of electrons, "pile-up" of low-energy pulses gives a significant efficiency to the scintillator for electrons of energy less than the 200-kev electronic bias (Farley, private communication). Using these data, we can obtain the scintillator to Geiger counter ratio for the maximum rates at 0614 UT by means of a large flux (10^{10} electrons/cm^2 sec) of monoenergetic electrons of 40-kev energy. Because of the long time required per pulse at apogee for the ion chamber, it is not possible to use it to investigate the energy of the radiation.

If the measurements of pass 17 are of low-energy electrons shortly after a sudden commencement, it is of interest to see whether there is any association of such radiation with auroras. If a time and spatial correlation exists between the satellite measurements and the visible aurora we might infer that the detectors observed the energetic component of auroral electrons. We concentrate our attention first on the large rate changes between 0525 and 0622 UT.

Figure 4 is a polar map on which several of McIlwain's L curves [*McIlwain*, 1961] are plotted. These curves may be considered the intersection of the earth's surface and the "L shells" on which trapped particles move, if the guiding center approximation can be used for these particles. Also shown in the figure is the projection of the orbit of Explorer 6 for pass 17 along L shells onto the surface of the earth. The positions of the satellite at 0525, 0600, 0614, and 0618 UT are marked on the trajectory for later discussion.

The all-sky-camera photographs (courtesy of the Upper Atmospheric Research Section, Radio and Electrical Engineering Division, National Research Council, Ottawa, Canada) in figure 3B show the auroral activity at Churchill (geomagnetic longitude 322.7°, geomagnetic latitude 68.7° N) during the time interval 0558 to 0622 UT. Approximate positions of the aurora seen in the photographs at 0614 and 0618 UT are given on the polar map in figure 4. If we consider that in a steady-state aurora primary particles move on an L shell, the aurora is the luminosity produced by the interaction between the particles precipitating from the shell and the upper atmospheric gas at the ionospheric level. Therefore, the projection of the lower border of an auroral arc along lines of force into the earth's surface can be considered an L curve.

From 0525 to 0614 UT the satellite was crossing the successive shells that intersect the earth to the south of Churchill and was moving away from the earth with an average speed of 1.5 km/sec, i.e., toward the Churchill shell of $L=8.5$. However, the aurora in the Churchill all-sky-camera photograph at 0600 UT, if present, was too far south for its location to be determined (Churchill is the only station available for this particular time); thus, no correlative study can be made for the two small scintillator peaks at 0558 and 0602 UT.

Between 0600 and 0608 UT the aurora increased its brightness and started to move northward (typical phenomena in the break-

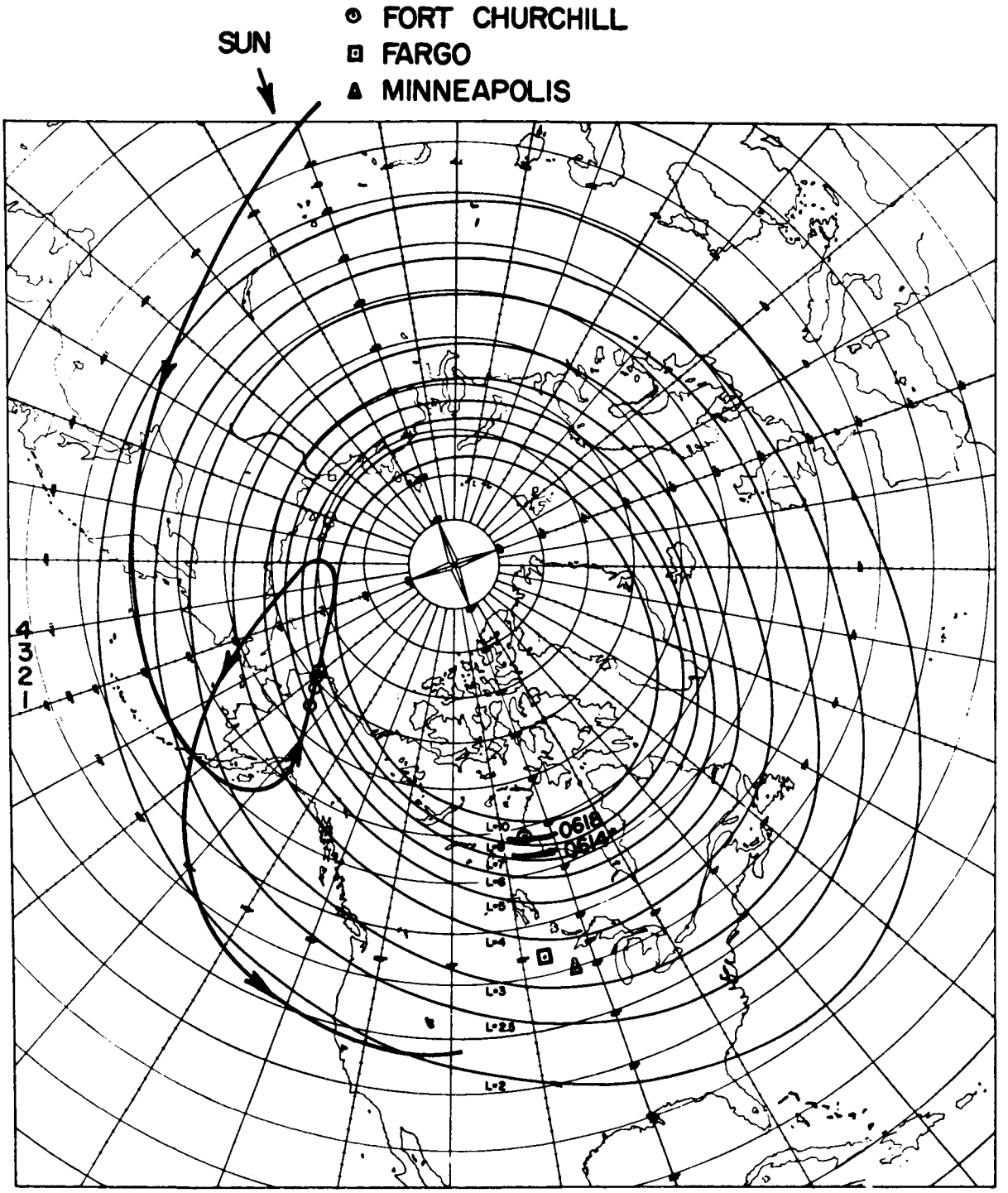

FIGURE 4.—*The intersection of* L *shells with the surface of the earth and the projection of pass 17 along* L *shells to the surface of the earth. The numbers near the left-hand margin refer to the satellite positions during the pass given by the circled points at the following times: (1) 0525, (2) 0600 (3) 0614, and (4) 0618 UT, August 16, 1959. The position of the sun at 0614 UT is indicated at the top of the figure. Approximate positions of the aurora at 0614 and 0618 UT are also shown.*

up of auroras during large magnetic storms [*Akasofu*, 1962]). The northward motion of the aurora can be interpreted to be an outward migration of auroral particles or the auroral disturbance from one L shell to another. The migration speed in the equatorial plane, estimated from motion of the visual aurora, is of the order of 10 km/sec, much faster than the satellite's 1.5 km/sec. In this interpretation, the satellite was apparently overtaken by the auroral disturbance or particles at 0614 UT, when it was on the shell $L = 7.2$, producing the pronounced peak in the scintillator and Geiger counter data. From figure 4 it is seen that the position of the aurora at 0614 UT obtained approximately from the all-sky-camera data coincides with the 7.2 L shell.

At 0618 UT the aurora reached the zenith at Churchill ($L = 8.5$), while the satellite was still on the shell $L = 7.3$. After reaching the zenith at Churchill, the aurora lost its simple curtain form, which is a typical late phase of the break-up. It is seen in the magnetic data from Meanook, Canada, in figure 3*C* that the break-up of the aurora was accompanied by a polar magnetic storm of more than 500 γ (courtesy of the National Research Council, Ottawa, Canada). The irregular count rates after 0614 UT may correspond to the active auroral forms during the break-up, but it is not possible to make a detailed correlation.

In general, satellite measurements involve an inherent uncertainty in that any variation observed could be one of space or time, possibly a combination of both. If the rate fluctuations on pass 17 are time variations, and if the earth's field before the break-up had not been distorted from the quiet-time field so that the L values of figure 4 hold, then the spatial and time correlations of the satellite rates and the visual aurora suggest the possibility that the peak detector rates at 0614 UT were the result of an auroral electron shell passing through the satellite position. Since the satellite measurements were made near the equatorial plane and at a longitude nearly 70° to the west of Churchill, the close time coincidence obtained suggests that we can think of an L shell containing auroral electrons that extends over a large range of longitudes—over at least half the dark side of the earth. The enhancement of the low-energy electrons, perhaps by some acceleration mechanism, must have occurred over a large part of the shell at the same time; it cannot be due to electrons spreading from a point source on the shell, since even 1-Mev electrons take about 3.5 min to drift 90° in longitude. Such a conclusion is supported by the observation of a large auroral X-ray burst at Minneapolis on September 23, 1957 [*Winckler, Peterson, Arnoldy and Hoffman*, 1958], that exactly coincided with the break-up of the aurora in Alaska [*Akasofu*, 1960].

The outward migration of the auroral shell is most likely to be due to an eastward electric field E, according to the relation

$$\mathbf{v} = \mathbf{E} \times \mathbf{H}/H^2$$

where v denotes the migration velocity and H the intensity of the earth's magnetic field. How such an eastward electric field is created and how it is related to an acceleration mechanism for the auroral particles are important problems to which solutions are not currently available. However, a group of low-energy protons and electrons, when they are captured and trapped in the earth's field, will tend to spread in different directions; the protons drift westward and the electrons eastward, producing an eastward electric field, at least for a short time, in the magnetosphere (the break-up of the aurora itself is a transient phenomenon).

There is evidence from the Explorer 7 (1959ι) data that the satellite crossed an auroral shell of electrons at an altitude of 1,000 km on November 28, 1959. Narrow zones of intense radiation were detected over a visible aurora [*O'Brien, Van Allen, Roach, and Gartlein*, 1960]. Our study here indicates that shells of auroral particles probably extend to the equatorial plane at geocentric ranges of more than 40,000 km.

0530–0615 UT, August 17, 1959.

During pass 19 the Geiger counter aboard Explorer 6 showed, superimposed on the general reduction in rate, a sharp decrease in rate (about 30 percent) at 0552 UT on August 17. The satellite was at a geocentric range of 29,400 km and on the shell $L = 4.6$. Simultaneous

observations of the earth's magnetic field made aboard the satellite gave a large deviation of more than 150 γ from the calculated field intensity [*Project Able-3*, 1960]. The Geiger counter data and the magnetic field measurements are shown in figure 5*A* and *B*.

Time-coincident with the sharp reduction in the Geiger counter rate, an aurora at Fargo, North Dakota (geomagnetic longitude 324.4, geomagnetic latitude 56.7° N), became very active at the zenith, undergoing a typical break-up as seen in the all-sky-camera pictures (data from the IGY Data Center A for Instrumental Auroral Observations) in figure 5*C*. The Meanook, Canada, magnetogram in figure 5*D* shows a large polar magnetic storm of more

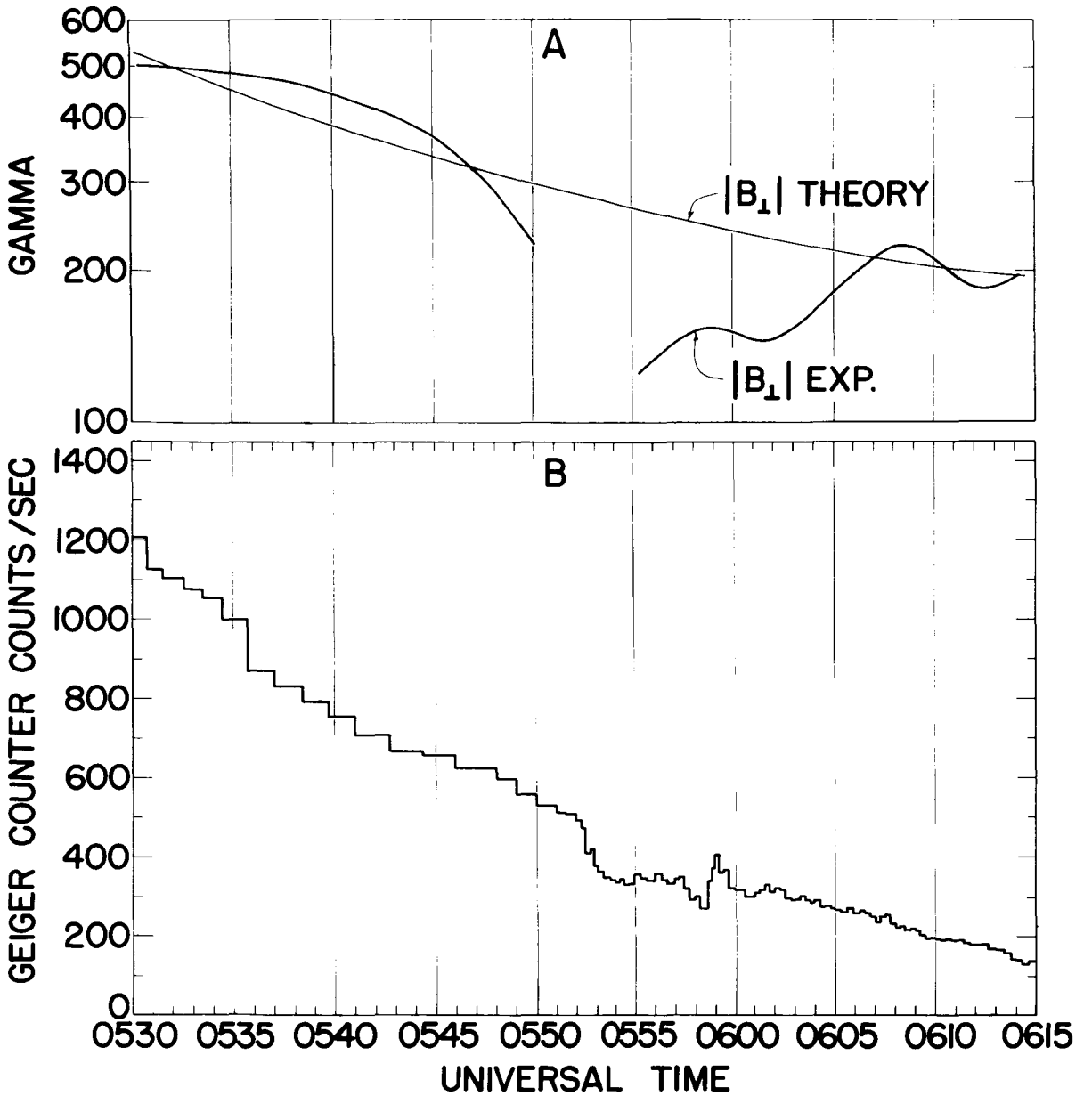

FIGURE 5A and B.—*Magnetometer and Geiger counter data as the satellite moved from a range of 25,700 to 33,000 km on pass 19.*

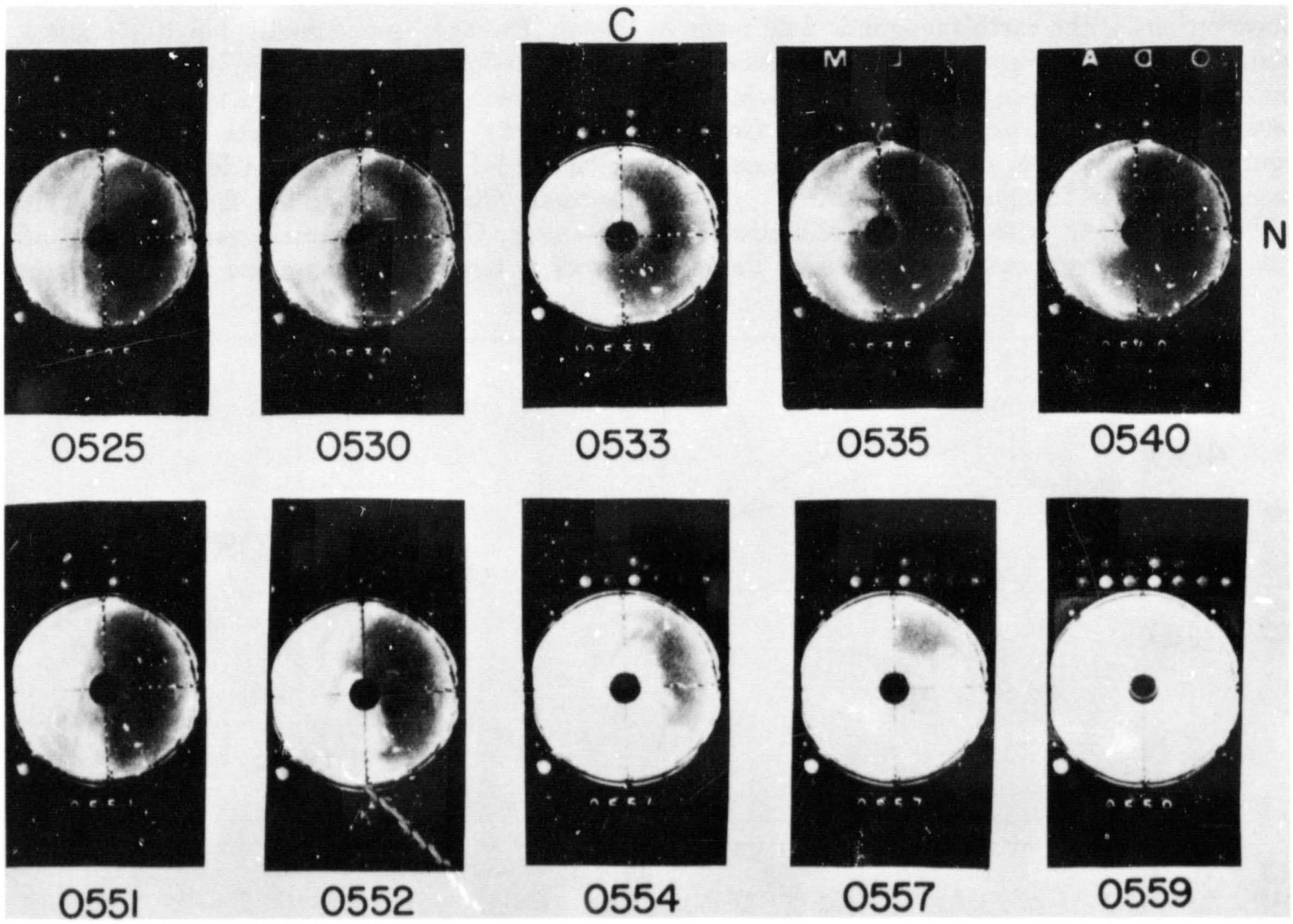

FIGURE 5C.—*Fargo all-sky-camera pictures; positive prints. The direction north is indicated by the* N.

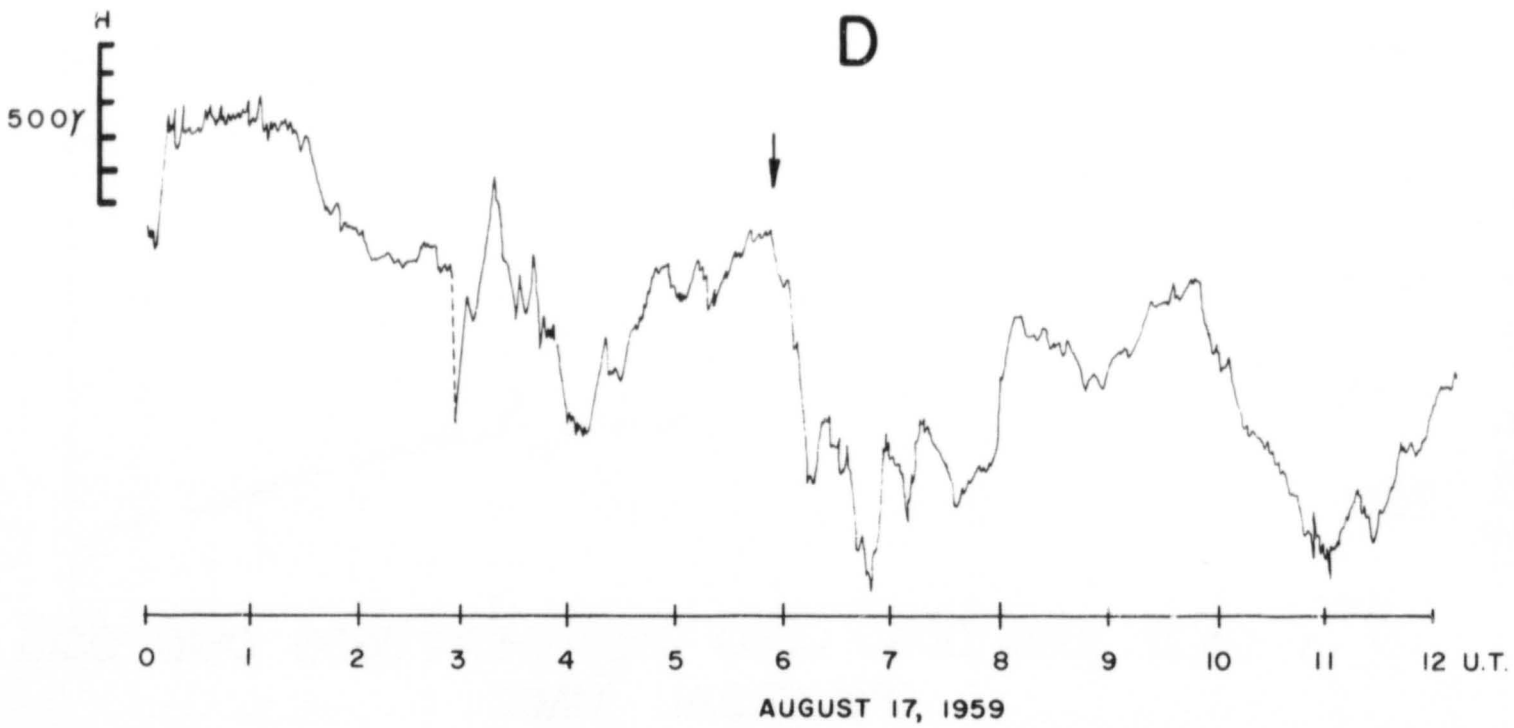

FIGURE 5D.—*The horizontal component of the earth's magnetic field as observed at Meanook, Canada. The arrow indicates the time of the auroral break-up at Fargo.*

than 800 γ at this time. Stations at latitudes lower than that of Fargo did not observe strong auroras; Churchill, through a partial cloud cover, recorded auroral activity in the southern sky during this period. The sharp time coincidence of the auroral break-up at Fargo and the decrease in Geiger counter rate and magnetic field measurements made aboard Explorer 6 suggest an association between the phenomena. In figure 6 are given the positions of the satellite at 0525, 0535, 0552, and 0559 UT in terms of L values. It is seen that at 0552 UT the satellite was at an L of 4.6 that intersects the earth's surface at a more northerly latitude than Fargo's ($L = 3.5$). Assuming a correlation between the satellite data and the Fargo auroral break-up, we can suggest several explanations for the difference in L values. First, there is no way of knowing what rate changes took place on the $L = 3.5$ shell at 0552 UT, since the satellite was not there but moving away from it. The measurement of the rate reduction on the 4.6 shell could be only the edge of a rather broad disturbance that occurred at 0552 UT and was centered about the $L = 3.5$ shell. Second, at 0552 UT the sun was at about 270° and the satellite at 172° W longitude. Since Fargo is at nearly 97° W longitude and at 0552 UT 173° away from the sun, it would lie on the electron shell connecting with the satellite measurements, if the field lines on the night side of the earth were stretched by the solar stream. Last, since the event occurred at about the maximum epoch of the main phase of the magnetic storm, the earth's magnetic field was greatly distorted, so that the two measurements could be nearly connected by the disturbed field.

According to previous measurements of high-altitude X rays observed at low latitudes during auroras [*Winckler, Peterson, Arnoldy, and Hoffman*, 1958; *Winckler*, 1960; *Winckler, Peterson, Hoffman, and Arnoldy*, 1959; *May*, 1961], we can speculate that the auroral activity during this period was of the type that would have X rays associated with it. Unfortunately no high-altitude measurements were made during the 0550 UT auroral event. It has been suggested [*Winckler*, 1960; *Arnoldy, Hoffman, and Winckler*, 1960*b*] that the trapped radiation serves as a source of the primary energetic electrons that produce the high-altitude X rays. The Explorer 6 measurements on pass 19 of a rate decrease in the outer zone time-coincident with active auroral forms might be evidence for such precipitation of particles from the trapped radiation into the atmosphere. From the data on this event, however, we cannot determine quantitatively whether precipitation from the outer zone is adequate to account for the X-ray fluxes observed during similar auroral disturbances. Simultaneous with the precipitation of particles out of the trapping region, and possibly associated with it, there could be acceleration mechanisms operating which supply more particles and energy.

An alternative interpretation of the sudden decrease in counter rate observed during pass 19 must be kept in mind, however; the decrease does not necessarily mean removal of radiation from the trapping region, for the energy of the particles and the efficiency of their detection by the counter could be lowered as a result of betatron deceleration by the changing field.

0900 UT, August 17, 1959

The Fargo all-sky-camera photographs at about 0900 UT on August 17, 1959, show another outburst of aurural activity and a very strong break-up. At the time of break-up, the satellite was at a range between 7 and 8 earth radii and nearly 110° in longitude to the east of the sun-earth line. The fact that the Geiger counter during this time detected no significant intensity of radiation above cosmic-ray background means that fewer than 10^6 electrons/cm^2 sec of 100-kev energy were injected from the solar stream into the earth's field, as measured at the position of the satellite during the aurora, and supports the measurements made aboard the space probe Pioneer 5 [*Arnoldy, Hoffman, and Winckler*, 1960*b*] giving fewer than 10^7 electrons/cm^2 sec of energy greater than 50 kev in a solar cloud in transit to the earth. (In fact, the space probe data are consistent with no energetic electrons in the cloud, since the response of the detectors can be attributed to solar protons that were also in transit to the earth at that

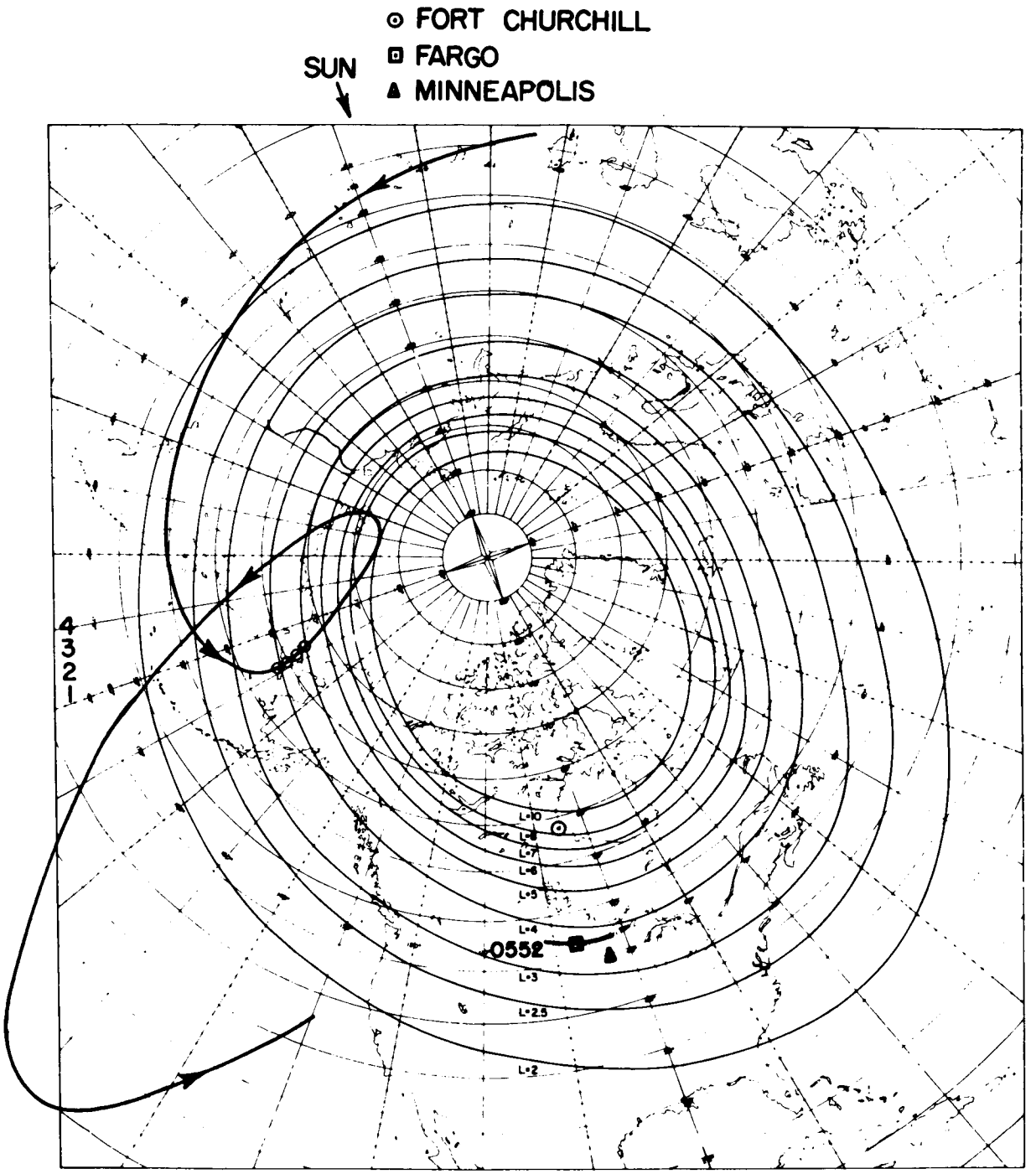

FIGURE 6.—*The intersection of* L *shells with the surface of the earth and the projection of pass 19 along* L *shells to the surface of the earth. The numbers near the left-hand margin refer to the satellite positions during the pass given by the circled points at the following times: (1) 0525, (2) 0535, (3) 0552, and (4) 0559 UT, August 17, 1959. The position of the sun at 0552 UT is indicated at the top of the figure.*

time and were measured by balloon-borne detectors.) If a large number of electrons of such energy are present in the low-latitude aurora, and auroral X rays indicate that there are [*Winckler et al.*, 1958; *Bhavsar*, 1961], we suggest that they must originate from the trapped radiation or be accelerated locally within the confines of the earth's field.

HIGH-ALTITUDE X-RAY BURSTS

During the build-up of the outer zone as measured by the ionization chamber and Geiger counter beginning with pass 20, it was fairly common to observe structure in the outer edge of the trapped radiation and radiation above cosmic-ray background at apogee. During this period high-altitude observations at Fort Churchill by *Anderson and Enemark* [1960] recorded numerous bursts of X radiation that were qualitatively correlated with surface measurements of the magnetic field and cosmic-noise absorption but that in general were not associated with the visible aurora; the two largest X-ray bursts occurred near local noon. In figure 7 are summarized the balloon data and times when Explorer 6 crossed the electron shell connecting with Churchill. Only once was the satellite on the Churchill shell at the time of an observation of high-altitude X rays. This was during pass 21 on the inbound portion of the trajectory, and the Geiger counter measured no significant radiation above cosmic-ray background. The intensity of high-altitude X rays measured at this time, however, was small in comparison with the other bursts observed.

Enhanced rates were recorded near apogee on passes 20 and 22, which occurred after the large X-ray bursts were measured at Fort Churchill at 1800 UT August 17 and 1830 UT August 18, respectively. In figure 8 are plotted the Geiger counter data for pass 20 as the satellite was approaching and returning from apogee. The prestorm rate curves are also given in the figure, and it is seen that from 31,000 to about 43,000 km the rates were above the prestorm level by nearly a constant amount, reflecting the over-all build-up of the outer zone. Starting at about 43,000 km and on out to apogee there was a maximum in the enhanced rates. Radiation above background was observed again on the inbound part of the pass where the background rate is that due to cosmic rays. The Churchill shell is marked on the figure along with several others. The measurements near apogee on pass 22, plotted in figure 9, are similar to those of pass 20.

The satellite was at apogee for passes 20 and 22 in the early evening and before darkness at Churchill, hence we cannot correlate the measurements with the all-sky-camera data taken at this station. Furthermore, it can be seen from figures 8 and 9 that there were no distinct rate maxima on the Churchill shell; rather, the radiation was broadly distributed.

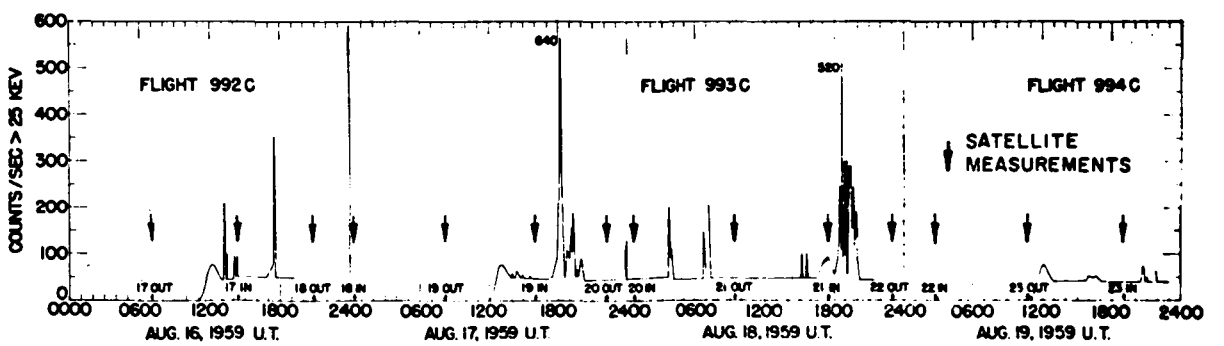

FIGURE 7.—*A time survey of the bursts of X radiation observed by means of balloon-borne scintillators at Churchill, Canada, by K. Anderson. The times when the Explorer 6 satellite was on the electron shell connecting with Churchill for the passes of this period are indicated.*

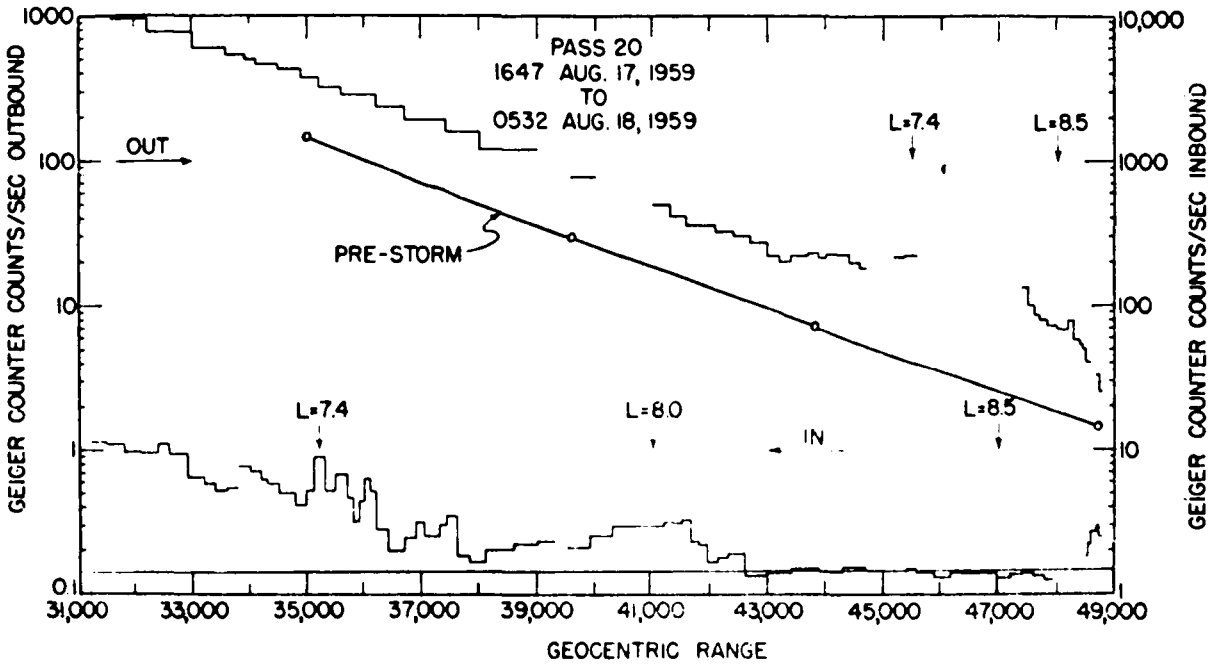

FIGURE 8.—*Geiger counter data as the satellite was approaching and returning from apogee on pass 20. Geiger counter rates as they would have been if prestorm conditions had prevailed are shown by the light curves. The crossing of various electron shells is indicated. The 8.5 shell connects with Fort Churchill, Canada.*

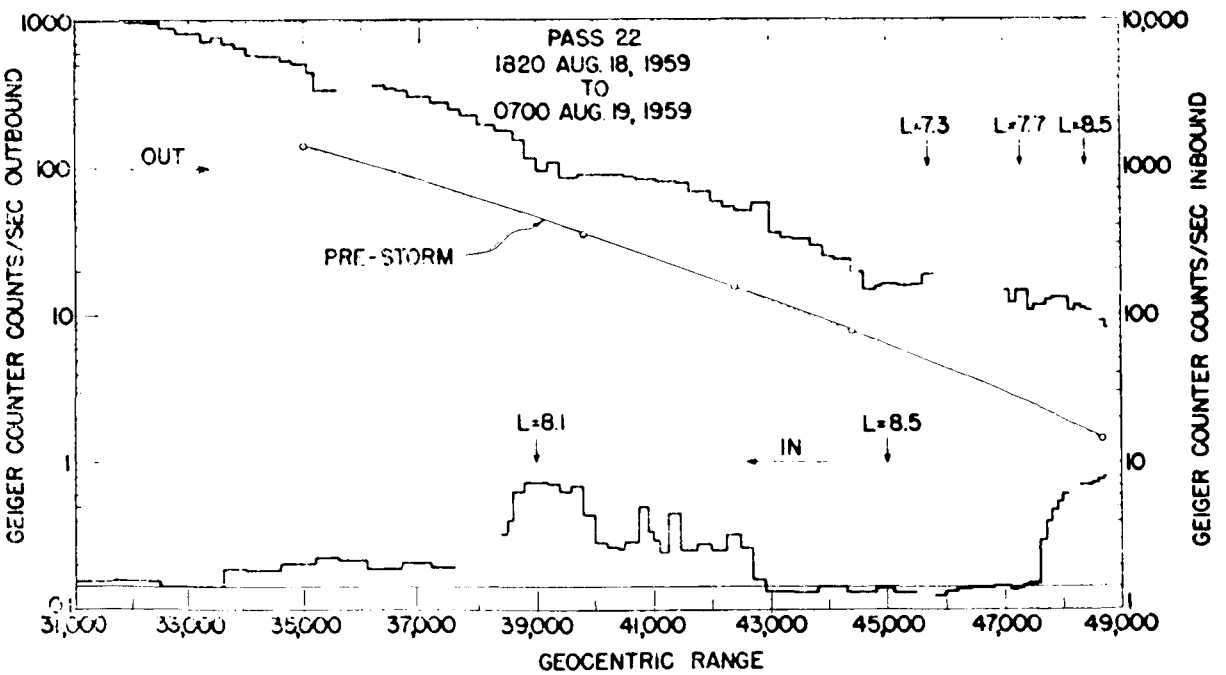

FIGURE 9.—*Geiger counter data as the satellite was approaching and returning from apogee on pass 22. Geiger counter rates as they would have been if prestorm conditions had prevailed are shown by the light curves. The crossing of various electron shells is indicated. The 8.5 shell connects with Fort Churchill, Canada.*

About all that can be said about the measurements of passes 20 and 22 is that they show the great instability of the outer edge of the trapped radiation. During the build-up of the radiation after the minimum of pass 19, energy is supplied to the outer zone. In the ensuing processes some of the radiation is turned into the escape cone and precipitated into the atmosphere. The structure observed on passes 20 and 22 happens to be the state of the radiation at the time of the measurements and after the disturbance that precipitated the large quantity of radiation into the atmosphere producing the high-altitude X rays observed at Churchill.

The frequent occurrence of radiation above cosmic-ray background at apogee and of structure in the outer edge of the trapped radiation indicates that source mechanisms are operative in this region a large percentage of the time. Since this is the region where the solar stream is first influenced by the earth's field it is reasonable that it be very dynamic and disturbed as far as radiation variations are concerned. The frequent precipitation of radiation into the atmosphere as a result of disturbances here is consistent with Anderson's estimate [*Anderson and Enemark*, 1960] that an average flux of 10 photons/cm^2 sec may be present as much as 40 percent of the time at high altitudes for northern latitudes. As was suggested by *Winckler* [1962], since the auroral zone connects with this region, the high-altitude X rays observed in the auroral zone can be expected to differ in average energy, flux, and correlation with auroras from X rays at low latitudes, where their origin might be due to electrons precipitated out of the intense trapped radiation.

Radiation above cosmic-ray background measured at apogee appears to be trapped; i.e., it will often be observed on the same electron shell during the outward and inward parts of a pass and, occasionally, on the same shell during the next pass some 10 to 12 hours later. However, the radiation is observed to have a sharp boundary on the shell that crosses the equatorial plane at 54,000 km, for the detector rates drop sharply to cosmic-ray background beyond this shell. It is likely that this boundary represents the termination of the earth's field, as far as its ability to trap radiation is concerned.

ACKNOWLEDGMENTS

We are indebted to Mr. Karl A. Pfitzer and Mr. Richard Brown for their assistance in the read-out of the raw data. We wish to acknowledge the fine engineering work of Mr. Robert Howard, who designed and built the electronic circuitry for the University of Minnesota experiment.

This work was supported by the National Aeronautics and Space Administration under contract NASw-56.

REFERENCES

Akosofu, S.-I., The ring current and the outer atmosphere, *J. Geophys. Research*, *65*, 535–544, 1960.

Akasofu, S.-I., Large-scale auroral motion and polar magnetic disturbances, 2, The changing distribution of the aurora during large magnetic storms, *J. Atmospheric and Terrest. Phys.*, in press, 1962.

Anderson, K. A., and D. C. Enemark, Balloon observations of X rays in the auroral zone, 2, *J. Geophys. Research*, *65*, 3521–3538, 1960.

Arnoldy, R. L., R. A. Hoffman, and J. R. Winckler, Observations of the Van Allen radiation regions during August and September 1959, 1, *J. Geophys. Research*, *65*, 1361–1376, 1960*a*.

Arnoldy, R. L., R. Hoffman, and J. R. Winckler, Solar cosmic rays and soft radiation observed at 5,000,000 kilometers from earth, *J. Geophys. Research*, *65*, 3004–3007, 1960*b*.

Arnoldy, R. L., R. A. Hoffman, and J. R. Winckler, Observations of the Van Allen radiation regions during August and September, 1959, 4, The outer-zone electrons, *J. Geophys. Research*, *67* (7), 1962.

Bhavsar, P. D., Scintillation counter observations of auroral X-rays during the geomagnetic storm of May 12, 1959, *J. Geophys. Research*, *66*, 679–692, 1961.

Fan, C. Y., P. Meyer, and J. A. Simpson, Dynamics and structure of the outer radiation belt, *J. Geophys. Research*, *66*, 2607–2640, 1961.

Farley, T. A., and A. Rosen, Charged-particle variations in the outer Van Allen zone during a geomagnetic storm, *J. Geophys. Research*, *65*, 3494–3496, 1960.

May, T., A study of auroral X rays at Minneapolis between 23 August 1959 and 1 August 1960, *Cosmic Ray Tech. Rept. CR-36*, Cosmic Ray Group, University of Minnesota, Minneapolis, 1961.

McIlwain, C. E., Coordinates for mapping the distribution of magnetically trapped particles, *J. Geophys. Research*, *66*, 3681–3692, 1961.

O'Brien, B. J., J. A. Van Allen, F. E. Roach, and C. W. Gartlein, Correlation of an auroral arc and a subvisible monochromatic 6300 A arc with outer-zone radiation on November 28, 1959, *J. Geophys. Research*, *65*, 2759–2766, 1960.

Project Able-3, Final Mission Rept., vol. 2, STL/TR-59-V002-02903, Space Technology Labs., August 1960.

Rosen, A., and T. A. Farley, Characteristics of the Van Allen radiation zones as measured by the scintillation counter on Explorer 6, *J. Geophys. Research, 66*, 2013–2028, 1961.

Rosen, A., T. A. Farley, and C. P. Sonett, Soft radiation measurements on Explorer 6 earth satellite, in *Space Research: Proc. First Intern. Space Sci. Symposium*, pp. 938–950, North-Holland Publishing Co., Amsterdam, 1960.

Winckler, J. R., Balloon study of high altitude radiations during the International Geophysical Year, *J. Geophys. Research, 65*, 1331–1359, 1960.

Winckler, J. R., Atmospheric phenomena, energetic electrons, and the geomagnetic field, *Radio Propagation, 66D*, 127–143, March-April, 1962.

Winckler, J. R., L. Peterson, R. Arnoldy, and R. Hoffman, X-rays from visible aurorae at Minneapolis, *Phys. Rev., 110*, 1221–1231, 1958.

Winckler, J. R., L. Peterson, R. Hoffman, and R. Arnoldy, Auroral X rays, cosmic rays, and related phenomena during the storm of February 10–11, 1958, *J. Geophys. Research, 64*, 597–610, 1959.

(Manuscript received June 18, 1962.)

Observations of the Van Allen Radiation Regions during August and September 1959[1]

6. Properties of the Outer Region

BY R. A. Hoffman,[2] R. L. Arnoldy,[3] and J. R. Winckler[3]

School of Physics
University of Minnesota

This last in a series of six papers summarizing the results of measurements with ion chamber and Geiger counter instruments aboard the Explorer 6 satellite discusses the general intensity, structure, and shape of the outer radiation region as displayed by contours of constant counting rate from the Anton Geiger counter. These contour plots show the large variation in counting rate, volume, and structure to which the outer radiation region is subjected during magnetic activity. Frequently two maximums are observed in the outer zone. It is shown that the depth of the minimum between these maximums as a function of altitude is an argument against any earth surface magnetic anomaly as the cause of the minimum in intensity. An explanation given previously is again suggested, namely, that the minimum is a result of changing spectrum of the trapped electrons, together with the spectral response of the counting instruments. By using the Geiger counter rate along a magnetic line of force, together with the ionization rate ratio, to determine the constancy of the spectrum, pitch-angle distributions at the equatorial plane are derived. The equatorial pitch-angle distribution is unfolded by means of a form of Able's integral equation with a mathematical approximation to the counting rates as a function of magnetic field strength. The pitch-angle distribution is derived before and after a large magnetic storm. Finally, a discussion of properties of the outer radiation zone during magnetically quiet times and the changes associated with a series of magnetic storms during August and September are discussed in detail. It is concluded that major intensity changes always correlate with solar activity, a time delay indicating the coupling by means of solar plasma beams. Intensity changes are independent of the occurrence of a Forbush type decrease caused by the plasma cloud. Counting rate changes during storms mainly associated with energetic electrons near 1 Mev are observed. Counting rates near the equator decrease for all lines of force if the storm has a main phase. Sometimes the decrease near the equator is accompanied by an increase near the atmosphere showing the lowering of mirror points. The percentage decreases are larger for lines of force at large radial distances. Large decreases on all lines of force are accompanied by widespread aurora. Counting rate increases occur during the recovery phase of magnetic storms and are apparently due to a local acceleration mechanism. The increased flux consists of particles having large pitch angles with a spectrum similar to that of the prestorm conditions. This paper includes a summary of conclusions, that are thought to be of continuing interest, from all six papers in the series.

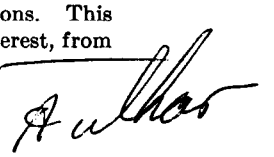

---

[1] Published in the November 1962 issue of *Journal of Geophysical Research*. Reprinted by permission.
[2] Now at NASA Goddard Space Flight Center.
[3] Now at Honeywell Co.

This sixth and last in the series of analyzing data received from the University of Minnesota ion chamber and Geiger counter experiment aboard Explorer 6 satellite (launched August 7, 1959) investigates, first, the properties of the outer radiation region that can be ascertained when the time variations of the earth's magnetic field are at a minimum, and, second, the variations of the properties of the trapped radiation during magnetic storms.

ELECTRON ENERGY RANGE OF RESPONSE

It may be well to review briefly the energy ranges of electrons in the outer region to which the detectors are thought to be responding. In the most extensive analysis to date of the responses of the Explorer 6 detectors (part 2, *Arnoldy, Hoffman, and Winckler* [1962]), we concluded that at 11,000 km the data require electrons of energy 5 Mev or larger with an assumed differential power-law spectrum fit to the data having an exponent between 2 and 3. Furthermore, the spectrum steadily steepens with range, whereas the high-energy limit decreases out to 26,500 km, where the best fit to the data gives a cutoff at about 3.5 Mev. The detectors are relatively insensitive to low-energy radiation when energetic electrons exist. Beyond 26,500 km the spectrum is thought to continuously steepen with an increasing contribution of bremsstrahlung to the detector rates. The nature of the spectrum with range, however, has been attained by fitting trial spectrums to the data and is, therefore, not a unique determination.

The Explorer 7 detectors, which measure the low- and high-energy radiation separately, are clarifying this entire response problem [*O'Brien, Van Allen, Laughlin, and Frank*, 1962]. However, for the purpose of this study, it can be said that the properties of the outer region derived here will pertain primarily to the high-energy electrons.

SEQUENCE OF GEOPHYSICAL EVENTS

To orientate the reader to the sequence of geophysical events during the lifetime of Explorer 6 telemetry, reference is made to figure 1, in which a number of observations are plotted as a function of time. The top curve shows the maximum counting rate of the Geiger counter in the outermost maximum of the outer region for those passes having data within $\pm 10°$ of latitude about the magnetic equator. The second curve is the daily mean of the horizontal component of the earth's magnetic field as measured by the Honolulu, Hawaii, observatory (obtained from the I.G.Y. World Data Center A, Cosmic Rays, University of Minnesota). The next histogram is the daily average counting rate from the Deep River neutron monitor (courtesy of Hugh Carmichael, through Data Center A, Cosmic Rays. At the bottom of the figure are indicated the specific periods that will be discussed in detail.

SHAPE OF THE OUTER RADIATION REGION

The general intensity, structure, and shape of the outer radiation region can be displayed by means of contours of constant counting rate from the Geiger counter. Because of the high ellipticity of the orbit of the satellite, and because, with respect to the geomagnetic axis of the earth, the orbits swing northward and southward in latitude on successive passes, a large part of the radiation region was swept out in a period of several days, affording the opportunity to plot the details of the distribution of particles in space that are accessible to the instruments. Three such contour plots on geomagnetic meridian planes in rectangular form appear in figure 2. To obtain a consistent set of data for a plot, time periods were selected when magnetic activity was low. Data were plotted on either side of the quietest time until the points showed a general variation. Then the averaging contour lines were drawn to the best fit to the points.

The top diagram of figure 2 includes data from the first 15 passes of the satellite, from August 7 through August 14, 1959. This period of observation displayed for the first time three distinct maximums in counting rates for the radiation detectors. The first of these, evident at about 8000 km range and $-30°$ magnetic latitude, can be identified with the inner zone. The second and third are seen at about 17,000 km and 22,500 km range near the equator; they comprise the outer zone.

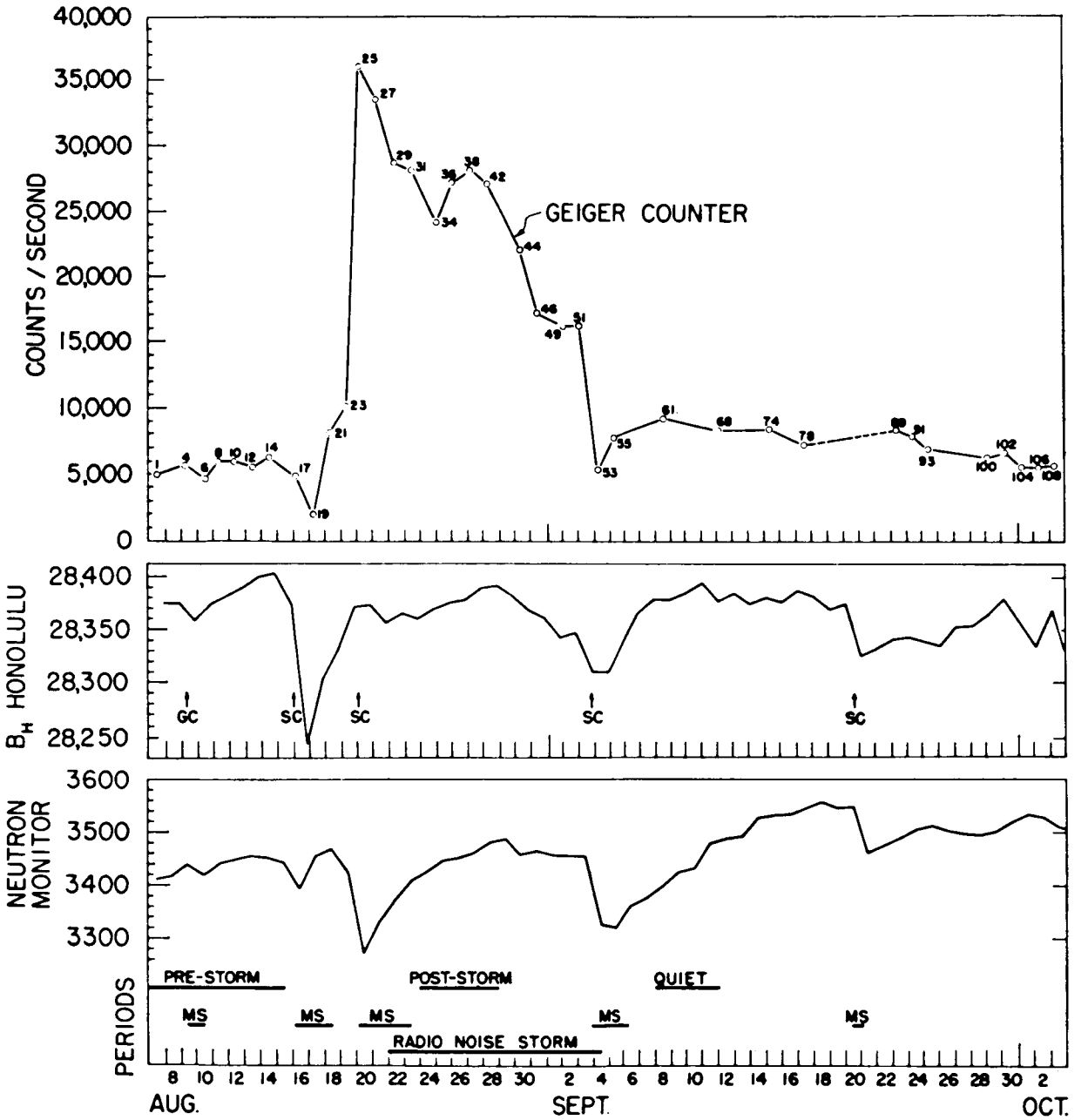

FIGURE 1.—*Time correlation of measurement during lifetime of Explorer 6 transmitters.* Top: *Geiger counter rate at outermost maximum in the outer belt.* Second: *daily average of earth's magnetic field.* Third: *daily average of bi-hourly counting rate from Deep River neutron monitor.* Bottom: *periods of interest.*

The second contour plot encompasses passes 32–43 in the period August 24–30, and is labeled "post-storm" in figure 1. Between these first two quiet periods, two magnetic storms occurred whose end result was an increase in counting rate of the detectors in the outer region to five times the prestorm value. The second and third maximums were still discernible at northern latitudes, but near the equator only one broad maximum in counting rate appeared.

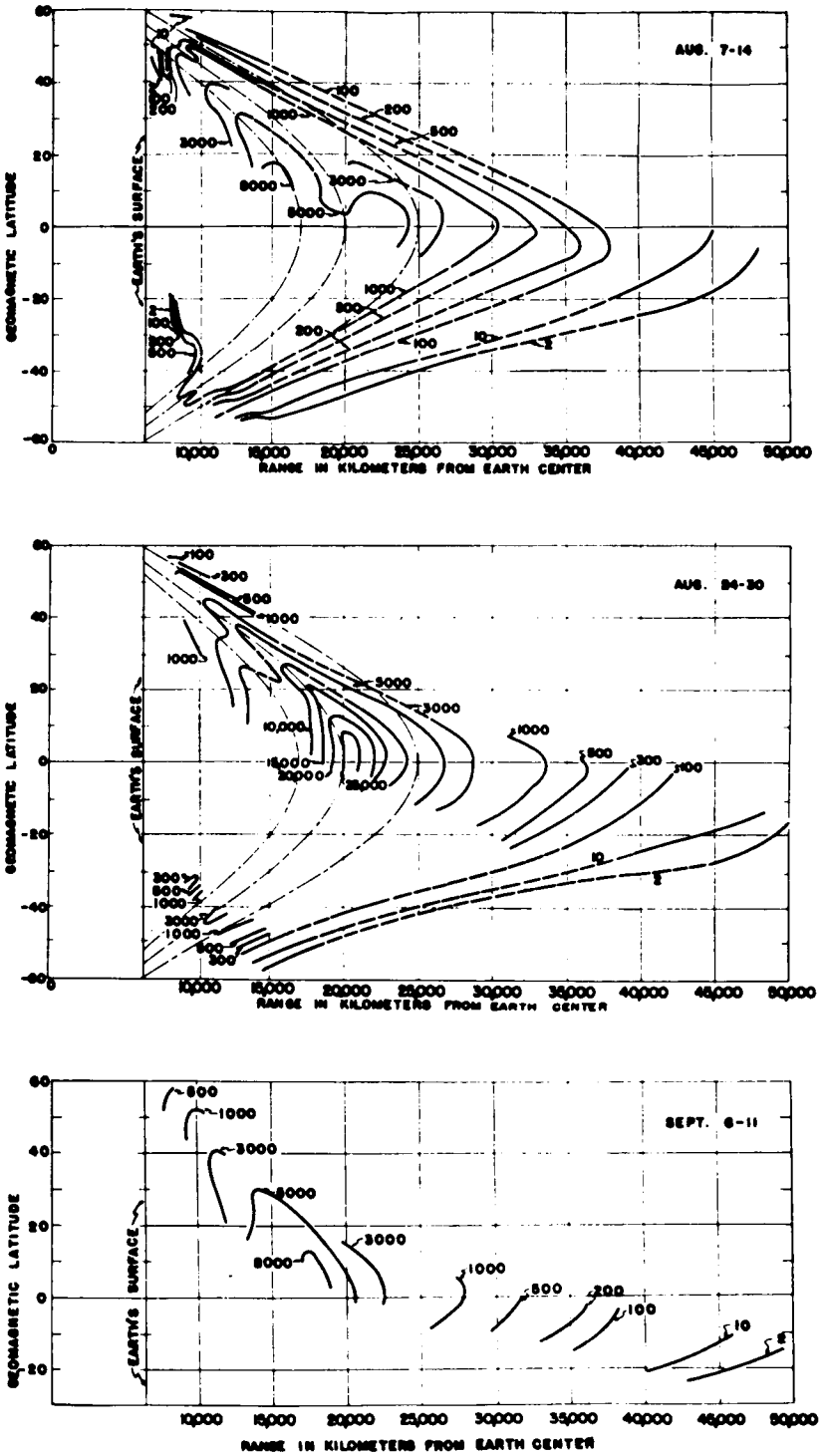

FIGURE 2.—*Rectilinear plots of contours of constant counting rate of the Geiger counter during magnetically quiet times.*

After some rather intense magnetic activity during the first few days of September, the trapped radiation stabilized to the intensities shown in the bottom plot, which includes passes 57–67 from September 6–11. Although the contours are very incomplete, the very striking observation was made that the outermost maximum had completely disappeared, whereas the initially second maximum had retained an intensity comparable to the August 7–14 period.

During the last half of September, the magnetic indices rose to values sufficiently high so that variations in intensity of the outer region might be expected. During the last week and a half of September, after a storm on the 20th, there was a slow emergence of another broad maximum at about 27,000 km at the magnetic equator, although it took almost a week before it showed as an actual maximum on passes even 10° off the equator.

This series of contour plots displays most impressively the large variations in counting rate, volume, and structure to which the outer radiation region is subjected during magnetic activity.

However, to attach quantitative significance to the contour plots we must consider the spectral response of the instruments as well as the value of the counting rate. Positions may be found on the contour plots for which the ratio of chamber to counter rates is the same. For example, it will be shown in the section on pitch-angle distributions that this condition prevails along a given line of force until altitudes near the atmosphere are reached. This observation means that over the range of energies which contribute predominantly to the response of the detectors the spectral form is constant. Suppose that the differential energy spectrum over this energy range is given by $dN/dE=N_0f(E)$, where $f(E)$, some function of energy, is the spectral form. Then the counting rate of the counter is proportional to the intensity factor N_0. Therefore, if the spectrum is known at any point on a line of force, such as those indicated in part 4, the spectrum is also found at any other point on the same line of force by merely adjusting the intensity factor by the ratio of the counting rates at the two points These counting rates can be read from the contour plots.

Whether the two maximums in the outer zone are a general feature is difficult to say. Of the 61 days of telemetry from Explorer 6 they were present at the equator 46 days, as closely as can be ascertained, or 75 per cent of the time. Pioneer 3 (December 6, 1958) [*Van Allen and Frank*, 1959], on the outbound leg of its trajectory, showed a slight inflection in the counting rate of the Geiger counters versus range through the belt, but no actual minimum. On the inward portion of the trajectory the next day there was seen even less sign of inflection. Mechta 1 [*Vernov et al.*, 1959], on January 2, 1959, also showed a somewhat large inflection in its scintillator and total ionization crystal, but again no actual minimum. No data were received from Pioneers 6 and 5 in this region.

If all, or at least an overwhelming majority of, the electrons in the outer region have the same source, the occurrence of a minimum in the distribution in space is a puzzling phenomenon. Some discussion has appeared concerning the minimum, and additional experimental evidence is available regarding its properties.

The Capetown Anomaly and the Outer-Zone Minimum

The effect of the Capetown magnetic anomaly on the trapped radiation has been debated in the literature, and part 2 [*Hoffman*, 1961] of this series brings the reader to the current state of the discussion: assuming the validity of present magnetic data, the particles affected by the anomaly do not have trajectories that would pass through the position of the experimentally observed minimum in the outer zone, but are probably almost an earth radius too low. However, a comparison between the current United States charts of total magnetic field and a recent magnetic survey of the area west of Capetown indicates considerable error in the field contours for 1955. Therefore, the next step in this anomaly discussion is necessarily a determination of the exact location and shape of the anomaly.

765-698 O-65—13

Altitude Dependence of Depth of the Outer-Zone Minimum

A study of the depth of the minimum as a function of altitude also produces another argument against an earth magnetic anomaly causing the outer-zone minimum. If the electrons in the outer zone were to have their source in the decay of albedo neutrons, and the minimum in the belt were due to particle loss in the Capetown anomaly, the depth of the minimum would show an altitude dependence: the minimum would be more pronounced near the atmosphere than at large distances on the magnetic-field shell that passes through the anomaly [*Dessler and Karplus*, 1960].

The orbit of Explorer 6 was ideal for this study. For example, the minimum in counting rate of the Geiger counter on the outbound part of pass 12 through the outer belt was obtained at a range of 20,200 km at a magnetic latitude of 3° N and geographic longitude of 89.1° E, whereas the minimum in rate on the inbound portion occurred at a range of 11,200 km at a magnetic latitude of 42.5° S and geographic longitude of 72.6° E. Thus the outbound portion lay close to the equator for large radial distances and the inbound portion crossed many shells at fairly constant low altitude.

To compare the profiles of the belt at the two different altitudes, it is desirable to plot the counting rates of the counter for both the outbound penetration of the belt and the inbound as a function of a common coordinate of range. Such a coordinate is the range at which the magnetic field shells cross the equator in the longitude region of 72° to 89° E. However, only two such shells, based on the 48 coefficient expansion to the field, were available (through the courtesy of Dr. Paul Kellogg, University of Minnesota), one having a maximum range of 24,500 km (the magnetic equator for this shell) and the other of 17,090 km. To obtain the equatorial magnetic shell ranges of all the other points along each part of the trajectory, the dipole equatorial ranges were compared with the two magnetic shell ranges to determine the accurateness of the dipole approximation to the earth's true field. Then all dipole ranges in between were adjusted to magnetic shell ranges by a linear interpolation, $R = AR' + B$, where R' are the dipole ranges.

For the outbound portion of pass 12, the adjusting equation was

$$R = 0.920\ R' + 1{,}650 \text{ km}$$

For the inbound portion,

$$R = 1.004\ R' + 10 \text{ km}$$

In figure 3 the counting rates of the Geiger counter versus the magnetic shell ranges are plotted for both the outbound and inbound parts of pass 12. The three hourly K_p magnetic indices did not exceed 2° during the 12 hours between the two intersections of the belt.

The upper part of the figure shows the ratio of inbound to outbound rates on a given shell (shell range at equator plotted as abscissas). If the trapped radiation were preferentially removed at low altitudes by the magnetic anomaly, and if this were the cause of the minimum in the outer zone, a marked decrease in the inbound to outbound ratio should occur at a

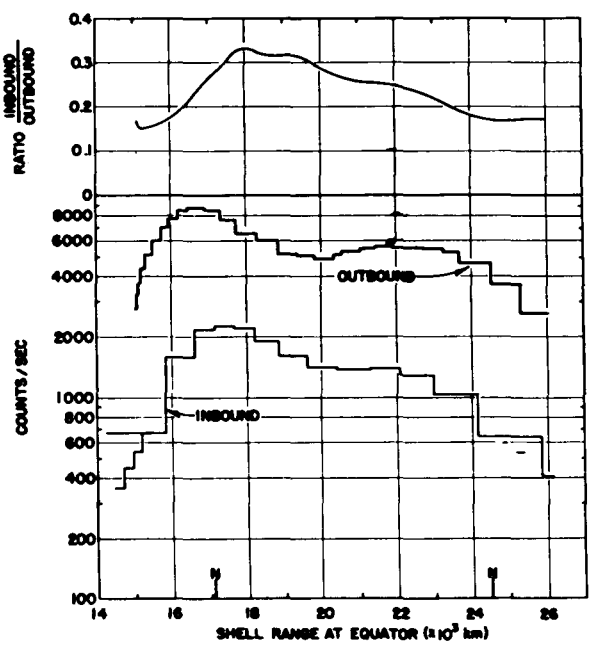

FIGURE 3.—*Comparison of the profiles of the outer belt at two different altitudes during pass 12 to study the altitude dependence of the outer-belt minimum.*

shell range corresponding to the outer-zone minimum. We note that actually the ratio curve in figure 3 smoothly changes through this region with no minimum. Thus the altitude dependence sampled at two points along each shell corresponding to the satellite trajectory fails to show a strong alteration of mirror-point distribution on the shell corresponding to the outer-zone minimum consistent with the continual removal of radiation at the anomaly. As can be clearly seen in figure 3, however, the ratio is not constant but increases to a maximum at a shell range of 18,000 km, then decreases slowly through the outer zone. This smooth variation with range appears to be the result of the increasing concentration of particles near the equator with increasing shell range (see part 4) and the changing altitude at which the radiation was sampled along the inbound orbit.

To compare directly two Geiger counter rates, it is necessary that the spectrum of particles in which the payload is immersed be the same at the two points of comparison, and only the intensity be different. As was explained previously the ratio of the chamber to counter rates is a measure of the shape of the spectrum. Therefore, it is desirable to compare this ratio for the outbound and inbound excursions through the belt on the same type of magnetic shell range coordinate as that used in figure 3. Figure 4 has such a comparison, and it is seen, especially at the location of the minimum, that the ratios are identical, and counting rates should be proportional to particle intensities.

Possible Cause of the Outer-Zone Minimum

An alternative explanation of the minimum, which we have advocated for some time (*Arnoldy and Winckler* [1960]; *Arnoldy, Hoffman, and Winckler* [1962]), is a spectrum of trapped electrons changing with range. The total intensity continually increases between the two observed maximums, but their spectrum steepens and the maximum energy of the electrons decreases. Most radiation detectors flown, including all four on Explorer 6, have a rapidly increasing efficiency with increasing energy. Therefore, the decrease in counting rate past the inner maximum is caused by a loss in that part of the counting rate contributed by the high-energy electrons not being offset by the increased intensity of the lower-energy electrons. Beyond the minimum, the increase in number of lower-energy electrons contributes more counts to the counter than are being lost from reduction in only the high-energy electrons, so another maximum is eventually reached.

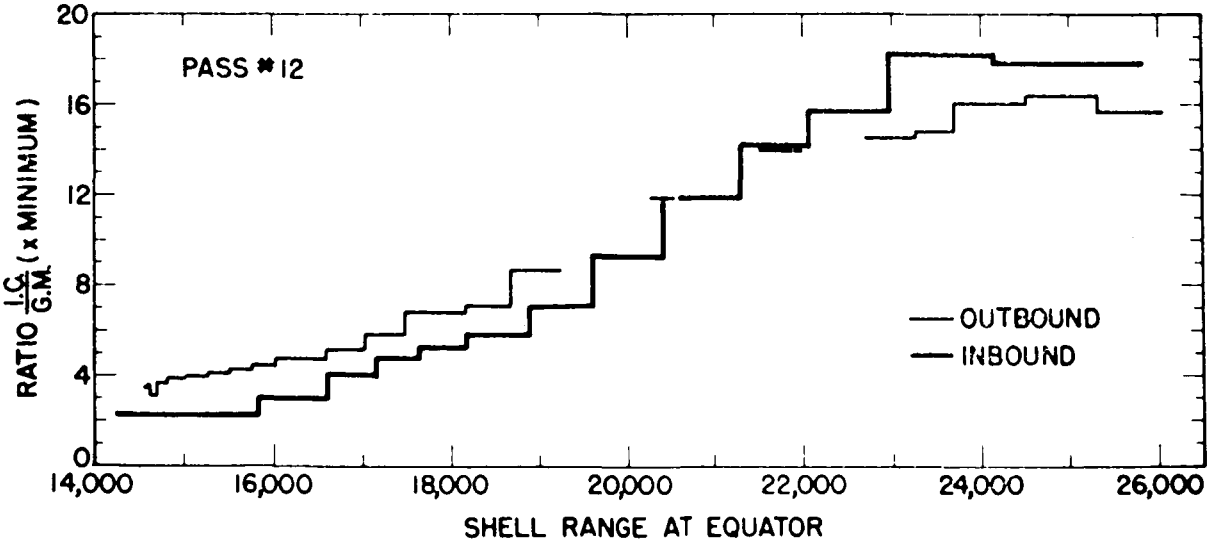

FIGURE 4.—*Comparison of ratios of chamber to counter counting rates along the two profiles of the outer belt during pass 12.*

Another explanation is that the distribution is merely the result of the injection, acceleration, and perturbing mechanisms operating in the outer magnetosphere. The region of the outermost maximum and beyond undergoes much larger time variations than the region of the inner maximum, so the number and position of the maximums observed during the quiet period following a storm is a reflection of the distribution of mechanisms that are perturbing the trapped particles during the storm.

PITCH-ANGLE DISTRIBUTIONS

Further properties of the outer-belt electrons can be derived from a study of their mirror-point and pitch-angle distributions as a function of range and time. The results of such a study provide requirements for any possible injection, acceleration, and precipitation mechanisms.

Intensity along Lines of Force

Because the guiding centers of the particles trapped by the earth's magnetic field follow the lines of magnetic force, it is possible to obtain the pitch-angle distribution of the particles from a plot of particle intensity as a function of magnetic field strength along a line of force.

As was discussed earlier, the Geiger counter rate is interpreted as proportional to the flux of electrons in the energy range that contributes significantly to the counting rate of the counter. However, if the constant of proportionality does not change with distance along a line of force, which will be true if the spectral shape remains constant, then the relative change in counting rate down a line of force suffices for obtaining the relative pitch-angle distribution. Now there is no a priori reason to believe that the spectrum remains constant, so again the ratio of chamber to counter rates down the force lines must be studied to justify the constancy of the spectral shape. If the ratio, and therefore the spectral shape, remains constant, then the mirror-point distribution is independent of energy.

The earth-centered dipole approximation is used for the magnetic field lines. Since the satellite orbit slowly precessed around the earth and swung northward and southward with respect to the geomagnetic axis, the satellite crossed a given dipole line or shell at various points for a series of passes.

For obtaining the pitch-angle distribution from the counter rate down a line of force it is more useful to plot the counter rate as a function of field strength than of magnetic latitude or altitude. The field strength can be obtained from the magnetic latitude by the equation

$$\overline{B} = \frac{B}{B_0} = \frac{(1 + 3 \sin^2 \wedge)^{1/2}}{\cos^6 \wedge}$$

where $\wedge$ is the geomagnetic latitude, B_0 is the field strength at the magnetic equator, and B is the field strength at a latitude $\wedge$.

Figures 5, 6, and 7 show the counting rates of the counter as a function of $\overline{B}$ for the dipole lines of force 17,000 km, the inner maximum, 22,400 km, the outer maximum, and 28,000 km in the lower parts of the figures, and the ratio of the ion chamber to counter rates in the upper parts for passes 1–15, labeled "prestorm" in figure 1. Data were not used in the approximate longitude range 250° E to 80° E for a latitude south of about 30° N magnetic in order to make a better fit of the dipole to the true field. In this region the mirror points dip closer to the earth's surface than the average over the rest of the earth. Though the ratio points do scatter, especially for the higher $\overline{B}$ values, it is judged that the pitch-angle distributions are energy-independent enough so that it is worthwhile to derive the distributions from the data. A part of pass 7 was almost tangent to the 22,400-km field line, though at a slightly greater range. The ratio is especially useful in this pass, since it shows an excellent constancy with $\overline{B}$. The ratio is somewhat higher than the other points plotted because the ratio rapidly increases with equatorial dipole range in this region. It was also shown in the study of the depth of the outer-belt minimum as a function of altitude that the ratio was the same on a given magnetic shell for the outbound and inbound intersections of the outer zone.

Figure 8 has curves approximating the counting rates versus $\overline{B}$ for five lines of force. The important feature to notice is the progres-

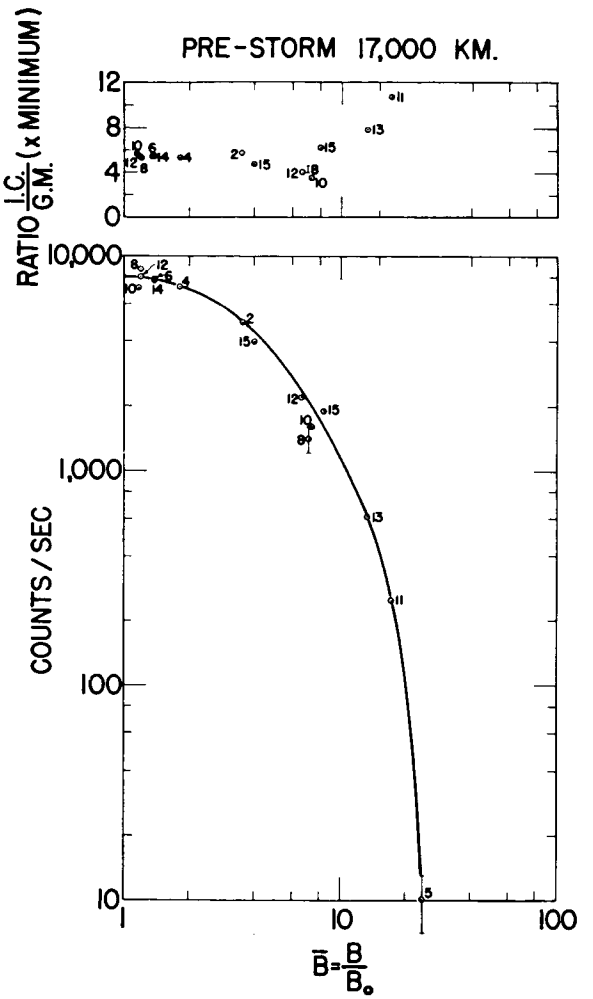

FIGURE 5.—*Counting rate of the Geiger counter as a function of* $\bar{B}$ *(bottom) and ratio of ion chamber to counter rates versus* $\bar{B}$ *(top) for the dipole line of force 17,000 km, passes 1–15, August 7–15, 1959.*

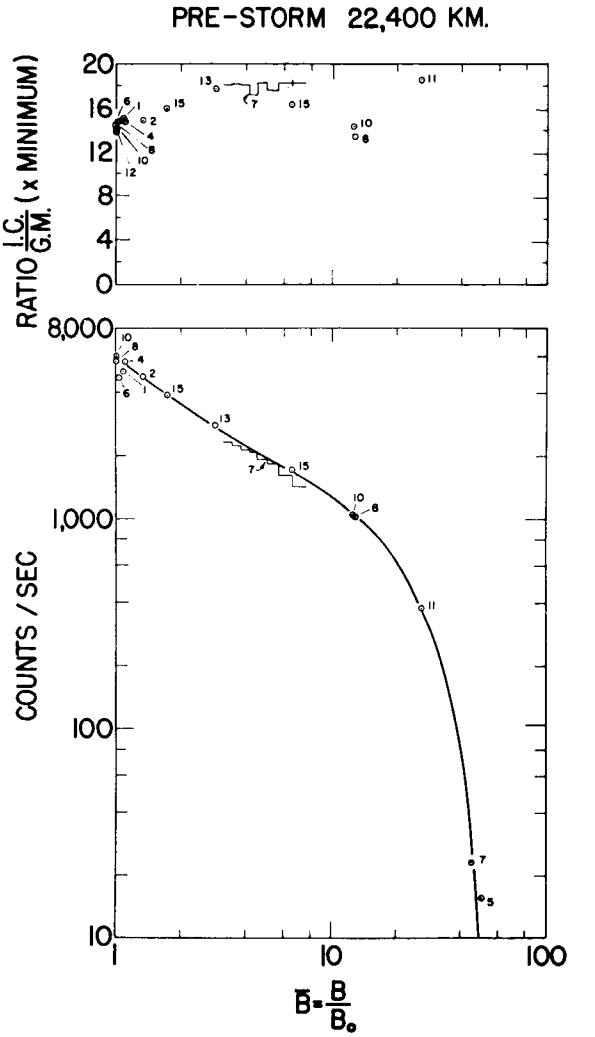

FIGURE 6.—*Same as figure 5 except for 22,400-km dipole line.*

sive concentration of particles toward the magnetic equator with increasing range. However, the energy spectrum of those particles near the equator is apparently the same as those particles contributing to the "knee" at about $\bar{B}$ equal to 10, as judged by the constancy of the ratios as observed in figures 5, 6, and 7.

Figures 9 and 10 contain the counting rate of the counter as a function of $\bar{B}$ for the dipole lines of force 17,000 km and 22,400 km during the "post-storm" period in figure 1. Since no data were available during this period for $\bar{B} > 6.5$ for the 17,000-km line, figure 9 contains points from passes 25–30 for the larger $\bar{B}$ values. It will be seen later that the intensities for large $\bar{B}$ do not fluctuate appreciably during smaller magnetic disturbances. There were insufficient data to construct a similar plot for the 28,000-km line of force after the storms.

Pitch-Angle Distributions

From the data curves in figures 5, 6, 7, 9, and 10 it is possible to derive the pitch-angle distributions of the outer-belt electrons at the magnetic equator.

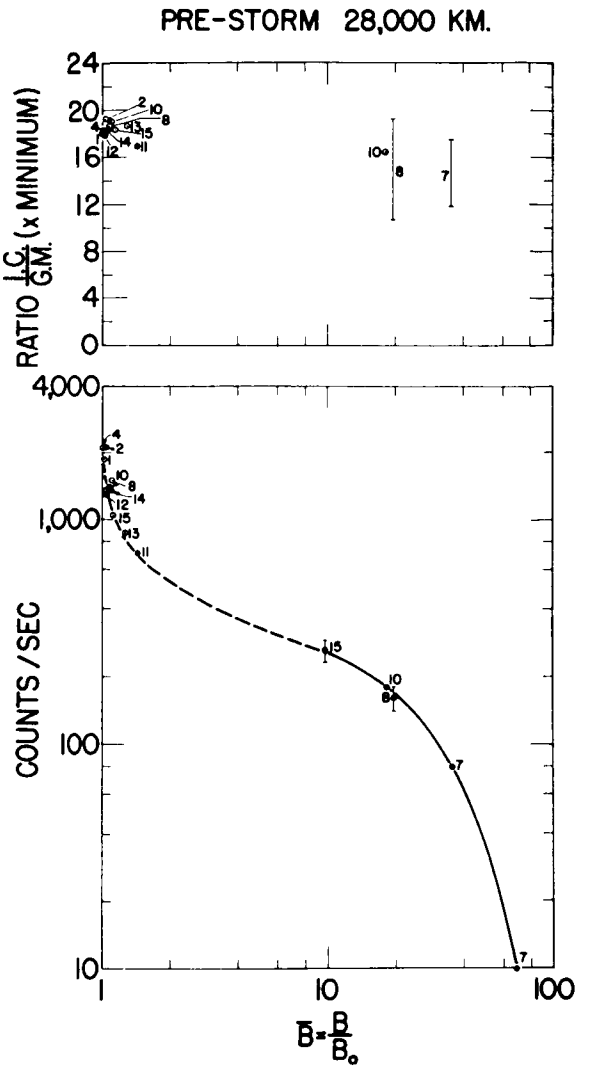

FIGURE 7.—*Same as figure 5 except for 28,000-km dipole line.*

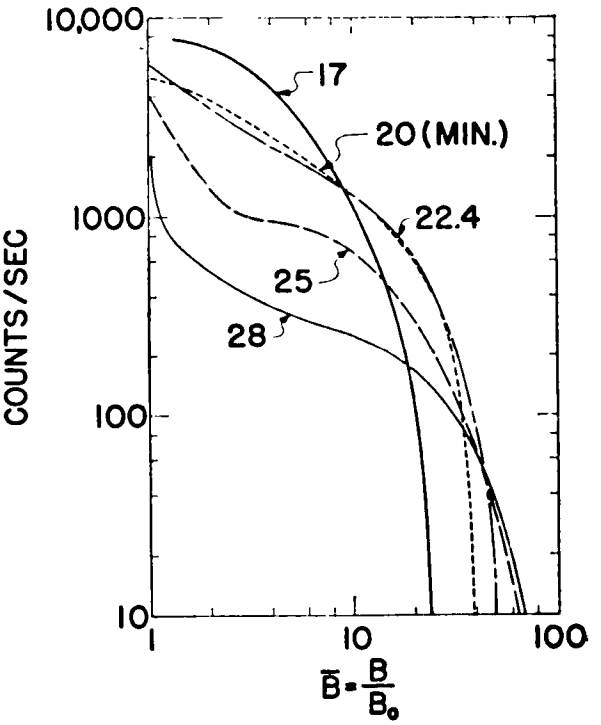

FIGURE 8.—*Curves approximating the counting rates versus* $\overline{B}$ *for five lines of force before the August 16, 1959, storm. Notice the progressive concentration of particles toward the magnetic equator with increasing range.*

By Liouville's theorem [*Janossy*, 1948], the flux of particles per unit solid angle is constant as we follow the particles down a line of force, for particles having all the same momentum.

Let $N_0(P, \psi_0)$ be the number of particles per unit volume and per unit solid angle at ψ_0 per unit momentum interval at P, at the equator. This is the pitch-angle distribution, for which a solution will be found. The pitch angle (ψ or ψ_0), measured between the trajectory and the local field line, is independent of the direction of particle motion and does not exceed 90°.

The flux of particles per unit solid angle at ψ_0 per unit momentum interval at P at the equator is $V \cdot N_0(P, \psi_0)$.

Let $f(P, \psi, B)$ be the number of particles per unit volume per unit solid angle at ψ per unit momentum interval at P at a point where the field is B. Then the flux of particles per unit solid angle at ψ per unit momentum interval at P where the field is B is $V \cdot f(P, \psi, B)$. At the equator

$$V \cdot f(P, \psi_0, B_0) = V \cdot N_0(P, \psi_0) \tag{1}$$

Hence, by Liouville's theorem, everywhere along a line of force

$$V \cdot f(P, \psi, B) = V \cdot N_0(P, \psi_0) \tag{2}$$

The counting rate C of an omnidirectional detector due to particles of velocity V is proportional to

$$C(V, B) \alpha V \int_{\psi=0}^{\pi/2} f(P, \psi, B) \sin \psi d\psi \tag{3}$$

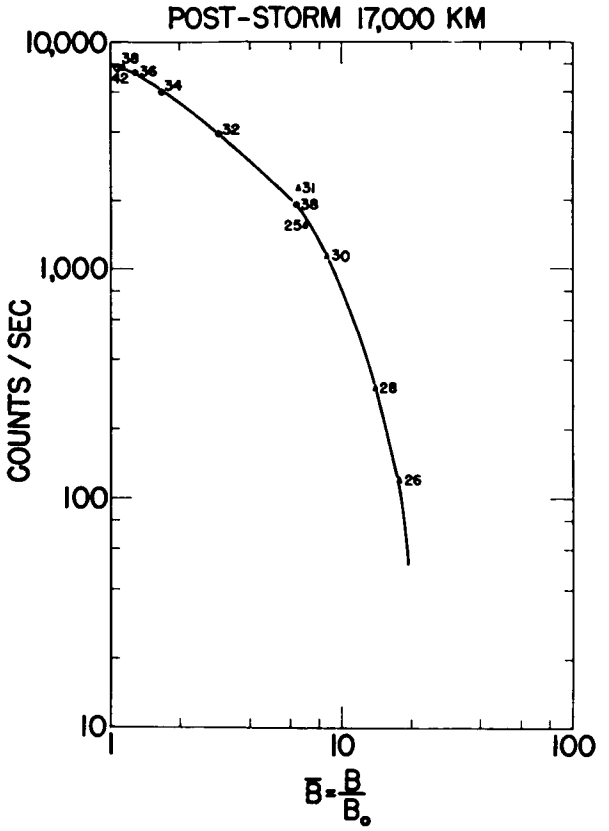

FIGURE 9.—*Counting rate of the Geiger counter as a function of* $\overline{B}$ *for the dipole line of force 17,000 km for passes 32–43, and passes 25–31 for* $\overline{B}>6.5$, *after the August 16 and 20 storms.*

where the integration is the flux per unit solid angle over the total 4π solid angle. Using (2)

$$C(V, B)\alpha V\int_0^{\pi/2} N_0[P, \psi_0] \sin \psi d\psi \qquad (4)$$

Expressed in terms of values at the equator, using the first adiabatic invariant,

$$\frac{\sin^2 \psi}{B} = \frac{\sin^2 \psi_0}{B_0} \qquad (5)$$

$$\frac{\sin \psi \cos \psi d\psi}{B} = \frac{\sin \psi_0 \cos \psi_0 d\psi_0}{B_0} \qquad (6)$$

and so

$$C(V, B)\alpha V \int_0^{\sin^2 \psi_{0\,max}} N_0(P, \psi_0) \cdot \frac{B}{B_0} \frac{d(\sin^2 \psi_0)}{\left(1 - \frac{B}{B_0} \sin^2 \psi_0\right)^{1/2}} \qquad (7)$$

where the upper limit is obtained by setting $\psi = 90°$ in (5).

If the efficiency of the detector to particles of velocity V is $\epsilon(V)$, then the total counting

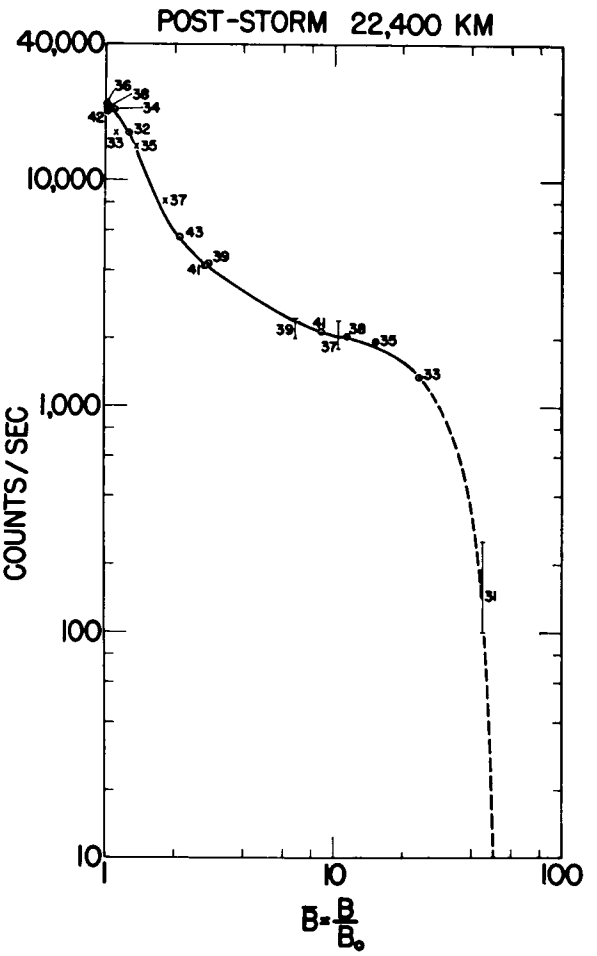

FIGURE 10.—*Counting rate of the Geiger counter as a function of* $\overline{B}$ *for the dipole line of force 22,400 km for passes 31–43.*

rate of the detector at a field strength B is proportional to

$$C(B)\alpha \int_0^\infty V\cdot\epsilon(V)\,dV \int_0^{\sin^2\psi_{0\,max}} N_0(P,\psi_0) \cdot\frac{B}{B_0}\frac{d(\sin^2\psi_0)}{\left(1-\frac{B}{B_0}\sin^2\psi_0\right)^{1/2}} \quad (8)$$

Since the pitch-angle distribution is independent of the energy of the particles, the first integral over velocity can be replaced by a constant. If this constant and the constant of proportionality in the previous equation are taken together and designated K, then

$$C(B) = K\int_0^{\sin^2\psi_{0\,max}} N_0(\psi_0) \cdot\frac{B}{B_0}\frac{d(\sin^2\psi_0)}{\left(1-\frac{B}{B_0}\sin^2\psi_0\right)^{1/2}} \quad (9)$$

This integral equation must be inverted to solve for $N_0(\psi_0)$. Here B is the point of the detector.

To solve, transform the equation into the form of Abel's integral equation [*Valterra*, 1930]. Let

$$\bar{B} = B/B_0$$
$$x = \sin^2\psi_0$$
$$dx = d(\sin^2\psi_0)$$
$$t = \sin^2\psi_{0\,max} = 1/\bar{B}$$

Then

$$\frac{2}{K}t^{1/2}C(1/t) = \int_0^t N_0(x)\frac{dx}{(t-x)^{1/2}} \quad (10)$$

By Abel's equation, this can be inverted:

$$N_0(x) = \frac{2}{\pi K}\frac{d}{dx}\int_0^x \frac{t^{1/2}C(1/t)\,dt}{(x-t)^{1/2}} \quad (11)$$

Substituting back,

$$N_0(\psi_0) = \frac{2}{\pi K}\frac{d}{d(\sin^2\psi_0)} \cdot\left[\int_\infty^{1/\sin^2\psi_0} \frac{C(\bar{B})\,d(1/\bar{B})}{(\bar{B})^{1/2}(\sin^2\psi_0 - 1/\bar{B})^{1/2}}\right] \quad (12)$$

but

$$d(1/\bar{B}) = d(B_0/B) = -B_0/B^2\,dB$$

and

$$\sin^2\psi_0 = B_0/B_m$$

where B_m is the value of the field at the turning point of a particle with equatorial pitch angle ψ_0. Therefore

$$\frac{d}{d(\sin^2\psi_0)} = \frac{d}{d(B_0/B_m)} = \frac{1}{B_0}\frac{d}{d(1/B_m)} = -\frac{B_m^2}{B_0}\frac{d}{dB_m}$$

Then

$$N_0(\psi_0) = \frac{2}{\pi K}B_m^2\frac{d}{dB_m} \cdot\left[B_m^{1/2}\int_\infty^{B_m}\frac{C(B)\,dB}{B^2(B-B_m)^{1/2}}\right] \quad (13)$$

where $B>B_m$.

A simplification in the expression can be obtained through the substitution $y^2 = (B/B_m - 1)$, so that

$$dy = \frac{dB}{2(B/B_m - 1)^{1/2}}$$

Then

$$N_0(\psi_0) = -\frac{4}{\pi K}B_m^2\frac{d}{dB_m} \cdot\left[\frac{1}{B_m}\int_0^\infty \frac{C[B_m(y^2+1)]\,dy}{(y^2+1)^2}\right] \quad (14)$$

To use, find the counting rate C down a line of force as a function of the field B. Substitute into this function $B(y^2+1)$ for B, and place into the equation for $N_0(\psi_0)$. Note that y is a parameter that is integrated out.

The actual derivation of the pitch-angle distributions of the outer-belt electrons was accomplished by using two approximation methods, the approximation of $C(\bar{B})$ by a series of power laws, and by a series of straight lines.

Approximation method using power laws.—Let the counting rate as a function of $\bar{B}$ be approxi-

mated by a series of straight lines on the ln-ln plot of C versus $\overline{B}$, or power laws.

$$C(\overline{B}) = N_i/\overline{B}^{n_i} \quad \text{for} \quad \overline{B}_i \leq \overline{B} \leq \overline{B}_{i+1} \tag{15}$$

Then, dropping the subscript m,

$$N_0(\psi_0) = \frac{-4}{\pi K} B^2 \frac{d}{dB} \cdot \left[\frac{1}{B} \sum_i \int_{\nu_i}^{\nu_{i+1}} \frac{N_i\, dy}{B^{n_i}(y^2+1)^{n_i}(y^2+1)^2}\right] = \frac{4}{\pi K} \sum_i \frac{(n_i+1)N_iR_i}{B^{n_i}} \tag{16}$$

where

$$R_i = \int_{\nu_i}^{\nu_{i+1}} \frac{dy}{(y^2+1)^{n_i+2}}$$

Note that if $C(\overline{B})$ can be approximated by a power law for all values of $\overline{B}$

$$N_0 \propto \sin^{2n} \psi_0 \tag{17}$$

Approximation method using straight lines.— Let the counting rate as a function of $\overline{B}$ be approximated by a series of straight lines on a linear plot of C versus $\overline{B}$,

$$C(\overline{B}) = \alpha_i - \gamma_i \overline{B}$$

for

$$\overline{B}_i \leq \overline{B} \leq \overline{B}_{i+1} \tag{18}$$

Then

$$N_0(\psi_0) = -\frac{4}{\pi K} B^2 \frac{d}{dB} \cdot \left[\frac{1}{B} \sum_i \alpha_i \int_{\nu_i}^{\nu_{i+1}} \frac{dy}{(y^2+1)^2} - \sum_i L_i\right] = \frac{4}{\pi K} \sum_i \alpha_i I(y_{i+1} - y_i) \tag{19}$$

where the L_i are terms independent of B, and

$$I(y_{i+1} - y_i) = \int_{\nu_i}^{\nu_{i+1}} \frac{dy}{(y^2+1)^2} = \left(\frac{y}{2(y^2+1)} + \frac{1}{2}\tan^{-1} y\right)\Bigg|_{\nu_i}^{\nu_{i+1}} \tag{20}$$

Figure 11 shows the pitch-angle distributions for the 17,000-km line of force derived from the curves in figures 5 and 9. Figure 12 shows the same information for the 22,400-km line, and figure 13 for the 28,000-km line. All the curves are normalized to 100 at ψ_0 equal to 90°. Table 1 itemizes the type of approximation used to derive each distribution, and the number of lines approximating the counting rate curves. An isotropic distribution would appear as a straight horizontal line.

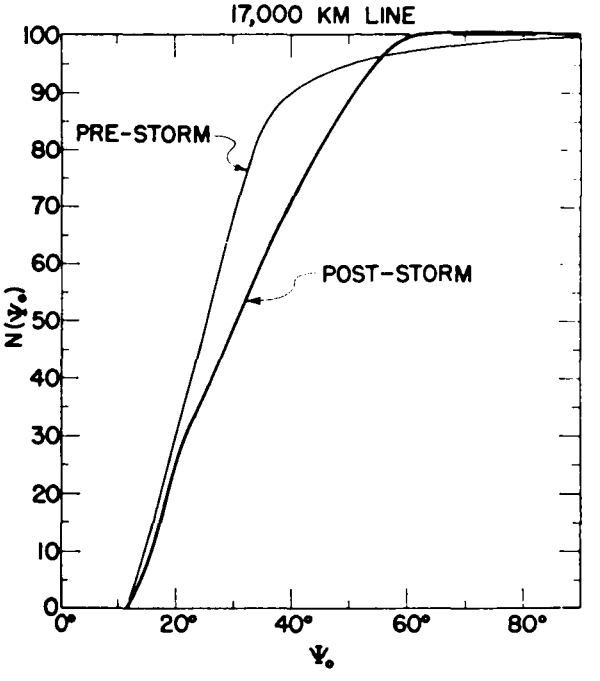

FIGURE 11.—*Equatorial pitch-angle distributions for the 17,000-km line of force derived from the curves in figures 5 and 9.* $N(\psi_0)$ *is the relative density of particles per unit solid angle at* ψ_0.

It is thought that through the use of these approximation methods the pitch-angle distributions are within the accuracy of the counter data. The largest errors will occur for large values of $\overline{B}$, or small pitch angles, where an error of several factors is possible for $\psi_0 < 15°$ because of the scarcity of data and the changes in ratio.

The definition of pitch-angle distribution used here is the usual one, but must be made clear. $N_0(\psi_0)$ was defined as the number of particles per unit volume and per unit solid angle, or density per unit solid angle, with pitch angles near ψ_0 at the magnetic equator. Since flux is velocity times density, these distributions can

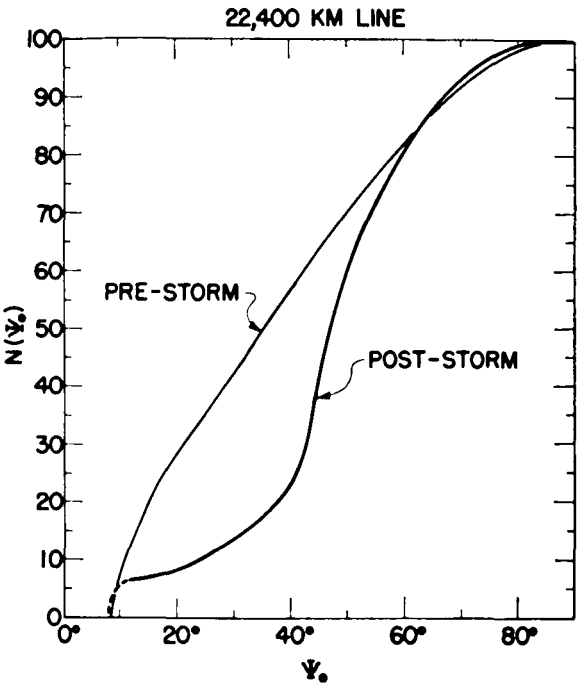

FIGURE 12.—*Equatorial pitch-angle distributions for the 22,400-km line of force derived from the curves in figures 6 and 10.*

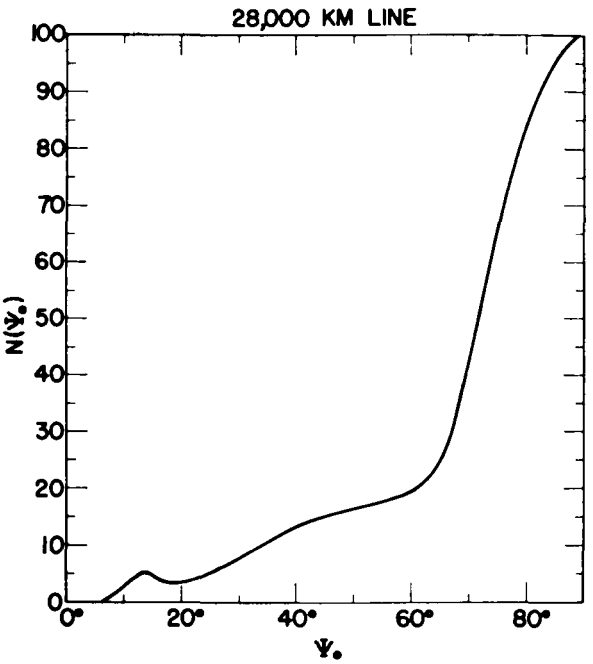

FIGURE 13.—*Equatorial pitch-angle distribution for the 28,000-km line of force derived from the curve in figure 7.*

also be considered as the flux measured by a telescope looking at an infinitesimal solid angle at ψ_0. This definition is different from the one used by *Fan et al.* [1961*b*] in their study of pitch-angle distributions, in that theirs is integrated over time. That is, they count each electron once as it crosses a unit area normal to the line of force at the magnetic equator, but continue counting until all electrons that will ever pass through the unit area have been accounted for. As a result, the pitch-angle distributions from the two definitions appear quite different.

TABLE 1.—*Type of Approximation and Number of Lines Used for Approximating the Counting Rate of the Geiger Counter as a Function of* $\overline{B}$ *in Deriving the Pitch-Angle Distributions*

Dipole Line, km	Time Period	Straight Line Approximation	Power-Law Approximation
17, 000	Prestorm	5 lines	Not used.
	Post-storm	($\overline{B}$ 6.8) 4 lines	($\overline{B}$ 6.8) 3 lines.
22, 400	Prestorm	7 lines	3 lines.
	Post-storm	8 lines	Not used.
28, 000	Prestorm	Not used	6 lines.

Storm-Time Mirror Points

The derivations of the pitch-angle distributions in the previous section required data from a series of passes during magnetically quiet times in order to obtain a distribution of counting rate points along a line of force. During magnetically disturbed times the intensities fluctuate between successive passes so that pitch-angle distributions cannot be studied.

However, an indication of the mirror-point changes can be observed by plotting the counting rate of the counter versus the prestorm $\overline{B}$ values at the points of intersection of the orbits with the prestorm dipole shells. This is done for the usual three dipole lines, 17,000 km, 22,400 km, and 28,000 km in figures 14, 15,

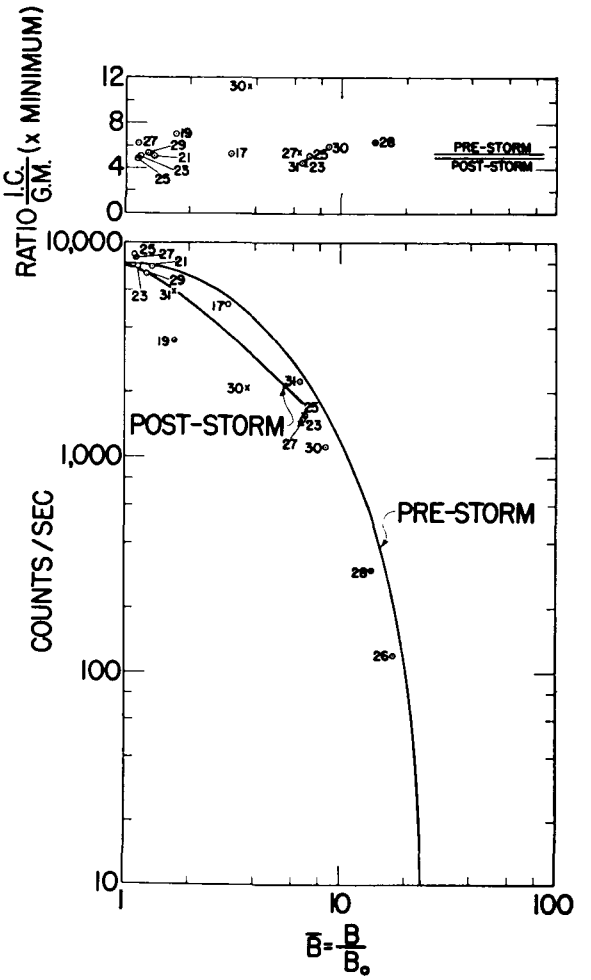

FIGURE 14.—*Counter rate as a function of* $\bar{B}$ *(bottom) and ratio of chamber to counter rates versus* $\bar{B}$ *(top) for the dipole line of force 17,000 km, passes 16–31, during the August 16 and 20 storms.*

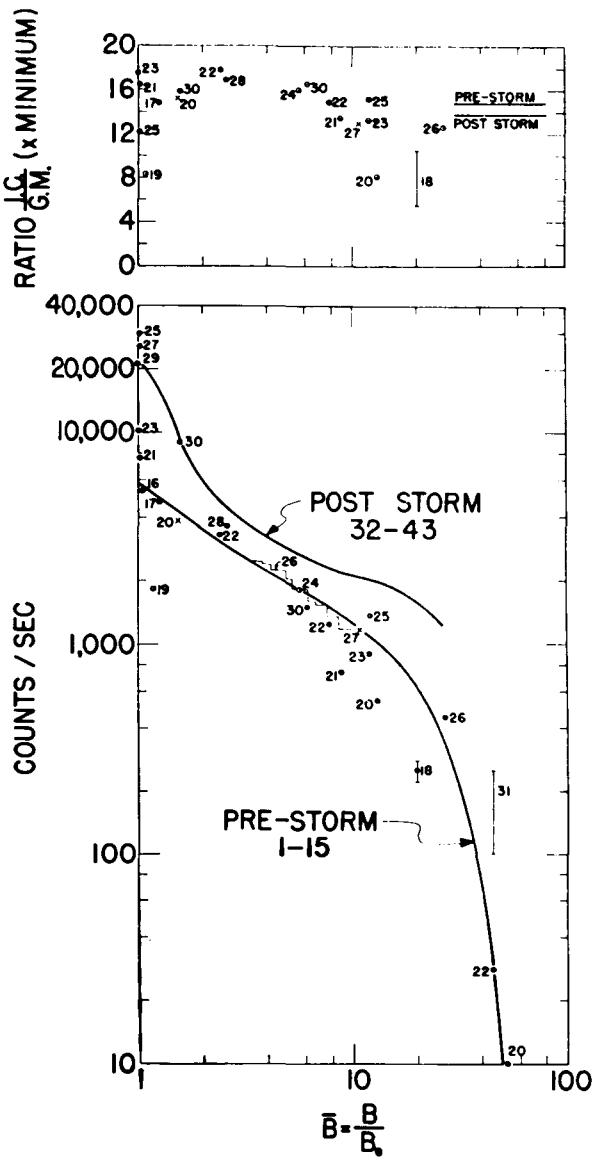

FIGURE 15.—*Same as figure 14 for the 22,400-km line.*

and 16. Also shown are the pre- and post-storm distributions for comparison.

MAGNETIC STORMS

In the first part of this paper, the properties of the radiation during magnetically quiet times before and after magnetic disturbances were discussed. In this section the variations in the trapped radiation during magnetic storms are analyzed in conjunction with other geophysical phenomena. Since data acquisition was most complete for the first month of operation of the satellite, the three storms of August (9, 16, and 20) and the first storm in September (3) will be analyzed most thoroughly.

Types of Data Analyzed

In the storm-time analysis, six different phenomena are considered. The first two are ground level, magnetometers and a sea-level neutron monitor; two are satellite measurements, the radiation detectors and satellite

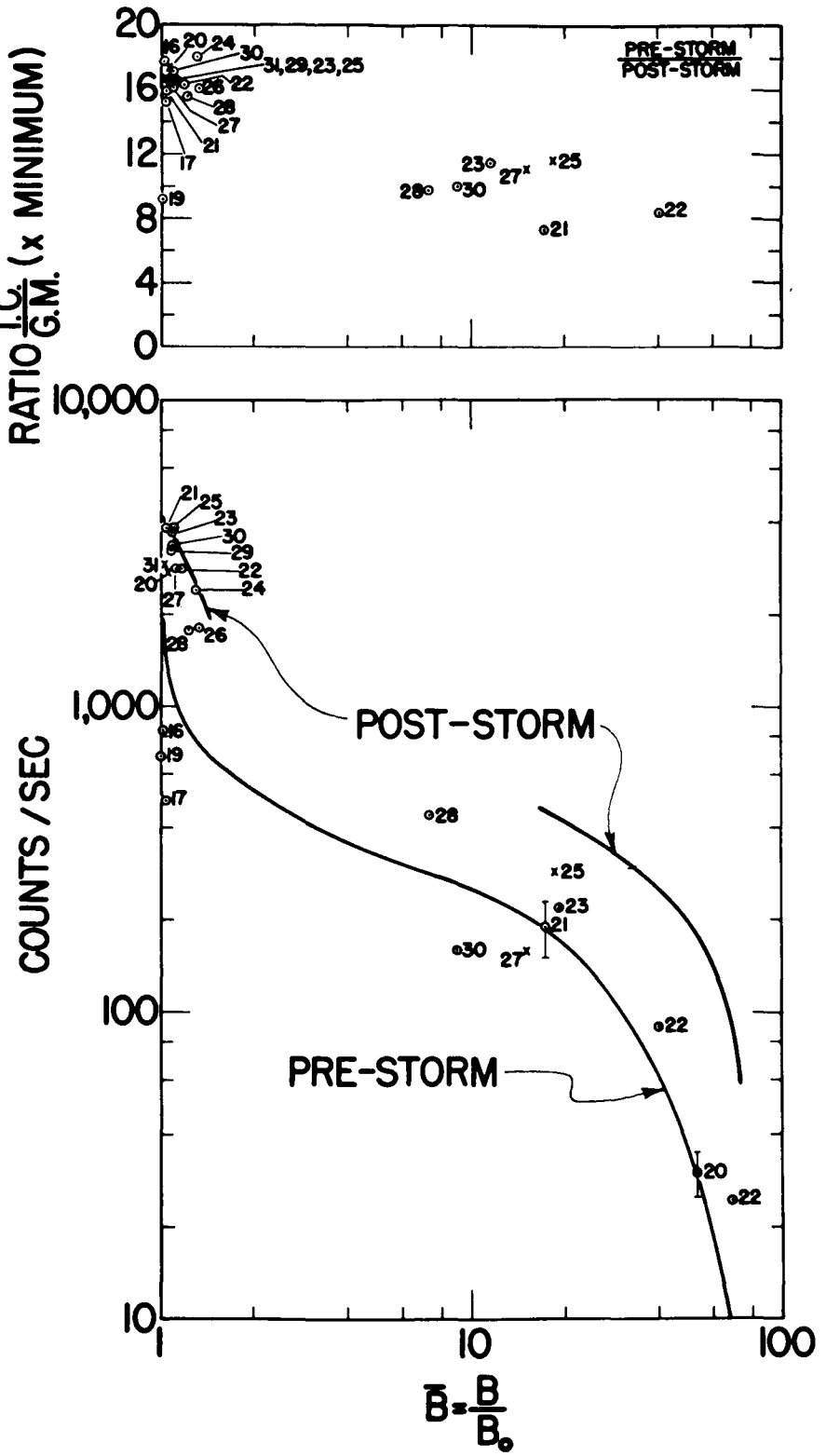

FIGURE 16.—*Same as figure 14 for the 28,000-km line.*

magnetometer; and two are solar, solar flares and solar radio emission. They will be considered in the following order for each storm:

(*a*) Since magnetic storms are defined by abnormal excursions of the ground-level magnetic field, the first observation to be discussed in the analysis of each specific event will be the magnetograms from several observatories. The major trends of the ground-level magnetic field were obtained by deriving the average D_{st} curve from the hourly averages measured at Fredericksburg, San Juan, and Honolulu. For the storm of August 16, Sydney Chapman and S. Akasofu have kindly furnished a D_{st} curve based on 12 observatories well distributed in latitude and longitude between geomagnetic latitudes of 30° N and S. It must be pointed out of the series of hourly averagings eliminates short time fluctuations and has a tendency to decrease sudden commencements.

(*b*) The next measurement was from the Geiger counter and ionization chamber. Specifically, the counting rate of the counter was considered at the points of intersection of the orbits with the prestorm dipole shells. Because the counting rate down a line of force was extremely dependent upon latitude, the percentage change from the prestorm values has been considered instead of the absolute value of the counting rate; i.e.,

$$\frac{\left(\begin{array}{c}\text{counting rate}\\ \text{at } \overline{B} \text{ for}\\ \text{storm-time pass}\end{array}\right)-\left(\begin{array}{c}\text{average counting}\\ \text{rate at } \overline{B}\\ \text{before storm}\end{array}\right)}{\left(\begin{array}{c}\text{average counting rate at } \overline{B}\\ \text{before storm}\end{array}\right)}\times 100$$

The comparison of counting rates for a series of storm-time passes at the points of intersection of the orbits with the nonperturbed dipole shells must be justified, because mechanisms are known which can move trapped particles in range, thereby causing an apparent change in intensity of radiation in a given location of space. For such a study the locations of the outer belt maximums and minimum in counting rates of the Geiger counter for two storm-time passes are compared with the locations during quiet periods. Table 2 contains the equatorial ranges (R_0) of the lines of force through the two maximums and minimum for the even-numbered passes surrounding the August 9–10 storm and preceding the August 16 storm as well as the locations for pass 6 on August 10 and pass 19 during the main phase of the August 16 storm. It is seen from the table that the six ranges of comparison for passes 6 and 19 do not display any systematic variation from the average ranges. Each individual position could be determined to within a couple of hundred kilometers. The odd-numbered passes from 1 to 15 as well as pass 20, also during the main phase of the August 16 storm, were too far off the magnetic equator in the heart of the outer belt to be of use in this comparison, since the positions of the maximum and minimum change in the profiles of the radiation toward the earth's surface, especially during magnetic storms.

TABLE 2.—*Comparison of the Equatorial Ranges of the Two Outer-Belt Maximums and Minimum during Magnetically Quiet Periods with the Ranges During Magnetic Storms to Determine Whether Radial Drift of the Trapped Particles Occurs*

Pass No.	Inner Maximum R_0, km	Minimum R_0, km	Outer Maximum R_0, km
2	17, 300	20, 400	22, 900
4	16, 900	19, 800	22, 800
8	16, 500	19, 200	22, 500
10	16, 300	18, 800	22, 100
12	16, 300	19, 700	22, 600
14	16, 500	19, 400	22, 300
Averages	16, 600 ± 300	19, 600 ± 400	22, 500 ± 200
6	16, 500	20, 300	22, 800
19	16, 800	19, 900	21, 400

This justification also established one requirement for decelerating and dumping mechanisms on the radiation: that there can be no large radial drifts of the particles.

(*c*) Measurements of the magnetic field in extraterrestrial space were made by a search coil magnetometer and a phase comparator aboard Explorer 6 [*Sonett et al.*, 1960]. The search coil utilized the spinning of the payload to measure $|B_\perp|$, the component of the magnetic

field perpendicular to the spin axis of the vehicle. The phase comparator indicated the angle between $B_\perp$ and $S_\perp$, where $S_\perp$ represents the projection into the payload equatorial plane of a unit vector pointing in the direction of the sun. The theoretical values of $B_\perp$ and the phase angle have been calculated on the basis of the spherical harmonic expansion of the earth's surface field and extrapolation to the location of the vehicle. A phase change to smaller angles corresponded to a decrease in field amplitude and to an increase in amplitude of a perturbation field.

(*d*) Listings of solar flares and radio emission were obtained from the Solar Geophysical Data reports, Part B [*Natl. Bur. Standards*, 1959–1960] and from the High Altitude Observatory summary report [*Trotter and Roberts*, 1960].

(*e*) The other ground level measurement is the Deep River neutron monitor hourly average counting rate.

It is generally believed that there is a direct correspondence between the observation of a magnetic storm and the interception by the earth of a solar plasma beam [*Dessler and Parker*, 1959]. Now there are apparently two types of plasma, one containing magnetic fields and one deficient in fields, provided that the criterion for such a determination is the simultaneous observation of a Forbush decrease. If one occurs, the plasma contains a field; if the cosmic-ray intensity remains constant, the plasma is field free. It is now known that the cause of a Forbush decrease is not geocentric, i.e. dependent upon the earth and its magnetic field, because, simultaneous with the occurrence of a magnetic storm [*Fan et al.*, 1960; *Coleman et al.*, 1961], one was observed 5,000,000 km from the earth with detectors aboard Pioneer 5. A Forbush decrease and magnetic storm were also recorded at the earth during the same period.

Magnetic Storm Observations
August 9–10, 1959, Magnetic Storm

(*a*) Earth surface magnetometers. This small magnetic storm is not listed as a principal magnetic storm [*Lincoln*, 1960] but was detected because of the decrease in counting rates of passes 5 and 6 over the average values when we were constructing figures 5, 6, and 7. A scan of the magnetograms from the three observatories considered shows no sudden commencement. In fact only the Fredericksburg record indicates what might be a positive phase of about 10 γ, commencing at approximately 1115 UT on August 9. The hourly averages and other related data appear in figure 17.

(*b*) Counting rate changes. Pass 4 intersected the outer belt about six hours before the storm, and the counting rates appeared normal at the crossings of all the lines of force. Pass 5 occurred during the main phase and intersected the 22,400-km and 25,000-km lines at two points. The counting rate data show the very interesting phenomenon of a decrease in intensity near the magnetic equator, but an increase at lower altitudes, though still well above the atmosphere. The ratio of chamber to counter rates increased only a few per cent except at large ranges, indicating a very slight softening of the radiation.

The intensities were returning to prestorm level in pass 6 during the recovery stage of the storm, and the ratios were essentially normal. Pass 7 was basically normal in the heart of the belt, but especially at 35,000 km; it remained depressed thereafter.

(*c*) Satellite magnetometer. The Explorer 6 magnetic field measurements have been published for pass 5 [*Smith et al.*, 1960; see their fig. 2], which strikingly displays a negative perturbation in the distant field. This characteristic anomaly has been interpreted as a ring current at 60,000 km carrying a current of 5×10^6 amperes in a circular cross section of 3 earth radii. About 25½ hours later the same region of space was again intersected on pass 7, but the start of the magnetic-field perturbation had moved out by about 9000 km (see their fig. 1). The orbit for pass 5 was within 6° of the geomagnetic equator from 30,000 to 43,000 km orbital range, and for pass 7, from 33,000 to 45,000 km range.

(*d*) Flares. The most prominent flare preceding this period occurred at about 1555 UT, August 7. Table 3 contains the observations of the flare as reported in the Solar Geophysical

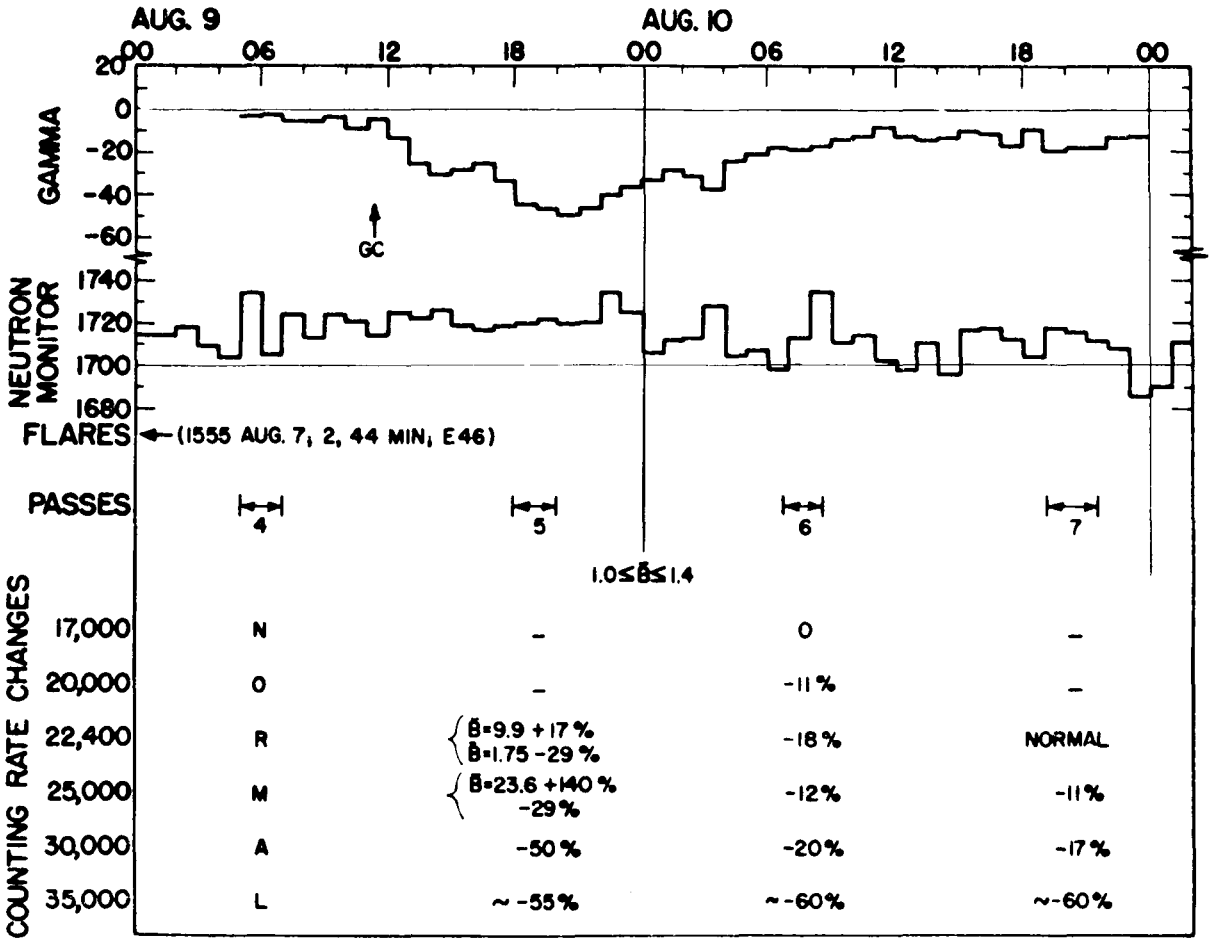

FIGURE 17.—*Correlation analysis for August 9–10 magnetic storm.* Top: D_{st} *hourly averages.* Second: *Deep River neutron monitor hourly averages.* Bottom: *Geiger counter rate changes at various lines of force.*

Data Report of September, 1959 (*Natl. Bur. Standards*, 1959–1960]. This McMath plage region 5315 was a recurrence of region 5265 which caused the very interesting July 1959 events [*Smith et al.*, 1960], since the time lapse between the July and August central meridian crossing of the region was about 26 days 12 hours.

Trotter and Roberts [1960] describe the activity of this region (Main Solar Region 59–Q) as follows: when the region returned in August it showed a redevelopment of activity quite similar to that in July. Strong, complex coronal looped prominences associated with yellow line emission and moderate surges were again in evidence. Three classes 1^+ flares early in the passage produced short-wave fadeouts, but from central meridian passage on the region declined rapidly.

No solar flare occurred during the period of the gradual commencement (GC) during the eleventh hour on August 9, so that the counting rate decrease cannot be attributed to an immediate solar cause. The nearest flare reports were before 0940 and at 1214 UT.

(*e*) Neutron monitor. It is shown in figure 17 that no Forbush decrease accompanied the storm.

August 16, 1959, Magnetic Storm

(*a*) Earth surface magnetometers. The most fully documented storm of the Explorer 6 epoch

TABLE 3.—*Solar Flares*

Date	Observatory	Universal Time			Location				Duration, minutes	Importance	Ionospheric Effect
		Start	End	Maximum Phase	Latitude	Meridian Distance	McMath Plage Region	High Altitude Observatory Region			
		August 9 Storm									
Aug. 7	Lockheed	1551	1635	1604	N15	E46	5315	59–Q	44	1	
	Sac Peak	1554	1634	1606	N15	E46			40	1+	S–SWF.
	Wendel	1558	1634		N17	E46			26	2	
	Locarno	1600	1636	1615	N16	E44			36	22	
		August 16 Storm									
Aug. 14	Hawaii	0044	0234	0119	N12	E28	5323	59–L	110	2+	G–SWF.
	Mitaka	0211	2326	0236	N10	E27			75	2	
		August 20 Storm									
Aug. 18	Wendel	1019	1149		N12	W31	5323	59–L	30	2+	
	Stockholm	1020	1243		N13	W32			83	2	
	Locarno	1020	1250	1050	N11	W34			150	3	S–SWF.
	Meudon	1022	1216	1058	N11	W38			114	3	
	RBO. Herst	1203	1235	1203	N12	W30			32	2	
						or					
Aug. 18	Sac Peak	1654	1822	1726	N05	E15	5329	59–U	88	2+	Slow.
	Climax	1656	1814	1733	N08	E17			77	2	S–SWF.
	Wendel	1657	1813		N04	E16			76	2+	
	Zurich	1714	1726		N05	E16			12	2+	
		September 3 Storm									
Sept. 1	Lockheed	1947	2030	1953	N09	W15	5344	59–X	43	1	Slow.
	Sac Peak	1948	2030	1956	N09	W15			42	2	S–SWF.
						or					
Sept. 2	Good Hope	0720	0954		N10	W10	5344	59–X	154	2	
	Athens	0724	0900		N06	W09			96	3	Slow.
	Pirculi	0724	0905	0830	N11	W09			101	3	S–SWF.
	Krasnya	0729	0830		N09	W09			61	2	
		September 3 Solar-Proton Event									
Sept. 3	Alma-Ata	0421	0436	0423	N25	W85	5339	(?)	15	2	
	Sydney	0421	0438	0423	N27	W86			17		S–SWF.
	Tashkent	0421	0439	0422	N23	W86			18	2+	

was the one commencing on August 16, 1959, at 0404 UT. The positive phase, though beginning sharply, was of rather small amplitude, and it remained for only about two hours before the large characteristic negative bay of about 140 γ appeared. It should be pointed out that the previous half day was somewhat disturbed magnetically, the last three K_p indices for the 15th being 5°, 4+, and 6−. In fact Fredericksburg, Huancayo, and Toolangi reported small storms beginning at 12xx, 1407, and 1342 UT, respectively, and lasting several hours.

(*b*) Counting rate changes. This storm produced major changes in the radiation intensity, whose prominent features have been discussed previously [*Arnoldy et al.*, 1960*a*]. However, a more complete analysis of the data shows the following properties (graphed in fig. 18).

Pass 15 was normal during the first half of August 15, but pass 16 already showed a decrease on the outer side of the outer belt at and beyond the 25,000-km line of force near the equator. Pass 17, during which the sudden commencement occurred, indicated a slight further decrease for the same lines of force. Unfortunately the receiving stations recorded data from both low-power transmitters for only the initial portion of pass 18 during the main phase of the storm as observed at the earth's surface. However, decreased intensity was observed at points off the equator, contrary to pass 5, when an increase was observed off the equator. Pass 19, also during the main phase, showed a decrease at all lines of force, the fractional decrease from before the storm varying only from −53 to −68 per cent from the 17,000-km to the 28,000-km lines. However, the fractional decrease between passes 17 and 19 was very range dependent, the entire decrease occurring for 20,000 km and closer, but none occurring beyond the 28,000-km line.

From passes 20 to 22 the intensity at the equator recovered for the inner half of the outer belt and rose to above prestorm values at ranges from the outermost maximum and beyond. From passes 22 through 24 conditions remained stable. It is of interest to follow these changes on figures 15, 16, and 19.

(*c*) Satellite magnetometer. The magnetic field observations from Explorer 6 during the August 16 storm are fully illustrated by studying the phase comparator data from each pass [*Space Technology Labs.*, 1960].

1. Pass 15 was normal, a negative deviation from the theoretical phase beginning at about 35,000 km. A negative phase change corresponds to a decrease in field amplitude.

2. Pass 16 showed the deviation occurring at 33,000 km, much sharper in depth than pass 15. This may be due to the disturbance reported in the last half of August 15.

3. Pass 17 had the deviation retreated to 35,000 km again, but considerable structure appeared, characteristic of the magnetic elements at the earth's surface during a storm.

4. On pass 18 these effects were enhanced, with the deviation region beginning at about 31,000 km.

5. On pass 19 the deviation was noticeable at 27,000 km, structure occurring at altitudes even lower than before.

6. Pass 20 showed some recovery of the field, the deviation having retreated to 35,000 km, and a much smoother field.

7. The deviation of pass 21 again moved in to about 28,000 km but was considerably smaller in amplitude and smoother.

8. The field had recovered for pass 22, the deviation beginning at about 38,000 km.

The actual field measurements were not nearly as complete as the phase comparator data, but the observations are very interesting. Figure 19 contains the observations from three passes, 18, 19, and 22, taken from *Space Technology Labs.* [1960]. The deviations in field amplitude generally follow the phase comparator. A noteworthy feature is the close agreement between the theoretical field and experimental measurement for ranges smaller than the deviations, except for the appearance of structure.

(*d*) Flares. The August 16 storm is generally attributed to a flare at the beginning of August 14 (see table 3). The active region, McMath 5323 (High Altitude Observatory Main Solar Region 59–L), was a recurrence of region 5280, which was rather inactive during its July central meridian passage 26 days 19 hours previously, but which produced many small flares from August 10 through August 18.

765-698 O-65—14

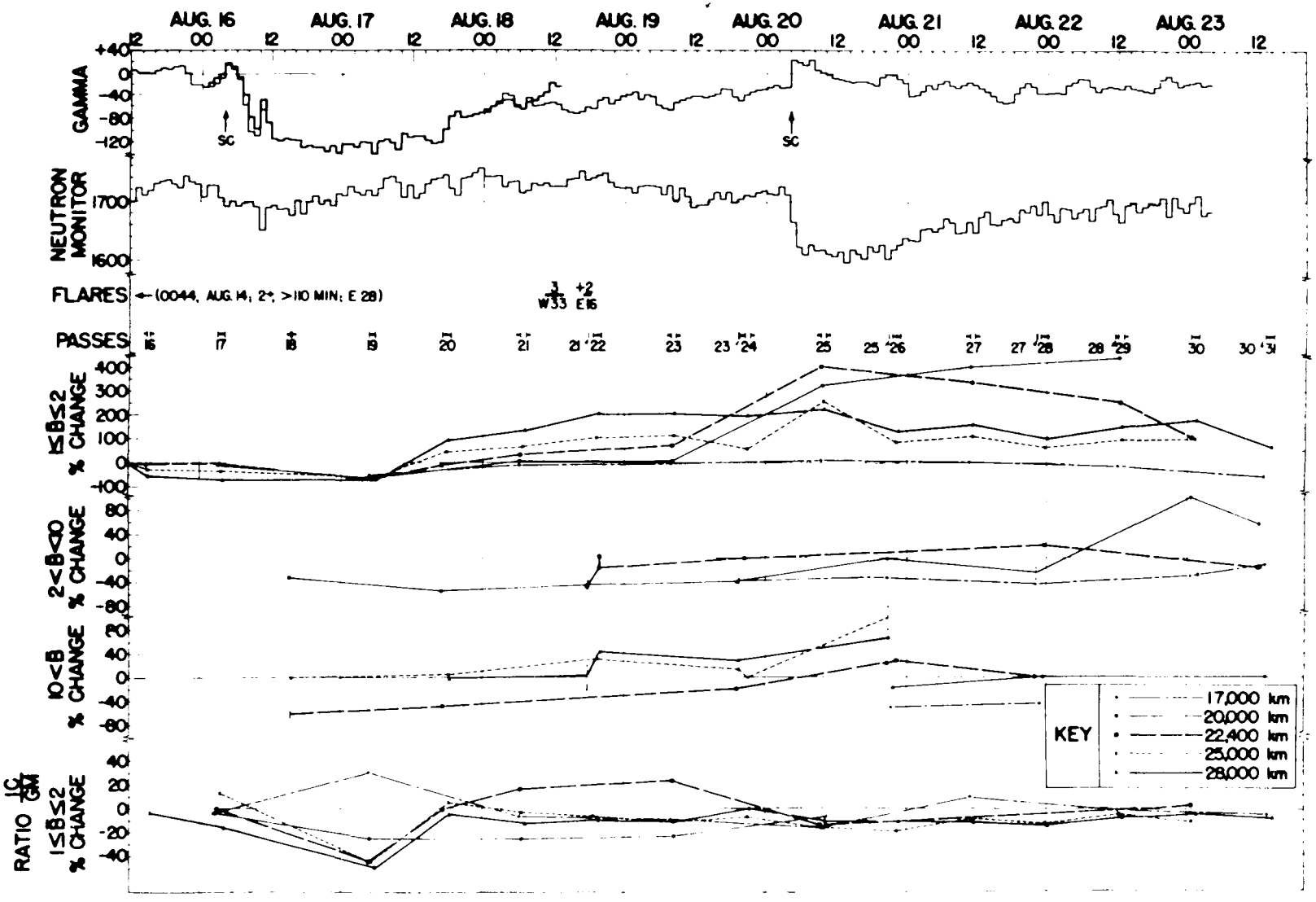

FIGURE 18.—*Correlation analysis for August 16 and 20 magnetic storms.* Top: D_{st} *hourly averages (dark curve from Chapman and Akasofu).* Second: *Deep River neutron monitor hourly averages.* Middle three graphs: *Geiger counter rate changes at various lines of force.* Bottom: *ratio changes at various lines of force.*

Again the counting rate changes cannot be attributed to an immediate solar cause because only one flare was reported on August 16, a class 1 before 0928.

The High Altitude Observatory summary report of solar activity states that the aurora associated with this disturbance was visible well into central United States on August 16 and into southern Canada on August 17. (For a detailed discussion see part 5, *Arnoldy, Hoffman, Winckler, and Akasofu* [1962].)

(*e*) Neutron monitor. Only a small Forbush decrease occurred, as is seen in figure 18.

August 20, 1959, Magnetic Storms

(*a*) Earth surface magnetometers. In the first data analysis of Explorer 6, this storm was also missed. About half the magnetic observatories listed in this Journal [*Lincoln*, 1960] reported it. The sudden commencement at 0412 UT was sharp and very large, with the positive phase lasting about four hours. The main phase never fully developed, but irregular negative excursions continued for several days.

(*b*) Counting rate changes. Contrary to the two previous storms, no counting rate reductions were apparent (see fig. 18).

(*c*) Satellite magnetometers. Unfortunately no Explorer 6 magnetic data have been published during this storm. It would be interesting to determine whether there is a relation between the change in location of the negative anomaly due to the ring current structure in the field throughout the belt, the nonappearance of a main phase on the earth's surface, and the lack of "dumping" of the trapped radiation.

(*d*) Flares. The source of this storm could have been either of two flares on August 18, both of which are listed in table 3. Region 5323 had previously produced the August 16 storm and was recurrent, and region 5329 was newly active during this revolution. The High Altitude Observatory attributes the magnetic storm to the region 5323 (or 59–L) instead of region 5329 (59–U) and, as for the previous two storms, no flare was reported near the sudden commencement.

(*e*) Neutron monitor. For the first time a large Forbush decrease occurred, as is seen in figure 18, indicating the arrival of a magnetized gas cloud.

Radio noise storm.—As the earth's magnetic field and the trapped radiation became stabilized after the August 20 storm, a great long-lasting solar radio noise storm was observed. A plot of the intensity of radio emission at 169 Mc/s, as determined by the Meudon Observatory group from the solar radio station at Nancy, France, is shown in part 1, figure 14, of this series, which is taken from the Boulder reports [*Natl. Bur. Standards*, 1960]. The sun is scanned every day, and the intensities are plotted across the disk. Regions of moderate activity appear frequently, as shown by the small black and white spots, but on August 22 a region developed that on succeeding days reached very high intensity. The radio emission from this region extended beyond the limits of the disk (shown by the horizontal lines labeled W and E on the left margin). This long-lasting solar noise storm was observed at several other stations, for example, by Warwick (private communication, 1959) at Boulder and by Erickson (private communication, 1959) at the Convair radio astronomy station in California. Warwick's sweep-frequency interferometer covering the approximate range 15 to 100 Mc/s showed that the emission was continuum radiation, definitely not thermal, and attributable to synchrotron radiation from electrons in a region that appeared to be at a very great distance from the surface of the sun.

The unusual nature of this noise storm is also made clear by observations of the Fraunhofer Institute, which showed numerous wide-band rapid intensity fluctuations during the period. Similar observations were reported by the Nera Observatory [*Information Bulletin of Solar Radio Observations in Europe*, 1960].

During the period of observations of the first half of this noise storm, the trapped radiation was extremely stable, permitting the construction of the contour plot of figure 2 (*middle*) and the pitch-angle distributions of figures 11 and 12. This observation is at some variance with the interpretation of *Fan et al.* [1961*a*] of their figure 13*A*, which is similar to our figure 1, in which a steady decline in intensity of the

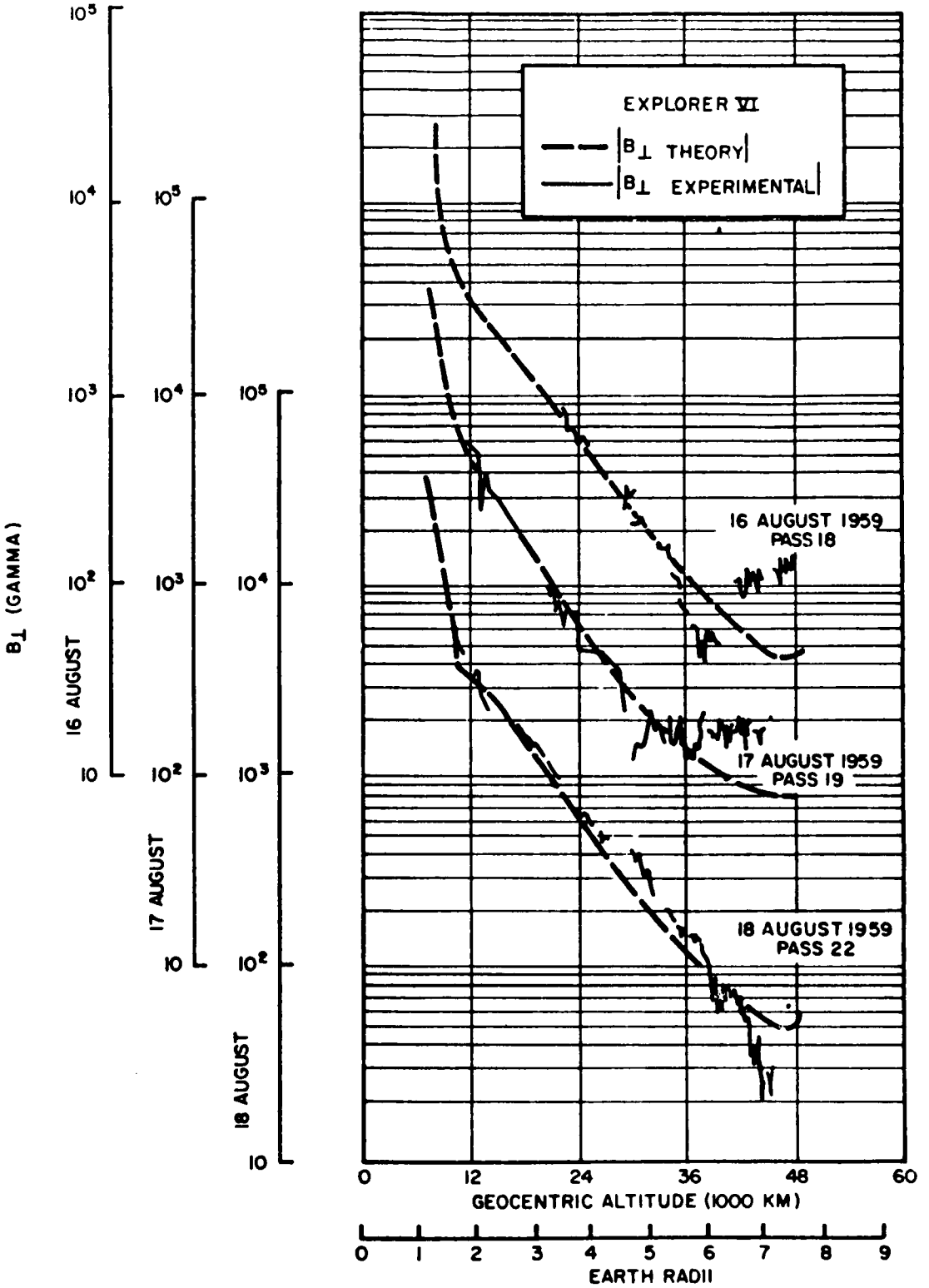

FIGURE 19.—*Measurements in the magnetic field at the location of Explorer 6 for three passes during the August 16 magnetic storm.*

outermost maximum is concluded over the period August 20 to September 3. However, plotting the data as in figures 9 and 10 definitely proves a stability in the radiation for about six days.

The second half of this noise storm was still proceeding when the radiation intensities decreased during the August 29 to September 2 period (see fig. 20). Since the increases of intensity shortly before the observation of the noise storm can be accounted for by the wake of the August 20 magnetic storm, and since the decreases did not commence until the noise storm had been in progress for a week, it is difficult to associate the trapped radiation variations with the solar radio noise.

On the basis of incomplete data, in the first report of the Explorer 6 results [*Arnoldy et al.*, 1960*b*], it was tentatively concluded that a close association existed between the beginning of the noise storm and the intensity increase, but with the acquisition of additional data the association became less certain, as was reported in the second publication [*Arnoldy et al.*, 1960*a*]. However, suspicions still lingered as to the cause of the build-up, whether it might be related to an unobserved initial phase of the solar noise storm, but the analysis of the August 20 magnetic storm provides an adequate explanation.

Some comments should be presented relating to magnetic and solar activity during August 29–31 because of the large changes in the counting rates during this period. No magnetic storms were reported after August 20 and the geomagnetic planetary three-hourly indices K_p did not exceed 3° at any time except for 4° from 1500–1800 on August 29, when there was a small, sharp excursion on the magnetograms. The magnetic field in figure 20 is quite stable, as was the neutron counting rate. However, it is interesting to note that the sunspot numbers for August 29 through September 1 were by far the highest for the entire third quarter of the year. In fact, for the solar rotation 1417, from August 9 to September 4, the sunspot index reached the highest level since January 1959. Numerous class 1 and 1^+ flares were reported as well as two class 2, the first before 2250 on August 29 on central meridian, and the other at 1536 on August 30 at 37° W.

September 3, 1959, Magnetic Storm

(*a*) Earth surface magnetometers. Another moderately sized storm occurred on September 3, the sudden commencement being at 2150 UT. The positive phase, though sharp, went rapidly negative after only a half hour.

(*b*) Counting rate changes. The accuracy of radiation intensity measurements at various lines of force during this period are complicated by the possibilities of errors in the trajectory. This problem arose in the consideration of inner belt data in part 3 [*Hoffman, et al.*, 1962] where it was stated that new trajectory data were available through pass 36, and a comparison of the new with the old required shifts up to several minutes in time along the orbit to acquire coincidence in position. However, in figure 20 the present trajectory has been considered as accurate, keeping in mind that the percentage changes for lines 22,400, 25,000, and 28,000 km near the equator and all lines off the equator could be decreased to about half the values plotted. Passes 32–41 and the lower altitude parts of passes 42 and 43 have been considered as prestorm for the discussion of the September 3 magnetic storm.

In spite of this possibility, it is definitely known that between passes 41 and 44 there occurred a large decrease in intensity, because nowhere along the trajectory of pass 44 did the intensity reach prestorm values. This slow decrease continued for all lines of force until pass 49 on the beginning of September 2, when the intensities leveled off until the storm at the end of September 3. Again, as for the storm of August 9–10, the intensities seemed to increase off the equator.

The September 3 magnetic storm is further complicated by the observation of solar protons apparently from a flare beginning on September 3 [*Fan et al.*, 1961*a*]. The flare beginning at 0421 resulted in high-energy particles first arriving in the vicinity of the earth within approximately 20–30 minutes. An increase by about a factor of 2 over cosmic-ray counting rates occurred in the University of Chicago triple

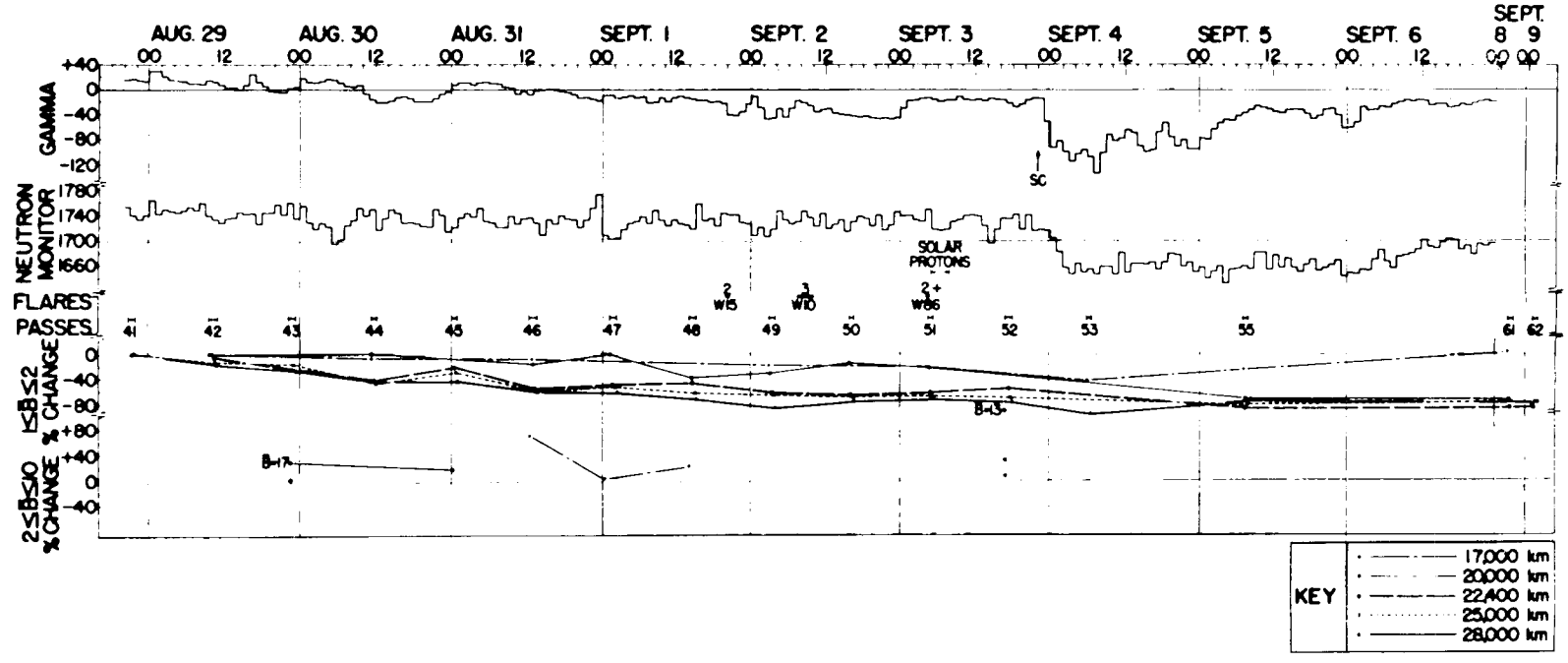

FIGURE 20.—*Correlation analysis for September 3 magnetic storm.* Top: D_{st} *hourly averages.* Second: *Deep River neutron monitor hourly averages* Bottom two graphs: *Geiger counter rate changes at various lines of force.*

coincidence telescope and continued for several hours. Although during this period the trapped radiation remained stable (passes 51 and 52), the solar proton event was of such small magnitude that we would hesitate to draw from this any conclusions as to the effects on the belts of similar, though larger, events.

The storm of September 3–4 brought a further depression of intensities, especially for the outermost maximum, the 20,000- and 22,400-km lines of force. During the recovery stage of the storm, the equatorial intensity of the 17,000-km line recovered, while the lower altitude intensity on this line was depressed, similar to the August 16 and 20 magnetic storms. However, the intensities on the other lines remained stable.

(*c*) Satellite magnetometer. Unfortunately no satellite magnetometer data have been published for this period.

(*d*) Flares. The designation of the flare causing this storm is again possibly arbitrary. *Trotter and Roberts* [1960] state: "A geomagnetic disturbance began early on 2 September and lasted until 5 September. The beginning of the disturbance coincided with the central meridian passage of Region 59–K. Then, a class 2 flare on 1 September was followed 50 hours later by a sudden commencement geomagnetic storm superimposed on the storm already in progress. The auroras visible across the United States as far south as Denver on 1 and 3 September were associated with this storm."

The other possibility is a class 3 flare on September 2 at 0720 from the same region 5344 (or 59–X) during the first passage of this region across the sun. Both flares are plotted in figure 20. No flare was reported after 1840 on September 3 during the period of the sudden commencement.

(*e*) Neutron monitor. A Forbush decrease occurred coincident with the storm at the end of September 3.

Rest of September.—Another description of the intensity variation appears in figure 21, in which the Geiger counter rate is plotted for various periods of time along the orbit of pass 19. Points on the lines marked "prestorm" and "post-storm" were obtained from figures 5, 6, 7, 9, and 10 for August 7–15 and August 24–29,

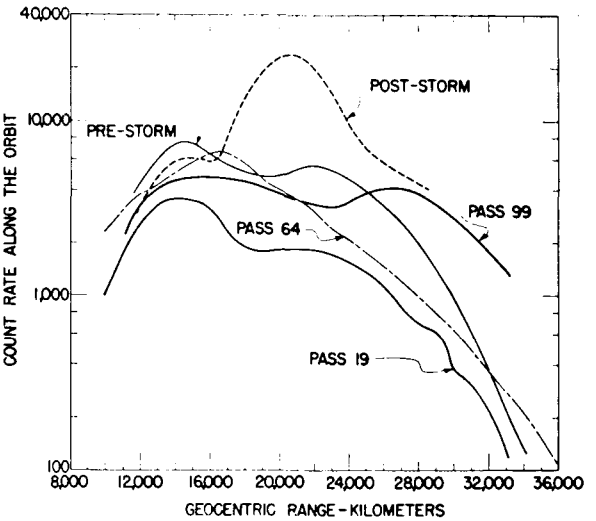

FIGURE 21.—*Geiger counter rate versus range along the orbit of pass 19 for various periods of time. This graph shows the large variability in intensity and shape of the outer belt. "Prestorm" and "post-storm" are before and after the August 16 and 20 magnetic storm period.*

respectively. Pass 19 is the dumped pass during the August 16 magnetic storm and pass 64, having identical magnetic coordinates, occurred during the quiet time after the September 3–4 storm. This pass exhibits, as does the contour plot of figure 2 (*bottom*) only one maximum in the outer belt. This feature continued until September 20, when a moderate storm occurred at mid-day. A second maximum at about 26,500 km began to grow after the storm, and by the end of the month appeared as in pass 99, whose orbit is within 1° in latitude of pass 19 from 20,000- to 32,000-km range.

Summary of Observations

A systematization of the observations taken during the four magnetic storms and the August 29–September 1 quiet period indicate rather loose correlations between the various phenomena, as is shown by the entries in Table 4. The following tendencies do appear however, for the outer belt:

1. Solar dependence. (*a*) Major intensity changes always correlate with solar activity. (*b*) The time delay indicates the coupling is by means of solar plasma beams. (*c*) A great long-

TABLE 4.—*Storm Summary*

	Aug. 9	Aug. 16	Aug. 20	Aug. 29–Sept. 1	Sept. 3
Flare recurrent region.	Yes	Yes	No, Yes		No, No.
Plasma transit time.	43 hr	51 hr	35 hr, 42 hr		40 hr, 51 hr.
Surface magnetic field:					
Sudden commencement.	No	Moderate	Large and sharp.	No	Small but sharp.
Main phase	Small, ~50 γ	Moderate, ~150 γ.	Small and irregular.	None	Moderate, ~130 γ.
Length	24 hr	14 hr	17 hr		32 hr.
Forbush decrease	None	Small	Average	None	Average.
Trapped radiation:					
Main phase:					
Equatorial	Decrease, >17,000 km.	Decrease all lines.	>17,000 km, large increase; 28,000 km, no change.	Decrease all lines.	Decrease all lines.
Low altitude	Increase: 22,400 km, 25,000 km.	Decrease: ≤22,400 km; no change. >22,400 km.	Increase all lines.	Increase, ≤22,400 km.	
Recovery phase:					
Equatorial	Increase	Increase all lines.	Little change except decrease at 22,400 km.		Recovery 17,000 km; others, no change.
Low altitude	Recovery	Increase all lines.	Decrease 22,400 km; increase 20,000 km.		Decrease 17,000 km; others, (?).
Pitch-angle distribution:					
ψ_0~90°	Little change	Increase	Large increase	Decrease	Decrease.
ψ_0~23°	Increase			Increase	
Aurora southernmost latitude.	None	40th parallel, southern Canada on Aug. 17.	(?) (Probably very little).	35th parallel	40th parallel.

lasting solar radio noise storm apparently had no effect on the trapped radiation.

2. Intensity changes are independent of the occurrence of a Forbush decrease.

3. Radial dependence. (*a*) The larger the radial distance of a line of force, generally the larger the variations and less correlation with earth surface magnetometer field changes. (*b*) The lower side of the belt (17,000-km line) is the most stable, and variations are reasonably coincident with earth surface field changes. At the equator on this line the counting rate always recovers to prestorm values, though small variations in pitch-angle distributions do occur.

4. Counting rate decreases. (*a*) Counting rates near the equator decrease for all lines of force if a magnetic storm occurs having a main phase. However, the decrease may begin before or after the main phase is observed on the earth's surface. (*b*) If the counting rate decrease is not large or rapid at the equator, the rate increases for points nearer the atmosphere,

meaning that the mirror points of the particles are moved down the lines of force. (*c*) The percentage decreases are usually larger for lines of force at larger radial distance. (*d*) Decreases can occur when the earth's surface field is quite stable. (*e*) Decreases are best correlated with inward movement of the ring current magnetic anomaly. (*f*) For large decreases at all lines, auroras appear at subauroral-zone latitudes.

5. Counting rate increases. (*a*) Counting rate increases occur during the recovery phase of magnetic storms. (*b*) The increases are apparently due to a local acceleration mechanism. (*c*) The particles have large pitch angles. (*d*) The percentage sizes of the increases can be independent of the radial distance of the lines of force for ranges 20,000 km and beyond. (*e*) The spectrum, as indicated by detector ratios of new particles, is similar to the prestorm spectrum and the spectrum is dependent upon the particular line of force and not on the size of the intensity change. (*f*) Increases are independent of the observation of structure in the field in the belt.

SERIES SUMMARY

In concluding this series of papers on the analysis of Explorer 6 data, we attempt here to summarize the major experimental results that were obtained. Although many of the results that will be presented here have been studied by more recent satellite experiments, it is significant that the Explorer 6 observations in 1959 were the first extensive ones made throughout the volume of the trapping region, and they remain unique in giving its state at a particular time in the solar cycle.

(*a*) Since Explorer 6 was placed in a very elliptical orbit, and owing to the inclination of the earth's magnetic axis to its spin axis, the satellite swept through a considerable part of the trapping region, making possible the construction of rather complete contours of constant counting rate and radiation dosages as measured by the Geiger counter and ionization chamber, respectively. Such contours necessarily depend strongly on the shielding surrounding the detectors and are thus peculiar to the spacecraft. Nevertheless, the Explorer 6 rate contours displayed a shape quite different from those derived by Van Allen using a similar Geiger counter aboard several previous spacecraft.

(*b*) The rates of the ionization chamber and Geiger counter displayed a minimum in the outer zone. According to the present magnetic data, the minimum in detector rates does not lie on a particle shell connecting with the Capetown magnetic anomaly, hence cannot be attributed to a scattering of radiation out of the trapping region by the anomaly. A spectral study of the outer zone suggests that the minimum has a spectral-detector origin.

(*c*) The proton differential energy spectrum fit to the data in the inner zone at a geomagnetic latitude of $-28°$ has the form $E^{-1.65}$ above 30 Mev. Electron fluxes in the inner zone are inferred to be greater than 10^7 electrons/cm^2 sec above 200 kev.

(*d*) In fitting trial spectrums to the outer-zone data it is seen that flat spectrums with electron energies up to 5 Mev must prevail at the inner edge or small ranges. The flux of electrons of energies between 1 and 5 Mev here is of the order of 10^6 electrons/cm^2 sec. With increasing range the spectrums steepen until at the outer edge the ionization chamber and Geiger counter are detecting the electrons only through the intermediate bremsstrahlung process.

(*e*) As is indicated by the nearly constant ratio of ionization chamber to Geiger counter rates, the spectrum of trapped particles in the outer zone to which the detectors are sensitive does not change appreciably down magnetic lines of force except at low altitudes. The counting rates of the Geiger counter were then used to determine the pitch-angle distributions of the trapped particles by studying the intensity down force lines. Such distributions in the outer zone show that beyond the line of force crossing the equator at 25,000 km there is an increasing number of particles turning near the equatorial plane. The pitch-angle distributions of the particles in the outer zone are inconsistent with those resulting from albedo neutron decay.

(*f*) Large rate changes are observed in the outer radiation region correlated with solar activity having a time delay indicating that the coupling is by means of solar plasma streams.

The percentage decreases are greater for lines of force at large radial distances. The data place an upper limit of about 10 per cent for time variations in the inner zone caused by solar activity during the lifetime of Explorer 6.

(*g*) Evidence for the lowering of mirror points in the outer zone during magnetically disturbed periods has been obtained. The pitch-angle distributions of "new particles" in the outer zone after a magnetic disturbance show that they mirror nearer the equatorial plane.

(*h*) The simultaneous measurement of low-energy radiation at 42,000 km on an electron shell connecting with an aurora suggests that the aurora is associated with a disturbance extending over many degrees longitude and out to large ranges. During a strong low-latitude aurora a rapid decrease in count rate was observed in the outer zone time coincident with the break-up of the aurora, indicating either the precipitation or deceleration of the trapped particles at this time.

ACKNOWLEDGMENTS

This work was supported by the National Aeronautics and Space Administration under contract NASw–56.

REFERENCES

Arnoldy, R. L., R. A. Hoffman, and J. R. Winckler, Observations of the Van Allen radiation regions during August and September 1959, 1, *J. Geophys. Research, 65*, 1361–1376, 1960*a*.

Arnoldy, R. L., R. A. Hoffman, and J. R. Winckler, Observation of the Van Allen radiation regions during geomagnetic storms, *Proc. COSPAR First International Space Science Symposium*, Nice, 877–896, 1960*b*.

Arnoldy, R. L., R. A. Hoffman, and J. R. Winckler, Observations of the Van Allen radiation regions during August and September 1959, 4, The outer-zone electrons, *J. Geophys. Research, 67*, 2595–2612, 1962.

Arnoldy, R. L., R. A. Hoffman, J. R. Winckler, and S.-I. Akasofu, Observations of the Van Allen radiation regions during August and September 1959, 5, Visual auroras, high-altitude X-ray bursts, and simultaneous satellite observations, *J. Geophys. Research, 67*, September 1962.

Arnoldy, R. L., and J. R. Winckler, Time variations in the earth's trapped radiation as measured by Explorer 6 satellite, *Bull. Am. Phys. Soc., 5*, 260, 1960.

Coleman, P. J., Jr., C. P. Sonett, and L. Davis, Jr., On the interplanetary magnetic storm: Pioneer 5, *J. Geophys. Research, 66*, 2043–2046, 1961.

Dessler, A. J., and R. Karplus, Some properties of the Van Allen radiation, *Phys. Rev. Letters, 4*, 271–273, 1960.

Dessler, A. J., and E. N. Parker, Hydromagnetic theory of geomagnetic storms, *J. Geophys. Research, 64*, 2239–2252, 1959.

Fan, C. Y., P. Meyer, and J. R. Simpson, Rapid reduction of cosmic-radiation intensity measured in interplanetary space, *Phys. Rev. Letters, 5*, 269–271, 1960.

Fan, C. Y., P. Meyer, and J. A. Simpson, Dynamics and structure of the outer radiation belt, *J. Geophys. Research, 66*, 2607–2640, 1961*a*.

Fan, C. Y., P. Meyer, and J. A. Simpson, Equatorial pitch-angle distribution of electrons in the outer radiation belt, *IGY Satellite Rept. 14, Rockets and Satellites*, National Academy of Sciences, Washington, D.C., July 1961*b*.

Hoffman, R. A., Observations of the Van Allen radiation regions during August and September 1959, 2, The Capetown anomaly and the shape of the outer belt, *J. Geophys. Research, 66*, 4003–4006, 1961.

Hoffman, R. A., R. L. Arnoldy, and J. R. Winckler, Observations of the Van Allen radiation regions during August and September 1959, 3, The inner belt, *J. Geophys. Research, 67*, 1–12, 1962.

Information Bulletin of Solar Radio Observations in Europe, No. 1, Section Ionosphere and Radio Astronomy, Netherlands PTT, The Hague, January 1960.

Janossy, L., *Cosmic Rays*, p. 267, Oxford at the Clarendon Press, London, 1948.

Lincoln, J. V., Geomagnetic and solar data, *J. Geophys. Research, 65*, 788–795, 1960.

Natl. Bur. Standards, U.S., CRPL, Solar and geophysical data, August, September, October, 1959; January, April, 1960.

O'Brien, B. J., J. A. Van Allen, C. D. Laughlin, and L. A. Frank, Absolute electron intensities in the heart of the earth's outer radiation zone, *J. Geophys. Research, 67*, 397–403, 1962.

Smith, E. L., P. J. Coleman, D. L. Judge, and C. P. Sonett, Characteristics of the extraterrestrial current system: Explorer 6 and Pioneer 5, *J. Geophys. Research, 65*, 1858–1861, 1960.

Sonett, C. P., E. J. Smith, and A. R. Sims, *Space Research: Proc. Intern. Space Sci. Symposium, First*, pp. 921–937, North-Holland Publishing Co., Amsterdam, 1960.

Space Technology Labs., *Project Able-3, Final Mission Report*, vol 2, Los Angeles, California, 1960.

Trotter, D. E., and W. O. Roberts, *Solar Activity Summary 3, 16 June through 1 October, 1959*, High Altitude Observatory, Boulder, 1960.

Valterra, V., *Theory of Functionals*, p. 54, Blockel and son, London, 1930.

Van Allen, J. A., and L. A. Frank, Radiation around the earth to a radial distance of 107,400 km, *Nature, 183*, 430–434, 1959.

Vernov, S. N., A. Y. Chudakov, P. V. Valukov, and Y. I. Logachev, Study of terrestrial corpuscular radiation and cosmic rays during flight of cosmic rocket, *Doklady Akad. Nauk SSSR, 125*, 304, 1959.

(Manuscript received August 20, 1962.)

Page intentionally left blank

Section 2. Cosmic and Trapped Radiation Studies Designed by the University of Chicago

Page intentionally left blank

Introduction to the Cosmic and Trapped Radiation Studies Designed by the University of Chicago

BY C. Y. FAN, P. MEYER AND J. A. SIMPSON

Enrico Fermi Institute for Nuclear Studies
University of Chicago

In retrospect, the investigations on Explorer VI provided several important contributions to the understanding of both the solar modulation of cosmic radiation and to the origin and structure of the Van Allen belts. To carry out specific studies it was essential to design an instrument which could, on the one hand, measure proton fluxes down to cosmic ray background levels in the presence of large fluxes of trapped electrons, and also separate high energy trapped protons from electrons in the belts. On the other hand, it must also measure cosmic radiation nucleon flux levels in space down to a well-defined cut-off energy (>75 MeV for protons). Electron fluxes were determined by means of their Bremsstrahlung effects within the detector. These measurements were accomplished by using a wide-angle, triple-coincidence, semi-proportional counter telescope of high stability, which is described in reference 1. The separation of protons and electrons was achieved and a typical cross-section curve showing the separation of protons and electrons in the radiation belts appears in figure 5 of reference 1. Even in the presence of the trapped electrons, small solar flare proton events could be detected (ref. 2).

To summarize the results, we divide the studies into two categories: those related to trapped radiation in the magnetosphere, and those concerned with testing various theories of cosmic ray modulation and therefore interplanetary observations in the sense that only cosmic ray fluxes were measured at great distances on Explorer VI in the proton channel.

TRAPPED RADIATION AND MAGNETOSPHERIC STUDIES

On the basis of evidence from more recent satellite launchings (e.g. Explorer XII and Explorer XIV) it is true that the range of electron and proton energies and their distributions in the magnetosphere are more extensive and detailed than could be deduced from Explorer VI instrumentation. Nevertheless, Explorer VI was the first of the series of sophisticated satellites that examined in detail and, for the first time, provided evidence of many features of the radiation belts. The most important conclusion drawn from the experiments is that the changes in the outer electron belt intensity and energy spectrum were taking place *irreversibly* and, hence, that local acceleration of the electrons is almost certainly required. Two irreversible processes among all the changes in the outer electron belt were identified during geomagnetic storms (refs. 1 and 3). It followed that it was unlikely the outer belt electrons could be solar electrons which arrive with subdetection energies to undergo local post-acceleration. It is probable that irreversible processes of gain and loss operate on the ambient electrons (and possibly beta decay electrons).

A general development of the Explorer VI data led to the conclusion that the flux and energy distribution of electrons in the outer belt were closely correlated to changes in the geomagnetic field. Since these magnetic field changes were brought about by geomagnetic

storms, it followed that the solar wind provided the energy input to the magnetosphere. It is further shown that in the region of the outer radiation belt the geomagnetic field is well described by the magnetic dipole approximation. The magnetic field parameters may be represented by the three parameters B_0, Θ, and b (ref. 1).

The inner belt proton distribution above 75 MeV was measured for the first time (fig. 5 of ref. 1).

The analysis of electron fluxes along a line of force in the geomagnetic field indicates major discrepancies with those predicted from the neutron decay theory for the origin of the inner belt and regions nearby (ref. 4). An investigation of the pitch-angle distribution of the outer belt electrons indicates a surprising concentration in the equatorial zone (ref. 5).

Explorer VI results pointed to a downward revision of the maximum electron flux to be expected in the outer radiation belt. Whereas it was formerly assumed in 1959 to be of the order of 10^{11} cm^{-2} sec^{-1}, the Chicago measurements and interpretation limited the electron fluxes to $<10^{9}$ cm^{-2} sec^{-1} (table 2, ref. 1).

EXPERIMENTAL TESTS FOR RESOLVING COSMIC RAY MODULATION THEORIES

By 1959 it had already been proven that the galactic flux of cosmic radiation was modulated through the intervention of magnetic fields controlled by solar plasma. Consequently, cosmic ray intensity variations and changes of cosmic ray spectrum are changed by solar activity. The most successful model for transporting magnetic fields into the interplanetary medium by solar plasma was the model of the solar wind by E. N. Parker. The fundamental question then arose as to whether plasma interactions with the magnetic environment outside the magnetosphere provided the main source of modulation (geocentric modulation), or whether the magnetic fields were vast in scale, occupying a large portion of the inner solar system and leading to intensity variations throughout the inner solar system independent of the presence of the earth. The first steps in deciding these matters were made with Explorer VI. A sharp reduction in cosmic ray intensity (known as the Forbush decrease) from ionization chamber measurements was observed simultaneously near the apogee of Explorer VI and by the University of Chicago neutron intensity monitors on the earth's surface. It was thereby proven that Forbush decreases could be seen in interplanetary space independent of the earth's system (ref. 6).

The slowly changing solar activity cycle produces an 11-year change in the galactic cosmic ray intensity; this was also shown to be primarily heliocentric since the general cosmic ray intensity level at the apogee of Explorer VI was essentially the same as that measured at the earth's surface for an integral flux above 75 MeV (ref. 7). The final proof of both of these effects came from the flight of Pioneer V in March 1960.

REFERENCES

1. Fan, C. Y., Meyer, P. and Simpson, J. A.: Dynamics and Structure of the Outer Radiation Belt, *J. Geophys. Res.*, Vol. 66, 2607, 1961.
2. Fan, C. Y., Meyer, P. and Simpson J. A.: Trapped and Cosmic Radiation Measurements from Explorer VI, *Space Research*, Vol. 1, p. 951, 1960.
3. Simpson, J. A., Fan, C. Y. and Meyer, P.: Dynamics of the Outer Radiation Belt, *J. Phys. Soc. of Japan*, Vol. 17, Suppl. A–11, 154, 1962.
4. Hess, W. N., Killeen, J., Fan, C. Y., Meyer, P. and Simpson, J. A.: The Observed Outer-Belt Electron Distribution and the Neutron Decay Hypothesis, *J. Geophys. Res.*, Vol. 66, 2313, 1961.
5. Fan, C. Y., Meyer, P. and Simpson, J. A.: The Equatorial Pitch Angle Distribution of Electrons in the Outer Radiation Belt, *Space Research*, Vol. 11, pp. 867–875, 1961.
6. Fan, C. Y., Meyer, P. and Simpson, J. A.: Cosmic Radiation Intensity Decreases Observed at the Earth and in the Nearby Planetary Medium, *Phys. Rev. Letters*, Vol. 4, pp. 421–423, 1960.
7. Fan, C. Y., Meyer, P. and Simpson, J. A.: Experiments on the Eleven-Year Changes of Cosmic Ray Intensity Using a Space Probe, *Phys. Rev. Letters*, Vol. 5, 272, 1960.

Cosmic Radiation Intensity Decreases Observed at the Earth and in the Nearby Planetary Medium[1]

BY C. Y. FAN, PETER MEYER, AND J. A. SIMPSON

Enrico Fermi Institute for Nuclear Studies
University of Chicago

This note reports preliminary experiments which prove that existing theories for the modulation mechanism responsible for rapid decreases of primary cosmic-ray intensity cannot invoke the presence of the earth or its magnetic field.

Forbush first noted sudden intensity decreases in ionization chambers located deep within the atmosphere which followed in the order of 20 to 40 hours some large solar flares.[1] These intensity decreases arose from changes in the secondary radiation produced by primary cosmic rays and were frequently accompanied by substantial geomagnetic field disturbances. It was later shown experimentally that this kind of world-wide decrease was a property of the primary cosmic radiation observed at the earth, and arose neither as a consequence of the geomagnetic storm nor by phenomena which might change temporarily the magnetic cutoff rigidities, such as ring currents around the earth.[2] The changes in the primary spectrum during times of depressed intensity—namely, a larger decrease for low magnetic rigidity particles than for high rigidity particles—suggested that the modulation was due to interplanetary magnetic fields in the vicinity of the earth.[2] For a typical event, the high rate for reduction of prevailing cosmic radiation intensity at the earth also placed bounds on the requirements for magnetic field intensity and scale size of suitable modulating electromagnetic fields, i.e., intense fields of large scale size, or vice versa.

Several hypotheses have been advanced for this solar-produced modulation of galactic cosmic radiation. On the one hand are models which may be described roughly as heliocentric; namely, where the cosmic radiation intensity in a substantial volume of the inner solar system is reduced by either disordered,[3] or ordered magnetic fields[4,5] of solar origin independent of the presence of the earth and its geomagnetic field. On the other hand are models which depend upon the solid earth and its permanent magnetic field for creating the decrease of cosmic-ray intensity; namely, geocentric models.[6] To decide between these two classes of hypotheses, we ask the question: How far into the interplanetary medium is the full decrease of galactic cosmic-ray intensity observed during a Forbush decrease? Is the pre-existent radiation intensity found at distances beyond which the geomagnetic field could be invoked to account for the Forbush decrease, or is the intensity also reduced in the nearby interplanetary medium as it is at the earth? For all existing models which invoke the presence of the geomagnetic field, a suitable limit for the effective extent of the modulating region is 6 to 10 R_e, where R_e is the radius of the earth.

[1] This work was supported in part by the National Aeronautics and Space Administration and in part by the U.S. Air Force Office of Scientific Research. This article was published in the April 1960 issue of *Physical Review Letters*. Reprinted by permission.

765-698 O-65—15

To answer these questions, we have performed a direct experiment using a cosmic-ray detector carried by the Explorer VI satellite launched August 7, 1959 in an orbit which extended beyond the region of trapped Van Allen radiation and reached a range in excess of $7.5R_e$. In addition to the satellite observations, we measured simultaneously the changes in the nucleonic component at the earth over a wide range of geomagnetic cutoff rigidities. For this purpose we used neutron intensity monitors extending from the geomagnetic equator to high latitudes.

The cosmic-ray detector in the satellite was a triple-coincidence, proportional counter system which measured protons in excess of 75-Mev energy, or electrons in excess of 13-Mev energy. The triple coincidence detector does not respond to bremsstrahlung, such as from electrons trapped in the geomagnetic field. The satellite orbit was an ellipse of apogee approximately 48,800 km and perigee approximately 6,600 km, with its orbital plane inclined by about 46° to the geographic equator. A description of the instrument, its performance, and the satellite and its motions will appear elsewhere.[7] Most of the data recorded at the earth during the two months when the telemetry was operative covered the first four weeks after the launching. During this time, one outstanding sharp decrease of cosmic-ray intensity and two smaller decreases were observed in the neutron intensity monitors at the earth. The results we report here are for this period. Only satellite data in the range 35,000 to 48,800 km were used for analysis. The continuous record of the neutron intensity monitor at Climax, Colorado (located at a geomagnetic rigidity cutoff of ~2.5 Bv) was chosen from among the network detectors to represent the changes at the earth. Only neutron intensity data for time intervals which overlapped the satellite triple-coincidence data were used as shown in figure 1. The statistical errors of the satellite data are less than 1 percent for all points used in figure 1. All neutron data have smaller errors. From figure 1 the over-all correlation between the detectors at 35,000 to 48,000 km and at the earth's surface is obvious. Only the large decrease on August 20 provides data of sufficient accuracy to compute the ratio of the relative change of intensity at the satellite and at the earth as shown in figure 2. The ratio is:

$$\frac{\text{Relative change in satellite detector}}{\text{Rel. change in nucleonic component detector}} = 1.9.$$

The correlation coefficient for the two sets of data in figure 2 is 0.96. We now compare the amplitude of the Forbush decrease at great distances from the earth with the amplitude in the *primary* radiation at the top of the atmosphere. Therefore, we have to relate the intensity changes of secondary neutrons as observed at Climax to the changes of primary intensity outside the atmosphere above Climax. For this purpose we may use neutron intensity measurements at balloon altitudes which have been carried out for typical Forbush decreases over a number of years by our laboratory. For the present phase of the solar cycle, and cosmic-ray spectrum, this factor is approximately 1.8. Therefore, within an experimental error of

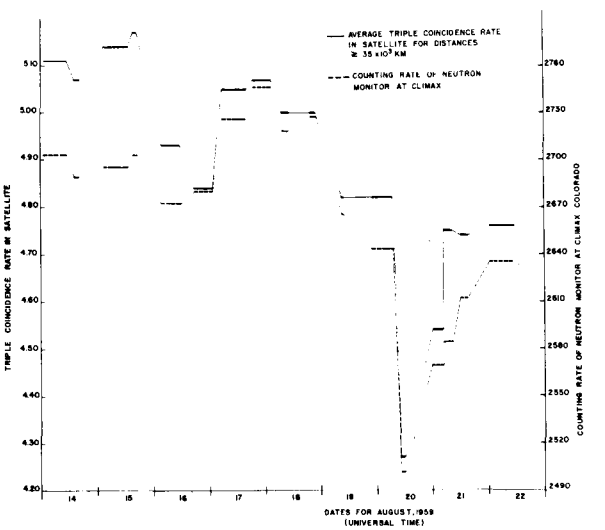

FIGURE 1.—*Cosmic-radiation intensity as a function of time showing on August 20, 1959 a Forbush-type intensity decrease of ~15 percent within five hours. The nucleonic component monitor provides a measure of primary intensity changes at the earth. The lightdashed and solid lines are used to connect the periods for which satellite data are available.*

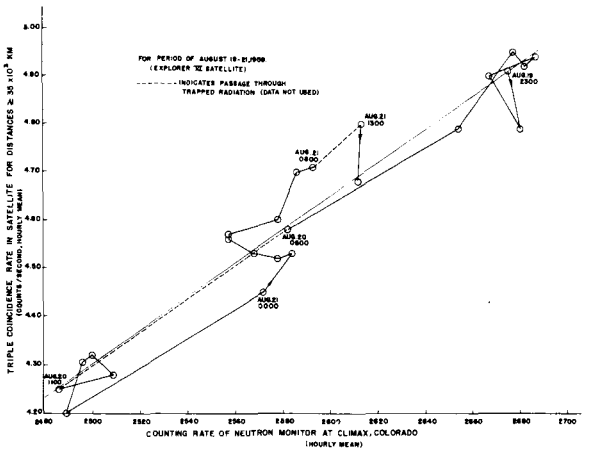

FIGURE 2.—*The relative changes in cosmic-ray intensity at the satellite and at the earth for the sharp intensity decrease of August 20 shown in figure 1. The correlation coefficient is 0.96.*

approximately 10 percent, the magnitude of the sharp decrease of primary cosmic radiation was the same at the earth as it was out to distances as great as 7.5 R_e. Thus the decrease of August 20, 1959 means that more than 15 percent of all the cosmic-ray particles were removed within 5 hours by the modulation mechanism. Using neutron intensity monitor data we have shown that this event is worldwide, and that the spectrum has undergone changes which are typical of other Forbush decreases studied at this phase of the solar cycle.

We believe this experiment excludes existing hypotheses which invoke the presence of the earth and the geomagnetic field to account for the Forbush decreases of cosmic-ray intensity. Thus, geocentric models such as solar plasmas containing disordered magnetic fields overlying the geomagnetic field, or the roughing-up of the geomagnetic field by a solar wind do not account for our observations. On the other hand, we know that these sharp intensity decreases at the earth are the delayed consequences of large solar flare outbursts on the visible side of the sun. Forbush decreases are observed at the earth only for restricted angular positions of the solar events relative to the position of the earth. Therefore, the modulation region may be confined to a volume of space surrounding the Sun-Earth line. This restricted heliocentric system of fields is different, at least in scale size, from the mechanism required for the modulation of cosmic radiation intensity over the 11-year solar activity cycle.[8] We do not here go into further details of suitable models.

The space probe Pioneer V (launched March 11, 1960) carrying equipment identical with the Explorer VI satellite may soon provide further tests of the scale size for the Forbush intensity decrease at distances $>>8R_e$.

Figure 1 also shows that the radiation measured by the satellite undergoes a stepwise intensity decrease following each of the two decreases which is not apparent in the relativistic energy range of the spectrum as represented by the neutron intensity monitors on the earth. This may indicate the persistent exclusion of some low-energy particles by the mechanism producing the Forbush decreases and is being investigated.

The authors wish to thank especially Leonard Petraitis, Robert Takaki, Joseph Jezewski, James Lamport, and Lucien Biberman of the University's Laboratories for Applied Sciences for their contributions to the engineering of our apparatus in Explorer VI. The Advance Research Project Agency provided funds for the initial development of the instruments.

We wish also to express our thanks for the overall payload engineering and coordination provided by Space Technology Laboratories, especially Dr. Adolph Thiel and Dr. John Lindner. The constant interest of Dr. John Lindsay of the National Aeronautics and Space Administration was deeply appreciated. Mr. R. Tjonaman and staff of the Enrico Fermi Institute Cosmic-Ray Group maintained a continuous watch for unusual solar and cosmic-ray events which made possible the increased data acquisition from the satellite during August.

REFERENCES

1. S. E. Forbush· Phys. Rev. *54*, 975 (1938). We here refer to this type of rapid decrease of intensity as a Forbush decrease.
2. J. A. Simpson, Phys. Rev. *94*, 423 (1954); Proc. Natl. Acad. Sci. U.S. *43*, 42 (1957).
3. P. Morrison, Phys. Rev. *101*, 1307 (1956).

4. G. Cocconi, T. Gold, K. Greisen, S. Hayakawa, and P. Morrison, Suppl. Nuovo cimento *8*, 161 (1958).
5. H. Elliot, International Union of Pure and Applied Physics Conference on Cosmic Rays, Moscow, 1959 (unpublished).
6. E. Parker, Phys. Rev. *103*, 1518 (1956); Phys. Rev. *110*, 1445 (1958).
7. C. Y. Fan, P. Meyer, and J. A. Simpson, *Proceedings of the First International Conference on Space Research* (North-Holland Publishing Company, Amsterdam, 1960) (to be published).
8. For further reference, see J. S. Simpson, Astrophys. J. Suppl. *4*, No. 44, May, 1960.

(Received March 29, 1960.)

Experiments on the Eleven-Year Changes of Cosmic-Ray Intensity Using a Space Probe[1]

BY C. Y. FAN,[2] PETER MEYER, AND J. A. SIMPSON

Enrico Fermi Institute for Nuclear Studies
University of Chicago

The total intensity of cosmic radiation reaching the earth changes with the 11-year solar activity cycle.[1] The energy spectrum of relativistic particles up to at least 20 Bev changes approximately from $E^{-2.7}$ (1954) to $E^{-2.0}$ at maximum solar activity (1957–8) with the intensity being reduced at solar maximum by a factor 2 for the relativistic particle flux,[2] and by a factor in excess of 4 for the integral flux down to $\sim$100 Mev for protons.[3] Figure 1 shows the change in nucleonic component intensity between 1954 and 1960. Experimental evidence strongly supports the view that the spectrum at solar minimum approximates the full galactic spectrum outside the solar system, and that through an electromagnetic modulation mechanism, initiated by solar activity, the galactic particle flux having access to the inner solar system, or the earth, is greatly reduced at solar activity maximum.[2] We have performed direct experiments which prove that any mechanism changing the cosmic-ray intensity over 11 years is centered about the sun, and the scale size is $>$1 astronomical unit (a.u.) for the volume of space in which the cosmic-ray intensity is reduced at this period of the solar activity cycle. We also find that the gradient of cosmic-ray intensity near the orbit of Earth is so small as to suggest that modulation of galactic intensity occurs at distances much greater than the orbit of Earth.

The experiment consists in carrying a cosmic radiation detector from the Earth to great distances in interplanetary space near the time of solar maximum. The detector measures protons above 75 Mev and, hence, integrates over that part of the cosmic-ray spectrum which changes by a factor of 2 to 4 in intensity between solar maximum and solar minimum. If the reduced intensity is restricted to the vicinity of the Earth, the flux measured in interplanetary space

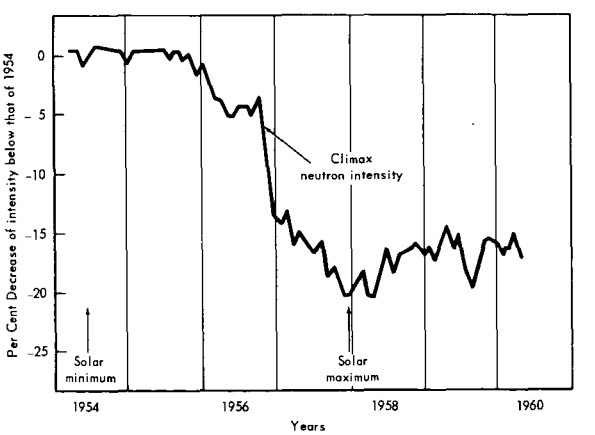

FIGURE 1.—*Changes in the nucleonic component intensity between 1954 and 1960 at Climax, Colorado (~2.4 Bv magnetic rigidity cutoff).*

[1] This research was supported principally by the National Aeronautics and Space Administration, and in part by the Air Force Cambridge Research Center, Geophysics Research Directorate, and the Air Force Office of Scientific Research. Published in the September 1960 issue of *Physical Review Letters*. Reprinted by permission.

[2] Also Laboratories for Applied Science, University of Chicago, Chicago, Illinois.

will be greater by a factor of 2 to 4. If the volume in which there is reduced intensity is heliocentric, then there will be an intensity gradient in the direction of the sun, the magnitude of which depends greatly upon the model adopted for the solar origin of the 11-year, cosmic-ray intensity variations.

Identical cosmic-ray detectors were carried by the satellite Explorer VI (launched August 7, 1959) and the space probe Pioneer V (launched March 11, 1960) and are described elsewhere.[4, 5] Since this detector was not sensitive to bremsstrahlung [4] from trapped electrons in the outer radiation belts of the Earth, the cosmic-ray flux was measured from less than 10,000 km to 48,000 km from Earth by Explorer VI. The data for August 9, 1959 are shown in figure 2. Between this data and the launching of Pioneer V on March 11, 1960, the integrated cosmic-ray intensity at the Earth increased by +13 percent as deduced from nucleonic component monitors. The August 9, 1959 rates in figure 2 have, therefore, been increased by 13 percent for comparison with the Pioneer V data. We note that the cosmic-ray flux was approximately constant from inside the terrestrial field far into the interplanetary medium.

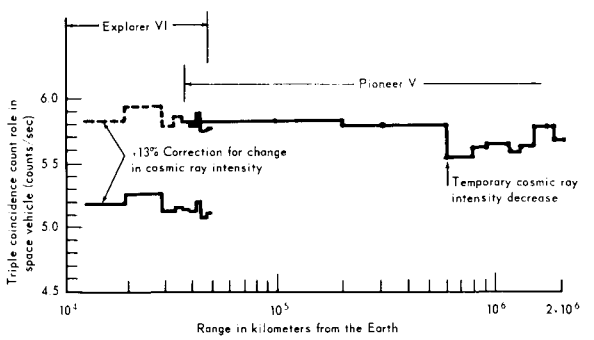

FIGURE 2.—*Counting rate of triple coincidence events in Explorer VI satellite (August 9, 1959) and Pioneer V space probe (March 1960). The 13-percent correction in Explorer VI data arises from intensity changes known to take place outside the atmosphere between August 1959, and March 1960, due to the 11-year cycle (see fig. 1). Assigned errors on each interval of data are less than 1 percent. Pioneer IV (March 1959) also observed constant intensity between 92,000 and 658,000 km.*[8]

Therefore the 11-year depression of cosmic-ray intensity is not geocentric.

We know from analysis of nucleonic component data such as shown in figure 1 that the cosmic-ray intensity measured at the Earth as the Earth moves in its orbit about the Sun is not significantly dependent upon solar system longitude. Thus, at solar maximum the cosmic-ray intensity is not only depressed within the inner solar system but the depression is roughly concentric about the Sun in the ecliptic plane.

Provided these intensity changes are brought about by solar modulation of the galactic flux, these results lead to the conclusion that there must be a cosmic-ray intensity gradient somewhere between interstellar space and the inner solar system. This gradient will exist in the regions of space where the electromagnetic modulation is taking place.

On the one hand, if the modulating region lies beyond the orbit of Earth (>1 a.u.) then the gradient between Sun and Earth will be very small. A model in this category would be convective removal of particles by advancing magnetic field irregularities arising from instabilities of a solar wind.[6] On the other hand, if the Earth lies inside the modulation region the cosmic-ray flux will decrease as one approaches the Sun. Several models, including a recent proposal of Elliot,[7] require a large, negative gradient between Sun and Earth.

One of the objectives for the space probe Pioneer V was to examine this problem. At this time we have data over the initial 50 days representing a change in solar radial distance of 0.1 a.u. (10 percent of the distance to the Sun) which sets upper limits on the radial gradient of cosmic-ray intensity in interplanetary space. To remove the time-dependent changes of cosmic-ray intensity, we determined the ratio of the intensities in Pioneer V to the intensities at the Earth represented by the nucleonic component monitor at Chicago. This ratio, normalized to unity at time of launch, March 11, is shown in figure 3 as a function of solar radial distance, and time. We have averaged data over intervals of two to three days for this analysis.

It is immediately apparent from figure 3 that there was a sudden loss of flux of nonrelativistic

particles at the time of the rapid, Forbush intensity decrease of March 31–April 1.[5] This change in the primary spectrum persisted to the last available measurements 30 days later. The stepwise decrease in the very low energies was also detected in the Explorer VI data,[4] and will be discussed in a later publication. Smaller intensity decreases occurred at the times shown by arrows in figure 3. This effect is a change

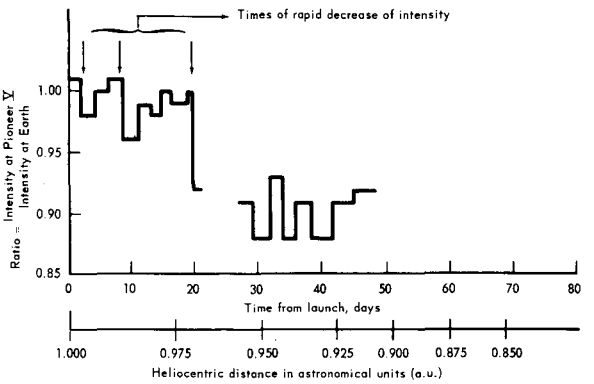

FIGURE 3.—*The change of cosmic-ray intensity radially along the sun-earth line and relative to the intensity at the orbit of Earth. The errors assigned to these averaged intervals of data are less than 0.5 percent. The arrows indicate the existence of known perturbations in the low-energy portion of the cosmic-ray spectrum and data for these periods are not used in determining the intensity gradient.*

in spectrum which must be taken into account in measuring the gradient. There also exists the possibility that the negligible gradient observed from 0.95 a.u. to 0.90 a.u. (25th to 50th day) is the result of a space gradient plus a compensating gradual return of the low-energy particles. However, such a coincidence of effects is not likely to continue over so long a period.

We obtain a radial omnidirection intensity gradient of $-(15\pm20)\%$/a.u. measured near the orbit of the Earth and in the direction of the Sun. This value is inconsistent with the existence of a positive gradient such as required for an appreciable, steady solar production of the radiation. This small but negative gradient shows that (during the period of this measurement) any electromagnetic modulating mechanism required to account for the eleven-year intensity variations is located principally outside the orbit of Earth. Such results from Pioneer V place strong constraints upon acceptable heliocentric models for the eleven-year cosmic-ray intensity variation.

We hope that additional data at later times in May may be extracted from the noisy data arising from the low signal level at these great distances.

For their contributions to the engineering and construction of our apparatus we wish to thank Mr. J. Jezewski, Mr. J. Lamport, Mr. L. Petraitis, and Mr. R. Takaki of the Laboratories for Applied Science, University of Chicago. We also appreciate the overall engineering and management of the Pioneer V project by Dr. A. Thiel, Dr. J. Lindner, and the staff of Space Technology Laboratories. The assistance of Dr. J. Lindsay of the NASA for the Pioneer V project and the use of the Jodrell Banks radio telescope by Professor A. C. B. Lovell enhanced greatly the results of these experiments.

REFERENCES

1. S. E. Forbush, J. Geophys. Research *59*, 525 (1954).
2. P. Meyer and J. A. Simpson, Phys. Rev. *106*, 568 (1957); J. Simpson, Astrophys. J. Suppl. Series No. 44, *4*, 378 (1960).
3. H. V. Neher, Phys. Rev. *107*, 588 (1957); J. R. Winckler and L. Peterson, Nature *181*, 1317 (1958).
4. C. Y. Fan, P. Meyer, and J. A. Simpson, *Proceedings of the First International Conference on Space Research* (North-Holland Publishing Company, Amsterdam, 1960); IGY Satellite Report No. 11, p. 115, June, 1960 (World Data Center A).
5. C. Y. Fan, P. Meyer, and J. A. Simpson, preceding Letter [Phys. Rev. Letters *5*, 269 (1960)].
6. E. N. Parker, Phys. Rev. *109*, 1874 (1958).
7. H. Elliot, Nature *186*, 299 (1960).
8. J. A. Van Allen and L. A. Frank, Nature *184*, 219 (1959).

(Received August 10, 1960.)

Dynamics and Structure of the Outer Radiation Belt[1]

BY C. Y. FAN,[2] P. MEYER, AND J. A. SIMPSON

Enrico Fermi Institute for Nuclear Studies
University of Chicago

From an analysis of electron measurements in the Explorer VI satellite (August 7-October 6, 1959) four time-dependent parameters which characterize the outer electron belt have been investigated. They are: (1) the equatorial electron intensity I_0; (2) the equatorial range from the earth R_0 of the peak intensity; (3) the electron-density distribution along a line of force through the intensity peak; and (4) a measure of the change in electron spectrum with time. These parameters, along with measurements of magnetic field intensity, make it possible to study the origin of the changes in electron intensity and distribution which are known to occur in the outer belt. Several magnetic storms occurred during the observation on Explorer VI. Within the sequence of changes in the outer belt induced by these geomagnetic storms, there are some changes of the parameters which are accounted for only by invoking an irreversible energy gain or loss within the outer belt. The energy gain process appears to be through irreversible local acceleration of electrons. The energy loss process leads to a stable mirror-point distribution characteristic of the periods between geomagnetic storms. The time intervals within which each of these processes is operative are identified. Reversible processes are possibly the cause for other changes.

The foregoing analysis rests upon the proof given in this paper that the outer-belt peak intensity coincides over a wide range of geomagnetic latitudes with magnetic field lines of force in the centered dipole approximation. Consequently, the measured electron-intensity maximum is used as a 'tracer' of the geomagnetic field lines of force for analyzing changes in the outer belt with time. It is shown that even during geomagnetic storms the trace of the electron-intensity maximum followed a centered dipole line of force. This indicates that at all times the particle-energy density of the radiation belt is much less than the energy density of the magnetic field in the region. The electron fluxes, high-energy proton fluxes, and possible electron spectra are investigated. Two distinct peaks of electron intensity are identified to persist in the outer belt for about 2 months, and it is shown that these peak distributions undergo radial motion during geomagnetic disturbances.

Author

1. INTRODUCTION

The first measurements of charged particles trapped within the geomagnetic field were made by the Iowa [*Van Allen, McIlwain, and Ludwig*, 1959] and by the U.S.S.R. groups [*Vernov, Chudakov, Vakulov, and Logachev*, 1959*a*]. Subsequent observations proved the existence of an inner belt composed of energetic protons and electrons, and an outer radiation belt dominated by energetic electrons. Single traversals of the outer belt made at different times led to the conclusion that the characteristics of this outer belt changed with time and solar activity. The origin of the inner belt protons is satisfactorily accounted for by the decay products of fast neutrons escaping from the terrestrial atmosphere. Although the origin of the outer belt at first was ascribed to electrons accelerated at the sun and subsequently trapped in the geomag-

[1] Published in the September 1961 issue of *Journal of Geophysical Research*. Reprinted by permission.

[2] Also Laboratories for Applied Sciences, University of Chicago, Chicago, Illinois.

netic field, this hypothesis foundered on both the basis of physical principles and through experimental evidence, including results reported in this paper. Therefore, if electrons are to be introduced from the sun, or other sources at very low energy, it is required that they be accelerated in the geomagetic field to yield the persistent, variable flux of energetic electrons observed in the outer radiation belt. On the other hand, if the outer-belt electrons are ambient electrons, or electrons from neutron decay [*Hess*, 1960; *Dessler and Karplus*, 1960], then the changes in electron intensity and spatial distribution must also arise from magnetic field changes.

Therefore we conclude that a study of the changes in the electron outer belt brought about by changes in the geomagnetic field may lead us to the origin of these trapped electrons.

The energy that produces the variations of the external geomagnetic field comes from solar events, such as the solar flares, which emit ionized plasma leading to the classical geomagnetic storm.

There are a variety of ways in which some of these changes in energy and distribution of trapped electrons may be brought about [e.g., *Northrop and Teller*, 1960; *Parker*, 1961*a*]. Either rapid field changes including hydromagnetic wave propagation lead to the violation of one or more of the adiabatic invariants, and hence to *irreversible* acceleration or loss of energy in the belt, *or* slow field changes can dominate to produce *reversible* acceleration and consequent changes in the particle distributions in space.

The main purpose of the present investigation is to decide whether reversible processes determine the changing character of the outer electron belt or whether irreversible processes must be invoked. The experiment, therefore, requires frequent, sequential traversals of the outer electron region at intermediate and low latitudes for extended periods of time under quiet field conditions as well as during geomagnetic storms. An investigation of this kind was first undertaken by the Explorer VI satellite launched August 7, 1959, in the highly elliptic orbit shown in figure 1. This satellite carried a group of charged-particle radiation detectors having a wide dynamic range and variety of energy responses, as well as a magnetometer. The types of radiation detection instruments are given in appendix A, table 1, along with a list of all space vehicles which at this writing have passed through the outer belt at low latitudes (app. A, table 2). The measurements were obtained under fortunate circumstances, since the geomagnetic field remained quiescent for a week before the commencement of two geomagnetic storms closely spaced in time. All the data are within the period August 7 through October 6, 1959, following which time the transmitter ceased to operate.

A preliminary account of our experiments [*Fan, Meyer, and Simpson*, 1960] has shown several new properties of the trapped electrons in the outer belt, such as the persistent existence of a double belt structure in the outer zone and radial motions of these peak intensity distributions with time. We also observed the large-scale time-dependent changes of intensity and particle distributions following geomagnetic storms which have also been reported by other investigators with apparatus on Explorer VI [*Arnoldy, Hoffman, and Winckler*, 1960*a*; *Rosen, Farley, and Sonett*, 1960]. However, our detailed study and conclusions regarding the outer-belt electrons have awaited the full re-

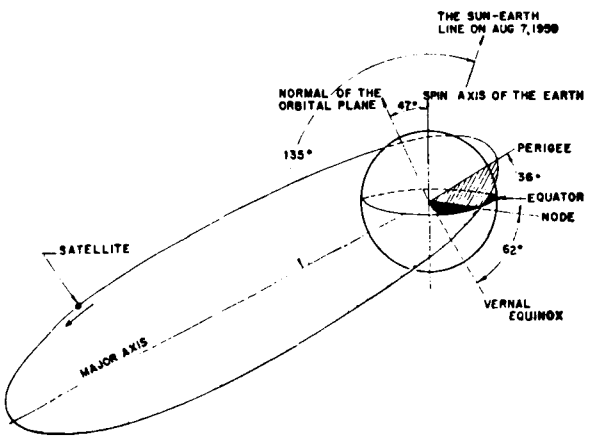

FIGURE 1.—*Perspective drawing of the Explorer VI satellite orbit. The orbital data are as follows: period, 12 hours 48 minutes; apogee, 48,788 km; perigee, 6,626 km; Geographic inclination 47°; Tilt of orbit, 38° with respect to ecliptic plane.*

duction of data, the availability of correlating solar geophysical data, and improved orbit calculations for Explorer VI.

To prove whether there exist irreversible changes or only reversible changes, our investigation centers on the identification and measurement of parameters that describe the characteristics of the outer belt and their changes with time. We first show that a centered dipole magnetic field is a good approximation for the description of trapped electron guiding centers in the outer belt, even during periods of geomagnetic storms. Thus, the positions of intensity maxima in the outer belt become "tracers" by which we follow changes in position, intensity, or other parameters as a function of time. It is then possible to follow systematically through the progress of a geomagnetic storm the changes of parameters such as the equatorial range R_0 of the outer belt, or the equatorial intensity maximum I_0. To investigate reversible and irreversible processes we also need to know the electron mirror-point distribution along a magnetic line of force and the changes in this distribution with time. Having proved that the centered dipole approximation describes the lines of force in space in the outer belt, we are able to construct experimental curves of electron intensity as a function of position along magnetic lines of force and to relate the changes in their distributions to geomagnetic storms.

The analysis of bremsstrahlung intensity rests upon some knowledge of the changes in electron spectrum with time and position in the geomagnetic field. Through the introduction of a parameter that reveals when the electron spectrum changes as a function of position or time, we separate spectral changes during magnetic storms from changes in mirror-point distributions, etc. The measurements show that there is a concentration of electrons at the equator during some geomagnetic storms.

Our results lead to the identification of two irreversible processes among all the changes in the electron outer belt during geomagnetic storms. One is an energy or particle gain; the other is an energy or particle loss. Although not disproved, it also appears unlikely that the outer-belt electrons are solar electrons which arrive with subdetection energies to undergo local postacceleration. It is probable that the irreversible processes of gain and loss operate on ambient electrons and beta decay electrons. Some conditions are established for developing specific models of the electron outer belt.

2. CHARACTERISTICS OF THE DETECTOR SYSTEM

In order to separate high-energy protons ($P > 75$ Mev) and electrons ($E > 13$ Mev) from bremsstrahlung produced by lower energy electrons, a triple coincidence telescope consisting of seven methane-argon filled gas counters was used for the detectors (fig. 2). These counters operated in the semiproportional range with a

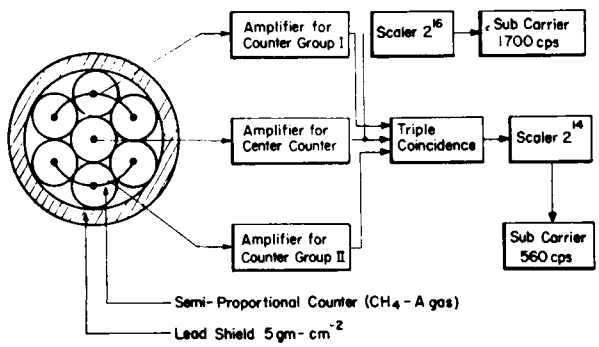

FIGURE 2.—*Block diagram of instrumentation in Explorer VI used for the analysis of the outer electron belt.*

dead-time of 0.8 microsecond. This makes it possible to distinguish the cosmic ray flux from the trapped radiation in the outer radiation belt and to separate the bremsstrahlung production from energetic protons in the inner radiation belt. Groups of these counters were combined as shown in figure 2 to form a wide-angle, triple-coincidence counter telescope, so that the accidental rate would be negligible even for the highest fluxes expected in the outer belt. The wide-angle was chosen to avoid the variation of counting rates due to any possible anisotropy of the radiation in the geomagnetic field. The lead shield surrounds the triple-coincidence telescope for two reasons: (1) It provides a threshold for the minimum energy protons detectable by the triple-coincidence telescope (75 Mev for

protons and $\geq$ 13 Mev for electrons). (2) The 5 g-cm^{-2} of lead reduces the total counting rate in each of the individual counters to such a level that even for the highest fluxes attainable in the outer radiation belt, only minor corrections due to the dead-time were needed, and never more than 2 percent.

The information from the outputs of the two scalers in figure 2 were transmitted to ground receiving stations through two subcarrier channels in the Explorer VI satellite.

The response of this detector system to protons was studied with the University of Chicago synchrocyclotron proton beam. The results are shown in figure 3 for the detector axis perpendicular to the proton beam over an energy range of

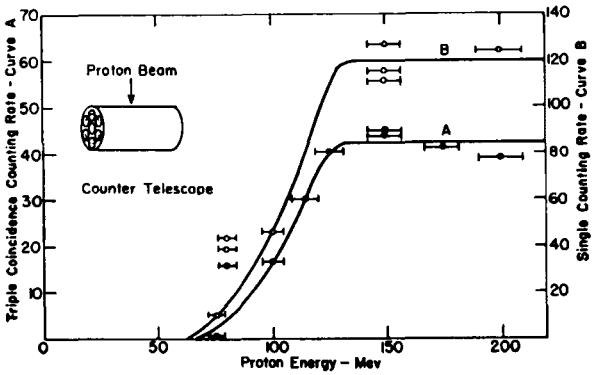

FIGURE 3.—*Detector response for protons from the synchrocyclotron beam of the University of Chicago.*

50 to 250 Mev. In measuring relatively flat spectra like the cosmic radiation and the inner-belt protons [*Freden and White*, 1960] this detector possesses a sharp cutoff at the mean energy of 100 Mev. For solar flare protons where the spectra may be as steep as $1/E^5$, the gradual change in sensitivity in the region from 75 to 100 Mev, as shown in figure 3, must be taken into account.

The noncoincident high counting rates of the single counter during the passage through the outer belt must be due exclusively to geomagnetically trapped electrons which produce bremsstrahlung either in the satellite shell, interior objects, or in the surrounding lead shield. With an unknown energy spectrum it is obviously impossible to relate the count rate of the single counter to the flux of particles or energy flux carried by the electrons incident on the vehicle. However, with proper calibration, we shall show in section 11 that significant limits on the particle flux and on the particle energy spectra may be derived.

The response of this bremsstrahlung detector to monoenergetic electrons was studied in the laboratory using the electron beam from Van de Graaff generators (High-Voltage Engineering Company and the General Electric Company) and a low energy X-ray source at the University of Minnesota. The completely assembled spare payload of Explorer VI, with a mass distribution identical to the flight unit, was mounted so that it could be rotated about two mutually perpendicular axes for exposing any portion of its surface to direct electron bombardment. (The electron flux in the energy range from 250 kev to 1 Mev in discrete energy intervals irradiated the payload from various directions, so that an averaged response of the counter for isotropic radiation could be deduced. This experiment differs from an exposure to particles in space in two ways: there was air present inside the payload; the electron beam for each exposure was unidirectional instead of omnidirectional. Additional measurements were obtained inside the vacuum system using the bremsstrahlung detector with an absorber simulating the satellite shell.)

Since the shell of Explorer VI payload is made of aluminum 170 mg/cm^2 thick, all electrons with energies below 500 kev are stopped in the shell. Therefore the response of our radiation detector to electrons below 500 kev is due entirely to bremsstrahlung produced in the payload shell. This was verified by showing that the count rate for an equivalent electron flux was proportional to the inverse square of the distance between the detector and the irradiated area on the shell. The angular distribution of X-rays within the satellite appears to be sufficiently isotropic to use the inverse square law for those parts of the payload where no appreciable absorption material is located between the satellite shell and our detector. The assumption of isotropy for the X-rays produced in the shell will be an even better approximation in the

actual case of omnidirectional incidence of electrons in space.

For the equatorial plane of the vehicle where the instruments and associated equipment are located, the experimental count rates for the electron flux incident at various payload longitudes were used to compute the bremsstrahlung contribution. The openings between equipment and eletronic parts in the payload were studied, and the calibration takes into account factors that could influence the count rate from low energy X-rays.

From these measurements we wish to obtain the flux of monoenergetic electrons isotropically incident upon the satellite from the counting rate of our bremsstrahlung detector. To this end we integrated over the response curve in the equatorial plane, and added the upper and lower hemisphere integrations of the payload shell separately. Thus we obtained the response curve in counting rate per electron per square centimeter bombarding the shell as shown in figure 4. The portion of the curve between 200 and 1,000 kev can be expressed as a power law $E^{4.7}$.

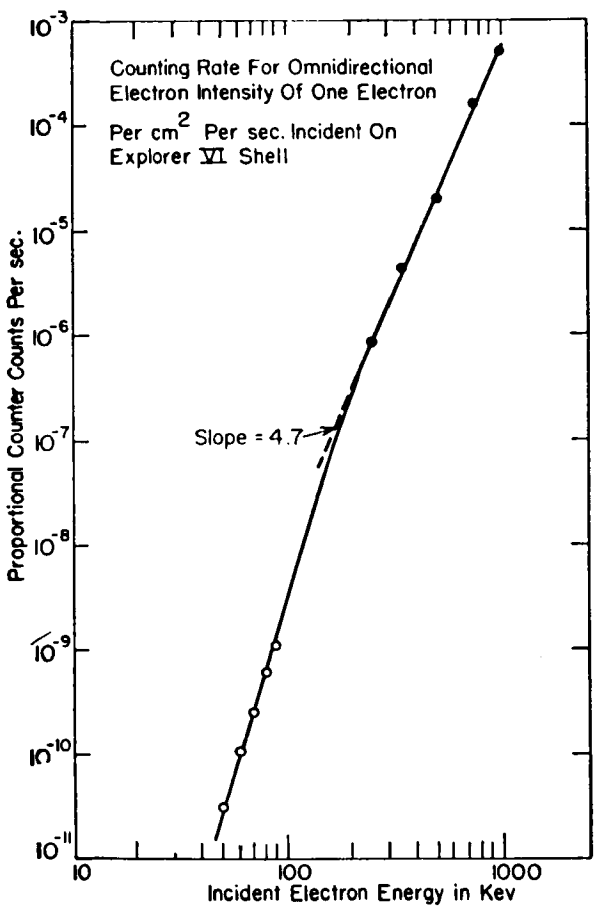

FIGURE 4.—*Calibration curve for the center counter shown in figure 2. These electron data were obtained with the detector in the duplicate Explorer VI vehicle.*

The performance of our detector system for separating trapped protons and cosmic radiation from bremsstrahlung is clearly shown in the Explorer VI measurements of figure 5 which represents a traversal through the inner and outer radiation belts at high geomagnetic latitudes.[3] The triple-coincidence counting rate rises to a maximum value at 8,500 km representing the peak of the inner radiation belt for protons $>$ 100 Mev, and decreases to a cosmic-ray background at the radial distance of 9,500 km and beyond.

For counting penetrating particles in a single counter the calculated omnidirectional cross section is 5.5 cm², which is 1.95 times the cross section for triple coincidences measured with Explorer VI, and 1.93 with Pioneer V. These measurements were obtained by using the omnidirectional cosmic-ray intensity at great distances from the earth with no bremsstrahlung present. Any increase in this ratio signifies bremsstrahlung detected by the single counter. For example, in the outer belt the bremsstrahlung rate reaches 1.8×10^4 counts/sec compared with a triples count rate of 5 to 6 counts/sec from cosmic radiation. In figure 5 it is seen that detectable bremsstrahlung sets in on the outer slope of the inner radiation belt and increases until reaching a peak intensity of the outer belt. These measurements demonstrate the separation of the detection of bremsstrahlung from energetic nucleonic particles. It is also interesting to note that the triple-coincidence detector has measured untrapped solar flare protons while it was in the outer radiation belt where the highest singles count rate was

[3] During each period of satellite motion there are two passes through the Van Allen belts; we define an ingoing or outgoing traversal of the trapped radiation as a pass, numbered consecutively from launch. The dates of the consecutively numbered passes are given in appendix A, table 3.

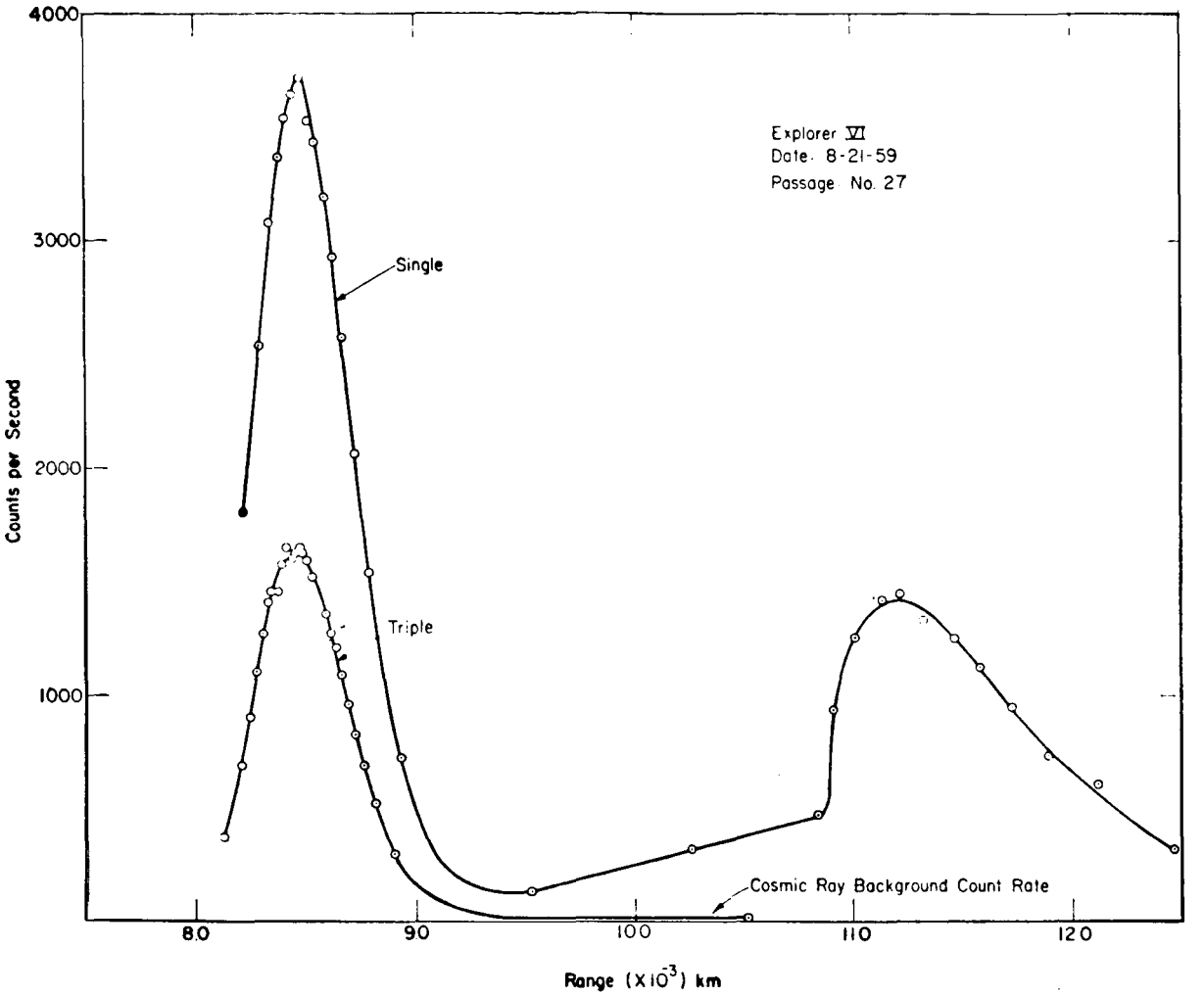

FIGURE 5.—*Counting rate data along the satellite trajectory (pass 27) showing the existence of the high-energy proton region P_1 (inner belt) and the E_3 peak from electrons in the outer belt. Note that the triple-coincidence (proton) count rate beyond P_1 is due to cosmic radiation alone.*

6,500 counts/sec [*Fan, Meyer, and Simpson,* 1960].

3. THE EXISTENCE OF TWO ELECTRON INTENSITY PEAKS

Typical data recorded during passes through the trapped radiation regions are shown in figure 6 and figures 7 *a, b*. They immediately reveal the existence of the two electron intensity peaks reported in 1959 [*Fan, Meyer, and Simpson,* 1960]. Using an ion chamber and Geiger counter, the Minnesota group have confirmed the existence of this double-electron-peak structure [*Arnoldy, Hoffman, and Winckler,* 1960*b*]. Since our data show throughout the 8 weeks of Explorer VI recordings that a double peak is a persistent characteristic, and since a re-evaluation of earlier space-shot data suggests the possible existence of this intermediate range peak even over greater periods of time, we suggest that two separated electron intensity maxima may be a persistent feature of the outer radiation belt. Therefore this paper uses the nomenclature, proposed earlier, designating with the subscripts 1, 2, 3 the peak intensities at successive radial distance, and indicating by letter P or E whether we observe protons or

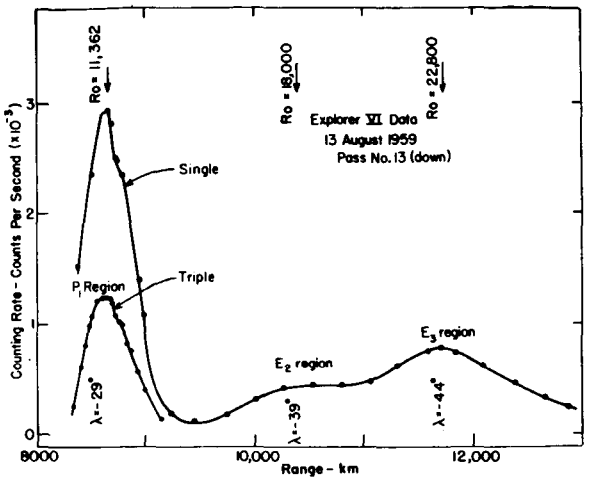

FIGURE 6.—*Counting rate along the satellite trajectory (pass 13) showing the existence of regions* P_1 *(inner belt),* E_2*, and* E_3 *(outer belt). Statistical errors are approximately the size of individual data points.*

electrons: i.e., the electron regions E_2 and E_3 are the outer Van Allen belt; thus the maxima in figure 6 are identified as P_1, E_2 and E_3.

The two peaks in figures 7*a* and 7*b* lie in the E_2 and E_3 regions. To reduce the Explorer VI observations to a quantitative study, it is necessary to trace the identity of these regions through intensity changes or positional changes of the outer belt with time before, during, or after geomagnetic disturbances. Therefore, we have defined the *maximum* intensity of E_2 and the *maximum* intensity of E_3 as "signatures" of the E_2 and E_3 regions, and we use these maxima to trace the E_2 and E_3 electron distributions in the geomagnetic field both in space and time. For example, for a given peak distribution at the equator during times of quiescent geomagnetic field, the peak intensity is to be assigned to a magnetic line of force of the dipole field at range R_0, as we show in the next section. With the assumptions that the guiding center approximation holds for the trapped electrons, and that both the energy spectrum and the pitch-angle distribution do not drastically change in the neighborhood of the line of force through E_3 (max), we find that the maximum intensity of the electrons will be along a line of force over the entire range of latitudes for which the radiation is trapped [*Fan, Meyer, and Simpson*, 1961]. Thus, we may use the position of maximum intensity to give us the trace in the meridian plane of the geomagnetic line of force passing through E_3 (max) or E_2 (max).

4. THE GEOMAGNETIC FIELD AND THE REPRESENTATION OF EXPLORER VI ORBIT

Since the magnetic field of the earth is described by a dipole inclined with respect to the rotation axis, plus higher order terms, and the period of the satellite is approximately 12.7 hours, the satellite successively passes through different portions of the magnetic field in its motion about the earth, only returning to its initial position with respect to geomagnetic coordinates after approximately 32 satellite passes. For studies of the outer radiation belt where the range R (distance from dipole to satellite) is the order of 15×10^3 to 30×10^3 km or more, we can neglect the higher order terms. The best test for the validity of this approximation is found in the consistency with which data obtained in the outer radiation belt fit together smoothly with the dipole approximation over a wide range of geomagnetic coordinates and at different times. This is shown as follows:

In figure 8 we plot the positions of E_3 (max) in R_0, $\cos^2 \lambda$ coordinates for which the line of force in the center dipole approximation becomes a straight line passing through the origin. The data were obtained in a short time interval since we find that the position of the intensity maximum changes with time. The high latitude data have been corrected according to appendix 2. Within the limits of experimental errors, which we believe to be ± 300 km, the data lie on straight lines. The data for August 21 were obtained during magnetic disturbances (fig. 13) when the intensity was changing by a large factor. Hence, we conclude that the centered dipole approximation is valid in the outer radiation belt not only for the undisturbed field but also during times of geomagnetic disturbances. This result has been shown in our earlier report [*Fan, Meyer, and Simpson*, 1960]. The important implication of the alignment of E_3 (max) with undistorted dipole lines of force is that the energy density ρ_e at all times must be less than the magnetic

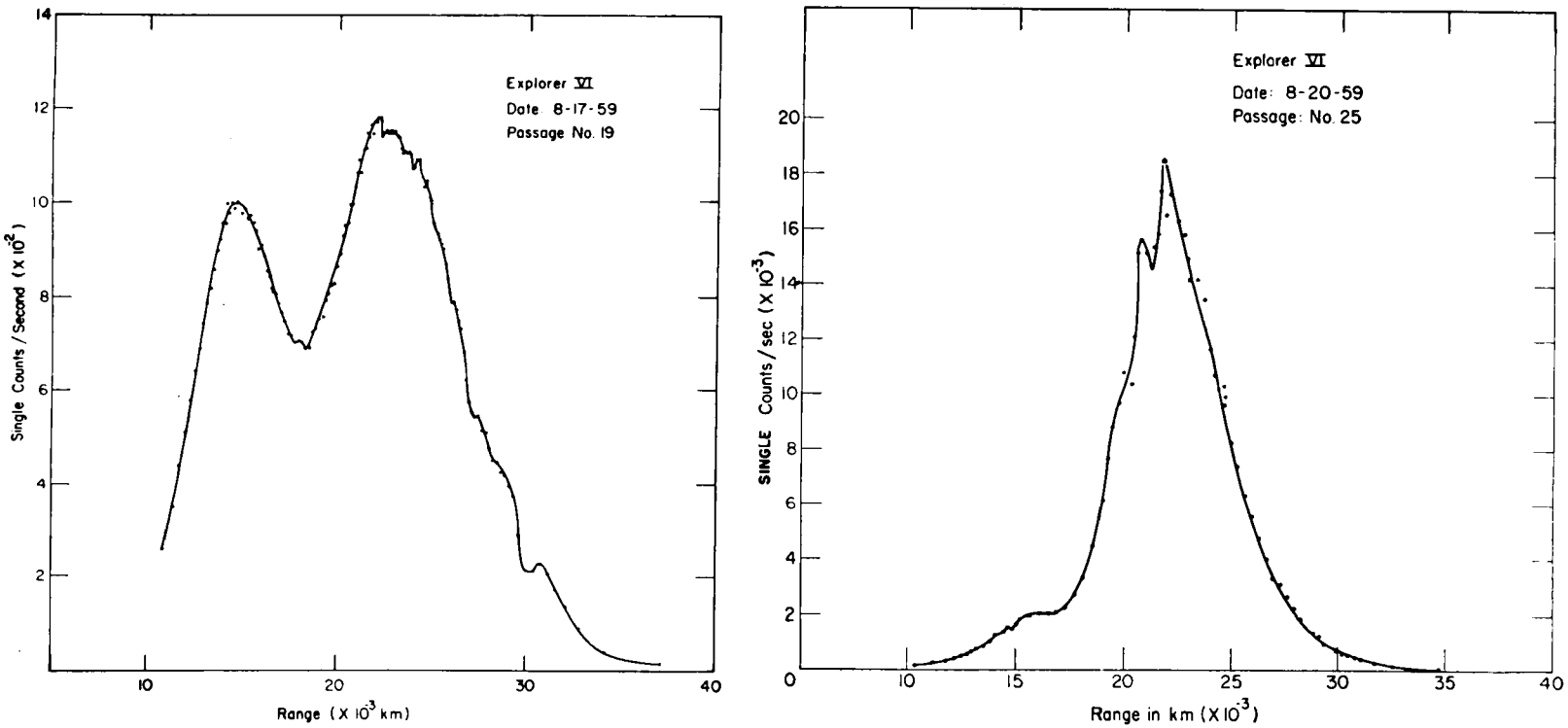

FIGURES 7 *a, b.—Counting rate from bremsstrahlung as a function of range along the satellite trajectory. Electron peaks* E_2 *and* E_3 *are shown. All data points determining the curves for each pass are shown here. Statistical errors are less than* $\pm$ *1 percent.*

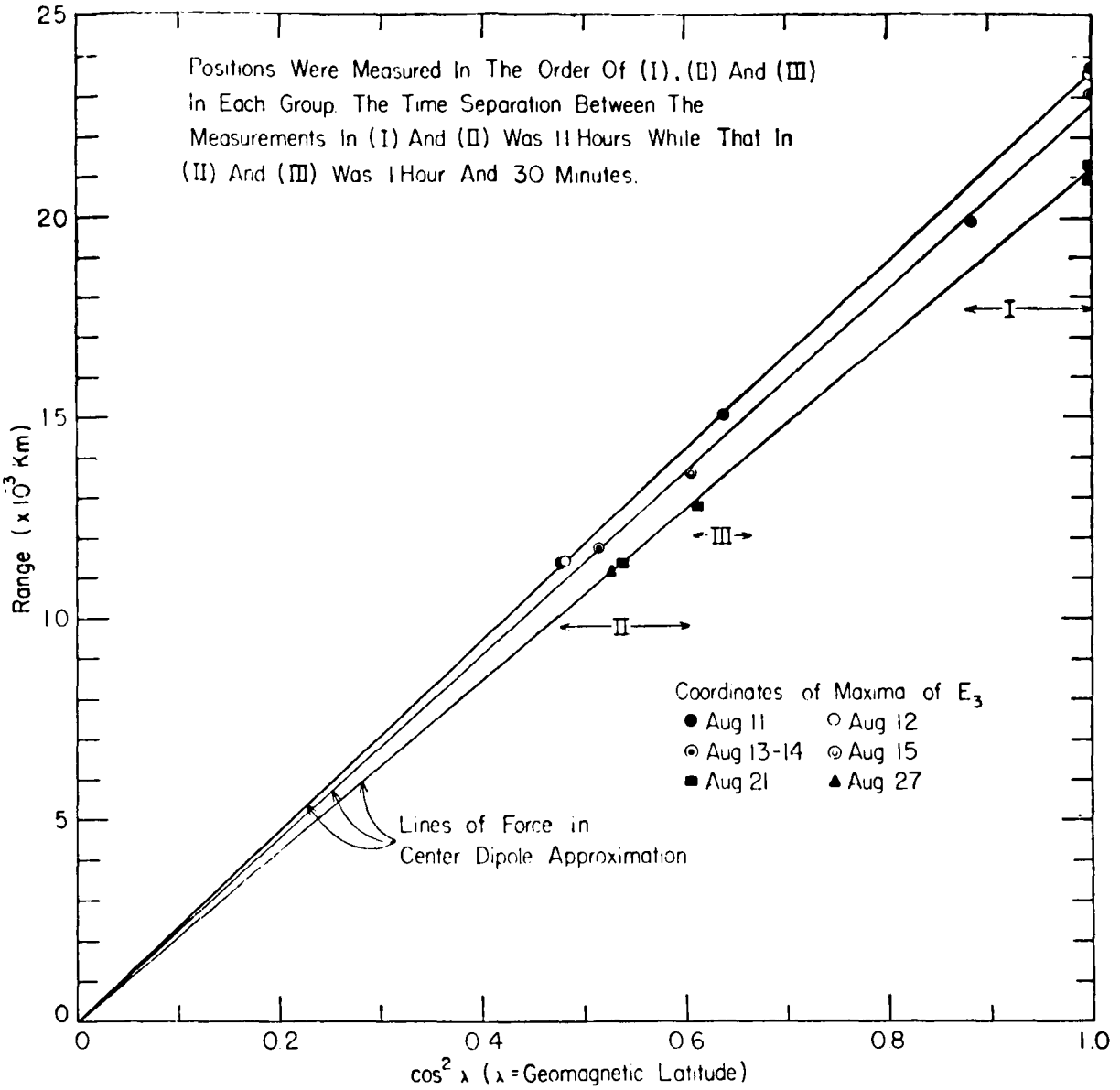

FIGURE 8.—*Proof that the outer belt maximum* E_3 *(max) lies on magnetic lines of force in the centered dipole approximation even for periods of geomagnetic storms.*

field energy density ρ_m in the outer radiation belt (for otherwise the magnetic field line would have been distorted by the presence of the particles).

Thus the problem reduces to the description of the satellite motion in the geomagnetic dipole meridian plane—a representation used also by other investigators in the description of satellite and space probe measurements. Figure 9 shows typical trajectories in the λ-R plane and indicates how, over an extended period of time, large volumes of space in the vicinity of the trapped radiation are covered by the Explorer VI orbit.

However, we wish to point out another representation for the orbit trajectory [*Fan, Meyer, and Simpson*, 1961]. If the dipole approximation is valid for outer-belt analysis as we have claimed, then the geomagnetic field lines are described by the equation $R = R_0 \cos^2$

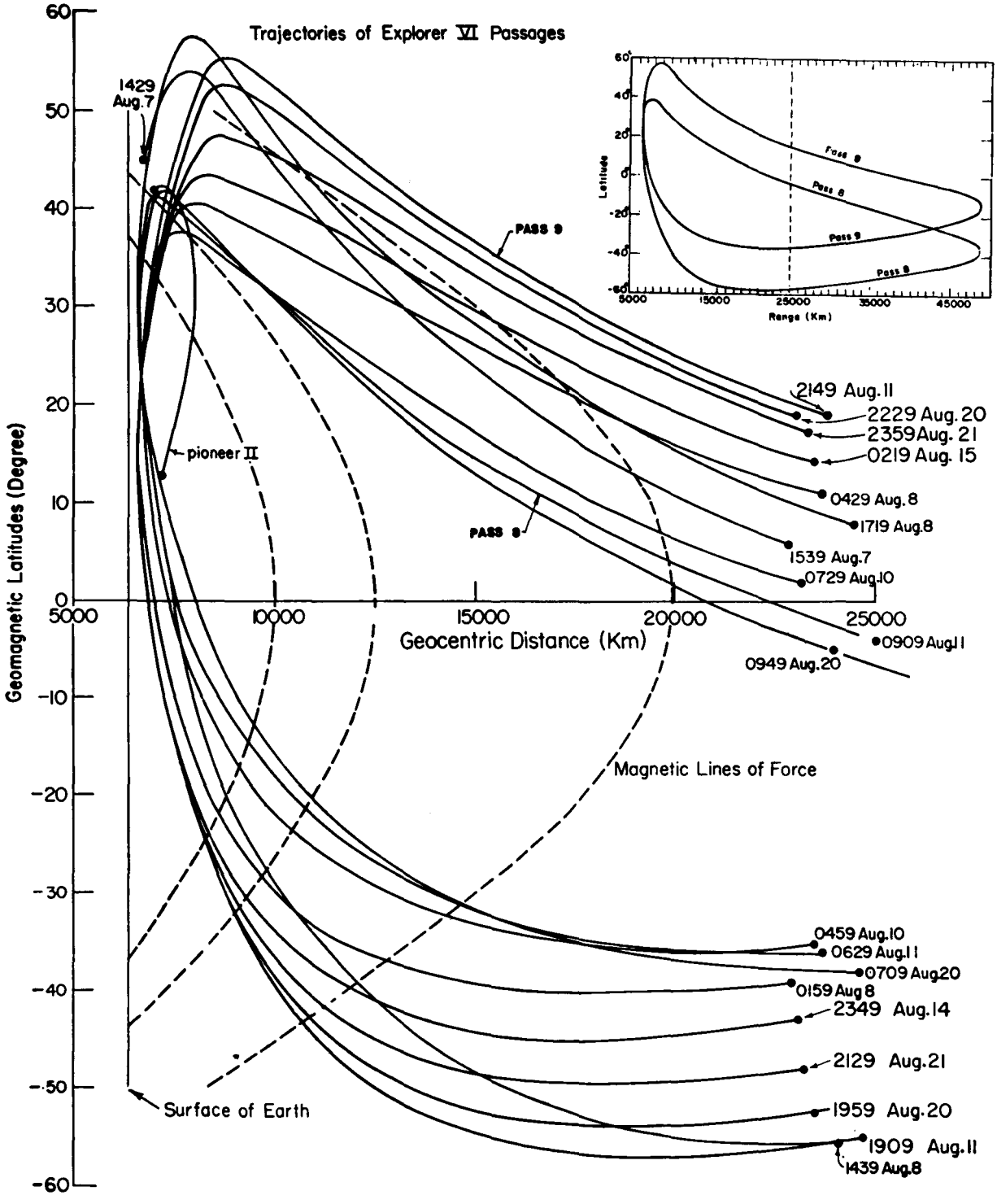

FIGURE 9.—*Projection of satellite orbit on the meridian plane of the geomagnetic field using the centered dipole approximation. Insert shows the complete trajectory.*

765-698 O-65—16

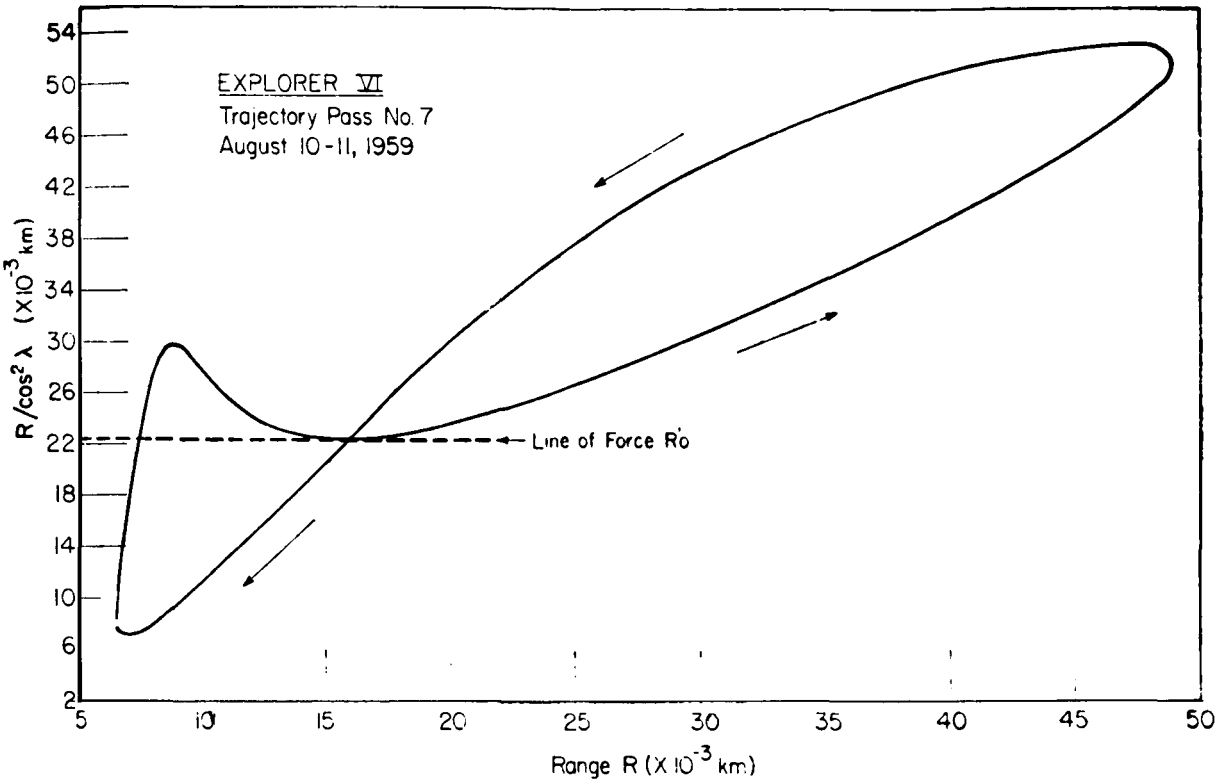

FIGURE 10.—*Representation of Explorer VI trajectory in coordinates R_0 vs. R in the approximation of a centered dipole magnetic field where $R=R_0 \cos^2\lambda$.*

λ, where λ is the geomagnetic latitude and R_0 the equatorial distance of a line of force from the center of the dipole. Lines of force with range R_0 around the earth are equivalent (azimuthal symmetry). Thus, the orbit may be described on a plane R_0 vs. R wherein each field line becomes a horizontal line in the two-dimensional plot. Trajectory data in these coordinates are shown in figure 10. We see that a significant portion of the satellite motion may be projected onto a single dipole line of force whose range at the equator is R_0'. Since the electron intensity is measured continuously we may obtain curves for intensity as a function of λ (or magnetic field intensity) along a line of force as shown in section 7. If we allow a range spread of about 200 km, we then obtain useful data of this type from over one-third of all Explorer VI trajectory passes. Among these passes we find many that lie on the same R_0 as the position of E_3 (max).

In section 7 it will be shown that the intensity along a line of force near E_3 (max) changes rapidly with λ. Also, we note from figure 9 that the satellite sometimes moves obliquely across the region of E_3 (max) where the intensity is a strong function of latitude and range. For such cases the observed position of electron intensity peak and the true position of intensity maximum are in general different. This problem is discussed in appendix B. The problem is restricted to high latitudes, since at low latitudes the traversals are always at a large angle with respect to the lines of force. From appendix B it is clear that corrections in range and latitude are significant in locating the true position of E_3 (max) at high latitudes. We have applied these corrections in the region of E_3 (max) in this paper.

In figure 11 the positions of the maxima for regions E_2 and E_3 are plotted in the meridian plane for a large number of trajectory passes.

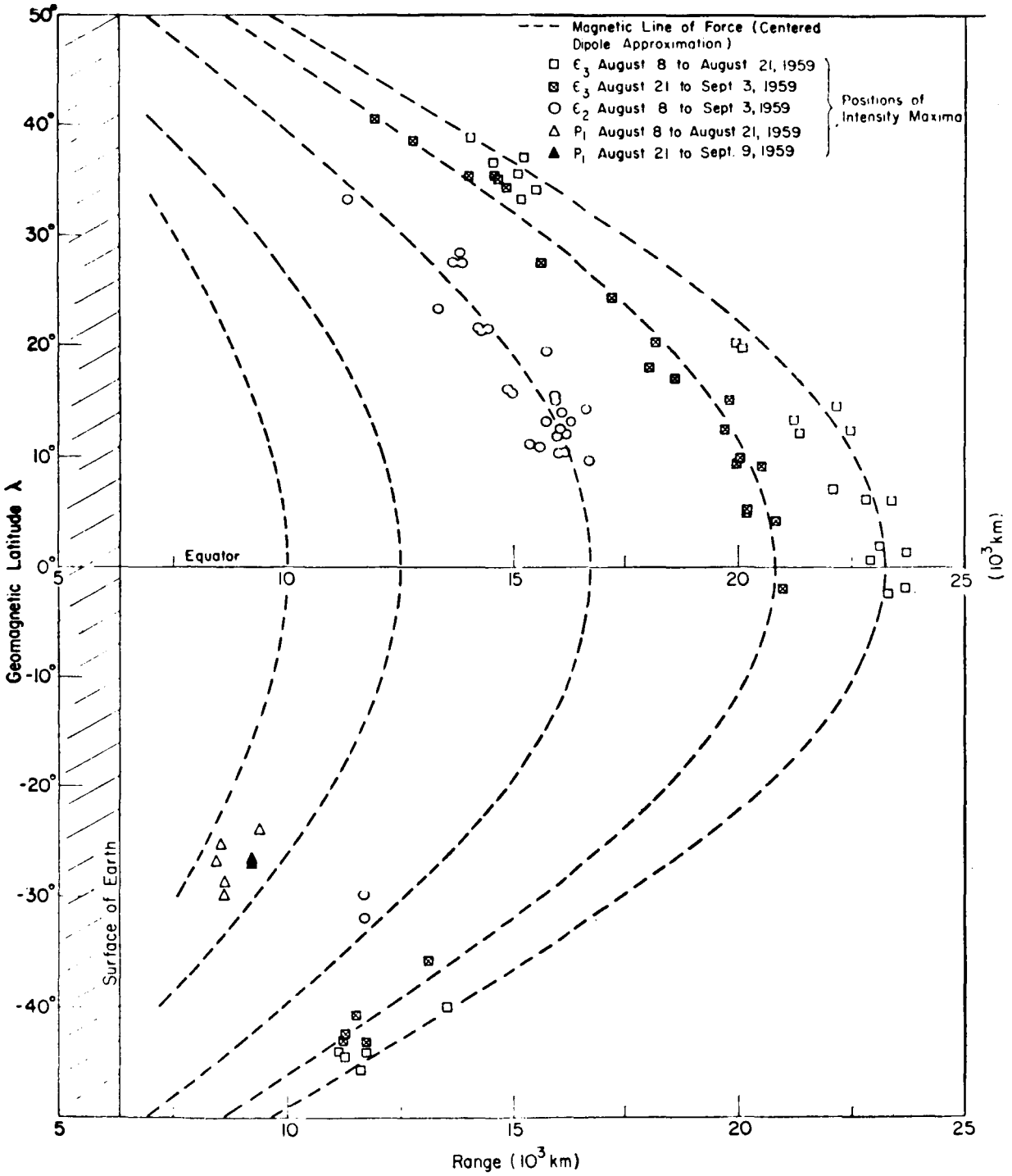

FIGURE 11.—*Meridian plane plot of the* E_2 *(max) and* E_3 *(max) positions in the geomagnetic field. For more detailed analysis, see figures 8 and 23.*

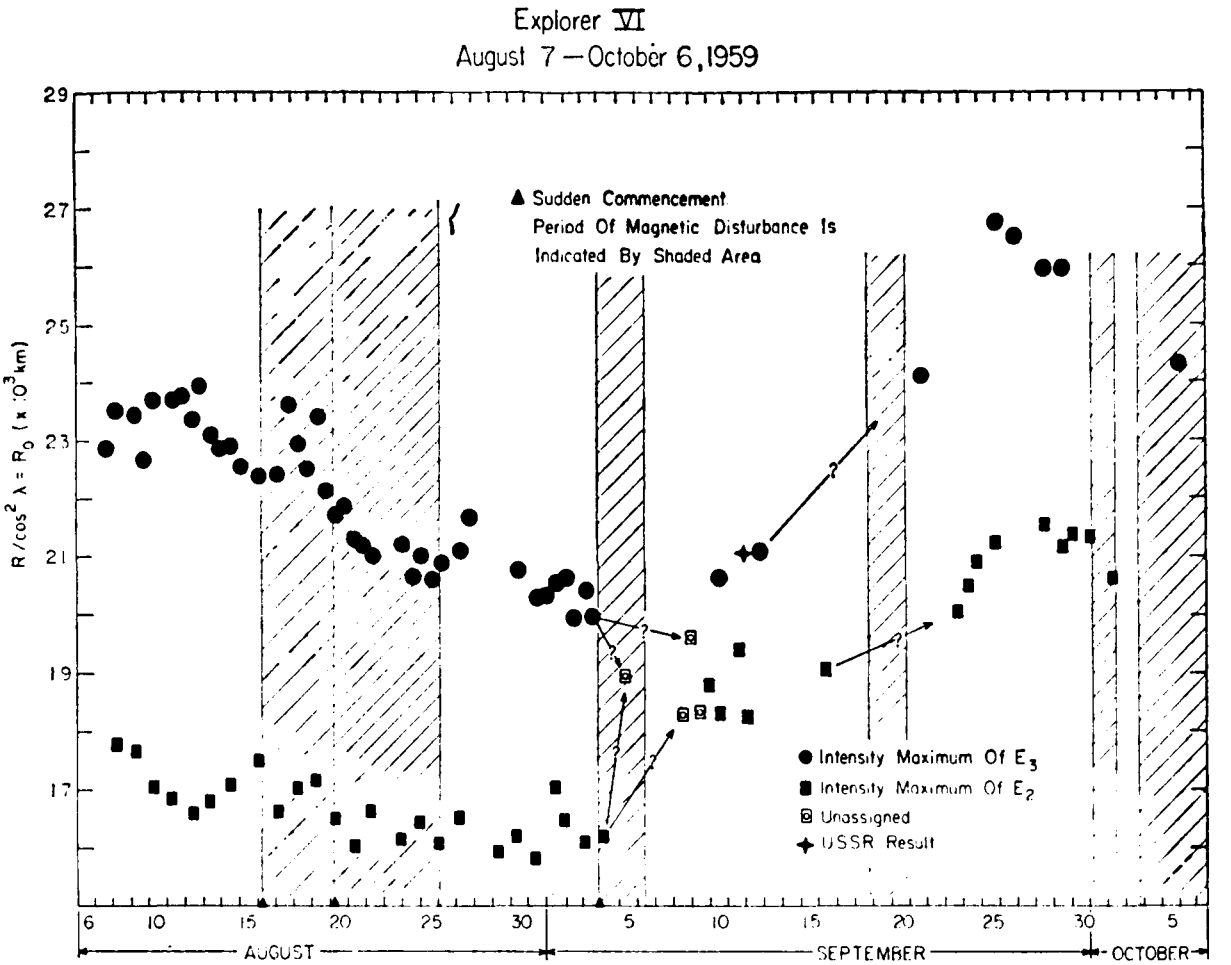

FIGURE 12.—*The position of* E_3 *(max) extrapolated to the geomagnetic equatorial range* R_0 *as a function of time.*

This is an extension of results already published [*Fan, Meyer, and Simpson,* 1960]. From figure 11 it is clear that the two maxima lie along lines of force and retain their separate identity to very high latitudes. It is also clear that the intensity minimum between E_2 and E_3 in the outer belt is not the "gap" described in the literature between the inner and outer belts.

5. THE RADIAL CHANGE OF ELECTRON BELTS

To investigate in greater detail the radial motion of the two electron belts as a function of time evident from figure 11, we have used all passes through E_2 and E_3 with the criterion for identification of maxima outlined in appendix B. We then determined the equivalent equatorial range R_0 of the magnetic dipole line of force on which each maximum was found to lie. The results of this extrapolation appear in figure 12. Since systematic and progressive errors in the time-position data of the satellite trajectory could introduce "drifts," we have investigated the question of the accuracy of the orbital data, especially with respect to variable atmospheric drag at perigee. Although we know there are errors between the calculated and real positions of the satellite at small range—serious for inner belt studies—the errors in the outer region until at least September 9 are from 500 to 100 km in range (see app. B). Consequently, the large

changes of range in figure 12 represent real changes of the intensity maxima with time and lead to the conclusions:

1. There exist rapid and simultaneous changes in range of E_3 (max) and E_2 (max) during geomagnetic storms. The magnitude of the change may be as great as 10 percent of the total range from the dipole center.
2. Both regions tend to undergo the same inward direction of motion with the magnitude of change being much less for E_2.

Whether outward motion occurs depends upon the interpretation placed on the data after the geomagnetic storm on September 3. Unfortunately the ground stations were closed for a few days. We have indicated by arrows the alternative interpretations that may be placed on the data after September 3. Two regions continue to persist but their identities become obscure. The maximum appearing beyond 27,000 km after September 25 might be interpreted as either a new region forming and moving inward or a shift in the previous E_3 (max). In any event, inward motion is certain at some times, and outward motion is not excluded at other times by our results.

The physical explanation for these radial motions of the outer belt is unclear. If, as appears likely, the motions are mainly inward, then drift or diffusion across lines of force might seem to be an attractive explanation, especially since the drift occurred during a geomagnetic disturbance. Although inward motion of electrons in nonuniform magnetic fields is a well-recognized possibility [*Herlofson*, 1960; *Parker*, 1961*a*], both the short time constants and the persistence of a "sharp" maximum with high intensity at all times in the experimental data argue against inward diffusion.

The changes have the gross appearance of lines of force moving inward as though the scale of the dipole were decreasing. It has been argued that as a consequence of the insulating shell of the earth, lines of force may be progressively brought inward [*Gold*, 1959]. However, the peak distribution would rapidly disappear, contrary to fact.

The Argus experiment [*Van Allen, McIlwain, and Ludwig*, 1959*b*] showed that the intensity maximum of trapped β rays from fission products did not change radially during the entire period of observation by more than $\sim$ 30 km, even though geomagnetic disturbances were taking place. Since the ranges of the Argus 'shells' were less than for region E_2, the radial motion we have found presumably has its origin in magnetic field and current system changes beyond the range of E_2 and E_3 at the times of geomagnetic storms.

6. INTENSITY CHANGES OF E_2 AND E_3 REGIONS WITH TIME

Since satellite trajectories cover a wide range of geomagnetic latitudes as a function of time, the spatial distribution and changes with time of the intensities are intermixed. We shall first consider exclusively the data obtained in an equatorial band of latitudes $\pm 10°$ for which case the spatial variation may be neglected. We shall then extend this analysis to higher geomagnetic latitudes, and, finally, to a description of the intensity along a magnetic line of force as a function of time.

The results for intensity changes in the equatorial plane are shown in figure 13 for the region E_3. For the first 7 days after launch the intensity is constant within the accuracy of the measurements. Thereafter large intensity variations occurred in association with geomagnetic storms. On August 16, a severe geomagnetic storm began with sudden commencement at 0400 UT. The magnitude of the changes in the equatorial horizontal component of the geomagnetic field at the surface of the earth is plotted in figure 13*A*. The magnetic field in the outer belt was also measured at this time (inset fig. 13*B*) [*Smith and Rosen*, 1960; Smith and Sonett, 1961, to be published]. The period of violent magnetic disturbances, represented by large values of A_p, continued into August 17–18. Since it is well known that more than 7 to 10 days are required for the field to return to its normal condition, the second sudden commencement magnetic storm, which began at 0410 UT, August 20, must have been superposed on the recovery phase of the August 16 storm. The August 20 storm was coincident with a sudden

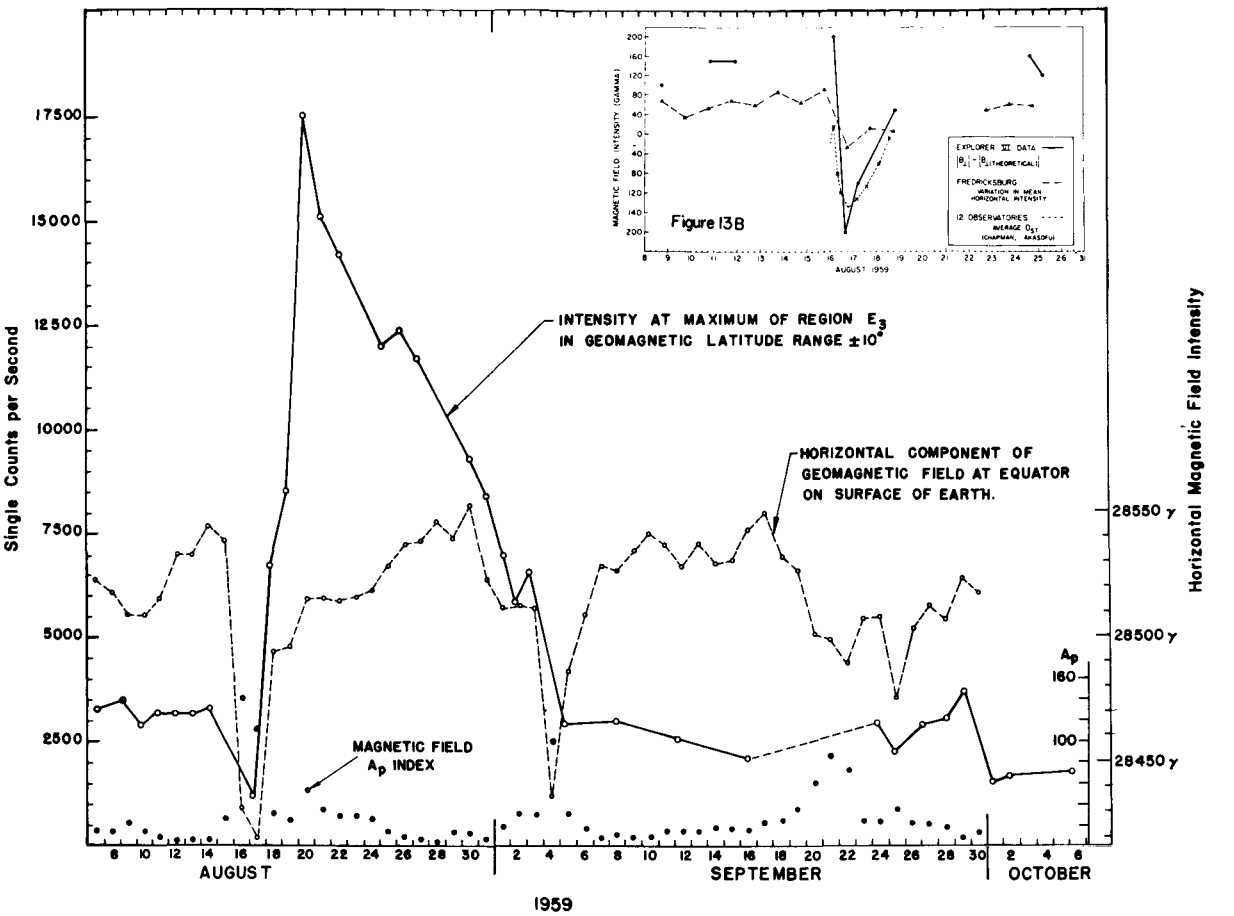

FIGURE 13*A*.—*The change of intensity of* E_3 *(max) in the geomagnetic equator* ($\pm 10°$) *as a function of time. The averaged values of the surface horizontal component of the equatorial geomagnetic field (Huancayo, Peru) is shown. The* A_p *index indicating the magnitude of geomagnetic fluctuations is given as individual solid points.* B. *Changes in magnetic field intensity observed in Explorer VI within the outer belt* (Smith and Rosen, *1960; Smith and Sonett, to be published*).

decrease of ~15 percent of cosmic-ray intensity in space [*Fan, Meyer, and Simpson*, 1960].

Gross changes of intensity in the E_3 region have also been observed with the other radiation detectors on Explorer VI [*Arnoldy, Hoffman, and Winckler*, 1960*a*, 1960*b*; *Rosen, Farley, and Sonett*, 1960]. The most obvious phenomena we note are a sudden decrease of intensity following the initial phase of the storm and, later, a buildup by a factor 3 in intensity within 24 hours during the main phase and recovery of the first storm. The equatorial peak intensity increased by another factor ~ 3 at the time of the second magnetic storm on August 20. The intensity then gradually declines, and, after the magnetic storm of September 3, reaches approximately the values obtained at the time of launch. We note here that geomagnetic storms occurred also on September 20 and October 3. These two storms were minor compared with the events of August 16 and 20.

We now investigate the intensity changes with time at higher geomagnetic latitudes, viz., at higher field intensities along lines of force through E_3 (max). Since the intensity decreases rapidly with increasing latitude, curves similar to figure 13 at higher latitudes can only be obtained by using data from small intervals of

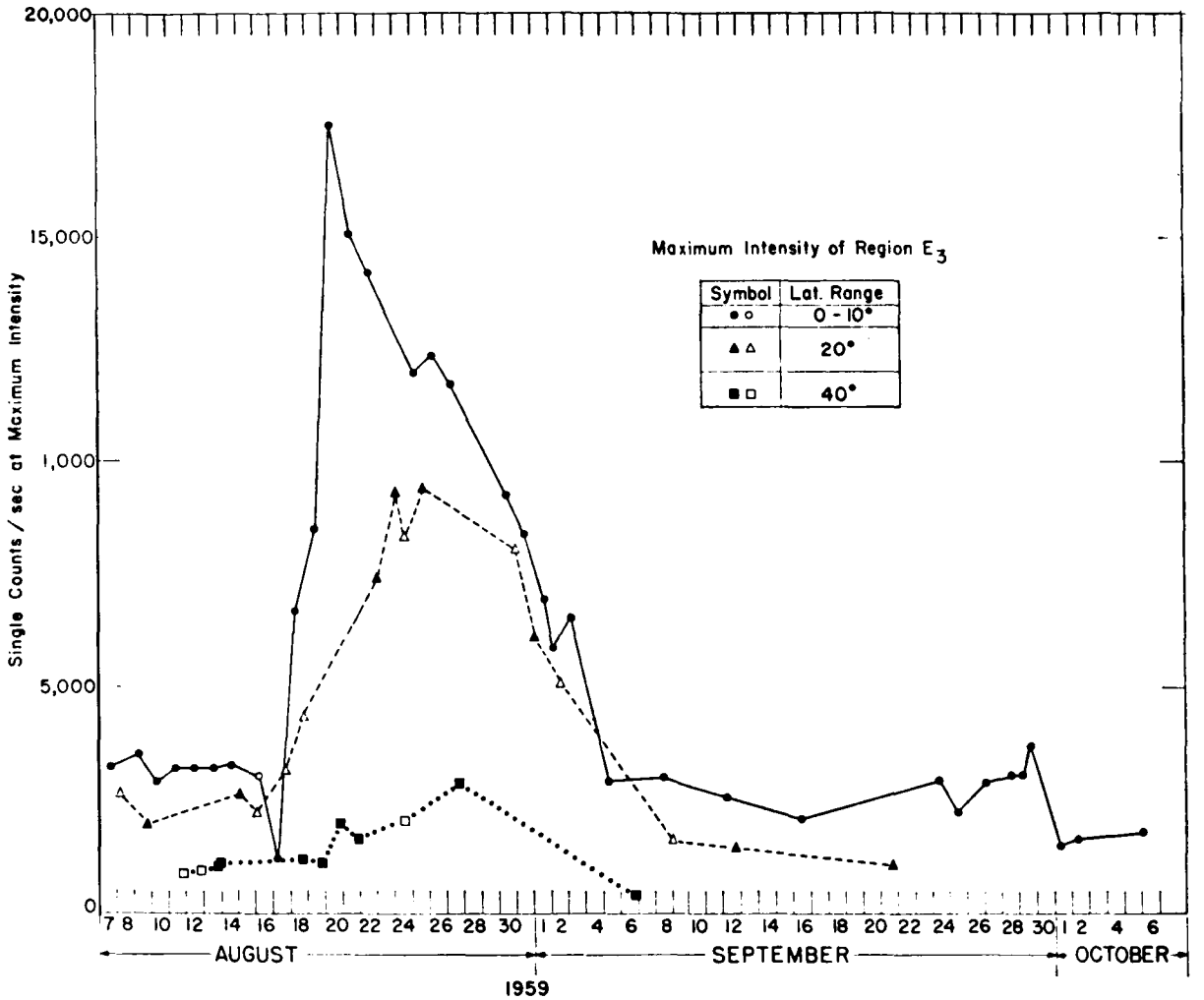

FIGURE 14.—*Electron intensity as a function of time at* E_3 *(max) for different geomagnetic latitude intervals. The solid points represent data within* $\pm$ *5° of the 20° curve or the 40° curve.*

latitude. Therefore, all data in the latitude intervals $\lambda = 20° \pm 10°$ and $40° \pm 10°$ were interpolated (sec. 7) to 20° and 40°, respectively, and are shown in figure 14. These curves for 0°, 20°, and 40° reflect the changes of electron pitch-angles with time. We discuss quantitatively the physical meaning of these observations after examining the detailed electron-intensity distribution along a line of force.

7. THE ELECTRON INTENSITY ALONG LINES OF FORCE AS A FUNCTION OF TIME

From the electron density measured along a tube of force, either the distribution of mirror points or the equatorial pitch-angle distribution of electrons may be determined. These measurements are fundamental to an understanding of the electron source and loss mechanisms in the outer belt.

We note from section 4, figure 10, that for some passes the satellite moved along a dipole line of force for a significant interval of time, and that approximately one-third of all passes contained data of this kind. Curves for intensity I vs. λ have been constructed by supplementing these passes with individual crossings of the same force line at different latitudes but at closely related times.

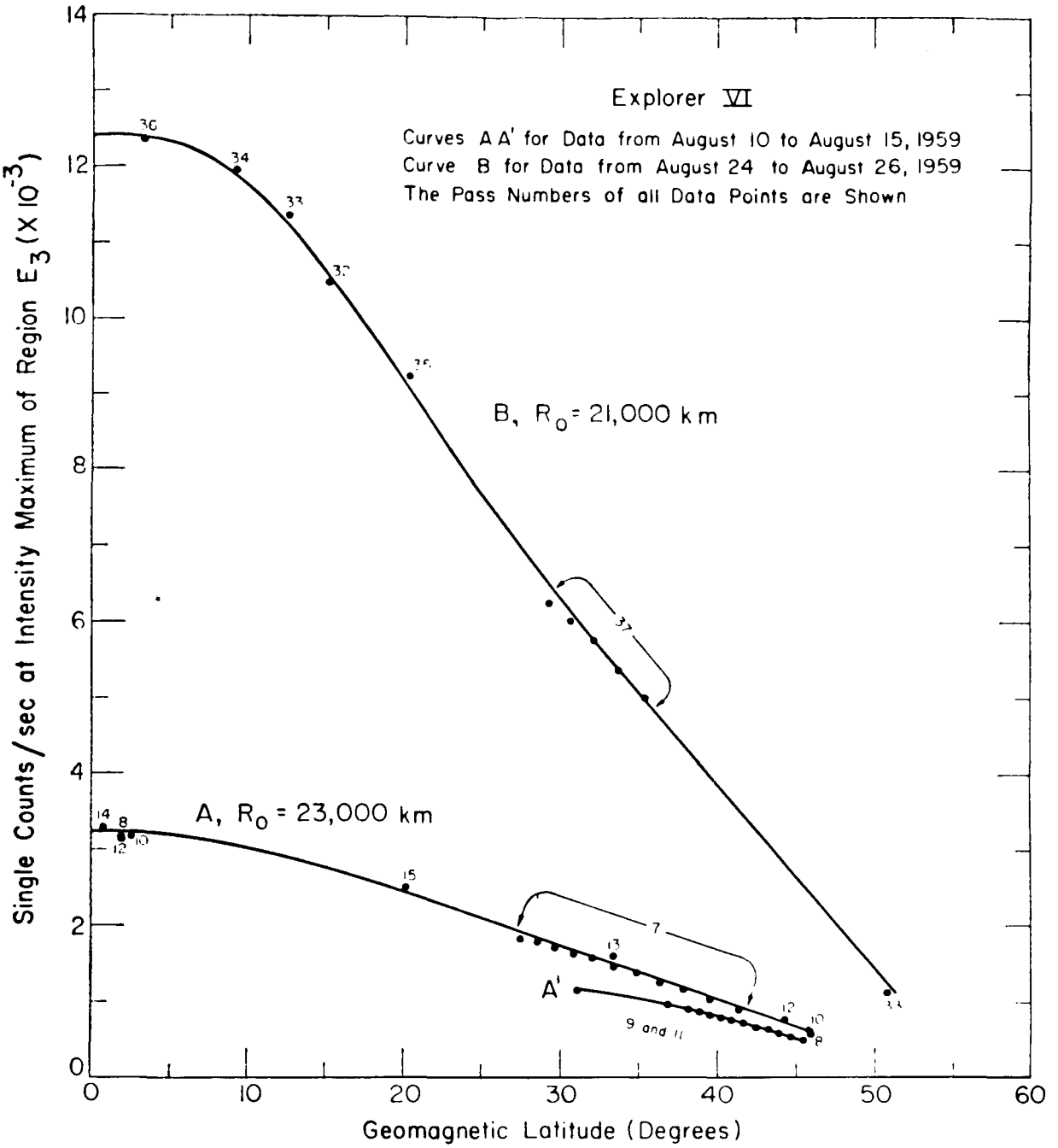

FIGURE 15.—*Electron intensity at* E_3 *(max) along lines of force in the centered dipole approximation.*

We first show in figure 15 the intensity along a line of force passing through the maximum of E_3 during times when the geomagnetic field is relatively quiet. Curve A is for a period before the geomagnetic storms, and curve B represents a quiet period[4] where the counting rate was still high following the geomagnetic storms.

[4] The lowest magnetic disturbance indices for August and September occurred on August 26.

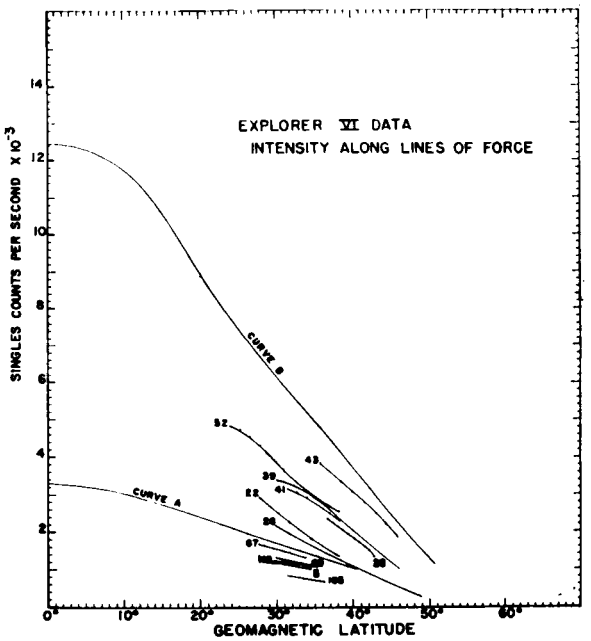

FIGURE 16.—*All experimental data for E_3 (max) along lines of force similar to figure 15, but covering a wide interval of time and range in space.*

All additional data along segments of lines of force, not necessarily through E_3 (max), are given in figure 16 for both magnetically quiet and geomagnetic storm periods.

We have found that all these data, to a good approximation, may be represented by

$$\frac{I}{I_0} = \left(\frac{B}{B_0}\right)^{-x} \tag{1}$$

at intermediate latitudes, and, for periods free from magnetic storms, even to the equator. The symbols I_0 and B_0 refer to equatorial electron and magnetic field intensity, respectively.

The data from figures 15 and 16 have been plotted in figures 17 and 18 using expression (1) and a dipole magnetic field for those cases where the lines of force passed through E_3 (max). The values of the exponent x for these curves are listed in table 1.

Provided there are no large changes in the electron spectrum with time along a line of force through E_3 (max), a condition we later show to be satisfied (sec. 8, fig. 21), then the

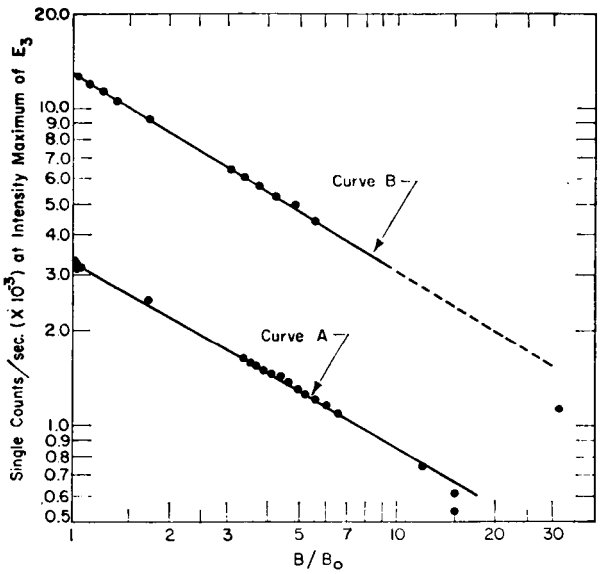

FIGURE 17.—*Electron intensity along magnetic lines of force through E_3 (max) as a function of time. Using the data from figure 15 and data during the geomagnetic storms August 16–20, it is shown that $I = I_0[B/B_0]^{-x}$.*

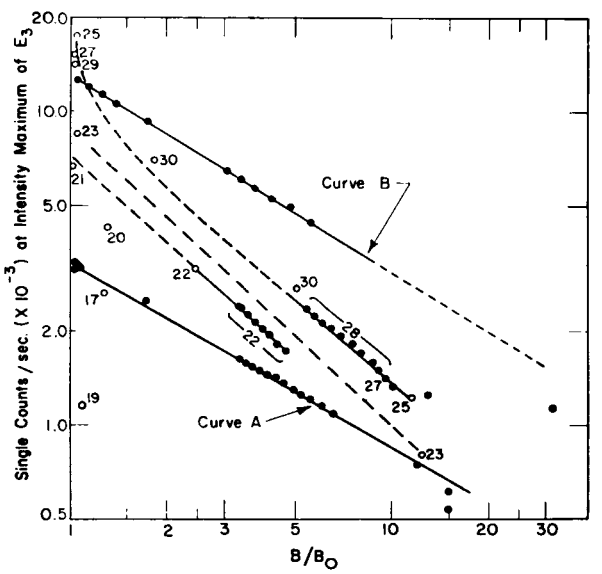

FIGURE 18.—*Electron intensity along magnetic lines of force through E_3 (max) as a function of time later than August 26, 1959.*

curves in figure 17 prove that the pitch-angle distribution (or mirror points) is changed during the main phase of the first geomagnetic storm.

The relationship between the exponent x and equatorial pitch-angle distribution has been discussed recently [*Fan, Meyer, and Simpson*, 1961]. Figure 17 also proves that the particle-intensity increase is initially concentrated at the equator, and only at a later time in the development of the magnetic storm does the electron flux at large B/B_0 (high latitude) begin to rise.

TABLE 1.—*Values of Exponent x as a Function of Time at Intermediate Latitudes*

Pass, day	x	$R/\cos^2 \lambda$
Curve *A* (8–10 to 8–15)	0. 58	23480
22 (8–18)	0. 91	21480
23 (8–19)	0. 95	23400
28 (8–21)	0. 79	20820
Curve *B* (8–26)	0. 63	20900
43 (8–29)	0. 60	20790

In the same way we investigate the region E_2. Unfortunately, owing to the high latitudes of the trajectory through the region of E_2 maximum, there are only individual points and no sections of data along lines of force. Therefore, we must be content with constructing the intensity along tubes of force using data grouped over a period of several days. Since we showed [*Fan, Meyer, and Simpson*, 1960] that the region E_2 is relatively immune to the large-scale solar-induced phenomena associated with E_3, we use data over intervals of time for which there was negligible change in range R_0 for E_2. These time intervals—A_2, B_2, C_2, D_2—are given in figure 19. The assumption that the spectrum is independent of latitude no longer holds for region E_2, as we shall show in section 8. Hence, we must confine our attention to the relatively large-scale changes in slope of the curves with time. The electron intensities along lines of force are shown in figure 19 where the steep slope of curve B_2 corresponds to the time August 17–18 of the first geomagnetic storm. We conclude that during this phase of the storm the mean pitch-angle of electrons in region E_2 also increased.

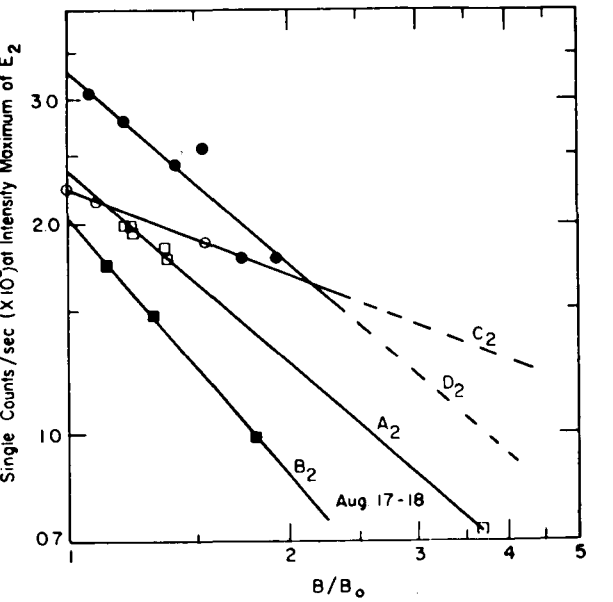

FIGURE 19.—*For the region of* E_2 *(max) the intensity along lines of force have been determined by using data in the following time intervals:* A_2, *August 7 to 15, 1959;* B_2, *August 17 to 18;* C_2, *September 8 to 11;* D_2, *September 24 to 25.*

8. CHANGES IN ELECTRON ENERGY SPECTRUM WITH RANGE, LATITUDE AND TIME

The analysis of the outer-belt electrons has so far provided us with the time-dependent parameters of electron intensity I, equatorial range R_0 and E_3 (max), and a function x representing the electron pitch-angle, or mirror-point, distribution along a line of force. Since the electron flux is measured by its bremsstrahlung produced in the satellite, it is also essential to understand the major changes that may take place in the spectrum of trapped electrons during and after the magnetic storm. For example, if the spectrum of electrons changed along a line of force in such a way that the mean energy is much higher near the equator than at high latitudes during the magnetic storm (for example, during pass 22) it could not be argued that the observed increase in x (fig. 17) was due to an increased concentration of particles at the geomagnetic equator.

We approach this problem of spectral change with time and position as follows. Although we

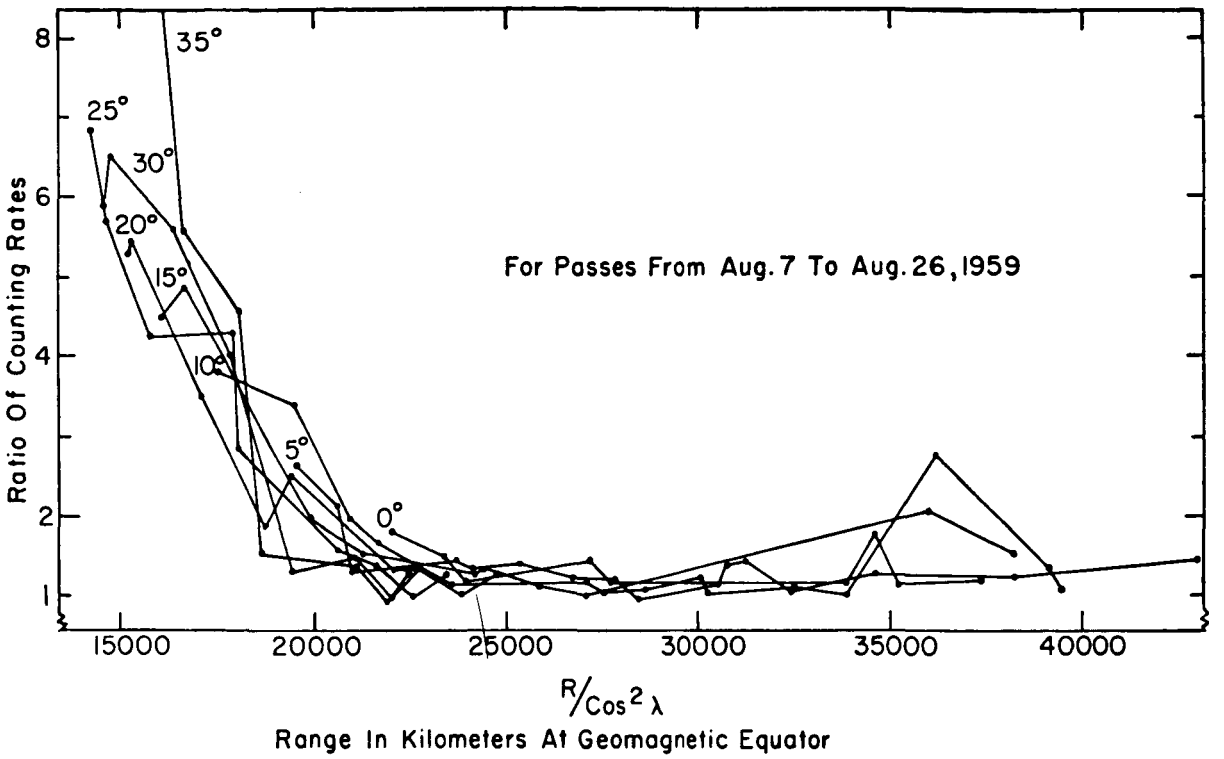

FIGURE 20.—*The ratio* Z *of counting rates from two bremsstrahlung detectors as a function of equatorial range* R_0. *All data points have been projected onto equatorial plane in the centered dipole magnetic field approximation. A* change *in* Z *indicates a change in electron spectrum. (GM counter data are from* Arnoldy, Hoffman, and Winckler [*1960a, b*] *and private communications*).

do not know the electron spectrum we can determine if there are *changes* in the spectrum by observing the relative change in count rates of two bremsstrahlung detectors, each having a different response to the electron spectrum. Two detectors suitable for this purpose are the GM counter of the Minnesota Group [*Arnoldy, Hoffman, and Winckler,* 1960*b*] and the single, lead-shielded proportional counter.

Therefore, we use the *change* in the ratio

$$Z = \frac{\text{GM count rate}}{\text{proportional count rate}}$$

as an indicator of changes in the trapped electron spectrum.

The ratio Z is shown in figure 20 as a function of equatorial range R_0 in 5° intervals of latitude. It decreases with increasing range R_0 but levels off at approximately 22,000 km. Thus, the electron spectrum at high latitudes and small range is quite different from the spectrum at E_3 (max). Beyond 22,000 km there is a negligible change in spectrum.

These conclusions are verified in figure 21, where we have plotted Z along selected lines of force. Pass 33 lies in the E_2 region. The data for pass 22 were obtained during the intense magnetic storm, thus proving that the intensity changes along the line of force in figure 17 are *not* due to changes in electron spectrum with latitude.

To isolate gross spectral changes with time from these spatial changes, we have selected only values of the ratio at E_3 (max) in the equatorial zone. This ratio is plotted in Figure 22 as a function of the single proportional counter intensity. We note here that (*a*) there are no significant changes in spectrum until after reaching maximum intensity at pass 25; (*b*) after pass 25 there is a systematic change of spectrum for many days (even though some of the varia-

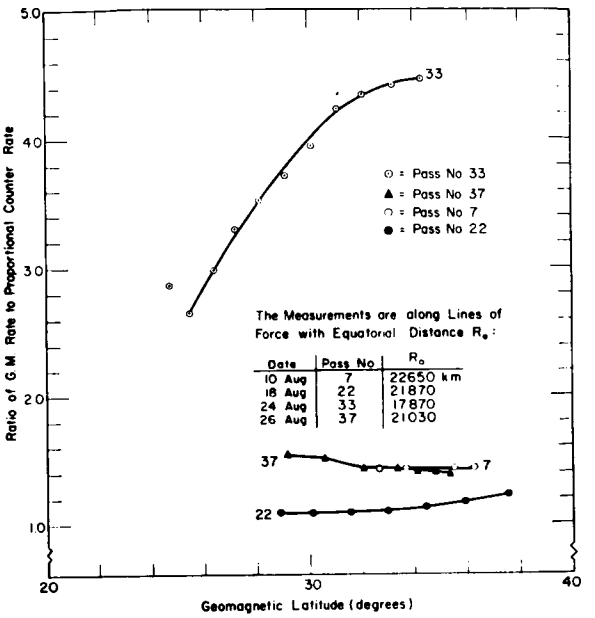

FIGURE 21.—*The ratio* Z *along magnetic lines of force near* E_3 *(max) and* E_2 *(max).*

tions in ratio may be due to changes in range, etc.).

These results reveal that the electron spectra for curves *A* and *B* in figure 17 were different.

The above analysis did not depend upon assumptions regarding the form of the electron spectrum. If we assume, owing to lack of detailed information, that the electron spectrum is given by $N(E)dE = AE^{-\gamma}\,dE$, then we may predict specific changes in the energy spectrum. This has been done in appendix C where the value of γ is derived from the count-rate ratios and the detector response curves.

9. THE ORIGIN OF CHANGES IN THE OUTER ELECTRON BELT

In the preceding sections of this paper we have established four parameters to represent the physical characteristics and changes with time of the outer electron belt, namely (1) the maximum electron intensity at the equator I_0; (2) the mirror-point distribution along a line of force represented by the exponent x; (3) the equatorial range of the dipole line of force passing through the principal maximum E_3 (max) of the outer belt R_0; and (4) the ratio Z which is sensitive to *changes* in the electron spectrum. All these parameters possess spatial and time-dependent characteristics.

We now investigate the basic question of the origin for changes in these parameters with time. It is clear that the time dependence originates with events at the sun which transport energy by means of plasma, radiation, or particles to induce geomagnetic storms. It is not settled, however, whether the outer-belt electrons have a long trapping time and undergo changes in energy and trajectory through variations of the geomagnetic field in such a way that when the field returns to its initial conditions, so will the parameters of the trapped electrons. Is the origin of the changes with time to be found entirely in reversible processes—for example, the betatron effect? Or, are we forced to conclude that at least part of the effect is brought about by particle loss, local electron acceleration or injection, and, therefore, are we required to admit that irreversible processes are prominent in the changing character of the outer electron radiation belt?

In this section we shall show how the analysis of the four parameters I_0, R_0, x, Z, along with a gross knowledge of the form of the time changes in geomagnetic field B, enable us to decide between these alternatives.

First, we bring together in figure 23 the main results of our analysis in earlier sections for the period before, during, and after the two geomagnetic storms on August 16 and 20. This interval of time was chosen because of the large-scale effects, and the availability of large amounts of data.

Second, our analysis is restricted to the region E_3 where the position of the maximum intensity in the dipole field is used as a "tracer" to follow the electron distribution with time. When we state that a particle distribution remains on a line of force through R_0, we are using this line of force as representative of all lines of force around the earth at range R_0 across which these particles drift with time. We have assumed the centered dipole approximation where the field shape is independent of longitude.

Third, since the intensity changes of the geomagnetic field were measured in the E_3 region by the magnetometer on Explorer VI as

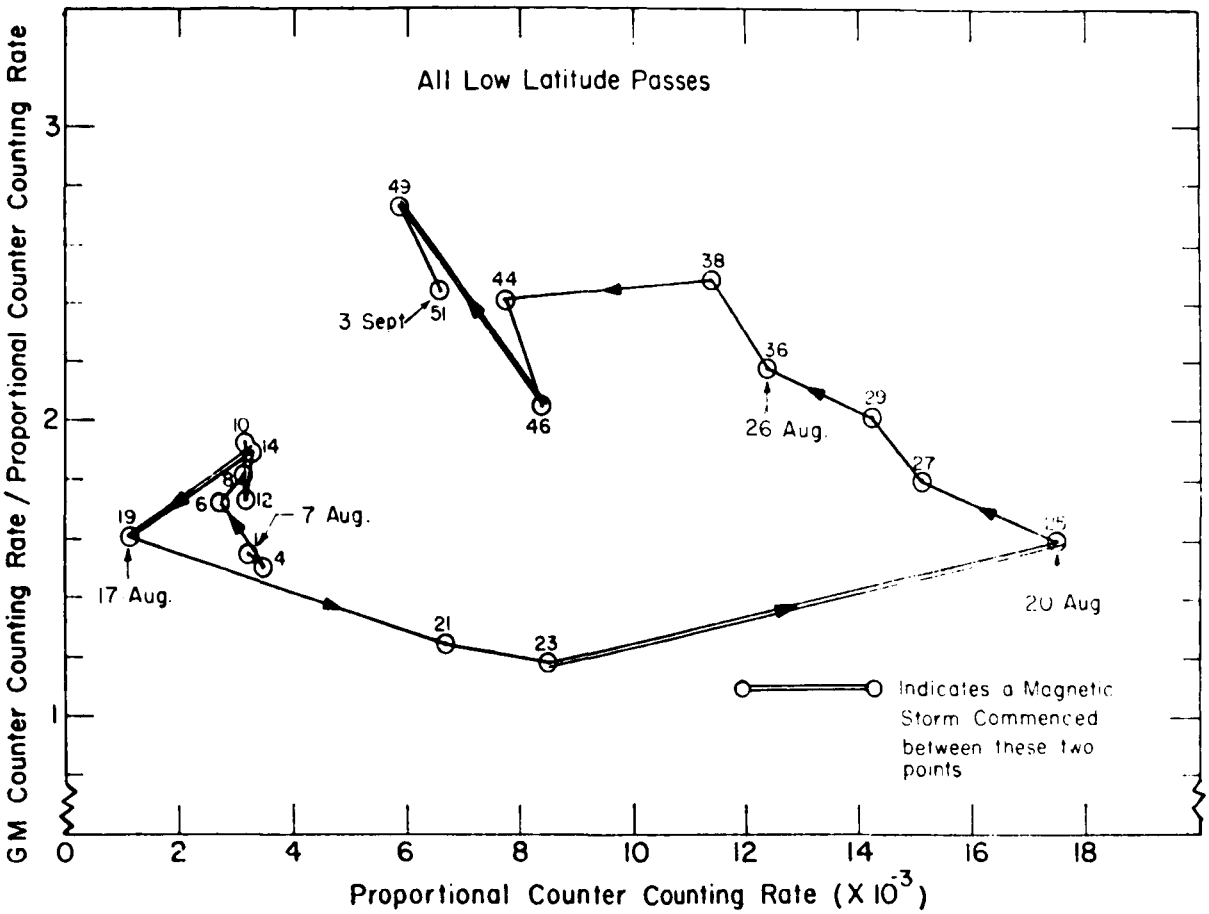

FIGURE 22.—*The ratio* Z *as a function of the single proportional counter counting rate at* E_3 (*max*).

shown in figure 13*B*, we call attention here to the conclusion, important for the analysis that follows, that the magnetic field changes at the location of the E_3 region and at the surface of the earth (see fig. 13*A*) are similar, especially with respect to the sign of the change in intensity with time. We also note that significant deviations of the magnetic field from the dipole approximation do not appear in the Explorer VI magnetometer records during the magnetic storms until ranges in excess of 25,000 km are reached [*Sonett, Smith, Judge, and Coleman*, 1960].

From figures 13 and 23 we divide into eight successive time intervals the major changes in the outer radiation belt and relate them to the physical properties of the belt and the magnetic field.

Period t_1 (*Aug. 7–15*).—This is the prestorm period where the mirror-point distribution was constant and the intensity changed by less than 1 percent per day for the order of 7 days.

$$I_0(t_1) = \text{constant}$$

$$x(t_1) = 0.57$$

$$R_0(t_1) \approx 23{,}000 \text{ km}$$

$$Z(t_1) = \text{constant}$$

These represent the initial conditions for our analysis.

Period t_2 (*Aug. 16–17*).—The sudden commencement of a magnetic storm occurred at 0405 UT, August 16. Our first data after that time were obtained on pass 19 (August 17) during the main (depressed intensity) phase of

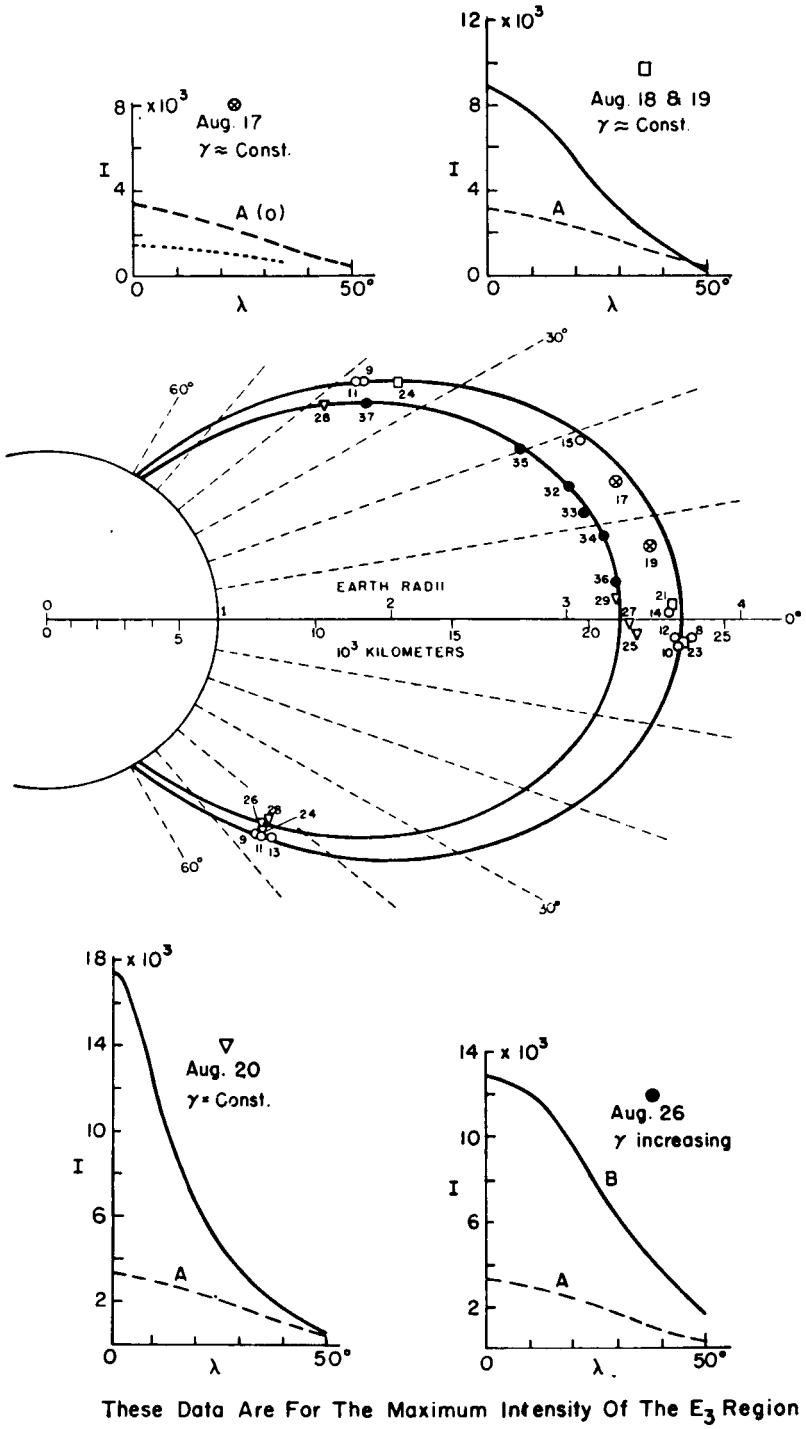

FIGURE 23.—*The changes in pitch-angle (or mirror-point) distributions and intensity for electrons at* E_3 *(max) as a function of range* R_0*, and time for the geomagnetic storms of August 16 and 20, 1959.*

the magnetic storm. The magnetic disturbance index A_p was high throughout this time period.

$$I_0(t_2) \approx \frac{I_0(t_1)}{3}$$

$x(t_2)$ unknown

$$R_0(t_2) \approx 22{,}000 \text{ km}$$

$$Z(t_2) \approx Z(t_1) \text{ (negligible spectrum change)}$$

We conclude that the changes between t_1 and t_2 could be explained by betatron deceleration.[5]

Period t_3 (*Aug. 17–18*).—The magnetic field intensity at *both* the earth and the region of E_3 (max) had rapidly returned to within $\sim$ 0.6 of its prestorm value for pass 21 on August 18. The magnetic disturbance index A_p was still high.

$$I_0(t_3) \approx 2I_0(t_1)$$

$$x \approx 1.2$$

$$R_0(t_3) \approx R_0(t_1)$$

$$Z(t_3) \approx Z(t_1)$$

Since (1) the range R_0 of E_3 (max) was the same as before the storm, (2) the magnetic field has remained undistorted, and (3) the field intensity was still below the prestorm value, the increase of I_0 at t_3 by a factor > 2 above $I_0(t_1)$ can only be explained by some irreversible process. In fact not only is $I_0(t_3) > I_0(t_1)$ but also $x(t_3) > x(t_1)$.

Period t_4 (*Aug. 18–19*).—The magnetic field continues slowly to increase toward normal intensity on pass 23. The electron flux is increasing and a flux appears at great distances ($> 40{,}000$ km) as shown in section 10.

$$I_0(t_4) \approx 3I_0(t_1)$$

$$x \approx 1$$

$$R_0(t_4) = R_0(t_1)$$

$$Z(t_4) = Z(t_1)$$

This step could be possibly accounted for by betatron effect.

Period t_5 (*Aug. 20*).—The second magnetic storm with sudden commencement at 0410 UT August 20 was followed within 4 hours by pass 25.

$$I_0(t_5) \approx 6I_0(t_1)$$

$$R_0(t_5) - R_0(t_4) \approx -2000 \text{ km}$$

$$x > 1$$

$$Z(t_5) \approx Z(t_1)$$

We could account for the flux increase as a reversible process *if* the field increase comes about through the change in range of 2000 km for E_3 (max). Note the high concentration of electrons confined to within $\pm$ 15° of the geomagnetic equator at this time.

Period t_6 (*Aug. 21–26*).—Between t_5 and t_6 there are the following changes:

$$I_0(t_6) \approx 4I_0(t_1)$$

$$\approx 2/3I_0(t_5)$$

$$x(t_6) = 0.6x \approx (t_1)$$

$$R_0(t_6) \approx R_0(t_5)$$

$$Z(t_6) > Z(t_1)$$

(This significant change of the spectrum[6] is independent of latitude.)

The measurements for curve B centered in time on August 26 are for a period of magnetically quiet days even though the magnetic field intensity at E_3 (max) was still below prestorm level. Note that the data suggest a lowering of mirror points and an increase in flux at high latitudes even though the field strength in this region continued to increase.

Period t_7 (*Aug. 26–30*).

$$I_0(t_7) = 2I_0(t_1)$$

$$R_0(t_7) \approx R_0(t_1)$$

$$x(t_7) = x(t_6) = x(t_1)$$

$$Z(t_7) \approx Z(t_6)$$

We find here a reduction of intensity by a factor of $\sim$ 2 *without a significant change* in the pitch-angle distribution and the spectrum.

Period t_8 (*Sept. 3*).—The magnetic storm of September 3 with sudden commencement at 2200 UT was followed by high A_p values and resulted in a rapid return of I_0 to the value $I_0(t_1)$ without a significant change in x as seen in figure 16.

[5] The STL scintillation detector count rate increased at this time. We discuss this increase in section 12.

[6] See appendix C for probable form of spectrum change.

$$I_0(t_8) = I(t_1)$$
$$x(t_8) = x(t_1)$$
$$R_0(t_8) = \text{uncertain}$$
$$Z(t_8) \geq Z(t_7)$$

It is difficult to prove experimentally that a process is reversible because so much must be known about both the particle and magnetic field parameters. For example, *Parker* [1961*b*] recently has shown that the superposition of two deformations of the geomagnetic field can approximate almost any variation of electron distribution which maintains a "bell-shaped" latitude dependence. Parker finds three adjustable parameters are required to describe the possible reversible changes in a slowly changing geomagnetic field: namely, $T(t)$, which determines the magnitude of the field B_0', $a(t)$, giving the scale of the field; and $\nu(t)$ describing the form of the field lines. Accordingly, wherever we state that a given step could be explained as a reversible process, we imply the possibility of invoking changes in these magnetic field parameters to reconstruct the observed change in electron distribution.

The changes occurring between some of the eight periods above may be reversible. However, there are some changes which, under any model for trapped particles, could not be explained by reversible processes. Indeed, we need only prove that one of the series of changes is irreversible, and we prove the process as a whole to be an irreversible effect. For this test we choose first the change from period t_1 to period t_3.

We note that between t_1 and t_3 the magnitude of B decreased ($T(t)$ was decreased) whereas both the dipole character of the field lines and the range of the field line through E_3 (max) were preserved ($a(t)$ and $\nu(t)$ constant). Yet the electron density at t_3 was everywhere greater than at t_1. This change in the radiation belt had its origin either in an increase in energy of the already trapped electrons, or additional particles have been added in the energy range to which the detectors are sensitive.

What irreversible process could bring about this result? Briefly, there exist two extreme alternatives:

1. If, at period t_2 during the main phase of the geomagnetic storm with the total field intensity at its minimum value, electrons are injected somehow with energies below the detection level of the bremsstrahlung detectors, than, when the field recovers to ~ 0.6 of its initial value, these new particles could be brought up to energies where they produce bremsstrahlung with increased efficiency. However, this explanation is unlikely since it is required to preserve the ratio Z (or the spectrum) and the new particles would have to be concentrated about E_3 (max) to preserve the range of E_3 (max).

2. During the period t_2 of the storm's main phase there were small-scale but rapid magnetic field intensity variations (high A_p) which could be invoked through some irreversible process to accelerate electrons. Such an unspecified process plus the partial recovery of over-all field intensity could not only bring the intensity above its prestorm value but also increase the electron density near to the equator.

We do not attempt here to build models for the observed irreversibility but only emphasize that the existence of this step removes the possibility for a reversible theory of outer belt intensity variations

Another irreversible step clearly exists between t_5 and t_6. On the basis of equatorial data the magnetic field intensity increases while the changing electron distribution remains along a dipole line of force of constant R_0. The evidence is against any change in scale of the field. The electron mirror-point distribution returned to nearly the prestorm values, which is equivalent to the equatorial intensity declining while the high latitude intensity increased. These changes were accompanied by a change in energy spectrum. If we assume that the spectrum was of the form $E^{-\gamma}$ then we observed an increase in γ. These changes reveal an irreversible loss of particle energy, or particles. The data indicate a relative loss of particles at high energy which could come about either by the escape of high-energy particles or a radiative energy loss at high energy. A similar irreversible process is found between t_6 and t_7.

Thus our investigation has led us to two irreversible processes, one an irreversible energy

gain and the other an irreversible loss. At present we do not understand either of the underlying phenomena.

10. THE ELECTRON FLUXES BEYOND THE OUTER BELT

At ranges greater than 40,000 km (corresponding to lines of force reaching the earth at geomagnetic latitudes greater than 67°) the proportional counter normally detects only the cosmic-ray flux. Therefore, we may invoke a hypothetical, spherical surface with radius of 40,000 km to surround the trapped radiation and determine the fluxes of high-energy electrons, if any, that are trapped or pass through this "boundary" from time to time. We do this by plotting in figure 24 the single count rate for all data at distances greater than 40,000 km as a function of time. As shown in section 2, this count rate is the sum of the omnidirectional cosmic-ray intensity, normally 9.5 counts/sec, and any bremsstrahlung produced by electrons. The singles count rate for the cosmic radiation exhibited three successive Forbush-type intensity decreases, as shown by the arrows in figure 24. Thus, the excess count rate over approximately 10 counts/sec is due to bremsstrahlung by electrons incident on Explorer VI. One single count indicates an omnidirectional intensity of 3×10^6 electrons/sec/cm^2 if the energy is 200 kev. W note that in addition to low level fluctuations (less than 1 count/sec) there exist occasional outstanding bursts, especially the increase on August 19, which would represent a flux of 9×10^6 electrons/sec/cm^2 for 200 kev electrons.

The scintillation counter detected rapid intensity fluctuations correlated with magnetometer fluctuations in the same regions of space [*Farley and Rosen*, 1960]. These electrons must be trapped.

Since these electrons appeared during the period of intensity buildup in region E_3, it is tempting to assume that the flux represents the arrival of solar electrons, which diffuse inward

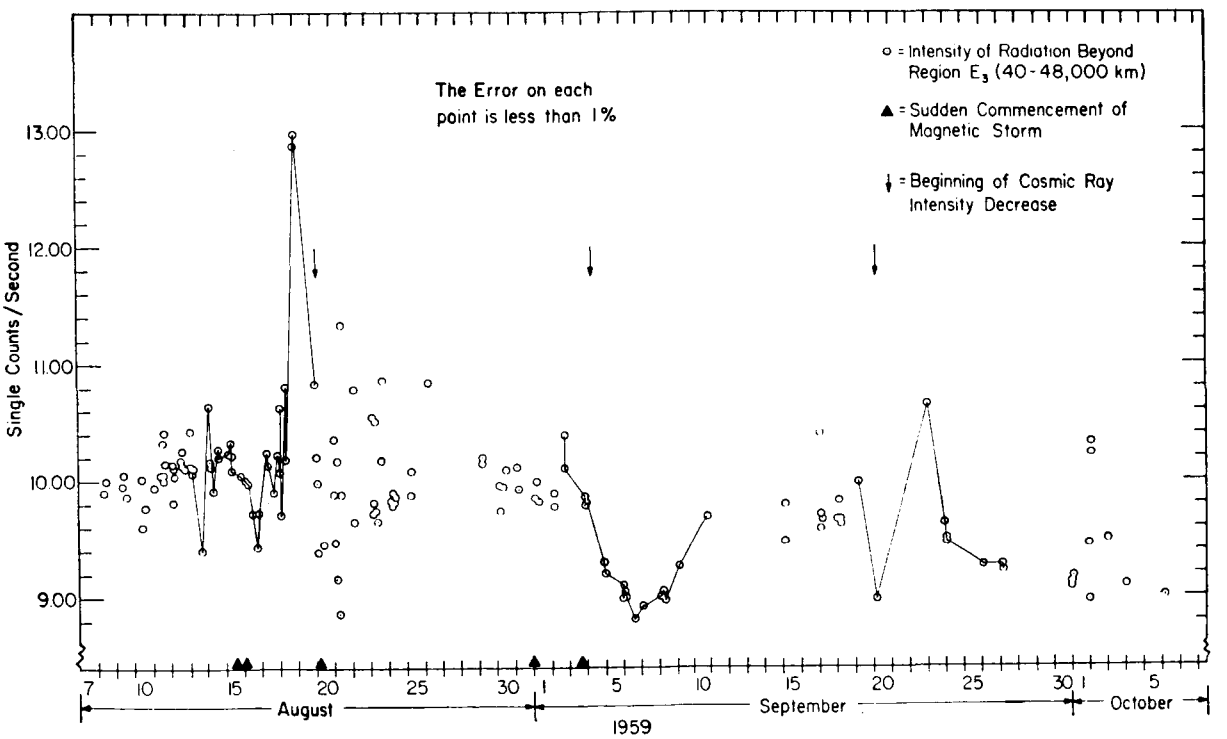

FIGURE 24.—*The high-energy electron flux observed beyond the outer electron belt, i.e., at a range* $R_0 \geq 40{,}000$ *km as a function of time.*

765-698 O-65—17

in the equatorial magnetic field. However, they could not be preaccelerated electrons that find their way into the E_3 region for the purpose of producing the many-fold increase of equatorial intensity because (1) the E_3 intensity buildup began (between periods t_2 and t_3) many hours *before* this distant flux reached a high level and only after the kind of field fluctuations which might allow trapping had subsided; (2) there is no *a priori* mechanism whereby the process of trapping new particles should preserve the location of E_3 (max), or the energy spectrum; and (3) as a precondition for trapping, the incoming particle density must approximate the trapped particle density; but, on August 18–19 the flux was several orders of magnitude lower than required.

However, the possibilities exist that these particles are "spillage" from the auroral zone, or that they have drifted outward from the equator as a result of instabilities [7] during the rapid buildup of E_3 (max) intensity.

11. ELECTRON FLUX, ENERGY DENSITY, AND SPECTRUM

Bremsstrahlung measurements do not give directly the electron flux and energy spectrum. Therefore, we shall assume an energy spectrum and compute the electron flux from the single counter count rate and response curve in figure 4 for monoenergetic electrons. For any assumed energy spectrum, we have the additional boundary condition that the energy density of the geomagnetic field ρ_m, at any point must considerably exceed the electron energy density ρ_e at that point. This condition was proved in section 4 for both normal and disturbed geomagnetic field conditions. This boundary condition, $\rho_m > \rho_e$, is most severe in the limiting case of the geomagnetic equator at the range of maximum E_2 intensity, where the electron density is highest and the field energy density is lowest along the line of force passing through E_3 (max). For the quiet period before August 14, 1959, where E_3 (max) lies at approximately 22 to 23 $\times$ 10^3 km, we find for an undisturbed dipole field a magnetic field energy density of $\approx 2 \times 10^{-6}$ erg/cm^3.

Experimental evidence on the electron spectrum is scarce. The only direct measurements [*Walt, Chase, Cladis, Imhof, and Knecht*, 1960; *Cladis, Chase, Imhof, and Knecht*, 1961] were carried out at low altitude ($\approx$ 1,000 km) along a line of force passing through the geomagnetic equator at a range of $\approx$ 9,000 km and, therefore, far below the range of E_2 (max).

In the energy range accessible to our detectors their data are consistent with a differential energy spectrum of the form $N(E)\,dE = AE^{-\gamma}\,dE$ with $4 < \gamma < 5$. This exponent agrees with the analysis of the ratio of GM and proportional counters for a range less than the range of E_2 (max) as shown in figures 20 and 25, Appendix C. It then follows that if we continue to assume a power law spectrum to ranges beyond E_3 (max), then the exponent drops to $\gamma \approx 3$. Thus in the discussion which follows we shall assume a differential power law spectrum with $3 < \gamma < 5$.

We may determine the electron flux for the time interval August 7–14, 1959, at E_3 (max) in the equatorial plane as follows. The counting rate, I, of a single proportional counter is given by

$$I = \int_{E_1}^{E_2} N(E)\, G\,(E)\, dE$$

where $N(E)$ is the electron differential energy spectrum and $G(E)$ is the response function of our detector, shown in figure 4. The lower limit E_1 is not critical for determining I since the function $G(E)$ falls off faster than $E^{4.7}$ below 100 kev. On the other hand, the value of ρ_e is extremely sensitive to E_1 since the power spectrum is divergent as $E_1 \rightarrow 0$. For the present case we set $E_1 \approx 100$ kev. The upper limit, E_2, is not well known. From Walt and his co-workers it should be less than 800 kev. From the results of Van Allen and the Soviet measurements, E_2 is consistent with a value less than 1000 kev. Therefore, we assume $E_2 = 1000$ kev. The parameter A in the expression $AE^{-\gamma}$ depends very little on the choice of E_1, but is sensitive to the choice of E_2. Increasing E_2 reduces A.

[7] For example, the recently studied velocity-space instablity observed in mirror-machine geometries by R. F. Post (private communication to J.A.S.) [*Post and Perkins*, 1961].

TABLE 2.—*Parameters for Electron Flux and Energy Density in Region* E_3 *at the Geomagnetic Equator*

γ	E_1, kev	E_2, kev	A electrons/cm² sec (kev)$^{\gamma-1}$	$N(E > 100$ kev), electrons/cm² sec	ρ_e, ergs/cm³	ρ_m, ergs/cm³
3	100	1,000	1.6×10^{13}	8×10^{8}	4×10^{-8}	2×10^{-6}
3	100	2,000	2.4×10^{12}	1.2×10^{8}	6.8×10^{-9}	
5	100	1,000	5×10^{18}	1×10^{10}	8×10^{-7}	
5	100	2,000	2.8×10^{18}	7×10^{9}	3.3×10^{-7}	2×10^{-6}
Equilibrium spectrum from neutron decay only [1]	0	800	5.3×10^{-5}	$N(E \geq 0$ kev) 4.4×10^{8}	3.6×10^{-8}	2×10^{-6}

[1] Based on spectrum from Hess and Poirier (private communication to J. A. S.)

The values for the integral electron flux in the region E_3 at the geomagnetic equator are given for $\gamma = 3$ and $\gamma = 5$ in table 2, along with the parameters used in the calculations. To show that the results are not very sensitive to the choice of the upper limit E_2, flux values for both $E_2 = 1$ Mev and $E_2 = 2$ Mev are given.

The electron energy density is then,

$$\rho_e = \int_{E_1}^{E_2} \frac{N(E)}{v_e(E)} E \, dE$$

where

$$v_e(E) = c \frac{[\eta(\eta + 2)]^{1/2}}{\eta - 1}$$

is the velocity of the electrons, $\eta = E/m_e c^2$, and m_e and c are the electron mass and the velocity of light, respectively. The computed values of ρ_e are given in table 2.

Since there is some evidence [*Vernov, Chudakov, Vakulov, and Logachev*, 1959] that there are electrons in the spectrum below 100 kev, our calculations tend to be lower limits. We also note that the total intensity at E_3 (max) increased sixfold at the equator by August 21 still under the condition $\rho_m > \rho_e$ (with the spectrum essentially unchanged as shown in fig. 22). Thus it is clear that the exponent cannot be much in excess of $\gamma = 3$, under the assumption of a power law spectrum.

In Table 3 a similar analysis in the region of E_2 (max) at $R_0 \approx$ 16–17,000 km shows that $\rho_e \ll \rho_m$ even for the case of $\gamma = 5$.

12. SUMMARY AND DISCUSSION

Structure of the Outer Belt, the Geomagnetic Field, and Fluxes of Electrons and Protons

Measurements of bremsstrahlung in the satellite Explorer VI have revealed that for about 2 months there existed two distinct peaks of electron intensity, identified as regions E_2 and E_3. This kind of structure is a persistent feature of the outer belt. It is proved that the maximum intensity in the E_3 region coincides over a wide range of geomagnetic latitudes with magnetic lines of force in the centered dipole approximation. Thus, the measured electron intensity maxima may be used as tracers of the geomagnetic field lines of force for the purpose of analyzing changes in the belt with time. During geomagnetic storms the electron intensity increased manyfold at E_3 (max), but even under these conditions the trace of the intensity maximum followed a center dipole line of force. This leads to the conclusion that the electron energy density must have been everywhere less than the magnetic energy density throughout the time of our measurements.

The observed range for the maximum electron intensity undergoes large and rapid inward shifts during geomagnetic storms which amount to as much as 10 percent of the total range of the outer belt. This effect is likely to have its origin beyond the range of E_3 and connected with the irreversible energy gain in the outer belt discussed later in this section.

TABLE 3.—*Parameters for Electron Flux and Energy Density in Region E_2*

γ	E_1, kev	E_2, kev	A $\frac{\text{electrons}}{\text{cm}^2\ \text{sec}}$ $(\text{kev})^{\gamma-1}$	$N(E > 100$ kev) electrons/cm² sec	ρ_e, ergs/cm³	ρ_m, ergs/cm³
3	100	1, 000	1.1×10^{13}	5.3×10^{8}	2.8×10^{-8}	
3	100	2, 000	1.6×10^{12}	8×10^{-9}	4.4×10^{-9}	1×10^{-5}
5	100	1, 000	3.3×10^{18}	7×10^{9}	5.2×10^{-7}	
5	100	2, 000	1.9×10^{18}	4.7×10^{9}	2.2×10^{-7}	1×10^{-5}

By introducing the assumption that the bremsstrahlung is produced by an electron spectrum of the form $E^{-\gamma}$, and by noting that the particle energy density is everywhere less than the magnetic energy density, we may calculate the maximum allowed electron fluxes in the region of E_3 under a variety of assumptions. For this assumed spectrum and energy limits of 100 to 1,000 kev, we find that γ should be close to 3 and cannot be as large as 5. This agrees with independent calculations derived from the measured ratio of GM counter to proportional counter counting rate. Under these assumptions the omnidirectional electron flux at $R_0 = 22{,}000$ km is 8×10^8 electrons/cm² sec. At smaller range in the E_2 region, a larger value for the exponent is allowed from energy density arguments, and is calculated from the observed change in counting rates of bremsstrahlung detectors. For the region E_2 a value of $\gamma = 5$ is consistent with high latitude observations.

The bremsstrahlung detector data show that the energy spectrum along a line of force E_3 (max) is essentially independent of latitude, but through E_2 (max) is sensitive to geomagnetic latitude, being strongly energy dependent at high latitudes. For example, if the electron energy spectrum has the form $E^{-\gamma}$ with an upper energy limit between 1,000 and 2,000 kev, then the form of the spectrum in the outer belt tends to become flatter (decreasing γ) with increasing range in the outer belt. The electron spectrum near E_3 (max) was observed to remain essentially unchanged even though the intensity changed over a factor of 6 as a result of a geomagnetic storm. At a later time, the spectrum was observed to change significantly and in such a way that for our assumed spectrum the value of the exponent increased by 25 to 50 per cent within a few days, and persisted long after the termination of the magnetic storm. Thus, it is evident that geomagnetic storms may induce changes of the outer-belt electron spectrum as well as changes in total intensity.

The proton flux in the outer belt for energies in excess of 75 Mev is (0.0 ± 0.1) protons/cm² sec.

The Origin of the Outer-Belt Electrons

We have described properties of the outer electron belt (sec. 9) by four parameters representing equatorial intensity $I_0(t)$, location of the magnetic dipole line of force through E_3 (max) at the equator, R_0, the electron density distribution along a line of force $I = I_0(B/B_0)^{-x}$ characterized by the parameter x, and a measure Z of spectral change of electrons with time. We find that within the sequences of changes in the outer belt induced by geomagnetic storms, there are some changes of these parameters which are accounted for only by involving an irreversible energy gain or energy loss within the belt. Since we measure bremsstrahlung, our count rate I (single counter) is given by

$$I = \int_0^\infty G(E)\ N\ (E)\ dE$$

where $N(E)$ is the spectrum and $G(E)$ is the detector efficiency. Although we know $G(E)$ (see fig. 4), we do not know $N(E)$, and therefore cannot prove whether a change in I arises from the gain or loss of particles, or whether there is

a kinetic energy gain or loss for a conserved number of particles. Thus, we confined our conclusions to the proof that there exist two kinds of *irreversible* processes: namely, (1) particle or energy gain to the belt; (2) particle or energy loss, leading to a stable intensity and electron mirror-point distribution.

Regarding the process of energy gain we have found arguments that strongly favor local acceleration of the electrons. Some of these arguments are of the negative kind. The monitoring of the high-energy electron flux beyond the outer belt proves that preaccelerated electrons are not present with sufficient density even if it were possible to trap them efficiently. An injection of electrons at subdetection energies ($<$ 50 kev) followed by local acceleration is unlikely because the electron distribution of added particles would have to maintain the original E_3 (max) location in the magnetic field and leave the resultant energy spectrum unchanged.

We are led, therefore, to consider mainly local acceleration of electrons already trapped and to ask where and at what times during the magnetic storm could this irreversible energy gain occur. The time of occurrence is fairly well limited to the last part of the main phase and extending through the first hours of recovery from the main phase of the geomagnetic storm (August 18 and 19, as shown in figs. 13 and 23).

The mechanism for energy gain in this period is obscure. For example, if a statistical acceleration process, such as Fermi acceleration, were operative at this time, while small-scale magnetic irregularities were moving through the dipole field, we might expect that protons would be even more efficiently accelerated than electrons. Is it not likely that the sudden increase of particle intensity observed in the Explorer VI scintillator [*Rosen and Farley*, 1961] could be the low energy protons beginning at the time when all bremsstrahlung detectors and the ion chamber still observed low intensity on August 17? The scintillator detects protons of energy $>$ 2 Mev. It may also be argued that the energy input is coincident with the rapid recovery of the geomagnetic field—such as ring current changes—on August 17–18. In any event, any successful model of acceleration must include (1) the preservation of E_3 (max) over an intensity range of factor 6; (2) no drastic changes in the form of the spectrum; and (3) a concentration of the excess intensity in the vicinity of the equator.

The loss processes are of a different kind. They are associated with a changing spectrum, a decrease of electron pitch angles and a gradual reduction of intensity. All these changes occur while the geomagnetic field gradually increases to its prestorm level and becomes unperturbed. The loss process seems to go on with a longer time constant than the irreversible acceleration discussed above. Again we are not sure whether particles are escaping from the trapped distribution or whether we are observing particle deceleration. The changes are consistent with the latter alternative, especially if we assume a spectrum of the form $E^{-\gamma}$. We then interpret the losses of particles or energy in two successive stages: first, there is a loss at high pitch angles and high energy, and second, there is a loss at all latitudes independent of pitch angle.

The changes take place as though there existed some instability, or energy loss process (possibly radiative) which returns the electron intensity distribution to the "steady state." In fact, one of the most remarkable results of our analysis is the observed tendency for the E_3 region to stabilize around a characteristic pitch-angle distribution where $x \approx 0.6$ except during magnetic field perturbations. Note that $x \approx 0.6$ even for the period after the September 3 magnetic storm (fig. 16).

The fluctuations of high-energy electron intensity beyond the outer belt introduce the possibility that there may also be a loss of particles in near-equatorial orbits on or about August 20 when the equatorial concentration of electrons was greatest.

It has been suggested [*Arnoldy, Hoffman, and Winckler*, 1960*b*; *O'Brien, Van Allen, Roach and Gartlein*, 1960] that the large reduction in observed bremsstrahlung intensity with the main phase of a magnetic storm (in our case, pass 19) is in reality "dumping" of particles to form the aurora. We believe that the small energy density of high energy electrons cannot account for the much larger auroral energy

release, and that betatron deceleration between t_1 and t_2 is more likely.

The results are consistent with the acceleration of ambient electrons to the observed energy distributions. Probably through collective motions of high-temperature solar plasma somewhat more energetic particles could be trapped from time to time, but their equilibrium energies and distribution would still be dominated by processes in the geomagnetic field. In view of our conclusions, the question of the origin of energy gain and loss processes is more significant than the question: from where do the electrons come?

The beta decay electrons from neutrons certainly contribute to the outer belt [*Hess*, 1960; *Dessler and Karplus*, 1960]. Recently, however, it was shown that processes other than injection of neutron decay electrons must be operative in order to account for the spatial distribution of electrons in the outer belt [*Hess, Killeen, Fan, Meyer, and Simpson*, 1961]. This again points to the existence of energy gain and loss processes.

It is important to note that satellite bremsstrahlung observations in low altitude orbits, such as Explorer VII, will appear to have a time dependence different from our equatorial results for the outer belt. This is readily understood from figures 14 and 23 for the August 1959 magnetic storms. For example, the increase of intensity would appear at the "tip" of the outer belt a few days after reaching maximum intensity at the equator. The position in latitude of the maximum intensity near the "tip" should shift rapidly by $\sim 1°$ to $3°$ corresponding in our analysis of changes in R_0 (note that for low altitudes the center dipole approximation is not sufficient to describe the real field).

Finally, we caution the reader to recall that we have been able to analyze only two magnetic storms. We would expect the detailed changes in the outer electron belt from one magnetic storm to another to be as diverse as geomagnetic storms themselves have proven to be through many years of analysis by many investigators. Indeed, the magnetic storm of September 3 (for which we have very few data) did not lead to an irreversible acceleration, but only a loss mechanism which preserved the prevailing electron pitch-angle distribution.

ACKNOWLEDGMENTS

It is a pleasure to acknowledge the essential contribution to the engineering of our apparatus in Explorer VI by L. Petraitis, R. Takaki, J. Jezewski, W. Six, and J. Lamport of the Universities Laboratories for Applied Sciences. For data reduction and analysis we thank M. Case, C. Gloeckler, K. Schwarz, R. Langford, and G. Lentz. A continuous watch for unusual solar events by R. Tjonaman and the staff of the Cosmic Ray Group assisted in increasing the data acquisition during August 1959. The assistance of R. D'Arcy in the X-ray calibration of the duplicate payload was appreciated. We thank R. S. Rochlin and the General Electric Company for the use of their linear accelerator, and D. Yovanovitch for assistance in carrying out the proton calibrations.

Discussions of our results with E. N. Parker have been both stimulating and helpful to us.

We appreciate the collaboration among those conducting experiments in Explorer VI, especially the Minnesota group of Arnoldy, Hoffman, and Winckler and the Space Technology group of A. Rosen, T. Farley, and E. Smith, where we have mutually exchanged data. We thank the Minnesota group for permission to use their unpublished GM counter data and for the use of their X-ray apparatus.

In carrying out the Explorer VI project we are especially indebted to J. Lindsay and H. Newell of the National Aeronautics and Space Administration, and to A. Thiel, J. Lindner, and K. Moe of Space Technology Laboratories.

This research was supported in part by the National Aeronautics and Space Administration under contract NASw-24, and in part by the Air Force Office of Scientific Research under contract AF-18(600)-666.

APPENDIX A

TABLE 1.—*Characteristics of Charged-Particle Detectors and Magnetometer on Explorer VI*

Proportional Counter Telescope	*University of Chicago*
A. Triple coincidence counts measure protons ($E > 75$ Mev) and electrons ($E > 13$ Mev) and are not affected by intense bremsstrahlung.	
B. Single counts measure bremsstrahlung and particles under *A*.	
GM Counter and Ion Chamber	*University of Minnesota*
A. GM counter measures sum of protons ($E > 36$ Mev), electrons ($E > 2.8$ Mev), and ambient bremsstrahlung.	
B. Ion chamber measures average ionization per particle (protons $E > 24$ Mev, electrons $E > 1.6$ Mev) plus bremsstrahlung.	
Plastic Scintillation Counter	*Space Technology Laboratories*
A. Measures electron flux directly for $E > 200$ Kev; plus	
B. Bremsstrahlung; plus	
C. Protons with $E > 2$ Mev	
Spin Magnetometer	*Space Technology Laboratories*
Measures component of magnetic field perpendicular to the spin axis of Explorer VI down to 10^{-4} gauss.	

TABLE 2.—*Low-Latitude Traversals Through the Outer Radiation Belt Which Yielded Data*

	Dates	Number of Passes Through Outer Belt
1. Pioneer I	Oct. 11, 1958	1
2. Pioneer III	Dec. 6, 1958	1
3. Lunik I	Jan. 2, 1959	1
4. Pioneer IV	Mar. 3, 1959	2
5. Explorer VI	Aug. 7–Oct. 6, 1959	113
6. Lunik II	Sept. 12, 1959	1
7. Pioneer V	Mar. 11, 1960	1

TABLE 3.—*Times for Orbit Pass Numbers of Explorer VI (Aug. 7–Oct. 6, 1959)*

Date	Pass No.	Date	Pass No.	Date	Pass No.
8–7	1	8–28	41	9–19	81
8	2	29	42	19	82
8	3	29	43	20	83
9	4	30	44	20	84
9	5	30	45	21	85
10	6	8–31	46	21	86
10	7	9– 1	47	22	87
11	8	1	48	22	88
11	9	2	49	23	89
12	10	2	50	23	90
12	11	3	51	24	91
13	12	3	52	24	92
13	13	4	53	25	93
14	14	4	54	25	94
15	15	5	55	26	95
15	16	5	56	26	96
16	17	6	57	27	97
16	18	6	58	28	98
17	19	7	59	28	99
17	20	7	60	29	100
18	21	8	61	29	101
18	22	8	62	30	102
19	23	9	63	9–30	103
19	24	10	64	10– 1	104
20	25	10	65	1	105
20	26	11	66	2	106
21	27	11	67	2	107
21	28	12	68	3	108
22	29	12	69	3	109
23	30	13	70	4	110
23	31	13	71	4	111
24	32	14	72	5	112
24	33	14	73	5	113
25	34	15	74	------	------
25	35	15	75	------	------
26	36	16	76	------	------
26	37	16	77	------	------
27	38	17	78	------	------
27	39	17	79	------	------
28	40	18	80	------	------

APPENDIX B

Process of Determining the Position of a Radiation Belt

We define the position of a radiation belt by the location in the geomagnetic equatorial surface at which the counting rate of a radiation detector is a maximum.

Consider a line of force of the geomagnetic field. A position on this line may be specified by means of a parameter $b = B/B_0$ where B is the magnetic field intensity at this position, while B_0 is the minimum magnetic field intensity along the line of force. Since an equatorial surface is a surface generated by the points of minimum field intensity on lines of force, i.e., the B_0 surface, the constant B_0 lines and their orthogonal lines, denoted by constant ϕ, may then be conveniently used as a coordinate system to specify the positions of lines of force. Thus, the three variables, B_0, ϕ, and b determine a point in space, and we can write the counting rate as

$$I = I(B_0, \phi, b) \tag{1}$$

The variation of counting rate per unit arc length ds along the trajectory of the satellite is

$$\frac{dI}{ds} = \left[\frac{\partial I}{\partial B_0}\right]_{\phi,b} \frac{dB_0}{ds} + \left[\frac{\partial I}{\partial \phi}\right]_{B_0,b} \frac{d\phi}{ds} + \left[\frac{\partial I}{\partial b}\right]_{B_0,\phi} \frac{db}{ds} \tag{2}$$

If there is an axial symmetry so that $(\partial I/\partial \phi)_{B_0,b} = 0$, equation 2 becomes

$$\frac{dI}{ds} = \left[\frac{\partial I}{\partial B_0}\right]_{\phi,b} \frac{dB_0}{ds} + \left[\frac{\partial I}{\partial b}\right]_{B_0,\phi} \frac{db}{ds} \tag{3}$$

The physical meanings of $[\partial I/\partial b]_{B_0,\phi}$ and $[\partial I/\partial B_0]_{\phi,b}$ are respectively the variation of the counting rate along a line of force and that along the intersection of a constant b and a constant ϕ surface. The positions of the maxima shown in figures 5, 6, 7*a*, and 7*b* are the solutions of $dI/ds = 0$ and are called the observed maxima, whereas the true maximum of the radiation belt by our definition is given by the equation

$$\left[\frac{\partial I}{\partial B_0}\right]_{\phi,b} = 0.$$

This is, of course, correct only if the pitch-angle distribution, $n(v, \theta_0)$ [*Fan, Meyer, and Simpson*, 1961] does not vary greatly with respect to B_0.

The following is a working process by which the solution of $(\partial I/\partial B_0)_{\phi,b} = 0$ may be found.

Figure 17 shows that for a limited segment along a line of force of a center dipole field, equation 1 assumes the following simple expression

$$I = f(R_0)(b)^{-x} \tag{4}$$

where, if R and λ are respectively the range and the magnetic latitude,

$$R_0 = R/\cos^2 \lambda, \quad b = \frac{(1 + 3\sin^2 \lambda)^{1/2}}{\cos^6 \lambda} \tag{5}$$

and x is in general a function of B_0. B_0 is then M/R_0^3. Therefore, if the magnetic field in the vicinity of the *short portion of the trajectory* is not greatly different from a center dipole field, and if the value of x is almost constant, the position of the maximum of $f(R_0)(=Ib^x)$ will be approximately the solution of $(\partial I/\partial B_0)_{\phi,b} = 0$.

In the determination of the maximum of $f(R_0)$ we encountered two difficulties: (1) the determination of the position of E_3 required a knowledge of the value of x for $R_0 \approx 22{,}000$ km, which is not always available; (2) the position data errors are determined by the accuracy of the trajectory data discussed below.

The values of x during the quiet period of August 7–14, 1959, at $R_0 = 22{,}000$ km were 0.5 to 0.6, whereas in the magnetically disturbed days (August 16–20) they increased to about 1.0–1.2. This is about the total range in the measured values of x. The following criterion was used for the actual determination. If the value of x for certain passages at R_0 between 19,000 and 24,000 km was available, this value was used; otherwise, the value of x of the passages immediately preceding or following was used, provided that no magnetic storms were under way.

Take passage 20 as an example. The maximum counting rate along the trajectory ($dI/ds = 0$) is at $\lambda = 12.4°$ and $R_0 = 24{,}500$ km, whereas the solution of $df/dR_0 = 0$ is at $\lambda = 14.4°$ and $R_0 = 23{,}600$ km.

We have used improved trajectory calculations prepared by the staff at Space Technology Laboratories which take into account the variable atmospheric drag at perigee. These data appear to be accurate within $\approx \pm 100$ km at the outer belt until at least September 12. However, a new trajectory for Explorer VI will be prepared based on minitrack data providing

more accurate position-time data at small range. In view of these trajectory errors the corrected positions of E_2 and E_3 have been worked out only for the cases where the solutions of $dI/ds = 0$ and $df/dR_0 = 0$ are widely different. No corrections are needed for values of $\lambda \leq 10°$, since $B/B_0 \approx 1$.

Two final remarks must be added:

1. Since

$$\frac{d}{ds}\left[I\left(\frac{B}{B_0}\right)^{\epsilon}\right] = \frac{df}{dR_0}\frac{dR_0}{ds}$$

there always exists an extreme value of $I(B/B_0)^{\epsilon}$ at the position where $dR_0/ds = 0$, and this is in general different from the solution of $df/dR_0 = 0$.

2. It can readily be shown that the "ridge" of equal counting-rate contours, frequently used as the definition of the position of a radiation belt, coincides with a line of force passing through the solution of $df/dR_0 = 0$. Therefore, these two definitions are equivalent.

APPENDIX C

Derivation of Changes in Electron Spectrum Using Bremsstrahlung Detectors

We showed in section 8 that whatever may be the form of the electron spectrum in the outer belt the spectrum undergoes *changes* with range and along lines of force in the vicinity of the E_2 region. However, the spectrum was approximately constant along lines of force through E_3 (max).

We shall now introduce an assumed form for the spectrum and calculate the changes in the ratio Z of count rates from two bremsstrahlung detectors, each having different responses to a given energy spectrum. The response curve for the single proportional counter has been described in section 2 and figure 4. The response curve of the GM counter in Explorer VI has been made available to us by Arnoldy, Hoffman, and Winckler. (The three groups of investigators using Explorer VI for radiation measurements have exchanged their calibration and detector characteristics.)

From section 11 it appears that a reasonable form of the electron energy spectrum prevailing in the outer belt is $dN(E) = AE^{-\gamma}\,dE$, which we shall use in our calculations. Our second assumption is that the maximum energy for the outer belt electrons is $E < 2.8$ Mev, i.e., no direct electron detection is possible by either detector (Arnoldy, Hoffman, and Winckler, private communication).

We may then calculate directly the expected values of γ for given values of the ratio Z. The solid curve shown in figure 25 uses the measured response curve in figure 4 and a maximum electron kinetic energy of 1,000 kev. To demonstrate the sensitivity of these calculations to the shape of the response curve we have also calculated Z vs. γ for the case where the single counter response is proportional to $E^{4.7}$ over the entire energy range. Clearly, the changes in γ are not extremely sensitive to the shape of the low energy portion of the calibration curve except for high values of Z.

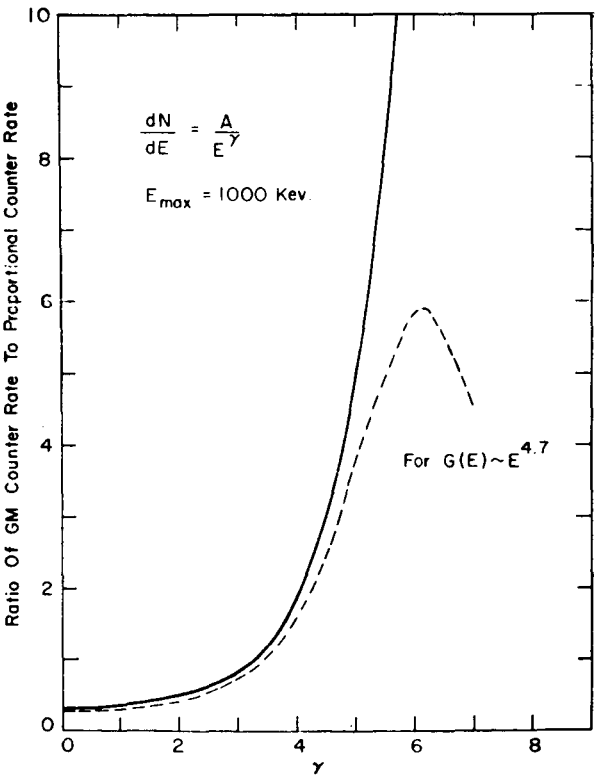

FIGURE 25.—*The calculated relationship between the ratio* Z *and the exponent* γ, *assuming that the electron spectrum is* $dN = AE^{-\gamma}\,dE$ ($E \leq 1$ *Mev*).

Thus the changes in spectrum at E_3 (max), which occurred during recovery from geomagnetic storms in figure 22, would be interpreted as a change from approximately E^{-3} to $\sim E^{-4}$ for the electron differential spectrum between August 20 and August 26, 1959.

If these assumptions were approximately correct, the dependence of Z on R_0 in figure 20 would imply that the electron energy spectrum becomes "flatter" with increasing range.

REFERENCES

Arnoldy, R., R. Hoffman, and J. R. Winckler, Measurements of the Van Allen radiation belts during geomagnetic storms, *Space Research*, First International Space Science Symposium, edited by H. K. Kallman Bijl, North Holland Publishing Company, pp. 877–896, Amsterdam, 1960*a*.

Arnoldy, R. L., R. A. Hoffman, and J. R. Winckler, Observations of the Van Allen radiation regions during August and September 1959; 1, *J. Geophys. Research, 65*, 1361–1375, 1960*b*.

Cladis, J. B., L. F. Chase, W. L. Imhof, and D. J. Knecht, Energy spectrum and angular distributions of electrons trapped in the geomagnetic field, *Tech. Rep. LMSD–895085*, 1961.

Dessler, A. J., and R. Karplus, The gap in the electron component of the outer zone of the Van Allen radiation (abstract), *J. Geophys. Research, 65*, 2486, 1960.

Fan, C. Y., P. Meyer, and J. A. Simpson, Trapped and cosmic radiation measurements from Explorer VI, *Space Research*, First International Space Science Symposium, edited by H. L. Kallman Bijl, North Holland Publishing Company, pp. 951–966, Amsterdam, 1960.

Fan, C. Y., P. Meyer, and J. A. Simpson, Equatorial pitch angle distributions of electrons in the outer radiation belt, Proceedings of the Second International Space Science Symposium, Florence, Italy, April, 1961.

Farley, T. A., and A. Rosen, Charged particle variations in the outer Van Allen zone during a geomagnetic storm, *J. Geophys. Research, 65*, 3494–3496, 1960.

Freden, S. C., and R. S. White, Particle fluxes in the inner radiation belt, *J. Geophys. Research, 65*, 1377–1383, 1960.

Gold, T., Motions in the magnetosphere of the earth, *J. Geophys. Research, 64*, 1219–1224, 1959.

Herlofson, N., Diffusion of particles in the earth's radiation belts, *Phys. Rev. Letters, 5*, 414, 1960.

Hess, W. N., The radiation belt produced by neutrons leaking out of the atmosphere of the earth, *J. Geophys. Research, 65*, 3107–3115, 1960.

Hess, W. N., J. Killeen, C. Y. Fan, P. Meyer, and J. A. Simpson, The observed outer belt electron distribution and the neutron decay hypothesis, *J. Geophys. Research, 66*, 2313–2314, 1961.

Northrop, T. G., and E. Teller, Stability of the adiabatic motion of charged particles in the earth's field, *Phys. Rev., 117*, 215–225, 1960.

O'Brien, B. J., J. A. Van Allen, F. E. Roach, and C. W. Gartlein, Correlation of an auroral arc and a subvisible monochromatic 6300 A arc with outer-zone radiation on November 28, 1959, *J. Geophys. Research, 65*, 2759–2766, 1960.

Parker, E. N., Effect of hydromagnetic waves in a dipole field on the longitudinal invariant, *J. Geophys. Research, 66*, 693–708, 1961*a*.

Parker, E. N., The distribution of trapped particles in a changing magnetic field, *J. Geophys. Research, 66*, 2641–2652, 1961.

Post, R. F., and W. A. Perkins, *Phys. Rev. Letters, 5*, 85, 1961.

Rosen, A., and T. A. Farley, Characteristics of the Van Allen radiation zones as measured by the scintillation counter on Explorer VI, *J. Geophys. Research, 66*, 2013–2028, 1961.

Rosen, A., T. A. Farley, and C. P. Sonett, Soft radiation measurements on Explorer VI earth satellite, *Space Research*, First International Space Science Symposium, edited by H. K. Kallman Bijl, North Holland Publishing Company, pp. 938–950, Amsterdam, 1960.

Smith, E., and Rosen, A., The scientific results of the satellite: Explorer VI, in *Ballistic Missile and Space Technology*, edited by D. P. LeGalley, Academy Press, p. 405, 1960.

Sonett, C. P., E. J. Smith, D. L. Judge, and P. J. Coleman, Jr., Current systems in the vestigial geomagnetic field: Explorer VI, *Phys. Rev. Letters, 4*, 161–163, 1960.

Van Allen, J. A., C. E. McIlwain, and G. H. Ludwig, Radiation observations with satellite 1958 epsilon, *J. Geophys. Research, 64*, 271–286, 1959*a*.

Van Allen, J. A., C. E. McIlwain, and G. H. Ludwig, Satellite observations of electrons, artificially injected into the geomagnetic field, *J. Geophys. Research, 64*, 877–891, 1959*b*.

Vernov, S. N., A. Ye. Chudakov, P. V. Vakulov, and Yu. I. Logachev, Study of terrestrial corpuscular radiation and cosmic rays by the flight of a cosmic rocket, *Doklady Akad. Nauk SSSR, 125*, 304–307, 1959.

Vernov, S. N., and A. Ye. Chudakov, Terrestrial corpuscular radiation and cosmic rays, *Space Research*, First International Space Science Symposium, edited by H. K. Kallman Bijl, North Holland Publishing Company, pp. 751–796, Amsterdam, 1960.

Walt, M., L. F. Chase, Jr., J. B. Cladis, W. L. Imhof, and D. J. Knecht, Energy spectra and altitude dependence of electrons trapped in the earth's magnetic field, *Space Research*, First International Space Science Symposium, edited by H. K. Kallman Bijl, North Holland Publishing Company, pp. 910–920, Amsterdam, 1960.

(Manuscript received June 29, 1961.)

The Observed Outer-Belt Electron Distribution and the Neutron Decay Hypothesis[1]

BY W. N. HESS[2] AND J. KILLEEN

Lawrence Radiation Laboratory
University of California

C. Y. FAN, P. MEYER, AND J. A. SIMPSON

Enrico Fermi Institute for Nuclear Studies
University of Chicago

Measurements of electron flux along a line of force in the outer radiation belt are compared with calculations that assume that all electrons are injected by neutron decay. The comparison shows that the two distributions are quite different at intermediate and low latitudes where corrections are unimportant. It is concluded that other processes, in addition to electron injection by neutron decay, are necessary to explain the experimentally observed flux distribution along a line of force.

Theories for the sources and losses of electrons in the outer radiation belt must take into account not only electron flux and energy spectrum but also the spatial distribution of electron mirror points along a line of force in the geomagnetic field. Different sources lead to different distributions [*Killeen and Boer*, 1960]. The theory that the outer belt is entirely due to β-decay electrons from neutrons leaking out of the terrestrial atmosphere requires that low-altitude electron injection be dominant [*Hess, Canfield, and Lingenfelter*, 1961]. Therefore, it is of interest to compare the predicted distribution for the neutron decay hypothesis (Hess and Killeen, to be published) with a recent experiment [*Fan, Meyer, and Simpson*, 1961] which shows the electron intensity along lines of force can be obtained directly from Explorer VI satellite measurements using a detector sensitive to bremsstrahlung principally from electrons above 100-kev energy. This is an energy range suitable for comparison with the energy spectrum from neutron decay. Since the calculated distribution of electrons at intermediate and low latitudes in the outer radiation belt is determined more by the source distribution—which is well known—than by the details of the loss mechanism, a comparison of experiment and theory is a valid test of the neutron decay hypothesis.

There are three equivalent ways to represent the electron distribution along a line of force; namely, the flux, or the mirror point distributions along a line of force, or the pitch angle distribution at the equator of particles trapped along a line of force [*Fan, Meyer, and Simpson*, 1961]. In this paper all results are expressed as an electron flux along a line of force through the maximum intensity of the E_3 region of the outer

*Published in the August 1961 issue of *Journal of Geophysical Research*. Reprinted by Permission.

[1]Now at NASA Goddard Space Flight Center.

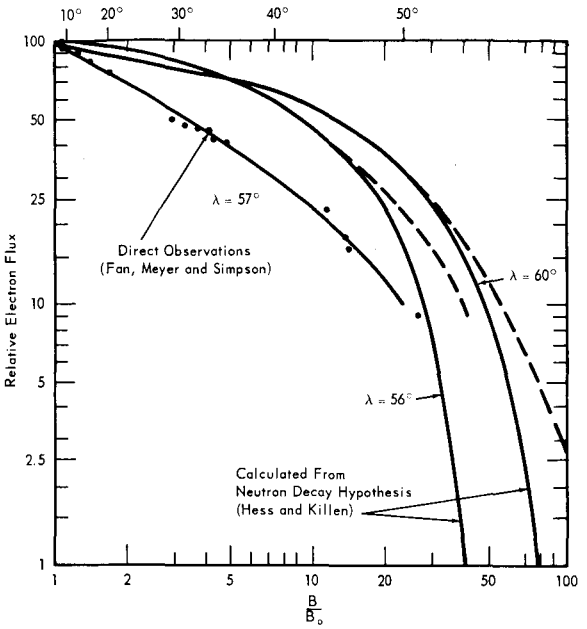

FIGURE 1.—*Relative electron flux measured along a geomagnetic dipole line of force whose range at the equator is* R_0=*21,000 km* (Fan, Meyer and Simpson, *1961*). *For comparison the calculated electron flux distributions assuming only β decay electrons from neutrons escaping from the terrestiral atmosphere are shown for nearby lines of force* (*Hess and Killeen, to be published*). (B_0 *is the magnetic field intensity at the geomagnetic equator*).

belt. For both the experimental results and the calculations, the geomagnetic field is assumed to be a dipole field. This has been found experimentally to be a good representation for the outer electron belt [*Fan, Meyer, and Simpson,* 1960].

The measured electron intensity along a dipole line of force passing through the equator at the geocentric range R_0=21,000 km, or intersecting the earth at the geomagnetic latitude λ=57°, is shown in figure 1. B_0 is the geomagnetic field intensity at the equator, and B is the field intensity at any latitude λ. This is also the line of force through the maximum intensity of the E_3 region in the outer belt [*Fan, Meyer, and Simpson,* 1961]. These measurements were obtained in a period free from large-scale temporal changes of electron intensity or magnetic field intensity, and represent the prevailing electron flux along a line of force at this range.

Since the electron fluxes are derived from bremsstrahlung measurements, it is especially important to note that the change in electron spectrum along the line of force through E_3 maximum was found to be negligible (Fan, Meyer, and Simpson, to be published).

It has been shown that the measured electron intensity I along a line of force may be well represented at intermediate and low latitudes by $I = I_0\ (B/B_0)^{-x}$, where I_0 is the equatorial intensity (Fan, Meyer, and Simpson, to be published). Thus, changes in x reflect changes in electron pitch angle distribution. The smallest values of x are found during undisturbed periods and have the value $x \approx 0.5$ as derived from figure 1. During geomagnetic disturbances, x may increase in value to ~ 1.2.

The calculated electron flux along lines of force intersecting the earth at λ = 56° and λ = 60° are also shown in figure 1, normalized to the experimental curve at the equator (Hess and Killeen, to be published). These calculations assume injection by neutron decay electrons with energies greater than 100 kev. This represents nearly all the electrons in the neutron decay spectrum. Two loss processes were considered. First, trapped electrons are slowed down by collisions with thermal electrons—this is the dominant loss mechanism at high altitudes for electrons with energies greater than 100 kev. Second, at altitudes below a few thousand kilometers where the exosphere becomes principally oxygen and nitrogen, instead of hydrogen, the dominant loss process becomes Coulomb scattering.

The inclusion of scattering losses only changes the calculated flux distribution along a line of force at high latitudes, as indicated by the uncorrected curves drawn by dotted lines in figure 1. This will not affect the low latitude calculations where the comparison with experiment is valid.

A comparison of the exponents x in figure 1 proves that $x < 0.23$ for the neutron decay hypothesis lies below the possible range of x values ($x \geq 0.5$) found by direct measurements in the outer radiation belt. Thus, there are relatively more electrons with mirror points at

low latitudes than predicted by the neutron decay hypothesis.

Therefore, other processes in addition to electron injection by neutron decay are necessary to explain the experimentally observed flux distribution along a line of force in the outer electron belt.

ACKNOWLEDGMENT

The calculations of Hess and Killeen were supported by the U.S. Atomic Energy Commission. The work of Fan, Meyer, and Simpson was supported in part by the National Aeronautics and Space Administration and in part by the U.S. Air Force Office of Scientific Research, contract AF 18 (600)–666.

REFERENCES

Fan, C. Y., P. Meyer, and J. A. Simpson, Trapped and cosmic radiation measurements from Explorer VI, *Space Research*, edited by H. Kallmann-Bijl, North Holland Publishing Company, Amsterdam, pp. 951–966, 1960.

Fan, C. Y., P. Meyer, and J. A. Simpson, The equatorial pitch angle distributions of electrons in the outer radiation belt, EFINS–61–20, Second International Meeting of COSPAR, Florence, Italy, April 1961. (To be published.)

Hess, W. N., E. Canfield, and R. E. Lingenfelter, Cosmic-ray neutron demography, *J. Geophys. Research, 66*, 665–677, 1961.

Killeen, J., and G. Boer, Densities of particles trapped by the geomagnetic field, *Bull. Am. Phys. Soc.* [2], *5*, 312, 1960.

(Manuscript received May 19, 1961.)

Page intentionally left blank

Section 3. Scintillation Counter Experiments Designed by Space Technology Laboratories, Inc.

Page intentionally left blank

Introduction to the Scintillation Counter Experiments Designed by Space Technology Laboratories, Inc.

BY T. A. FARLEY[1]

Space Technology Laboratories, Inc.

The scientific information obtained from the scintillation counter experiment on Explorer VI has been published in the papers included here.

The paper, "Charged-Particle Variations in the Outer Van Allen Zone during a Geomagnetic Storm," by Farley and Rosen, called attention to observations of the particle intensity immediately following the sudden commencement of a geomagnetic storm. The scintillation counter observed an increase in the intensity of trapped particles within 12 hours of the sudden commencement. The other radiation instruments on the same vehicle (and, indeed, all previously flown radiation detectors) showed a decrease during this period. This apparently paradoxical situation was better understood as it became apparent over a period of time that the instruments observing decreases were responding primarily to high energy electrons ($>$ 1 Mev), or to the bremsstrahlung from high energy electrons, in contrast to the experimenters' assumptions that they were responding to bremsstrahlung from low energy ($<$ 100 kev) electrons. The scintillation counter, then, gave the first evidence that the injection of fresh particles into the radiation belt is not delayed until the recovery phase, but begins immediately.

This paper also presented correlations of the particle intensity with the magnetic field as measured by the magnetometer on board the same vehicle. These out-of-phase correlations indicated a particle intensity (of energies below threshold) capable of controlling the magnetic field at the edge of the radiation belt. Investigations of this sort are still badly needed in order to understand the phenomena of this boundary region. Rosen and Sanders are preparing further data for publication concerning the short term particle fluctuation in the radiation belt.

The paper, "Characteristics of the Van Allen Radiation Zones as Measured by the Scintillation Counter on Explorer VI," by Rosen and Farley, presents a broad survey of the scintillation counter data, together with a detailed description of the instrument and the corrections which were applied to the data for saturation and binary failure effects. A preliminary report had been made by Rosen, Farley and Sonett at the First International Space Science Symposium in 1960. The results of a careful remeasurement of the geometrical factor of the instrument are shown. In the calculation of the geometrical factor an error was made, which we take the opportunity to correct here. The geometrical factor should be a factor of 4 larger, and the reported fluxes a factor of 4 smaller, at all energies except for high-energy particles which could reach the scintillator from all directions. Consequently all the reported fluxes (except those for high energy cosmic rays) in all the papers presented here should be reduced by a factor of 4. The authors have claimed only an order of magni-

[1] Now at Institute of Geophysics and Planetary Physics, Univ. of Calif. at Los Angeles.

765-698 O-65—18

tude accuracy for their flux estimates, and no change in this uncertainty is indicated. A factor of four will, however, bring the estimated quiet day outer zone intensity, >500 kev, down from 2×10^7 electrons/cm^2 sec to 5×10^6 electrons/cm^2 sec, which is more in line with subsequent measurements on more recent vehicles.

The paper also presents comparisons of scintillation counter data from the other radiation experiments of Explorer VI. Some observations are made concerning the discrepancies in flux estimates, energy spectrum estimates, and peak intensity positions among these instruments. None of the instruments on the satellite were particle spectrometers, and consequently all of them were sensitive to both energy spectrum changes and intensity changes in such a way that it has proved impossible to construct either a detailed energy spectrum or a correct record of the intensity variations using the data from these instruments.

The paper, "Pitch Angle Distributions and Mirror Point Densities in the Outer Radiation Zone," by Farley and Sanders, presents a method for the calculation of equatorial pitch angle distributions and mirror point densities from the observations of an omnidirectional particle counter at all points along a line of force. The technique is applied to both the scintillation counter data, and to the University of Chicago's proportional counter on Explorer VI. For the scintillation counter, the data along the line of force with $r_o = 21{,}000$ km was examined. The results indicate an apparent relative absence of electrons with pitch angles of 90° during quiet periods.

Charged-Particle Variations in the Outer Van Allen Zone during a Geomagnetic Storm[1]

BY T. A. FARLEY[2] AND A. ROSEN

Space Technology Laboratories, Inc.

The geomagnetic storm whose sudden commencement began about 0400 GMT on August 16, 1959, was associated with intense and unusual fluctuations in the particle intensity measured by the Space Technology Laboratories' scintillation counter on the Explorer VI earth satellite. Comparison of these data with a spin coil magnetometer [*Sonett, Judge, Sims, and Kelso*, 1960] on the same vehicle has revealed a 180° out-of-phase correlation between the particle intensity and the magnetic field strength. The storm was also accompanied by an increase in the count rate of the scintillation counter in the outer zone within 12 hours after the sudden commencement, whereas other radiation instruments on the satellite, sensitive to bremsstrahlung from electrons, saw a decrease. This letter presents data relating to these observations and some comments about the phenomena observed.

The scintillation counter on the Explorer VI earth satellite is sensitive to 500-kev electrons and 10-Mev protons that penetrate the payload shell, and to 200-kev electrons and 2-Mev protons that enter a foil-covered window having a geometrical factor 180 times smaller. The fluctuations seen by this counter, rising and falling by as much as three orders of magnitude within a few minutes, were first observed about 0600 GMT August 16 on pass 17 of the Explorer VI satellite at approximately 41,500 km from earth center. The occurrence of these fluctuations, shown in figure 1, corresponds very closely to the beginning of the main phase of the storm as observed on ground-station magnetometer records. Similar intensity variations at these distances, differing in fine structure, were observed on passes 18 and 19, on August 16 and August 17, respectively.

Various investigators [*Dessler and Karplus*, 1960; *Rosen, Farley, and Sonett*, 1960; *Arnoldy, Hoffman, and Winckler*, 1960; *Fan, Meyer, and Simpson*, 1960] have raised the question whether these and other fluctuations might be the result of a betatron mechanism, which would alternately raise and lower the energies of large numbers of particles above and below the threshold of the instrument as the magnetic field alternately increases and decreases. Accordingly, a detailed comparison has been made between the scintillator count rate and the Space Technology Laboratories' magnetometer [*Sonett, Judge, Sims, and Kelso*, 1960; *Sonett*, 1960] carried on the same vehicle. A number of intervals have been found, covering a considerable period of time in each case, in which the magnetic field shows a very good in-phase correlation with the scintillation counter, demonstrating the existence of the betatron-type mechanism (D. L. Judge and P. J. Coleman, to be published). The fluctuations during the geomagnetic storm, however, show an out-of-phase correlation. Figure 2 shows some of the detailed correlations made at 44,000 km on August 16 during pass 18 of the satellite.

These observations indicate that there is a magnetic field associated with the particles seen

[1] Published in the October 1960 issue of *Journal of Geophysical Research*. Reprinted by permission.

[2] Now at Institute of Geophysics and Planetary Physics, Univ. of Calif. at Los Angeles.

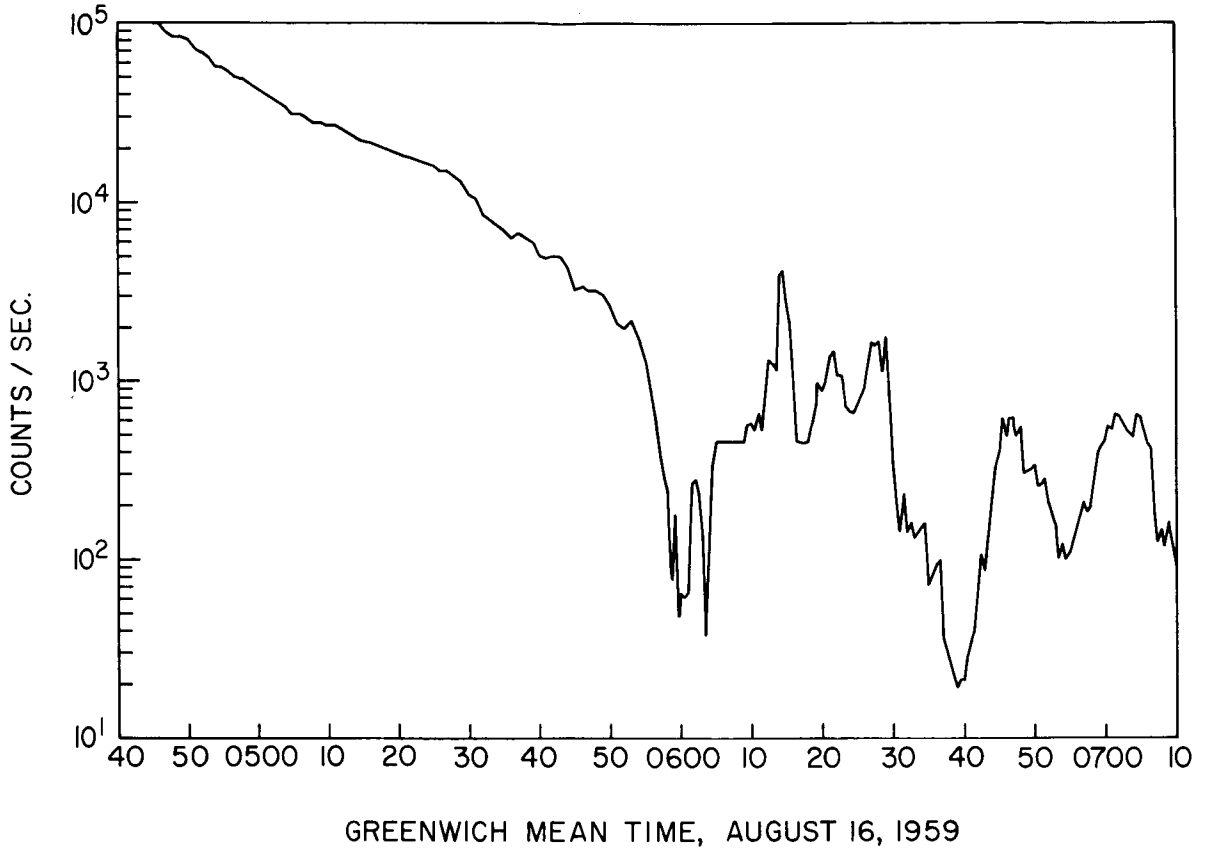

FIGURE 1.—*Rapid variations in particle intensity during a geomagnetic storm.*

by the scintillation counter which is capable of substantially reducing the geomagnetic field at that distance. This depression of the magnetic field may possibly be the result of an intrusion of diamagnetic gas clouds into the geomagnetic field caused by the increased pressure of the storm-day solar wind. The particles in these ragged gas clouds evidently have disordered internal motions which become ordered as the particles take up internal orbits that will exclude the geomagnetic field. The field outside the clouds is increased because some of the lines of force are excluded from the interior of the bubbles. The field inside the clouds is not zero, since the geomagnetic field lines are not completely excluded, or else because the clouds have some internal fields of their own.

The local time on this satellite at 7 earth radii is always about 7 PM, and the satellite is, therefore, always on the side of the earth away from the sun at this distance. Whether these gas clouds ever penetrate to distances less than 7 earth radii on this side of the earth has not yet been determined, and correlations with the magnetometer are being made at closer distances in order to settle the question.

The particles seen by the scintillation counter at this time may be either electrons or protons. If they are electrons above 500 kev, which seems likely, and if the particle flux is isotropic, a count rate of 10^4/sec corresponds to a flux of approximately 3×10^5 electrons/cm^2 sec. This flux of 500-kev electrons has an energy density of about 10^{-11} erg/cm^3. The magnetic energy density in a field of 100 gamma (10^{-3} gauss) is 4×10^{-3} erg/cm^3 Even if the particles are protons, the particle fluxes measured by the scintillation counter are inadequate to cause the observed variations in the magnetic field, and there must be large numbers of low-energy particles associated with the particles seen by the scintillation counter.

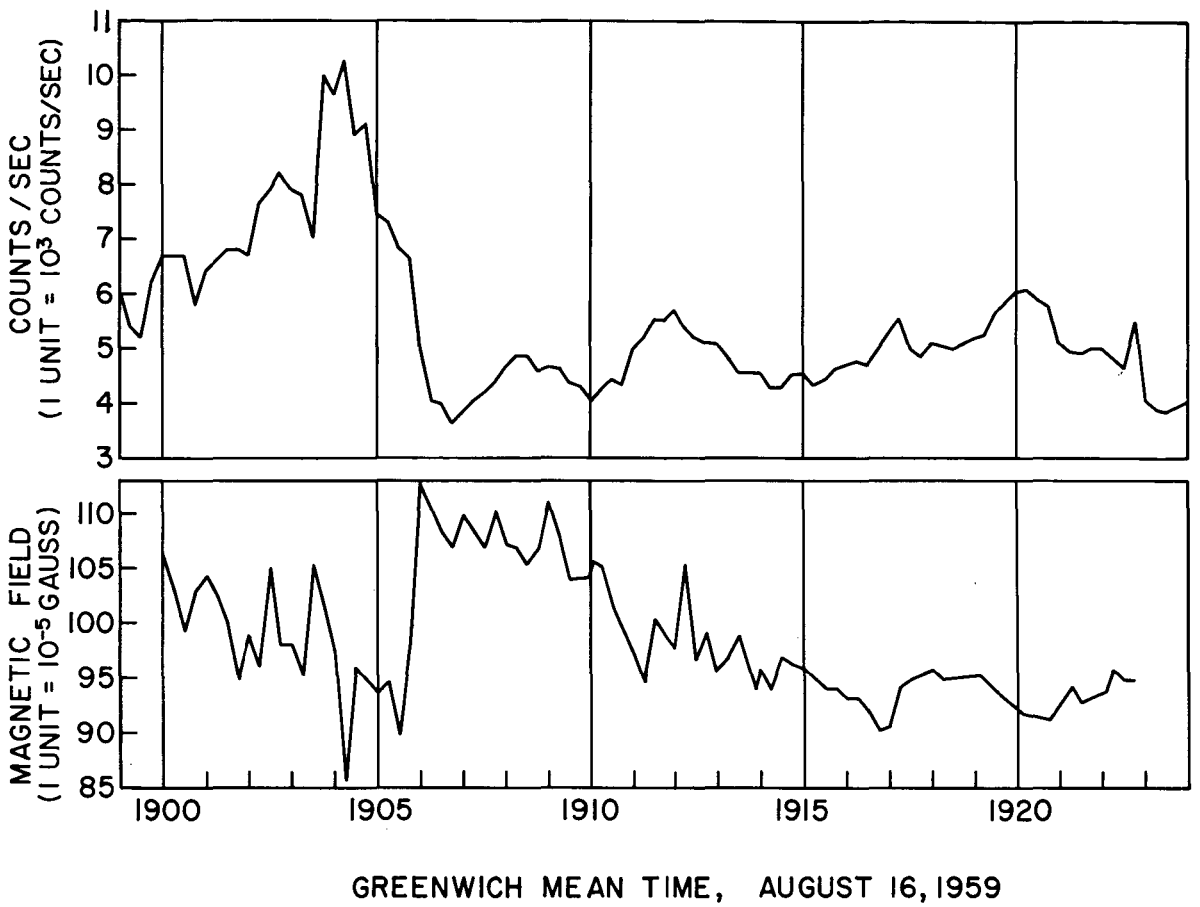

FIGURE 2.—*Simultaneous particle intensity and magnetic field measurements at 44,000 km during a geomagnetic storm.*

Figure 3 shows a comparison of the particle flux on passes 17 and 18, both on August 16, in the outer Van Allen zone. Pass 18 shows a very unusual amount of structure in the particle flux and a modest increase in peak intensity—evidence that new particles have appeared in the geomagnetic field at distances beyond approximately 3 earth radii. This increase in peak intensity, taking place during the main phase of the magnetic storm, is quite small compared with the 20-fold increase that had occurred by pass 21 on August 18. It is important to note, however, that there is no net decrease in peak intensity in the outer zone of particles to which the scintillation counter is sensitive at any time during the storm, although there is a decrease at radial distances beyond the position of peak intensity. This may be contrasted with the results of *Arnoldy, Hoffman, and Winckler* [1960] and *Fan, Meyer, and Simpson* [1960], who observe a decrease in the peak intensity of bremsstrahlung from electrons.

Since the instruments on this satellite sensitive to bremsstrahlung from electrons see a decrease in peak intensity, the increase in peak intensity seen by the scintillation counter must be the result of an increase of protons above 2 Mev in the geomagnetic field. The evidence presented here does not settle the question of the origin of these protons. If they enter the field in diamagnetic gas clouds, the geomagnetic field will diffuse almost immediately into these clouds, trapping a fraction of the newly arrived particles along the lines of force of the geomagnetic field. The irregular structure of the outer Van Allen zone at this time suggests the presence of hydromagnetic waves which may cause some scattering loss of particles

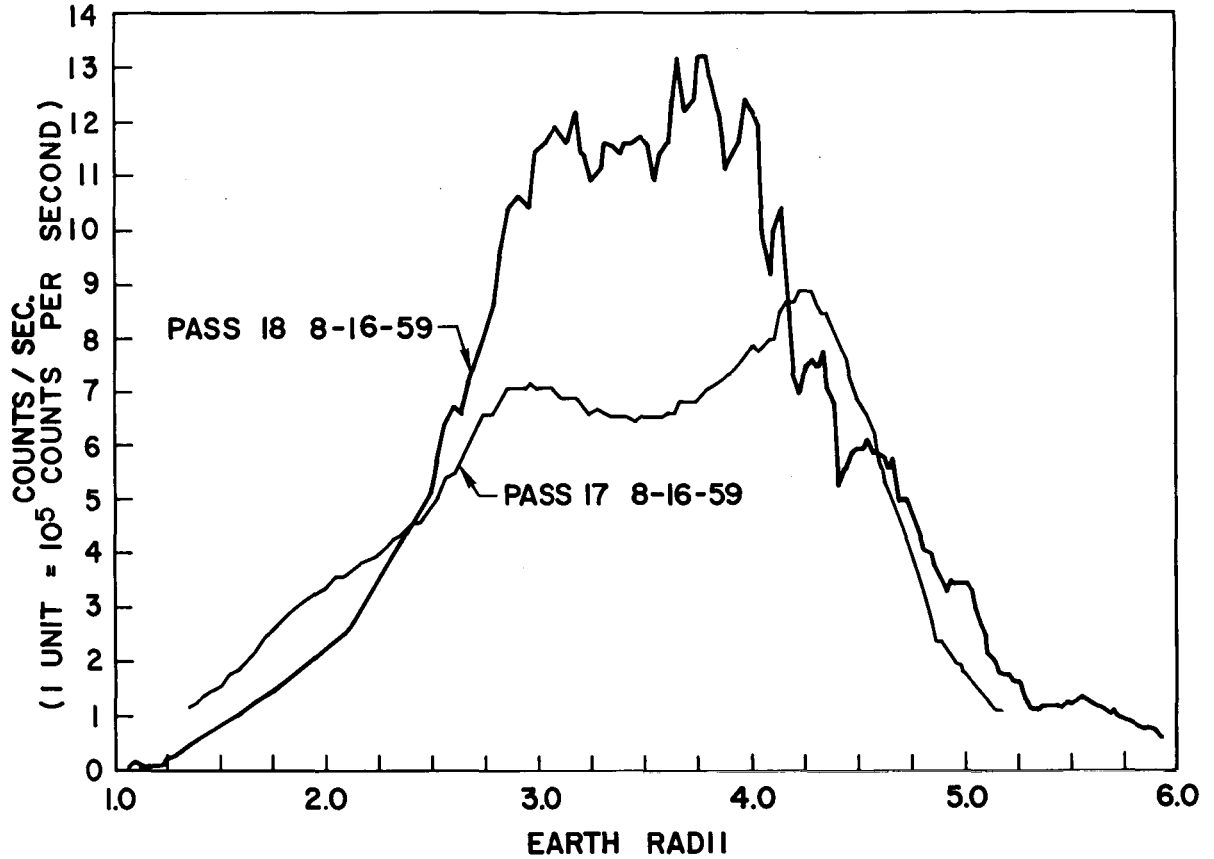

FIGURE 3.—*A comparison of the particle intensities in the outer Van Allen zone just before and just after the sudden commencement of a geomagnetic storm. All count rates have been corrected for saturation effects.*

already trapped in the field. If a generalized depression of the field is also present at this time, causing a large-scale betatron deceleration of trapped particles, these phenomena may account for the decreased count rate in the satellite instruments sensitive to bremsstrahlung.

The phenomena described here are consistent with the geomagnetic storm model of *Dessler and Parker* [1959], and the confirmation of the increase of energetic protons in the geomagnetic field during a storm makes plausible the establishment of the field stresses which account for the main phase of a geomagnetic storm in that model.

ACKNOWLEDGMENTS

We wish to acknowledge several useful discussions of some of the above phenomena with E. N. Parker and A. J. Dessler.

This program was carried out under the direction of the National Aeronautics and Space Administration.

REFERENCES

Arnoldy, R. L., R. A. Hoffman, and J. R. Winckler, *J. Geophys. Research, 65,* 1361, 1960.

Dessler, A. J., and R. Karplus, *Phys. Rev. Letters, 4,* 271, 1960.

Dessler, A. J., and E. N. Parker, *J. Geophys. Research, 64,* 2239, 1959.

Fan, C. Y., P. Meyer, and J. A. Simpson, *Proc. COSPAR Space Symposium,* North Holland Publishing Co., Amsterdam, 1960.

Rosen, A., T. A. Farley, and C. P. Sonett, *Proc. COSPAR Space Symposium,* North Holland Publishing Co., Amsterdam, 1960.

Sonett, C. P., *Advances in Space Sci., 2,* Academic Press, New York, 1960.

Sonett, C. P., D. L. Judge, A. R. Sims, and J. M. Kelso, *J. Geophys. Research, 65,* 55, 1960.

(Received July 30, 1960.)

Pitch Angle Distributions and Mirror Point Densities in the Outer Radiation Zone [1]

BY T. A. FARLEY [2] AND N. L. SANDERS

Space Technology Laboratories

A method is presented for the calculation of the equatorial pitch angle distribution (unidirectional intensity distribution) of trapped radiation from the count rate of an omnidirectional detector along a line of force. An expression is derived for the calculation of the mirror point density from the equatorial pitch angle distribution. The method is applied to data obtained from the Space Technology Laboratories scintillation counter and the University of Chicago proportional counter on the Explorer VI satellite. The results from the scintillation counter show a relative absence of electrons with pitch angles of 90° during quiet periods, a sharp increase in such particles shortly after a sudden commencement magnetic storm, and restoration of the prestorm distribution at a higher intensity level after the storm. The results from the proportional counter are qualitatively similar with the exception of the apparent deficiency of 90° pitch angles during quiet periods, which does not appear

The determination of the spatial distribution of the electrons trapped in the geomagnetic field requires a great many samplings of the particle intensity at different locations throughout the field. The Explorer VI satellite, with a period of 12 hours and 42 minutes, crossed the line of force at an equatorial geocentric radius of 21,000 km either two or four times per period. Sufficient data were obtained from these crossings during a 3-week period to permit detailed analysis of the spatial distribution along this line in terms of the individual particle orbits. The observations covered a range of geomagnetic latitudes from 0° to 50°.

This satellite was launched on August 7, 1959, into an elliptical orbit with apogee at 48,600 km from earth center. A scintillation counter, one of three radiation experiments on board, was supplied by Space Technology Laboratories. *Rosen and Farley* [1961] have given a detailed description of this instrument and the data obtained from it. All count rates of this instrument used in this paper have been corrected for saturation effects as described by Rosen and Farley. The efficiency of the instrument for detection of electrons is shown in figure 1.

A proportional counter was supplied by the University of Chicago for this satellite, and detailed results from that instrument have been given by *Fan, Meyer, and Simpson* [1961 *a* and *b*]. Some of the count rate data published by these authors have been used here for the calculation of pitch angle distributions.

The problem of calculating unidirectional intensities at a point from knowledge of the omnidirectional intensity at every point along a line of force has been solved by *Ray* [1960]. The solution presented by him differs in form from that presented in this paper. Approximate solutions to this same problem have been obtained by *Fan, Meyer, and Simpson* [1961 *a* and *b*] and by *Lenchek, Singer, and Wentworth*

[1] Published in the June 1962 issue of *Journal of Geophysical Research*. Reprinted by permission.

[2] Now at: Institute of Geophysics and Planetary Physics, Univ. of Calif. at Los Angeles.

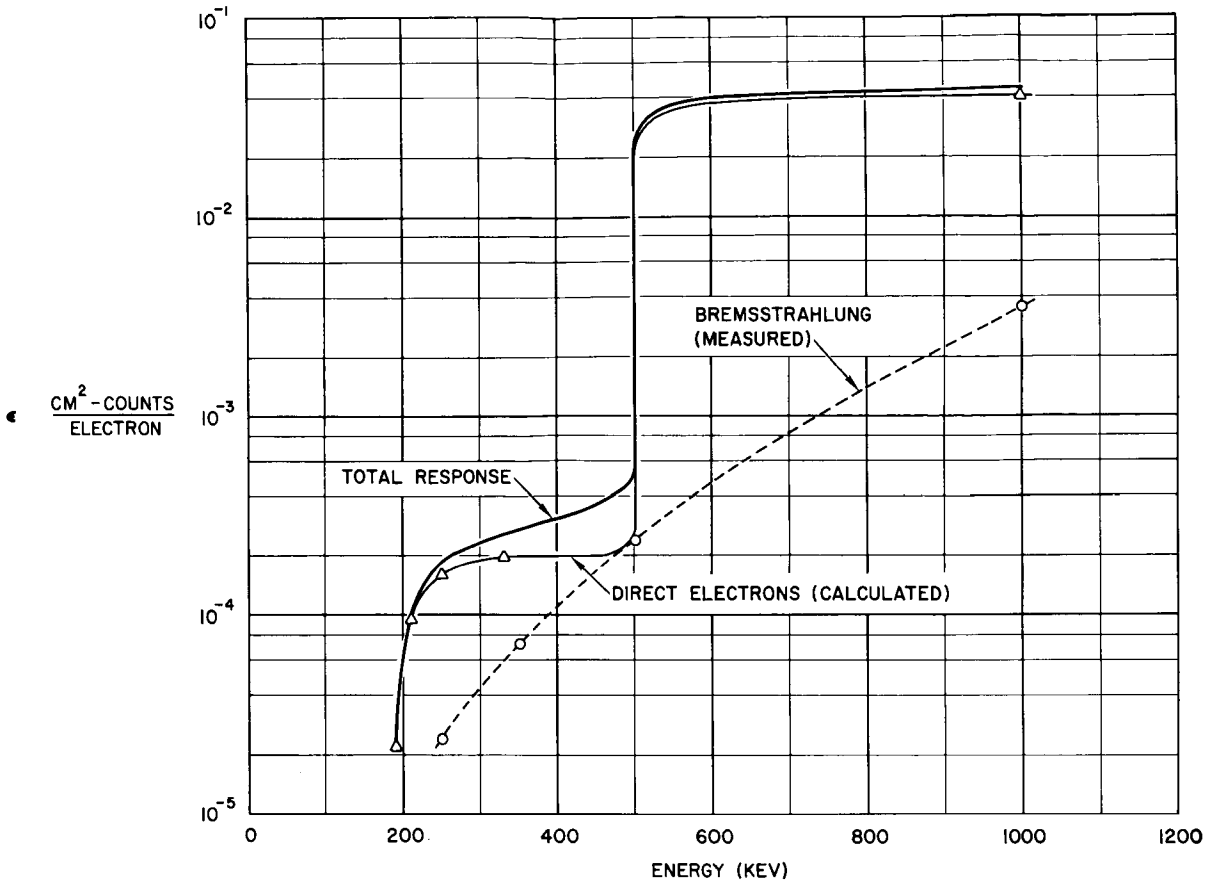

FIGURE 1.—*The efficiency of the scintillation counter for the detection of electrons*

[1961], who apply their solutions to the data obtained from the proportional counter on Explorer VI.

Exact expressions for the equatorial unidirectional intensity (pitch angle distribution) and the mirror point density are presented in this paper in a simple form. These theoretical results are then applied to the omnidirectional intensities measured by the scintillation counter and proportional counter on the Explorer VI satellite. The unidirectional intensities calculated from the exact expressions derived herein are in excellent agreement with those calculated from the same data by the approximation technique of Wentworth. Comparison is made between the pitch angle distributions calculated from the data and those calculated from the omnidirectional intensities given by *Hess and Killen* [1961] for neutron-decay electrons.

THEORETICAL DISCUSSION

The equilibrium distribution of trapped particles obeying the adiabatic invariance conditions along any line of force may be described in at least three different ways: by the omnidirectional particle intensity at all points along the line; by the unidirectional intensity at all pitch angles at the geomagnetic equator; and by the density of particles having mirror points at each point along the line. In a given magnetic field these three descriptions are equivalent, contain exactly the same information, and are convertible one to another. The equatorial pitch angle distribution is derived here from the omnidirectional intensity along the line of force for an arbitrary magnetic field. The mirror point density is derived here from the equatorial pitch angle distribution by assuming that the field is a magnetic dipole.

Definitions

The pitch angle α is the angle between the particle velocity vector and the magnetic field vector at the point where the magnetic field magnitude is B. It is equal to 90° at the particle mirror point and has a minimum value when the particle crosses the equator.

The unidirectional intensity $j(B, \cos \alpha)$ is the number of particles per cm² sec ster having velocity vectors between α and $\alpha + d\alpha$.

The omnidirectional intensity $J(B)$ is the integral of $j(B, \cos \alpha)$ over the solid angle. B_0, j_0, etc., refer to the value of the variables at the geomagnetic equator. B_m refers to the value of the magnetic field at the particle mirror point.

The unidirectional intensity in the equatorial plane, $j_0(\cos \alpha_0)$, is called the pitch angle distribution.

The mirror point density $\omega(\lambda)$ is the number of particles per unit volume having mirror points between the geomagnetic latitudes λ and $\lambda + d\lambda$.

$T(\lambda)$ is twice the time required for a particle to travel from its northern mirror point at λ to its southern mirror point at $-\lambda$, i.e., one complete period.

Pitch Angle Distribution

From the definition,

$$J(B) = 4\pi \int_{\alpha_{\min}}^{\pi/2} j(B, \cos \alpha) \sin \alpha \, d\alpha \qquad (1)$$

$j_0(\cos \alpha_0)$ can be obtained from the solution of this integral equation as follows. Consider a group of particles which have equatorial pitch angles between α_0 and $\alpha_0 + d\alpha_0$, and which mirror between λ and $\lambda + d\lambda$. Neglecting their slow longitudinal drift, the guiding centers of these particles move on a bundle of flux lines which constitute a flux tube extending from λ to $-\lambda$. In equilibrium, the same number of guiding centers per unit time must cross one tube section in one direction as cross any other tube section in the same direction. Thus:

$$2\pi j(B, \cos \alpha) \sin \alpha \, d\alpha \cos \alpha \, dA = 2\pi j_0(\cos \alpha_0) \sin \alpha_0 \, d\alpha_0 \cos \alpha_0 \, dA_0$$

Using the mirror relation for adiabatically trapped particles,

$$\frac{\sin^2 \alpha_0}{B_0} = \frac{\sin^2 \alpha}{B}$$

$$j(B, \cos \alpha) B dA = j_0(\cos \alpha_0) B_0 \, dA_0$$

and therefore

$$j(B, \cos \alpha) = j_0(\cos \alpha_0)$$

This equality states that the unidirectional intensity at some α_0 at the geomagnetic equator is equal to the unidirectional intensity at α at any point along the line of force if α is related to α_0 by the mirror equation. Equation 1 can be rewritten as

$$J(B) = 4\pi \int_{\alpha_{\min}}^{\pi/2} j_0(\cos \alpha_0) \sin \alpha \, d\alpha \qquad (2)$$

Using the mirror equation $\sin^2 \alpha = B/B_m$, the variable of integration may be changed to B_m:

$$\frac{J(B)}{2\pi B} = \int_B^{B_{\max}} \frac{j_0'(B_m) dB_m}{(B_m)^{3/2}(B_m - B)^{1/2}} \qquad (3)$$

where $j_0'(B_m)$ is the function obtained by changing the variable in j_0 from $\cos \alpha_0$ to B_m. $B_{\max}$ is the value of the field at which the particle having pitch angle $\alpha_{\min}$ mirrors. Notice that those particles having mirror points at $B_m < B$ (i.e., higher altitudes) do not contribute to $J(B)$.

Making the substitutions

$$B_m = B_{\max} - y$$

$$B = B_{\max} - t$$

$$\frac{j_0'(B_m)}{(B_m)^{3/2}} = \frac{j_0'(B_{\max} - y)}{(B_{\max} - y)^{3/2}} = f(y)$$

$$\frac{J(B)}{2\pi B} = \frac{J(B_{\max} - t)}{2\pi(B_{\max} - t)} = \psi(t)$$

equation 3 becomes

$$\psi(t) = \int_0^t \frac{f(y) \, dy}{(t - y)^{1/2}} \qquad (4)$$

with $\psi(0) = 0$ since $J(B_{\max}) = 0$.

This is Abel's integral equation, and its solution is (e.g., *Courant* [1956])

$$f(t) = \frac{1}{\pi}\frac{d}{dt}\int_0^t \frac{\psi(y)\,dy}{(t-y)^{1/2}} \qquad (5)$$

Integrating by parts, differentiating under the integral sign, and replacing the original variables:

$$j_0(\cos\alpha_0) = j_0'(B_m) = -\frac{(B_m)^{3/2}}{\pi}\int_{B_m}^{B_{max}} \frac{\frac{d}{dB}\left(\frac{J(B)}{2\pi B}\right)dB}{(B-B_m)^{1/2}} \qquad (6)$$

Equation 6 is the general solution for $j_0(\cos\alpha_0)$ when $J(B)$ is known. The differentiation and integration may be performed by computer. The change of variable from B_m to $\cos\alpha_0$ is accomplished through the mirror relation $\sin^2\alpha_0 = B_0/B_m$.

Mirror Point Density

Particles having equatorial pitch angles between α_0 and $\alpha_0 + d\alpha_0$ have mirror points between λ and $\lambda + d\lambda$. In equilibrium, the time rate at which the guiding centers of these particles pass through the cross section of a flux tube at the equator is equal to the time rate at which they mirror in the volume element $dAdl$ of the flux tube at λ:

$$4\pi j_0(\cos\alpha_0)\sin\alpha_0 d\alpha_0\cos\alpha_0 dA_0 = \frac{\omega(\lambda)\,dl\,dA}{T(\lambda)}$$

where ω and T are the mirror point density and bounce period as previously defined. In cylindrical coordinates $(dl)^2 = dr^2 + r^2(d\lambda)^2$, and for a dipole field

$$dl = r_0\cos^7\lambda(B/B_0)\,d\lambda$$

where r_0 is the geocentric radius in the equatorial plane. Therefore

$$\omega(\lambda) = \frac{2\pi T(\lambda)}{r_0\cos^7\lambda}\left(\frac{B_0}{B}\right)^2\left(\frac{1}{B_0}\frac{dB}{d\lambda}\right)j_0(\cos\alpha_0) \qquad (7)$$

In a dipole field

$$\frac{B}{B_0} = \frac{(4-3\cos^2\lambda)^{1/2}}{\cos^6\lambda} \qquad (8)$$

so that

$$\frac{1}{B_0}\frac{dB}{d\lambda} = 3\tan\lambda\left[\frac{B_0}{B\cos^{10}\lambda} + \frac{2B}{B_0}\right] \qquad (9)$$

From the definition of the bounce period,

$$T(\lambda) = 4\int_0^{B_m}\frac{dl}{v\cos\alpha} = \frac{4r_0}{v}\int_0^{\lambda}\frac{B}{B_0}\frac{\cos^7\lambda\,d\lambda}{[1-B/B_m]^{1/2}} \qquad (10)$$

Equation 10 has been numerically integrated, and the results are shown in figure 2. The bounce period is evidently inversely proportional to the particle velocity. The period, often described as approximately independent of the mirror latitude, actually varies by a factor of approximately 1.7 from the geomagnetic equator to a latitude of 60°.

Bringing together equations 7, 8, and 9, the result is

$$\omega(\lambda) = \frac{6\pi T(\lambda)\sin\lambda(8-5\cos^2\lambda)}{r_0(4-3\cos^2\lambda)^{3/2}\cos^2\lambda}\,j_0'(\lambda) \qquad (11)$$

where $j_0'(\lambda)$ is the result of a change in variable from $\cos\alpha_0$ to λ in $j_0(\cos\alpha_0)$.

If the particles are all of the same velocity (e.g., all relativistic), equation 8 may be used together with values of T from figure 2 to obtain the mirror point density from the pitch angle distribution.

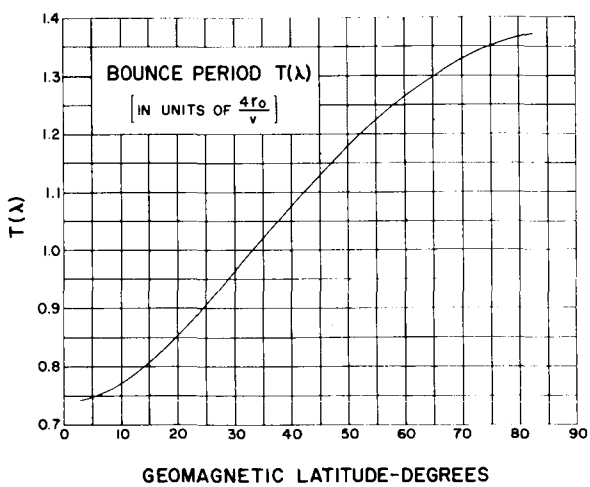

FIGURE 2.—*The bounce period of particles adiabatically trapped in a dipole field plotted as a function of the latitude at which the particle mirrors. r_0 is the geocentric radius of the line of force in the equatorial plane, and v is the particle velocity.*

Detector Efficiency

The ideal instrument for measurements of the omnidirectional intensities for use in these expressions is one whose directional response is isotropic and whose energy response is constant within some energy interval and zero elsewhere. Such an instrument would produce data from which a correct pitch angle distribution could be calculated for the particles in that energy interval.

If the detector response is anisotropic in such a way that the efficiency depends on the pitch angle and local satellite orientation, the data are not readily usable to calculate the pitch angle distribution.

If the instrument is omnidirectional, but has an efficiency that depends on energy, the omnidirectional count rate $R(B)$ will be given by

$$R(B) = 4\pi \int_{\alpha} \int_{E} \epsilon(E) \cdot \frac{dj'(B, E, \cos\alpha)}{dE} \sin\alpha \, d\alpha \, dE$$

If $j'(B, E, \cos\alpha)$ can be written as $j(B, \cos\alpha)(E)$, which indicates that the energy spectrum does not change along a line of force, then

$$R(B) = \left[\int_{E} \epsilon(E) \frac{dn(E)}{dE} dE\right] 4\pi \cdot \int_{\alpha} j(B, \cos\alpha) \sin\alpha \, d\alpha = kJ(B)$$

and an undistorted pitch angle distribution will result.

If the energy spectrum does change along a line of force (and therefore changes with pitch angle at a given point on the line), the unidirectional intensities determined from the observed count rates will be weighted (distorted) according to the efficiency of the detector for particles from that direction. For example, if the efficiency of the detector rises with energy, the unidirectional intensities will appear too large in the directions from which the high-energy particles come and too low in the directions from which low-energy particles come.

Data and Results

The data from which the pitch angle and mirror point distributions have been calculated are the count rates of the scintillation experiment at the time the satellite crosses one particular geomagnetic field line. The field line that crosses the geomagnetic equator at 21,000 km from earth center has been chosen, because the satellite crossings of this line take place over a wide range of northern latitudes and because comparisons with the published results of Fan and coworkers can be made along this same line of force. This field line is also the approximate position of one of the outer-zone electron peaks observed by the scintillation counter and designated peak 2 by *Rosen and Farley* [1961]. The position of the field line in space has been calculated from an earth-centered dipole approximation in which the north geomagnetic pole intersects the surface of the earth at 78.5° N latitude and 291° E longitude.

The data points have been grouped into three time intervals. Figure 3 shows the data from all available crossings of this line of force during the magnetically quiet period from August 8 to August 16, 1959. Figure 4 shows data points taken during the magnetically disturbed period of August 18 to August 22, which followed the severe magnetic storm of August 16, 1959. Figure 5 includes data taken during a quiet period following the storm. The data points have been divided in this way to show the major changes that took place during these three weeks.

The assumption has been made that these count rates are proportional to the omnidirectional particle intensity at the point in space at which the data were taken. This is equivalent to the assumption that the counter efficiency ϵ is independent of particle pitch angle for all satellite orientations. Even though the scintillation counter is averaging over each spin cycle of the vehicle, its efficiency is still anisotropic in such a way that it is more sensitive to particles striking the vehicle parallel to the spin axis direction than to particles striking perpendicular to the spin axis direction. Near the geomagnetic equator at 21,000 km the vehicle spin axis was approximately perpendicular to the magnetic field line, so that the in-

strument was most sensitive to particles having 90° pitch angles. Therefore the apparent absence of these particles, which is a result of the decreased count rate near the equator, cannot be explained by the somewhat anisotropic response of the counter. Except for the apparent hole near 90° and the loss cone near 0° the pitch angle distribution is nearly isotropic at the equator, and a somewhat anisotropic response is of little consequence. At high latitudes, where the pitch angles are all near 90°, considerable error which depends on the satellite orientation can be introduced. Because of the existing uncertainties in vehicle orientation with respect to the line of force, no attempt has been made to omit data points or to correct for these errors, which certainly contribute to the data point scatter at the high latitudes. Crossings of the line of force at northern latitudes have been plotted with solid circles, and those at southern latitudes with open circles. The line drawn through these points represents our best estimate of the omnidirectional particle intensity.

Comparison has been made in each figure with the count rate of the University of Chicago proportional counter rate [*Fan, Meyer, and Simpson*, 1961 *a* and *b*]. Since the University of Chicago group used the line of force passing

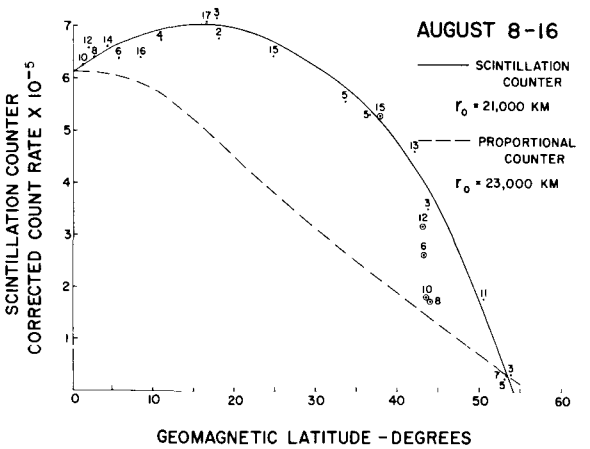

FIGURE 3.—*Radiation detector count rates for the magnetically quiet period from August 8 to 16. The proportional counter rates have been arbitrarily normalized to the scintillation counter rate at the geomagnetic equator in all count rate figures.*

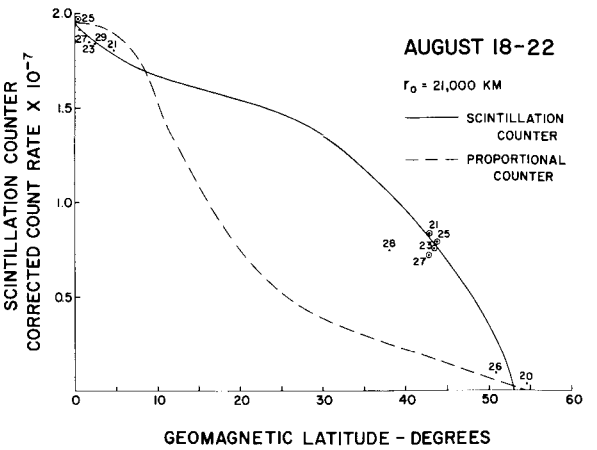

FIGURE 4.—*Radiation detector count rates for the late recovery phase of the magnetic storm of August 16, 1959, which was followed by a magnetically disturbed period from August 18 to 22.*

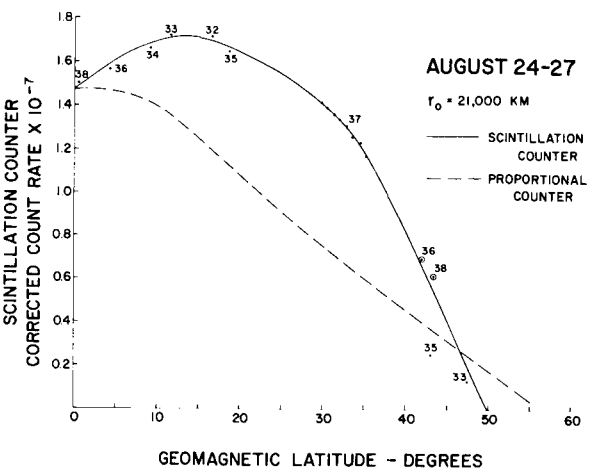

FIGURE 5.—*Radiation detector count rates for the magnetically quiet period from August 24 to 27.*

through their E_3 outer-zone maximum, their curve in figure 3 is for a neighboring line of force at R_0=23,000 km, while in figures 4 and 5 their curve is for the same line as the scintillation counter data. In each case the proportional counter data had been normalized to the scintillation counter rate at the geomagnetic equator, even though the poststorm intensity increase is considerably greater for the scintillation counter than for the proportional counter.

We attribute the change in count rate ratio of these two counters along the line of force to a small change in the average electron energy along the line of force. For example, a small increase in the proportion of high-energy electrons (>1 Mev) would cause the observed increase in proportional counter to scintillation counter ratio near the geomagnetic equator because the proportional counter efficiency is proportional to $E^{4.7}$ [*Fan, Meyer, and Simpson*, 1961 *a* and *b*] whereas the scintillation counter efficiency is rising only slowly in this energy range (fig. 1).

The authors believe that the scintillation counter is responding entirely to electrons of energies above 500 kev because of the improbably large fluxes of electrons below this energy that would be required to cause a significant fraction of the observed counting rate. Therefore, the pitch angle distributions calculated from the scintillation counter data are those for electrons above 500 kev, weighted by the slowly rising efficiency of the counter. The distributions calculated from the proportional counter data are those for the entire electron energy spectrum, weighted by $E^{4.7}$. If there are changes in the energy spectrum along the line of force the scintillation counter distributions will be only mildly distorted whereas those of the proportional counter may be very considerably distorted according to the argument presented in the theoretical section.

A number of qualitative similarities between the STL and Chicago data may be pointed out. First, there is a sharp peaking-up of the count rate curves of both counters at the geomagnetic equator during the recovery phase of the magnetic storm. Unfortunately, there are few crossings of this line of force at intermediate latitudes during this period, and the STL count rate curve has simply been drawn in a shape similar to that of the preceding period at these latitudes. Second, there is a return to the prestorm count rate curve shape during the third, magnetically quiet, period.

Figures 6, 7, and 8 are presentations of the corresponding equatorial pitch angle distributions computed by the method described in the theoretical section. Since the unidirectional intensity has been plotted against the cosine

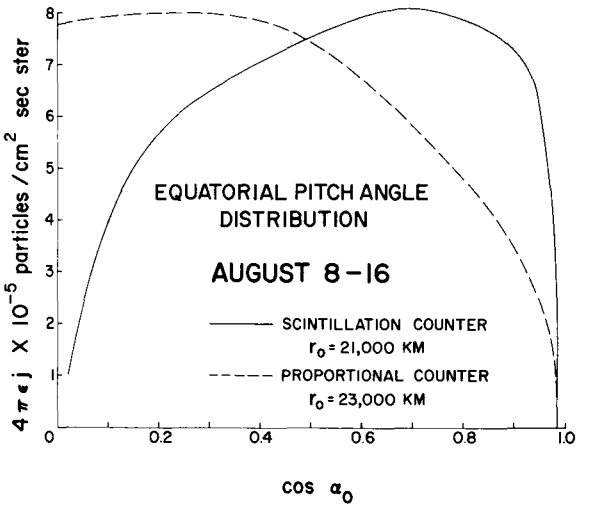

FIGURE 6.—*Pitch angle distributions calculated from the count rates in figure 3.* ϵ *is the average efficiency of the detector for the particles to which the instrument is responding.*

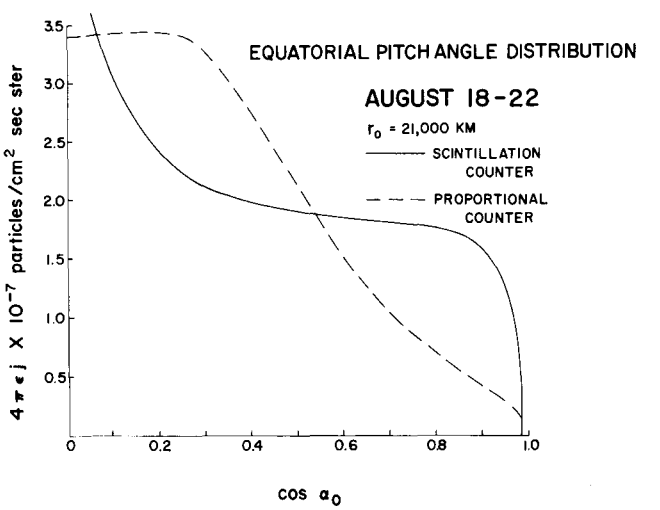

FIGURE 7.—*Pitch angle distributions calculated from the count rates in figure 4.*

of the pitch angle, the area under each curve is simply the count rate of each instrument at the geomagnetic equator. Because of the equatorial normalization of the count rates of the instruments, both the scintillation and proportional counter curves have the same total areas. The equatorial peaking of the count rate curve during the storm is apparent here as a sharp increase in particles having pitch angles near

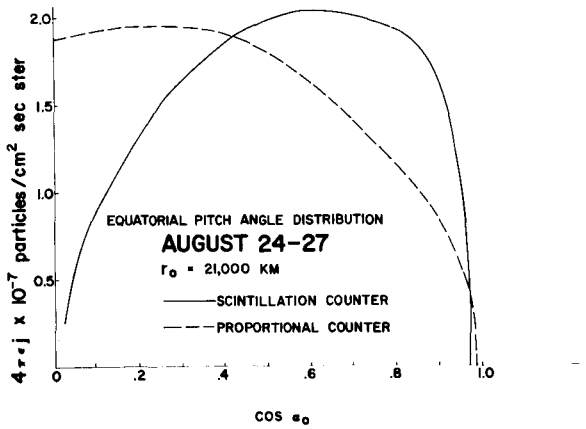

FIGURE 8.—*Pitch angle distributions calculated from the count rates in figure 5.*

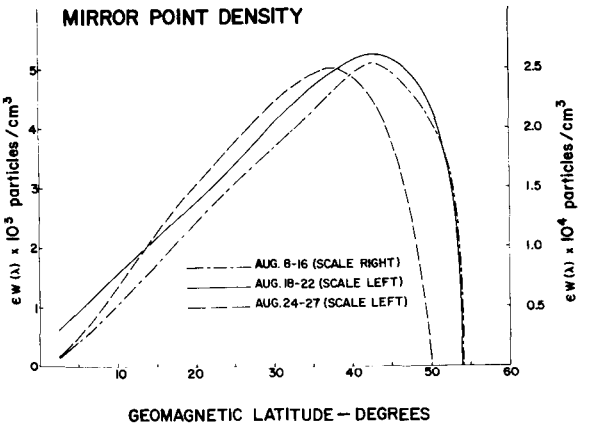

FIGURE 9.—*The mirror point density as a function of the latitude at which the particles mirror, using the scintillation counter rates for the three periods considered.*

90°. It does not seem possible to say whether these particles have been removed by August 24, or whether they have been distributed over smaller pitch angles.

The pitch angle distributions given here for the proportional counter differ substantially from those given by *Fan, Meyer, and Simpson* [1961 *a* and *b*], primarily because of a different definition of the pitch angle distribution used by them.

Figure 9 is a plot of the mirror point distributions that correspond to the three time periods, calculated from the scintillation counter data.

Experimental Discussion

The equatorial pitch angle distributions calculated from the scintillation counter data are compared with a theoretical distribution of neutron-albedo decay electrons in figure 10. The theoretical distribution has been computed from the omnidirectional intensity presented by *Hess and Killeen* [1961] for the neutron-decay electrons along the line of force at $r_0 = 20{,}500$ km. All three curves in this figure have been arbitrarily normalized at $\cos \alpha_0 = 0.66$.

The neutron-albedo decay theory is so far the only theoretical source mechanism for the outer-zone electrons from which a pitch angle distribution has been calculated, and it is for that reason that these comparisons have been made. The authors believe that the Explorer VI results indicate the presence of substantial

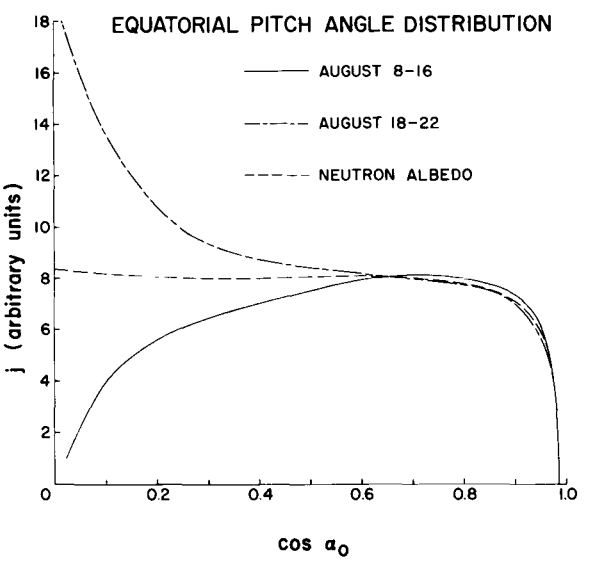

FIGURE 10.—*Comparison of the August 8–16 and August 18–22 pitch angle distribution with that calculated from the omnidirectional intensities given by Hess and Killeen (1961) for neutron-decay electrons. The curves are arbitrarily normalized at cos $\alpha_0 = 0.66$.*

fluxes of electrons of energies of at least 1 Mev, and that the flux of these particles increased markedly after a geomagnetic storm. These facts appear to be incompatible with the existence of an unmodified neutron-decay electron energy spectrum in this region. Indeed, the only part of the neutron-decay hypothesis com-

patible with the observations is the possibility that neutron decay is the source mechanism for electrons that are subsequently modified both in energy and pitch angle distribution by an unknown time-dependent mechanism.

The magnetic history of the period for which data have been presented may be summarized as follows: August 12, 13, and 14 were among the five quietest days in August. On August 15, a gradual commencement storm was reported at some stations. At approximately 0400 on August 16, a sudden commencement storm began which continued until the end of August 17 or the beginning of August 18. This storm was classed as severe (corresponding to a K index of 8 or 9). Huancayo reported a moderate, gradual commencement storm which began at 0635 on August 18 and ended at 2000 hours the same day. A moderately severe, sudden commencement storm began on August 20 at 0412. There is no general agreement as to when this storm ended. (Some stations estimated that it ended on August 20, but others recorded disturbed conditions until August 24.) August 27 and 28 were the two quietest days of the month.

During the two magnetically quiet periods, there appears to be a relative absence of particles having pitch angles near 90°. This fact is a consequence of the decreasing count rate near the geomagnetic equator. Mathematically speaking, the intensity of particles having pitch angles of 90° is found by subtracting from the equatorial count rate the contribution of all particles mirroring at higher latitudes, and designating the remainder as the count rate of particles having 90° pitch angles. If this remainder is small (as actually it is) it will be quite sensitive to any variation or error in the count rate at the equator. For example, the decrease in count rate at the equator of less than 15 percent (figs. 3 and 5) causes a drop of approximately 100 percent in the pitch angle distribution at 90° (figs. 6 and 8). Nevertheless, the assertion that there is a relative absence of particles with pitch angles near 90° during quiet periods appears justified by the data.

During the main and recovery phases of a magnetic storm, either a substantial number of new particles are injected or else acceleration of particles already present takes place, causing the twentyfold increase in count rate of the scintillation counter. The injection or acceleration must be such as to increase sharply the intensity of particles trapped near the geomagnetic equator. High-latitude injection or acceleration of geomagnetic storm electrons, therefore, appears inconsistent with the data.

The disappearance of the electrons with pitch angles near 90° takes place sometime after the pass 29 crossing of the line of force at 1232 UT on August 22, 1959, during a period of lessening magnetic disturbance. August 22 is also the date on which a great solar radio noise storm commenced, and the possible connection of this storm with the outer radiation zone has been discussed by *Arnoldy, Hoffman, and Winckler* [1960]. How this solar event might have influenced electrons with pitch angles near 90° deep within the geomagnetic field is not known. The fact that the resulting pitch angle distribution resembles the prestorm distribution may indicate that it is the result of the same mechanism that produced the prestorm distribution at some earlier date.

APPENDIX

A useful analytic solution to equation 6 can be found if $J(B)$ can be conveniently expressed as a polynomial in B, i.e.,

$$J(B) = \sum_{k=-s}^{k=n} A_k B^k$$

where s and n are positive integers.

Then

$$2\pi \frac{d\psi}{dB} = \sum_{k=-s}^{k=n} (k-1) A_k B^{k-2}$$

Substituting into equation 6 and performing the integration, we find that

$$4\pi j_0'(B) = \frac{2B^{3/2}}{\pi} \left\{ 2(B_{max} - B)^{1/2} \sum_{k=2}^{k=n} (1-k) B^{k-2} A_k + \sum_{i=-s}^{i=0} (1-i) A_i I_i \right\} \quad (12)$$

where

$$I_i = \frac{(B_{max} - B)^{1/2}}{(1 - i)B_{max}^{1-i}B} + \frac{1 - 2i}{2 - 2i}\left(\frac{1}{B}\right)I_{i+1} \qquad i < 0$$

and

$$I_0 = \frac{(B_{max} - B)^{1/2}}{B\,B_{max}} + \frac{1}{B^{3/2}}\cos^{-1}\left(\frac{B}{B_{max}}\right)^{1/2}$$

For each value of B, $j(\cos \alpha_0)$ is equal to that value of $j'(B)$ for which

$$\cos \alpha_0 = (1 - B_0/B)^{1/2}$$

In using the above derived expressions, it is usually convenient to express B in units of B_0, the value of the magnetic field intensity in the equatorial plane.

ACKNOWLEDGMENTS

This work was supported by the National Aeronautics and Space Administration.

We are indebted to Dr. Robert Wentworth for discussions about his technique for determining pitch angle distributions. Dr. Wilmot Hess and Dr. John Killeen have kindly provided their calculated flux data and mirror point density curves for the neutron-albedo electron population mechanism. Adeline Cowen has spent many hours in data reduction and calculation.

REFERENCES

Arnoldy, R. L., R. A. Hoffman, and J. R. Winckler, Observations of the Van Allen radiation regions during August and September 1959, part 1, *J. Geophys. Research, 65*, 1361–1376, 1960.

Courant, R., *Differential and Integral Calculus*, Interscience Publishers, New York, p. 340, 1956.

Fan, C. Y., P. Meyer, and J. A. Simpson, The equatorial pitch angle distribution of electrons in the outer radiation belt, *IGY Satellite Rept. 14*, 15–21, 1961*a*.

Fan, C. Y., P. Meyer, and J. A. Simpson, Dynamics and structure of the outer radiation belt, *J. Geophys. Research, 66*, 2607–2640, 1961*b*.

Hess, W. N., and J. Killeen, Spatial distribution of electrons from neutron decay in the outer radiation belt, *J. Geophys. Research, 66*, 3671–3680, 1961.

Lenchek, A. M., S. F. Singer, and R. C. Wentworth, Geomagnetically trapped electrons from cosmic ray albedo neutrons, *J. Geophys. Research, 66*, 4027–4046, 1961.

Ray, E. C., On the theory of protons trapped in the earth's magnetic field, *J. Geophys. Research, 65*, 1125–1134, 1960.

Rosen, A., and T. A. Farley, Characteristics of the Van Allen radiation zones as measured by the scintillation counter on Explorer VI, *J. Geophys. Research, 66*, 2013–2028, 1961.

(Manuscript received March 22, 1962.)

Characteristics of the Van Allen Radiation Zones as Measured by the Scintillation Counter on Explorer VI[1]

BY ALAN ROSEN AND THOMAS A. FARLEY[2]

Space Technology Laboratories, Inc.

A scintillation counter responding principally to direct electrons has been flown on the Explorer VI earth satellite in an elliptical orbit extending to 48,600 km. The instrument measured fluxes of electrons above 200 kev and protons above 2 Mev. After a week of magnetically quite observations, a geomagnetic storm occurred, and an immediate increase in the counting rate of this instrument was detected; other radiation instruments showed a decrease in counting rate at this time. Gross fluctuations in particle intensity were observed at the edge of the outer zone of the Van Allen radiation belt during the storm, and these fluctuations are closely related to simultaneous geomagnetic activity. The increased particle intensity in the outer zone declined quite slowly after the storm until the next period of magnetic activity about two weeks later. This paper presents a detailed summary of the observations made by the scintillation counter during the period of data reception from the satellite.

Space Technology Laboratories, Inc., has constructed, calibrated, and flown a scintillation counter on the Explorer VI earth satellite. The object of the experiment was to make direct observations of electrons in both the inner and outer zones of the radiation belt with a detector insensitive to bremsstrahlung.

The Explorer VI satellite, constructed by Space Technology Laboratories, Inc., was launched at 14:23 GMT on August 7, 1959, into an elliptical orbit having an apogee 48,600 km from earth center and a perigee at 6,600 km (230 km altitude). The period of the satellite was 12 hours and 42 minutes, and the payload spun about its own axis at a rate of 2.8 cps. The orbit was inclined 38° with respect to the plane of the ecliptic. Perigee took place at about 9:30 AM local time at the approximate latitude of Florida, and apogee took place at approximately 9:00 PM local time in high southern latitudes. The satellite did not go into the earth's shadow in the 6-week period during which the analog transmitter broadcasting the scintillation counter data was operating.

The geomagnetic storm that is frequently referred to in this paper, and that produced such profound effects on the trapped radiation, began with a sudden commencement at 0404 GMT on August 16, 1959. The initial phase lasted approximately 2 hours. The main phase decrease in horizontal intensity began at about 0600 GMT, and the storm main phase ended late on August 17, and was designated moderately severe at most ground station observatories.

INSTRUMENTATION

The detector used in this experiment consisted of a cylindrical plastic scintillator,

[1] Published in the July 1961 issue of *Journal of Geophysical Research*. Reprinted by permission.

[2] Present address: Inst. of Geophysics and Planetary Physics, U. of Calif. at Los Angeles.

765-698 O-65—19

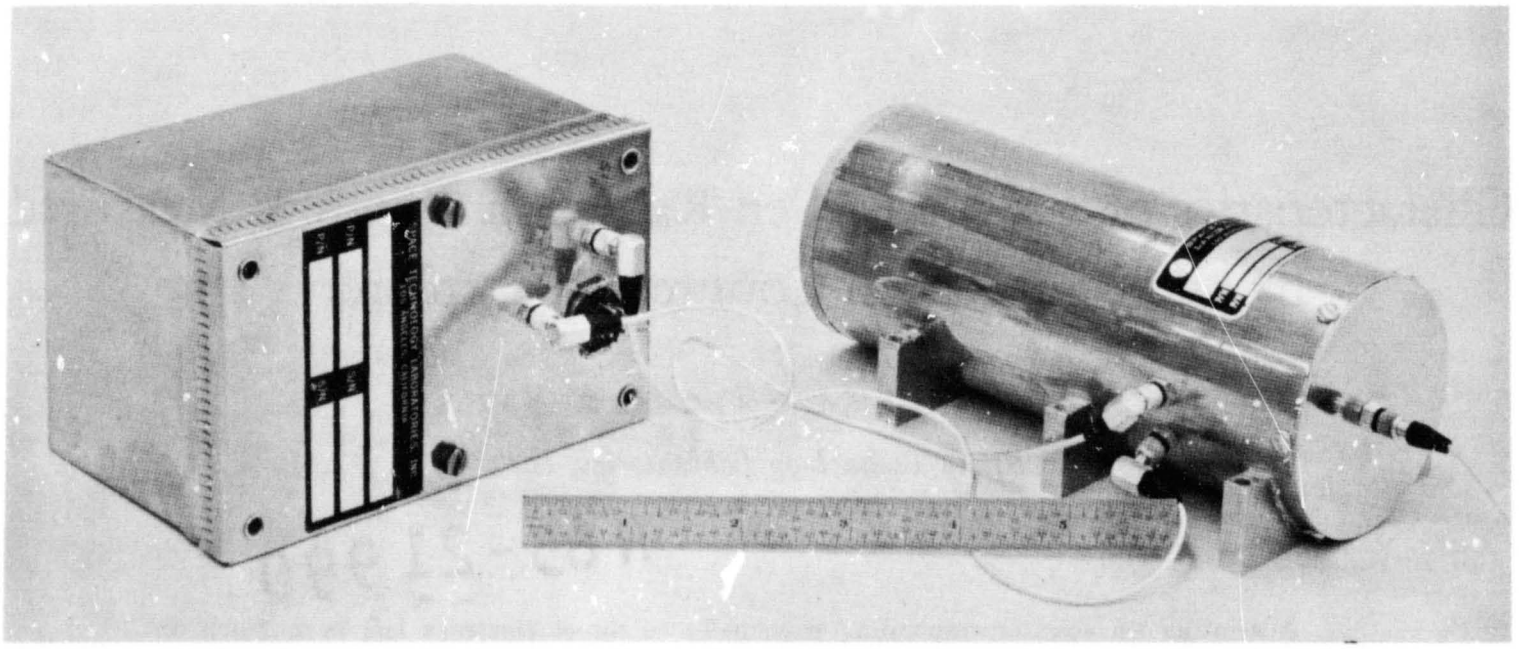

FIGURE 1.—*Photograph of flight instrument showing photomultiplier housing and associated circuitry.*

approximately 1 inch in diameter and ¼ inch thick, cemented to a Dumont 6467 photomultiplier tube. Figure 1 shows a photograph of the photomultiplier tube package and associated circuitry. The output pulses of the photomultiplier were amplified and fed into a binary register having a capacity of 2^{20} pulses. Voltages representing the state (on or off) of the ninth, fourteenth, and twentieth binaries were added and used to modulate a subcarrier oscillator, so that transitions between the states of these binaries could be used to determine the counting rate. The output of the 2^{20} binary was also fed into a digital register whose contents were broadcast in digital form by a second transmitter.

The detector was covered with a foil having a thickness of 3.3 mg/cm². An electronic bias was used in order to count only particles losing 100 kev or more of energy in the scintillator; this bias was adjusted by using the 624 kev electron conversion peak of Cs^{137} as an energy standard. This instrument, mounted inside the shell of the satellite, responded to radiation penetrating a 3.3 mg/cm² foil-covered window, and to more energetic particles passing through the payload shell. The minimum energy detectable, determined by the foil thickness, the permitted angle of penetration of the foils, and the electronic bias of 100 kev, was 200 kev for electrons and 2 Mev for protons.

The omnidirectional geometrical factor[2] of this instrument for the direct observation of electrons and protons was estimated from geometrical considerations to be approximately 2×10^{-4} cm² for 200–500 kev electrons and 2–10 Mev protons. Five hundred kev electrons and 10 Mev protons could just penetrate the shell and be detected, and at these energies the omnidirectional geometrical factor was estimated to be 4×10^{-2} cm². The geometrical factor rose slowly to a maximum value of 3.5 cm² for very penetrating particles.

The saturation characteristic of the entire detector system, including flight power supply and all flight electronics, was determined before the satellite was launched by tests made on the actual flight instrument. The results of this test are shown in figure 2. A 1 millicurie source of Sr^{90} was used for this test, and the incident intensity was increased by decreasing the source to detector distance. The observed count rate continued to rise slowly, even for very high incident intensities, because the

[2] The omnidirectional geometrical factor G, which depends on the counter surface area and the solid angle through which radiation can reach the counter, is defined by $\epsilon G = R/J$. R is the corrected counting rate of the detector and J. the omnidirectional intensity of isotropic radiation, is the flux per unit time of particles from all directions through a sphere of unit cross-sectional area (J is measured in cm^{-2} sec^{-1}). ϵ, the detection efficiency for the radiation in question, is assumed to be 100 percent for electrons and protons.

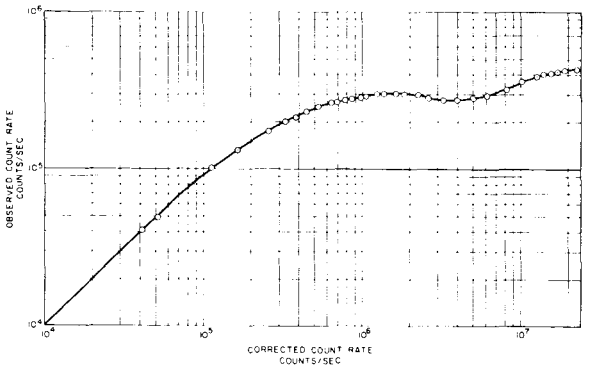

FIGURE 2.—*Observed count rate of the flight instrument as a function of incident intensity of Sr^{90} source. The data points were obtained before flight in a laboratory measurement on the actual detector, power supply, and electronics that were used in the satellite. This curve has been used to correct the count rate for saturation effects.*

potential across the later dynode resistors of the photomultiplier dropped, the output pulse height and width decreased, and a higher count rate could be handled by the succeeding electronic circuitry.

The scintillation counter was relatively insensitive to bremsstrahlung, and the counting rate of this instrument due to electrons of a given energy must considerably exceed the count rate due to bremsstrahlung from electrons at the same incident energy. The only photon interaction of importance in a plastic scintillator is the Compton interaction, and because of the electronic bias of 100 kev, the theoretical threshold for photon detection was about 220 kev. Electrons having energies below the threshold could not produce bremsstrahlung that would be registered by the detector. Because a plastic scintillator has a low efficiency for detection of photons above 220 kev, and because electrons having energies of several hundred kev have a small probability of producing 220 kev photons, the instrument responded principally to direct electrons at all energies.

The calculated estimates of the efficiency and geometrical factor for bremsstrahlung detection were confirmed by measurements after Explorer VI was launched on a similar instrument with the same bias level. An entire payload, identical to Explorer VI, was subjected to an electron bombardment at the High Voltage Engineering Corporation in order to measure the response of the various radiation instruments to electrons at 1 Mev, and to bremsstrahlung from monoenergetic electrons at 500, 350, and 250 kev. At 1 Mev the electrons were permitted to strike the payload directly, whereas at 500, 350, and 250 kev the electron beam was absorbed in an aluminum plate placed near the payload allowing only bremsstrahlung to reach the satellite. The bombardment was made from a variety of directions, and the response was integrated over the surface of the payload to measure the product ϵG for each of these energies. These measurements represent the bremsstrahlung efficiency even at 1 Mev, for the scintillation counter was never directly in the rather narrow electron beam. These results are shown in figure 3 together with the estimated geometrical factors for direct detection of electrons. The total response of the detector for measurement of electron flux is the sum of these two curves, and is also shown in the figure. It is this total response curve that must be used to interpret the counting rate of the instrument in orbit.

While bremsstrahlung from electrons below about 220 kev could not in theory produce counts in the detector, sufficiently high intensities of low-energy photons could cause pulse pile-up above the threshold of the scintillation counter. The spare Explorer VI payload was bombarded with low-energy electrons from an electron gun at the University of Minnesota, and the duplicate scintillation experiment count rate was observed. The omnidirectional electron fluxes required to produce the count rates observed in the outer zone on a quiet, prestorm day were calculated from these measurements, and were as follows: at 40 kev, 2×10^{12} electrons/cm^2 sec; at 60 kev, 6×10^{11} electrons/cm^2 sec; at 85 kev, 3×10^{11} electrons/cm^2 sec. The fluxes would have to be more than an order of magnitude higher to produce the counting rate observed after the geomagnetic storm. Because the required fluxes are so large, it is unlikely that pulse pile-up due to bremsstrahlung from low-energy electrons contributed more

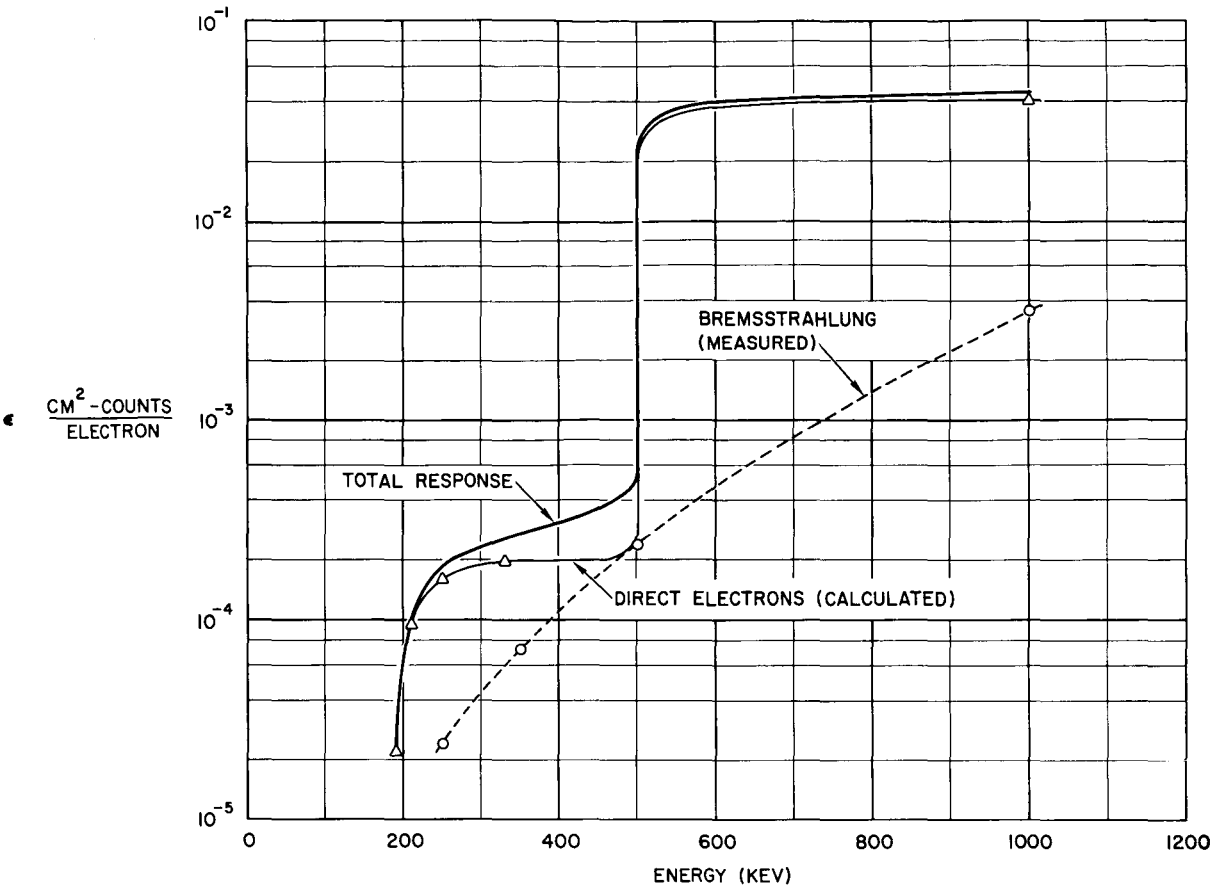

FIGURE 3.—*A representation of the over-all efficiency of the scintillation counter for the detection of electrons, both directly and by means of bremsstrahlung from the electrons.*

than a minor fraction of the count rate in the outer zone.

Two examples of the data as reduced from the telemetry records, one taken before and one taken after the great increase in count rate during the geomagnetic storm beginning August 16, 1959, are shown in figures 4 and 5. The corresponding trajectories are shown in figure 6, together with the trajectories of other traversals of the radiation belts discussed in this work. The trajectories are plotted in a geomagnetic coordinate system based on an earth-centered magnetic dipole axis intersecting the earth's surface at 78.5° N latitude and 291° E longitude.

The high observed count rates plotted in figures 4 and 5 clearly indicate that the true radiation intensity saturated the instrument at the peak of the outer Van Allen zone. Furthermore, the observed count rates were considerably higher than those obtained with very high intensities of Sr^{90} in the laboratory with the flight instrument.

Figure 5 illustrates a condition common to all traversals of the high intensity radiation regions after August 18: there are maxima at approximately 620,000 to 640,000 counts per second on both sides of the region of highest intensity. These "shoulders" have been identified as the characteristic maximum in the saturation curve shown in figure 2. Since these maxima always appear at just double the 310,000 counts per second maximum in the saturation curve, the very high count rates have been attributed to a binary failure that resulted in a doubling of all observed count rates. This conclusion is supported by a count rate outside the radiation zones that consistently indicated an interplanetary cosmic-ray flux of approxi-

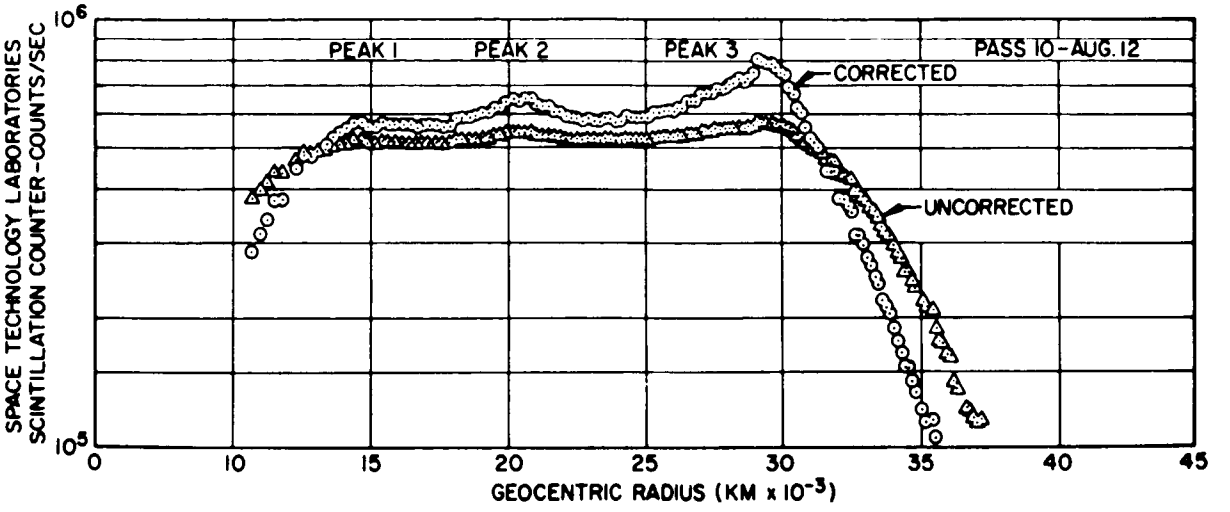

FIGURE 4.—*Typical observed and corrected count rate curves in the outer Van Allen zone before the geomagnetic storm of August 16, 1959.*

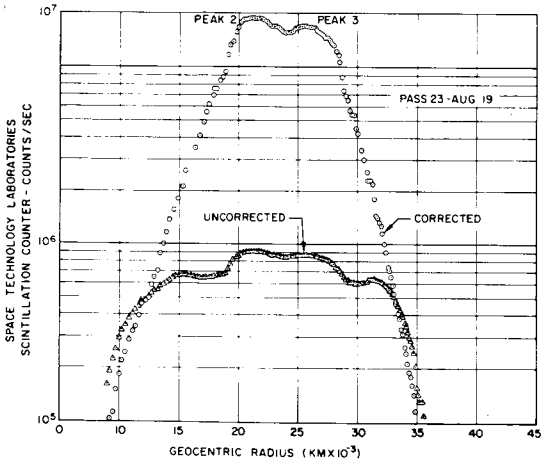

FIGURE 5.—*Typical observed and corrected count rate curve in the outer Van Allen zone after the geomagnetic storm of August 16, 1959.*

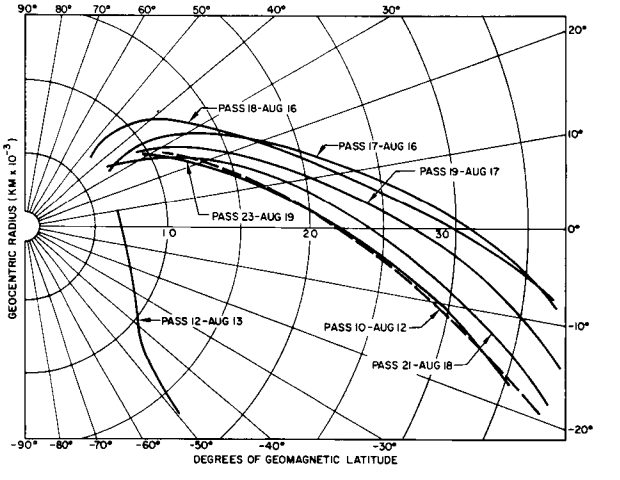

FIGURE 6.—*Radial distance and geomagnetic latitude for the trajectory portions used in this paper.*

mately twice the value observed by the other experiments on this vehicle. Approximate true intensity curves have been constructed, therefore, by halving the observed count rate, and by reading the true intensity from the saturation curve. The corrected count rates, calculated as described here, are also shown in figures 4 and 5. All other particle intensities referred to or illustrated in this work have been corrected in this way. An analysis of the possible errors and uncertainties which may be introduced by this correction procedure has been placed after the data presented in the next section.

DATA

The data from this experiment show systematic differences from that obtained by the bremsstrahlung detectors on the same satellite, and these differences must be due to the different energies to which the scintillation counter responds. The data are presented here in a way that facilitates comparison with the other instruments on this vehicle.

Pass 10 in figure 4 has three identifiable peaks labeled 1, 2, and 3. This pass is representative of data taken between August 8 and 16,

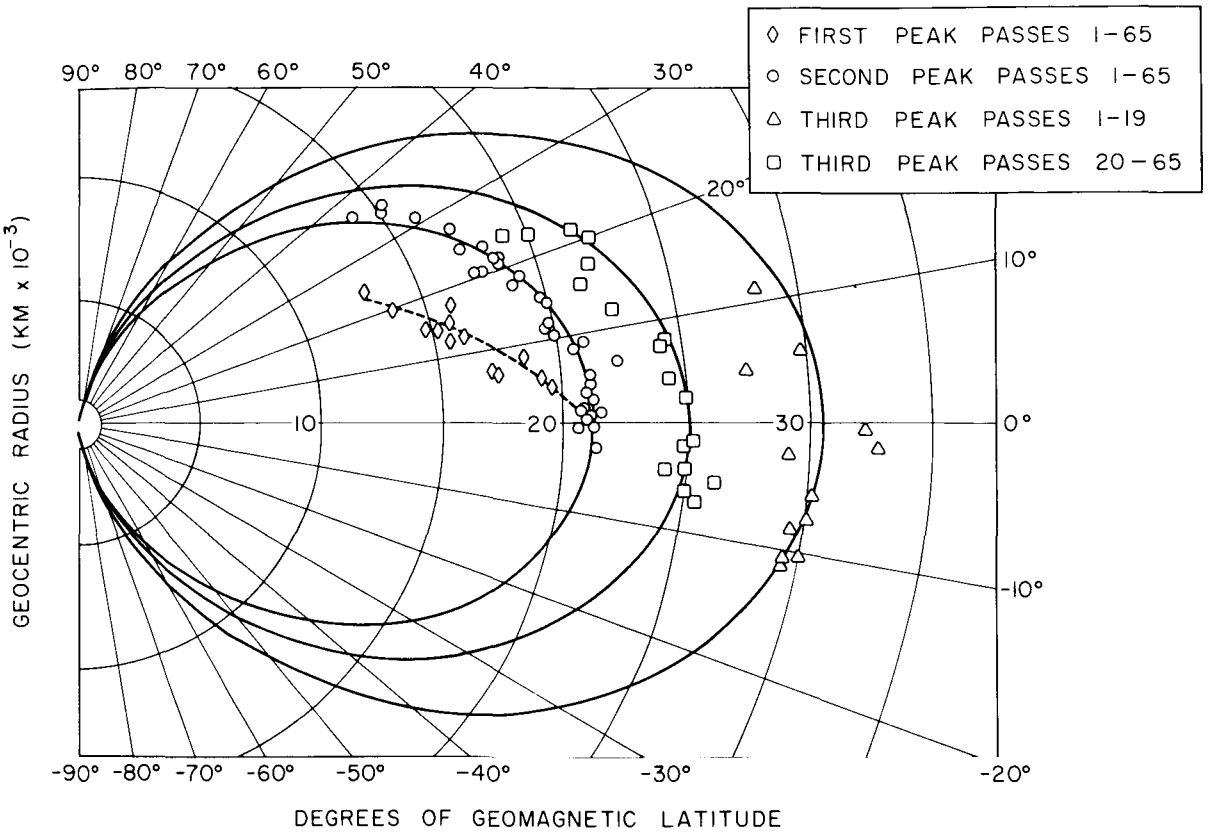

FIGURE 7.—*Positions of the three peaks seen by the scintillation counter. The solid lines are magnetic dipole lines of force. The dotted line connects the points representing peak 1 that are not distributed along a line of force.*

although peak 1 is never outstanding and is sometimes missing. None of these peaks are to be identified with the high energy proton "inner belt," since the counting rates are much too high, and the satellite passes too far north on the outward traversal to see these protons, according to *Fan, Meyer, and Simpson* [1960]. Pass 23 in figure 5 illustrates the type of data obtained from August 18 to September 3. Peak 1 is never seen, and on the most northerly passes only one peak is observed.

The position of these peaks, both before and after the magnetic storm, are plotted in figure 7 in the above-described geomagnetic coordinate system. This figure includes the magnetic lines of force along which peaks 2 and 3 are found. It also shows the large change in position of peak 3 after the occurrence of the geomagnetic storm, and the apparent merger of peak 3 with peak 2 at high latitudes after the storm.

The position of peak 2 appears to be essentially independent of the geophysical events that took place during the lifetime of the satellite. The points representing peak 1, unlike the other peaks, do not fall along a line of force.

An indication of the substantial day-to-day variation in the outer Van Allen zone may be obtained from the data plotted in figure 8. This figure shows the count rate at 10° south geomagnetic latitude using data taken from each pass when the satellite was within 1° of this latitude.

Figures 9, 10, and 11 show comparisons between simultaneous measurements made by the STL scintillation counter, the University of Minnesota Geiger counter and ion chamber [*Arnoldy, Hoffman, and Winckler*, 1960]; and the University of Chicago proportional counter [*Fan, Meyer, and Simpson*, 1960]. Figure 9

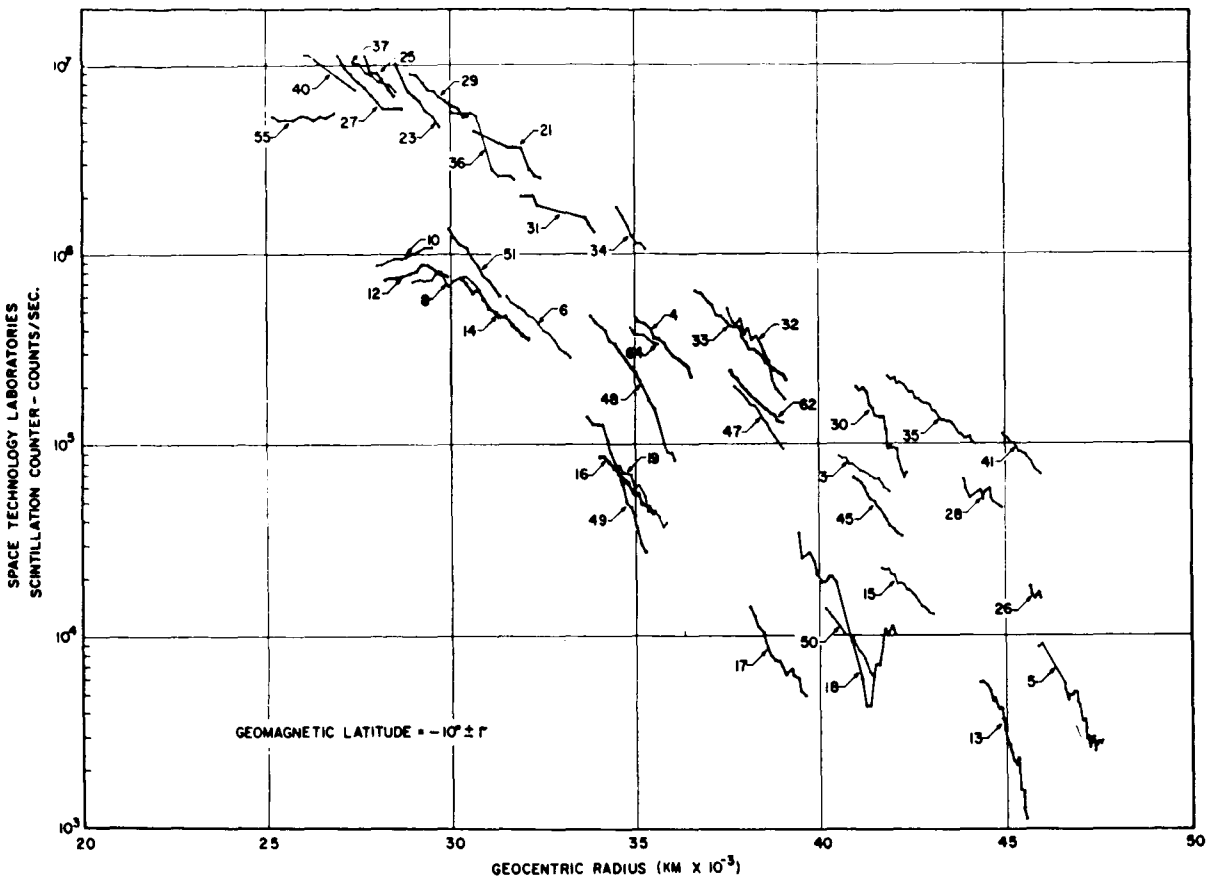

FIGURE 8.—*Count rates from different passes at various radial distances, always within ±1° of 10° south geomagnetic latitude. The count rate shows a radial dependence of approximately* r^{-15}

shows data taken on August 16 immediately before the geomagnetic storm. Figure 10 shows the remarkable changes that had occurred by August 17: the scintillation counter peak intensity has increased while the instruments sensitive to bremsstrahlung show a decrease.

After passing through apogee at approximately 48,000 km from earth center, the satellite spent several hours at high southern latitudes outside the radiation zones, and then re-entered the outer belt at fairly low altitude, passing rapidly through a region of depressed intensity and the inner zone containing the high-energy protons. Figure 11 shows typical scintillation counter results during this period and compares them with simultaneous measurements made by the proportional counter of the University of Chicago. There was never more than one peak in the scintillation counter results while passing through the outer zone at these distances.

The systematic discrepancies in the position and behavior of the peak intensities between the scintillation counter and the instruments sensitive to bremsstrahlung raise important questions concerning the type and energy of the particles to which each instrument is responding. These questions will be considered more fully in the next section.

Figure 12 shows the results of three day-by-day passes beginning immediately before the geomagnetic storm of August 16 and continuing through pass 21 on August 18 when the increase due to the storm was over. The initial increase seems to be mostly in peak number 2, with the increase and change in position of peak 3 occurring between passes 19 and 21. Although the trajectory of the satellite was not

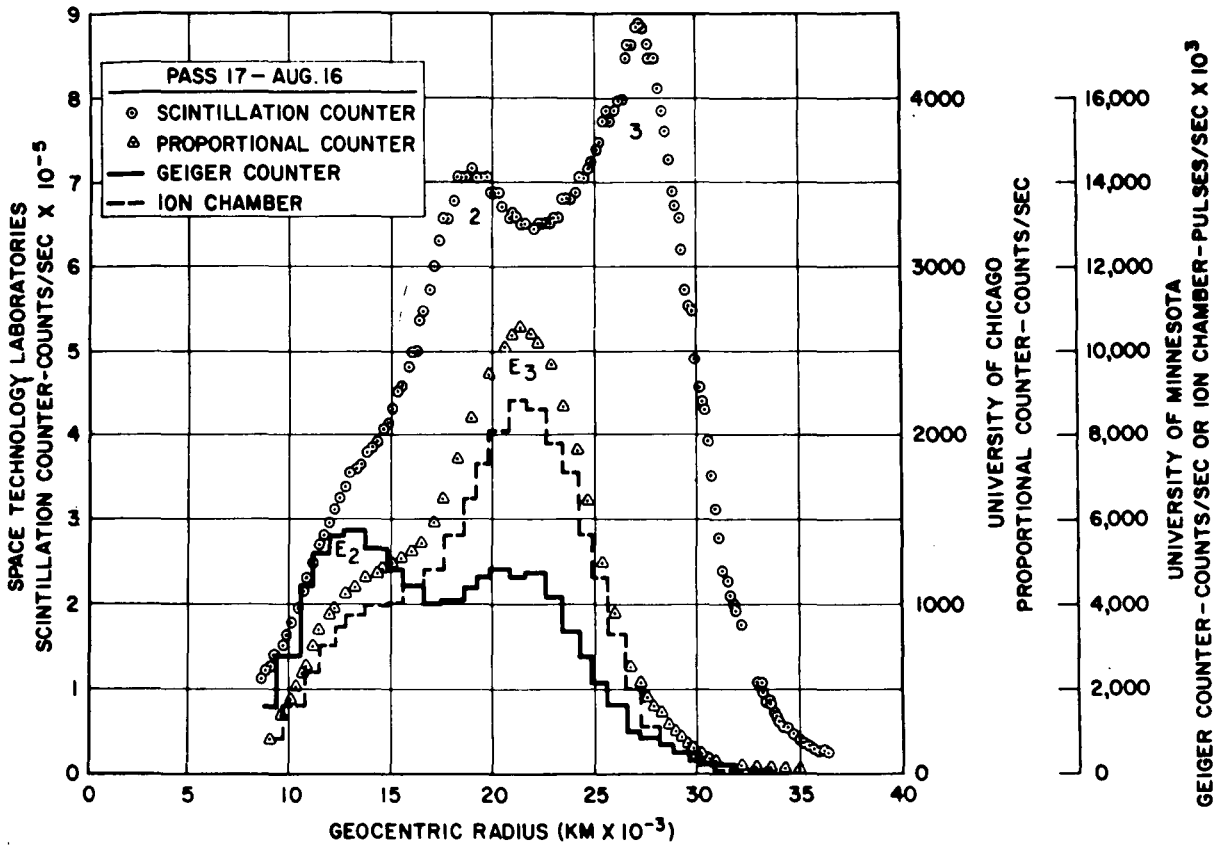

FIGURE 9.—*Results from the four radiation detectors aboard the Explorer VI satellite immediately before a geomagnetic storm.*

identical for these four passes (see fig. 6), the increase certainly cannot be attributed to a change in the trajectory, for even on pass 18 the intensity rose to a higher value than any seen between August 8 and August 16. There is, therefore, no decrease in the peak intensity of either peak in the outer Van Allen zone of particles to which the scintillation counter responded. Figure 8, however, shows that the intensity far out in the outer zone did show a tendency to decrease during the early stages of the storm on passes 18 and 19.

Figure 13 shows the maximum peak intensity in the outer zone for essentially all the available passes. Sometimes the maximum intensity is at peak 2 and sometimes it is at peak 3, although the difference in peak heights is always small. While the uncertainties in the reconstruction of the intensity curves and the uncertainty in the estimate of the efficiencies for particles of various energies do not permit accurate measurements of the particle flux, the relative day-to-day changes are probably quite well represented in figure 13. For example, the alternate increase and decrease in peak intensity starting with pass 20 was at least partly the result of traversals alternately at high and low geomagnetic latitudes. Since the period of the satellite was just slightly greater than 12 hours, consecutive passes differ in geographic longitude by approximately 180°. Therefore, the magnetic dipole axis was alternately tipped toward the satellite (high geomagnetic latitude pass) and away from the satellite (low latitude pass). A few days later, because the satellite period was incommensurate with the earth's period, the magnetic axis was tipped to the side on each traversal, and both passes were at intermediate geomagnetic latitudes. The low latitude passes produced the high count rates, and the high latitude passes,

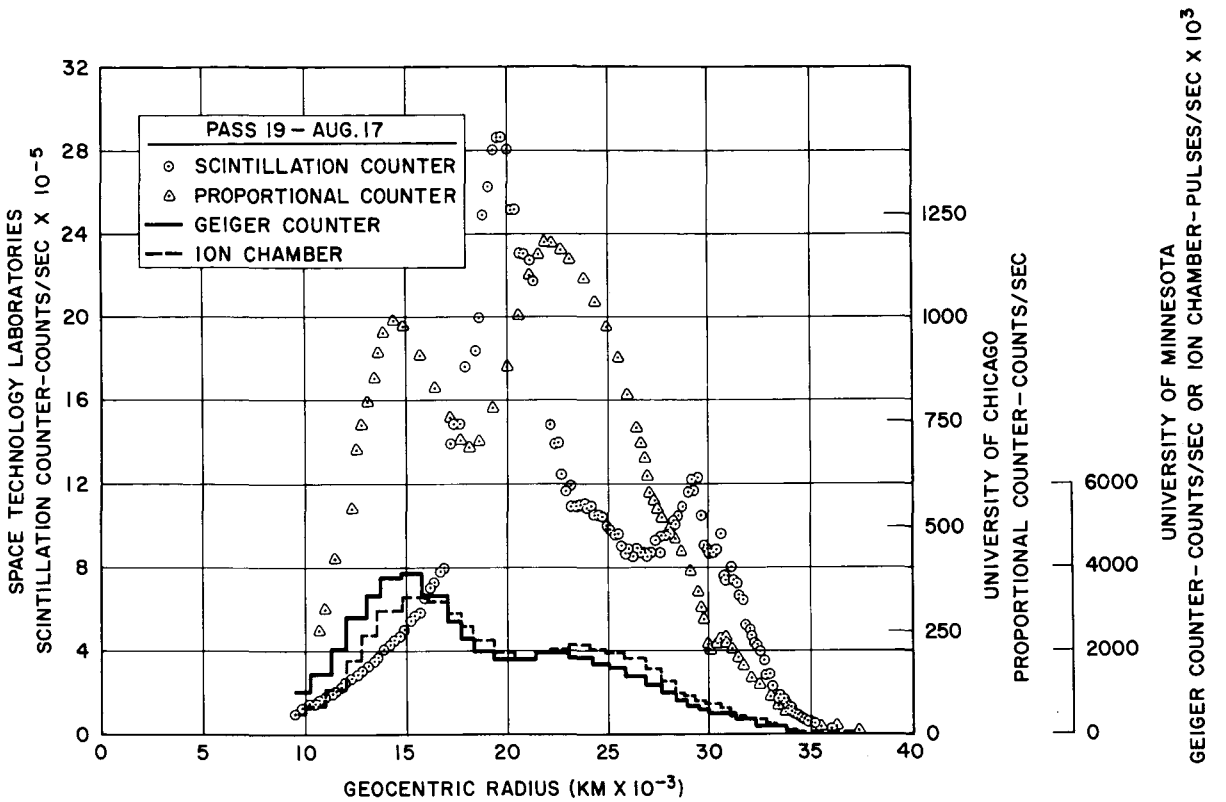

FIGURE 10.—*Results from the four detectors approximately 20 hours after a geomagnetic storm sudden commencement. Note the contraction of the scintillation counter scale, and the expansion of the other scales from those used in figure 9.*

the low ones. The appearance of such expected effects supports the validity of the reconstruction of the peak intensities from the saturation curve.

At radial distances of about 7 earth radii, the trapped radiation intensity decreased to a low value, presumably the interplanetary cosmic-ray flux. The decrease in intensity was quite rapid, varying approximately as the inverse fifteenth power of the radial distance at constant latitude, as shown in figure 8. On several occasions during periods of magnetic activity observed at surface observatories, large fluctuations indicative of very disturbed conditions in the radiation field have been seen at the outer edge of the outer Van Allen zone. The three best examples of these fluctuations are shown in figures 14, 15, and 16, together with some simultaneous data from the University of Minnesota Geiger counter in figures 14 and 15. The data shown in figures 14 and 15 were taken during the main phase of the August 16 geomagnetic storm. The data in figure 16 were taken during a period of irregular magnetic activity that lasted from September 2 to September 4.

The authors have shown in a separate work [*Farley and Rosen*, 1960] that the scintillation experiment count rate is negatively correlated with the magnetic field for at least a 20 minute period during these fluctuations. The magnetic field was measured by the Space Technology Laboratories' magnetometer [*Sonett, Smith, and Sims*, 1960; *Smith, Coleman, Judge, and Kelso*, 1960] carried on the vehicle. The correlation is probably typical of all the fluctuations shown in these figures, in sharp contrast to the quiet-day positive correlations found between these same two instruments by Judge and Coleman

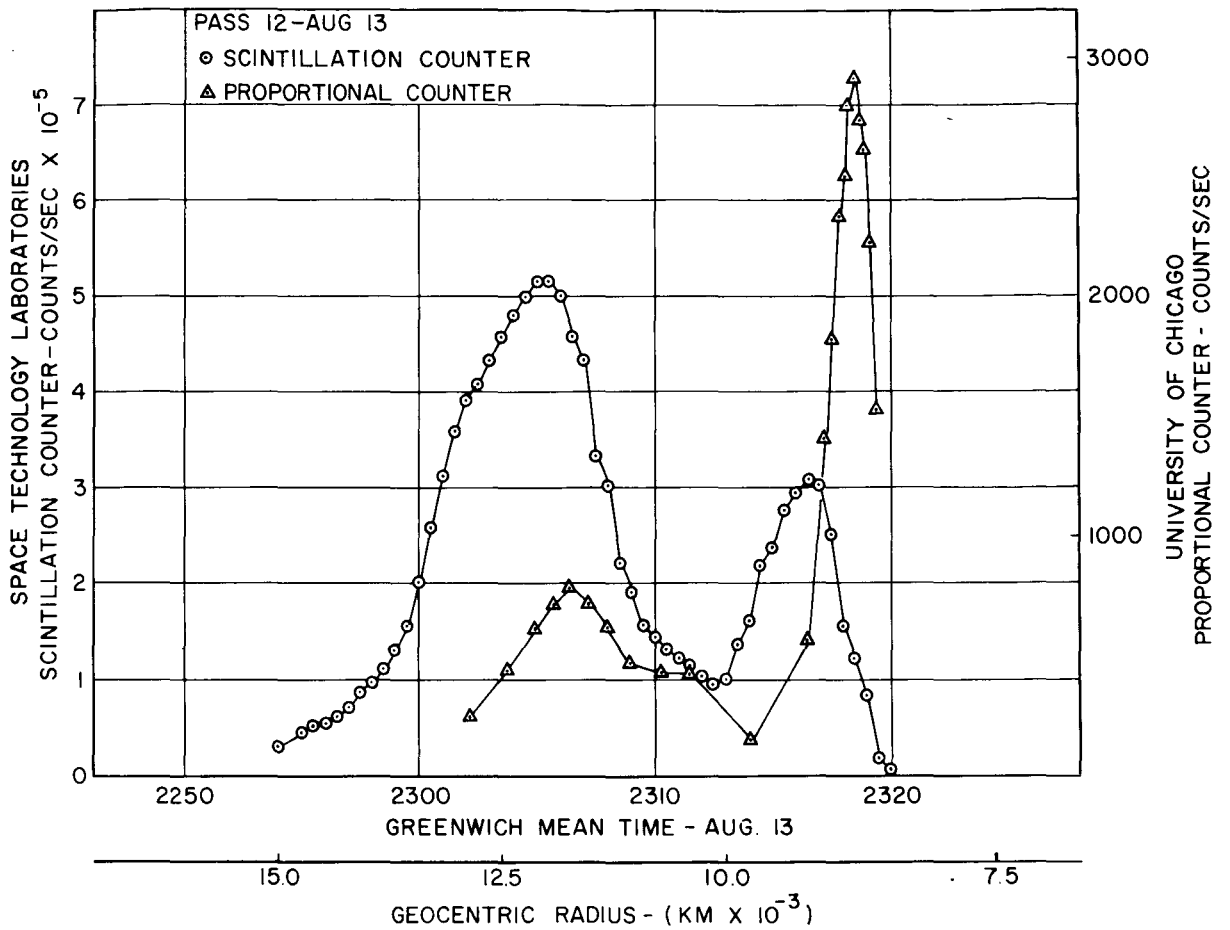

FIGURE 11.—*A typical traversal of the outer and inner Van Allen zones while the satellite approaches perigee, comparing the scintillation counter and proportional counter results.*

(private communication), which they have identified as a betatron-type acceleration of trapped particles.

A continuing investigation is being carried out to see what connection these fluctuations may have between distant and ground station magnetic disturbances, and what relation they may have to hydromagnetic waves propagating in the geomagnetic field.

The count rate outside the radiation belt at high southern latitudes varied from about 5.5 to 10 counts/sec (corrected) from day to day, although it often seemed quite steady over several hours' time. This count rate corresponded to an omnidirectional flux of 1.6 to 2.9 particles/cm^2 sec if it was caused by particles having sufficient energy to penetrate to the scintillator from all directions. During the period of the geomagnetic storm this count rate rose to 50 counts/sec and more, probably owing to low-energy particles in this region as a result of the storm.

It is now appropriate to consider to what extent these results, differing markedly in some respects from those of the bremsstrahlung instruments, have been affected by the saturation and binary failure corrections applied to the STL data. Perhaps the most noticeable difference in this experiment was the appearance of three peaks, none of which was located at the positions of peaks observed by the other experiments. We offer the following arguments that

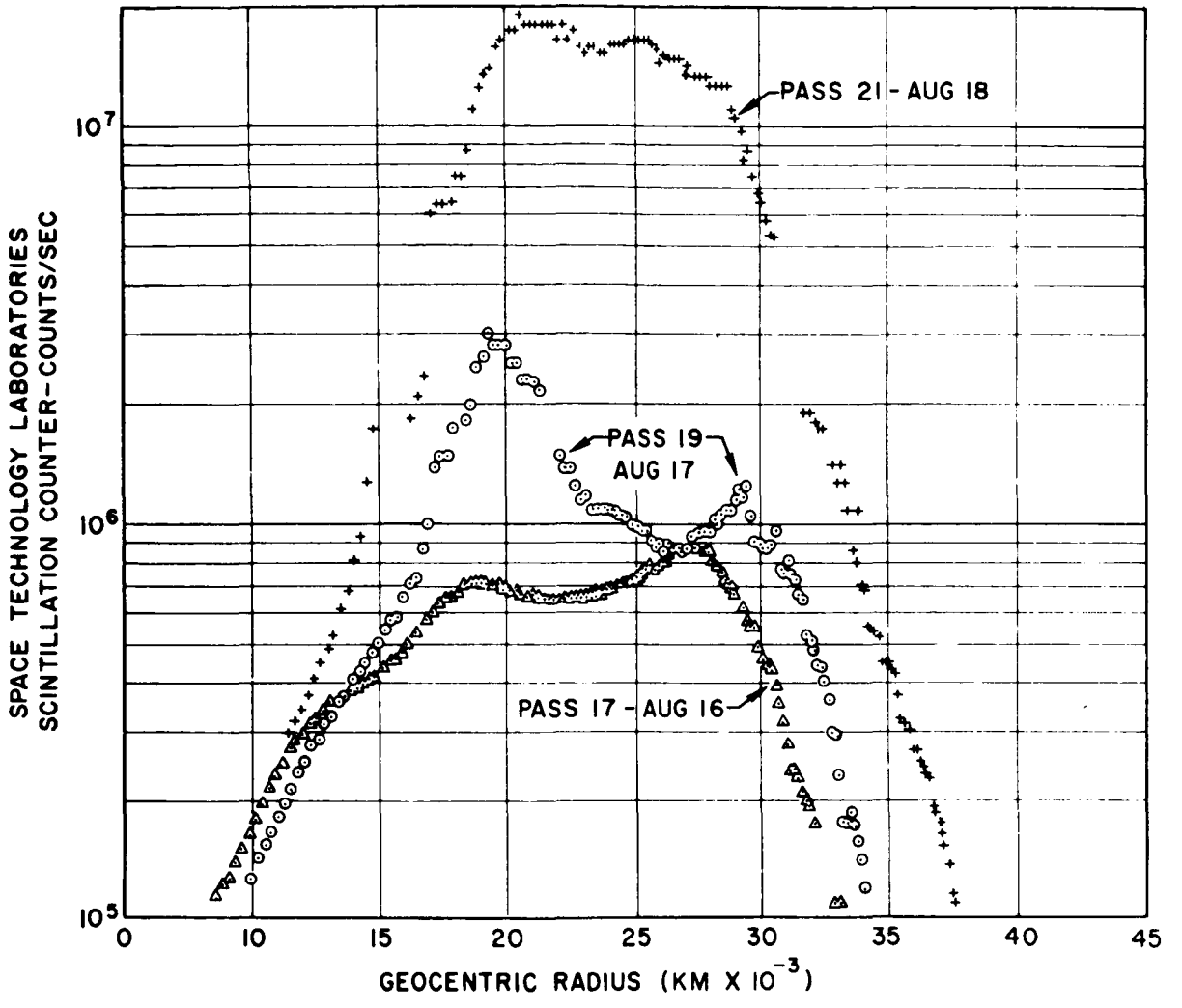

FIGURE 12.—*Three traversals of the outer Van Allen zone at approximately 24-hour intervals during a geomagnetic storm, showing a continuous increase in count rate.*

the peaks indicated by the scintillation counter are real and are located correctly:

1. The peaks indicated by the scintillation counter show a systematic distribution in space, and have a time behavior that can be related to that of the bremsstrahlung detector peaks. The observation of a peak depends on the ability to tell when the true incident intensity stops increasing and starts decreasing. A false indication of a change from increasing to decreasing intensity might be given by a maximum in the saturation curve, or by a failing binary starting to function normally. Both of these effects would produce a false peak appearing at a given count rate, or perhaps appearing randomly for a binary failure not related to the count rate. But this certainly does not occur. Peak 2, for example, falls along the same line of force (fig. 7) after the storm of August 16 as it did before, even though the observed counting rates are quite different. Peak 3 does change position after the storm, but it moves inward about 5000 km in a way quite similar to the outermost peak of the bremsstrahlung counters, and certainly is not found at the same observed counting rates. In short, the peaks observed by this detector

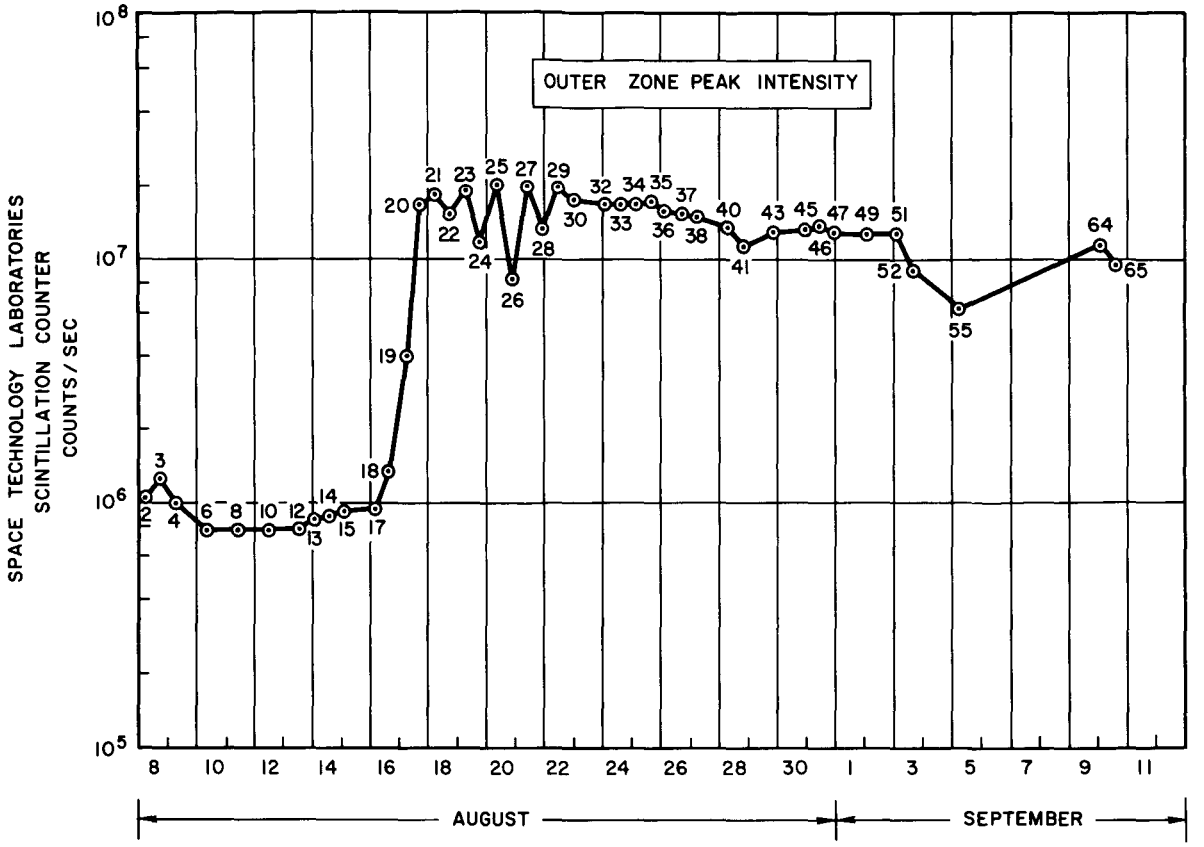

FIGURE 13.—*Approximate maximum count rate of the scintillation counter for all passes on which data are available.*

and described as real in this paper are not systematically correlated with the observed count rate, nor are they randomly sprinkled over the outer radiation zone.

2. A careful examination of the data in figure 10 at the position of the outermost scintillation counter peak reveals significant changes in the slope of the proportional counter count rate which indicates that the proportional counter responds in some degree to the particles in peak 3. Although peak 3 is not seen in this position thereafter (because of the storm increase), there are significant slope changes in both the scintillation counter and proportional counter count rates at this position in space on subsequent passes. Such correlations could hardly be expected if peak 3 of the scintillation counter were a spurious peak due to saturation or binary failure effects.

3. There is evidence for total failure of the binary involved. If the observed count rates on a quiet day outside the radiation belt are accepted without correction, this results in an interplanetary flux of approximately twice the value of 1.8 particles/cm^2 sec reported by *Fan, Meyer, and Simpson* [1960]. There is evidence, therefore, of a factor of 2 error both at 11 counts per second and at 640,000 counts per second, indicating that the binary failure is total and not count rate dependent.

Besides the establishment of the peaks and their locations, the authors have made flux estimates that are affected by the saturation and binary failure corrections. Before the storm, a typical correction at peak 3 is a factor of 2

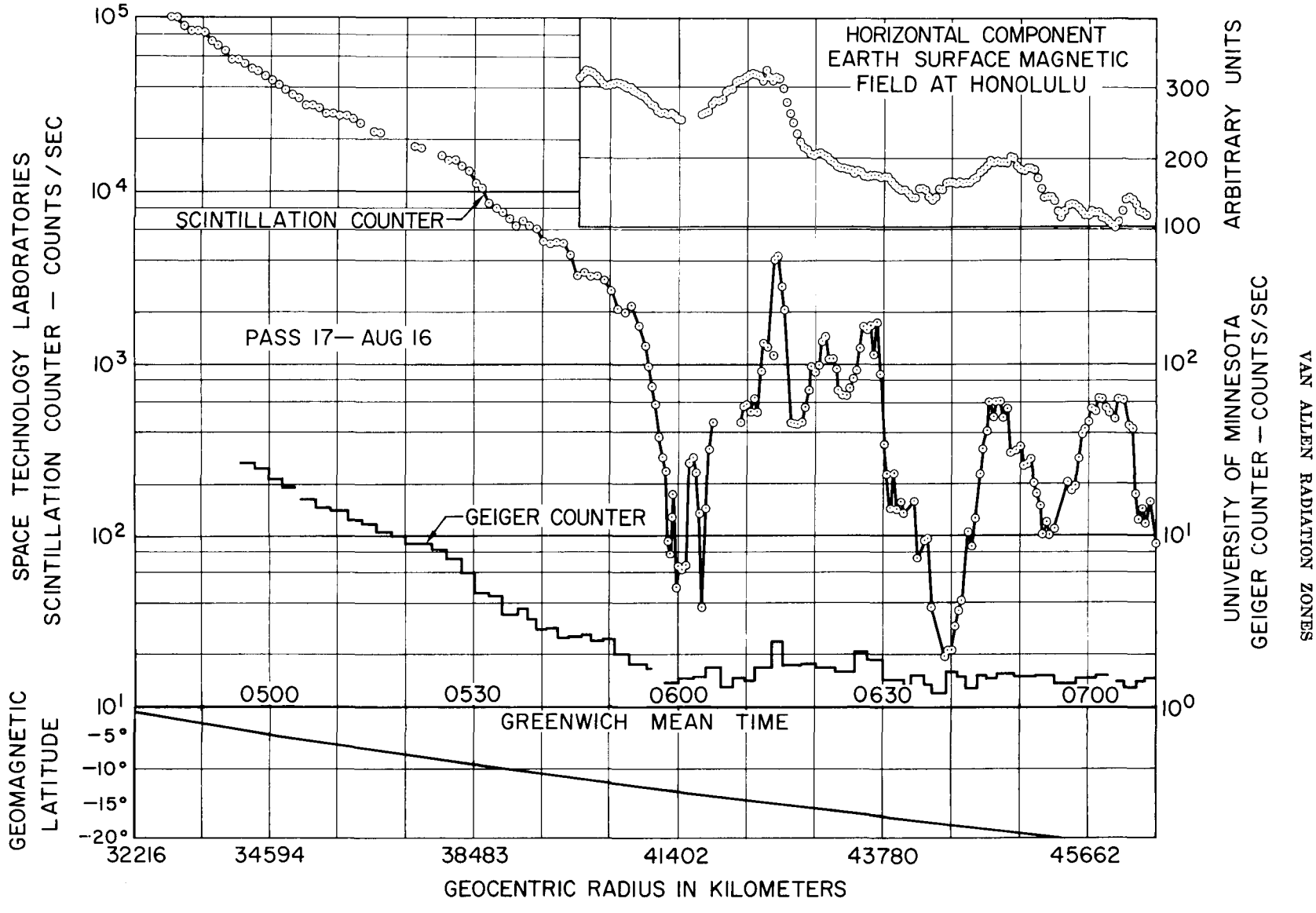

FIGURE 14.—*Gross fluctuations observed at the edge of the outer Van Allen zone, commencing approximately at the start of the main phase of a geomagnetic storm.*

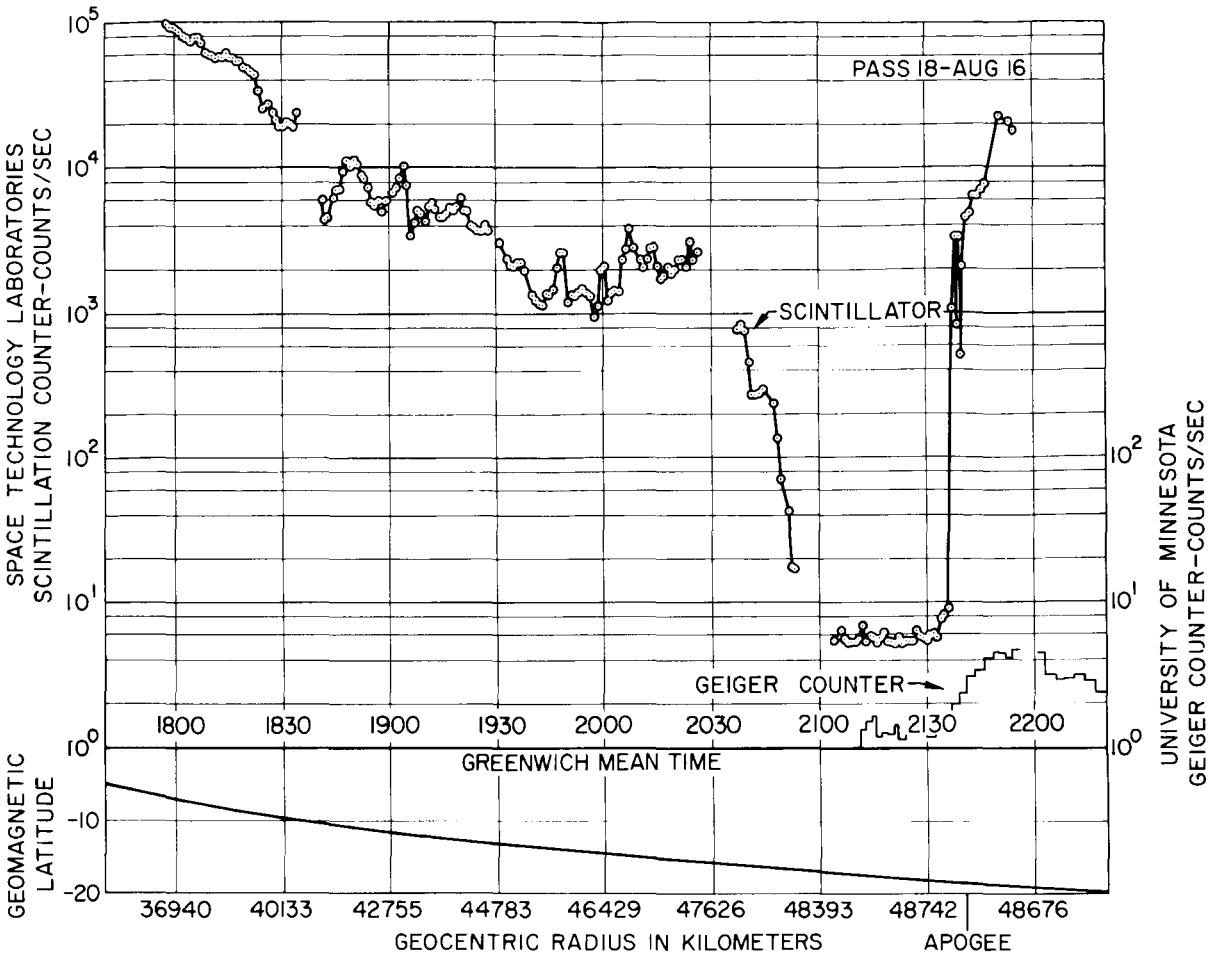

FIGURE 15.—*Gross fluctuations are still present some 12 hours after the sudden commencement.*

decrease for binary failure, and a factor of 3 increase for saturation. After the storm the correction is a factor of 2 decrease for binary failure and about a factor of 40 increase for saturation. As a result of these large corrections, as well as of some uncertainties in the geometrical factors, the authors claim only an order of magnitude accuracy for their flux estimates, although they may be somewhat better than this before the storm. It is important to point out that if the fluxes of electrons above 200 kev were not of the order estimated in this paper the scintillation counter simply would not have saturated.

DISCUSSION

A comparison of the results of this experiment with the results of the other radiation experiments on the same satellite gives important information on the type and energy of the particles in the outer Van Allen zone. There are several remarkable differences in spatial distribution and behavior during the magnetic storm that indicate that the scintillation counter is at times responding to particles other than those to which the proportional and Geiger counters are sensitive.

These differences can probably be explained by the different sensitivities of the instruments to electrons of varying energies. The scintillation counter, unlike the bremsstrahlung instruments has a rather sharp low-energy cutoff at 200 kev for electrons, and except when the electron spectrum is quite steep between 200 and 500 kev, it responds principally to electrons above 500 kev. The scintillation counter

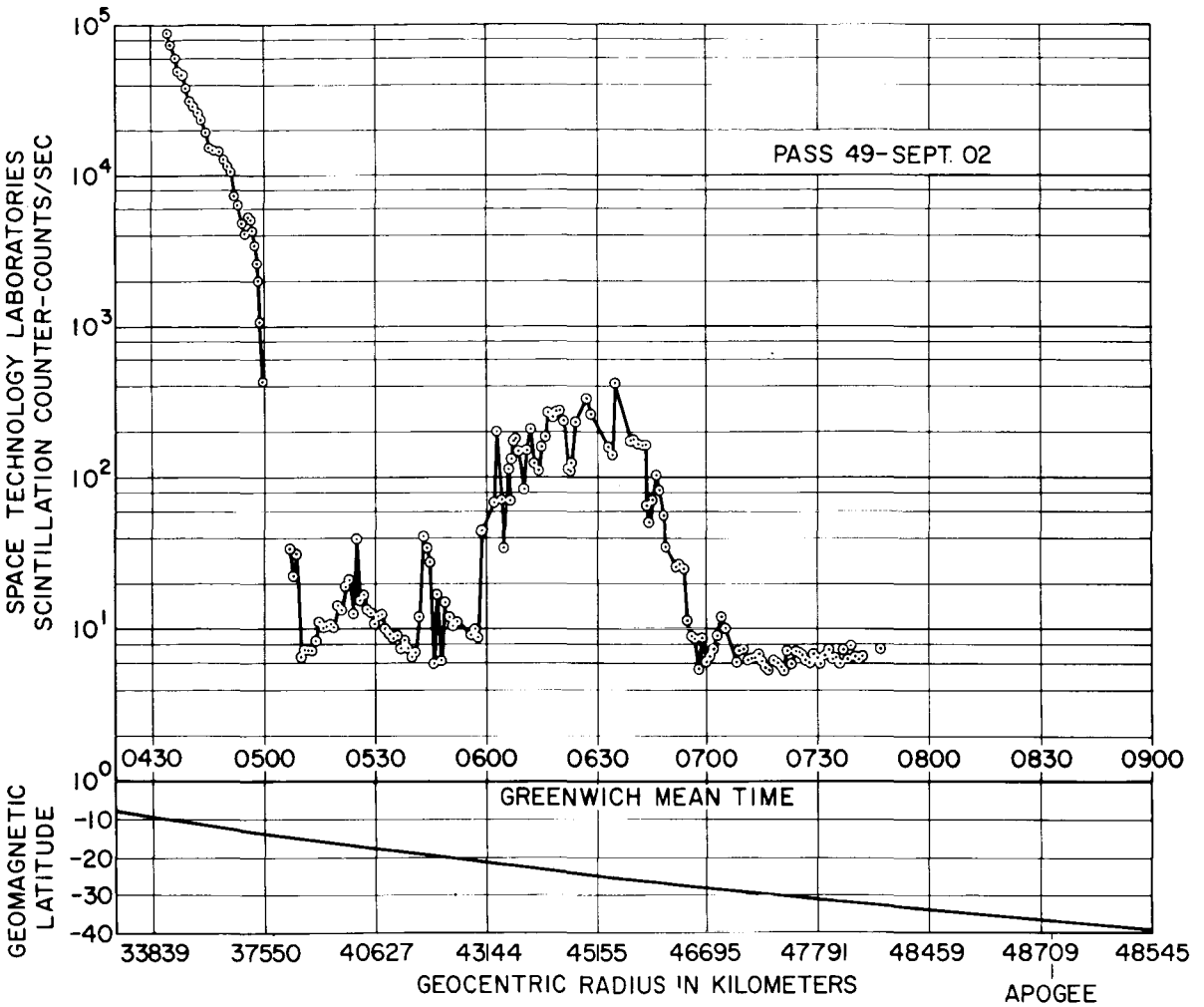

FIGURE 16.—*Particle fluctuations during a period of irregular magnetic activity on September 2, 1959.*

also has a proton sensitivity that extends to considerably lower energies (2 Mev) than the other radiation detectors. The differences between the results of the scintillation counter and the bremsstrahlung instruments have been discussed below with the assumption that they are caused by the different sensitivity of the scintillation counter.

The spatial distribution differences are obvious from figures 9 and 10. The scintillation counter peaks 2 and 3 are not readily identifiable as the electron peaks E_2 and E_3 [*Fan, Meyer and Simpson*, 1960]. The correlations between peak 3 and the slope changes in the proportional counter on pass 19 mentioned in the last section indicate that the proportional counter was responding inefficiently to particles observed by the scintillation counter, and that this response is superimposed on a considerably greater count rate due to other particles. The counts registered by the proportional counter telescope in the outer Van Allen zone have been identified unambiguously as bremsstrahlung from electrons because of the absence of triple counts [*Fan, Meyer, and Simpson*, 1960]. Since this counter was shielded with 5 g/cm^2 of lead, it was least sensitive to bremsstrahlung from low-energy electrons, and it seems most reasonable to identify peak 3 of the scintillation counter as electrons having energies significantly below those that caused most of the proportional counter response. We conclude, therefore, that

there were large fluxes of electrons above 200 kev in peak 3 whose distribution and storm behavior were noticeably different from those electrons detected by the other instruments.

Throughout the period of observation by the scintillation counter, peaks 2 and 3 appear to be closely related. They were of approximately the same intensity before the magnetic storm, and they both underwent a 20-fold increase in intensity during the storm. The intensity of both peaks decreased slowly at the same rate after the storm. Furthermore, they appeared to merge at high geomagnetic latitudes after the storm, and only one peak was seen on passes at these latitudes. It seems reasonable, therefore, to assume that peaks 2 and 3 were both caused by electrons of several hundred kev energy, and that the intensity of these particles decreased slightly between peak 2 and peak 3.

The ion chamber to Geiger counter ratio reaches a peak near the E_3 maximum, and this has been interpreted to indicate a very soft spectrum at E_3 [*Arnoldy, Hoffman, and Winckler*, 1960]. The dip between peaks 2 and 3 of the scintillation counter may be the result of an electron spectrum at E_3 so soft that it cannot be detected by the scintillation counter. At the same time there must be sufficient high-energy electrons (500 kev–1 Mev) to account for the proportional counter response. If the scintillation counter is responding to electrons above 500 kev at the position of E_3, the count rate (pass 17) corresponds to an isotropic flux of approximately 2×10^7 electrons/cm^2 sec, and this is in quite good agreement with the spectrum proposed by J. A. Simpson (Space Science Research Conference, California Institute of Technology, January 24, 1961) to account for the proportional counter response at E_3.

The simplest electron spectrum that would be consistent with all the instruments on this sstellite would have large fluxes of soft electrons (20–100 kev) which dominate the Geiger-counter and ion-chamber response, but are not seen by the scintillation counter and the lead-shielded proportional counter. It would also have a much smaller group of high-energy electrons (500 kev–1 Mev) which would cause the proportional counter and scintillation counter response at the E_3 maximum. It does not seem possible to represent this electron spectrum by an energy distribution function of the form $E^{-\gamma}$ over the whole range from 20 kev to 1 Mev. Indeed, *Vernov and Chudakov* [1960] have suggested that the particles comprising the outer zone are electrons which appear to be in two energy groups. According to their investigation, the first group consists of electrons of 10–100 kev whose maximum intensity is 10^9 electrons/cm^2 sec sterad above 20 kev. The second group consists of electrons of energy of the order of 1 Mev whose maximum intensity is 10^5 electrons/cm^2 sec sterad. It may be possible to construct a detailed spectrum when the efficiencies of all the instruments as a function of energy have been determined.

It is possible that at some times and some places in the outer zone, the scintillation counter—and perhaps the Geiger counter and ion chamber—responded to protons instead of electrons. In particular, the authors have suggested [*Farley and Rosen*, 1960] that the increases in intensity (for example, pass 19) observed during the main phase of the storm must be the result of protons because the bremsstrahlung instruments observed a decreased count rate during this period. If it can be determined that the bremsstrahlung counters cover the entire electron energy range to which the scintillation counter is sensitive, then there appears to be no alternative to the proton hypothesis. However, the ion-chamber to Geiger-counter ratio indicates a considerable hardening between passes 17 and 19, while both the Geiger counter and lead-shielded proportional counter have approximately equal (60 percent) decreases in count rate. Until this apparently contradictory situation can be explained, there still exists the possibility that an electron component of the radiation can cause an increase in the scintillation counter without being observed by the other counters.

It seems rather unlikely that peak 2 can be caused by protons, except perhaps on pass 19, because of the previously mentioned similarities with peak 3, and because of recent calculations by *Dragt* [1960] which indicate a sharp cutoff of proton intensities with radial distance, even at low energies. Furthermore, the energy densities computed from that possibility seem improbably

TABLE 1.

	Count Rate	$\beta=\frac{v}{c}$	Flux, part./cm² sec	Particle Density, part./cm³	Particle Energy Density, erg/cm³	Magnetic Field, gauss	Magnetic Energy Density, erg/cm³	Gyroradius, km
Peak 1:								
2 Mev protons	5.8×10^{5}	6.6×10^{-2}	2.9×10^{9}	7.4×10^{-1}	2.4×10^{-6}	3.05×10^{-2}	3.7×10^{-5}	68
10 Mev protons	5.8×10^{5}	1.5×10^{-1}	1.5×10^{7}	1.7×10^{-3}	2.7×10^{-8}	3.05×10^{-2}	3.7×10^{-5}	150
Peak 2:								
200 kev electrons	6.5×10^{5}	7.0×10^{-1}	2.2×10^{9}	5.2×10^{-2}	1.7×10^{-8}	9.90×10^{-3}	3.9×10^{-6}	1.7
500 kev electrons	6.5×10^{5}	8.6×10^{-1}	1.6×10^{7}	3.2×10^{-4}	2.5×10^{-10}	9.90×10^{-3}	3.9×10^{-6}	3.0
Peak 3:								
200 kev electrons	8.0×10^{5}	7.0×10^{-1}	2.7×10^{9}	6.4×10^{-2}	2.0×10^{-8}	3.50×10^{-3}	4.9×10^{-7}	4.7
500 kev electrons	8.0×10^{5}	8.6×10^{-1}	2.0×10^{7}	3.9×10^{-4}	3.1×10^{-10}	3.50×10^{-3}	4.9×10^{-7}	8.4

765-698 O-65—20

large. Peak 1, however, is considerably closer in, and it is possible that protons of lower energy than those detectable by the Geiger counter (~25 Mev) are responsible for this peak. It should be noted that the points representing the position of this peak in figure 7 do not fall along a line of force, suggesting that these particles are trapped more closely to the geomagnetic equator with increasing radial distance. Several possibilities for peak 1, and the previously mentioned possibilities for peak 2 and 3 are shown in table 1 together with the corresponding particle and field energy densities, using data from pass 10 (fig. 4).

The fluctuations in count rate starting at about 7 earth radii in figures 14, 15, and 16 are the result of some dynamic mechanism which occurred during stormy periods. Correlations with the STL magnetometer carried aboard Explorer VI have yielded information on this mechanism [*Farley and Rosen*, 1960]. The earth-surface horizontal component of the magnetic field at Honolulu has been included in figure 14. The correlation suggested in this figure has not been borne out in subsequent comparisons with data at the ground stations, and it must be concluded that any correlation that does exist is obscured by local effects either at the vehicle or near the individual ground stations.

CONCLUSIONS

The scintillation counter on the Explorer VI earth satellite monitored the particle intensity in the earth's radiation belt for a period of 4 weeks. The experiment demonstrated the presence of large fluxes of several hundred kev electrons in the outer zone whose distribution differs somewhat from the particles observed by the bremsstrahlung detectors on the same vehicle.

This detector observed an increase in counting rate in the outer zone during the early stages of the geomagnetic storm of August 16, 1959, while the bremsstrahlung detectors observed a decrease. This increase must be attributed to particles other than those to which the bremsstrahlung instruments were principally responding. The scintillation counter rate rose by a large factor after the geomagnetic storm, as did the rates of the other instruments on the vehicle.

Gross fluctuations in particle intensity at the edge of the outer zone were observed during the geomagnetic storm. These fluctuations are evidently caused by some dynamic process that takes place at the edge of the trapped radiation belt during a geomagnetic storm.

ACKNOWLEDGMENTS

We are indebted to Charles P. Sonett for many discussions of the data and for his continued support of this experiment. Stuart Baker has conceived special instrumentation for reduction of the data, and John McGehee has spent many careful hours reading and plotting data from the records.

This work was carried out under the direction of the National Aeronautics and Space Administration.

REFERENCES

Arnoldy, R. L., R. A. Hoffman, and J. R. Winckler, Observations of the Van Allen radiation regions during August and September 1959, Part I, *J. Geophys. Research, 65*, 1361–1376, 1960.

Dragt, A. J., Effect of hydromagnetic waves on the lifetime of Van Allen radiation protons, *J. Geophys. Research, 66*, 1641–1649, 1961.

Fan, C. Y., P. Meyer, and J. A. Simpson, Trapped and cosmic radiation measurements from Explorer VI, *Proceedings of the First International Space Science Symposium*, p. 951, North Holland Publishing Company, Amsterdam, 1960.

Farley, T. A., and A. Rosen, Charged particle variations in the outer Van Allen zone during a geomagnetic storm, *J. Geophys. Research, 65*, 3494–3496, 1960.

Smith, E. J., P. J. Coleman, Jr., D. L. Judge, and C. P. Sonett, Characteristics of the extra terrestrial current system: Explorer VI and Pioneer V, *J. Geophys. Research, 65*, 1858–1861, 1960.

Sonett, C. P., E. J. Smith, and A. R. Sims, Surveys of the distant magnetic field: Pioneer I and Explorer VI, *Proceedings of the First International Space Science Symposium*, p. 921, North Holland Publishing Company, Amsterdam, 1960.

Vernov, S. N., and A. E. Chudakov, Terrestrial corpuscular radiation and cosmic rays, *Proceedings of the First International Space Science Symposium*, p. 751, North Holland Publishing Company, Amsterdam, 1960.

(Manuscript received December 1, 1960; revised March 31, 1961.)

Section 4. Magnetic Field Experiments Designed by Space Technology Laboratories, Inc.

Page intentionally left blank

Introduction to the Magnetic Field Experiments Designed by Space Technology Laboratories, Inc.

BY C. P. SONETT
NASA Ames Research Center

Explorer VI was the first of the extreme eccentricity, high-apogee, NASA satellites. It was designed to allow a sweep through the radiation belts to be made about four times a day. Since at the time of the Explorer VI flight the Earth's magnetic field was thought to terminate at some 5 to 7 Earth radii during quiet times and perhaps 2 to 3 radii during storms, the opportunity was present to verify this viewpoint and, if correct, to investigate the properties of the boundary region. From a historical standpoint, the status of the ring current reached a peak of interest around this time because of the discovery of the Van Allen radiation belts. In spite of the findings of Pioneer I, which showed no ring current effect on the sunlit hemisphere of the magnetosphere during times of magnetic quiet, there was keen interest in the possibility that a strong ring current effect would be found in association with the Van Allen belts. These were the primary motivations behind the magnetic field experiment carried on Explorer VI.

The findings of the magnetometer experiment must be regarded in the light of the previous comments which categorize this experiment as a survey designed to explore questions of gross interest. A result of immediate interest from this experiment was the lack of any noticeable geomagnetic termination. Since apogee was at 8 Earth radii, this meant that at least in the evening quadrant a geomagnetic termination would have to be placed at greater distance. A second effect, puzzling but especially interesting, which persisted both during times of quiet and disturbance, was an unmistakable distortion of the geomagnetic field at altitudes near apogee. The original interpretation of this distortion pointed out that it must be associated with currents having a large scale size. Although attempts to associate a proper current configuration with the field distortion required the assumption of a ring-like current, it was made clear that such an approximation quite clearly had not been uniquely demonstrated by the experiment. Although later events (i.e., Pioneer V) suggested, from sunward side data, the presence of a storm time current, the general view which has since developed, based on the more definitive data of Explorer X, is that the data were a two-dimensional or planar view of the geomagnetic tail. The consistency between the Explorer VI and Explorer X data has been reviewed in a paper by Smith. With the help of hindsight, it now seems clear that any satellite magnetometer experiment carried out at the altitudes and longitudes of Explorer VI could not make a distinction between a tail deformation and a ring current. The probability of storm time ring currents flowing is, however, suggested by data taken during disturbed times. Lastly, a comprehensive analysis of the storm time fluctuations in the magnetic field, together with those in one of the radiation detectors, has provided a view of the operation of betatron acceleration in the magnetosphere.

Current Systems in the Vestigial Geomagnetic Field: Explorer VI [1]

BY C. P. Sonett,[2] E. J. SMITH,[3] D. L. JUDGE, AND P. J. COLEMAN, JR.[4]
Space Technology Laboratories, Inc.

The purpose of this letter is to present some preliminary data taken by the magnetometer carried by the satellite Explorer VI. These data indicate the existence of a temporally and spatially variable current system which strongly perturbs the geomagnetic field at geocentric distances of 5 to 7 *Re* (earth radii).

The Explorer VI orbit is extremely eccentric with an apogee of 48,800 km and a perigee of 6,700 km geocentric. The period of rotation is approximately 12¾ hours. The plane of the orbit is inclined 47° with respect to the geographic equator. In terms of the orbital orientation with respect to the sun, apogee occurs between local dusk and midnight, i.e. 2100 hours local time, with perigee occurring at 0900 local time.

The magnetometer used was a search-coil mounted on the inner shell of the spin-stabilized vehicle, as in Pioneer I [1,2]. The telemetered data consisted of a sinusoid whose amplitude is a measure of $|B_\perp|$, the component of the magnetic field perpendicular to the spin-axis of the vehicle. A theoretical estimate of the expected field was made by extrapolation of the surface field, using an eccentric dipole model.[3] These field estimates were combined in a computer program with the trajectory of the satellite and the orientation of its spin axis to yield expected values of $|B_\perp|$.

Figure 1 presents some representative, preliminary data for orbital sweeps occurring on August 10, August 24 and September 1, 1959. A feature which is typical of the results obtained thus far is the reasonable agreement between the expected and the measured field at distances less than 5 to 6 R_e and the regular occurrence of large-scale deviations at greater distances. Thus, on August 10 the field displayed an abrupt, negative anomaly at 7 R_e with indication of a field recovery with increasing altitude. On August 24, it displayed a positive-going anomaly beginning at 6.5 R_e. The data of September 1 showed a negative deviation which began at 5 R_e and reached a minimum at 5.8 R_e. This was followed by a field increase to twice the expected value. These data were obtained on moderately quiet geomagnetic days.

It is of interest to compare these data with the results of Pioneer I [1] and the Russian cosmic rocket, Mechta. [4] In the former case, good agreement between observation and theory was obtained throughout the interval from 3.7 to 7 R_e. There is a disparity, however, between the Mechta data and the results of both Explorer VI, to this time, and Pioneer I. Neither the general depression of the field nor the

[1] Presented at the Explorer VI Session of the Cleveland Meeting of the American Physical Society, November 29, 1957 (*Bull. Am. Phys. Soc.*, Vol. 4, 416, 1959). This program was carried out under the auspices of the National Aeronautics and Space Administration. Published in the January 1960 issue of *Physical Review Letters* and reprinted by permission.

[2] Now at NASA Ames Research Center.

[3] Now at Jet Propulsion Laboratory.

[4] Now at Institute of Geophysics, Univ. of Calif. at Los Angeles.

anomaly at 3 to 4 R_e, which were observed by Mechta, has been detected. This disparity may disappear upon examination of more data.

The data presented in this note indicate the existence of an extraterrestrial current system beyond 5 R_e which causes a perturbation of the geomagnetic field. It appears likely that such a current system will take the form of a toroidal ring. However, it is obvious that neither a solitary pass nor repeated orbiting which shows an anomaly in one region of the outer atmosphere constitutes unambiguous proof of annular current closure.

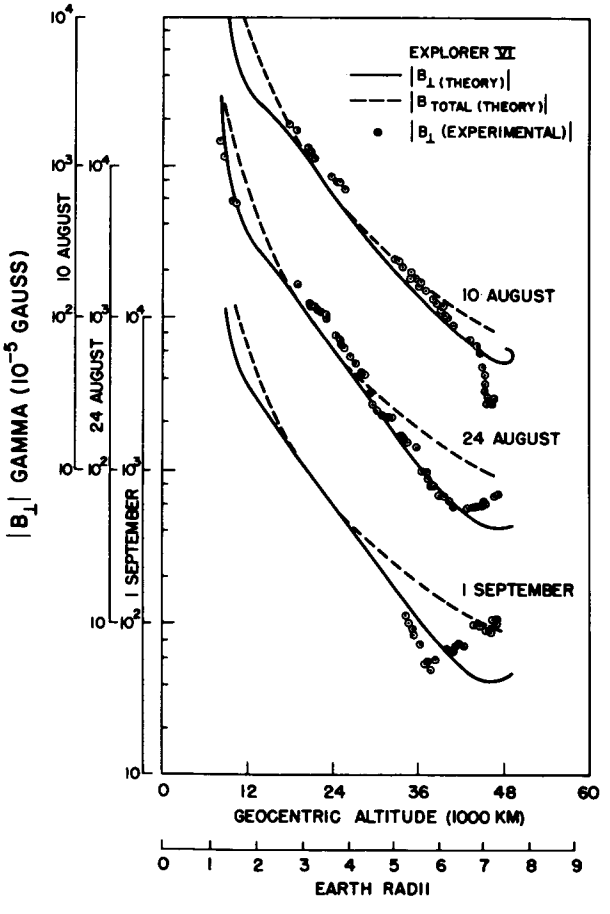

FIGURE 1.—*Representative values of* $|B_\perp|$ *for ascending leg of the orbit on August 10, August 24 and September 1. The values shown in the figure are geometry dependent. The small variations shown in the inner region for August 10 and August 24 are being studied.*

Figure 1 suggests the occurrence of two types of deviation and additional data, not shown, tend to bear this out. The possibility that such differences are not the result of fundamentally different kinds of current systems but are the effects of the orbital geometry is being investigated. The positive-going deviation observed on August 24 was repeated, to a lesser extent, on August 25. The deviation of September 1 occurred also on September 2, and investigation has shown that the negative-going deviation of August 10 is probably the initial portion of the same type of field variation. Figure 2 presents the amplitude of the deviation in the outer zone for August 9, August 10, September 1, and September 2. The similarity in the slopes of these curves strongly suggests similar characteristics and a similar cause for the perturbations. The data of August 24 and August 25, representing the other type of deviation, have not been included so as to avoid confusion. In addition to not showing a region of decreased field, the slopes of the latter do not agree with those shown in figure 2.

The deviation of the type shown in figure 2 argues for a spatially-confined current system such that a field reversal occurs as one passes through or near the current. Another obvious feature of this comparison is the difference in the altitudes at which the deviations were observed. This suggests that variations of several thousand kilometers in the location of the current system (as indicated by the position of the deviation minimum) may occur within intervals of 24 hours or less.

It is noteworthy to consider that these extraterrestrial currents appear in the region from 5 to 7 R_e. The unperturbed dipole field line through this region intersects the earth in the vicinity of the quiet day, southern auroral limit. The existence of a relationship between these currents and auroral activity is under investigation.

From the dynamics of a neutral plasma contained by a magnetic field, it is known that the individual particles will execute complex oscillations with a net drift azimuthally.[5] Because the direction of drift is charge dependent, this drift should appear as a net current flowing toroidally. Since the plasma

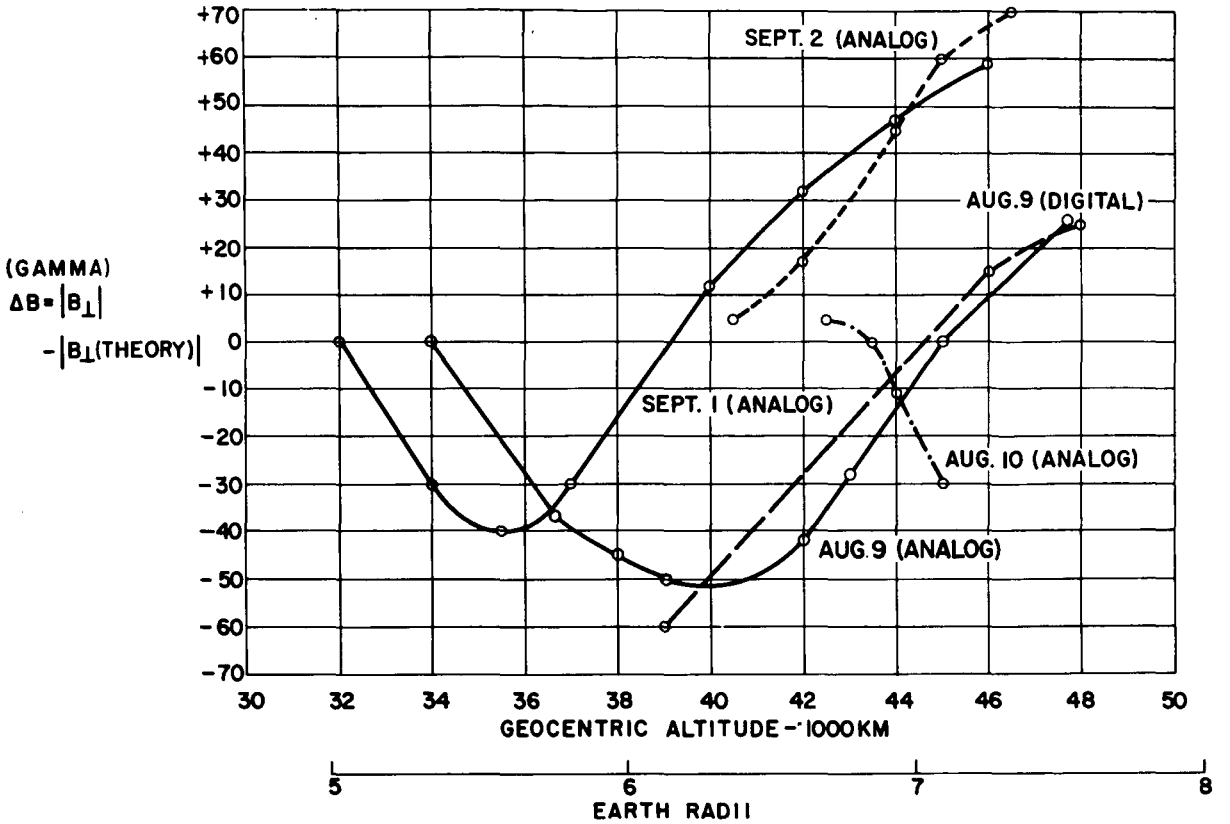

FIGURE 2.—*Shown above is the difference between the measured and expected values of* $|B_\perp|$ *shown for representative days. The repeatability of the slopes argues for a similar cause of the perturbations.*

in the exosphere is confined in just this way, convection currents capable of perturbing the geomagnetic field might be expected.[6] In addition to the large scale deviations discussed above, the preliminary data indicates a general increase in the magnetic field strength throughout most of the inner zone (see fig. 1) as well as irregular deviations. Although a longitudinal drift of the total plasma field should exist and provide a current, the resultant field depression, seen by a magnetometer presumed to be interior to such a region, is difficult to evaluate and requires knowledge of the velocity distribution function for the charged particles. It does appear from the data, however, that the commonly postulated condition, $\nabla \times H = 0$, is inadmissible in the outer atmosphere.[7]

The authors wish to thank Prof. L. Davis for helpful discussions.

REFERENCES

1. C. P. Sonett, D. L. Judge, A. R. Sims, and J. M. Kelso, *J. Geophys. Research* (to be published).
2. C. P. Sonett, D. L. Judge, and J. M. Kelso, *J. Geophys. Research, 64,* 941 (1959).
3. E. H. Vestine, *J. Geophys. Research, 58,* 127 (1953).
4. S. Dolginov, and N. Pushkin, Pravda, July 15, 1959.
5. H. Alfvén, *Cosmical Electrodynamics* (Oxford Univ. Press, New York 1953) p. 27.
6. S. F. Singer, *Trans. Am. Geophysical Union, 38,* 175 (1957).
7. J. W. Dungey, *Cosmical Electrodynamics* (Cambridge University Press, Cambridge 1958) Chap. 8, p. 150 and Proc. Phys. Soc. (London) *406* 229 (1955).

Surveys of the Distant Geomagnetic Field: Pioneer I and Explorer VI[1]

BY C. P. SONETT,[2] E. J. SMITH[3] AND A. R. SIMS

Space Technology Laboratories, Inc.

Experimental results obtained by magnetometers carried on board the lunar probe, Pioneer I, and the satellite, Explorer VI are presented.

Pioneer I data indicate an inverse-cube field decrease between 3.7 to 7 geocentric earth radii. The probe appears to have penetrated the interface region between the geomagnetic and the interplanetary field at an altitude of 13.6 radii. Fluctuations in both the amplitude and direction of the distant geomagnetic field were observed. Explorer VI data also indicates fair agreement between observed and expected values of the magnetic field at altitudes less than 5 earth radii. In the region from approximately 5 to 8 earth radii, the field typically shows regular, large-scale deviations. The characteristics of the extraterrestrial current system responsible are discussed.

Until 1953 little was known of the nature of the atmosphere beyond the F2 maximum, although some evidence indicating the existence of a far-reaching atmosphere had existed for some time prior. Auroral streamers, particularly those in the sunlit atmosphere, had been observed to heights as great as 1,000 km.[1] Twilight flashes of the red oxygen lines had been traced by Elvey [2] to 1,300 km. For many years the existence of a distant atmosphere was treated as a subsidiary condition to problems of great geophysical interest, examples being the classical work of Birkeland, Stoermer, and many others on the polar aurora.

In 1953 Storey,[3] investigating whistling atmospherics, showed that the propagation of such electromagnetic disturbances required an ionized atmosphere extending some 2 or 3 earth radii. Prior to this time a common picture of the outer atmosphere consisted of an almost collisionless nonionized gas bound to the earth by gravitational attraction. Because of the collisionless state the molecules of the gas were supposed to execute individual elliptic orbits with the kinetic temperature of the gas determining the escape rate. Thus, the geomagnetic field was assumed to be dynamically decoupled from the gaseous atmosphere. This region of the earth's atmosphere was called the exosphere.

The work of Storey indicated that an electron density of some 10^3 cm^{-3} was required to distances of 2 to 3 geocentric radii in order to explain the longitudinal propagation and dispersion of electromagnetic waves in the VLF region of the spectrum. It was recognized that the positive and negative charge densities had to be approximately equal in order to satisfy a fundamental requirement of cosmic plasmas. More recent investigation of this region of the earth's atmosphere has been in terms of modern

[1] This program was carried out under the direction of the National Aeronautics and Space Administration. Published in the Proceedings of the First International Space Science Symposium, Nice, France, January 1960. Reprinted by permission.

[2] Now at NASA Ames Research Center.

[3] Now at Jet Propulsion Laboratory.

hydromagnetic theory. It has since become clear that the geomagnetic field plays an important role in the dynamics of the distant atmosphere and that the medium is a deformable body of anisotropic elasticity.

An early example was the suggestion of Dungey [4] that geomagnetic pulsations might be excited by hydromagnetic oscillations taking place at a boundary between the geomagnetic field and interplanetary gas. He further proposed that this boundary was well defined and its distance was determined by momentum exchange between streaming solar gas and the geomagnetic field.

Today this region of space, bounded on the inside by the ionosphere and on the outside by interplanetary gas, is taken to be a neutral hydrogen plasma with a high degree of ionization through which threads the distant geomagnetic field. Its temperature is considered to lie between 10^3 and perhaps several times 10^5 degrees K, the lower bound representing the temperature just above the ionosphere as determined by Vanguard orbital data. The highest value presumably obtains by heat transfer from coronal gas exterior to the interplanetary boundary.[6] The electrical conductivity is of the order of 10^{12} to 10^{14} esu (σ_{Cu} equals 5×10^{17} esu). The hydrogen ion density at 3 earth radii is estimated by Johnson[6] to be 500 per cm^3. Thus in summary, the field and medium are strongly coupled, the plasma playing the role of a superconductor over large-scale distances.

MAGNETOMETER EXPERIMENTS

It is now clear that the use of magnetometers presents a means of investigating the plasma dynamics of the distant atmosphere of the earth and interplanetary space and experiments of this type can serve as an important tool in the investigation of plasmas of cosmic scale.

The status of rocket magnetometer research at extreme altitudes presently consists of some half-dozen or so Russian flights, Pioneer I, Explorer VI, and Vanguard III. Presumably the Russian flights have been survey experiments, as were Pioneer I and Explorer VI. One important result of the Russian work has been the discovery of a large field anomaly at some 3 earth radii.[7]

The experiments discussed in this paper were conducted on Pioneer I and Explorer VI. It is the purpose herein to review some of the results of the magnetometer experiments on these two flights. The reduction and interpretation of the data are still in progress. Thus, the data presented are tentative and subject to both change and further interpretation.

The magnetometer carried on Pioneer I consisted of a searchcoil fixed in the vehicle and coupled to a low-frequency amplifier. The spin rate of the vehicle, 1.835 cps, produced an emf in the coil which was proportional to the component of the magnetic field projected into the equator of the vehicle, provided that the time dependence of the field was small compared to the spin time. The details of this equipment have been reported elsewhere. [8, 9]

On Explorer VI this equipment was again utilized with a change in the scale range of the magnetometer. In addition to the searchcoil, a flux-gate probe was included on this flight to measure the component of the magnetic field which lay along the spin axis of the vehicle. An aspect indicator was also carried to determine the dihedral angle between the two planes defined by (a) the spin axis and sun vector and (b) the spin axis and magnetic field vector. Figure 1 shows the coordinate axis associated with the payload. $|B_\perp|$, in the figure, is the equatorial component of the field and $|B_\parallel|$ is the spin axis component of the field. The combination of this equipment was intended to provide the vector magnetic field at the payload. Due to permanent multipole distributions within the vehicle the flux-gate saturated. Thus, information was available only from the search coil and aspect indicator.

TRAJECTORIES

The orbit of Explorer VI was highly elliptic with an apogee of 48,800 km geocentric and a perigee of 6,780 km geocentric. The period was 12¾ hours. The geometry of the orbit is complicated, the major axis being inclined to the geographic equator of the earth at an angle of some 47 degrees. The satellite spends most

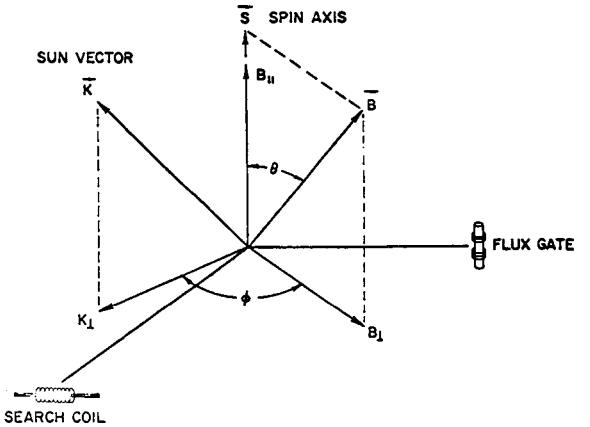

FIGURE 1.—*The coordinate system for the magnetometer experiments in a spinning payload. Shown above is a set of unit vectors in directions given by (1) the vehicle spin axis, (2) the normal to a plane containing the spin axis and the direction from the vehicle to the sun, and (3) the direction normal to the plane of the first two vectors. The search coil measures* $|B_\perp|$, *the component of the total field perpendicular to the spin axis. The flux gate magnetometer measures the component parallel to the spin axis. The aspect indicator measures the angle* ϕ *as shown.*

of its time south of the earth's equator. Figure 2 displays the projection of the orbit of this vehicle upon the geographic equator (e.g., as seen from the earth's polar axis). This figure also shows the relation of the orbit to the earth-sun direction. Considering the subsolar point to define the local noon meridian for the vehicle, apogee occurs at approximately 2100 hours. Thus, effects of solar wind are complex—the apogee lying more than 90 degrees away from the stagnation point. This is to be compared with the Pioneer I probe where, while the vehicle was traversing the distant field, it was located approximately under the solar wind stagnation point.

LARGE-SCALE CURRENTS IN THE OUTER ATMOSPHERE

Although the analysis of Explorer VI data is in a preliminary state it is apparent that a large current system has been discovered which lies between 5 and 7 geocentric radii.[10] The data which has been reduced to date is for relatively quiet geomagnetic days. The extent of this current system is under investigation and will require a model calculation because of the complexity of the geometry of this experiment. Figure 3 presents representative preliminary data for three selected days (August 10, August 24, and September 1). $|B_\perp|$ is shown as a function of geocentric distance. The most clearly defined feature is the occurrence of large-scale deviations beyond 5 earth radii (R_e). The deviations, including data not displayed, are a substantial fraction of the total earth's field at that distance (50–75 percent). Considering the whole field two distinct types of deviation have been noted. At distances $< 5\ R_e$ the observed field has the general character expected for the geomagnetic field, e.g., the field in this inner region is consistent with an inverse-cube decrease with distance. The deviations which occur represent a smaller fraction of the total field than the deviations in the far field (never more than 20–30 percent). In addition to large-scale fluctuations, about a regularly de-

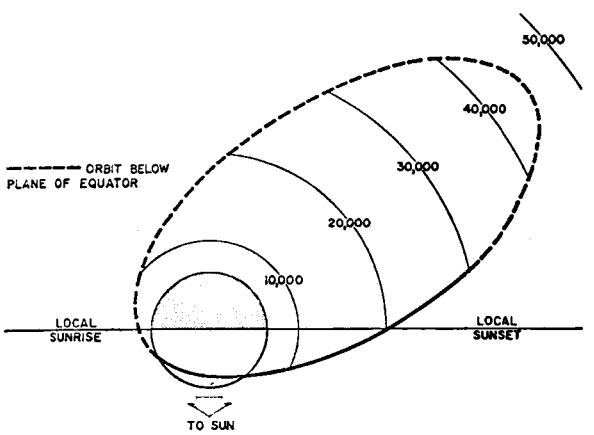

FIGURE 2.—*Projection of the Explorer VI orbit into the geographic equatorial plane of the earth. The solid portion of the ellipse corresponds to that part of the trajectory having a northern latitude, whereas the dashed portion refers to the portion below the equator. The distances marked on the arcs are kilometers from the center of the earth projected into the earth's equational plane.*

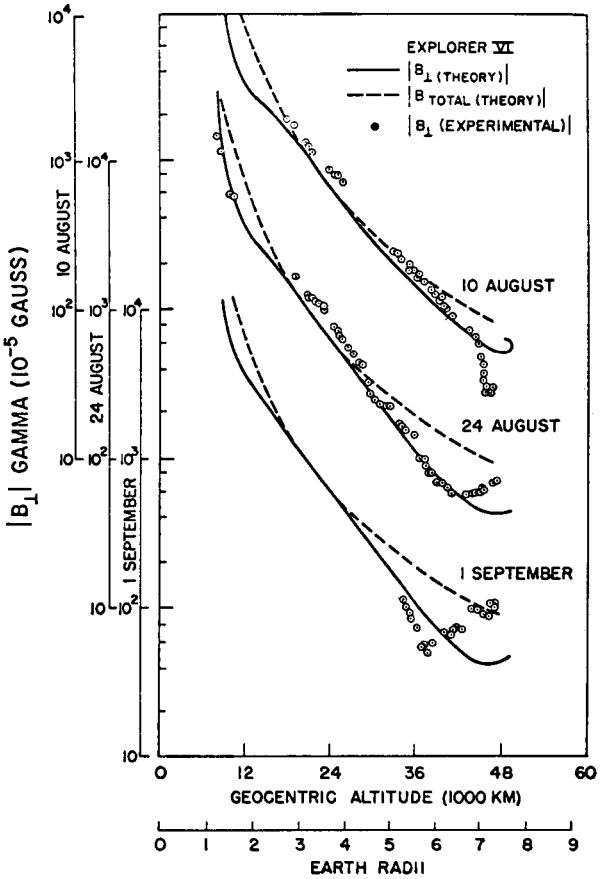

FIGURE 3.—*Representative values of* $|B_\perp|$ *for ascending leg of the orbit on 10 August, 24 August and 1 September.*

creasing mean value, the field shows a somewhat greater amplitude almost everywhere than that predicted by theory. The validity of these deviations in connection with the plasma dynamics of the region is presently being investigated. Until more work is carried out and the results advance beyond a preliminary state, for $R < 5\ R_e$ agreement with the extrapolated geomagnetic field has been emphasized. For comparison some Pioneer I data is shown in figure 4 for 3.7 to 7 R_e. In this regard the results of these two flights represent a definite contrast with those obtained by the flight of the rocket Mechta. The latter data show a large-scale depression of the field throughout the outer atmosphere. In addition, an anomaly occurs in the vicinity of 3 to 4 R_e which has been attributed to the effects of a ring current. Neither of these results have been found in the data of Pioneer I or Explorer VI. There are several possible explanations:

1. The differences in the trajectories of the American and Russian flights. The Russian rocket was located at 20 to 30 degrees north latitude when the anomaly was observed while, at the same altitude, Explorer VI crossed the geomagnetic equator.

2. The current system responsible for the anomaly is not a permanent feature of the extraterrestrial field but only occurs sporadically.

3. The anomaly may correspond to the deviations observed by Explorer VI between 5 to 7R_e but may occur at 3 to 4 R_e under special circumstances. In this regard, however, surface magnetic activity was less prior to and during the flight of Mechta than on corresponding days for Explorer VI.

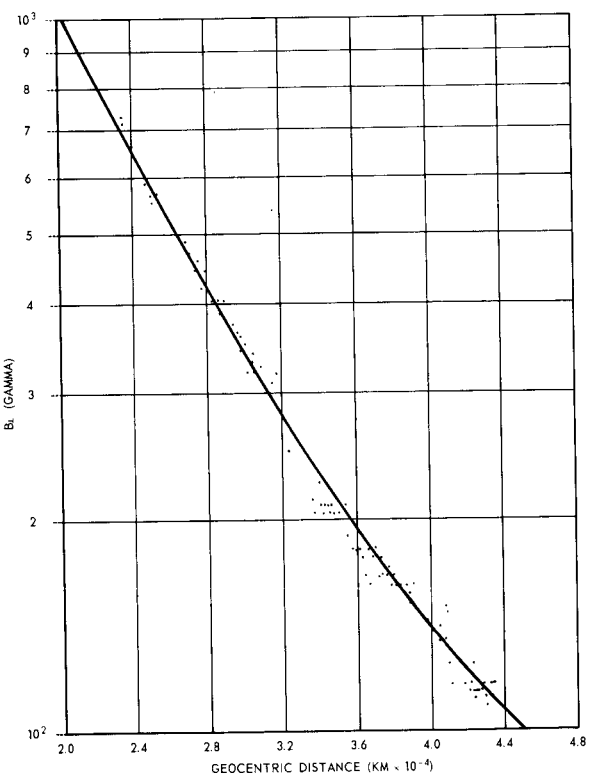

FIGURE 4.—*Shown above is the difference between the measured and expected values of* $|B_\perp|$ *shown for the flight of Pioneer I.*

The deviations in the field which occur at distances greater than 5 R_e reveal several features of interest. Figure 5 displays the difference between $|B_\perp|$ (observed) and $|B_\perp|$ (theory) as a function of radial distance. The distances of the location of the deviation, e.g. as given by the minimum, are noteworthy. Arguments can be advanced to show that such excursions represent temporal variations. There is evidence that on August 9–10 the current system responsible for these deviations moved outward several thousand km over a time of 25.5 hours. On the other hand, on September 1–2 it may be inferred that the location of the current system was constant over a similar period.

The preliminary evidence clearly indicates the existence of an extraterrestrial current system beyond 5 R_e which causes a perturbation of the geomagnetic field. This means that the commonly postulated condition, $\Delta \times H = 0$, is inadmissible in the outer atmosphere. It is suggestive that these currents appear in the region from 5 to 7 R_e. The unperturbed dipole field line through this region intersects the earth in the vicinity of the quiet day, auroral limit. The existence of a relationship between these currents and auroral activity is under investigation. The occurrence of two types of deviation has already been noted. The data of August 24 representing a second type of deviation have not been included in figure 5 so as to avoid confusion. However, it may be stated that, in addition to not showing a region of decreased field, the slopes of the perturbation of August 24 do not agree with those shown in figure 5. It is not known whether the observation of these two kinds of deviation necessarily implies that the currents responsible were essentially different; the possibility that the location and orientation of the vehicle are responsible for an apparent change in the field deviation is under investigation.

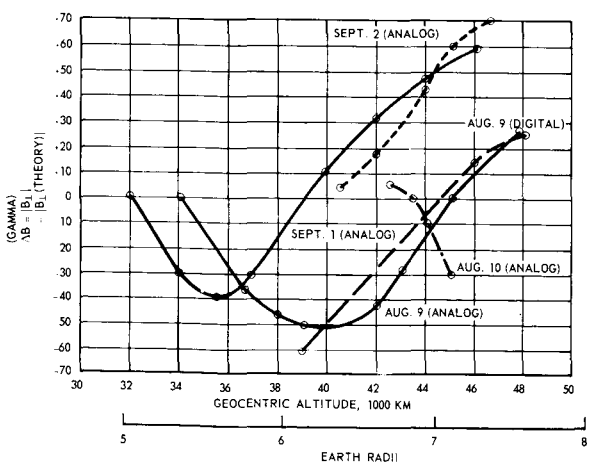

FIGURE 5.—*Shown above is the difference between the measured and expected values of* $|B_\perp|$ *shown for representative days. The repeatability of the slopes argues for a similar cause of the perturbations. (Explorer VI).*

An attempt has been made to determine the total current capable of producing the observed deviations. If one is willing to make certain simple assumptions regarding symmetry, the total current may be computed from a special case of Ampere's rule ($I = 2\pi rH$) using a knowledge of the field outside the current and at a known distance from the current location. Estimates carried out in this way yield a value, I, for the total current of 10^6 amperes and a corresponding current density of 10^{-8} amp/m^2. These are order of magnitude estimates and obviously more refined calculations are needed.

The question arises as to whether these currents close axisymmetrically to form a ring current. Depending on how the currents originate, data obtained by a single pass, or even by continual orbiting but over the same region of space, does not necessarily give an unambiguous result. If the currents are due to plasma trapped by the magnetic field in Stoermer orbits then an azimuthal drift is implied which will lead to a ring current. The possibility that the currents may close in some other configuration should be considered.

It is perhaps significant that a maximum current density is predicted at 6 to 8 R_e by Singer.[11] Such a result is obtained even though the ion density is assumed to be uniform throughout the plasmasphere and in spite of the fact that the azimuthal drift velocity increases with altitude. The maximum results from the magnetic field due to the ring current which tends to reduce the gradient of the earth's field. Furthermore, the total current, estimated at 10^6 amp above, can be obtained from

theoretical calculations assuming quite reasonable plasma characteristics. The total current and the current density above are consistent with a low-energy plasma ($\sim$10 keV protons) having a density of 10 cm^{-3}. It should be stated that, although the agreement is suggestive, further study will be required to test the validity of the details of the existing theory.

GEOMAGNETIC TERMINATION

Since Dungey has extended the concept of a Chapman-Ferraro boundary to quiet geomagnetic days it is of immediate interest to consider this question in reference to the data of Pioneer I and Explorer VI.

It has been argued that Pioneer I penetrated such a boundary [9] at 13.5 R_e (fig. 6). On the planetary side of the boundary, the field boundary conditions require a field increase and on the solar side a depression (we assume a field-free interplanetary cavity). This forms the basis for the interpretation of the Pioneer I data in reference to this problem. It should be pointed out that the theory of a cold plasma impinging on a plasma-free field implies a boundary of thickness $\sim$ plasma wavelength. As will be pointed out later, the ratio of gas kinetic and magnetic energy densities is of order unity. The fact that a field dependence $\sim r^{-5}$ was noted extending over some 10^9 cm ($\lambda_{plasma} \sim 10^6$ cm) is perhaps indicative of limitations of the theory of media where approximate equipartition occurs between magnetic and gas kinetic energies.

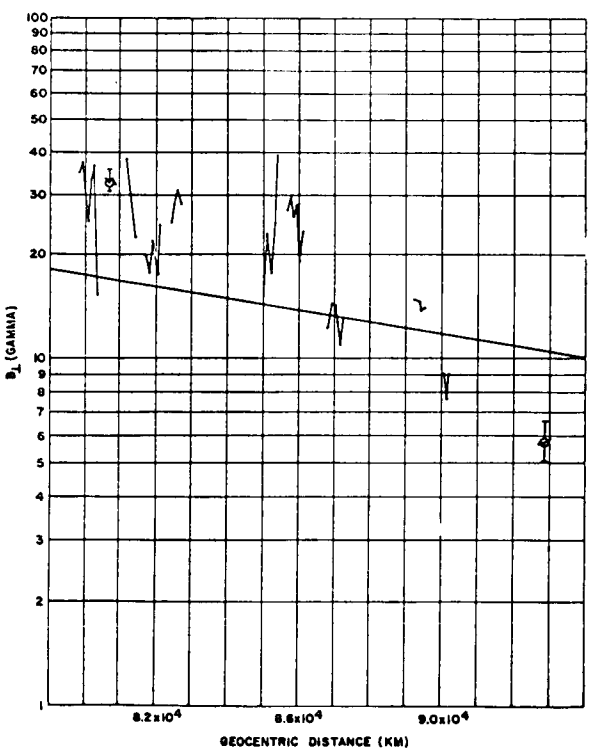

FIGURE 6.—*The magnitude of* $B_\perp$ *for region B (12.3 to 14.6 geocentric radii). The solid curve shows the theoretically expected value of the perpendicular component of* B. *(Pioneer I).*

It has often been supposed that a steady solar wind will act so as to terminate the geomagnetic field at 5 to 10 R_e. The cardinal idea behind this hypothesis has been that the field would terminate where the kinetic energy density was equal to the wind pressure. However, this would only take place at the stagnation point, and over large regions the boundary would be more complex. Although Pioneer I traversed near the sub-solar point, Explorer VI was at apogee in the opposed hemisphere.

The fact that the two vehicles sampled the field in different directions with respect to the earth-sun line does not lead to any inconsistency with the expectation that the cutoff lay beyond 8 R_e during the time the Explorer VI was detecting the large-scale deviations. It seems reasonable to expect that the field termination will occur at the same or lower altitude along the earth-sun line (Pioneer I) that at the azimuth corresponding to the Explorer VI orbit. Such a conclusion is independent of whether cutoff is due to a solar wind or to motion of the earth through a stationary, interplanetary gas. Therefore, it is believed that termination usually occurs beyond the apogee for Explorer VI, perhaps at a distance exceeding 10 R_e.

HYDROMAGNETIC ACTIVITY

Geomagnetic disturbances have been studied on the surface of the earth for many years. It was proposed by Dungey that surface waves are generated at the interplanetary boundary of the geomagnetic field and would propagate

downward, thus contributing to surface micro-pulsations. The detailed relation, if any, between surface micro-pulsations and distant activity is an exceedingly difficult problem to attack theoretically. Parker[12] has extended Dungey's work pertaining to the geomagnetic boundary with substantially the same results, though in greater detail. Kato and Watanabe[13] have reviewed the problem of disturbances from the standpoint of surface observations.

Obayashi and Jacobs,[14] utilizing Fermat's principle, have shown that the period of micro-pulsations should display a linear relation when plotted against $\cos^2 \phi$, where ϕ is the geomagnetic latitude. The wave velocity used by them was the pure Alfvén velocity $H/\sqrt{4\pi\rho}$. Since the radial velocity near the equator is compounded of both the acoustic and magnetic velocities, their estimates represent an upper bound for the equatorial period. Figure 7 is a plot of micro-pulsation period versus geomagnetic latitude after Obayashi and Jacobs.

The Pioneer I flight is notable primarily because of the discovery of large amplitude hydromagnetic disturbances in the distant atmosphere. The flight data obtained from 3.7 to 7 and 12.3 to 14.6 geocentric radii shall be referred to as regions A and B respectively. The small-scale fluctuations of region A (fig. 4) have been attributed partially to instrumental and reading errors. The question of the contribution of direct hydromagnetic activity to these variations is presently being investigated. It is noteworthy that the magnitude of the disturbances for region A and B are comparable in size though, of course, in the former case the fractional variation in the field is small because of the large value of the quiescent field. The fluctuations are more easily noticeable in region B. Although the magnetometer on Pioneer I measured only $|B_\perp|$ this was a good measure of total field because of the preferred direction of the spin axis (almost normal to the geomagnetic field). Data for region B was taken in the region of the sub-solar point, whereas for region A data was obtained during the early part of the morning (local time).

The variations in region B have been spectrally analyzed. A typical power spectrum is shown in figure 8; the envelope variations of the data for this region showed characteristic hydromagnetic activity somewhat more clearly. An observed periodicity of order 10 seconds is apparent in the latter and corresponds strikingly to the model of Obayashi and Jacobs near the geomagnetic equator. It is suggestive to consider that the fluctuations noted are in fact related to surface activity though the detailed characteristic of the surface fluctuations relative to those seen by Pioneer I might easily be lost in propagating downward to the surface because of dispersion and dissipative losses in the outer atmosphere.

We have shown in figures 9a and 9b two examples of the envelope of the magnetometer signal in region B. It is interesting to note that the activity decreases beyond some 13.5 radii and essentially disappears at 95,000 km, the farthest distance at which data was obtained. On the assumption that these disturbances are travelling magneto-acoustic waves, we have calculated both the hydromagnetic, (V_s), acoustic, (V_a), and modified acoustic velocity, (V'). These are shown in table 1 for temperatures of 10^4 and 10^5 degrees K. Utilizing a period of 10 seconds as typical, the wavelength of these disturbances is some $2 - 4 \times 10^7$ cm for a gas temperature of 10^5 degrees K and an assumed field of 20γ. (Vehicle velocity 1—2 km/sec.) Such calculations are highly tentative since the wave velocity is a function of the field intensity at the point of measurement. The wave front thickness appears to lie between the gyro radii for protons and electrons in this medium assuming a particles velocity of 10^8 cm/sec. Davis, Lüst, and Schlüter[15] have shown that for $\Delta B/B < 2$ in a collisionless plasma, the disturbances should have a symmetric character, although the theory breaks down for larger amplitudes. It is of some interest to note that the power density, $\overline{\Delta H^2}/\Delta\omega$, is approximately 4 times 10^{-7} gauss^2/cps at 13.6 radii and then drops beyond that point.

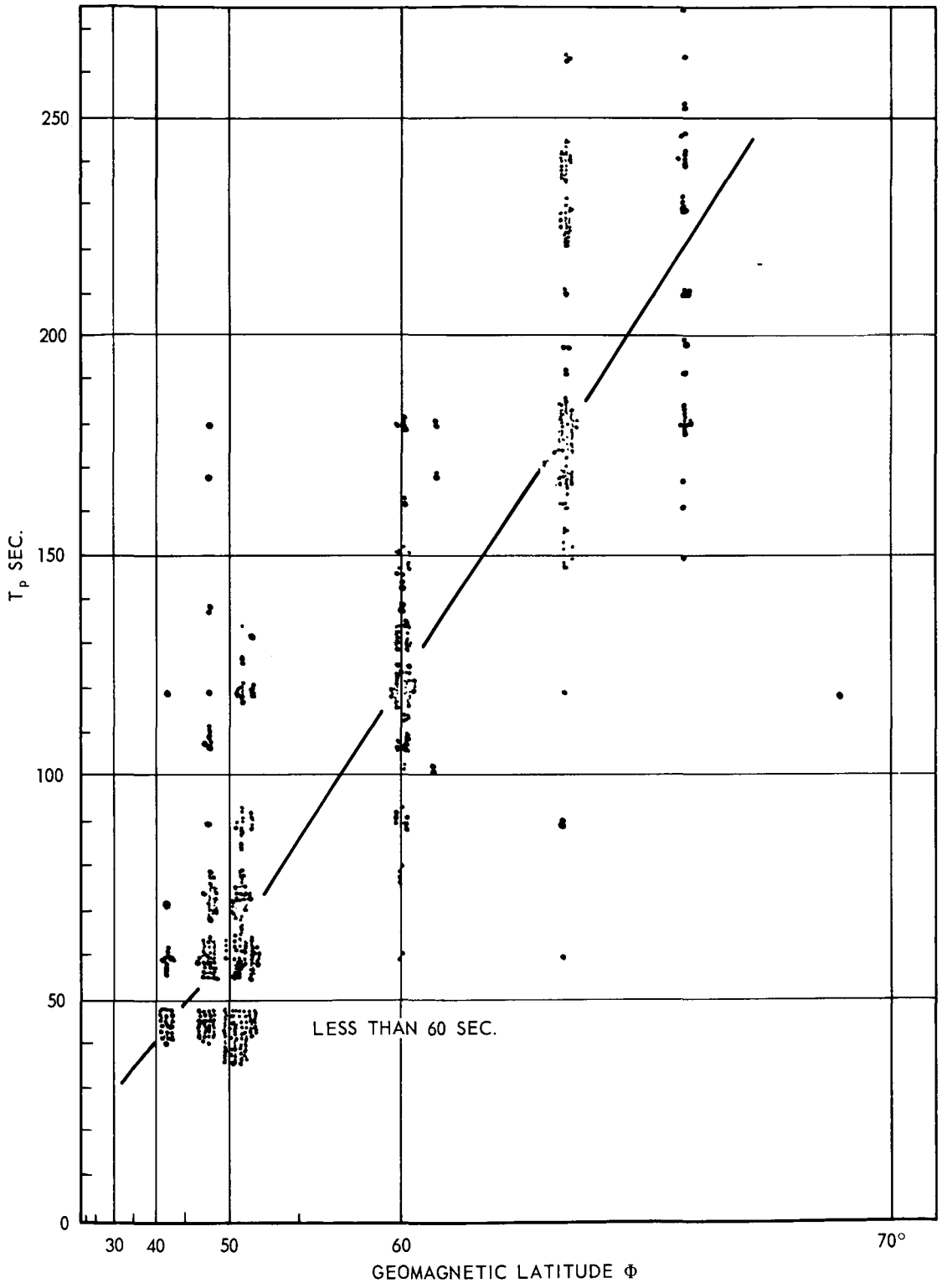

FIGURE 7.—*Scatter diagram of the period of micro-pulsations versus geomagnetic latitude is shown by the solid line (after Obayashi and Jacobs).*

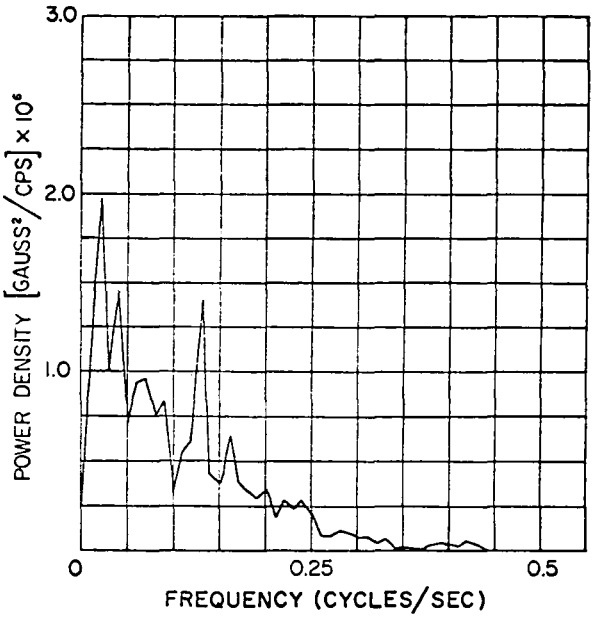

FIGURE 8.—*The power spectral density of the small-scale fluctuations of* $|B_\perp|$ *computed from the autocorrelation integral for the region of* 8×10^4 *km. (Pioneer I).*

Since the field becomes quiet at distances greater than 13.5 radii, it appears that the activity is generated locally and is not a propagation phenomena from the sun (longer term variations, i.e. ~ hundreds of seconds may be present in the data; if further analysis confirms this, the above statement may not apply to this case). Dungey has suggested the possibility that the Chapman–Ferraro surface oscillates over large distances and has raised the possibility that the disturbances noted are due to such a phenomena.[16] In the event that they are magneto-acoustic waves propagating earthward, the manner of excitation of them, other than the above suggestion, may require an involved coupling process to the boundary oscillations.

TABLE 1

$T°(r)$	V_s (km/sec)	V_a (km/sec)	V'
10^4	12	20	23
10^5	35	20	40

NOTE.—Estimates of wave velocity assuming a base field of 208, $N = 500$ cm^{-3}. V_s is the acoustic velocity, V_a the Alfvén velocity, and $V' = \sqrt{V_a^2 + V_s^2}$. As explained in the text these values are limited in meaning.

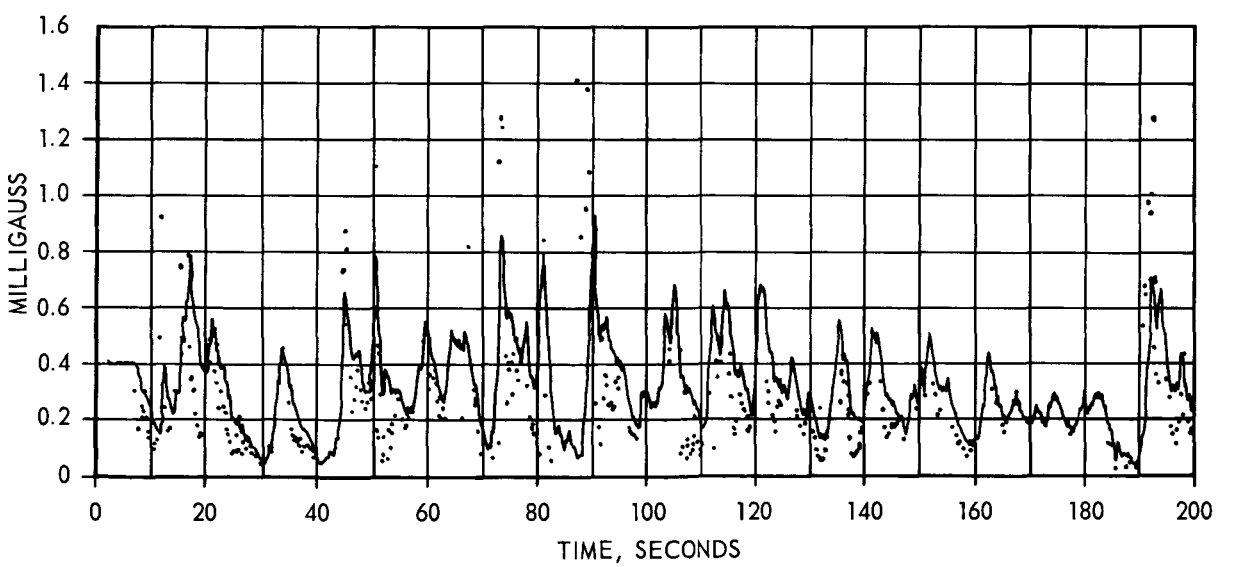

FIGURE 9a.—*The envelope if* $|B_\perp|$ *in the region of 80,000 km geocentric. The points shown not connected by the line correspond to the values uncorrected for the automatic gain control of the magnetometer amplifier. (Pioneer I).*

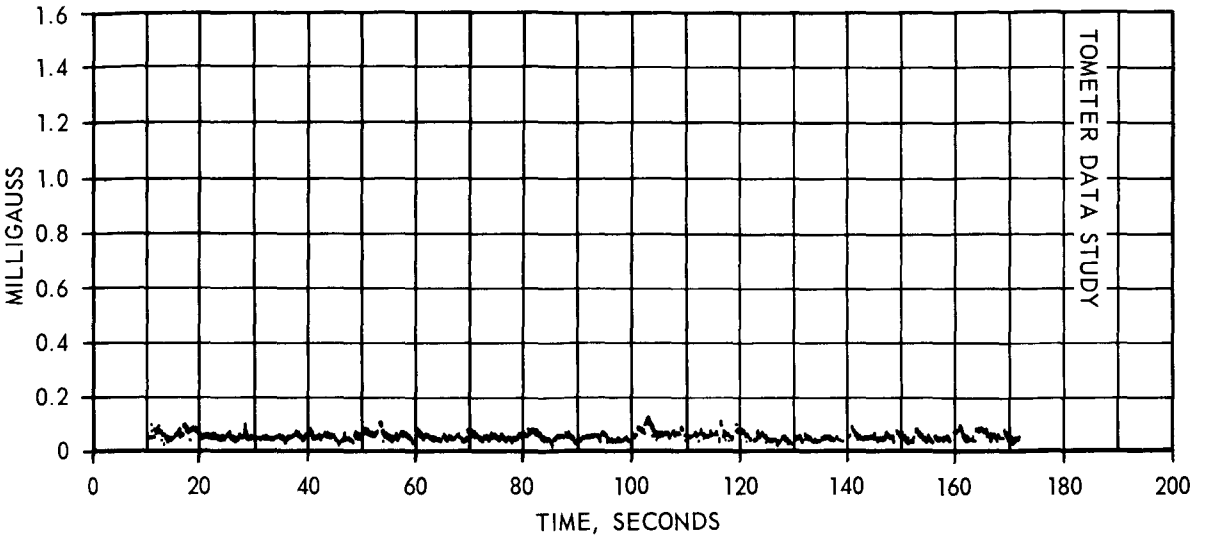

FIGURE 9b.—*The envelope of the field variations at 94,300 km geocentric show the marked decrease in field noise (Pioneer I).*

THE INTERPLANATORY FIELD

On the assumption that the transition from the noisy to quiet field, combined with the fact that the field from 13.5–14.3 R_e decreases as R^{-5}, it is suggested that the interplanetary boundary was penetrated.

If the direction of the interplanetary field was non-radial from the sun, the Pioneer I measurement provides an upper bound to the interplanetary field for the day of the flight of 6×10^{-5} gauss. In this event one can also make an estimate of the gas density in space on the day of the flight. An upper bound is 110 protons/cm^3, assuming that interaction of the earth with a stationary plasma took place where the relative velocity was due to orbital motion of the earth. If it is assumed that a streaming gas was flowing radially outward from the sun 100 cm^{-3} represents an upper bound on the volume density.

CONCLUSIONS

The Pioneer I data are consistent with an inverse-cube field decrease in the region from 3.7 to 7 R_e. The space probe appears to have penetrated the interface between the geomagnetic and interplanetary field in the direction of the sun at an altitude of 13.5 R_e. The data also provides evidence of small-scale fluctuations in both amplitude and direction of the distant geomagnetic field. These fluctuations include shock-like amplitude disturbances which can possibly be attributed to longitudinal, hydromagnetic waves. The disturbances were observed in the region from 12 to 13.5 R_e and were greatly diminished in amplitude beyond field termination.

Preliminary analysis of the data from Explorer VI has consisted of a study of the variation in the amplitude of the quiescent field with altitude. The data indicates fair agreement between the observed and expected values of the magnetic field at altitudes less than about 5 R_e. In the region from 5 R_e to 8 R_e (apogee) the field typically reveals regular, large-scale deviations. The characteristics of these deviations imply the existence of an extraterrestrial current system in this region which is spatially and temporally variable. These currents are believed to be due to trapped, low-energy plasma which drifts around the earth longitudinally because of the inhomogeneous nature of the earth's dipole field. This interpretation implies that the current closes toroidally to form a ring current about the earth. Order of magnitude estimates of the amplitude of the

current based on the observed deviations lead to physically reasonable results.

The authors wish to acknowledge the extensive help of D. L. Judge, P. J. Coleman, and S. C. Baker in carrying out these experiments. The work reported here would not have been possible without the help of a large and dedicated staff at STL. We wish to acknowledge also helpful discussions over a period of time with L. Davis, Jr., A. L. Dessler, E. H. Vestine, R. A. Helliwell, and J. W. Dungey.

REFERENCES

1. C. Stoermer, The Polar Aurora, International Monographs on Radio (Oxford University Press, 1955) p. 91.
2. C. T. Elvey, Gassiot Committee Report (Physical Society, London, 1948) p. 16.
3. L. R. O. Storey, An Investigation of Whistling Atmospheres, Phil. Trans. Royal Soc. A., 246 (1953) 113.
4. J. W. Dungey, Electrodynamics of the Outer Atmosphere, Physical Soc., London, 406 (1954) 229; also, Cosmical Electrodynamics, Chapt. 8 (Cambridge Univ. Press, 1958).
5. S. Chapman, Symposium on the Upper Atmosphere (Institute of Geophysics, Univ. of Calif. at Los Angeles, Dec. 1959).
6. F. S. Johnson, The Ion Distribution Above the F2 Maximum, J. Geophys. Research, 65 (1960) 577.
7. S. Dolginov and N. Pushkov, DOKL, AN-SSSR 129 (1959).
8. C. P. Sonett, D. L. Judge and J. M. Kelso, Evidence Concerning Instabilities in the Distant Geomagnetic Field; Pioneer I, J. Geophys. Research, 64 (1959) 941.
9. C. P. Sonett, D. L. Judge, A. R. Sims and J. M. Kelso, A Radial Rocket Survey of the Distant Geomagnetic Field, J. Geophys. Research, 65 (1960) 55.
10. C. P. Sonett, E. J. Smith, D. L. Judge and P. J. Coleman, Current Systems in the Vestigial Geomagnetic Field, Phys. Rev. Lett. 4 (1960) 161.
11. F. S. Singer, Trans. Amer. Geophys. Union, 38 (1957) 175.
12. E. N. Parker, Physics of Fluids, 1 (1958) 171.
13. Cf. Y. Kato and T. Watanabe, Science Reports Tohnkin Univ., ser. 5, Geophysics 8 (1957).
14. T. Obayashi and J. A. Jacobs, Geophys. Jour. of the Royal Astronomical Soc., 1 (1958) 53.
15. L. Davis, R. Lüst, and A. Schlüter, The Structure of Hydromagnetic Shock Waves, Zeit. f. Naturforsch., 13a (1958) 916.
16. E. W. Dungey, private communication.

Satellite Observations of the Geomagnetic Field during Magnetic Storms[1]

BY E. J. SMITH [2]
Space Technology Laboratories

C. P. SONETT [3] AND J. W. DUNGEY [4]
Space Sciences Division, NASA Ames Research Center

Explorer 6 satellite data and surface magnetograms are used to study the gradual and sudden commencement geomagnetic storms of August 16–18, 1959. Analysis of these data provides the following conclusions: (1) The geomagnetic field was strongly perturbed but retained its essentially dipolar character out to geocentric distances of 8 earth radii. (2) A long-period variation in the distant field coincided with D_{st} at the surface. The magnitude of the main-phase decrease at $\sim 4R_E$ was ~ 2.5 times larger than at the surface. Variations in the field direction at $\sim 7R_E$ correlate with half-day variations in (*a*) the horizontal component at the surface and (*b*) the 3-hour K index. (3) Large irregular field fluctuations with periods exceeding one minute were characteristic of the storm period. (4) The large-scale storm field was qualitatively similar to the disturbance field observed previously on nonstorm days. The disturbance field appeared to evolve from quiet to disturbed conditions and then to gradually recover.

INTRODUCTION

Simultaneous measurements of the geomagnetic field at the surface and in the magnetosphere are essential to a better understanding of magnetic storms, since the solar effects responsible for storms can be strongly modified by a complicated interaction with the earth's outer atmosphere. Space probes Pioneer 1 and Lunik 2 [*Sonett, Judge, Sims, and Kelso,* 1960; *Krassovsky,* 1960] traversed the distant geomagnetic field during nonstorm intervals. Pioneer 5 and Lunik 1 were launched during the recovery phases of storms [*Coleman et al.,* 1960], and Vanguard 3 (apogee $\sim$ 10,000 km) measured the field above the ionosphere during an interval which included several moderate magnetic storms [*Heppner et al.,* 1960]. Explorer 6 made the first repetitive measurements of the earth's field, between 4 and $8R_E$ (earth radii), during a magnetic storm.

The satellite magnetic field data obtained by Explorer 6 at geocentric distances between 4 and $8R_E$ during a severe magnetic storm are used here to study the gross characteristics of the large-scale storm field surrounding the earth. The physical origin of the storm field

[1] Parts of this paper were presented at the International Conference on Cosmic Rays and the Earth Storm, Kyoto, September 1961 [*Smith and Sonett,* 1962]. Published in the July 1964 issue of *Journal of Geophysical Research.* Reprinted by permission.

[2] Now at Space Sciences Division, Jet Propulsion Laboratory, Pasadena, California.

[3] Now at Jet Propulsion Laboratory.

[4] Now at Department of Physics, Imperial College, London.

is investigated, as is the possible existence of a main phase ring current. Long-period variations in the distant field are also compared with variations in the intensity of the outer radiation zone during the storm. Some of the data discussed here have been published previously in a preliminary report [*Smith and Sonett*, 1962].

BACKGROUND

Instrumentation

The detecting element of the magnetometer, a solenoid wound on a high permeability core, was attached to the shell of the spin-stabilized spacecraft which rotated 2.7 times per second. In an ambient stationary magnetic field, a sinusoidal voltage was generated with a frequency equal to the spin rate and an amplitude proportional to $B_\perp$, the component of the magnetic field perpendicular to the spacecraft spin axis (fig. 1). The electronics consisted of an amplifier having a passband centered at the spin frequency. A quasilogarithmic amplifier gain, achieved by using automatic gain control, extended the dynamic range of the magnetometer to 3 orders of magnitude so that fields could be measured over an extended range of altitudes.

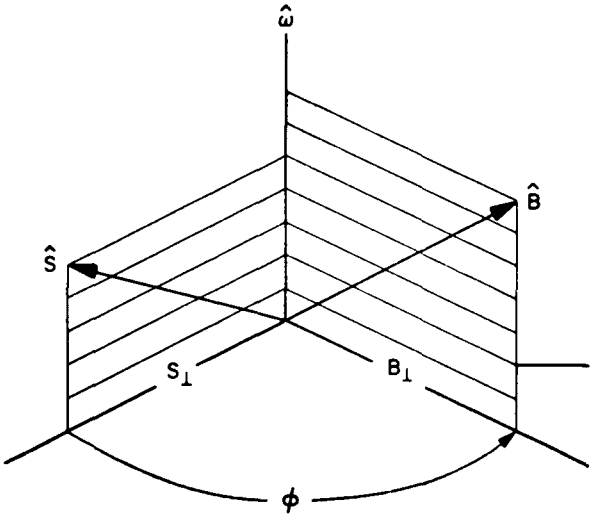

FIGURE 1.—*Spacecraft coordinate system. This figure shows the essential features of the experiment geometry.* $\hat{\omega}$ *is the rotation axis of the spin-stabilized spacecraft. The equatorial plane of the spacecraft is perpendicular to* $\hat{\omega}$. $\hat{S}$ *is a unit vector directed toward the sun, and* B *is the magnetic field vector. The projections of* $\hat{S}$ *and* B *onto the equatorial plane are* $S_\perp$ *and* $B_\perp$, *respectively, which define the angle* ϕ. *The Explorer 6 magnetometer measured* $B_\perp$ *and* ϕ *directly.*

The magnetometer coil constant, the numerical relation between field strength and the induced voltage, was determined by comparing the voltages generated when the search coil and a standard air-core coil were simultaneously rotated in the earth's field in a region where gradients were small. Sinusoidal input voltages were used to obtain steady-state electronic calibration. (The transient response of the magnetometer is not pertinent to this paper and will be discussed elsewhere.) In a given field, the output signal amplitude depended on the spin rate of the spacecraft and was only slightly dependent on the temperature of the electronics which was checked by means of several temperature sensors inside the spacecraft. The satellite spin rate was computed on the ground from the number of cycles of the telemetered sinusoid that occurred in a given time period. Further details about the equipment and its calibration are reported elsewhere [*Judge et al.*, 1960].

Early recognition of the importance of directional data [*Sonett et al.*, 1959] led to the inclusion of a photodiode sun scanner and phase comparator. This instrument provided a phase reference, based on the solar direction, and determined, in flight, the directional variations in $B_\perp$. The merit of including this type of instrument has been supported by subsequent events, and sun scanners are now virtually standard equipment on spinning spacecraft.

The phase comparator measured the angle φ between $B_\perp$ and $S_\perp$, where $S_\perp$ is the projection into the spacecraft equatorial plane of a unit vector pointing from the spacecraft in the direction of the sun (fig. 1). Hereafter, φ is called the *phase angle*. It is the magnetic declination in spacecraft coordinates referred to the spacecraft-sun direction, and it depends on the orientation of the spacecraft spin axis.

The phase comparator input signals were the search coil sinusoid and a sequence of pulses

generated by a photodiode when illuminated by solar radiation once per spacecraft revolution (fig. 2). The photodiode pulse and a pulse coincident with the zero-voltage crossing of the search coil sinusoid operated Schmidt triggers that controlled the state of a flip-flop. The output, obtained by integration of the flip-flop output signal, was a dc voltage proportional to the time delay between the two pulses. Except for very small fields, the phase comparator output was independent of the magnitude of the search coil sinusoid, and the measurement of φ was independent of $B_\perp$.

The search coil and phase comparator analog voltages each modulated a subcarrier oscillator. The resulting FM signals, which were transmitted continuously, were received at one or more STL ground stations (England, Florida, Hawaii, and Singapore) approximately 18 hours per day. The search coil sinusoid was also converted to a slowly varying dc voltage by a peak detector and filter and was digitized inside the spacecraft along with the phase comparator output. Transmissions of binary-coded digital data, which were used to test the telemetry system subsequently flown on Pioneers, were commanded from the ground at irregular intervals. The digital data were used primarily to check the quality and accuracy of the telemetered analog data.

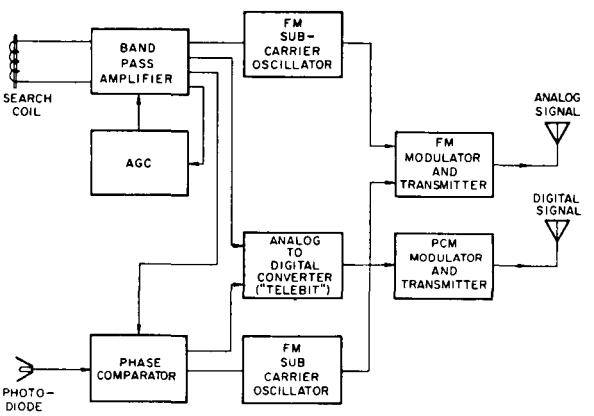

FIGURE 2.—*Block diagram of the search coil magnetometer. The experiment sensors are the search coil and a sun-sensing photodiode. The amplifier bandpass was centered at the spacecraft spin frequency and automatic gain control extended the dynamic range of the amplifier. The phase comparator measured the time delay between zero-voltage crossings of the search coil sinusoid (corresponding to the instant when the directions of* $B_\perp$ *and the coil axis coincided) and pulses generated when the sun was within the narrow field of view of the photodiode. Two independent data processing systems were employed. Analog voltages were telemetered continuously as frequency-modulated signals. The analog voltages were also converted to binary numbers on the spacecraft and transmitted on ground command.*

Orbit Parameters

After Explorer 6 was launched in August 1959, much time and effort was expended in refining the ephemeris because of perigee drag fluctuations and solar-lunar perturbations, a poorly understood subject in 1959. With the establishment of an accurate orbit and a precise spin axis orientation, the more subtle effects in the data, such as the properties of the disturbance field near the geomagnetic equator, were made accessible.

The Explorer 6 orbit (apogee 48,000 km, perigee 6,740 km) was highly eccentric. The orbital plane was inclined 47° to the geographic equator and apogee was at geographic latitude −20°. The spacecraft crossed the equatorial plane at geocentric altitudes of 7,200 and 30,000 km. Figure 3 shows a projection of the orbit onto the surface of the earth during August 16–17.

The satellite was launched from Atlantic Missile Range at 1345 GMT on August 7, 1959. Since perigee occurred at about 0900 hours local time, apogee was on the opposite side of the earth at 2100 hours local time. On August 7, the projection onto the geographic equatorial plane of the semimajor axis of the orbit made an angle of $\sim$ 135° with respect to the earth-sun direction. This angle decreased by approximately 1° per day. The right ascension and declination of the spin axis were 217° and 23°, respectively.

The orbital period, 12¾ hours, had an important effect on the instantaneous location of the spacecraft in geomagnetic coordinates.

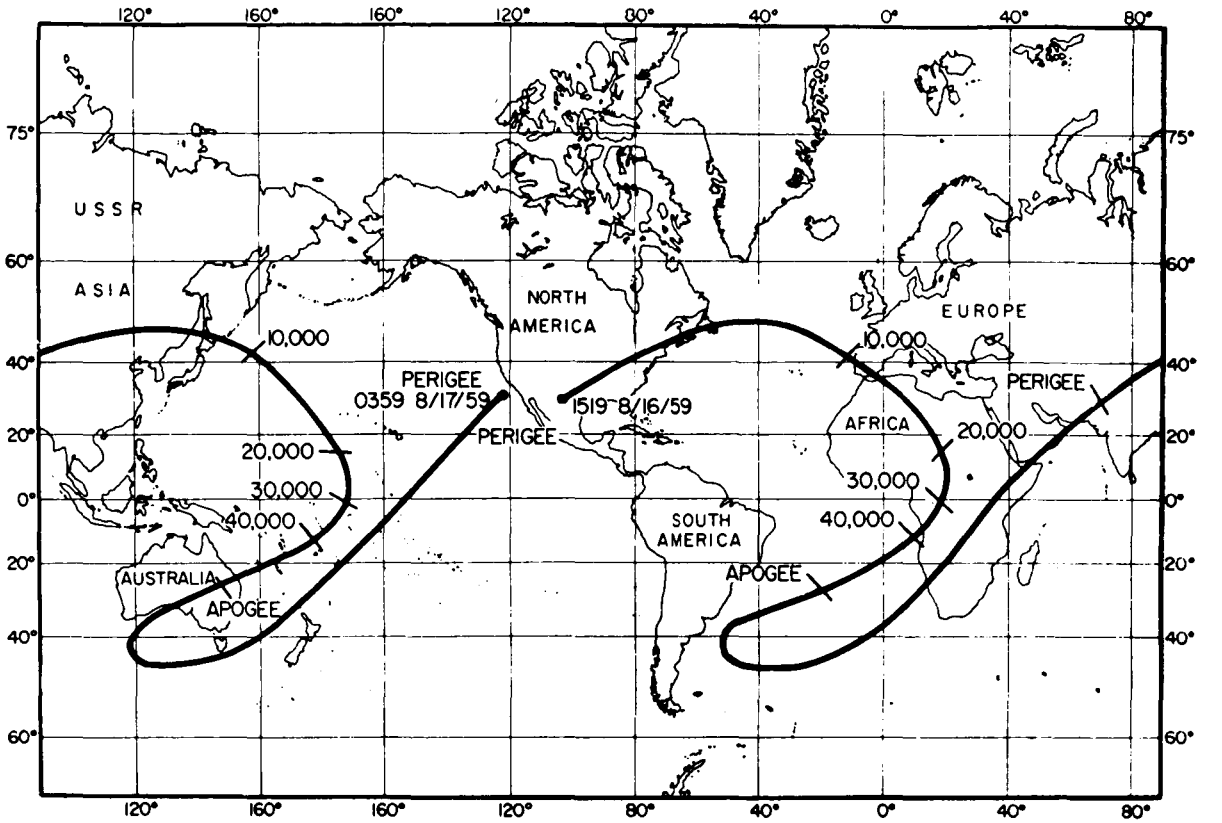

FIGURE 3.—*Projection of the Explorer 6 trajectory onto the earth. The geographic position of the spacecraft is shown at radial distances separated by 10,000 km and at apogee. The positions shown are for the 18th orbit on August 16–17.*

Because the earth's magnetic pole is inclined 11½° with respect to the rotation axis, the geomagnetic latitude of a given orbital position underwent a semidiurnal variation as large as 23°. However, the geomagnetic latitude of the spacecraft was nearly the same before and after two complete rotations around the earth (~25½ hours). This prompted us to divide the data obtained on odd-numbered and even-numbered passes into two separate groups in order to isolate temporal changes in the geomagnetic field more clearly.

Magnetic Conditions at the Earth's Surface

August 12, 13, and 14 were among the five quietest days in August [*Lincoln*, 1960] (fig. 4). On August 15, a gradual commencement storm was reported at some stations. At approximately 0400 on August 16, a sudden commencement storm began and continued until the end of August 17 or the beginning of August 18. This storm was classed as severe (corresponding to a K index of 8 or 9). Huancayo reported a moderate, gradual commencement storm which began at 0635 on August 18 and ended at 2000 hours the same day. A moderately severe sudden commencement storm began on August 20 at 0412. There is no general agreement as to when this storm ended. (Some stations estimated that it ended on August 20, but others recorded disturbed conditions until August 24.) August 27 and 28 were the two quietest days of the month. A moderately severe (K = 6, 7) sudden commencement storm began on September 3 at 2159 and continued until September 5 or 6. The discussion which follows is concerned primarily with the severe magnetic storm of August 16.

Review of the Explorer 6 Data Obtained on Nonstorm Days

In the preliminary analysis of the data, the magnitude $B_\perp$ and direction φ of the observed field were compared with the magnitude and direction of the extrapolated geomagnetic field [*Sonett, Smith, Judge, and Coleman*, 1960; *Sonett, Smith, and Sims*, 1960; *Smith, et al.*, 1960]. An 8 coefficient spherical-harmonic expansion of the surface field [*Vestine*, 1959] was used to extrapolate the geomagnetic surface field to the satellite position, where it was resolved into spacecraft coordinates for comparison with the measured field. This computed field is labeled $G_\perp$ and has spacecraft declination φ_G.

Discrepancies between $B_\perp$, the measured component, and $G_\perp$, the extrapolated one, were observed throughout most of the trajectory. Below $5R_E$, $B_\perp$ tends to exhibit the same altitude dependence as $G_\perp$ but to have a somewhat larger magnitude. Beyond approximately $5R_E$, there was a marked disparity between $B_\perp$, $G_\perp$, and their spacecraft declinations, φ and φ_G.

An important consequence of the AGC loop is that the relative and absolute accuracy of measurement increased with increasing altitude. For example, a change of 1 percent in the output voltage corresponded to 300 γ in a 5,000 γ field (approximate altitude, 12,000 km), and to only 3 γ in a 100 γ field (approximate altitude, 38,000 km). The differences between $B_\perp$ and $G_\perp$ beyond $5R_E$ corresponded to large fractional changes (15 to 20 percent) in the magnetometer output signal. The experimental results suggested that the extraterrestrial field was essentially dipolar out to $5R_E$, deviating progressively at greater altitudes. (The deviation between $G_\perp$ and $B_\perp$ depends strongly on the direction of $B_\perp$, as well as on its magnitude.) In a preliminary survey of data obtained throughout a 6-week interval, large-scale perturbations in $B_\perp$ and φ were always noted, although their shapes varied from day to day and were strongly dependent on the geometry of the experiment.

A perturbation field based on an equatorial current with a finite, circular cross section and constant current density was used to explore possible causes of the observed differences. The field due to the current was computed at points on the trajectory and added vectorially to the geomagnetic field; a coordinate transformation was then performed to obtain theoretical values of $B_\perp$ and φ. Reasonable agreement between the data and the model calculations was obtained for a westward current of $5 \cdot 10^6$ amperes centered at $10R_E$ [*Smith et al.*, 1960].

Perturbations in the distant geomagnetic field were also subsequently observed by Pioneer 5 on the sunward side of the earth. When the same mathematical model was applied to the Pioneer 5 magnetometer data obtained inside the geomagnetic field, reasonable agreement was again obtained between the calculated and observed $B_\perp$ for a westward current of $5 \cdot 10^6$ amperes centered at $8R_E$ and extending from 5 to $11R_E$.

These model calculations, employing an ad hoc current, were justifiably criticized because they ignored an important feature of currents associated with trapped particles. The diamagnetic character of the trapped particles should lead to a maximum reduction of the geomagnetic field at the peak of the particle kinetic energy distribution. *Akasofu and Chapman* [1961] compared the Explorer 6 data for August 9 with a computed field based on a model radiation zone. Their results place the particles at $\sim 6R_E$ and suggest the total current was $\sim 2 \cdot 10^6$ amperes. Similarly, *Apel et al.* [1962] derived a distribution of trapped particles corresponding to the Pioneer 5 magnetometer data and found it to be centered at $\sim 6R_E$. Although both these calculations employed ideal rather than observed particle distributions and did not take into account geometrical effects associated with the data, such as the geomagnetic latitude and spin axis orientation of the spacecraft, they undoubtedly lead to a more realistic estimate of where the particles causing the Explorer 6 and Pioneer 5 field deformations were located than our preliminary model calculations. For example, compare the vector disturbance field computed by *Akasofu et al.* [1961, figure 1] with the vector field derived from the Explorer 6 measurements [*Smith*, 1962, figure 1].

It should be noted that the model calculations were applied to data obtained under disturbed magnetic conditions. The Pioneer 5 data were

acquired during the recovery of a moderate magnetic storm. The Explorer 6 data obtained on August 9 were initially regarded as nonstorm data because a preliminary classification did not list August 9 as a disturbed day. However, as figure 4 shows, the K_p index reached a value of 4 during the period in which the data were obtained. All periods in which K_p exceeded 4 included storms.

THE EXPERIMENTAL DATA

The data in figure 5 were obtained on three successive days during the severe SC storm which began on August 16.

The storm data show the same qualitative features as the data obtained on nonstorm days (e.g., see figure 1 in *Sonett, Smith, Judge, and Coleman,* [1960]). For example, the fine structure appearing in figure 5, a variation of several hundred gammas that occurred at 30,000 km on August 17, may be the result of either spatial or temporal variations and is a subject of special interest investigated separately in connection with bay-like, polar storm variations. [*Smith and Judge,* 1961].

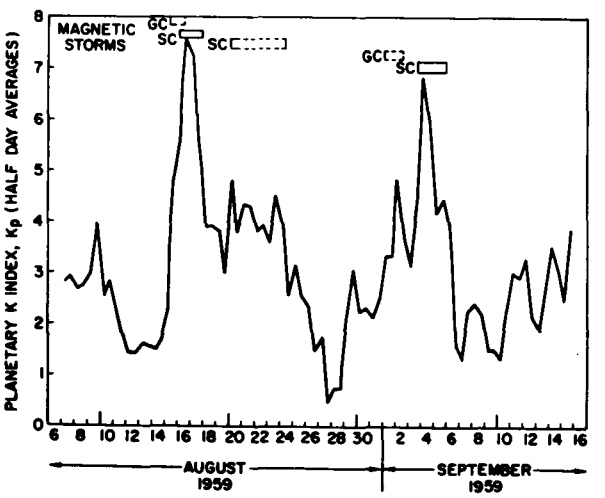

FIGURE 4.—*Geomagnetic activity during the Explorer 6 epoch. The planetary* K *index,* K_p, *is shown for August 7 to September 15, 1959. Half-day averages are plotted because the orbital period of the Explorer 6 was approximately 12¾ hours. The major storms are indicated at the top of the figure where GC and SC stand for gradual and sudden commencement storms, respectively. The lengths of the rectangles indicate the duration of the storm and are dashed where uncertainties exist.*

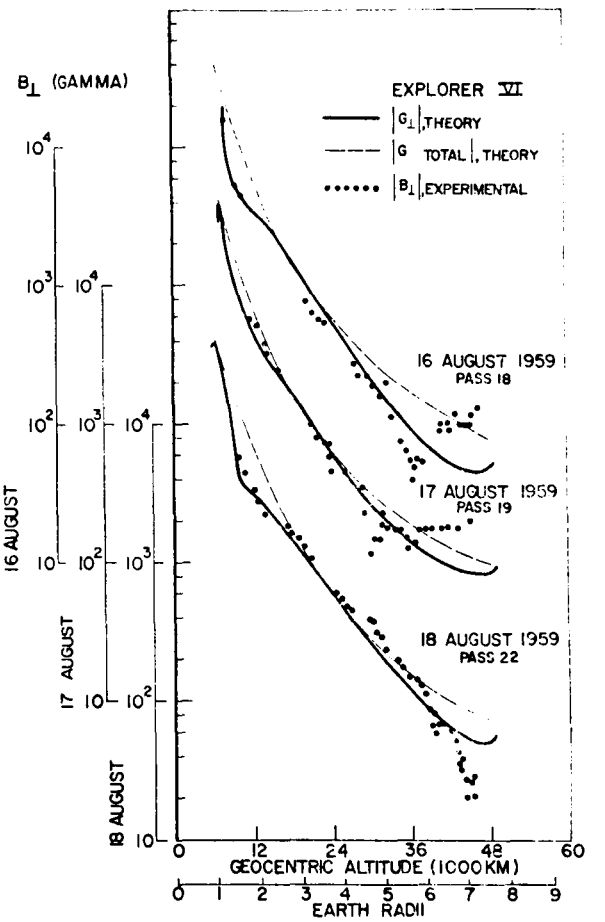

FIGURE 5.—*Explorer 6 field magnitude data for the magnetic storm of August 16–18.* $B_\perp$ *is shown as a function of geocentric distance for 3 orbits on August 16, 17, and 18. Values of the total geomagnetic field* G *and the component perpendicular to the satellite spin axis direction* $G_\perp$ *are also shown.* $G_\perp$ *and* G *are approximately equal from 3 to* $4R_E$ *because the Explorer 6 spin axis is nearly orthogonal to the geomagnetic field vector. The differences between* $B_\perp$ *and* $G_\perp$, *which appear to be large at geocentric distances of less than 3 earth radii, are exaggerated by the quasi-logarithmic characteristic of the magnetometer amplifier. The deviation between* $B_\perp$ *and* $G_\perp$ *at* $R > 5R_E$ *first noted on nonstorm days is also observed during the storm.*

In interpreting the data, we assumed that the field was perpendicular to the equatorial plane on the geomagnetic equator for both quiet and storm-time fields. Therefore, the scalar field measured at the equator completely specified the resultant field. For nonequatorial points of observation, variations in $B_\perp$ were caused by a change in the direction as well as in magnitude of the field. Thus, treating the equatorial measurements separately will simplify the interpretation of the experimental data. The next section describes the time dependence of the field magnitude near the geomagnetic equatorial plane. This is followed by a discussion of field direction at points of observation below the equatorial plane. The centered dipole approximation of the geomagnetic field is used to define the geomagnetic equator.

Variation in the Magnitude of the Near-Equatorial Field during the Storm

Figure 6*a* shows the time variation of the field magnitude in the outer radiation zone. Each datum was obtained from a measurement of $B_\perp$ at a geocentric distance of approximately 24,000 km or $4R_E$ (the actual radial distance varied between 22,000 and 26,000 km). The corresponding value of the extrapolated geomagnetic field was computed and subtracted from $B_\perp$. The differences ($\Delta B_\perp = B_\perp - G_\perp$) are plotted in figure 6*a* for approximately the first two weeks of Explorer 6 observations. Since the observed field at 24,000 km tends to exceed the extrapolated surface field on magnetically quiet days, a feature of the data that could be caused by a lack of good absolute accuracy at this altitude, the data in figure 6*a* were adjusted so that $\Delta B_\perp = 0$ on the quietest days of the month (August 11–12) by subtracting the amount by which $B_\perp$ exceeded $G_\perp$ on August 11 from all the differences. The digital data appearing in figure 6*a*, which were similarly adjusted, provide data for times for which no analog data were available.

Figure 6*b* is the time variation of the horizontal component of the surface field. Each datum, the daily mean value of the horizontal intensity at Huancayo, Peru (geomagnetic latitude δ_M, $-0.6°$), obtained by averaging the hourly mean values over each Greenwich day,

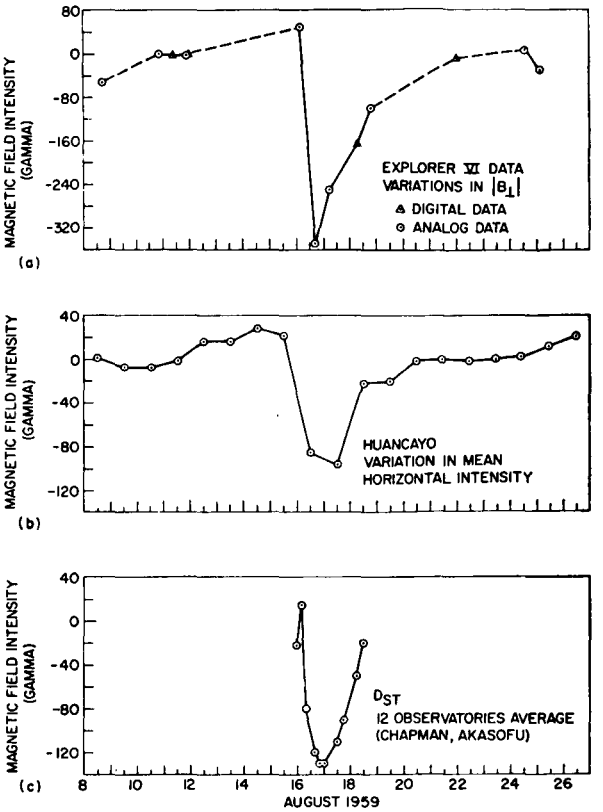

FIGURE 6.—*Time variations of the equatorial disturbance field compared with* D_{st} *variation at the earth's surface.* (a) $\Delta B_\perp = B_\perp - G_\perp$ *at* $\sim 4R_E$ *near the geomagnetic equator during the first two weeks of Explorer 6 measurements. The data are normalized so that* $\Delta B_\perp = 0$ *on August 12 (one of the magnetically quietest days of the month).* (b) *The variation in the horizontal intensity of the surface field at Huancayo, Peru* ($\delta_M = -0.6°$). *Daily averages are plotted at 1200 GMT.* (c) *The* D_{st} *curve for the SC storm of August 16; this curve was derived by S. Chapman and S.-I. Akasofu by averaging the storm data from 12 geomagnetic observatories.*

has been plotted at 1200 GMT. This procedure produced a reasonable representation of long-period changes in the earth's field. The variation in mean horizontal intensity has also been biased so that $\triangle H = 0$ on August 11–12.

The outstanding feature of the Huancayo data is the superimposed magnetic storms of August 15–20. The storm period was preceded

and followed by quiet intervals during which the horizontal component rose to its highest values (August 14–15, 26–28). The effect of the SC storm which began on August 16 is particularly noticeable.

Figure 6*c*, which is a plot of the smoothed D_{st} curve derived by Chapman and Akasofu [*Arnoldy et al.*, 1960], shows the history of the August 16 storm in greater detail. The data are averages of the horizontal component measured at 12 observatories well distributed in latitude and longitude.

The long-period variation of the storm field at the surface coincides with a similar variation at an altitude of $\sim$ 4 earth radii (24,000 km). A comparison of figures 6*a*, *b*, and *c* indicates that $B_\perp$ undergoes a main phase decrease and recovery at $\sim 4R_E$ which is essentially coincident with D_{st} at the surface. The magnitude of the main phase decrease is $\sim$140 γ at the surface and $\sim$ 360 γ at $4R_E$, that is, approximately two and one-half times as large.

Variation in the Direction of the Field during the Storm

Magnitude data ($B_\perp$) are unavailable for parts of the Explorer 6 orbit and for much of the Explorer 6 lifetime. When the satellite was at large radial distances, it was difficult to obtain good quality ground station records because of the relatively broad bandwidth requirements of the sinusoidal output signal and the low power of the radiated telemetry signal, which was significantly below the design goal. Most of the useful magnitude data were acquired by the large radio telescope at Jodrell Bank, England. Conversely, the frequency-modulated signal from the phase comparator varied slowly over the orbit, the signal bandwidth was narrow, and most of the phase data were eventually recovered.

Figure 7 shows the departure of the observed field direction from the direction of the extrapolated geomagnetic field and contrasts the departures on storm days and quiet days. The experimental measurements obtained from the magnetic field aspect indicator (or phase comparator) are shown as a function of altitude for three orbital passes. Also shown are theoretical values of the phase angle for the extrapolated geomagnetic field (φ_G).

At geocentric distances of less than 10,000–15,000 km, $\varphi = \varphi_G$ because of the "stiffness" of the geomagnetic field near the earth (i.e., a transverse disturbance field of several hundred gamma would not produce an observable change in the direction of the dipole field lines). Fortunately, the same range of angles ($150° < \varphi < 300°$) was observed near the earth and at great distances. Thus the agreement between φ and φ_G near perigee provides a check on the consistency of the aspect indicator calibration.

At large distances from the earth, where Explorer 6 was at southern geomagnetic latitudes, the phase deviation $\Delta\varphi = \varphi - \varphi_G$ was negative. On the geomagnetic equator ($\delta_M = 0$ is indicated in figures 8 through 11, and the geomagnetic latitude of the spacecraft as it traveled from 20,000 km to apogee is shown in figure 14), $\Delta\varphi$ was either zero (passes 16, 18, and 20) or slightly negative (orbits 15, 17, 19, 21, and 22).

The extent by which φ differed from φ_G depended, in part, on the trajectory of the Explorer 6 (i.e., the magnetic latitude of the spacecraft at a given altitude). There was also a time variation apparent in figure 7. Magnetic storms occurred August 17 and September 4, whereas August 27 was one of the quietest days of the month (A_p indices are included in the figure).

On August 27 and 13, $\Delta\varphi$ was smallest when, as figure 6 indicates, the horizontal intensity at the earth's surface rose to its highest value. These observations are qualitatively consistent with a decreased westward current in the magnetosphere.

Another feature of figure 7 is the occurrence of fine structure during the magnetic storms. Several distinct transients (such as those seen at 30,000 km on August 17 and 42,000 km on September 4) correlated with pulsating magnetic bays in the Antarctic [*Smith and Judge*, 1961] and transient increases in the Explorer 6 scintillator count rate. According to *Rosen and Farley* [1961], the occurrence of rapid variations in the scintillator count rate was typical of magnetically disturbed periods.

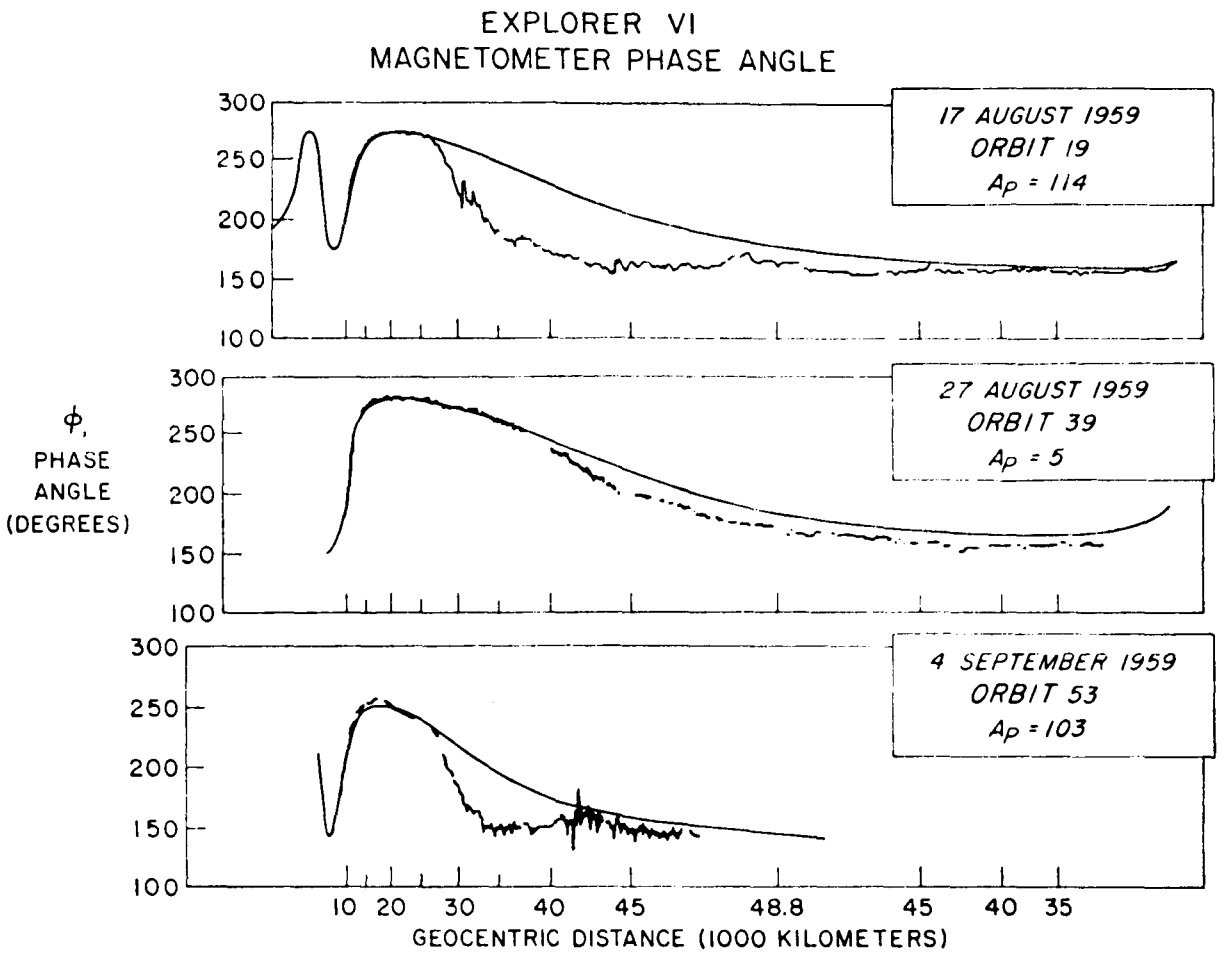

FIGURE 7.—*Phase angle data during storm and nonstorm intervals. The phase angle ϕ is shown as a function of geocentric distance for orbits on August 17 and 27 and September 4. The theoretical angle based on a spherical harmonic expansion of the surface field is also shown. August 17 and September 4 were storm days, and August 27 was the quietest day of the month. The planetary A_p indices are shown for each day. There are substantial changes in the character of the large-scale deviation, $\phi-\phi_G$, between quiet and disturbed periods. In addition, during storm periods irregular small-scale variations in ϕ are typical.*

Figures 8 through 11 contain the phase angle data for eight successive orbital passes during August 15–18. ΣK_p is the sum of the 3-hour planetary K indices during the 12-hour period corresponding to each orbital pass of Explorer 6. The altitude at which the spacecraft crossed the geomagnetic equatorial plane is denoted in each figure by $\delta_M = 0$ and an arrow (see fig. 14 for the position of the spacecraft at other geomagnetic latitudes). θ_M is an angle between $\hat{\omega}$, the Explorer 6 spin axis, and n, the normal to the local magnetic meridian plane (fig. 12). The meridian plane contains the local field direction and the center of the earth. The perpendicular to the magnetic meridian plane is given by $\hat{e}_B \times \hat{e}_R$, where $\hat{e}_B$ is a unit vector in the direction of the extrapolated geomagnetic field, and $\hat{e}_R$ is a unit vector in the direction from the earth's center to the spacecraft. The extent to which the spacecraft spin axis was rotated out of the magnetic meridian plane at different points along the trajectory is indicated by θ_M. The angle λ_s is obtained when the earth-sun vector

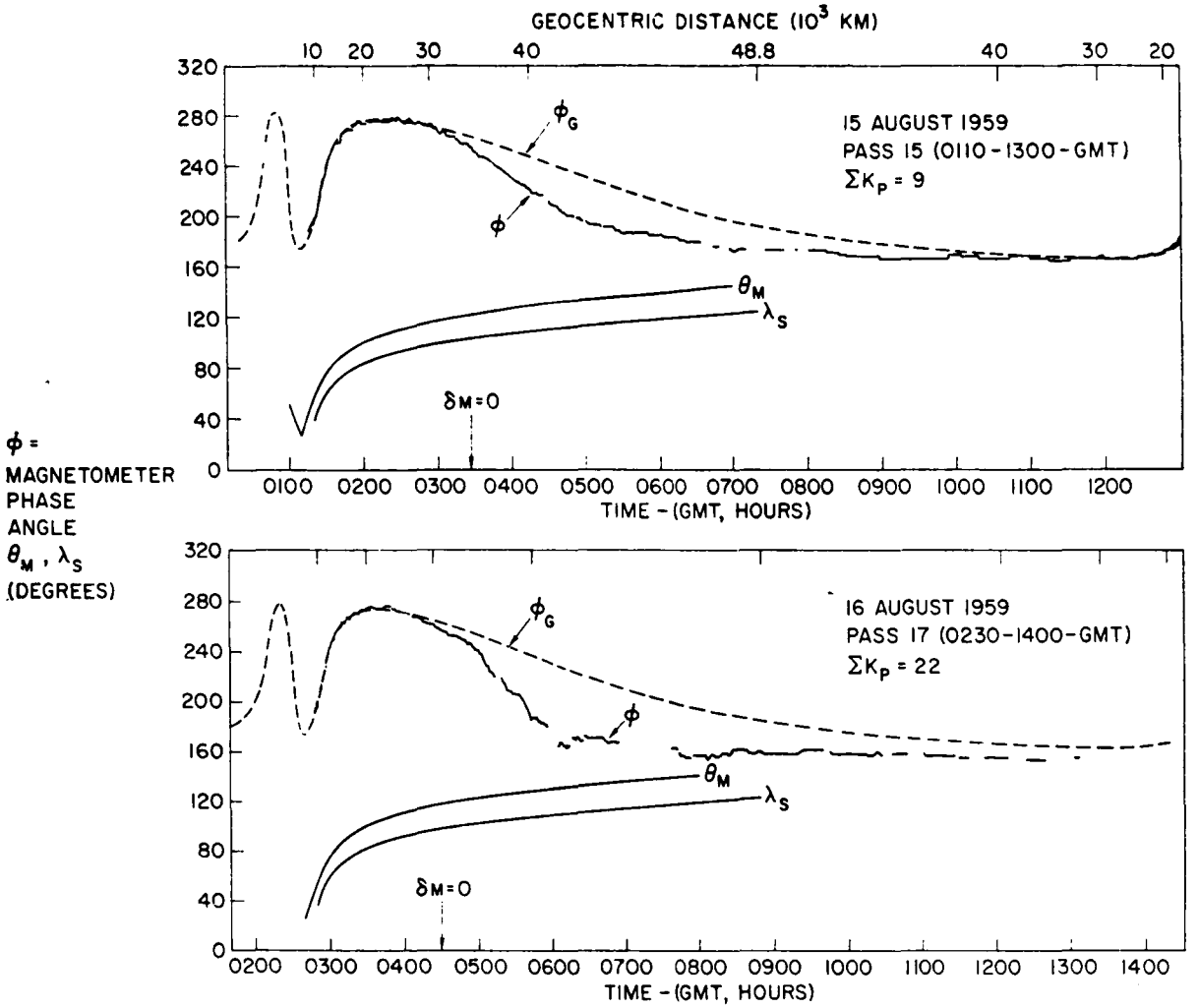

FIGURE 8.—*Phase data obtained during a magnetic storm (odd-numbered passes). The phase angle ϕ is shown as a function of geocentric distance and universal time. The theoretical phase angle for the unperturbed geomagnetic field, ϕ_G, is also shown. θ_M is the angle between the Explorer 6 spin axis and the local magnetic meridian plane (see figure 13). λ_s is the angle between the projection of the spacecraft radius and the earth-sun direction onto the geographic equatorial plane (see figure 14). The arrow marked $\delta_M = 0$ indicates where the spacecraft crossed the geomagnetic equator. Data are shown for two orbits, numbers 15 and 17 on August 15 and 16. The odd-numbered passes are presented together because their trajectories are similar in geomagnetic coordinates. ΣK_p is the sum of the planetary K indices during the 12 hours of each orbit. Note the agreement between ϕ and ϕ_G at low geocentric altitudes, which represents a calibration check on the phase comparator data at high altitudes where large deviations from the geomagnetic field direction are observed.*

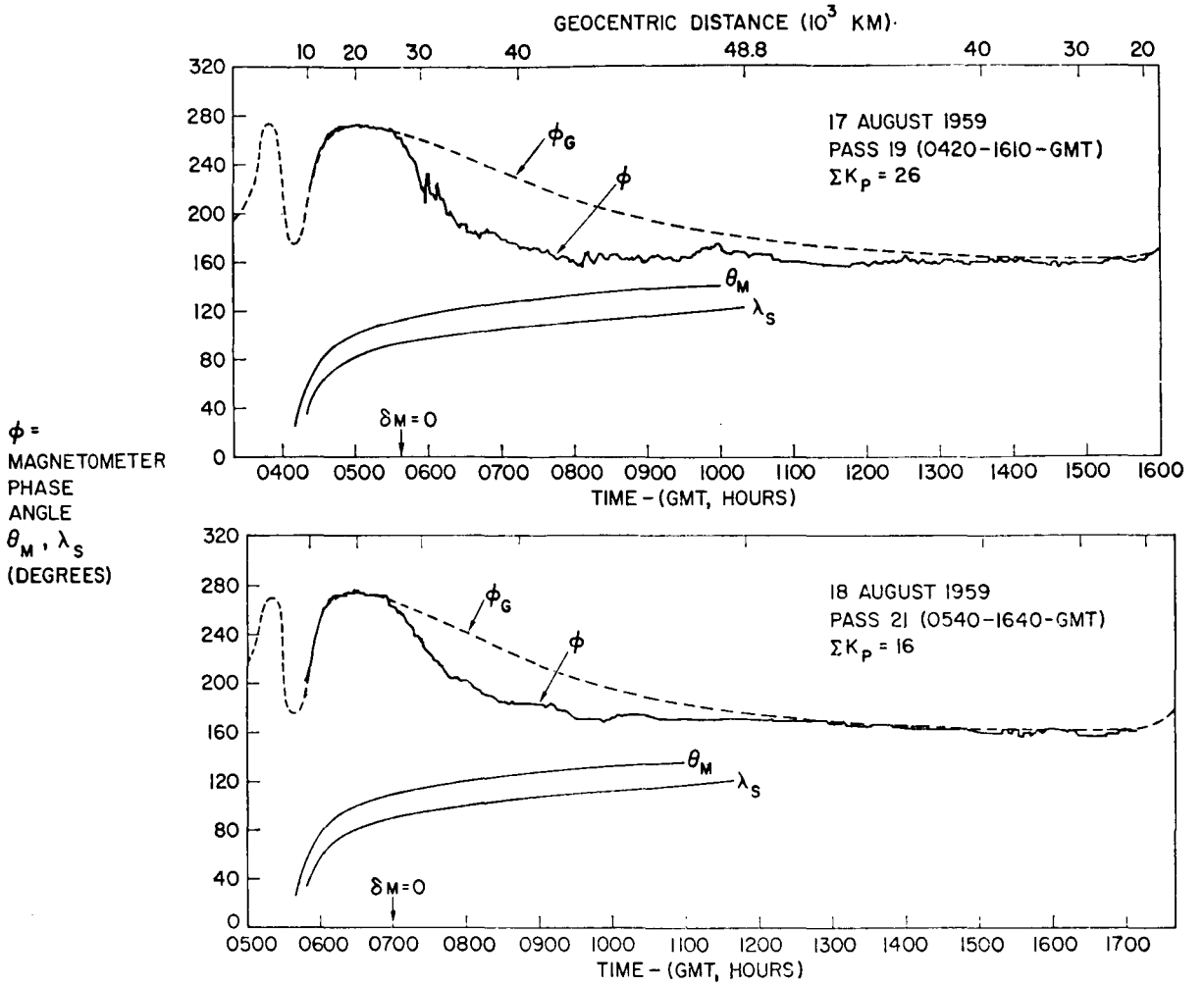

FIGURE 9.—*Phase data obtained during a magnetic storm (odd-numbered passes). The empirical phase angle and the theoretical angles presented in figure 8 are shown here for passes 19 and 21 on August 17 and 18.*

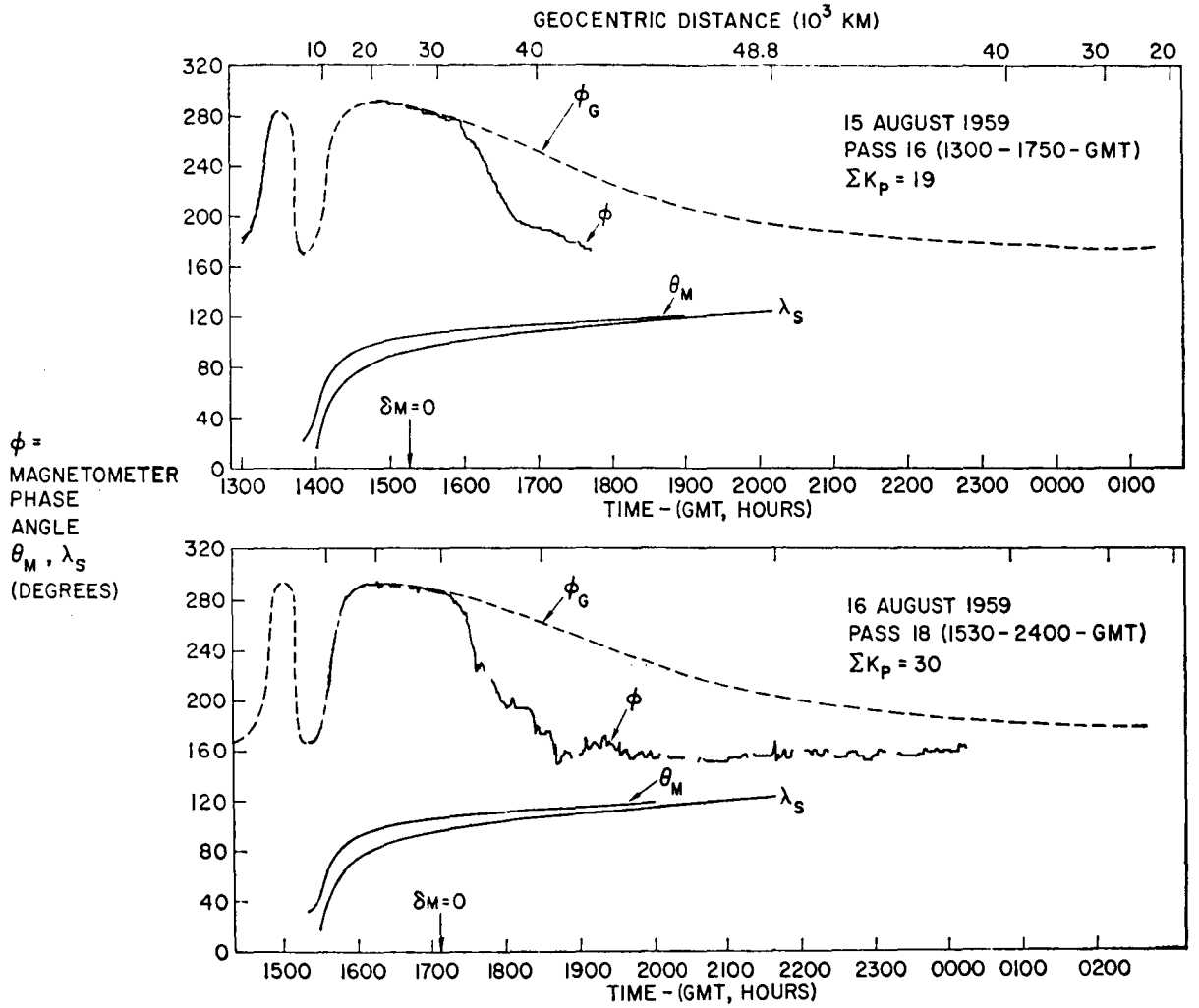

FIGURE 10.—*Phase data obtained during a magnetic storm (even-numbered passes). The phase data and theoretical angles are presented for the two even-numbered passes on August 15 and 16.*

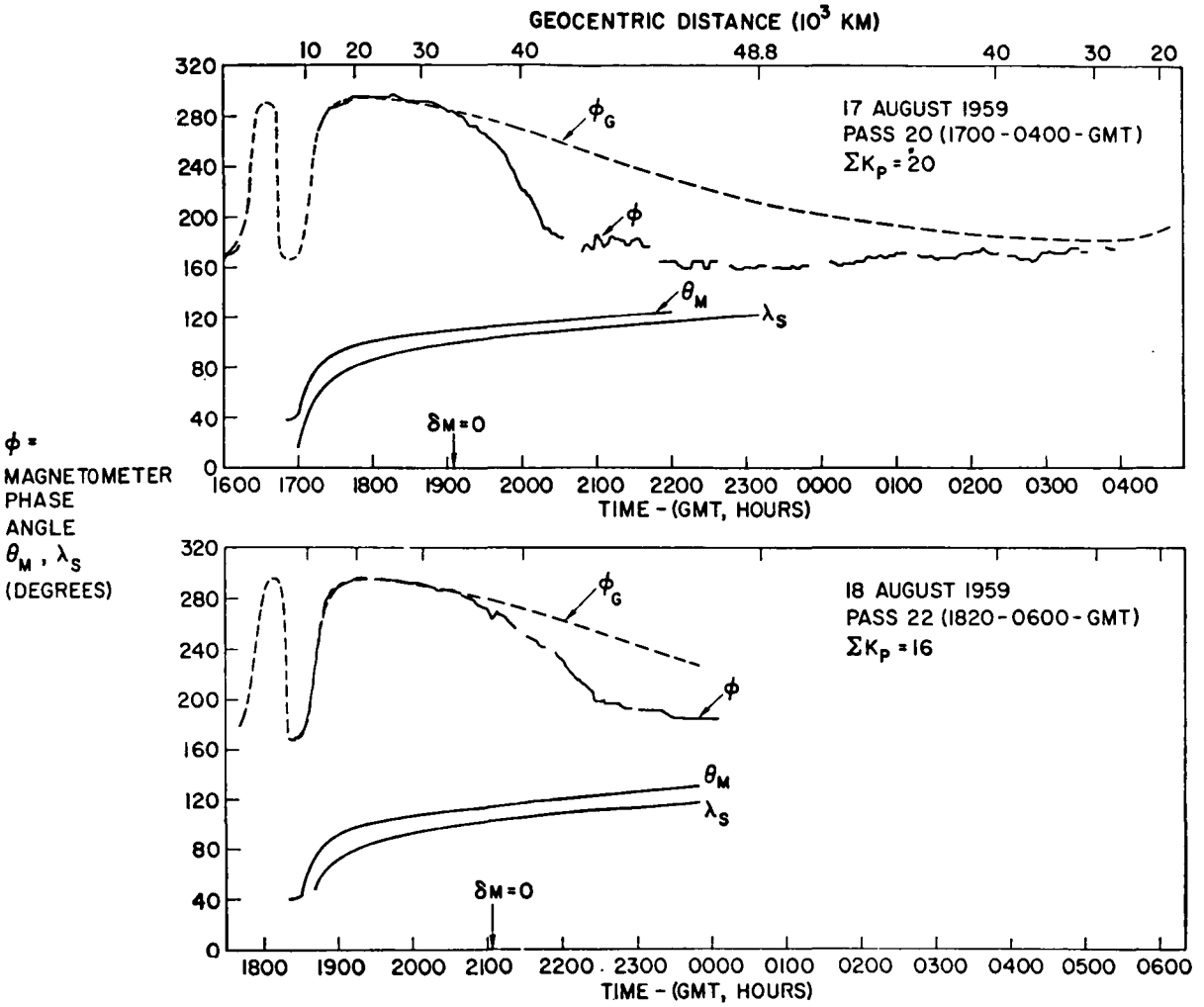

FIGURE 11.—*Phase data obtained during a magnetic storm (even-numbered passes). The phase data and theoretical angles are presented for two even-numbered passes on August 17 and 18.*

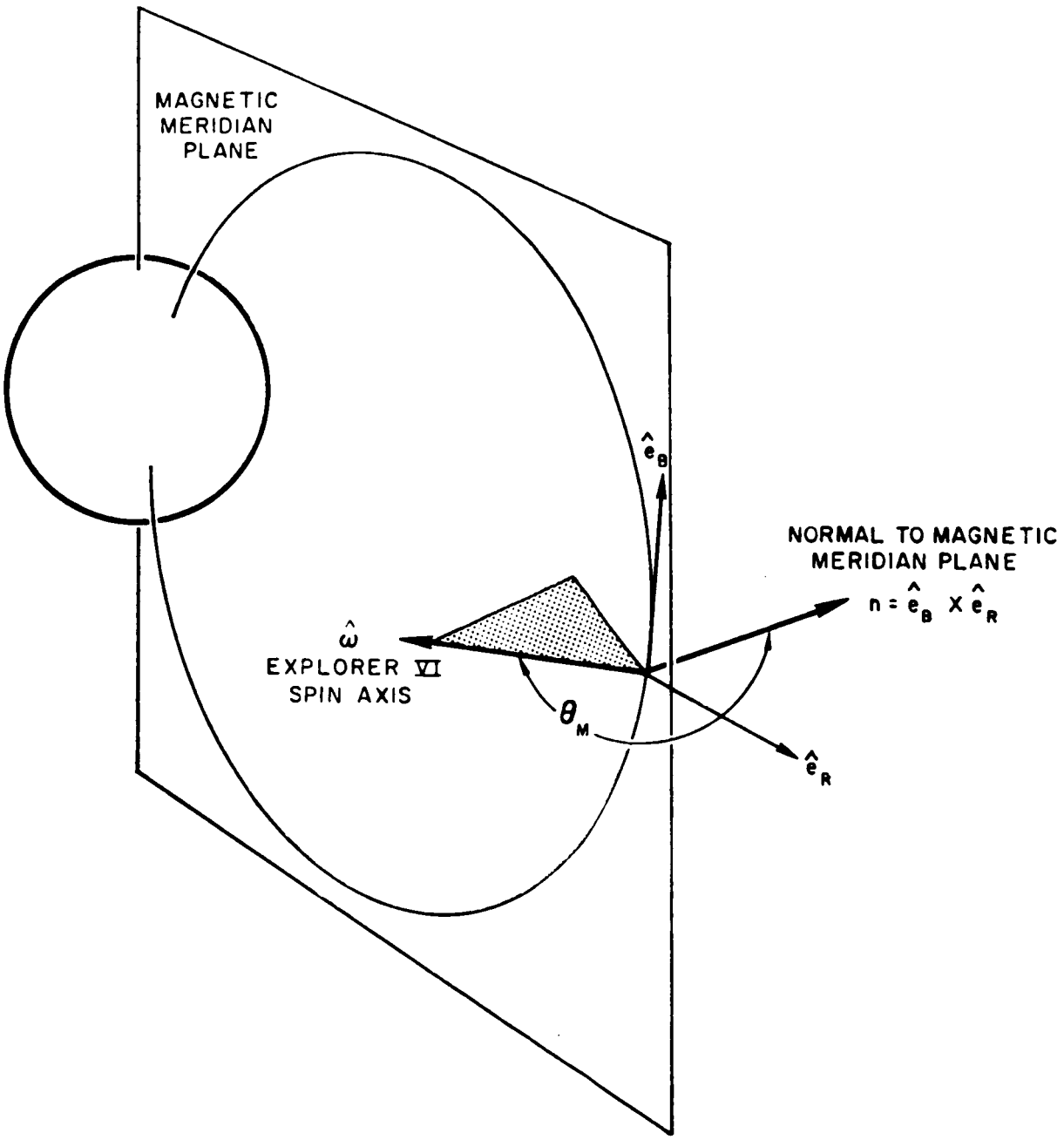

FIGURE 12.—*Representation of the angle* θ_M. *The unit vector* $\hat{e}_B$ *gives the direction of the geomagnetic field.* $\hat{e}_R$ *is a unit vector parallel to the radius vector from the center of the earth to the instantaneous position of the spacecraft.* $\hat{n}$ *is the unit normal to the local magnetic meridian plane, i.e., the plane of the geomagnetic field line.* θ_M, *the angle between the normal to the magnetic meridian plane and* $\hat{\omega}$, *the spacecraft spin axis, is useful in determining how sensitive the magnetometer is to disturbance field components lying in, or perpendicular to, the magnetic meridian plane.*

765-698 O-65—22

and the satellite radius vector are projected onto the equatorial plane (fig. 13).

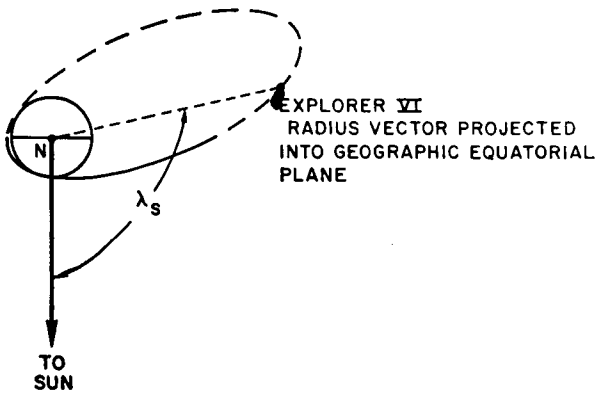

FIGURE 13.—*Representation of the angle, λ_s. The sun-earth direction and the Explorer 6 radius vector are shown when projected on the geographic equatorial plane. λ_s, the angle between these projections, gives the instantaneous position of the spacecraft with respect to the sun-earth direction. The projected Explorer 6 orbit for August 16 was used as an example. The solid part of the orbit lies above, and the dashed part below, the equatorial plane.*

As discussed earlier, the data are divided into two groups in order to minimize trajectory effects. Figures 8 and 9 contain only the odd-numbered passes which generally occurred during the first half of the Greenwich day, whereas figures 10 and 11 contain even-numbered passes. There were small progressive changes in the geomagnetic coordinates of the spacecraft at a given point on the trajectory on the odd-numbered and even-numbered orbits taken alone. In figures 14 and 15 the altitude at which δ_M was zero progressed to higher altitudes during the odd-numbered passes and to lower altitudes during the even-numbered passes.

Figures 8 through 11 show a progressive enhancement of $\Delta\varphi$ during the storm with a subsequent return to prestorm values. This can be seen if we consider a given $\Delta\varphi$ (e.g., $\Delta\varphi = -20°$), which moved toward lower altitudes during the main phase of the storm (ΣK_p increasing) and returned to higher altitudes during the recovery phase (ΣK_p decreasing).

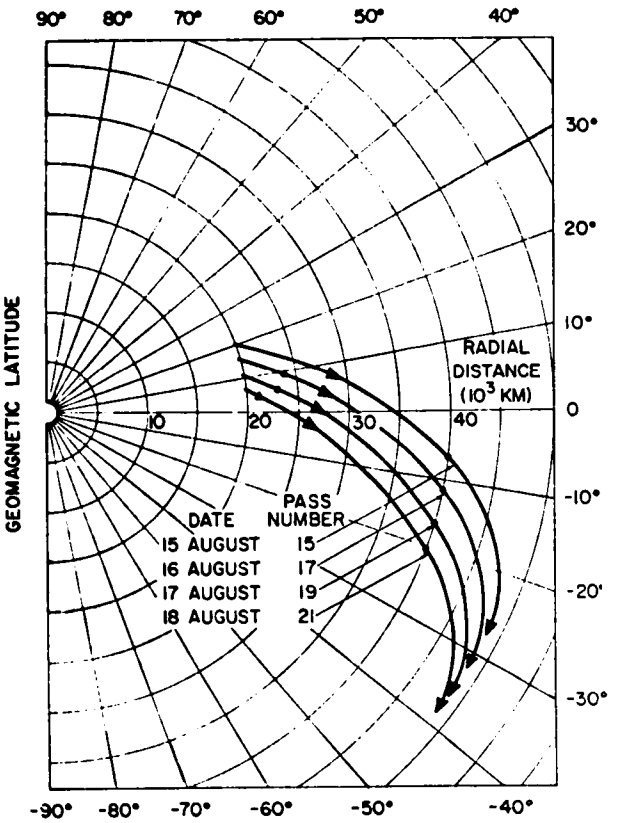

FIGURE 14.—*Geomagnetic latitude of the spacecraft (odd-numbered passes). The part of the Explorer 6 orbit between radii of 20,000 and 48,000 km is shown for passes 15, 17, 19, and 21 on August 15–18. The triangle (digital data) and circles (analog data) mark the positions at which data used in figures 6 and 16 were obtained.*

Figure 16 provides an alternative view of the variations in $\Delta\varphi$ during the storm. At the top of the figure is a plot of $\Delta\varphi$ at a given altitude (40,000 km) as a function of time. The simultaneous variation in the horizontal intensity at the earth's surface is plotted in the middle of the figure. The data are hourly mean values of H at Huancayo. The diurnal variation has been removed. At the bottom of the figure is a plot of the corresponding values of the 3-hour index K_p. The direction of the distant field was correlated with both variations in the

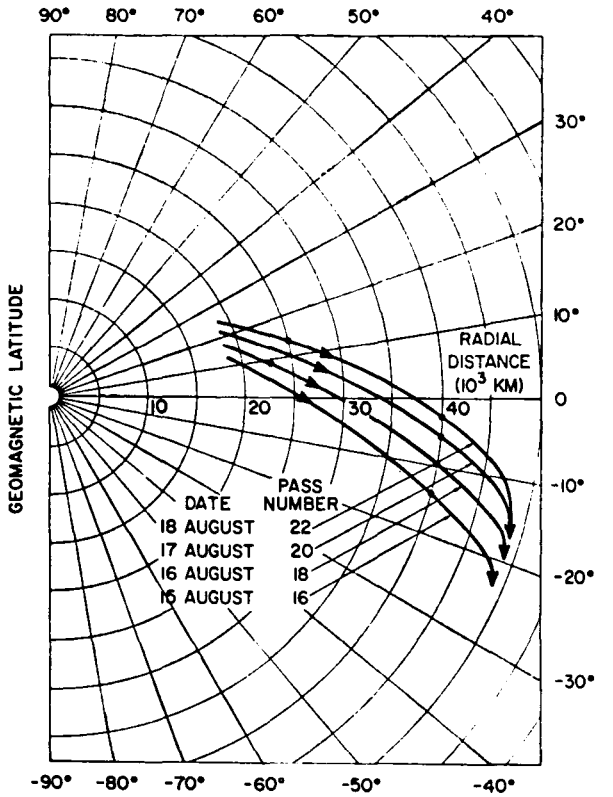

FIGURE 15.—*Geomagnetic latitude of the spacecraft (even-numbered passes). This figure contains the trajectory in spherical coordinates (geomagnetic latitude and radial distance) for passes 16, 18, 20, and 22 on August 15–18. The circles mark the location of Explorer 6 at which the data used in figures 6 and 16 were obtained.*

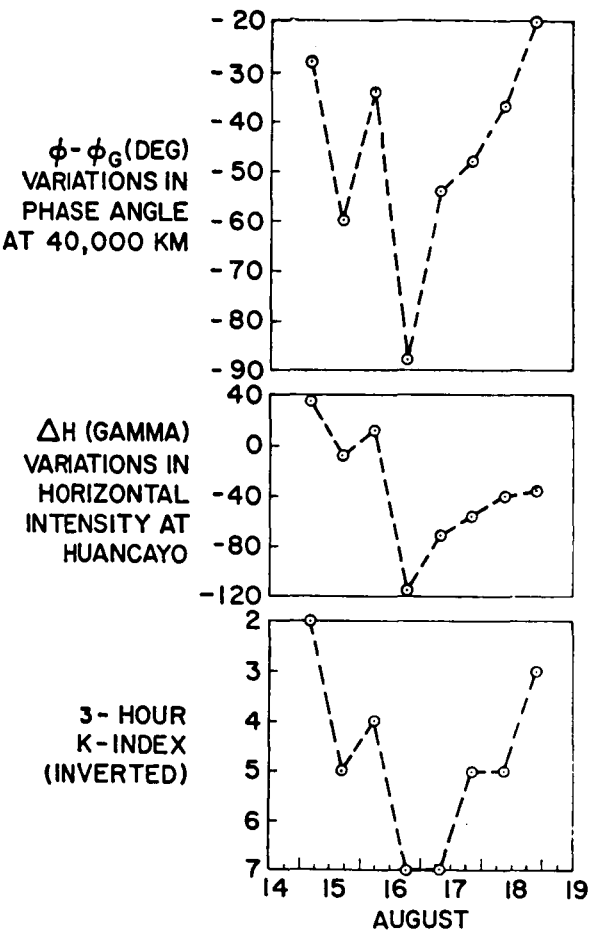

FIGURE 16.—*Temporal variation in the phase data at 40,000 km compared with the surface field.* $\phi-\phi_G$ *is the phase angle deviation, observed minus theoretical (corresponding to the unperturbed geomagnetic field).* $\phi-\phi_G$ *is shown during the storm interval August 15–18. Each Explorer 6 datum was obtained at a geocentric altitude of 40,000 km irrespective of geomagnetic latitude (see figs. 14 and 15).* ΔH *shows the variation in the average value of the horizontal component at Huancayo for the hour during which the Explorer 6 data were obtained. The three-hour* K *index, inverted so that* K *increases downward, is shown in the lower third of the figure. Note the correspondence between variations in the surface field and in the field direction at* $\sim 6.3 R_E$ *(40,000 km). Two storms are superposed. A gradual commencement storm that began August 15 was in the recovery phase when a sudden commencement storm began on August 16.*

horizontal component and the degree of agitation of the surface field.

This correlation appears to include the initial phase of the August 16 storm. However, the increase in ΔH and decrease in $\Delta\varphi$ observed during the first quarter of August 16 actually represented a superposition of two effects, the initial phase of the sudden commencement storm of August 16 and the recovery phase of the gradual commencement storm of August 15. The effect of the GC storm on the distant field can be seen in the first two data in figure 10 (August 15) and by comparing figures 8 (top) and 10 (top) (successive passes). An inspection of ground station magnetograms shows that the GC storm was of short duration. Because the

two storms overlap, it was not possible to isolate and study the effects of the initial phase of the SC storm. The subsequent data show the effect of the main phase decrease and recovery associated with the August 16 storm.

Simultaneous Variations in Field Magnitude and Peak Intensity of the Outer Radiation Zone

Figure 17*d* is the same as figure 6*a*, that is $\Delta B_\perp$ at $\sim 4R_E$. Measurements of the peak intensity of the radiation particle fluxes in the outer zone are also shown. Figures 17*a*, *b*, and *c* are the Explorer 6 data obtained by the Space Technology Laboratories scintillation counter, the University of Chicago proportional counter, and the University of Minnesota Geiger tube. Before the storm of August 16, the primary peak in the outer zone was at approximately 24,000 km, on the basis of Geiger tube data [*Arnoldy et al.*, 1960]. Thus, equatorial field measurements and Geiger tube measurements of the peak intensity occur in the same region of space and are essentially simultaneous. The peak of the outer zone as detected by the other two instruments was displaced slightly from 24,000 km [*Fan et al.*, 1960; *Rosen and Farley*, 1961].

During the main phase of the storm, there was a substantial decrease in the count rates of the University of Minnesota and University of Chicago experiments, followed by a large increase in the particle fluxes during the recovery phase of the storm. The scintillator data departed from this general tendency only during the onset of the main phase. This behavior is characteristic of the outer zone during a magnetic storm and has been observed by similar instruments on other satellites. The responses of the Explorer 6 detectors are consistent with the subsequent empirical demonstration that, with the onset of a magnetic storm, the low-energy (100 kev or less) particle flux increases at the same time that the medium- and high-energy particle fluxes are decreasing. All three components then undergo a large increase during the recovery phase of the storm [e.g., *Obrien*, 1964].

Figure 17 shows that the slow variations in particle intensity were correlated with the variations in field magnitude at $4R_E$. However, although the peak intensities in the outer zone after the storm increased by an order of magnitude, the magnetic field intensity was still somewhat less than its prestorm value.

SUMMARY

The experimental data can be summarized as follows:

1. Long-period time-dependent changes in the distance field coincided with D_{st} at the surface.
2. The magnitude of the main phase decrease in $B_\perp$ was ~ 2.5 times larger at $\sim 4R_E$ than at the surface.
3. Irregular field fluctuations, with periods exceeding one minute, were observed during the storm.
4. Variations in the direction of the field at $\sim 7R_E$ correlate with half-day variations in (*a*) the horizontal component of the surface field and (*b*) the three-hour planetary K index.
5. The large-scale perturbations of $B_\perp$ and φ during the storm were qualitatively similar to the perturbations observed previously on non-storm days.
6. The D_{st} variations in the field magnitude at $4R_E$ correlate with changes in the peak intensity of the outer radiation zone measured by three high-energy particle detectors on Explorer 6. Two detectors show a decreased intensity during the storm when the field magnitude is depressed. All three detectors recorded peak intensities that exceeded the prestorm values by an order of magnitude at the same time that the field magnitude returned to its quiescent value.

DISCUSSION

Characteristics of the Large-Scale Storm Field

The storm data at 4 to $8R_E$ and the worldwide component of the surface storm field (D_{st}) have the same time dependence. Furthermore, the variations at 1, 4, and 7 earth radii are essentially simultaneous, that is, possible time delays are much less than the characteristic period of the D_{st} variation. During the storm, the earth was immersed in a large-scale magnetic field that was manifest at the surface as the main phase decrease.

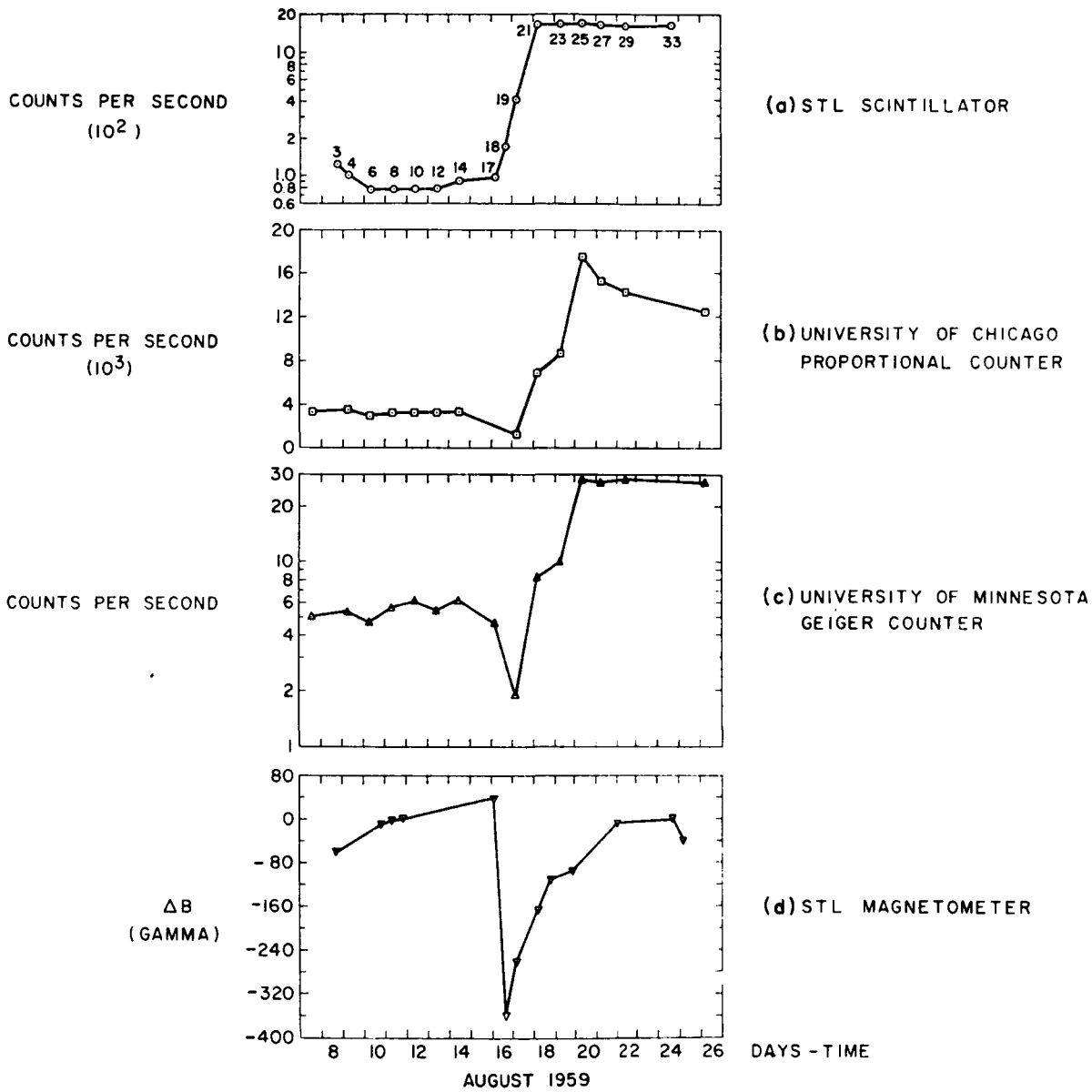

FIGURE 17.—*Comparison of equatorial magnetic field variation at $4R_E$ with simultaneous variation in the three Explorer 6 particle detectors. The time dependence of the peak counting rate per orbit of the scintillating crystal detector (STL) appears at the top. The variation in the coincidence telescope (University of Chicago) peak counting rate is shown as the next lower curve. The maximum count rate per orbit obtained by the Geiger counter (University of Minnesota) as a function of time is given by the next lower curve. The magnetometer data that appear at the bottom of the figure are the same data that appear in figure 6.*

The characteristics of the D_{st} field at the earth's surface can be described simply. The field is approximately uniform and antiparallel to the earth's axis of rotation over the entire surface.

Ideally, a complete description is desired of the magnitude and direction of the D_{st} field in the space surrounding the earth. However, a complete description is not possible from a single orbiting satellite. It is particularly difficult to distinguish between a radial dependence and a dependence on latitude or longitude when the trajectory is a highly inclined ellipse such as the Explorer 6 orbit. In addition, useful data from Explorer 6 are restricted to parts of the orbit where the magnitude of the disturbance field was at least several percent of the magnitude of the unperturbed geomagnetic field, as discussed previously. We can, however, infer several important properties of the large-scale storm field from the Explorer 6 data. Later magnetometer experiments can extend and improve this description.

We now show that near the equatorial plane at $4R_E$ the storm field (ΔB as distinct from $\Delta B_\perp$) was directed southward, was aligned with the local magnetic meridian plane, and had a magnitude of $\sim 350\,\gamma$. At 24,000 km, the angle θ_M between the spacecraft spin axis and the normal to the local magnetic meridian plane was approximately 105°. Thus, the spin axis was nearly contained in the meridian plane. Consequently, field rotations out of, or transverse to, magnetic meridian planes were readily detectable, while along this part of the orbit the phase angle was insensitive to rotations confined to magnetic meridian planes, which would leave φ equal to φ_G. The phase data (figs. 8 through 11) show that $\Delta\varphi$ did not exceed 8° during the storm. Therefore, any component of field rotation out of the magnetic meridian plane was small. The 350 γ decrease in $B_\perp$ during the main phase is consistent with a reduction in the magnitude of the field component parallel to G by a factor of approximately 2. Assuming that the field rotated without a change in magnitude implies a rotation of 60° which would produce a field with a large radial component near the equator. Such a field would differ greatly from the geomagnetic field and would correspond, for example, to an interplanetary field or a strongly deformed magnetic tail existing at 24,000 km and lying in a magnetic meridian plane. The experimental evidence discussed above, including the Explorer 6 trapped particle measurements, makes it certain that Explorer 6 was inside the geomagnetic field, particularly at 24,000 km. Therefore, it seems reasonable to conclude that the decrease in $B_\perp$ is primarily a decrease in magnitude, that B and G were parallel near the equator, and that $\Delta B(t)$ *in figure 6 is approximately the magnitude of the time-varying storm field near the geomagnetic equatorial plane.* Small deviations in field direction cannot be ruled out but are not an essential feature in view of the arguments presented here.

Ring Current

The disturbance observed during the storm is very suggestive of a ring current. To understand why the evidence is inconclusive, it is instructive to consider what observations would be needed for rigorous detection of this current. To deduce the current from measurements of the magnetic field, it is necessary to obtain $\oint \mathbf{B}\cdot d\mathbf{S}$ round a closed curve, thus giving the current through that closed curve. Not only does Explorer 6 lack one component of **B**, but no single satellite moves in a closed curve that is really suitable for this purpose. One possibility might be to use two satellites whose orbits are nearly coplanar and to compute the current through the lines between their orbits. In any event, quite accurate magnetic measurements would be needed. Here, then, we must be content to compare the observed field with that predicted for a ring current.

The ring current predicted is caused by trapped particles and can be regarded as arising either from their anisotropic pressure distorting the field hydromagnetically or from a combination of their drifts and diamagnetic effect. The latter is similar to pressure and causes an important depression of the field strength where the pressure is high, roughly according to pressure balance between particles and field. *Davis and Williamson* [1963] have observed a population of trapped protons having a pressure substantially higher than

that of other known trapped particles. For $L > 4$ they found the pressure to be about one-tenth that of the magnetic pressure during quiet times, and they found that pressure increased by a factor of 3 during one storm. *Akasofu* [1963] has reviewed ring current theory and estimated the effect of the protons observed by Davis and Williamson. Whereas the disturbance at the ground corresponds to a westward current, the current due to trapped particles is eastward on the inner side of the particle distribution where the particle pressure is increasing with L. The westward current flows on the outer side, and the resulting disturbance is illustrated by Akasofu's computations. He obtains for storm conditions in the equatorial plane a depression of 100 γ at the ground, a maximum depression of somewhat more than 200 γ between $L = 3$ and 4, and a slight strengthening of the field beyond $L = 6$. The greater depression at $L = 4$ than at the ground is in qualitative agreement with data from Explorer 6 and is due to the eastward current close in. The lack of detailed agreement could arise as follows. First, only protons of > 100 kev were observed by Davis and Williamson, and softer protons might be important. Since the observed proton pressure went up to one-third of the magnetic pressure, the pressure of softer particles could hardly be a dominant proportion, but it could change the maximum field depression from 220 γ to, say, 350 γ. Second, the storm observed by Explorer 12 was of course not the same as that observed by Explorer 6, and substantial differences between different storms seem to be allowable. Third, Akasofu's calculation is not self-consistent. Finally, should the ring current be incapable of accounting fully for the observed disturbance on the trajectory of Explorer 6, the field farther out is known to be distorted in a quite different way. This distortion is not symmetric about the geomagnetic axis, but, for the late evening meridian of Explorer 6, there is some similarity with the changes of φ observed near apogee; this distortion will now be discussed briefly.

Distortion of the Field in the Outer Magnetosphere

The solar wind, now certified by Mariner [*Neugebauer and Snyder*, 1962], distorts the magnetosphere. Many theoretical studies of this distortion have been published [e.g., *Midgley and Davis*, 1963]; most have neglected any interplanetary magnetic field, though some have considered it [e.g., *Dungey*, 1963]. Observations of this distortion were obtained from Explorers 10, 12, and 14. For comparison with Explorer 6, Explorers 10 and 14 are most relevant, having apogee in the evening direction. *Heppner et al.* [1963] found a boundary far out, but for the first 15 earth radii the field strength gradually exceeded the dipole value while the direction gradually swung around and pointed away from the earth (the apogees of Explorers 6, 10, and 14 were south of the equatorial plane). *Cahill* [1964] has published the results of two successive passes of Explorer 14 near the midnight meridian that are separated by 36 hours. There was a magnetic storm two days before the first pass. On the first pass the field strength was depressed from 4 to 8 radii by a roughly constant amount, $\sim$ 25–50 γ; farther out the field strength remained at $\sim$ 50–75 γ right out to apogee at 16 radii. On the second pass, there was no depression and the field strength settled at 30–50 γ from 10 radii out to apogee. On both passes the direction swung around and settled pointing away from the earth, the swing occurring between 7 and 9 radii on the first pass and between 9 and 11 radii on the second pass. It is this change in direction observed by Explorer 10 and by Explorer 14 which resembles the change in field direction observed by Explorer 6 near apogee (Cahill also found this change of direction on passes of Explorer 14 for which data have not been published). The far field near the noon meridian was observed by Explorer 12 [*Cahill and Amazeen*, 1963] and behaves entirely differently, demonstrating that the distortion is quite asymmetric and therefore not due to a ring current alone.

The observations seem to fit Dungey's model, though further measurements are required to fill in the picture. The outstanding features in this theoretical model are two concentrated current sheets, in both of which the current flows in the direction opposite to the orbital motion of the earth, the return current not being concentrated in sheets. One sheet is on the

day side, is oriented normal to the direction of the sun, contains current flowing eastward, and has been found by Explorer 12. The other is on the night side, oriented roughly in the equatorial plane, contains current flowing westward, and has not yet been found. The existence of the latter current sheet is, however, consistent with the observations far out and south of the equatorial plane. Because the sheet current is westward, the effect at 6 radii is hard to distinguish from the effect of a ring current, and the nature of the distinction needs consideration.

Distinction Between the Ring Current and Distortion by the Solar Wind

It has been stated that the ring current can be derived from the balance between the anisotropic pressure of the trapped particles and the force density $j \times B/c$. The distortion by the wind is derived by consideration of the plasma flow resulting from the imbalance between these same forces, but only a qualitative theoretical picture has yet been obtained. However, this shows that the two effects cannot be distinguished rigorously in terms of physical mechanisms, and this is true a fortiori if the trapped particles originate from the solar wind, as seems likely because of their storm-time variation. The distinction can then only be geometrical. The axial symmetry of the ring current contrasts with the asymmetry of the observed field far out, and it is clear that the relative importance of the wind distortion increases with the distance from the earth. Both disturbances are established beyond reasonable doubt, but it will never be easy to rigorously separate the two.

ACKNOWLEDGMENTS

We want to express our appreciation to our colleagues, P. J. Coleman, Jr., who was involved in the initial effort to reduce the phase data, K. Moe for his careful refinement of the Explorer 6 trajectory, Professor J. A. Simpson and Professor J. Winckler for making ground station and satellite data available to us, and Dr. A. J. Dessler and Dr. R. C. Wentworth for many helpful discussions regarding ring current theory.

We are grateful to Space Technology Laboratories, Inc., and particularly to Dr. Rosen and the Space Physics Department for their cooperation and assistance in the performance of this task. Technical assistance was provided by J. Kinsey, N. Lyke, and G. Komatsu of the Space Physics Department and by I. Kliger and P. Lipinski of the Computation and Data Reduction Center.

This work was supported financially by the National Aeronautics and Space Administration under contract NASw-270.

REFERENCES

Akasofu, S.-I., Deformation of magnetic shells during magnetic storms, *J. Geophys. Res.*, *68*, 4437–4445, 1963.

Akasofu, S.-I., J. Cain, and S. Chapman, The magnetic field of a model radiation belt, numerically computed, *J. Geophys. Res.*, *66*, 4013, 1961.

Akasofu, S.-I., and S. Chapman, The ring current, geomagnetic disturbance, and the Van Allen belts, *J. Geophys. Res. 66*, 1321, 1961.

Apel, J. R., S. F. Singer, and R. C. Wentworth, Effects of trapped particles on the geomagnetic field, in *Advances in Geophysics*, vol. 9, edited by H. E. Landsberg and J. Van Miegham, pp. 132–188, Academic Press, New York, 1962.

Arnoldy, R. L., R. A. Hoffman, and J. R. Winckler, Observations of the Van Allen radiation during August and September 1959, part 1, *J. Geophys. Res.*, *65*, 1361, 1960.

Cahill, L. J., Jr., Preliminary results of magnetic field measurements in the tail of the geomagnetic cavity, in press, 1964.

Cahill, L. J., and P. G. Amazeen, The boundary of the geomagnetic field, *J. Geophys. Res.*, *68*, 1835–1843, 1963.

Coleman, P. J., C. P. Sonett, D. L. Judge, and E. J. Smith, Some preliminary results of the Pioneer 5 magnetometer experiment, *J. Geophys. Res.*, *65*, 1856, 1960.

Davis, L. R., and J. M. Williamson, Low energy trapped protons, in *Space Research, Proc. Intern. Space Sci. Symp., 3rd, Washington, 1962*, pp. 365–375, North-Holland Publishing Company, Amsterdam, 1963.

Dungey, J. E., Null point in space plasmas, paper presented at Symp. Plasma Space Sci., Catholic University of America, June 11–14, 1963.

Fan, E. Y., P. Meyer, and J. A. Simpson, Trapped and cosmic radiation measurements from Explorer 6, in *Space Research, Proc. Intern. Space Sci. Symp., 1st, Nice, 1960*, edited by H. Kallmann-Bijl, p. 951, North-Holland Publishing Company, Amsterdam, 1960.

Heppner, J. P., N. F. Ness, C. S. Scearce, and T. L. Skillman, Explorer 10 magnetic field measurements, *J. Geophys. Res., 68*, 1–46, 1963.

Heppner, J. P., J. D. Stolarik, I. R. Shapiro, and J. C. Cain, Project Vanguard magnetic field instrumentation and measurements, in *Space Research, Proc. Intern. Space Sci. Symp., 1st, Nice, 1960*, edited by H. Kallmann-Bijl, p. 982, North-Holland Publishing Company, Amsterdam, 1960.

Judge, D. L., A. R. Sims, and M. G. McLeod, The Pioneer 1, Explorer 6, and Pioneer 5 high sensitivity transistorized search coil magnetometer, *IRE Trans. Space Electron. Telemetry, 6*, 114, 1960.

Krassovsky, V. I., Results of scientific investigations made by Soviet sputniks and cosmic rockets, *Astronaut. Acta, 6*, 32, 1960.

Lincoln, J. V., Geomagnetic and solar data, *J. Geophys. Res., 65*, 788, 1960.

Midgley, J. E., and L. Davis, Jr., Calculation by a moment technique of the perturbation of the geomagnetic field by the solar wind, *J. Geophys. Res., 68*, 5111–5123, 1963.

Neugebauer, M., and C. W. Snyder, The solar plasma experiment (in Mariner 2), *Science, 138*, 1095–1097, 1962.

Obrien, B. J., High latitude geophysical studies, with satellite Injun 3, part 3, *J. Geophys. Res., 69*, 13, 1964.

Rosen, A., and T. A. Farley, Characteristics of the Van Allen radiation zones as measured by the scintillation counter on Explorer 6, *J. Geophys. Res., 66*, 2013–2028, 1961.

Smith, E. J., A comparison of Explorer 6 and Explorer 10 magnetometer data, *J. Geophys. Res., 67*, 2095, 1962.

Smith, E. J., P. J. Coleman, D. L. Judge, and C. P. Sonett, Characteristics of the extraterrestrial current system: Explorer 6 and Pioneer 5, *J. Geophys. Res., 65*, 1858, 1960.

Smith, E. J., and D. L. Judge, Transient variations in the extraterrestrial magnetic field (abstract), *J. Geophys. Res., 66*, 2562, 1961.

Smith, E. J., and C. P. Sonett, Satellite observations of the distant field during magnetic storms: Explorer 6, *Proc. Intern. Conf. Cosmic Rays Earth Storm, Kyoto, Sept. 1961, J. Phys. Soc. Japan, 17*, 17, 1962.

Sonett, C. P., D. L. Judge, and J. M. Kelso, Evidence concerning instabilities in the distant geomagnetic field: Pioneer 1, *J. Geophys. Res., 64*, 941, 1959.

Sonett, C. P., D. L. Judge, A. R. Sims, and J. M. Kelso, A radial rocket survey of the distant geomagnetic field, *J. Geophys. Res., 65*, 55, 1960.

Sonett, C. P., E. J. Smith, D. L. Judge, and P. J. Coleman, Current systems in the vestigial geomagnetic field: Explorer 6, *Phys. Rev. Letters, 4*, 161, 1960.

Sonett, C. P., E. J. Smith, and A. R. Sims, Surveys of the distant geomagnetic field: Pioneer 1 and Explorer 6, in *Space Research, Proc. Intern. Space Sci. Symp., 1st, Nice, 1960*, edited by H. Kallmann-Bijl, p. 921, North-Holland Publishing Company. Amsterdam, 1960.

Vestine, E. H., Lines of force of the geomagnetic field in space. *Planetary Space Sci., 1*, 285, 1959.

(Manuscript received January 30, 1964;
revised March 18, 1964)

Characteristics of the Extraterrestrial Current System: Explorer VI and Pioneer V[1]

BY E. J. SMITH,[2] P. J. COLEMAN,[3] D. L. JUDGE, AND C. P. SONETT[4]

Space Technology Laboratories, Inc.

The purpose of this note is to present some of the characteristics of the current system discovered by Explorer VI. These currents are located at altitudes beyond 6 earth radii and thus lie outside the Van Allen radiation zones. The presence of the current system gives rise to a major large-scale perturbation of the distant geomagnetic field. It was on the basis of this field perturbation, which was observed by the Explorer VI magnetometer, that the existence of this current was established. In earlier work which has been published [*Sonett and others*, 1960*a*, *b*], it has been shown that the currents have the following characteristics. They (1) are a persistent feature of the distant field and occur on both magnetically quiet and magnetically disturbed days; (2) tend to be localized spatially, perhaps in the form of a toroidal ring; (3) show a time variation; (4) probably do not represent termination of the geomagnetic field (which appears to take place beyond 10 R_e); and (5) have a total magnitude which is probably of the order of 10^6 amperes.

These conclusions were based on a preliminary examination of the geomagnetic field deviations associated with the current. In order to establish the characteristics of the current system itself, a model has been hypothesized and the resultant field consisting of the geomagnetic and perturbation field has been computed. These calculations have been compared with the observed field in order to (1) test the applicability of the model and (2) evaluate the parameters of the current system which best fit the data. The purpose of the present discussion is to present some preliminary, but interesting, results of these model calculations.

The search coil magnetometer measures the component of B perpendicular to the spin axis of the payload, designated $|B_\perp|$ [*Sonett and others*, 1960*c*]. In addition there is a related experiment in the payload which provides information on the *direction* of the field component perpendicular to the spin axis. This consists of an aspect indicator which measures the angle, Φ, between $\overline{B}_\perp$ and the vector from the vehicle to the sun projected into the vehicle's equator.

Figure 1 represents the characteristic results from these two experiments obtained along the outward branch of an orbital pass. $|B_\perp|$ and Φ are shown as a function of geocentric altitude. In addition to the data points, heavy curves are shown representing theoretical values of the extrapolated geomagnetic field. The data represent an actual comparison between the absolute experimental values and the theoretical calculations (based on a spherical harmonic expansion of the earth's field as measured at the surface). This figure shows clear evidence in both measurements of the perturbation of the distant field. Figure 2 presents an expanded view of the region of interest (actually the data

---

[1] Presented at the Washington Meeting, American Geophysical Union, Session on Planetary Sciences, April 27–30, 1960. Published in the June 1960 issue of *Journal of Geophysical Research*. Reprinted by permission.

[2] Now at Jet Propulsion Laboratory.

[3] Now at Inst. of Geophysics, Univ. of Calif. at Los Angeles.

[4] Now at NASA Ames Research Center.

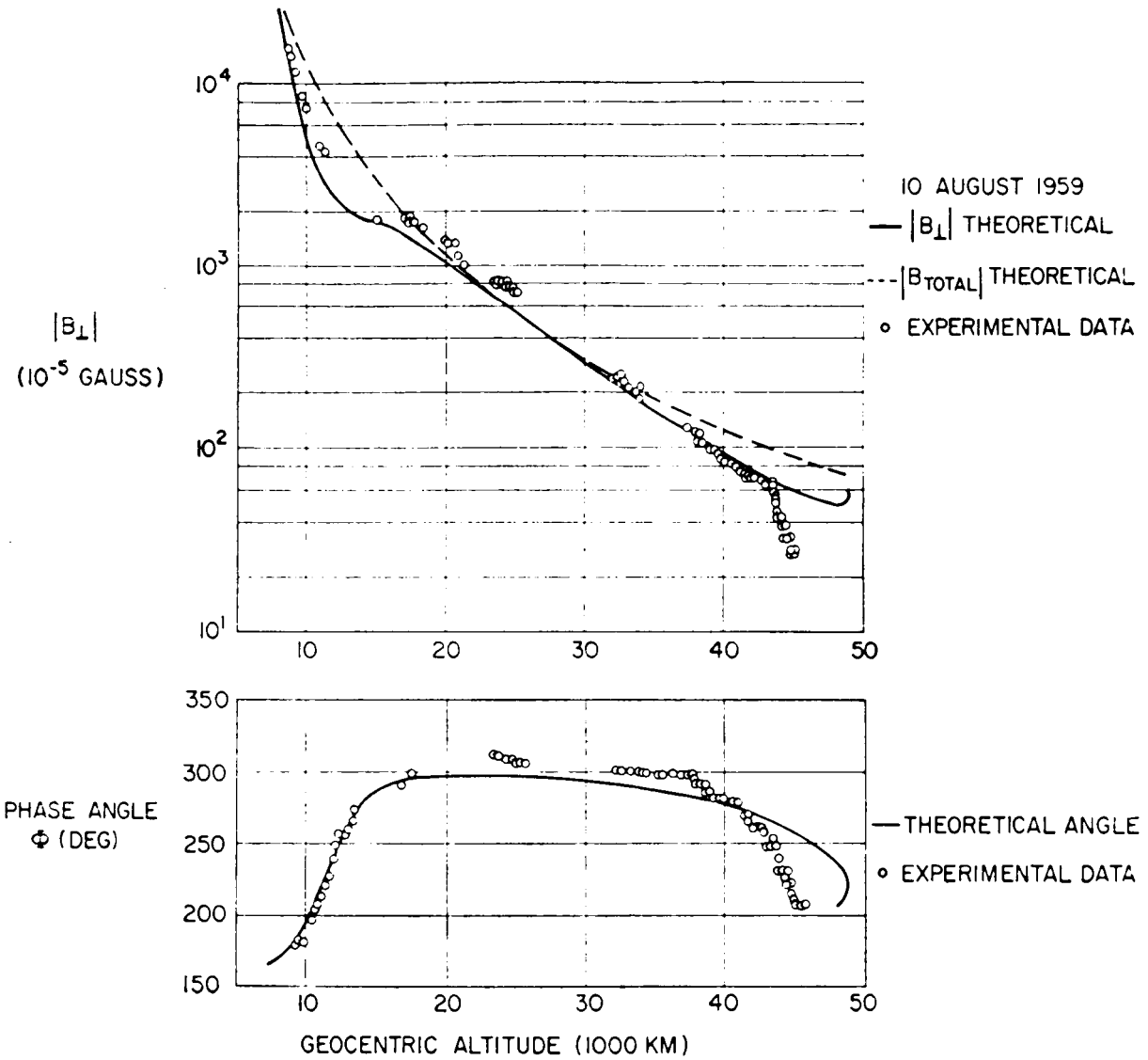

FIGURE 1.—*The extraterrestrial field as a function of geocentric altitude.*

were taken 25½ hours earlier than those shown in fig. 1).

Explorer VI provided two kinds of telemetered data. The magnetometer signal (a sinusoid at the spin frequency of the payload whose amplitude is proportional to $|B_\perp|$) modulated a subcarrier oscillator whose output was telemetered to the ground as a direct analog signal. The magnetometer signal also went to a digital-telemetry-unit ("telebit"), where the analog signal was converted into a digital signal. A binary "word" (or number) was continuously stored in a memory unit. The memory unit was sampled periodically, and the digital word was telemetered to the ground stations. The use of these two calibrated outputs provided a check on the quality and accuracy of the telemetered data.

As digital data obtained simultaneously with the analog data have been included in figure 2, the two output signals may be compared. The length of the vertical line associated with the digital data represents the maximum uncertainty in the measurement as a consequence of digit-

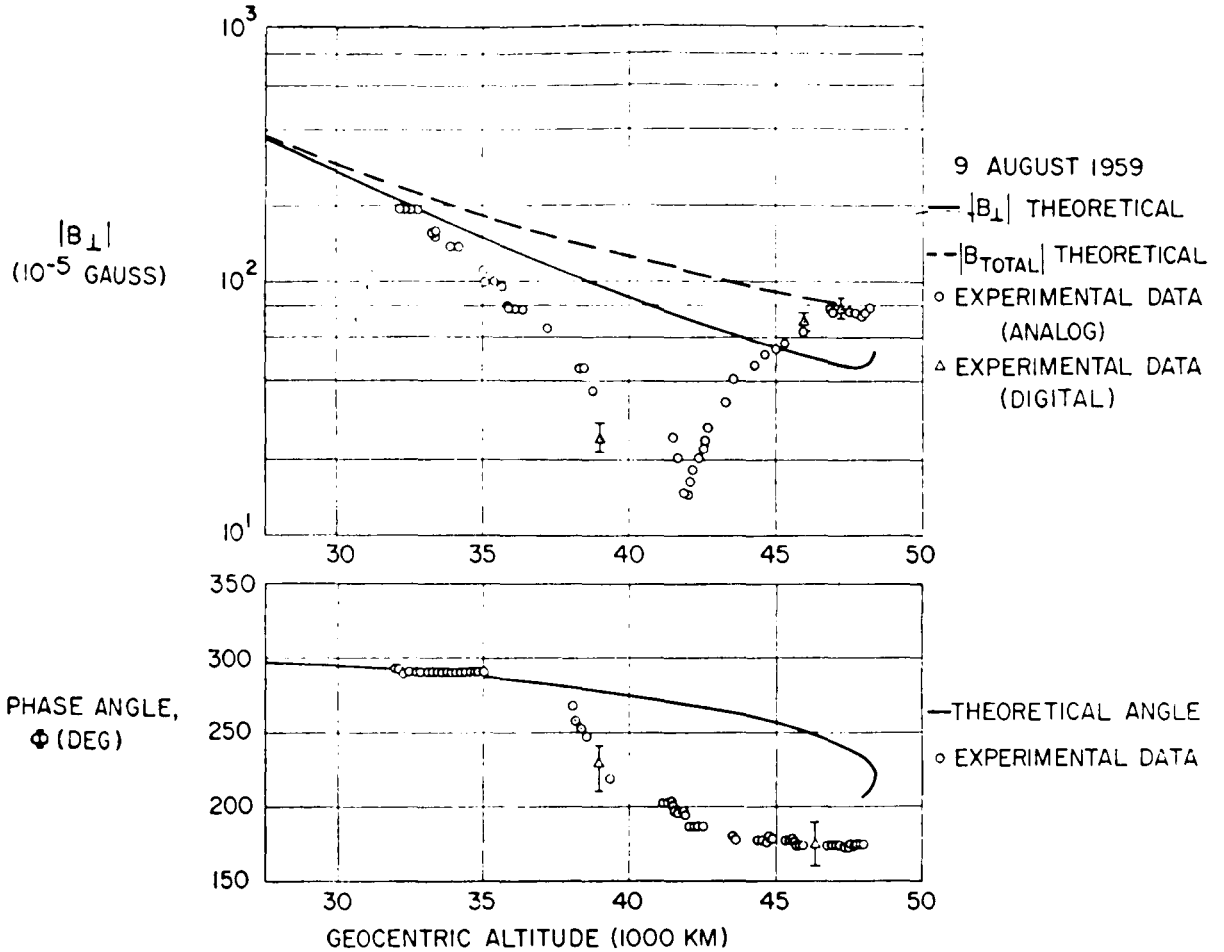

FIGURE 2.—*Field amplitude and phase angle in the deviation region.*

ization. There is substantial agreement between the two results.

Figure 3 presents the essential features of the model calculation diagrammatically. The assumptions involved are the following: (1) The current volume is cylindrical in shape with a circular cross section of radius a. (2) The center of the current cylinder is located at a distance R_0 from the center of the earth and lies in the geomagnetic equator. (3) The total current has a magnitude I which is uniformly distributed throughout the volume and flows westward.

One analog of such a model would be a circular current enclosing the earth as envisaged long ago by *Störmer* [1911] and by *Chapman and Ferraro* [1941]. This approach to the problem is essentially phenomenological; there is no consideration of the microscopic motion of particles. The utility of such a simple model lies in simplifying the calculations of the perturbation field due to the current. On the basis of individual particle motion in the inhomogeneous magnetic field, it has previously been suggested that such a model is physically meaningful [*Singer*, 1957], though we considered it significant that ∇B shows gross changes, thus raising a question as to the applicability of the Alfvén perturbation theory.

The calculations are complicated by the necessity of specifying the trajectory of the payload and the fact that the magnetometer detects a rather arbitrary component of the magnetic field which depends on the orientation

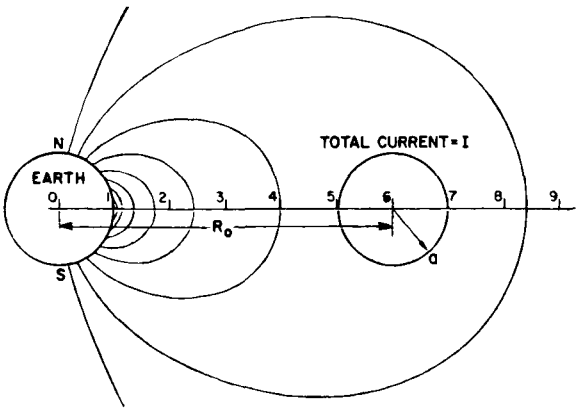

FIGURE 3.—*The ring-current model. Refer to text for proper values of* R_0 *and* a.

of the spin axis in space. The calculations were programmed for a computer as follows:

At a given point along the trajectory: (1) the perturbation field due to the current was computed; (2) it was added vectorially to the geomagnetic field obtained from the same spherical harmonic expansion as was used previously; (3) both the net $|B_\perp|$ and Φ were computed.

The results of these calculations are presented in figure 4. A close fit to the experimental data is obtained for the following values of the parameters

$R_0 = 60.10^3$ km ($\simeq 10\ R_e$)
$I = 5.10^6$ amperes
$a = 3\ R_e$ or less (no penetration of the current by Explorer VI on this day)

The region of space being sampled by the Explorer VI payload lies on the evening side of the earth at about 2100 hours local time. Clearly, it is desirable to sample a different region of space to determine the gross characteristics of the current system. This is particularly important as far as it relates to closure of the current system and to the establishment of whether or not the perturbations are due to a toroidal ring current. Such an opportunity was provided by Pioneer V, which carried a similar magnetometer and which passed through the geomagnetic field on the afternoon side of the earth.

Figure 5 presents the sampled, digital field

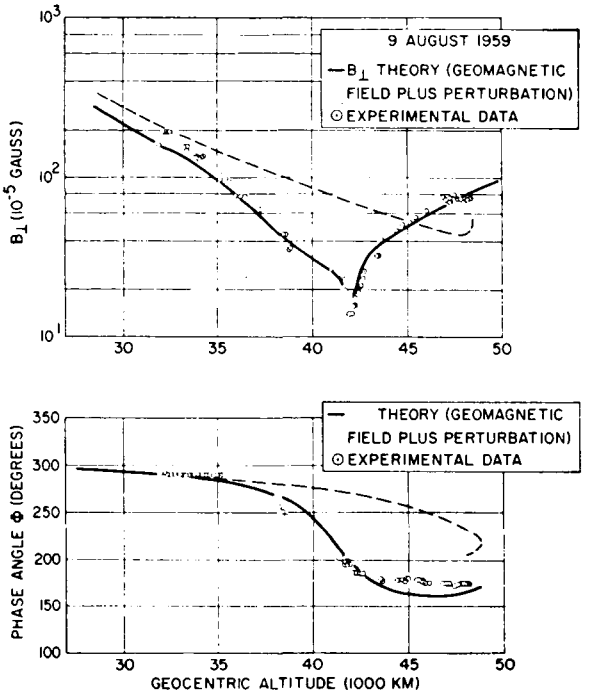

FIGURE 4.—*Comparison between the results of the model calculation and Explorer VI data. Dashed lines are unperturbed parameter values.*

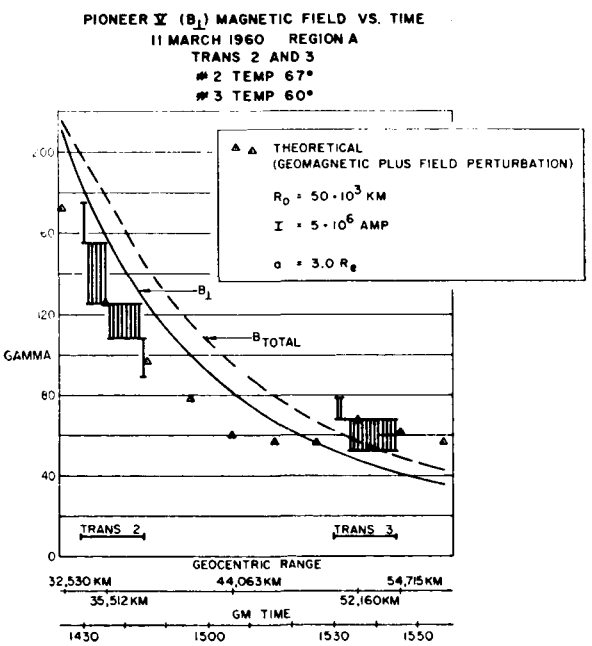

FIGURE 5.—*Comparison between the results of the model calculation and Pioneer V data.*

measurements obtained during the early part of the Pioneer V flight through the geomagnetic field. Also shown are the results of the model calculation using the following parameters:

$$R_0 = 50{,}000 \text{ km}$$
$$I = 5.10^6 \text{ amp}$$
$$a = 3\ R_e$$

An important feature of the agreement is the fact that the data cannot be adequately fit for values of a less than 3. Therefore, this establishes the minimum cross section of the ring at this time, just as the data in Figure 5 set an upper bound of 3 earth radii at the time those measurements were made.

It is considered that the close agreement with the model and the similarity of the values of the parameters in these two regions of space strongly suggest the existence of a ring current around the earth at altitudes of approximately 10 earth radii.

ACKNOWLEDGMENT

Supported by the National Aeronautics and Space Administration.

REFERENCES

Chapman, S., and V. C. A. Ferraro, The geomagnetic ring current, *Terrest. Magnetism and Atmospheric Electricity, 46*, 1–6, 1941.

Singer, S. F., A new model of magnetic storms and aurorae, *Trans. Am. Geophys. Union, 38*, 175, 1957.

Sonett, C. P., E. J. Smith, D. L. Judge, and P. J. Coleman, Jr., Current systems in the vestigial geomagnetic field: Explorer VI, *Phys. Rev. Letters, 4*, 161–163, 1960*a*.

Sonett, C. P., E. J. Smith, and A. R. Sims, Surveys of the distant magnetic field: Pioneer I and Explorer VI, *Proc. First Intern. Space Sci. Symposium*, 1960*b*.

Sonett, C. P., D. L. Judge, J. M. Kelso, and A. R. Sims, A radical rocket survey of the distant geomagnetic field, *J. Geophys. Research, 65*, 55–68, 1960*c*.

Störmer, C., Sur les trajectoires des corpuscles électrises dans l'espace sous l'action du magnetisme terrestre avec application aux aurores boréales, *Arch, sci. phys, et nat., 32*, 117–123, 190–219, 277–314, 415–436, 501–509, 1911.

(Received May 25, 1960)

A Comparison of Explorer VI and Explorer X Magnetometer Data[1]

BY EDWARD J. SMITH[2]

Space Technology Laboratories, Inc.

Magnetometers contained on seven spacecraft have measured the extraterrestrial magnetic field: Pioneer I, October 1958 [*Sonett, Judge, Sims, and Kelso*, 1960], Lunik I, January 1959 [*Dolganov and Pushkov*, 1959]; Explorer VI, August 1959 [*Sonett, Smith, and Sims*, 1960]; Lunik II, September 1959 [*Krassovsky*, 1960]; Vanguard III, September 1959 [*Heppner, Stolarik, Shapiro, and Cain*, 1960]; Pioneer V, March 1960 [*Coleman, Sonett, Judge, and Smith*, 1960]; and Explorer X, March 1961 [*Heppner, Ness, Skillman, and Scearce*, 1961]. Some of the magnetometer data are restricted to magnitude measurements only. Explorer VI and Explorer X, however, measured both magnitude and direction. Furthermore, for both spacecraft, apogee occurred at southernly geographic latitudes at an angle of approximately 135° with respect to the earth-sun direction. The purpose of this note is to compare the Explorer VI and Explorer X *vector* field measurements, to make this comparison in geomagnetic coordinates, and to discuss the existence of a large-scale deformation of the geomagnetic field.

The Explorer VI data provide evidence of a persistent, large-scale deformation of the geomagnetic field at radial distances exceeding 5 to $6R_E$ (earth radii) [*Sonett, Smith, Judge, and Coleman*, 1960]. The characteristics of the current associated with the deformation were sought in order to overcome trajectory restrictions and to explain the underlying cause. Reasonable agreement was obtained between a simple current model and magnetometer data from Explorer VI and Pioneer V [*Smith, Coleman, Judge, and Sonett*, 1960]. The data appear consistent with a westward ring current at $\sim 10R_E$, a result supported by the observation of a zone of trapped low-energy electrons [*Gringauz and Rytov*, 1960].

Preliminary analysis of the Explorer VI data was based on graphs of $|B_\perp|$ and ϕ, the magnitude and direction (with respect to the sun) of the field component perpendicular to the spacecraft spin axis, as a function of geocentric altitude. Leverett Davis suggested that a meaningful vector representation of the field could be obtained from the two measurements $|B_\perp|$ and ϕ by assuming that the deformed field lies in magnetic meridian planes. Figure 1 shows the disturbance field, $F = B - G$, where B is the observed field and G is the geomagnetic field extrapolated to the instantaneous location of Explorer VI. B was obtained by rotating $|B_\perp|$ and ϕ into geomagnetic coordinates (radial distance r, geomagnetic latitude δ_M, and longitude λ_M), assuming F had no component perpendicular to meridian planes ($F_{\lambda M} = 0$). F agrees qualitatively with the field produced by a westward current. The data bear a favorable resemblance to theoretical results for the vector field due to a diamagnetic ring current [*Akasofu, Cain, and Chapman*, 1961].

The Explorer X magnetometer measured all three field components [*Heppner, Ness, Skillman,*

[1] Published in the May 1962 issue of *Journal of Geophysical Research*. Reprinted by permission.

[2] Now at Space Sciences Division, Jet Propulsion Laboratory.

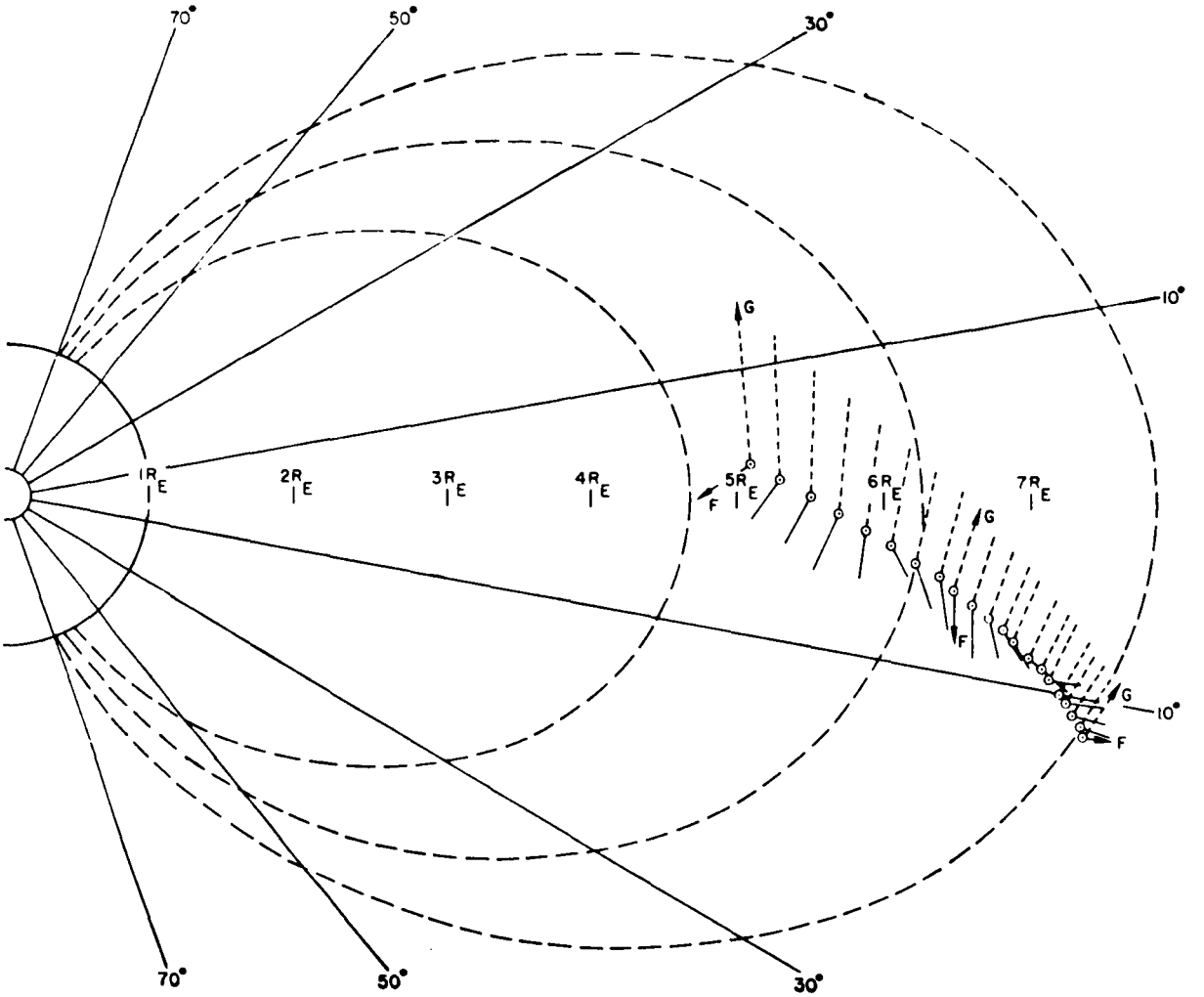

FIGURE 1.—*Disturbance field measured by Explorer VI. The disturbance field* F (*solid line*) *is equal to* B–G, *where* B *is the observed magnetic field and* G (*dashed line*) *is the extrapolated geomagnetic field.* B *is obtained by transforming the measured field parameters* $|B_\perp|$ *and* ϕ *into geomagnetic coordinates, assuming there is no component of* F *perpendicular to the magnetic meridian plane (the plane containing the dipole field line and the center of the earth).* F *is shown at selected positions on the Explorer VI trajectory as viewed from a direction perpendicular to the local magnetic meridian plane. The data were obtained on August 9, 1959, and were used in conjunction with the model calculations reported previously* (Smith, Coleman, Judge, and Sonett, *1960*).

and Scearce, 1961]. In figures 2 and 3 the data are transformed into spherical geomagnetic coordinates from spacecraft coordinates. Figure 2 shows B projected onto the magnetic equatorial plane. B tends to lie in magnetic meridian planes (the radial lines) out to geocentric distances of ~130,000 km. Thus, the assumption used in the Explorer VI data analysis gives a reasonably valid description of the disturbance field. Figure 2 also indicates that Explorer X was still inside the geomagnetic field at $20R_E$.

The Explorer VI and Explorer X data can be compared by considering figures 1 and 3. Fig-

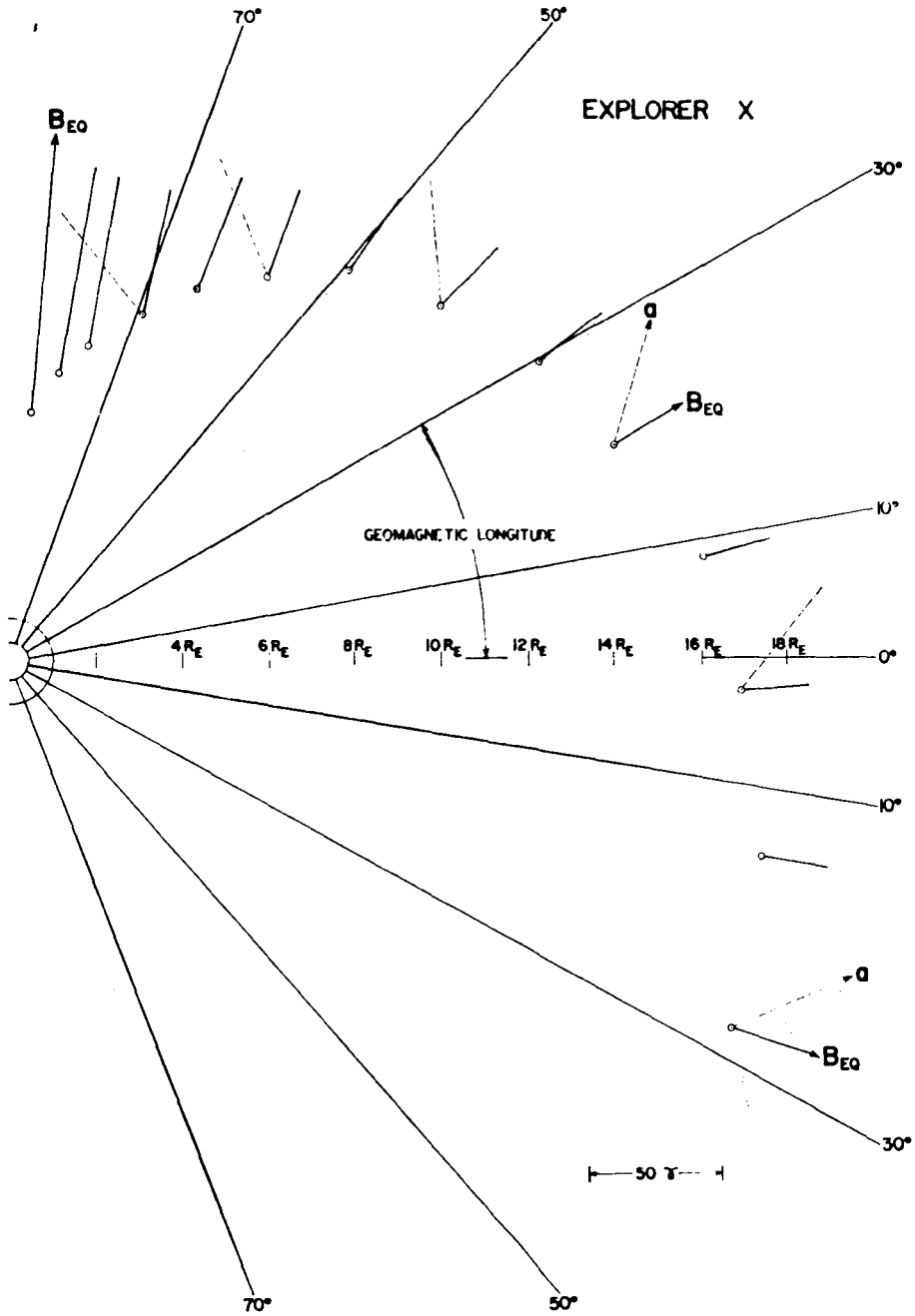

FIGURE 2.—*Field observed by Explorer X, projected into the equatorial plane. This figure shows the component of the observed magnetic field projected into the geomagnetic equatorial plane* B_{EQ} *(solid line). The direction of* B_{EQ} *can be compared with the direction of the corresponding geomagnetic field component* G_{EQ} *represented by a radial line connecting the point of observation and the earth's center.* a *is a unit vector in the antisolar direction (dashed line) also projected into the equatorial plane. It is evident that out to a geocentric distance of at least* $20R_E$ *the observed field tends to lie in the local magnetic meridian plane. Small deviations between* B_{EQ} *and* G_{EQ} *are consistent with a slight rotation of the field toward the antisolar direction.*

765-698 O-65—23

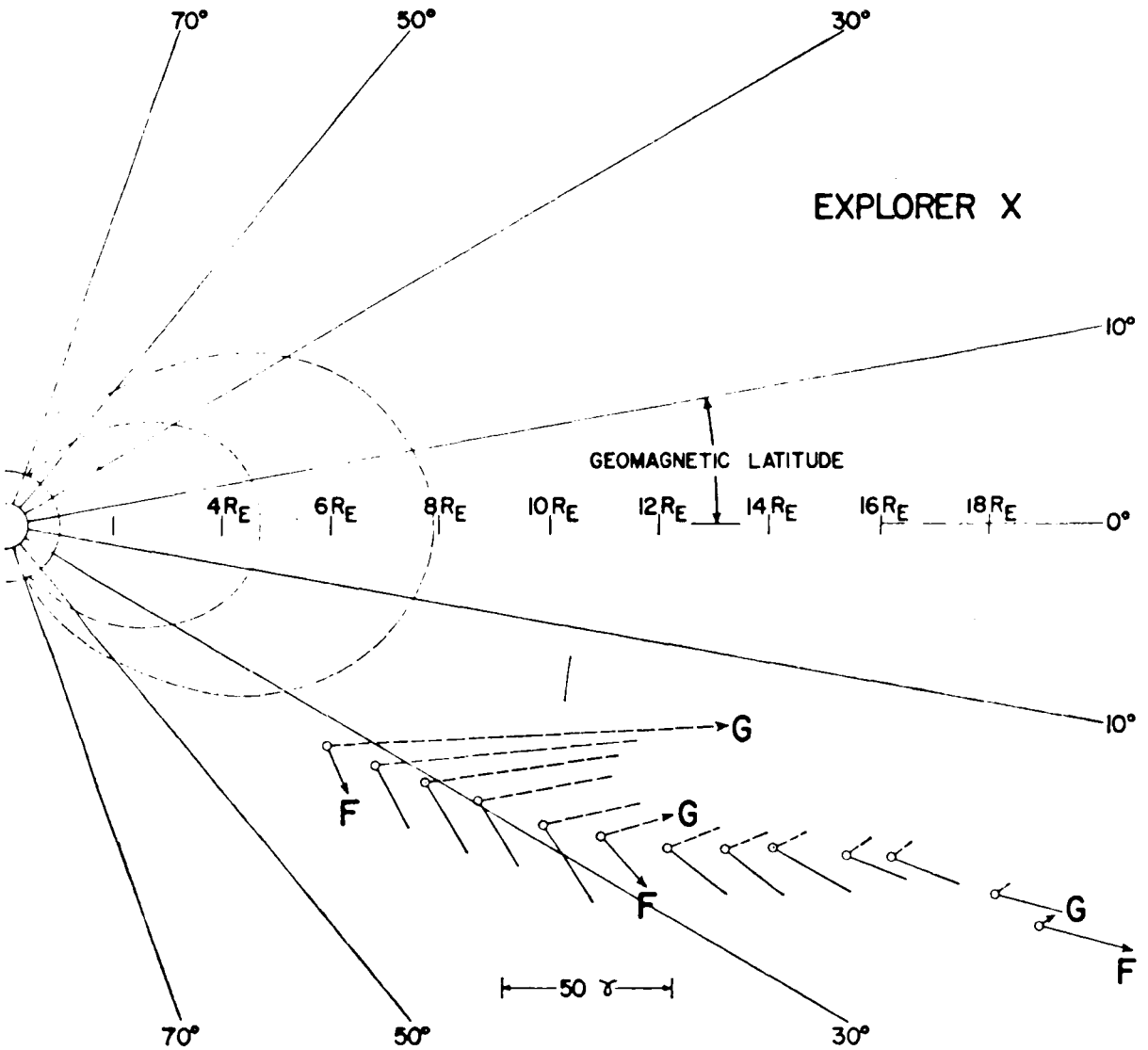

FIGURE 3.—*Disturbance field measured by Explorer X. This figure contains the geomagnetic field vector* G *and the component of the disturbance field* F (B—G) *projected into the local magnetic meridian plane. This figure should be compared with figure 1, which is the corresponding field component determined from the Explorer VI data. Both figures show a tendency for* F *to rotate counterclockwise and be radial at large geocentric distance.*

ure 1 shows a southward-directed F that rotates counterclockwise with increasing altitude. These features also appear in the Explorer X data. F is greater in figure 1 (mildly disturbed conditions) than in figure 3 (magnetically quiet). *This confirms the Explorer VI result that a large-scale deformation of the geomagnetic field is present even on nonstorm days.*

The disturbance field is such that the dipole field lines are rotated parallel to magnetic meridian planes (stretched out) but retain their essential, geomagnetic character. This result holds also during magnetic storms, at least out to $8R_E$ [*Smith and Sonett*, 1961] (Explorer VI apogee). There appear to be two possible explanations for a large-scale deformation of the geomagnetic field. Theory indicates that particles trapped in the geomagnetic field give rise to a westward ring current [*Singer*, 1957; *Dessler and Parker*, 1959]. An alternative explanation involves the transport of dipole field lines by the streaming solar plasma around the earth to form a magnetic tail in the antisolar direction [*Piddington*, 1959, 1960; *Johnson*, 1960]. The existence of the ring current was originally treated as a fundamental distinction between the two theories, but it is possible that both are present simultaneously [*Axford and Hines*, 1961].

Although the Explorer VI data appear qualitatively consistent with either explanation, the Explorer X results show that F is never directed northward inside the magnetosphere if the fluctuations occurring at greater altitudes [*Heppner, Ness, Skillman, and Scearce*, 1961] are associated with the outer boundary [*Sonett*, 1960]. In fact, F tends to be radial at large distances. This is contrary to what is expected for a ring current. The absence of characteristics of B obviously associated with the antisolar direction may appear inconsistent with the magnetic tail concept. However, hydromagnetic redistribution, at lower altitudes, of the stresses associated with a tail may preserve the symmetry of the earth's dipole field [*Parker*, 1958]. It appears likely that a magnetic tail exists. The question of the possible existence of the ring current, particularly during magnetic storms, is still unanswered. This aspect of the Explorer VI data is presently being investigated, using the data representation shown in figure 1.

ACKNOWLEDGMENTS

This work was financially supported by the National Aeronautics and Space Administration. I should like to acknowledge helpful discussions of this material with L. Davis, T. A. Farley, E. W. Greenstadt, and C. P. Sonett.

REFERENCES

Akasofu, S., J. C. Cain, and S. Chapman, The magnetic field of a model radiation belt numerically computed, *J. Geophys. Research, 66*, 4013, 1961.

Axford, W. I., and C. O. Hines, A unifying theory of high latitude geophysical phenomena and magnetic storms, *Can. J. Phys., 39*, 1433, 1961.

Coleman, P. J., C. P. Sonett, D. L. Judge, and E. J. Smith, Some preliminary results of the Pioneer V magnetometer experiment, *J. Geophys. Research, 65*, 1856, 1960.

Dessler, A. J., and E. N. Parker, Hydromagnetic theory of geomagnetic storms, *J. Geophys. Research, 64*, 2239, 1959.

Dolganov, S., and N. Pushkov, Results of earth's magnetic field measurement by the cosmic rocket, *Doklady Akad. Nauk SSSR, 129*, 1, 1959.

Gringauz, K. I., and S. M. Rytov, On the relationship between the magnetic field measurements obtained by Soviet cosmic rockets with charged particle traps and those obtained by U.S.A. Explorer VI and Pioneer V, *Doklady Akad. Nauk SSSR, 135*, 48, 1960.

Heppner, J. P., N. F. Ness, T. L. Skillman, and C. S. Scearce, Magnetic field measurements with the Explorer X satellite, *Proc. Intern. Conf. on Cosmic Rays and the Earth Storm*, Kyoto, September 1961 (to be published). (Also *NASA Rept.*, Goddard Space Flight Center contributions to 1961 Kyoto Conference on Cosmic Rays and the Earth Storm.)

Heppner, J. P., J. D. Stolarik, I. R. Shapiro, and J. C. Cain, Project Vanguard magnetic field instrumentation and measurements, in *Space Research, Proceedings of First International Space Science Symposium*, edited by H. Kallman-Bijl, North-Holland Publishing Co., Amsterdam, p. 982, 1960.

Johnson, F. S., The gross character of the geomagnetic field in the solar wind, *J. Geophys. Research, 65*, 3049, 1960.

Krassovsky, V. I., Results of scientific investigations made by Soviet sputniks and cosmic rockets, *Astronaut. Acta, 6*, 32, 1960.

Parker, E. N., Interaction of the solar wind with the geomagnetic field, *Phys. Fluids, 1*, 171, 1958.

Piddington, J. H., The transmission of geomagnetic disturbances to the earth's surface, *Geophys. J., 2*, 173, 1959.

Piddington, J. H., Geomagnetic storm theory, *J. Geophys. Research, 65*, 93, 1960.

Singer, S. F., A new model of magnetic storms and aurorae, *Trans. Am. Geophys. Union, 38*, 175, 1957.

Smith, E. J., P. J. Coleman, D. L. Judge, and C. P. Sonett, Characteristics of the extraterrestrial current system: Explorer VI and Pioneer V, *J. Geophys. Research, 65*, 1858, 1960.

Smith, E. J., and C. P. Sonett, Satellite observations of the distant field during magnetic storms: Explorer VI, *Proc. Intern. Conf. on Cosmic Rays and the Earth Storm*, Kyoto, September 1961 (to be published).

Sonett, C. P., Coupling of the solar wind to the exosphere, *Phys. Rev. Letters, 5*, 46, 1960.

Sonett, C. P., D. L. Judge, A. R. Sims, and J. M. Kelso, A radial rocket survey of the distant geomagnetic field, *J. Geophys. Research, 65*, 55, 1960.

Sonett, C. P., E. J. Smith, D. L. Judge, and P. J. Coleman, Current systems in the vestigial geomagnetic field: Explorer VI, *Phys. Rev. Letters, 4*, 161, 1960.

Sonett, C. P., E. J. Smith, and A. R. Sims, Surveys of the distant geomagnetic field: Pioneer I and Explorer VI, in *Space Research, Proceedings of First International Space Science Symposium*, edited by H. Kallman-Bijl, North-Holland Publishing Co., Amsterdam, p. 921, 1960.

(Received February 28, 1962)

The Effects of Betatron Accelerations Upon the Intensity and Energy Spectrum of Magnetically Trapped Particles[1]

BY PAUL J. COLEMAN, JR.[2]

Space Technology Laboratories, Inc.

A system composed of relativistic, charged particles in a uniform, slowly varying magnetic field is considered. The initial or unperturbed state of the system is one in which the number of particles per cubic centimeter with energies greater than E is given by $kE^{-\gamma}$, and in which the particle flux is isotropic. The effects of slow, uniform changes in the field strength upon the integral energy spectrum and upon the omnidirectional intensity of particles with momenta greater than σ are calculated. A simple expression which describes the latter effect is developed. Variations of these two effects are calculated as functions of the parameters, γ and σ.

The purpose of this note is to present the results of a calculation on the variation of particle intensity and energy spectrum with magnetic field for a system of relativistic, charged particles in a uniform, time-dependent magnetic field. The term "betatron acceleration" is used here, as it has been on previous occasions, only to emphasize the fact that the particle accelerations are produced by the changing magnetic fields. This calculation was undertaken as part of an analysis of data from the earth satellite, Explorer VI. These particular data indicate that simultaneous fluctuations of particle intensity and magnetic field occur in the outer atmosphere. In collaboration with D. L. Judge, the calculations presented in this note are being applied to these data and the results will be reported subsequently. Also, these experimental observations have been described briefly by *Farley and Rosen* [1960].

In order to treat this problem, it was assumed that the system described above has an unperturbed state in which the field strength is B_0, the number of particles per cubic centimeter with energies greater than E obeys a power law, $N_0(> E) = kE^{-\gamma}$, the particle flux is isotropic, and the omnidirectional intensity of particles with momenta greater than σ has a value I_0. Next, an integral was derived that gave the particle intensity, relative to I_0, as a function of the change in the magnetic field. This integral has been evaluated for various values of the parameters B/B_0, γ, and σ, and the results are presented. From these results a simple, empirical expression is developed that describes these intensity variations. Changes in the integral energy spectrum with magnetic field are also treated. It is felt that these results may be applicable, at least qualitatively, to the behavior of relativistic, charged particles in the outer geomagnetic field.

THE CONSTANTS OF THE MOTION

Consider a charged particle moving in a magnetic field which can be presented in cylindrical coordinates, ρ, ϕ and z, by a vector potential having only a ϕ component. Let this

[1] Published in the May 1961 issue of *Journal of Geophysical Research*. Reprinted by permission.

[2] Now at Institute of Geophysics, Univ. of Calif. at Los Angeles.

component be given by $A_\phi(\rho, z, t)$, where t is the time. Suppose that the projection of the particle's path upon the plane $z = 0$ has an approximate radius of curvature R, and that the approximate period of the motion parallel to this plane is T. Restrictions are placed upon the system as follows:

$$|(R\mathbf{k}_\rho \cdot \nabla)\mathbf{B}| \ll |\mathbf{B}| \tag{1}$$

and

$$T\left|\frac{\partial \mathbf{B}}{\partial t}\right| \ll |\mathbf{B}| \tag{2}$$

where $\mathbf{k}_\rho$ is a unit vector in the ρ direction.

Alfvén [1950] has shown that, when the magnetic field changes in such a system, a nonrelativistic particle moves on a tube of flux, and the magnetic moment of the particle is a constant of the motion. Thus,

$$\frac{mv^2 \sin^2 \theta}{B_z} = \text{constant}$$

where m is the particle mass, v is the magnitude of the particle velocity, and θ is the particle pitch angle, i.e., the angle between the magnetic field vector and the particle velocity vector.

For relativistic particles in such a system, *Layton* [1957] has shown that a constant of the particle motion is the product of a quantity described as the generalized magnetic moment of the particle and the total particle energy, and that relativistic particles also move on tubes of flux. This result may be written

$$\frac{(E^2 - m_0^2c^4)}{B_z} \sin^2 \theta = \text{constant}$$

where

$$E = \frac{m_0c^2}{(1 - \beta^2)}$$

m_0 is the particle rest mass, c is the velocity of light, and $\beta = v/c$. Thus, E is just the total energy of the particle. In terms of the magnitude of the relativistic particle momentum,

$$p = \frac{m_0c\beta}{(1 - \beta^2)^{1/2}} \tag{3}$$

this expression becomes

$$\frac{p^2 \sin^2 \theta}{B_z} = \text{constant} \tag{4}$$

Thus, in terms of initial conditions, the particle motion satisfies the relation

$$\frac{p^2 \sin^2 \theta}{B_z} = \frac{p_0^2 \sin^2 \theta_0}{(B_z)_0}$$

Particle energy spectrum.—For a relativistic particle, the kinetic energy may be written in terms of the particle momentum, as follows:

$$E = m_0c^2\left(\frac{p^2}{m_0^2c^2} + 1\right)^{1/2} - m_0c^2 \tag{5}$$

From (3),

$$p^2 = \frac{(m_0c\beta)^2}{1 - \beta^2}$$

From this expression, β, in terms of p, is given by

$$\beta = \frac{p}{(m_0^2c^2 + p^2)^{1/2}} \tag{6}$$

Next, for convenience, let

$$s^2 \equiv \frac{p^2}{m_0^2c^2}$$

where s may be considered the magnitude of the normalized particle momentum. Then, from (5) and (6), in terms of s,

$$E(s) = m_0c^2[(s^2 + 1)^{1/2} - 1]$$

$$dE = m_0c^2s(s^2 + 1)^{-1/2}\, ds$$

$$\beta(s) = \frac{s}{(1 + s^2)^{1/2}} \tag{7}$$

and

$$v(s) = \beta c = \frac{cs}{(1 + s^2)^{1/2}} \tag{8}$$

In the unperturbed system composed of charged particles in a uniform magnetic field of strength B_0, suppose that the number of particles per cubic centimeter with energies greater than E is

$$N_0(>E) = kE^{-\gamma}$$

$$= k(m_0c^2)^{-\gamma}[(s^2 + 1)^{1/2} - 1]^{-\gamma} \tag{9}$$

in the energy range of interest. Note that, in the unperturbed state of the system, the state of a particular particle may be described by the parameters B_0, p_0, and θ_0.

In this state, then, the differential energy spectrum is given by

$$n_0 \equiv -\frac{dN_0}{dE} = -\frac{dN_0}{ds}\frac{ds}{dE}$$

or

$$n_0 = k\gamma(m_0c^2)^{-\gamma}[(s^2+1)^{1/2}-1]^{-(\gamma+1)} \cdot s(s^2+1)^{-1/2}\,ds/dE \quad (10)$$

Next, we consider the effect upon the energy spectrum of a slow change of magnetic field strength from B_0 to B, which is a special case of a system restricted according to equations 1 and 2. The square of the normalized momentum of a particle may be written

$$s^2 = s^2(\cos^2\theta + \sin^2\theta) = s_{\|}{}^2 + s_{\perp}{}^2 \quad (11)$$

where the subscripts $\|$ and $\perp$ indicate directions relative to that of the magnetic field and, again, θ is the pitch angle of the particle. The constant of the particle motion given in (4) may be written in terms of s, and the parameters of the unperturbed state as follows:

$$\frac{s^2\sin^2\theta}{B} = \frac{s_0{}^2\sin^2\theta_0}{B_0} \quad (11a)$$

When the magnetic field changes slowly, and uniformly, from B_0 to B, $s_{\|}$ does not change. Thus, s^2 may be written in terms of the parameters of the unperturbed state and the field intensity B and, from (11),

$$s^2 = s_0{}^2\left(\cos^2\theta_0 + \frac{B}{B_0}\sin^2\theta_0\right) \quad (11b)$$

Now, those particles that, after the change of field from B_0 to B, have normalized momenta determined by the relation

$$s^2 = s_0{}^2\left(\cos^2\theta_0 + \frac{B}{B_0}\sin^2\theta_0\right)$$

are just those particles that, before the change, had normalized momenta determined by the relation

$$s_0{}^2 = \frac{s^2}{\cos^2\theta_0 + \frac{B}{B_0}\sin^2\theta_0}$$

Thus, after the field changes, those particles that have kinetic energy

$$E = m_0c^2[(s^2+1)^{1/2}-1]$$

are the same particles that before the field change had pitch angles θ_0 and kinetic energy

$$E_0 = m_0c^2 \cdot\left\{\left[\frac{s^2}{\left(\cos^2\theta_0 + \frac{B}{B_0}\sin^2\theta_0\right)}+1\right]^{1/2}-1\right\}$$

Consider only the particles that have pitch angle θ_0 when the field is B_0. According to the assumption of a power-law spectrum given by (9), the number of these particles with energies greater than E is proportional to

$$N_0(>E) = k(m_0c^2)^{-\gamma}[(s_0{}^2+1)^{1/2}-1]^{-\gamma}$$

After the field changes from B to B_0, all of these particles, which originally had energies greater than E_0, then will have energies greater than E. Thus, their number is proportional to

$$N(>E) = k(m_0c^2)^{-\gamma}\frac{B}{B_0} \cdot\left\{\left[\frac{s^2}{\left(\cos^2\theta_0 + \frac{B}{B_0}\sin^2\theta_0\right)}+1\right]^{1/2}-1\right\}^{-\gamma} \quad (12)$$

The factor B/B_0 is included because the particles remain on the surface of a tube of flux, and therefore, the particle density changes in proportion to the magnetic flux density.

To simplify (12), let

$$\eta^2 \equiv \cos^2\theta_0 + \frac{B}{B_0}\sin^2\theta_0 \quad (13)$$

Then the number of particles that had pitch angle θ when $B = B_0$ and energies $> E$ after the field change is proportional to

$$N(>E) = k(m_0c^2)^{-\gamma}\left[\left(\frac{s^2}{\eta^2}+1\right)^{1/2}-1\right]^{-\gamma}$$

and, differentiation with respect to E shows the differential energy spectrum for these particles after the field change to be proportional to

$$n(E) = -\frac{dN}{ds}\frac{ds}{dE} = k\gamma(m_0c^2)^{-\gamma} \cdot\left[\left(\frac{s^2}{\eta^2}+1\right)^{1/2}-1\right]^{-(\gamma+1)} \cdot\left(\frac{s^2}{\eta^2}+1\right)^{-1/2}\frac{s}{\eta^2}\frac{ds}{dE} \quad (14)$$

EXPRESSION FOR PARTICLE INTENSITY

In general, the unidirectional spectral particle intensity [See, for example, *Montgomery*, 1949], denoted by $j(r, \theta_1, \phi_1; \theta, \phi; E, t)$, may be defined, for a given type of particle, by the expression

$$j(r, \theta_1, \phi_1; \theta, \phi; E, t)\, dA\, d\Omega\, dE\, dt$$

= the number of particles with energy in the range dE at E, incident during the time interval dt at t, from within the solid angle $d\Omega$ at (θ, ϕ), upon the area dA normal to the direction of the particle velocity and located at the point (r, θ_1, ϕ_1).

Here, θ and ϕ are, respectively, the declination and azimuth of the incident particle direction. (In the system under discussion, the declination and the pitch angle are equivalent.)

For a particular state of our system, j is independent of the point of observation and independent of time. Under these assumptions, the unidirectional spectral intensity becomes a function of $(\theta, \phi; E)$ only. In this case, the omnidirectional spectral particle intensity, referred to a sphere of unit radius, will be denoted by $i(E)$ and is defined by the relation

$$i(E)\, dE\, dA = \left[\int_0^{2\pi}\int_0^{\pi} j(\theta, \phi; E) \cdot \sin\theta\, d\theta\, d\phi\right] dE\, dA$$

= the flux of particles with energies in the range dE at E, incident, from all directions, upon a sphere of projected area dA.

Next, let the number of particles per cubic centimeter, with energies in the range dE at E, be denoted by $n(E)\, dE$. Let the fraction of these particles with directions within the solid angle $d\Omega$ at (θ, ϕ) be denoted by

$$F(\theta, \phi)d\Omega = F(\theta, \phi) \sin\theta\, d\theta\, d\phi$$

Also, let the magnitude of the particle velocity be denoted by $v(E)$. Then

$$n(E)F(\theta, \phi)v(E) = j(\theta, \phi; E)$$

and

$$i(E)dE\, dA = \left[\int_0^{2\pi}\int_0^{\pi} F(\theta, \phi)v(E)n(E) \cdot \sin\theta\, d\theta\, d\phi\right] dE\, dA \quad (15)$$

or, in terms of s,

$$i(s)\, ds\, dA = \left[\int_0^{2\pi}\int_0^{\pi} F(\theta, \phi)vn\, mc^2 s(s^2 + 1)^{-1/2} \cdot \sin\theta\, d\theta\, d\phi\right] ds\, dA$$

Next, it is assumed that, when the field strength is B_0, the particle flux is isotropic. Thus, the fraction of the particles with directions within a given solid angle is just proportional to the magnitude of the solid angle, and the quantity $F(\theta, \phi)$ is actually independent of (θ, ϕ), i.e.,

$$F(\theta, \phi) = \frac{1}{4\pi} = F(\theta_0, \phi) \quad (16)$$

since $\theta = \theta_0$ when $B = B_0$.

Then, substituting for v, n_0 and $F(\theta, \phi)$ from (8), (9), and (16), respectively, and for E in terms of s, in (7), the omnidirectional spectral particle intensity, when the field is B_0, is given by

$$i_0(s)\, ds = \frac{c}{4\pi} k\gamma(m_0c^2)^{-\gamma}\left\{\int_0^{2\pi}\int_0^{\pi} \frac{s^2}{(1 + s^2)} \cdot [(s^2 + 1)^{1/2} - 1]^{-(\gamma+1)} \sin\theta_0\, d\theta_0\, d\phi\right\} ds$$

Integration over θ_0 and ϕ yields

$$i_0(s)\, ds = ck\gamma(m_0c^2)^{-\gamma} \frac{s^2}{(1 + s^2)} \cdot [(s^2 + 1)^{1/2} - 1]^{-(\gamma+1)}\, ds$$

The omnidirectional intensity of particles with energies greater than E is found by integrating the negative of this expression over s. Let this quantity be denoted by I. Then

$$I_0(> \sigma) = ck\gamma(m_0c^2)^{-\gamma}\int_\sigma^\infty \frac{s^2}{(1 + s^2)^{1/2}} \cdot [(s^2 + 1)^{1/2} - 1]^{-(\gamma+1)}\, ds \quad (17)$$

where the lower limit, σ, is determined by equation 7, i.e.,

$$E = m_0c^2[(\sigma^2 + 1)^{1/2} - 1]$$

Next, the omnidirectional spectral particle intensity, after the field has changed from B_0 to B, may be determined as follows.

Combining equations 11*a* and 11*b* yields

$$\sin^2\theta = \frac{B}{B_0} \frac{\sin^2\theta_0}{\cos^2\theta_0 + \frac{B}{B_0}\sin^2\theta_0} \quad (17a)$$

Thus, for a field change from B_0 to B, the new pitch angle of a particle depends only upon the initial pitch angle and the change in field strength. It is independent of the initial particle momentum, s_0.

As mentioned above, it is assumed that when $B=B_0$ the distribution of particles is isotropic. Thus, the fraction of particles in the element of solid angle at θ_0 and ϕ is

$$\frac{1}{4\pi} \sin \theta_0 \, d\theta_0 \, d\phi$$

According to (17a), when the field changes from B_0 to B, all the particles in this fractional group are changed to the same new pitch angle. The distribution over ϕ is unaffected. Thus, after the change,

$$F(\theta, \phi) \sin \theta \, d\theta \, d\phi = \frac{1}{4\pi} \sin \theta_0 \, d\theta_0 \, d\phi$$

The omnidirectional spectral particle intensity, after the field change, is then found by substituting this result, as well as the results given in (8) and (14), into (15). Note that, according to (17a), the limits of integration over θ_0, of the integral in (15), are 0 and 2π. Thus,

$$\begin{aligned} i(s) \, ds = {} & \left(\frac{B}{B_0}\right) \frac{c}{2\pi} k\gamma (m_0c^2)^{-\gamma} \\ & \cdot \left\{ \int_0^{2\pi} \int_0^{\pi/2} \frac{s^2}{(1+s^2)^{1/2}} \right. \\ & \cdot \left[\left(\frac{s^2}{\eta^2} + 1 \right)^{1/2} - 1 \right]^{-(\gamma+1)} \\ & \left. \cdot \left(\frac{s^2}{\eta^2} + 1 \right)^{-1/2} \frac{1}{\eta^2} \sin \theta_0 \, d\theta_0 \, d\phi \right\} ds \end{aligned} \tag{18}$$

Now, from (13),

$$\begin{aligned} \eta^2 &= \left(\cos^2 \theta_0 + \frac{B}{B_0} \sin^2 \theta_0 \right) \\ &= \frac{B}{B_0} \left[1 - \left(\frac{B - B_0}{B} \right) \cos^2 \theta_0 \right] \end{aligned}$$

Consider the case in which $B > B_0$. Let

$$x^2 = \left(\frac{B - B_0}{B} \right) \cos^2 \theta_0 \qquad B > B_0, \; x^2 < 1$$

Then

$$dx = - \left(\frac{B - B_0}{B} \right)^{1/2} \sin \theta_0 \, d\theta_0$$

and

$$\eta^2 = \frac{B}{B_0} (1 - x^2)$$

Also, the limits of integration become

$$\text{for } \theta_0 = \frac{\pi}{2}, \qquad x = 0$$

and

$$\text{for } \theta_0 = 0, \qquad x = \left(\frac{B - B_0}{B} \right)^{1/2}$$

After substitution of these relations into (18) and integration over ϕ, the omnidirectional intensity of particles with $s > \sigma$ is found by integrating the negative of the result over s, and is given by

$$\begin{aligned} I_1(>\sigma) = {} & ck\gamma (m_0c^2)^{-\gamma} \left(\frac{B}{B_0} \right)^{(\gamma+2)/2} \\ & \cdot \left(\frac{B - B_0}{B} \right)^{-1/2} \int_\sigma^\infty \int_0^{(1-B_0/B)^{1/2}} \\ & \cdot \left\{ \left[s^2 + \frac{B}{B_0} (1 - x^2) \right]^{1/2} \right. \\ & \left. - \left(\frac{B}{B_0} \right)^{1/2} (1 - x^2)^{1/2} \right\}^{-(\gamma+1)} \\ & \cdot (1 - x^2)^{\gamma/2} \left[s^2 + \frac{B}{B_0} (1 - x^2) \right]^{-1/2} \\ & \cdot \frac{s^2}{(1+s^2)^{1/2}} \, dx \, ds \end{aligned} \tag{19}$$

for $B > B_0$.

Next, consider the case in which $B_0 > B$. Let

$$x^2 = \left(\frac{B_0 - B}{B} \right) \cos^2 \theta_0 \qquad B_0 > B, \; x^2 < 1$$

Then

$$dx = - \left(\frac{B_0 - B}{B} \right)^{1/2} \sin \theta_0 \, d\theta_0$$

and

$$\eta^2 = \frac{B}{B_0} (1 + x^2)$$

Also, the limits of integration become,

$$\text{for } \theta_0 = \frac{\pi}{2}, \qquad x = 0$$

and,

$$\text{for } \theta_0 = 0, \qquad x = \left(\frac{B_0 - B}{B} \right)^{1/2}$$

After substitution of these relations into (18) and integration over ϕ, the omnidirectional intensity of particles with $s > \sigma$ is found by integrating the negative of the result over s, and is given by

$$I_2(>\sigma) = ck\gamma(m_0c^2)^{-\gamma}\left(\frac{B}{B_0}\right)^{(\gamma+2)/2} \cdot\left(\frac{B_0 - B}{B}\right)^{-1/2} \int_\sigma^\infty \int_0^{[(B_0-B)/B]^{1/2}} \cdot\left\{\left[s^2 + \frac{B}{B_0}(1 + x^2)\right]^{1/2} - \left(\frac{B}{B_0}\right)^{1/2}(1 + x^2)^{1/2}\right\}^{-(\gamma+1)} \cdot(1 + x^2)^{\gamma/2}\left[s^2 + \frac{B}{B_0}(1 + x^2)\right]^{-1/2} \cdot\frac{s^2}{(1 + s^2)^{1/2}}\, dx\, ds \qquad (20)$$

for $B_0 > B$.

The integral I_0, given by (17), has been evaluated for various values of γ and σ, the lower limit of the integration over s. The integrals I_1 and I_2, given by (19) and (20), respectively, have been evaluated for various values of B/B_0, γ and σ. These evaluations were accomplished with a digital computer with an error maintained below 1 per cent. The parameter σ was varied in order to determine the effect which a change of the particle detector threshold would have upon observations of the variations in omnidirectional particle intensity. It is assumed that the efficiency of the detector above the threshold is independent of the particle energy.

Values of particle energies corresponding to various values of σ, or s, for protons and electrons are plotted in figure 1. Thus, for example, if $\sigma = 1$, the calculated particle intensity would include, in the event of electrons, only those particles with energies greater than 200 kev.

The results of the integral evaluations are presented in figures 2, 3, and 4, which contain plots of log (I/I_0) versus log (B/B_0) for various choices of the parameters, γ and σ. Thus, from the curves, one can determine how the omnidirectional particle intensity varies with magnetic field strength for our model. Curves selected from figures 2 and 4 are presented in figure 5 to emphasize the dependence of the variations of intensity upon σ or, in turn, upon the lower limit of the energy of the particles included, i.e., upon the threshold of the particle detector.

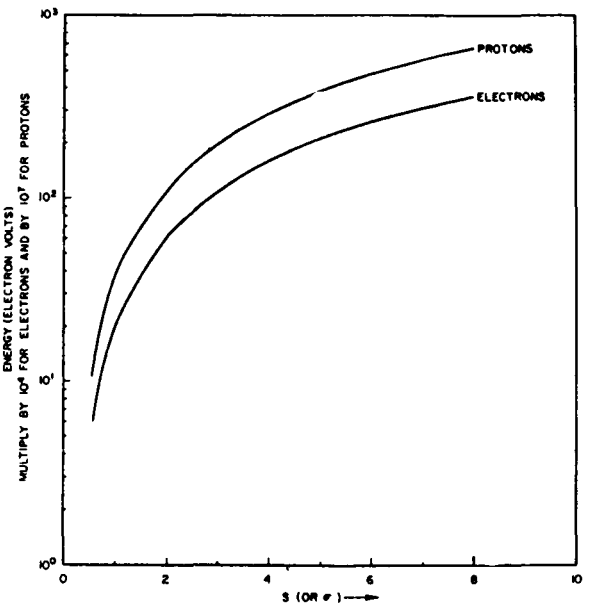

FIGURE 1.—*Normalized particle momentum* (s *or* σ) *versus particle energy for electrons and protons in the energy range of interest.*

Note that the curves in figures 2 through 5 are very nearly straight lines, particularly for values of B/B_0 in the neighborhood of $B/B_0 = 1$ or log $B/B_0 = 0$. The slopes of these curves have been calculated and plotted, versus γ, in figure 6. From the plot one may obtain a relatively simple expression that describes approximately the variation of the omnidirectional particle intensity with small changes in the magnetic field. The result is

$$\frac{\log (I/I_0)}{\log (B/B_0)} = \gamma\left(0.56 - 0.08\,\frac{\log \sigma}{\log}\right) + 1 \qquad (21)$$

at least for $1 < \sigma < 8$.

EFFECTS ON THE ENERGY SPECTRUM

Also, it is interesting to consider the effect of the change in magnetic field upon the integral

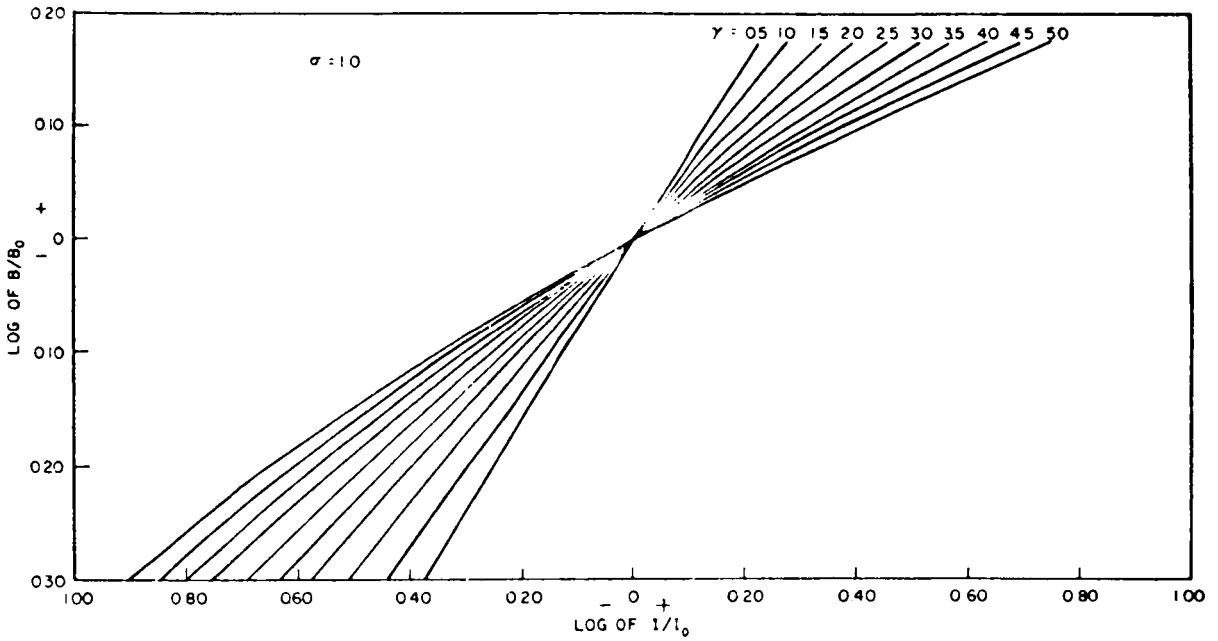

FIGURE 2.—*Curves showing the manner in which the relative omnidirectional particle intensity* I/I_0 *changes with the relative magnetic field strength* B/B_0. *The family of curves in this figure applies to the behavior of particles for which the magnitude of the normalized momenta are greater than 1.0, i.e.,* $s > 1.0$, *and the lower limit of integration in equations 17, 19, and 20 is, therefore,* $\sigma = 1.0$. *The parameter* γ *is the exponent appearing in the expression for the integral energy spectrum (see equation 9).*

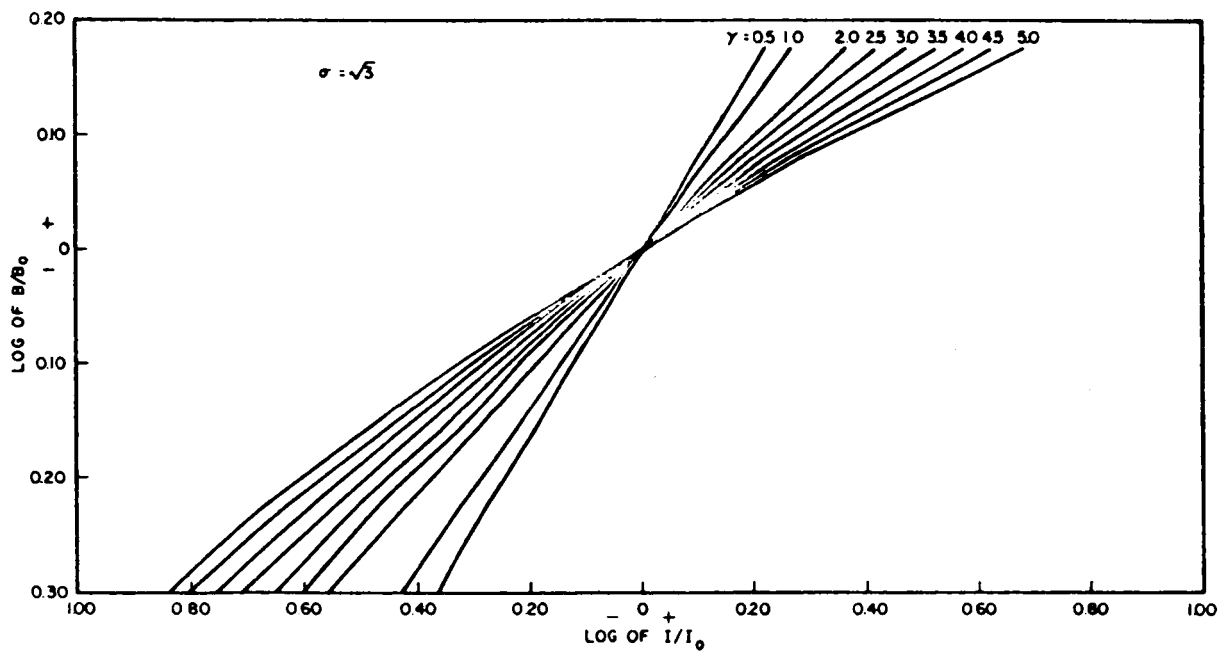

FIGURE 3.—*Curves similar to those in figure 2 except that* $s > \sqrt{3}$, *or* $\sigma = \sqrt{3}$.

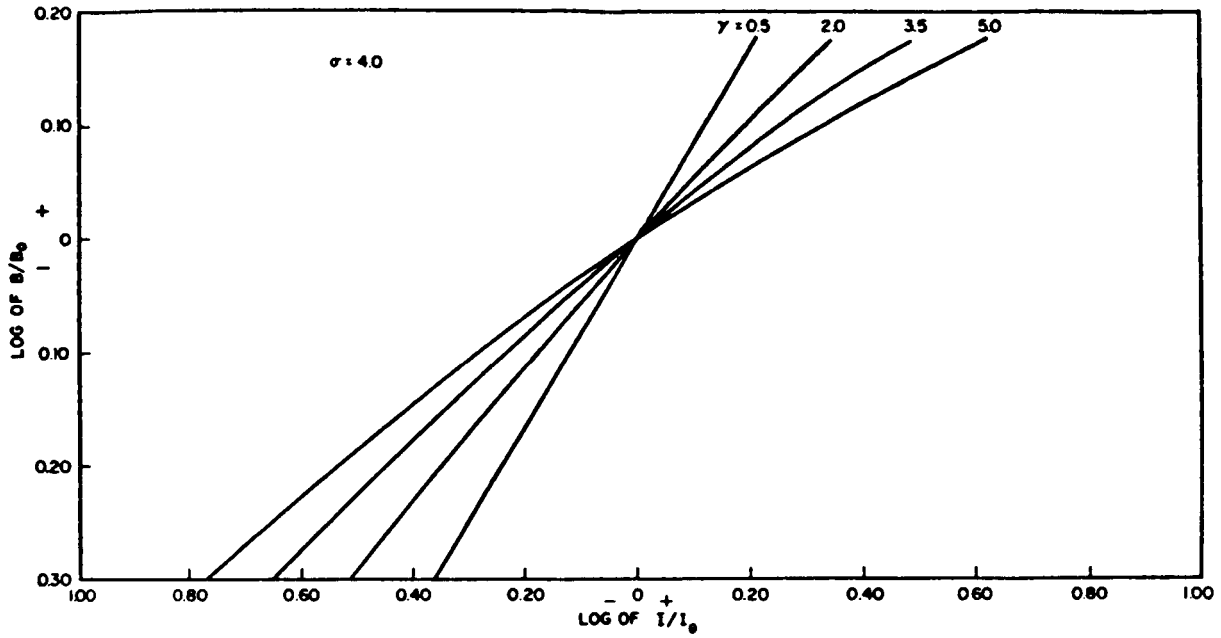

FIGURE 4.—*Curves similar to those in figure 2 except that* s > 4.0, *or* $\sigma = 4.0$.

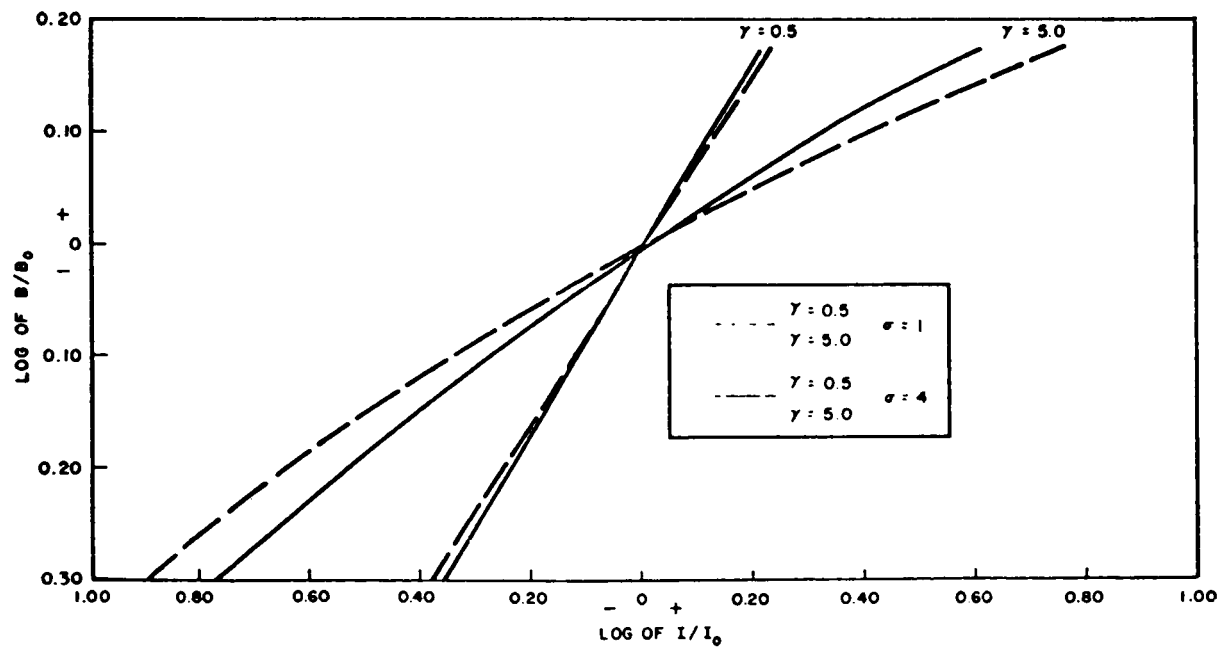

FIGURE 5.—*Curves selected from figures 2 and 4 to illustrate the effect of the choice of* σ *upon the manner in which the relative omnidirectional particle intensity* I/I_0 *changes with the relative magnetic field strength,* B/B_0.

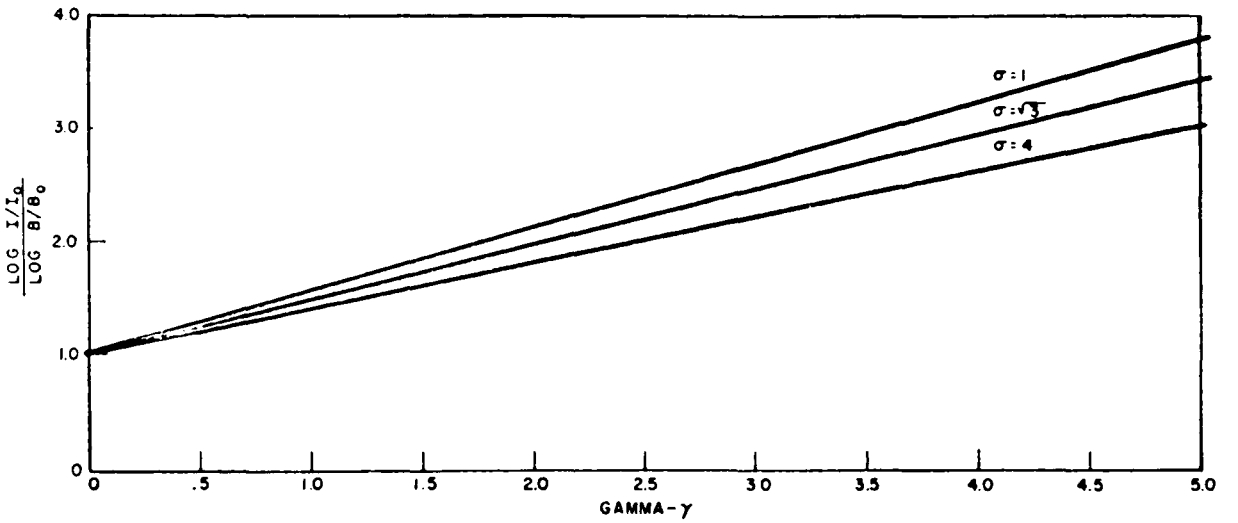

FIGURE 6.—*The approximate slopes of the curves shown in figures 2, 3, and 4 (curves of log* (I/I_0)*, the logarithm of the relative omnidirectional particle intensity, versus log* (B/B_0)*, the logarithm of the relative magnetic field strength) plotted versus* γ*, the exponent in the power-law expression for the integral energy spectrum, for various values of* σ*, the minimum magnitude of normalized momentum of the particles considered.*

energy spectrum of the particles. It was assumed that, in the unperturbed state, the energy spectrum, in terms of s, is given by (13).

However, after the field change, the spectrum is a function of the pitch angles that the particles had in the unperturbed state, and the integration over θ is more complicated. The integral energy spectrum is found by omitting the velocity factor, $v(s)$, in (15) and integrating over s. More explicitly, we eliminate the factor $cs(1 + s^2)^{-1/2}$ from the right side of (19) and integrate over s. Thus, for $B > B_0$,

$$N_1(>s) = k(m_0c^2)^{-\gamma}\left(\frac{B - B_0}{B}\right)^{-1/2}\left(\frac{B}{B_0}\right)^{(\gamma+2)/2} \cdot \int_0^{(1-B_0/B)^{1/2}} \left[s^2 + \frac{B}{B_0}(1 - x^2) - \left(\frac{B}{B_0}\right)^{1/2}(1 - x^2)^{1/2}\right]^{-\gamma}(1 - x^2)^{\gamma/2}\, dx$$

Similarly from (20) for $B_0 > B$,

$$N_2(>s) = k(m_0c^2)^{-\gamma}\left(\frac{B - B_0}{B}\right)^{-1/2}\left(\frac{B}{B_0}\right)^{(\gamma+2)/2} \cdot \int_0^{[(B_0-B)/B]^{1/2}} \left[s^2 + \frac{B}{B_0}(1 + x^2) - \left(\frac{B}{B_0}\right)^{1/2}(1 + x^2)^{1/2}\right]^{-\gamma}(1 - x^2)^{\gamma/2}\, dx$$

Values of $N(>s)$ are plotted versus s for various values of γ and B/B_0 in figure 7. These results are compared with the unperturbed spectra in the same figure. Note that the slopes of the plots change very little with B/B_0 in the range under consideration. Thus, γ remains relatively constant during changes in the magnetic field. This fact can be seen more easily in figure 8 which shows the change of γ with B/B_0 for various initial values of γ. Note that the log-log plots in figure 7 are very nearly straight lines. This result indicates that the exponential character of the integral energy spectrum does indeed persist during field changes while the value of the exponent changes slightly.

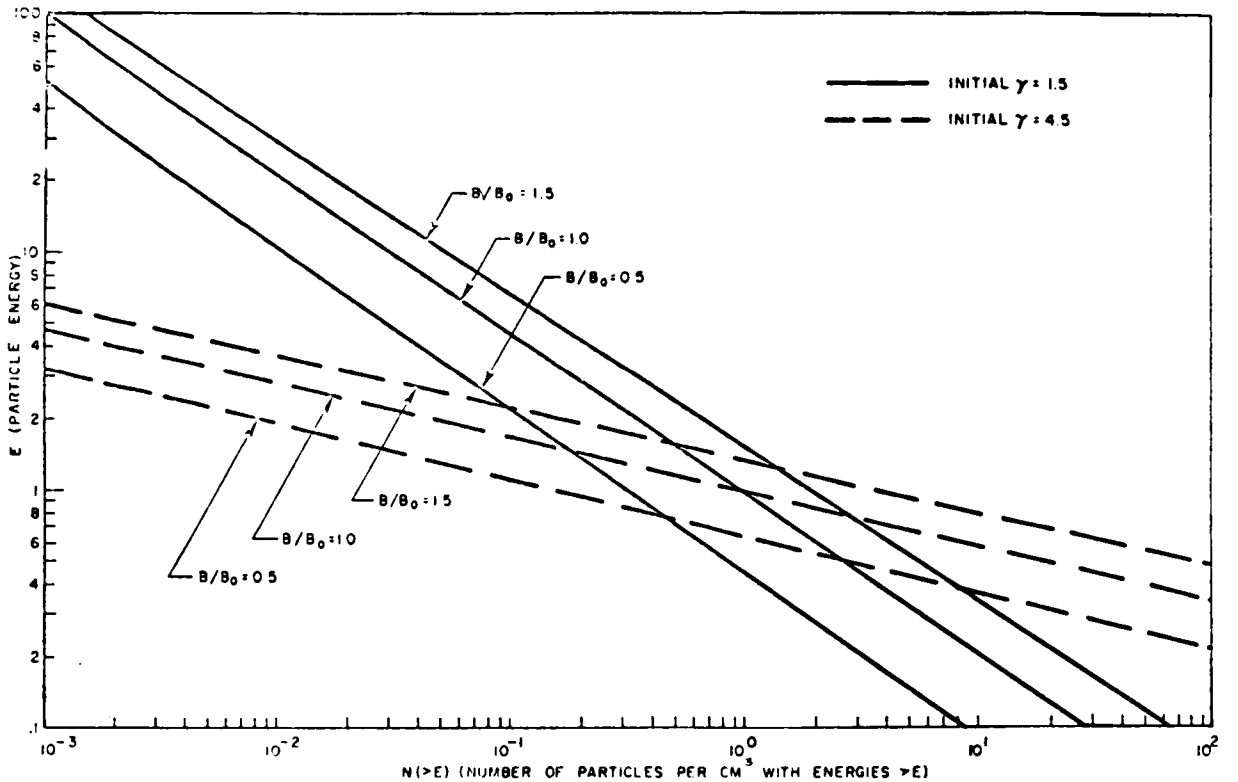

FIGURE 7.—*Examples of the integral energy spectra after magnetic field changes compared to the unperturbed spectrum for two choices of the initial value of the exponent* γ *where* $N(> E = kE^{-\gamma}$. *Note that the exponential characteristic is retained after the field changes.*

CONCLUSIONS

These results may be summarized as follows:

(a) The variation of the omnidirectional intensity of particles, having normalized momenta greater than σ, with slow uniform changes in the magnetic field strength is given, approximately, by equation 21.

(b) The value of the exponent appearing in the expression for the integral energy spectrum varies little from its initial value with changes in the magnetic field strength over the range considered. This result is shown in figure 8.

Although the results presented herein pertain to a very restricted system, it is felt that they can be applied to the more general system, restricted according to (1) and (2), with useful accuracy. Thus, for example, it may be possible to deduce a good deal of information about the energy spectrum of geomagnetically trapped particles from a study of the aforementioned simultaneous fluctuations of particle intensity and magnetic field observed in the outer atmosphere.

ACKNOWLEDGMENTS

I wish to thank L. Davis, D. L. Judge, and T. A. Farley for their suggestions pertaining to this note, and S. Gurnik for his efforts in programming the computer. The work was supported by the National Aeronautics and Space Administration.

REFERENCES

Alfvén, H., *Cosmical Electrodynamics*, Clarendon Press, Oxford, 19–23, 1950.

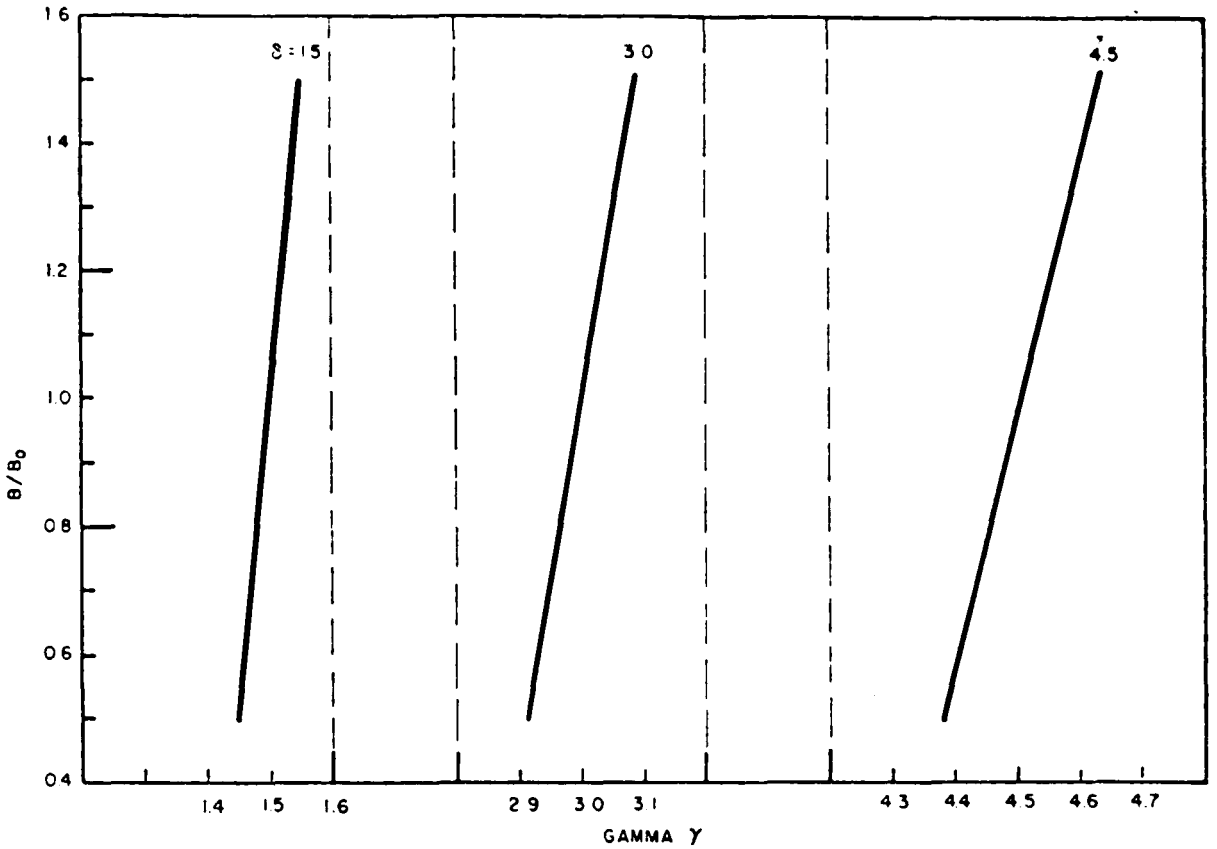

FIGURE 8.—*Curves showing the variation of* γ, *the exponent in the expression for the integral energy spectrum of the particles, with the relative magnetic field strength,* B/B_0.

Farley, T. A., and A. Rosen, Charged particle variations in the outer Van Allen zone during a geomagnetic storm, *J. Geophys. Research, 65*, 3494–3496, 1960.

Layton, Thomas W., Acceleration of cosmic rays by hydromagnetic waves, Doctoral Thesis, California Inst. of Tech., Pasadena, Calif., 28–29, 1957.

Montgomery, D. J. S., *Cosmic Ray Physics*, Princeton University Press, Princeton, New Jersey, 330–333, 1949.

(Manuscript received November 5, 1960; revised February 6, 1961)

Observations of Low-Frequency Hydromagnetic Waves in the Distant Geomagnetic Field: Explorer 6[1]

BY DARRELL L. JUDGE

Space Technology Laboratories

AND PAUL J. COLEMAN, JR.[2]

NASA Headquarters

Certain of the measurements obtained simultaneously with three of the instruments aboard the earth satellite Explorer 6 are discussed. The results from these instruments, the magnetometer, aspect indicator, and scintillation detector, provide direct evidence for the existence of low-frequency hydromagnetic fluctuations in the distant geomagnetic field, as well as some information pertaining to their specific characteristics. The observed phenomena consist of variations in the amplitude and direction of the measured component of the magnetic field accompanied by substantial changes in the intensity of the energetic particles detected by the scintillation counter. The fluctuations exhibited periods between 100 and 500 seconds. Within this range of periods, variations of the order of 10γ ($\Delta B/B \simeq 0.15$) in amplitude and 15° in orientation were observed in the measured component of the field. These field changes were accompanied by fluctuations of about the same relative amplitudes ($\Delta I/I \simeq 0.15$) in the intensity of the detected particles. Of particular interest is an observation of damped, quasi-sinusoidal oscillations detected simultaneously by all three instruments. As a basis for the interpretation of these results, simple models for hydromagnetic disturbances propagating in the transverse, or Alfvén, mode and in the compressional mode are described. The experimental results are compared with those that might be expected if the observed disturbances behaved as suggested by the models. It is concluded that these two modes, transverse and compressional, were indeed observed. The comparison between the models and the data indicates that the transverse mode had a period of 200 seconds, was elliptically polarized, and was marked by a rotation of the polarization that would be clockwise to an observer looking along the unperturbed field line toward the north geomagnetic pole. The compressional mode had a period of about 100 seconds. The harmonic relationship of these periods is evidence for coupling between the modes. Under the assumption that the decay of these oscillations is exponential, the time constant associated with the damping is approximately 500 seconds. It is shown that these disturbances violate only the third adiabatic invariant required for trapped particles in the region of the geomagnetic field in which the disturbances were observed. The model for the compressional mode allows certain conclusions concerning the characteristics of the trapped particles observed with the scintillation detector. Assuming an omnidirectional flux of electrons with an $E^{-\gamma}$ integral energy spectrum, it is shown that $\gamma \simeq 1$ for the particles with energies in the range about 500 kev. Consequences of the existence of these hydromagnetic disturbances are discussed, particularly with regard to their possible effects upon the dynamics of the outer radiation belt.

[1] Published in the December 1962 issue of *Journal of Geophysical Research*. Reprinted by permission.

[2] Now at Institute of Geophysics, Univ. of Calif. at Los Angeles.

INTRODUCTION

In recent years considerable interest has arisen in the properties of hydromagnetic disturbances in tenuous plasmas. Since *Alfvén* [1950] elaborated upon his earlier theoretical predictions of the existence of hydromagnetic waves, numerous authors have considered the possibility that hydromagnetic disturbances are propagated in the geomagnetic field. The properties that might be expected of such disturbances have been investigated theoretically in some detail. The first in situ observations of fluctuations in the distant geomagnetic field, interpreted to have been produced by hydromagnetic waves, were obtained by *Sonett et al.* [1960] with a magnetometer aboard the space probe Pioneer 1. Additional observations of such disturbances were obtained by *Coleman et al.* [1960] with a similar instrument aboard the space probe Pioneer 5.

Sugiura [1961] and *Wilson and Sugiura* [1961] have described measurements of geomagnetic disturbances at the earth's surface that indicate the existence of low-frequency hydromagnetic waves apparently generated in the distant geomagnetic field and transmitted to the earth along lines of magnetic force.

Data obtained with the magnetometer and aspect indicator aboard Explorer 6 provide additional and direct evidence for the existence, in the distant geomagnetic field, of low-frequency hydromagnetic disturbances. Variations in the intensity of a component of the energetic trapped radiation in the outer radiation zone were simultaneously observed with the scintillation detector aboard the same vehicle. Data obtained from these three instruments during periods of such disturbances in the magnetosphere will be presented. These results provide three types of measurements that will be used in an attempt to determine the hydromagnetic characteristics of the disturbances. Arguments leading to the interpretation of these results as the effects of hydromagnetic waves will be given.

Further, it is of interest to consider the effects of disturbances such as those observed on the particles trapped in the geomagnetic field. Since the first measurements of geomagnetically trapped particles [*Van Allen et al.*, 1959; *Vernov et al.*, 1959] the radiation zones have been explored in considerable detail. Apparently these zones consist of a comparatively stable inner belt, containing energetic protons and electrons, and an outer belt containing energetic electrons. Evidence favoring the existence of a third, more distant zone of lower-energy electrons has also been obtained [*Gringauz et al.*, 1960; *Gringauz and Rytov*, 1960].

The so-called outer radiation belt has been observed to undergo significant temporal variations which, for the most part, correlate with other phenomena evidently produced by solar activity [*Arnoldy, Hoffman, and Winckler*, 1960; *Rosen and Farley*, 1961; *Fan, Meyer, and Simpson*, 1961]. As a result of such observations, the study of the dynamics of the outer belt has been intensified. Various mechanisms that might produce the changes observed in the outer belt have been considered. Collisions of energetic electrons with particles of thermal energies certainly produced an effect. In addition, it is likely that hydromagnetic disturbances affect at least the trapped particles that are in the outer belt and beyond.

The motion of a charged particle in the unperturbed geomagnetic field can be described quite generally with the aid of the guiding center approximation [*Alfvén*, 1950]. Thus, the particle moves transverse to the magnetic lines of force in a nearly circular path (cyclotron motion) about a guiding center that oscillates along a line of force between "mirror points" in northern and southern geomagnetic latitudes, while slowly drifting in geomagnetic longitude. *Northrop and Teller* [1959] have discussed three adiabatic invariants of this motion. The first invariant applies to the cyclotron motion of the particle, the second applies to the motion of the particles along a field line, and the third applies to the longitudinal drift of the particle. These invariants may be violated, respectively, by hydromagnetic disturbances of sufficient amplitude, introduced in times comparable to the periods of the cyclotron motions; the periods between reflections at the mirror points; or the periods of the longi-

765-698 O-65—24

tudinal drift around the earth. Northrup and Teller suggest that violations of the adiabatic invariants will result in losses of trapped particles.

A mechanism for the diffusion of trapped particles due to irregularities in the geomagnetic field or to electric fields, either of which probably violates certain of these invariants, has been described by *Gold* [1959]. *Kellogg* [1959] has indicated that a hydromagnetic phenomenon, perhaps produced by a geomagnetic storm or by flute instabilities, which violates the third invariant, but does not violate the first and second invariants, can scatter trapped particles inward with associated accelerations. However, his mechanism required constant, non-dipolar gradients in the field. *Parker* [1960] and *Davis and Chang* [1962] have investigated the violation of the third invariant for the case in which the required hydromagnetic effect is a compression of the geomagnetic field produced by a geomagnetic sudden commencement. In another paper, *Parker* [1961] has discussed the possibility of acceleration of geomagnetically trapped electrons by a "hydromagnetic disturbance (*a*) capable of violating the third invariant (only) and (*b*) localized inside the geomagnetic field." As will be shown, data obtained with the instruments aboard Explorer 6, during periods marked by the magnetic field fluctuations mentioned previously, indicate that the observed disturbances, in the region of the outer radiation zone involved, violate only the third adiabatic invariant of the motion of the trapped electrons. The effects of such disturbances on the trapped radiation will be discussed, with particular reference to the aforementioned results of *Davis and Chang* [1962].

DESCRIPTION OF THE EXPERIMENT

Explorer 6 was launched into an elliptical orbit from Cape Canaveral, Florida, on August 7, 1959, at 1423 GMT. Its orbital plane was inclined at 47° to the earth's equatorial plane and at 38° to the plane of the ecliptic. Apogee was at southern latitudes about 48,000 km from the center of the earth and perigee was at approximately 6600 km (230 km altitude). On the day of launch, the angle between the ecliptic-plane projection, from earth's center to apogee, of the major axis of the orbital ellipse and the earth-sun line was about 134°. This angle decreased by about 1° per day. The orbital period of the satellite was approximately 12 hours 42 min.

The "search-coil" magnetometer carried aboard Explorer 6 has been described in detail elsewhere [*Judge et al.*, 1960]. The sensor was a multiturn coil fixed in the spacecraft. The vehicle was stabilized by a 2.8 cps rotation about its axis of maximum moment of inertia, and the resulting rotation of the coil, in a relatively constant ambient magnetic field, generated an emf that was a measure of the field strength. Thus, the magnetometer was sensitive only to the component of the ambient field that was transverse to the spin axis of the vehicle. The measured component will be denoted by $\mathbf{B}_\perp$ and its amplitude will be denoted by $|\mathbf{B}_\perp|$. Automatic gain control was incorporated in the magnetometer amplifier to provide a wide dynamic range for the instrument by reducing the sensitivity with increasing measured field.

An aspect indicator provided information on the direction of the measured component of the magnetic field. This instrument measured the angle α between $\mathbf{B}_\perp$ and the component of the spacecraft-sun vector transverse to the spacecraft spin axis. Details of the instrument are available in an earlier report [*Judge*, 1959].

The scintillation detector aboard Explorer 6 consisted of a small plastic scintillator, a photomultiplier tube, and associated electronics. A small, foil-covered window was placed in the satellite shell so that the instrument could detect, through the window, electrons with energies greater than 200 kev and protons with energies greater than 2 Mev. Electrons with energies greater than 500 kev and protons with energies greater than 10 Mev could penetrate the satellite shell and be detected by the instrument. The geometrical factor of the detector was 180 times smaller for particles entering through the window than for those entering through the vehicle shell. A more detailed description of the Explorer 6 scintillation detector is available in an earlier publication [*Rosen and Farley*, 1961].

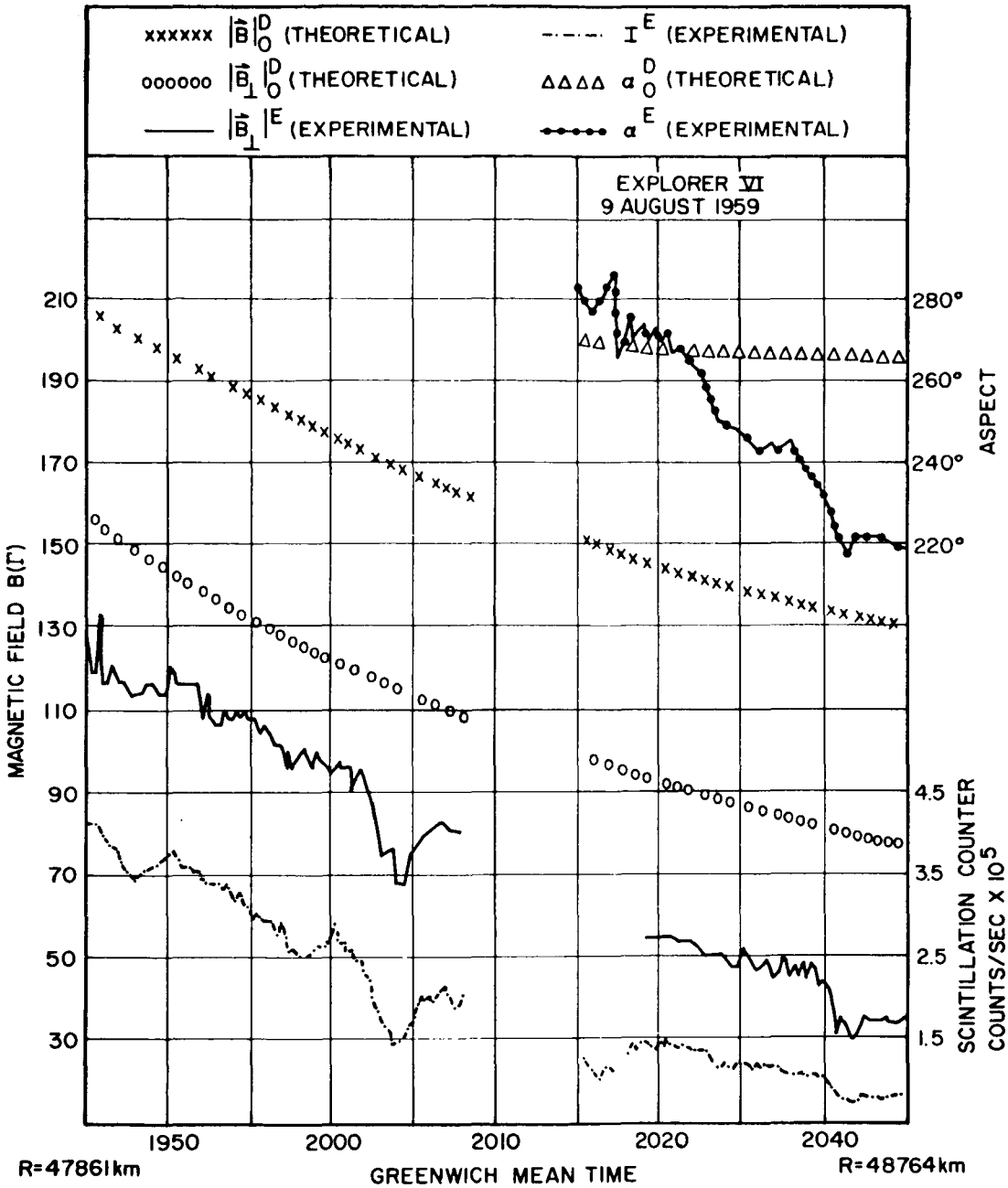

FIGURE 1.—*Effects produced by hydromagnetic disturbances and recorded by instruments aboard Explorer 6 during part of August 9, 1959. The experimental observations, designated by the superscript* E, *provide measurements of the following quantities:* $|\mathbf{B}_\perp|$, *the amplitude of the component of the ambient magnetic field that is transverse to the space craft spin axis;* α, *the direction of the transverse component of the field; and* I, *the ambient intensity (approximately omnidirectional) of energetic particles. Also shown are curves of theoretically expected values of* $|\mathbf{B}|$, $|\mathbf{B}_\perp|$, *and* α *that are based on a model derived from surface measurements of the geomagnetic field. These quantities carry the subscript* 0 *(zero) to indicate that they refer to the unperturbed geomagnetic field, and the superscript* D *to indicate that they have been derived from a model rather than measured.*

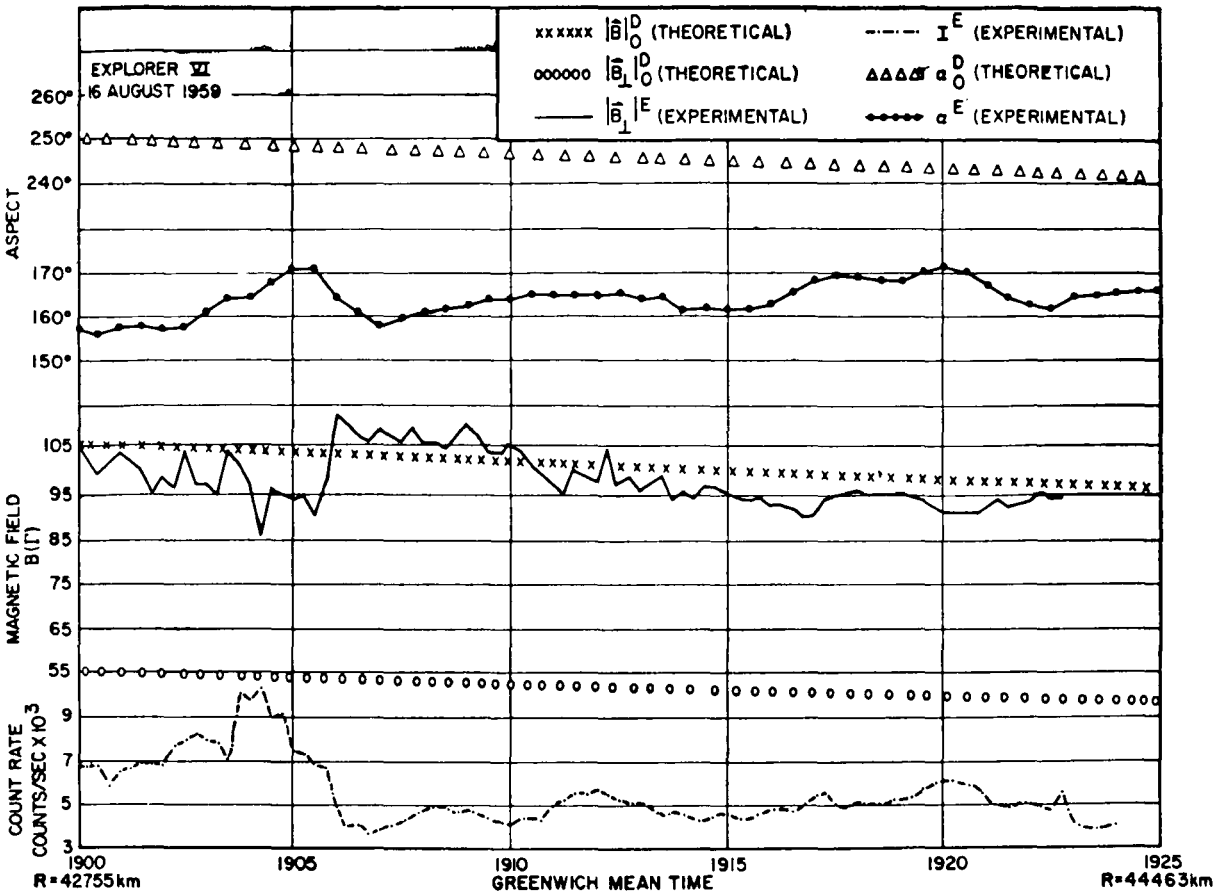

FIGURE 2.—*Effects produced by hydromagnetic disturbances on August 16, 1959. The quantities plotted are described in figure 1. Note that these results demonstrate fluctuations of field and particle intensities that are of opposite phases.*

OBSERVATIONS

Outstanding examples of the observations of hydromagnetic disturbances and their effects on trapped, charged particles were obtained on August 9, 16, and 18, 1959. Parts of the corresponding data are shown in figures 1, 2, and 3. In each of the figures, the data obtained from these instruments (magnetometer, aspect indicator, and scintillation detector) are plotted versus time (GMT) and radial distance r from the center of the earth. In addition to the empirical data, designated by the superscript E, theoretically expected values of $|\mathbf{B}_\perp|$, the amplitude of the component of the ambient magnetic field measured by the magnetometer; $|\mathbf{B}|$, the intensity of the total field; and α, the direction of the measured component, are plotted in the figures. These quantities will be identified by the subscript 0 (zero) to indicate that they pertain to the unperturbed geomagnetic field and by the superscript D to indicate they have been derived from a model rather than measured. Thus, we have $|\mathbf{B}_\perp|_0^D$, $|\mathbf{B}|_0^D$, and α_0^D. The expected values were computed by means of a model of the geomagnetic field developed by *Vestine* [1953].

Geomagnetic storm activity was absent on August 9 during the period of interest, although substantial field fluctuations were detected by surface magnetometers. A value of 39 was computed for the A_p index during the period of August 9 covered by data in figure 1. The value of A_p for August 9 was 22. The data presented

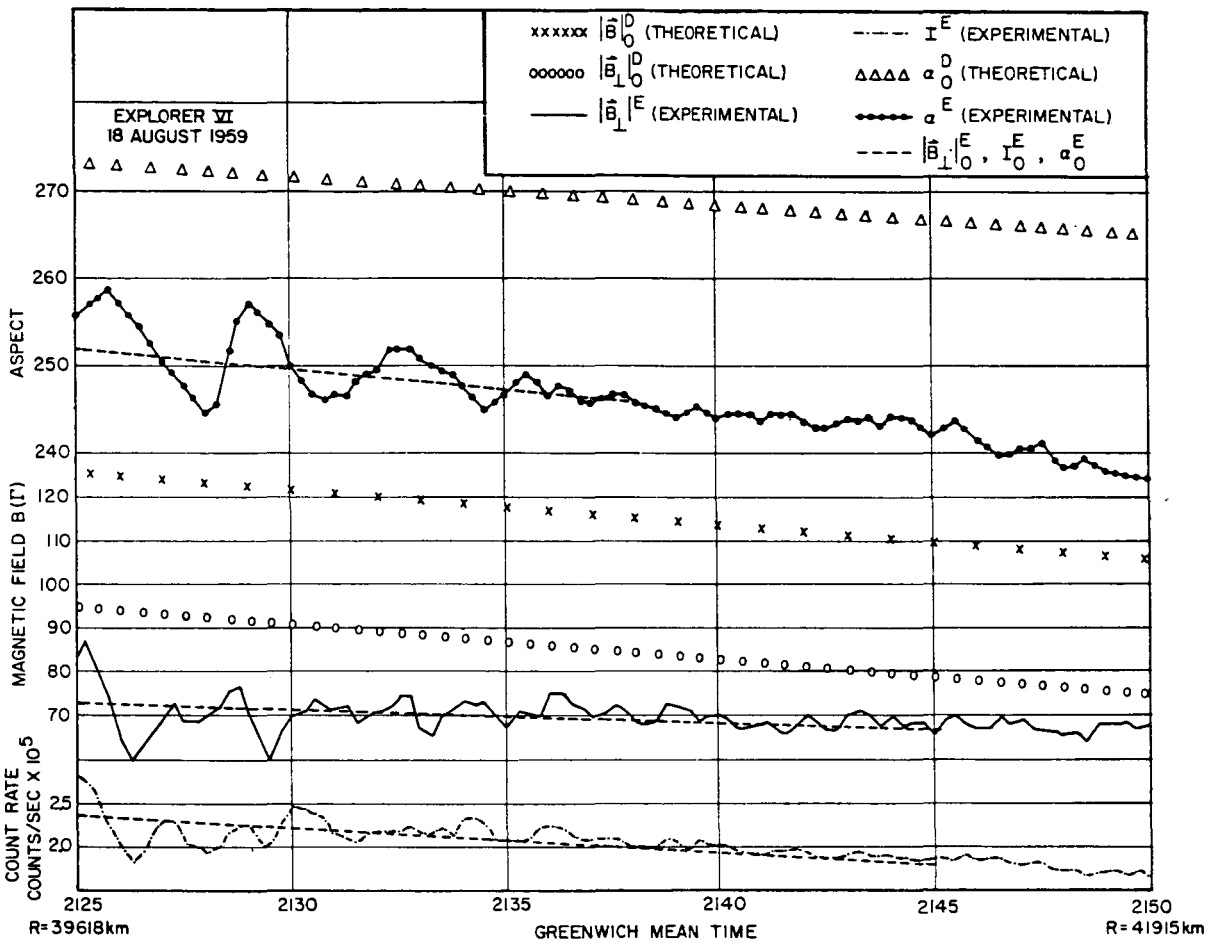

FIGURE 3.—*Effects produced by hydromagnetic disturbances on August 18, 1959. Most of the quantities plotted are described in figure 1. The remaining curves* $|\mathbf{B}_\perp|_0^E$, α_0^E, *and* I_0^E *are straight lines fitted to the plots of* $|\mathbf{B}_\perp|^E$, α^E, *and* I^E, *respectively, by the method of least squares. The subscript* 0 *(zero) implies the assumption that these values are representative of the geomagnetic field in the absence of the observed fluctuations and the superscript* E *indicates quantities based on empirical results rather than model calculations.*

in the figure provide a significant example of an "in-phase" correlation between variations in the measured component of the magnetic field and the scintillation detector count rate, particularly during the period around 2005 GMT. However, no aspect indicator data were obtained during most of the period indicated in the figure.

The observations presented in figure 2 were obtained on August 16 during the main phase of a geomagnetic storm that commenced at 0400 GMT on August 16. In contrast to the data in figures 1 and 3, these data show variations of the count rate that are of a phase nearly opposite the phase of the changes in the measured component of the field. The relationship between the magnetometer and scintillation detector measurements has been interpreted by *Farley and Rosen* [1961] as the result of the passage of diamagnetic gas clouds from the solar plasma into the geomagnetic field and past the spacecraft. Another phenomenon that might be responsible for such "out-of-phase" variations are a hydromagnetic disturbance traveling along the geomagnetic lines of force in the acoustic mode

of propagation. In this mode, which has been discussed in detail by *MacDonald* [1961], the variations in the pressure of the particles are balanced by variations of the opposite sense in the magnetic field pressure and accompanied by changes in the direction of the field. If it be assumed that the behavior of the detected particles is characteristic of the particles modifying the field, a disturbance of this type would produce the phase relationship shown by the results as well as changes in the field direction like those detected. Such behavior is possible, since disturbances of the frequency observed, propagating at the acoustic velocity, could violate the first adiabatic invariant of the particle motion.

If such were true, the source of the disturbances might well have been injected particles, as suggested. However, the disturbing solar plasma cloud itself need not have been in the vicinity of the spacecraft. These observations of August 16 will not be discussed further here, since the primary subject of this paper is the phenomenon that produces the in-phase variations of the particle flux and magnetic field like those seen on August 9 and 18.

The data shown in figure 3 were obtained on August 18 during the period immediately after the recovery of the August 16 magnetic storm. The value of the magnetic A_p index was again 39 during the period of interest, whereas the value of A_p for the day was 28. Thus, the level of geomagnetic activity was fairly high. In fact, during this day some observatories reported a continuation of the recovery from the magnetic storm. We shall consider, in detail, the results of August 18 only, because of the lack of aspect indicator data during the period of interest on August 9.

Before we discuss these observations, it is convenient to define a coordinate system (shown in fig. 4) related to the orientation of the theoretically predicted magnetic field, $\mathbf{B}_0{}^D$, as follows: The origin is fixed in the spacecraft. The z axis is parallel to the predicted field at the position of the vehicle. Thus the positive z direction is that from geomagnetic south to geomagnetic north. The y axis is perpendicular to the z axis, lies in the plane of the geomagnetic meridian containing the vehicle position, and is positive outward from the earth. The x axis is such as to complete the right-hand coordinate system and, therefore, is normal to the geomagnetic meridian plane and is directed westward.

As is indicated in figures 1, 2, and 3, the theoretically predicted field is significantly different from the measured geomagnetic field at distances from the earth such as those traversed during the periods of interest. However, the model provides us with a convenient means of defining directions, and we will use the directions so defined to describe the perturbations of the field under consideration.

Next, we consider the geometry of the experiment during the period of interest on August 18 in terms of the coordinate system just defined. According to available orbital data, the spin axis of the spacecraft, ω, was at an angle of approximately 52.50° to the z axis, or to $\mathbf{B}_0{}^D$. At the same time, the angle between ω_{xy}, the projection of the spin vector in the xy plane and the positive x direction was 43°. This situation is depicted in figure 4. Strictly speaking, this geometry existed at about 2130 GMT. However, changes of only a few degrees in the relative orientation of ω would have occurred during the twenty-minute period under consideration.

INTERPRETATION

With the foregoing description of the experiment in mind, we next attempt to describe effects that might be observed in the presence of hydromagnetic disturbances propagating in certain specific modes. The simple transverse mode, or Alfvén mode, is characterized to the first order by changes in the direction of the unperturbed local magnetic field with no accompanying changes in its magnitude, or with the addition of only a small transverse perturbing field. The compressional mode is characterized by changes in the magnetic field intensity with no changes in its direction. Since, as will be shown, the magnetic moment of trapped particles is conserved during these changes, the changes in field intensity produced by compressional oscillations should be accompanied by "in-phase" variations in the particle flux, particularly if the oscillations affect most

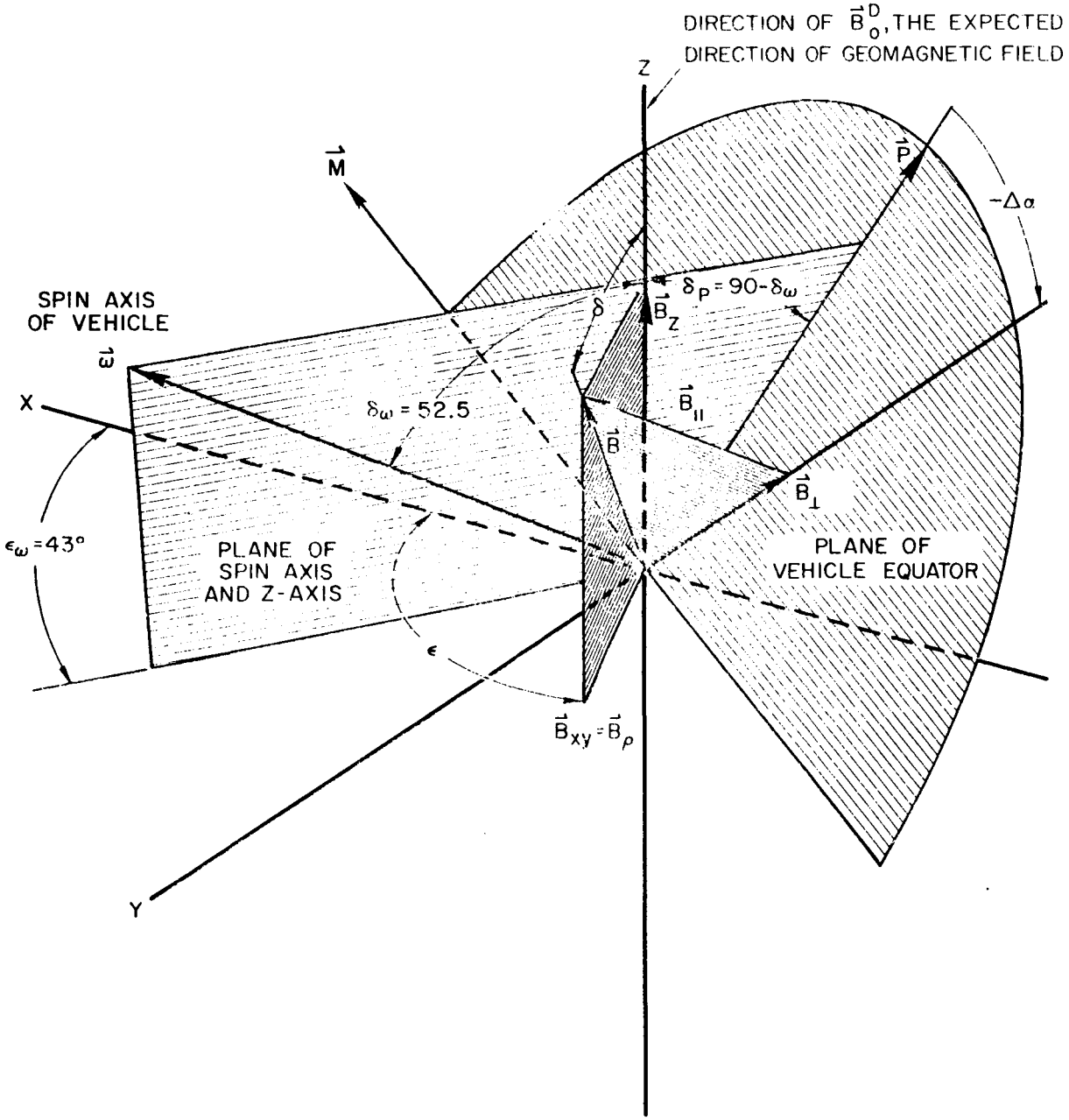

FIGURE 4.—*Geometry of the experiment. The angle 52.5° between the spin axis, represented by the vector* ω*, and the theoretically expected direction of the geomagnetic field, the* z *direction, is based on trajectory data for 2130 GMT on August 18, 1959. An arbitrarily oriented ambient field* **B** *is shown divided into a component* $\mathbf{B}_\perp$ *transverse to spin axis of the spacecraft, and a component* $\mathbf{B}_{||}$*, parallel to the spin axis. The angle* $\Delta\alpha$ *is a measure of the direction of* $\mathbf{B}_\perp$*. The angle actually recorded by the aspect indicator is measured from the direction of the component of the vehicle-sun line which is transverse to the spin axis, rather than from the direction of the vector* **P***, as shown. Hence,* $\Delta\alpha$ *as shown differs from the measured angle* α *by an amount nearly constant during the period of interest.*

of the region between mirror points on a given tube of magnetic flux. Of course, the hydromagnetic disturbances actually encountered may have been more complicated than a composition of only one or both of these modes. For example, according to analyses of *Herlofson* [1950], *van de Hulst* [1951], and *MacDonald* [1961], three modes of oscillation would, in general, arise from the passage of a hydromagnetic disturbance at an arbitary angle to the lines of magnetic force.

In any event, we submit that the changes in the direction of the magnetic field observed with the aspect indicator on August 18 provide evidence for the presence of transverse hydromagnetic disturbances and that the fluctuations in the scintillation detector count rate, roughly in phase with a component of the measured changes in the field strength, indicate the presence of large-scale compressional disturbances. To substantiate these remarks, changes in $|\mathbf{B}_\perp|$ and α resulting from several effects will be considered. Hence, additional notation will now be introduced to facilitate the discussion to follow. The subscript 0 will denote quantities associated with the unperturbed geomagnetic field; C, those associated with hydromagnetic disturbances in the compressional mode; and T, those associated with disturbances in the transverse mode. The superscript D or E will be used, respectively, to indicate whether the quantity was derived from some model or obtained empirically. Various components of the vector $\mathbf{B}$ will be denoted by subscripts. Thus, we have $\mathbf{B}_\perp$, the component perpendicular to the spin axis of the spacecraft; $\mathbf{B}_\omega$, the component parallel to ω, the spacecraft spin vector; and $\mathbf{B}_{xy}$, the component in the xy plane.

The quantities to be used most frequently are defined as follows:

$|\mathbf{B}_\perp|_0{}^D$ and $\alpha_0{}^D$ are the values of $|\mathbf{B}_\perp|$ and α that would be expected if the geomagnetic field in the region of interest were represented by the model of *Vestine* [1953].

$|\mathbf{B}_\perp|_0{}^E$ and $\alpha_0{}^E$ are assumed to be approximately the values of $|\mathbf{B}_\perp|$ and α that would have been observed during the periods of these measurements if the geomagnetic field had not been disturbed by the rapid fluctuations detected. The values for these quantities were obtained from lines that are the best fits to the data according to the method of least squares.

$|\mathbf{B}_\perp|_C{}^E$ is the value of $|\mathbf{B}_\perp|$ derived from a simple model of a hydromagnetic disturbance propagating in a compressional mode. This model will be described subsequently.

$|\mathbf{B}_\perp|_T{}^D$ is, similarly, the value of $|\mathbf{B}_\perp|$ derived from a simple model of disturbances propagating in the transverse mode. This model will also be described in detail subsequently.

With the measured values of $|\mathbf{B}_\perp|$ and α denoted by $|\mathbf{B}_\perp|^E$ and α^E, respectively, we define the quantities

$$\Delta|\mathbf{B}_\perp|^E \equiv |\mathbf{B}_\perp|^E - |\mathbf{B}_\perp|_0{}^E$$

and

$$\Delta\alpha^E \equiv \alpha^E - \alpha_0{}^E$$

EFFECTS OF THE TRANSVERSE MODE

In this section we shall attempt to separate, from the observed variations of $|\mathbf{B}_\perp|^E$, the component produced by the transverse disturbances. In order to consider the experimental results that might be anticipated in the presence of hydromagnetic disturbances in the transverse mode, it is necessary to determine the effects of changes in field direction and magnitude upon the quantities measured by the magnetometer and aspect indicator, i.e., $|\mathbf{B}_\perp|^E$ and α^E, respectively. The relations governing these effects are derived below from the geometry of the system, by means of the angles defined in figure 4.

The magnetic field $\mathbf{B}(t)$ may be described by the expression

$$\mathbf{B}(t) = \mathbf{i}B_x(t) + \mathbf{j}B_y(t) + \mathbf{k}B_z(t)$$

where $\mathbf{i}$, $\mathbf{j}$, and $\mathbf{k}$ are unit vectors in the directions of the x, y, and z axes, respectively; t is the time; and

$$\begin{aligned} B_x &= |\mathbf{B}(t)| \sin\delta(t) \cos\epsilon(t) \\ B_y &= |\mathbf{B}(t)| \sin\delta(t) \sin\epsilon(t) \\ B_z &= |\mathbf{B}(t)| \cos\delta(t) \end{aligned} \qquad (1)$$

where $|\mathbf{B}(t)|$ is the magnitude of the field. We have assumed that the unperturbed field lies along the z axis. Thus, in the absence of a perturbing influence, $\mathbf{B} = |\mathbf{B}(t)|\mathbf{k}$.

The magnitude of the component of $\mathbf{B}$ that is parallel to ω is given by $\mathbf{B}_\omega = \mathbf{B}\cdot\boldsymbol{\omega} = B_x \cos\epsilon_\omega$

$\sin \delta_\omega + B_y \sin \epsilon_\omega \sin \delta_\omega + B_z \cos \delta_\omega$, where $\boldsymbol{\omega} = \mathbf{i} \cos \epsilon_\omega \sin \delta_\omega + \mathbf{j} \sin \epsilon_\omega \sin \delta_\omega + \mathbf{k} \cos \delta_\omega$.

The magnitude of the component of the field perpendicular to the spin axis, $\boldsymbol{\omega}$, is

$$[|\mathbf{B}_\perp| = [|\mathbf{B}|^2 - (\mathbf{B} \cdot \boldsymbol{\omega})^2]^{1/2} = |\mathbf{B}| \sin [\cos^{-1} (|\mathbf{B}_\omega|/|\mathbf{B}|)]$$

Next, we define the unit vector $\mathbf{P}$, the direction of which is determined by the intersection of the equatorial plane of the vehicle with the plane containing $\boldsymbol{\omega}$ and the z axis. Thus, $\mathbf{P}$ is perpendicular to $\boldsymbol{\omega}$ and

$$\begin{aligned}\mathbf{P} &= \mathbf{i} \cos \epsilon_p \sin \delta_p + \mathbf{j} \sin \epsilon_p \sin \delta_p + \mathbf{k} \cos \delta_p \\ &= -\mathbf{i} \cos \epsilon_\omega \cos \delta_\omega - \mathbf{j} \sin \epsilon_\omega \cos \delta_\omega + \mathbf{k} \sin \delta_\omega\end{aligned}$$

We then define the unit vector $\mathbf{M} = (\boldsymbol{\omega} \times \mathbf{P})/|\boldsymbol{\omega} \times \mathbf{P}|$. Thus, $\mathbf{M}$ is determined by the intersection of the xy plane and the equatorial plane of the vehicle. The field vector $\mathbf{B}$ will have components parallel to $\mathbf{P}$ and $\mathbf{M}$ with magnitudes

$$|\mathbf{B}_P| = \mathbf{B} \cdot \mathbf{P} \text{ and } |\mathbf{B}_M| = \mathbf{B} \cdot \mathbf{M}$$

The angle $\Delta\alpha$, as depicted in figure 4, is then just

$$\Delta\alpha = \tan^{-1} (|\mathbf{B}_M|/|\mathbf{B}_P|)$$

During this period on August 18, approximate values of the parameters used in the foregoing were

$$\epsilon_\omega \simeq 43^\circ \qquad \delta_\omega \simeq 52.5^\circ$$

With the geometry of the experiment so defined, values of $\Delta\alpha$ and $|\mathbf{B}_\perp|/|\mathbf{B}|$ were calculated for various orientations of the field, i.e., for various values of δ and ϵ. The results are plotted in figure 5. Note that, for $\delta = 0$, $|\mathbf{B}_\perp|/|\mathbf{B}| = 0.793$ since $\mathbf{B}$ is then parallel to the z axis and $|\mathbf{B}_\perp| = |\mathbf{B}| \sin \delta_\omega = 0.793\ |\mathbf{B}|$. Also, for $\epsilon = \epsilon_\omega = 43^\circ$, or $\epsilon = 43^\circ + 180^\circ = 223^\circ$, the field vector lies in the plane defined by the z axis and $\boldsymbol{\omega}$, the spin vector, so that $\Delta\alpha = 0$.

Next we consider a simple model of a circularly polarized, transverse hydromagnetic wave. This model is one in which the disturbance would produce an effect at the space craft similar to that which would result from a precession of the magnetic field about its unperturbed direction. The simplest version then would appear as a field vector of constant magnitude, precessing at a constant rate and maintaining a constant angle, δ, with the direction of the unperturbed field, or the z axis. Thus in equations 1 we would have

$$\begin{aligned}|\mathbf{B}_\perp|(t) &= \text{constant} \\ \delta &= \text{constant} \\ \epsilon &= [(2\pi t/\tau) + \epsilon_0]\end{aligned}$$

where τ is the period of precession. For the geometry represented in figure 4, using $|\mathbf{B}_\perp| = 1$, $\tau = 195$ sec, and $\delta = 10^\circ$ and 20°, the variations in $|\mathbf{B}_\perp|$ and $\Delta\alpha$ that would be recorded by the magnetometer and aspect indicator, respectively, can be obtained from figure 5. The results, denoted by $|\mathbf{B}_\perp|_{\tau^D}$ and $\Delta\alpha_{\tau^D}$, are plotted versus time and ϵ in figure 6.

Next, we turn our attention to the experimental results obtained between 2125 and 2150 GMT on August 18, 1959. As stated previously, we have assumed that the disturbances in the transverse mode were solely responsible for the observed variations of α^E and that the variations of $|\mathbf{B}_\perp|^E$ were the result of disturbances in more than one mode. Hence, we will use the measurements of α^E in an effort to approximate the component of the variations in $|\mathbf{B}_\perp|$ that was produced by the transverse mode. Actually the results for $\Delta\alpha = \alpha^E - \alpha_0{}^E$ versus time, shown in figure 7, will be used. Thus, from the measurements of $\Delta\alpha^E$, we will attempt to obtain $|\mathbf{B}(t)|$, $\epsilon(t)$, and $\delta(t)$, which are needed to describe the field under the influence of such disturbances.

Consider first $|\mathbf{B}(t)|$. In figure 3 $|\mathbf{B}_\perp|_0{}^E$ is assumed to represent the steady-state values of $|\mathbf{B}_\perp|$. The angle between ω and the direction of the unperturbed field is taken to be 52.5°, so that we have $|\mathbf{B}| = |\mathbf{B}_\perp|/0.793$. Since $|\mathbf{B}_\perp|_0{}^E$ is changing relatively slowly during the period of interest, we take an approximate average value of 70γ. Thus, $|\mathbf{B}(t)| \simeq 88\gamma$.

Next, consider $\epsilon(t)$. From figures 5 and 6, we see that the maximums and minimums in the variations of $\Delta\alpha$ versus time, produced by a precessing field vector, occur at $\epsilon = 293^\circ$ and 150°, respectively. We use this fact to establish the phase of $\epsilon(t)$. The average period of the variations in $\Delta\alpha^E$ is approximately 195 sec. However, if this value of the period is to be consistent with the values of ϵ assumed to correspond to the maximums and minimums of

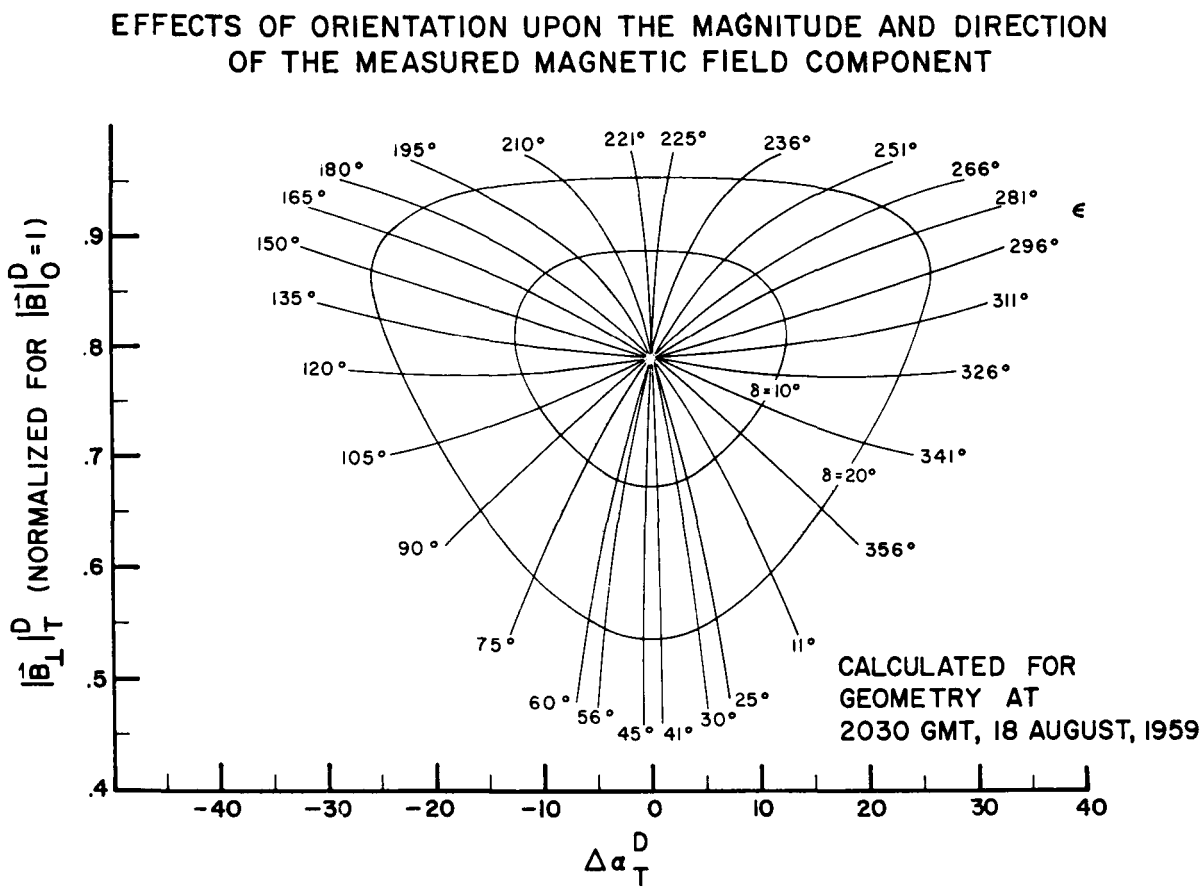

FIGURE 5.—*Curves showing the effects of field orientation upon the measured parameters of the field* $|\mathbf{B}_\perp|$ *and* $\Delta\alpha$, *assuming the geometry shown in figure 4. The ordinate quantity is actually* $|\mathbf{B}_\perp|/|\mathbf{B}|$. *The parameter* δ *is the angle between* **B** *and the z axis. The parameter* ϵ *is the azimuthal angle.*

$\Delta\alpha^E$, it is necessary to assume that the rotation rate was not constant. Thus, the 195-sec period was divided into a 60-sec interval for the increasing portions of the curve and a 135-sec interval for the decreasing portions. These intervals correspond to ranges of ϵ from 150° to 296°, and from 296° through zero degrees to 150°, respectively. This apparent variation of rotation rate is probably due to elliptical polarization of the transverse component. Because of the geometry of the system, divergence of just this type from the results expected for simple, circular polarization would be affected by disturbances somewhat elliptically polarized.

Finally, consider the function $\delta(t)$. It was found that the measurements of $\Delta\alpha^E$ could be well approximated if δ were assumed to be constant at about 5.5° from 21h 25m 00s GMT to 21h 29m 00s GMT and to vary as $5.5\ (1 + t/300)^{-1}$, where t is in seconds, during the remainder of the period of interest.

With $|\mathbf{B}(t)|$, $\epsilon(t)$, and $\delta(t)$ established as just described, the resulting values of $\Delta\alpha$ were calculated and plotted in figure 7. These results are denoted by $\Delta\alpha_T{}^E$ and are superimposed upon the plot of $\Delta\alpha^E$ to facilitate comparison. Since $\Delta\alpha_T{}^E$, the partially idealized version of the observations, is a reasonable facsimile of $\Delta\alpha^E$, we next apply the same values of $|\mathbf{B}(t)|$, $\epsilon(t)$, and $\delta(t)$, used in calculating $\Delta\alpha_T{}^E$, to a calculation of $|\mathbf{B}_\perp|_T{}^E$, the component of $|\mathbf{B}_\perp|^E$ that will be attributed to the presence of the transverse disturbances. $|\mathbf{B}_\perp|_T{}^E$ ob-

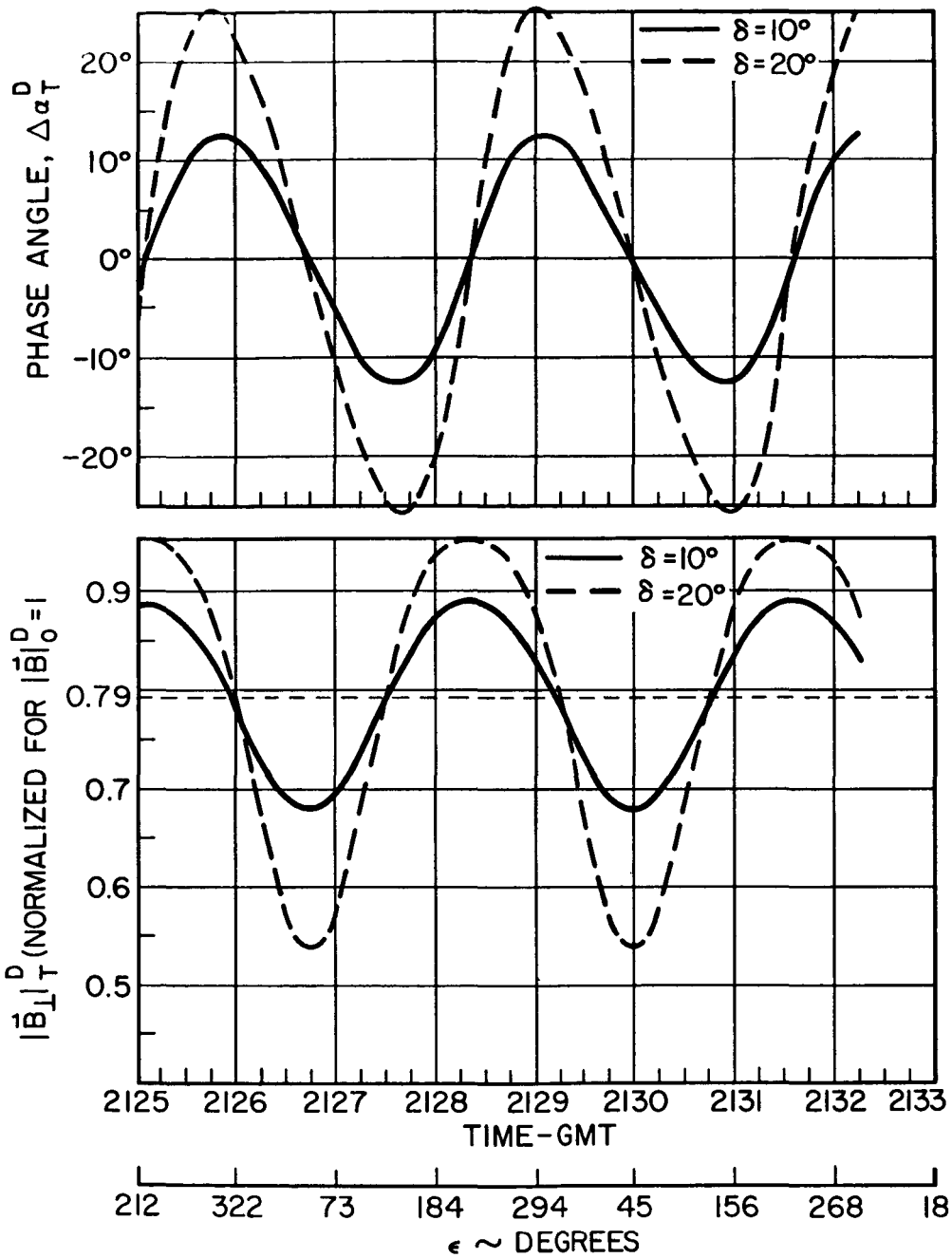

FIGURE 6.—*Curves showing the variations, with time, of* $\Delta\alpha$ *and* B_1 *that would be produced by a field of unit intensity at an angle* δ *to the z direction and precessing about the z direction at a constant rate with a period of 195 sec. These results denoted by* $\Delta\alpha_T{}^D$ *and* $|B_\perp|_T{}^D$ *respectively, are then assumed to represent the effect of a simple, circularly polarized, transverse wave of constant amplitude and the period indicated. The abscissa is graduated in GMT to facilitate comparison with the experimental results. The phase of* ϵ *relative to GMT is established from figure 5. Thus, minima in* $\Delta\alpha_T{}^D$ *occur at* $\epsilon = 150°$ *and maxima occur at* $\epsilon = 293°$.

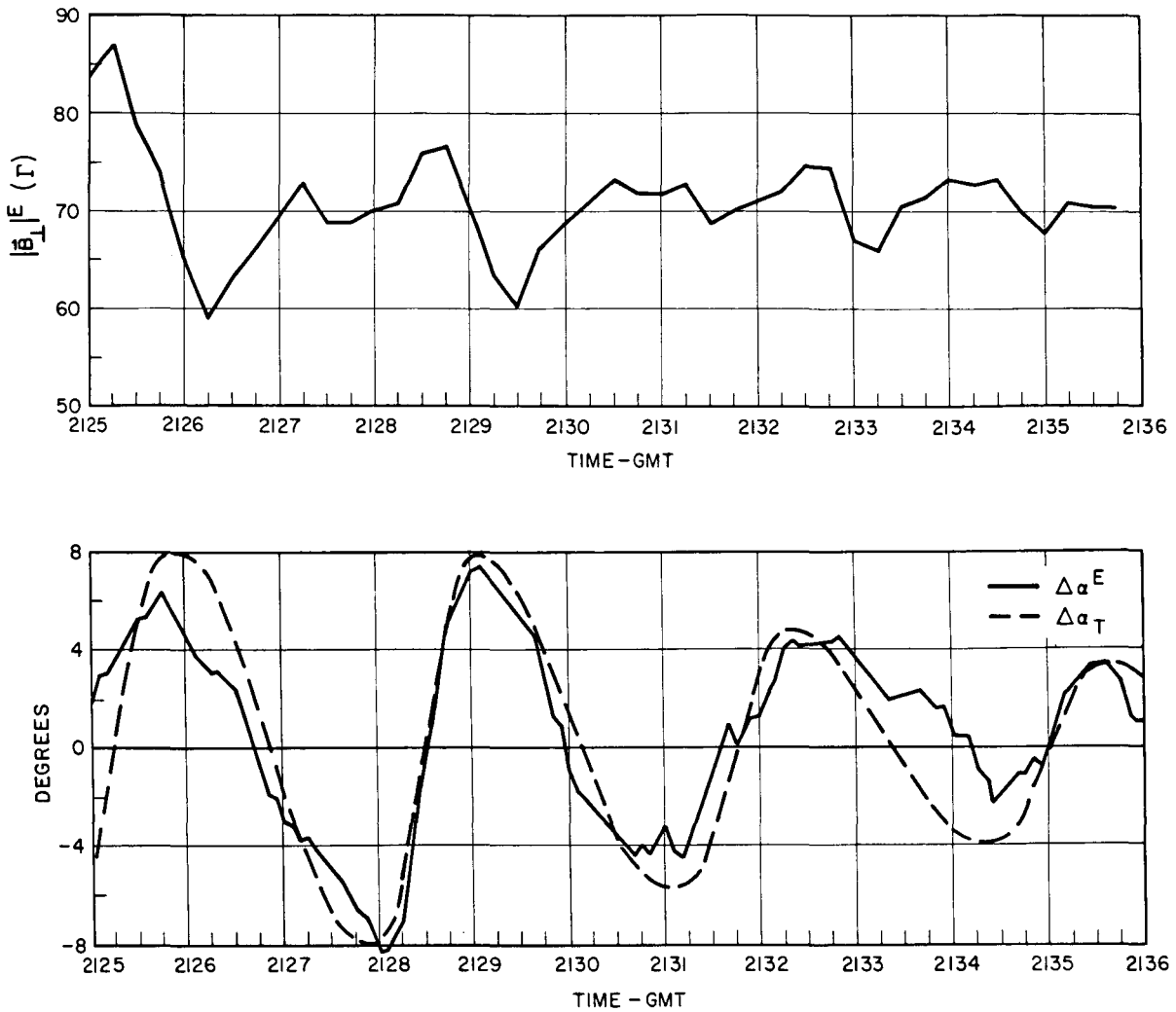

FIGURE 7.—*The curves of* $|\mathbf{B}_\perp|^E$ *and* $\Delta\alpha^E$ *are the results shown in figure 3, replotted to permit the use of an expanded time scale. Actually,* $\Delta\alpha^E = \alpha^E - \alpha_0{}^E$. *The last two quantities appeared in figure 3. Also shown is a partially idealized plot of* $\Delta\alpha^E$, *denoted by* $\Delta\alpha_T{}^E$, *and superimposed on the curve of* $\Delta\alpha^E$.

tained in this manner from the curves in figure 5 is plotted in figure 8. Actually, the quantity plotted is $\Delta|\mathbf{B}_\perp|_T{}^E = |\mathbf{B}_\perp|_T{}^E - |\mathbf{B}_\perp|_0{}^E \simeq |\mathbf{B}_\perp|_T{}^E - 70\gamma$.

In the same curve the difference between $\Delta\ |\mathbf{B}_\perp|_T{}^E$ and $|\mathbf{B}_\perp|^E$ is plotted. This quantity should provide a measure of the variations in $|\mathbf{B}_\perp|^E$ produced by disturbances other than those in the transverse mode. As will be seen, this difference exhibits a rather striking correlation with the variations in the count rate of the scintillation detector. Thus, these effects are attributed to the presence of hydromagnetic disturbances in the compressional mode. This mode will be considered further in the next section.

A comparison of the data and the model also indicates that the direction of rotation was clockwise to an observer looking along the field direction toward geomagnetic north. This result may be compared with that of *Wilson and Sugiura* [1961] who have reported on ground-

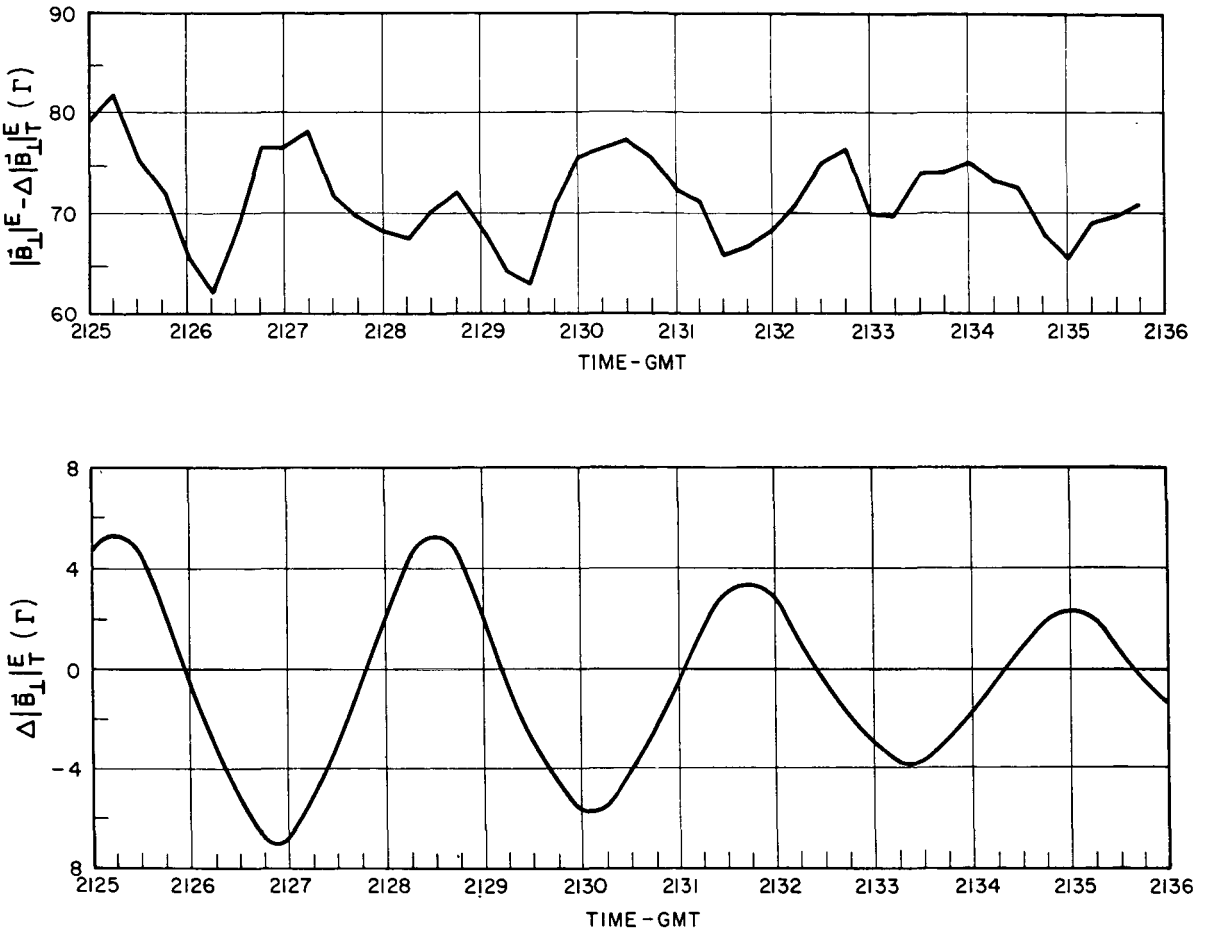

FIGURE 8.—*Components of the variations in* $|\mathbf{B}_\perp|^E$, *method 1. This method consists of using the measured values of* α *to calculate the component* $|\mathbf{B}_\perp|_T^E$, *due to the hydromagnetic disturbances in the transverse mode, and taking the difference between* $|\mathbf{B}_\perp|^E$ *and* $|\mathbf{B}_\perp|_T^E$ *to determine the component due to disturbances in other modes. The quantity actually plotted in the lower curve is* $\Delta|\mathbf{B}_\perp|_T^E = |\mathbf{B}_\perp|_T^E - |\mathbf{B}_\perp|_0^E$. *The upper curve is then* $|\mathbf{B}_\perp|^E - \Delta|\mathbf{B}_\perp|_T^E$.

based observations of geomagnetic field fluctuations that they interpret as the result of transverse hydromagnetic waves. The polarization of these waves was observed to depend upon local time, i.e., they are usually clockwise between 1000 and 2200 hours and counterclockwise between 2200 and 1000 hours. Since the satellite was at approximately 1900 hours local time, the transverse oscillations observed in the distant geomagnetic field apparently followed this rule. It should be noted that waves polarized in this sense would appear to be clockwise polarized in the northern hemisphere and counterclockwise polarized in the southern hemisphere, according to the definitions of Wilson and Sugiura.

In this section, then, we have employed the observations of the variations in the orientation of the measured component of the magnetic field, along with an extremely simple model of transverse hydromagnetic waves, in an attempt to estimate the contribution of disturbances in this mode to the variations of $|B_\perp|^E$. A measure of our success in this undertaking is the correlation between scintillation detector data and the variations of $|B_\perp|^E$ remaining after we have subtracted the estimated contribution of the transverse mode.

EFFECTS OF LARGE-SCALE COMPRESSIONAL DISTURBANCES

In this section we shall attempt to utilize the measurements of the flux of energetic particles to estimate the contribution of disturbances in the compressional mode to the variations in $|B_\perp|^E$. Using an $E^{-\gamma}$ particle energy spectrum, and other assumptions stated below, *Coleman* [1961] has calculated the effect upon trapped particles of large scale, compressional fluctuations in the geomagnetic field. We wish to apply the results of this calculation to test for the presence of such compressional disturbances during the period of August 18, 1959, under discussion. The parameter γ is important to the results. Thus, we will use an iterative process, first to compute γ from the data and next, using the calculated value of γ, to estimate the variations of $|B_\perp|$ that would have been required had such compressional disturbances actually produced the observed fluctuations in the count rate of the scintillation detector. Values of B calculated in this manner will be denoted by $|B_\perp|_c^E$.

To treat the motion of geomagnetically trapped particles somewhat more rigorously, consider a charged particle moving in a magnetic field **B** that can be represented in cylindrical coordinates ρ, ϵ and by a vector potential having only an ϵ component. Let this component be given by $A_\epsilon(\rho, z, t)$, where t is the time. Suppose that the projection of the particle's path upon the plane $z = 0$ has an approximate radius of curvature R and that the approximate period of the motion parallel to this plane is T. The restrictions placed on the temporal and spatial variations of the field **B** are

$$|(R\mathbf{k}_\rho \cdot \nabla)\mathbf{B}| << |\mathbf{B}|$$

and

$$|T\partial\mathbf{B}/\partial t| << |\mathbf{B}| \qquad (2)$$

where $\mathbf{k}_\rho$ is a unit vector in the ρ direction.

For the case of relativistic particle motion, *Layton* [1957] has shown that, when the magnetic field changes in such a system, a constant of the particle motion is the product of a quantity described as the generalized magnetic moment of the particle and the total particle energy. This result may be written

$$[(E_0^2 - m_0^2c^4) \sin^2 \theta]/|\mathbf{B}_z| = \text{constant}$$

where E is the total particle energy given by

$$E = m_0c^2(1 - \beta^2)^{-1}$$

m_0 is the particle rest mass, c is the velocity of light, v is the magnitude of particle velocity, θ is the angle between $\mathbf{B}_z$ and v, and $\beta = v/c$.

The magnitude of the relativistic particle momentum is

$$p = m_0c\beta(1 - \beta^2)^{-1/2}$$

so that the constant of the motion may be written

$$(p^2 \sin^2 \theta)/|\mathbf{B}_z| = \text{constant} \qquad (3)$$

which is the first adiabatic invariant for relativistic particles. Thus, violation of conditions 2 is equivalent to violation of this invariant. Note that (3), in the nonrelativistic limit, can be written

$$v_\perp^2/|\mathbf{B}_z| = \text{constant}$$

where $v_\perp$ is the component of v transverse to $\mathbf{B}_z$. This is the frequently used form of the first adiabatic invariant which describes the conservation of the magnetic moment of the particles [*Alfvén*, 1950].

Next, consider a system composed of a number of charged particles in a magnetic field. We assume initial conditions as follows:

(*a*) The magnetic field is uniform in the z direction with strength $|\mathbf{B}|_0$.

(*b*) The number of particles per centimeter^3 with energies greater than E is given by

$$N_0(> E) = KE^{-\gamma}$$

(*c*) The particle flux is isotropic.

Thus, the omnidirectional particle intensity is given, initially, by the expression

$$I_0(> E) = \int_E^\infty v(E)n(E)dE$$

where

$$n(E)dE = - dN_0(> E)$$

With these initial conditions, we next consider how the particle intensity changes as the magnetic field strength changes slowly and

uniformly from $|\mathbf{B}|_0$ to $|\mathbf{B}|$. Note that such a change in the field is a special case of a system restricted according to (2). In this case, *Coleman* [1961] has shown that the relationship, including relativistic effects, between I_0, defined above, and I, the omnidirectional intensity of particles with energies greater than E after the field change, may be written:

$$\log (I/I_0)/\log (|\mathbf{B}|/|\mathbf{B}|_0) = \gamma[0.56-0.08 (\log \sigma/\log 2)] + 1 \quad (4)$$

at least for $1 < \sigma < 8$. Here σ is defined by the relation

$$E = m_0c^2[(\sigma^2 + 1)^{1/2} - 1]$$

For this expression, the value of E is taken to be the energy threshold of the particle detector.

Since the experimental results described herein provide measurements of the quantities $I(> E)$ and of a component of $\mathbf{B}$ in (4), we wish to apply this expression to the data of August 18 to calculate a value for γ and, thereby, estimate the shape of the energy spectrum of the observed particles. A reasonable result will allow the conclusion that a betatron-type mechanism was operating and, therefore, that compressional hydromagnetic disturbances were affecting most of the region between the mirror points of the particles in a reasonably uniform manner.

Before proceeding, it is necessary to determine that the actual conditions associated with these disturbances do not violate the restrictions given in (2), i.e., do not violate the first adiabatic invariant. According to *Farley and Rosen* [1960], the particles associated with the observed effects are primarily electrons of energies greater than 500 kev. Consider, for a moment, particles at the extremes of an energy range about 500 kev. The average value of the magnetic field is somewhat less than 100 γ in this region. For a 200-kev electron in this field, the Larmor radius is about $R \simeq 16$ km, and the period of the motion is $T \cong 5 \times 10^{-4}$ sec. The contribution of particles with energies greater than 10 Mev to the observed intensity is negligible for such a spectrum even if the exponent γ is as low as 0.5. For an electron of this energy, the Larmor radius is $R \cong 3.5 \times 10^2$ km and the period is about $T \cong 7 \times 10^{-3}$ sec. It is immediately apparent that the periods of about 100 sec seen in figure 3 far exceed those of the cyclotron motion even for the higher-energy particles.

Assuming that these fluctuations are produced by compressional waves, the wavelength of the disturbances may be calculated by means of an estimate of the Alfvén velocity v_A for such a wave in this region. Thus, for a 100-γ field and an ion density of 100 cm^{-3}, $v_A \simeq 200$ km sec^{-1} The wavelength corresponding to a 100-sec period is, then, about 2×10^4 km, and for a 20-γ peak-to-peak wave amplitude, the gradients (dB/dS) transverse to the geomagnetic field are about 2×10^{-3} γ/km. Also the upper limit of the rate of change of the field with time, for these fluctuations, is about 4×10^{-1} γ/sec.

Applying the restrictions in (2) to this system, using the largest values of T and R, i.e., those for the 10-Mev electrons, it is found that the field gradients must be much less than 3×10^{-1} γ/km and that the rate of field changes must be much less than 1.4×10 γ/km. From the results in the previous paragraph it is seen that these conditions would be satisfied even if the estimated values of v_A were a factor of 10 too great. However, it should be mentioned that the velocity of sound in this region is probably $0.01v_A$. Thus, if the disturbances were propagating at this velocity, the first invariant might be violated. Recall that disturbances traveling at the lower velocity were discussed in connection with the results of August 16 shown in figure 2. For an indication of the scale size of the compressional disturbances as measured along the geomagnetic field lines, however, we must rely on the argument that most of the region between mirror points must have been affected.

Consider, next, the second invariant. As described by *Welch and Whitaker* [1959], the motion of a trapped particle is such that the time required for its travel between mirror points is independent of the latitude range through which it travels and nearly proportional to its distance from the earth's center where it crosses the geomagnetic equator. For a relativistic electron, this "bounce" period at $7R_e$ (R_e =radius of earth) is about 0.7 sec., and, for a 200-kev particle, is only about 1 sec. Clearly, the fluctuations being considered are too gradual

to affect this component of the particle motion significantly.

The third invariant, however, must be violated by these disturbances. *Welch and Whitaker* [1959] have shown that the average time required for electrons of a given energy to drift 360° in longitude varies less than 8 percent for particles confined within ±60° latitude of the geomagnetic equator. From extrapolations of their results, the drift time for a 200-kev electron at $7R_e$ is about 2.5×10^3 sec, for a 500-kev particle it is 1.0×10^3 sec, for 1 Mev it is approximately 0.57×10^3 sec, etc. For a 10-Mev particle, however, the drift time is comparable to the periods of the observed disturbances, i.e., about 60 sec. Thus, particles in this energy range should be much less affected by such hydromagnetic activity. Further, the periods of the drift motion decrease, with increasing distance of the particle from earth's center, as the inverse of the distance. As a result, 10 Mev particles apparently would not be greatly affected by these disturbances at distances greater than $6R_e$ if the geomagnetic field retains its dipolar character. Thus, such waves, particularly any of longer periods, might be expected to preferentially affect lower-energy particles as the waves travel toward the earth and to produce a hardening of the trapped particle spectrum with increasing radial distance, which has been suggested by *Fan et al.* [1916].

We have shown that these August 18 disturbances should not violate the first two invariants of the observed particles in this region, but should violate the third. However, it should be noted that disturbances of higher frequencies have been detected in this same range of geocentric distance on several occasions with the magnetometer aboard Pioneer 1 [*Sonett et al.*, 1962] as well as with the magnetometer aboard Explorer 6. The Explorer data are being analyzed in detail presently.

We now wish to apply the results of the calculation just described to the measurements obtained on August 18, 1959. To compute the value of the exponent γ, first it is necessary to estimate the values of $|\mathbf{B}|_0$ and I_0 $(> E)$ during the period. To this purpose, the best-fit straight lines for the experimental plots of count rate, I^E versus time and $|\mathbf{B}_\perp|^E$ versus time in figure 3 were calculated by the method of least squares. These lines were assumed to represent I_0 $(> E)$ and $|\mathbf{B}_\perp|_0$, respectively, as functions of time, and are denoted by I_0^E and $|\mathbf{B}_\perp|_0^E$. Under these assumptions, we next compare $|\mathbf{B}_\perp|^E$ with $|\mathbf{B}_\perp|_0^E$ and the count rate, I^E $(> E)$, with I_0^E $(> E)$ at various times shown in the figure. In figure 9 we have plotted log (I^E/I_0^E) versus log $(|\mathbf{B}_\perp|^E/|\mathbf{B}_\perp|_0^E)$ obtained in this fashion. Note that, for the compressional mode, $(|\mathbf{B}_\perp|/\mathbf{B}_\perp|_0) = (|\mathbf{B}|/|\mathbf{B}|_0)$. These points are compared with the results calculated by *Coleman* [1961] for the case of electrons with energies greater than 500 kev. From the slope of the best-fit straight line drawn through the experimental data, we have computed the value for the exponent γ using (4). The result is $\gamma \simeq 1$.

Two effects likely account for the scatter of the points plotted in figure 9. The most significant is the presence of effects from hydromagnetic disturbances other than the compressional ones. Since disturbances in other modes affect $|\mathbf{B}_\perp|^E$, but do not necessarily affect the particle flux as observed with an omnidirectional detector, the data points would be expected to deviate from the line corresponding to any value of the exponent γ. However, if the data cover a sufficient number of cycles in the variation produced by the other modes, the average value of γ calculated in this manner should not be significantly affected by the disturbances in other modes.

The second effect is an instrumental one. Since the output of the magnetometer was basically a 2.8 cps sinusoid of varying amplitude, the quality of the magnetometer telemetry during these periods was lower than that of the telemetry from the other two instruments. Compared to the signals from these other two instruments, the signal from the magnetometer occupied a wide bandwidth and, therefore, suffered from a lower signal-to-noise power ratio. Thus, noise sufficient to partially destroy the correlation between the magnetometer data and the scintillation detector count rate may have been present in the magnetometer signal. However, as will be shown, the absence of a simple correlation was mainly the result of the

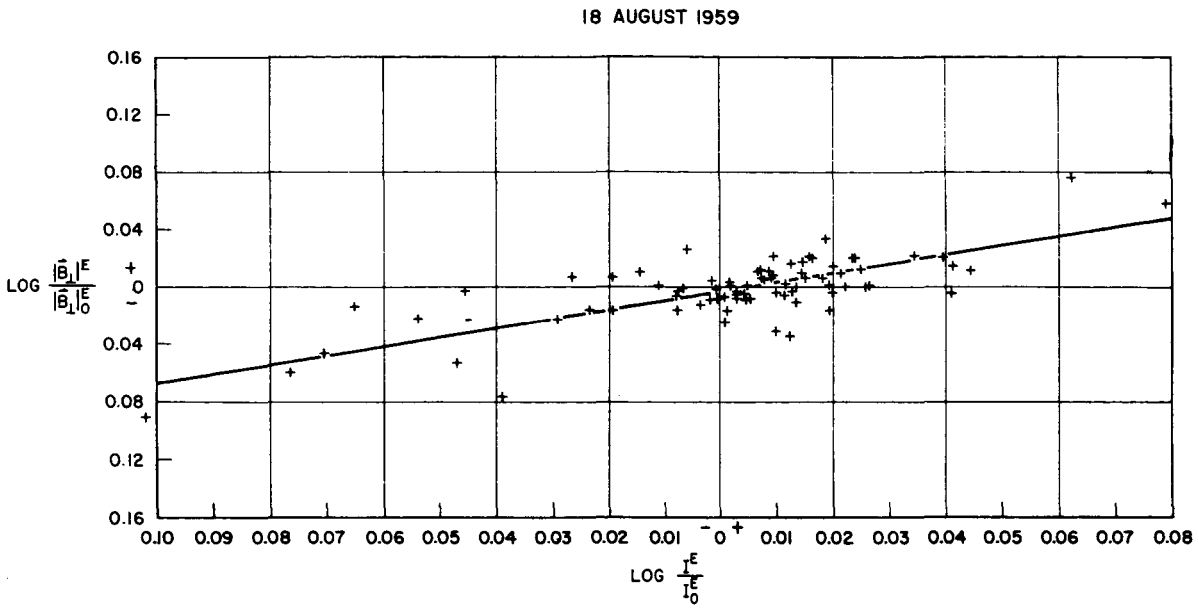

FIGURE 9.—*The data points are computed values of log* (I^E/I_0^E) *plotted versus values of log* $(|\mathbf{B}_\perp|^E/|\mathbf{B}_\perp|_0^E)$ *obtained coincidentally. Values were computed at 15-sec intervals from the curves of* $|\mathbf{B}_\perp|^E$, $|\mathbf{B}_\perp|_0^E$, I^E, *and* I_0^E, *versus time, in figure 3. For compressional disturbances behaving in accordance with the model, these points should fall approximately on a straight line. The line in the figure is the best fit to the data using the method of least squares. The scatter, in part at least, is due to the presence of modes other than the compressional one.*

presence of hydromagnetic disturbances propagating in more than a single mode.

Values for the exponent γ as defined in the foregoing, on the basis of various types of experimental observations, have been estimated previously by several experiments. It is of interest to compare the value $\gamma \simeq 1$ with such estimates. *Vernov and Chudakov* [1960], assuming an energy spectrum given by $N(> E) = E^{-\gamma}$, estimate $\gamma \simeq 5$ for electrons in the energy range from 20 kev to 100 kev at the maximum of the outer radiation zone. They also reported that the unidirectional flux of electrons with energies greater than 20 kev was $\simeq 10^9$ cm^{-2} sec^{-1} $ster^{-1}$, whereas that of electrons with energies in the range from 1 to 3 Mev was $\simeq 10^5$ cm^{-2} sec^{-1} $ster^{-1}$ Thus, they have suggested that there are two energy groups of electrons, one having 20 kev $\leq E \leq$ 100 kev and the other having $E \simeq 1$ Mev and an undefined spectrum in between. *Van Allen and Frank* [1959] observed that an omnidirectional flux of electrons of energies greater than 200 kev did not exceed 10^8 cm^{-2} sec^{-1}, whereas that for electrons of energies greater than 2.5 Mev did not exceed 10^6 cm^{-2} sec^{-1}. For the energy spectrum assumed above, these results correspond to a lower limit of between 3 and 3.5 for the exponent γ in the range of energies from 20 to 200 kev. More recent estimates of the value of the exponent for such a spectral distribution have been presented by *Fan et al.* [1961]. Their results indicate γ cannot be much greater than 2 for electrons of energies between 100 kev and approximately 1,000 kev in the region of the outer zone beyond about 25,000 km. Finally, from measurements with detectors aboard the second Soviet cosmic rocket, *Logachev* [1961] has obtained values of $\gamma \simeq 2$ for electrons in the energy range from 350 to 650 kev and $\gamma \simeq 3.5$ for electrons in the energy range from 650 to 1,100 kev. These results were obtained in a region between 30,000 and 35,000 km from the earth's center on September 12, 1959.

Thus, a spectrum for which the exponent γ

decreases somewhat with decreasing particle energy is consistent with the results presented by these experimenters. Of course, energy density considerations preclude a steepening spectrum at very low energies. The results of our calculation indicate that the value of γ for the spectrum in a range of energies about 500 kev decreases to nearly unity.

Several sources of error are possible in this determination of γ. We have not taken into account the increase, with particle energy, of the geometrical factor of the scintillation detector. This effect would result in an observed spectrum somewhat less steep than the actual one. However, for $\gamma > 1$, the effect of particles entering through the detector window will produce an error of the opposite type. It is also possible that this method yields a low value for γ because the longitudinal hydromagnetic waves are not of sufficiently large scale to affect the entire region between the mirror points. Thus localized field increases would not accelerate all of the particles on a tube of flux. In addition, since the pitch-angle distribution of the observed trapped particles is not actually isotropic, a change in field direction only, coupled with the geometrical dependence of the detector response, might produce an apparent particle acceleration.

We rule out the possibility that the observed compressional effects might be caused by some gross distortion of the geomagnetic field such that the position of the field lines would vary significantly in radial distance from the earth and, thereby, cause motion of the field lines back and forth past the satellite. The argument is as follows: Consider the case of such a change from 90 γ to 80 γ. At 40,000 km, the flux tube corresponding to a field strength of 80 γ would be displaced radially inward to $r = (80/90)^{1/3} \times 40{,}000$ km or be about 1,600 km. Assuming an r^{-15} dependence of the particle intensity upon the radial distance, r, from earth's center, as estimated by *Rosen and Farley* [1961], the corresponding change in the observed count rate would be a decrease to 0.55 times its value at 90 γ. Even for an r^{-10} dependence, the count rate would have been reduced to 0.6 times its value at 90 γ. Such decreases are somewhat greater than those included in the data and are therefore not consistent with the results, if it be assumed that no significant fraction of the observed particles could be transferred from one tube of flux, or magnetic shell, to another in periods comparable to 100 sec. However, over periods of hours, diffusion of particles in this manner is expected to affect their energy and distribution. This effect will be discussed subsequently.

Next, using the value of γ calculated above and a value of σ corresponding to the detector threshold of 500 kev for electrons, i.e., $\sigma = 2$, we again apply (4) to calculate the compressional variations in $|\mathbf{B}_\perp|$ required to affect the particles in the manner indicated by the data from the scintillation detector. The resulting values for $|\mathbf{B}_\perp|$, denoted by $|\mathbf{B}_\perp|_c^E$, are shown in figure 10 in the upper plot. The difference between these values and the measured values of $|\mathbf{B}_\perp|^E$ should then correspond to the effects of other modes of hydromagnetic disturbance. This difference is calculated and shown also in figure 10 in the lower plot.

In this section we have employed the data from the scintillation detector, along with a simple model of compressional hydromagnetic disturbances, in an attempt to estimate the contribution of disturbances in the compressional mode to the variations of $|\mathbf{B}_\perp|^E$. The upper set of curves in figure 11 provides a comparison between the contribution to $|\mathbf{B}_\perp|^E$ from the compressional disturbances, calculated in this section, and the variations of $|\mathbf{B}_\perp|^E$ that remain after subtraction of the contribution attributed to the transverse waves, as estimated in the previous section.

As a cross check, the lower set of curves in figure 11 provides a comparison between the calculated contribution of the transverse disturbances and the variations of $|\mathbf{B}_\perp|^E$ that remain after subtraction of the contribution calculated for the compressional disturbances. It would appear, from the upper curves, that

$$|\mathbf{B}_\perp|_c^E \simeq |\mathbf{B}_\perp|^E - \Delta|\mathbf{B}_\perp|_T^E$$

and, from the lower set, that

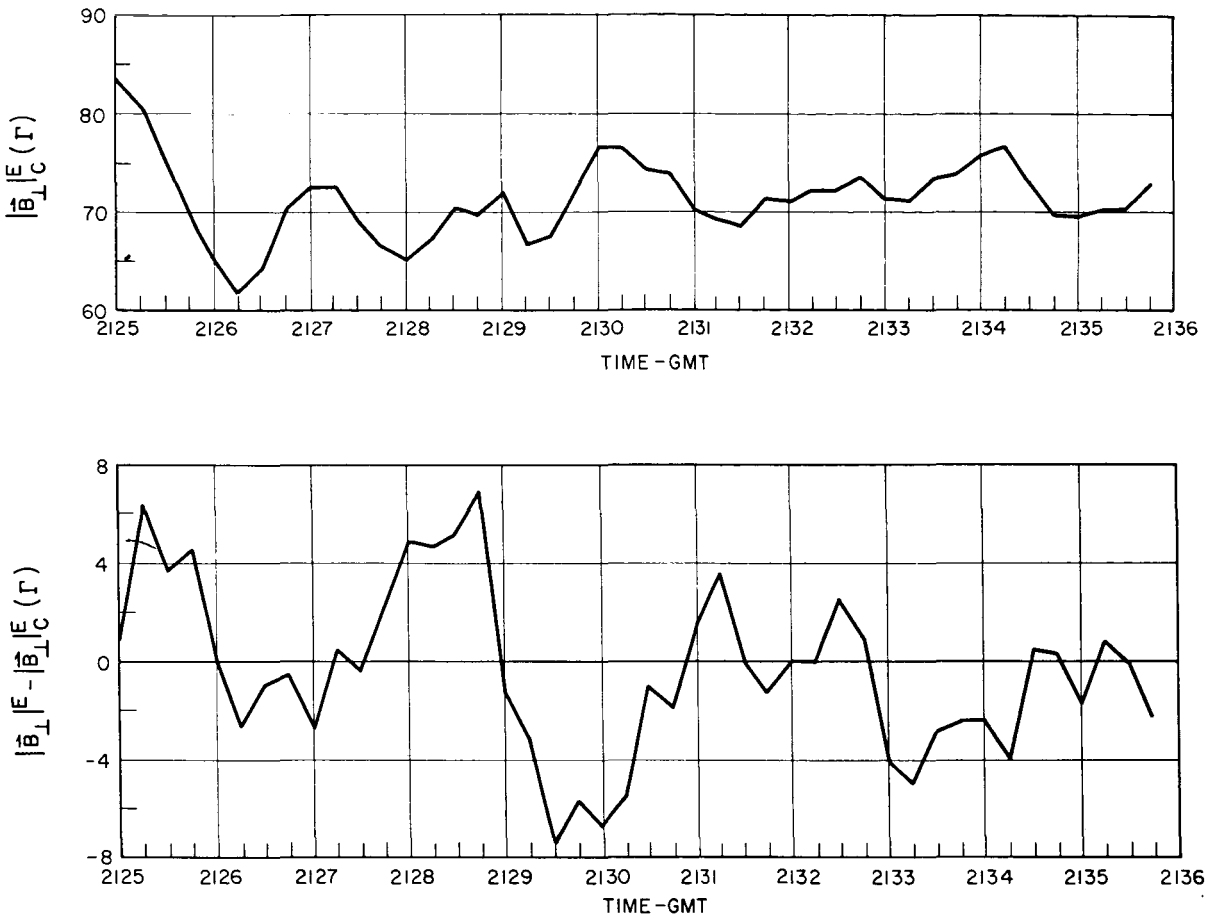

FIGURE 10.—*Components of the variations in* $|\mathbf{B}_\perp|^E$, *method 2. This method consists of using the measured values of* I *to calculate the component* $|\mathbf{B}_\perp|_C{}^E$, *due to the hydromagnetic disturbances in the compressional mode, and taking the difference between* $|\mathbf{B}_\perp|^E$ *and* $|\mathbf{B}_\perp|_C{}^E$ *to determine the component due to disturbances in any other mode. The upper curve is a plot of* $|\mathbf{B}_\perp|_C{}^E$ *versus time and the lower curve is a plot of* $|\mathbf{B}_\perp|^E - |\mathbf{B}_\perp|_C{}^E$ *versus time.*

$$\Delta|\mathbf{B}_\perp|_T{}^E \simeq |\mathbf{B}_\perp|^E - |\mathbf{B}_\perp|_C{}^E$$

Thus, the variations of $|\mathbf{B}_\perp|^E$ are composed, mainly, of only these two modes, i.e.,

$$|\mathbf{B}_\perp|^E \simeq |\mathbf{B}_\perp|_C{}^E + \Delta|\mathbf{B}_\perp|_T{}^E$$

SUMMARY AND DISCUSSION

In summarizing, we submit that the variations in the measured quantities observed during the period of interest on August 18 were the results of transverse hydromagnetic disturbances and of compressions and rarefactions in the geomagnetic field. The correlation between fluctuations in the count rate of the scintillation detector and the variations of the measured component of the field that remain after subtraction of the contribution from the transverse waves, provides evidence to the effect that the compressional changes in the field strength occur simultaneously over a large portion of the magnetosphere. In fact, the observations indicate that these compressional changes may occur along a particular line of force over nearly the entire region between the mirror points of the detected particles. The period of the disturbances associated with the compressional mode is approximately 100 sec whereas that of the transverse waves is about 200 sec. The apparent harmonic relationship

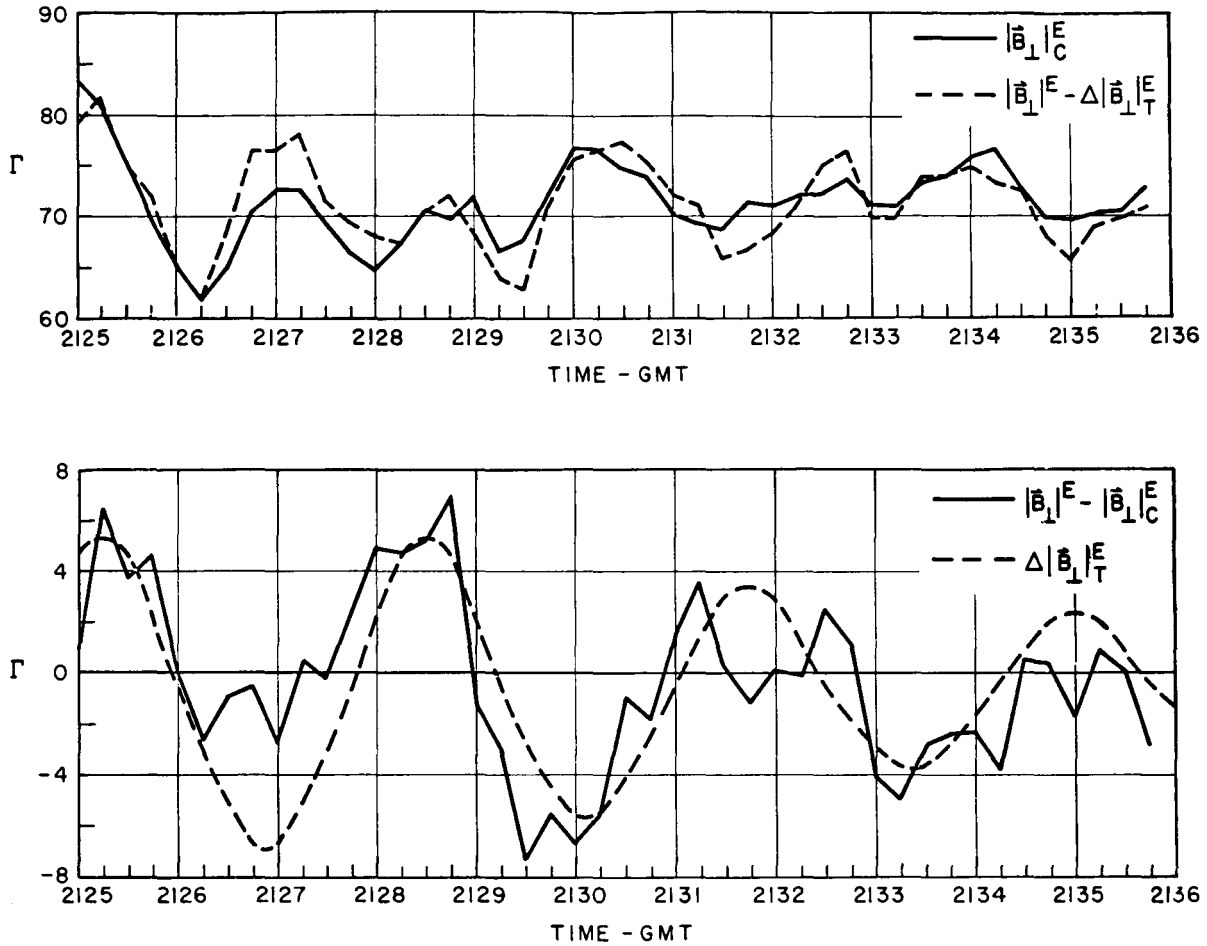

FIGURE 11.—*The upper pair of curves consists of the plot of* $\Delta|\mathbf{B}_\perp|_C{}^E$ *from figure 10 superimposed on the plot of* $|\mathbf{B}_\perp|^E - \Delta|\mathbf{B}_\perp|^E$ *from figure 8. The lower pair of curves consists of the plot of* $\Delta|\mathbf{B}_\perp|_T{}^E$ *from figure 8 superimposed on the plot of* $|\mathbf{B}_\perp|^E - |\mathbf{B}_\perp|_C{}^E$ *from figure 10. These comparisons are shown to demonstrate the consistency of the assumption that the magnetic field fluctuations were composed, in the main, of variations due to transverse and compressional disturbances. Datum points are plotted at 15-sec intervals.*

between these values may indicate coupling between the two modes, although the existence of such coupling would create difficulties with the linear treatment of magnetohydrodynamic waves. Comparison with our simple model indicates that the transverse waves are elliptically polarized and that the sense of their rotation is clockwise to an observer looking along the direction of the unperturbed field, toward the north geomagnetic pole.

Next we wish to consider the time constant for the decay of the amplitudes of these disturbances. Efforts to approximate, with exponential curves, the changes in the peak amplitudes of the results plotted in figure 3 indicate that time constants of somewhat less than 500 sec are appropriate. Thus, if the observed phenomena were produced by some type of free oscillations in the magnetosphere, these data provide evidence for a relatively rapid loss of energy from the oscillating system.

At this point, we would re-emphasize the fact that the models employed in obtaining the foregoing results are not unique in their applicability

to the observations. In fact, the magnetometer and aspect indicator provide measurements of only two of the three quantities required to describe the ambient magnetic field. However, the implied relationship between the field and the trapped particles permits the use of the count-rate data to compensate somewhat for the lack of complete field measurements.

It is of interest to consider the characteristics of the observed phenomena in connection with certain theoretical work. *MacDonald* [1961] has described three modes of propagation for hydromagnetic waves in the atmosphere. In this paper, periods for free oscillation of one of these modes, i.e., that in which vorticity is propagated along the lines of geomagnetic force, herein called the transverse mode, were calculated by MacDonald using two models of the exosphere to provide a wide range of densities. At geomagnetic latitude 60°, the periods for the lowest order mode of these oscillations were 184.6 and 74.4 seconds for the higher and lower density models, respectively. Since the satellite, during the period of the pertinent observations, was in the vicinity of the geomagnetic field line which intersects the earth's surface at geomagnetic latitude 67.5°, a crude extrapolation of these results would provide periods of several hundreds of seconds.

As stated earlier, if our assumptions as to propagation velocity are correct, the disturbances observed on August 9 and 18 violate only the third adiabatic invariant of the energetic electrons trapped in the region of the exosphere covered by these measurements. *Parker* [1960, 1961] has considered the effects of violations of this invariant and concluded that the net result of the diffusion, particle loss, and accelerations of the particles produced by the disturbances will be a decrease in the total energy associated with the trapped particles. The assumption that the region of hydromagnetic disturbance considered extended throughout the geomagnetic field was explicit in this result. In fact, the model used for the disturbance was that of a sudden commencement magnetic storm produced by the approach of a perfectly conducting plane to the geomagnetic field.

However, *Davis and Chang* [1962] have treated the same problem and conclude that such disturbances are considerably more effective in transporting particles to smaller radii than Parker's results would indicate. In fact, they suggest that such disturbances may provide a means of transferring electrons from interplanetary space to the outer radiation zones of planets. However, they remark that some of the attractiveness of the mechanism is lost owing to the fact that a considerable length of time would be required for the inward diffusion and acceleration to provide sufficient flux of energetic particles with any reasonable level of magnetic activity of the sudden commencement type.

It is suggested that the hydromagnetic disturbances described herein can affect the particles in a similar way, since they violate only the third invariant and, in the compressional mode, are apparently of large dimensions. *Parker* [1960] estimated that a few years would be required to seriously displace particles in the more distant regions of the outer radiation zone as a result of a typical amount of geomagnetic activity. In obtaining this estimate, he considered the effects on particles at $3.5R_e$ produced by the repeated approaches of a conducting plane that provided an image dipole at $10R_e$. Thus, $\Delta B/B = 1$ at $5R_e$ for this case. The observed fluctuations at $7R_e$ were characterized by $\Delta B/B \simeq 10^{-1}$. These were detected during a period of low geomagnetic activity and are probably much more frequent than geomagnetic storms or periods of high geomagnetic activity. As a result, despite their smaller amplitude, these fluctuations probably produce such diffusion and acceleration at a much greater rate. This possibility, coupled with the greater efficiency of the mechanism, indicated by *Davis and Chang* [1962], considerably enhances the attractiveness of this means of particle acceleration and relocation. It is also interesting, although somewhat premature, to consider the dependence of the properties of the observed variations upon the sources of the disturbances. *MacDonald* [1961] has discussed the theory of such dependence. The results of August 16, shown in figure 2, according to our interpretation would be the product of disturbances propagating in an acoustic mode and generated by the passage into the magnetosphere of clouds of

solar plasma. These clouds would then be of relatively small dimensions. On the other hand, the phenomena observed on August 9 and 18, shown in figures 1 and 3, were probably produced by some large-scale source as suggested earlier. It should be mentioned that another class of hydromagnetic disturbances has been observed at geocentric distances greater than about 10 earth radii [*Sonett et al.*, 1960; *Coleman, et al.*, 1960]. These fluctuations, with amplitudes up to 100 γ and frequencies up to 0.3 cps, were interpreted as characteristic of an unstable region between the geomagnetic field and interplanetary space. This region may be another source of disturbances that might penetrate deeper into the magnetosphere.

The interpretation of the observations reported herein is perforce somewhat speculative, since the experimental apparatus provided measurements of only two of the three quantities required to define the magnetic field. However, the consistency of the results is encouraging. We are at present investigating observations of disturbances with periods similar to those of August 9 and 18, but with smaller amplitudes and a more regular behavior. These data may be amenable to more accurate analysis by virtue of their relatively frequent occurrence during the course of our observations.

ACKNOWLEDGMENTS

We wish to thank A. J. Dessler for his early interest in this effort. We are indebted to T. A. Farley and A. Rosen, who made available to us the data from the Explorer 6 scintillation detector; and to Adeline Cowen, Paula Oldfather, Myrna Saxe, and Iva Voldese for their painstaking assistance in the reduction of data and with certain of the required computations. Those portions of this work conducted at Space Technology Laboratories, Inc., were supported by the National Aeronautics and Space Administration under contract NASw-270.

REFERENCES

Alfvén, H., *Cosmical Electrodynamics*, Clarendon Press, Oxford, 1950.

Arnoldy, R. L., R. A. Hoffman, and J. R. Winckler, Observations of the Van Allen radiation regions during August and September 1959, 1, *J. Geophys. Research, 65*, 1361–1376, 1960.

Coleman, P. J., Jr., C. P. Sonett, D. L. Judge, and E. J. Smith, Some preliminary results of the Pioneer V magnetometer experiments, *J. Geophys. Research, 65*, 1856–1857, 1960.

Coleman, P. J., Jr., The effects of betatron accelerations upon the intensity and energy spectrum of magnetically trapped particles, *J. Geophys. Research, 66*, 1351, 1961.

Davis, L., Jr., and D. B. Chang, On the effects of geomagnetic fluctuations on trapped particles, *J. Geophys. Research, 67*, 2169–2179, 1962.

Fan, C. Y., P. Meyer, and J. A. Simpson, Dynamics and structure of the outer radiation belt, *J. Geophys. Research, 66*, 2607–2640, 1961.

Farley, T. A., and A. Rosen, Charged particle variations in the outer Van Allen zone during a geomagnetic storm, *J. Geophys. Research, 65*, 3494–3496, 1960.

Gold, T., Origin of radiation near the earth discovered by means of satellites, *Nature, 183*, 355–358, 1959.

Gringauz, K. I., V. G. Kurt, V. I. Moroz, and I. S. Shklovskiy, Ionized gas and high speed electrons in the vicinity of the earth and in interplanetary space, *Doklady Akad. Nauk SSSR, 132*, 1062–1065 1960.

Gringauz, K. I., and S. M. Rytov, On the connection between the results of measurements of the magnetic field on the American Explorer VI satellite and the Pioneer V rocket, *Doklady Akad. Nauk SSSR*, 135, 48–51, 1960.

Herlofson, N., Magneto-hydrodynamic waves in a compressible fluid conductor, *Nature, 165*, 1020–1021, 1950.

Judge, D. L., Able—3–4 phase—comparator calibration procedure, *Mem. 7320.2–92, Space Tech Labs.*, November 1959.

Judge, D. L., M. G. McLeod, and A. R. Sims, The Pioneer I, Explorer VI, and Pioneer V high sensitivity, transistorized search coil magnetometer, *IRE Trans. Space Electron. Telemetry, 6*(3–4), 114–121, 1960.

Kellogg, P. J., Van Allen radiation of solar origin, *Nature, 183*, 1295–1297, 1959.

Layton, T. W., Acceleration of cosmic rays by hydromagnetic waves, Thesis, California Institute of Technology, 1957.

Logachev, Yu. I., Determination of the electron spectrum in the outer radiation belt during the flight of the second Soviet cosmic rocket, *Geomagnetism i Aeronomiya, 1*(1), 30–33, 1961.

MacDonald, G. J. F., Spectrum of hydromagnetic waves in the exosphere, *J. Geophys. Research, 66*, 3639–3671, 1961.

Northrop, T. G., and E. Teller, Stability of the adiabatic motion of charged particles in the earth's field, *Univ. of California, Radiation Lab. Rept. UCRL 5615*, 1959.

Parker, E. N., Geomagnetic fluctuations and the form of the outer zone of the Van Allen radiation belt, *J. Geophys. Research, 65*, 3117–3130, 1960.

Parker, E. N., Effect of hydromagnetic waves in a dipole field on the longitudinal invariant, *J. Geophys. Research, 66*, 693–708, 1961.

Rosen, A., and T. A. Farley, Characteristics of the Van Allen radiation zones as measured by the scintillation counter on Explorer VI, *J. Geophys. Research, 66*, 2013–2028, 1961.

Smith, E. J., P. J. Coleman, Jr., D. L. Judge, and C. P. Sonett, Characteristics of the extraterrestrial current system: Explorer VI and Pioneer V, *J. Geophys. Research, 65*, 1858–1861, 1960.

Sonett, C. P., D. L. Judge, A. R. Sims, and J. M. Kelso, A radial rocket survey of the distant geomagnetic field, *J. Geophys. Research, 65*, 55–68, 1960.

Sonett, C. P., A. R. Sims, and I. J. Abrams, The distant geomagnetic field, 1, Infinitesimal hydromagnetic waves, *J. Geophys. Research, 67*, 1191–1208, 1962.

Sugiura, M., Evidence of low-frequency hydromagnetic waves in the exosphere, *J. Geophys. Research, 66*, 4087–4096, 1961.

Van Allen, J. A., and Louis A. Frank, Radiation measurements to 658,300 kilometers with Pioneer IV, *State Univ. Iowa Rept. SUI–59–18*, August 1959.

Van Allen, J. A., C. E. McIlwain, and G. H. Ludwig, Radiation observations with satellite 1958ε, *J. Geophys. Research, 64*, 271–286, 1959.

Van de Hulst, H. C., *Problems of Chemical Aerodynamics*, chapter 6, Central Air Documents Office, Dayton, Ohio, 1951.

Vernov, S. N., and A. E. Chudakov, Terrestrial corpuscular radiation and cosmic rays, *Proc. First Intern. Space Sci. Symp.*, edited by H. Kallman-Bijl, North-Holland Publishing Co., Amsterdam, 1960.

Vernov, S. N., A. E. Chudakov, P. V. Vakulov, and Yu. I. Logachev, Study of terrestrial corpuscular radiation and cosmic rays by the flight of a cosmic rocket, *Doklady Akad. Nauk SSSR, 125*, 304–307, 1959.

Vestine, E. H., On variations of geomagnetic fields, fluid motions, and rate of earth's rotation, *J. Geophys. Research, 58*, 127, 1953.

Welch, J. A., Jr., and W. A. Whitaker, Theory of geomagnetically trapped electrons from an artificial source, *J. Geophys. Research, 64*, 909–922, 1959.

Wilson, C. R., and M. Sugiura, Hydromagnetic interpretation of sudden commencements of magnetic storms, *J. Geophys. Research, 66*, 4097–4112, 1961.

(Manuscript received August 9, 1962;
revised October 1, 1962)

U.S. GOVERNMENT PRINTING OFFICE : 1965 O—765-698